Preface

The 2013 Geophysical Fluid Dynamics Summer Study Program theme was *Buoyancy-Driven Flows*. Professor Paul Linden of the University of Cambridge was the principal lecturer. He ably introduced the topic from simple beginnings to sophisticated models and observations, guiding the audience in the cottage and on the porch through fundamental theory and applications. A number of topics from the lectures resurfaced in the fellows' projects. The first ten chapters of this volume document these lectures, each prepared by pairs of the summer's GFD fellows. Following the principal lecture notes are the written reports of the fellows' own research projects. This summer's fellows were:

- Tobias Bishoff, California Institute of Technology
- Catherine Jones, Scripps Institution of Oceanography
- Daniel Lecoanet, University of California, Berkeley
- Kate Snow, Australian National University
- Ton van den Bremer, Oxford University
- Karin Van Der Wiel, University of East Anglia
- Gregory Wagner, University of California, San Diego
- Yuki Yasuda, University of Tokyo
- Varvara Zemskova, University of North Carolina

In 2013, the Sears Public Lecture was delivered by Professor Susan Lozier, of Duke University on the topic of "Overturning in the North Atlantic: new observations, new views, lingering questions". Susan showed how modern observational techniques now allow the time-variability of the Gulf Stream and the North Atlantic circulation to be monitored, revealing trends and changes hitherto undetected. Redfield was crowded, and the audience enjoyed refreshments together after the lecture.

Claudia Cenedese, Eric Chassignet and Stefan Llewellyn Smith were co-directors for the summer. The summer was marked by a large number of long-term staff members, as well as many visitors who gave talks on a large variety of topics. The large number of long-term staff members ensured that the fellows never lacked for guidance, and the seminar series was filled by a steady stream of visitors, talking about topics as diverse as how to model hagfish slime and the science and art of sculpturing fluids.

As usual, laboratory experiments were facilitated by able support from Anders Jensen, who had to worry about long tanks, small slopes and smaller particles. Janet Fields and Jeanne Fleming made sure that the administrative side of the program ran with admirable efficiency. We continue to be indebted to W.H.O.I. Education, who once more provided a perfect atmosphere.

TABLE OF CONTENTS

PREFACE i

TABLE OF CONTENTS ii

PARTICIPANTS iv

LECTURE SCHEDULE viii

PRINCIPAL LECTURES
Paul Linden, University of Cambridge

Lecture 1
Introduction to gravity currents
Paul Linden 1

Lecture 2
Scaling laws
Paul Linden 9

Lecture 3
Hydraulic theories
Paul Linden 16

Lecture 4
Shallow water theory
Paul Linden 29

Lecture 5
Two-layer bores and non-Boussinesq gravity currents
Paul Linden 44

Lecture 6
Stratified environments
Paul Linden 65

Lecture 7
Continuously stratified ambient 72
Paul Linden

Lecture 8
Rotating currents
Paul Linden 82

Lecture 9
Mass loss currents
Paul Linden 93

Lecture 10
Gravity currents on slopes and in turbulent environments
Paul Linden 110

FELLOWS' REPORTS

Response of thermohaline circulation to changes in precipitation
Yuki Yasuda, University of Tokyo 124

Particle driven flow down an incline into a linear stratification
Kate Snow, Australian National University.....156

Nonlinear optimal perturbations
Daniel Lecoanet, University of California, Berkeley 179

Energy stability and mixing efficiency in forced stratified shear flows
Tobias Bischoff, California Institute of Technology 200

Investigation of lock release gravity currents in an upslope valley
Catherine Jones, University of California, San Diego.....225

Modelling the evolution of an iron-rich layer in a double diffusive regime
Barbara Zemskova, University of North Carolina, Chapel Hill 244

On the collision of sea breeze gravity currents
Karin van der Wiel, University of East Anglia.....264

Granular flow in a rotating drum
Gregory Wagner, University of California, San Diego 280

The Stokes drift of internal gravity wave groups
Ton van den Bremer, University of Oxford.....309

2013 GFD FELLOWS, STAFF AND VISITORS

Fellows

Tobias Bischoff	California Institute of Technology
Catherine Jones	University of California, San Diego
Daniel Lecoanet	University of California, Berkeley
Kate Snow	Australian National University
Ton van den Bremer	University of Oxford
Karin van der Wiel	University of East Anglia
Gregory Wagner	University of California, San Diego
Yuki Yasuda	The University of Tokyo
Varvara Zemskova	University of North Carolina, Chapel Hill

Staff and Visitors

Gualtiero Badin	University of Hamburg
Neil Balmforth	University of British Columbia
Dhruv Balwada	Florida State University
Cedric Beaume	University of California, Berkeley
Oliver Buhler	New York University
Xavier Carton	Université de Bretagne Occidentale
Colm-cille Caulfield	University of Cambridge
Claudia Cenedese	Woods Hole Oceanographic Institution
Eric Chassignet	Florida State University
Greg Chini	University of New Hampshire
Jean-Marc Chomaz	CNRS-École Polytechnique
Predrag Cvitanovic	Georgia Institute of Technology
Rebecca Dell	Scripps Institute of Oceanography
Charles Doering	University of Michigan
Baylor Fox-Kemper	Brown University
Basile Gallet	Campus Universitaire d'Orsay
Pascale Garaud	University of California, Santa Cruz
John Gille	National Center for Atmospheric Research
Sarah Gille	University of California, San Diego
David Goluskin	Columbia University
Ross Griffiths	Australian National University
George Hagstrom	New York University
Karl Helfrich	Woods Hole Oceanographic Institution
Andrew Hogg	Bristol University
Edward Johnson	University College London
Keith Julien	University of Colorado, Boulder
Richard Katz	University of Oxford
Joseph Keller	Stanford University
Richard Kerswell	Bristol University

Norman Lebovitz	University of Chicago
Sonya Legg	Princeton University
Paul Linden	University of Cambridge
Stefan Llewellyn Smith	University of California, San Diego
Ali Mashayek	University of Toronto
Eckart Meiburg	University of California, Santa Barbara
Paul Milewski	University of Bath
Philip Morrison	University of Texas, Austin
Rosalind Oglethorpe	University of Cambridge
Michael Patterson	University of Bristol
Joseph Pedlosky	Woods Hole Oceanographic Institution
Peter Rhines	University of Washington
James Rottman	University of California, San Diego
Alban Sauret	Princeton University
Michael Spall	Woods Hole Oceanographic Institution
Edward Spiegel	Columbia University
Andrew Stewart	California Institute of Technology
Bruce Sutherland	University of Alberta
Jean-Luc Thiffeault	University of Wisconsin
Andrew Thompson	California Institute of Technology
Andreas Thurnherr	Lamont-Doherty Earth Observatory
Laurette Tuckerman	Physique et Mécanique des Milieux Hétérogènes-ESPCI
George Veronis	Yale University
Brian White	University of North Carolina, Chapel Hill
Jack Whitehead	Woods Hole Oceanographic Institution
Andrew Woods	University of Cambridge
Philip Yecko	Montclair University
Zhiming Kuang	Harvard University

2013 Principal Lecturer

Paul Linden

2013 Geophysical Fluid Dynamics Participants

1st Row: Sarah Gille, Catherine Jones, Yuki Yasuda, Ton van den Bremer, Tobias Bischoff, Greg Wagner, Daniel Lecoanet, Kate Snow, Karin van der Wiel, Pascale Garaud, Varvara Zemskova, Kelly Ogden

2nd Row: Charlie Doering, Rosie Oglethorpe, Greg Chini, Ted Johnson, David Goluskin, Joseph Keller, George Veronis, Stefan Llewellyn Smith, Paul Linden, Claudia Cenedese, Joseph Pedlosky, Eric Chassignet, Gordon Zhang, Luisa Ottolenghi, Oliver Buhler

3rd Row: Ed Spiegel, Jie Yu, Jack Whitehead, George Hagstrom, Phil Yecko, Louis Howard, Karl Helfrich, Bruce Sutherland, Brian White, Rich Kerswell, Jim Anderson, Peter Rhines, Basile Gallet, Rebecca Dell, John Gille, Cedric Beaume, Sonya Legg, Dhruv Balwada, Zhiming Kuang

Missing from photo: Gualtiero Badin, Neil Balmforth, Xavier Carton, Colm-cille Caulfield, Jean-Marc Chomaz, Predrag Cvitanovic, Baylor Fox-Kemper, Ross Griffiths, Andrew Hogg, Keith Julien, Richard Katz, Norman Lebovitz, Ali Mashayekhi, Eckart Meiburg, Paul Milewski, Philip Morrison, Michael Patterson, Andrew Stewart, Jean-Luc Thiffeault, Andrew Thompson, Andreas Thurnherr, Laurette Tuckerman, Andrew Woods

GFD Lecture Schedule
June 17 – August 22

June 17-21– Principal Lectures

Gravity Currents
Paul Linden, University of Cambridge

June 24-28 – Principal Lectures

Gravity Currents
Paul Linden, University of Cambridge

July 1- August 22

Monday, July 1
Falling into structured fluids
Philip Yecko, Montclair State University

Tuesday, July 2
Gravity-driven interfacial flows: Vorticity-based models
Eckhart Meiburg, University of California

Wednesday, July 3
Dense overflows in ocean general circulation models
Sonya Legg, Princeton University

Thursday, July 4
HOLIDAY

Friday, July 5
Large amplitude acoustic streaming
Greg Chini, University of New Hampshire

Monday, July 8
Modeling the hagfish slime
Jean-Luc Thiffeault, University of Wisconsin

Tuesday, July 9
Three-dimensional quasi-geostrophic convection in the rotating cylindrical annulus with steeply sloping endwalls
Keith Julien, University of Colorado at Boulder

Wednesday, July 10
Coastal density fronts: gravity currents, internal waves, and mixing
Brian White, University of North Carolina

Thursday, July 11
A propagation model for internal waves generated by a body moving in an ocean thermocline
Jim Rottman, University of California, San Diego

Friday, July 12
Eddy generation by topographic transformation of coastal-trapped waves
Ted Johnson, University College London

Monday, July 15
Layers, layers everywhere: The dynamics of mixing-induced layering in turbulent stratified flow
Colm Caulfield, University of Cambridge

Tuesday July 16
A refined life at high resolution: Subgrid modelling in the eddy-rich regime
Baylor Fox-Kemper, Brown University

Wednesday, July 17

10:30 AM
Unusual features in rotating flows
Michael Patterson, University of Bristol

1:30 PM
The turbulence closure problem
Joseph Keller, Stanford University

Thursday, July 18
Harmonic forcing in rotating flows: zonal flow, instabilities and inertial waves
Alban Sauret, Princeton University

Friday, July 19
Stability criteria for inhomogeneous equilibria in the single wave model
George Hagstrom, New York University

Monday, July 22
Buoyancy-driven segregation of magma from the convecting mantle
Richard Katz, University of Oxford

Tuesday, July 23
Large-scale circulation in 2D Kolmogorov flows
Basile Gallet, Laboratoire FAST

Wednesday, July 24
Oscillatory double-diffusive convection
Pascale Garaud, University of California, Santa Cruz

Thursday, July 25

10:30 AM
A turbulent model of the Arctic halocline
Michael Spall, Woods Hole Oceanographic Institution

1:30 PM
Waves over periodic topographies
Jie Yu, North Carolina State University

Friday, July 26
Shoaling and tunneling internal solitary waves
Bruce Sutherland, University of Alberta

Monday, July 29
Sea breezes and land breezes along coastlines and semi-enclosed seas: Diurnal gravity currents
Sarah Gille, University of California, San Diego

Tuesday, July 30
Convective and absolute instability of finite amplitude gravity wave
Jean-Marc Chomaz, CNRS-Ecole Polytechnique

Wednesday, July 31
The effects of wind on the rise of volcanic plumes and the intrusions of volcanic ash
Andrew Hogg, University of Bristol

Thursday, August 1

10:30
Ekman Layer meets island
Joseph Pedlosky, Woods Hole Oceanographic Institution

1:30 PM
Buoyancy driven flows and mixing in confined spaces
Andrew Woods, University of Cambridge

Friday, August 2

10:30 AM
Sills or Hills? The 2014/15 Fracture Zone Canyon experiment
Andreas Thurnherr, Lamont Doherty Earth Observatory

1:30 PM
Science and art of sculpturing fluids
Jean-Marc Chomaz, CNRS-Ecole Polytechnique

Monday, August 5

10:30 AM
Extreme multiplicity in convection patterns
Laurette Tuckerman, PMMH-ESPCI

1:30 PM
Along the bumpy road from micro- to macro-physics
James Anderson, Stevens Institute of Technology

Tuesday, August 6
Wind and eddy-mediated export of Antarctic Bottom Water
Andrew Stewart, California Institute of Technology

Wednesday, August 7
Determining the depth of mixing in the upper water column of subpolar waters: implications for productivity
Susan Lozier, Duke University

Thursday, August 8
The influence of mesoscale eddies of the Arabian Sea on the slope currents of Red Sea and Persian Gulf outflow water
Xavier Carton, Universite de Bretagne Occidentale

Public Lecture - 5 PM - Redfield Auditorium, reception to follow

Overturning in the North Atlantic: new observations, new views, lingering questions
Susan Lozier, Duke University

Friday, August 9
The zonally asymmetric Antarctic Circumpolar Current
Andrew Thompson, California Institute of Technology

<u>Week 9 – August 12 - 16</u>

No lectures

Week 10 – August 19 - 23

Fellows' presentations

Monday, August 19

10:00 am - 11:00 am
Response of thermohaline circulation to changes in precipitation
Yuki Yasuda, The University of Tokyo

11:15 am - 12:15 pm
Particle driven flows down an incline into a linear stratification
Kate Snow, Australian National University

Tuesday, August 20

10:00 am – 11:00 am
Nonlinear optimal perturbations
Daniel Lecoanet, University of California, Berkeley

11:15 am - 12:15 pm
Energy stability and transport efficiency in forced stratified shear flows
Tobias Bischoff, California Institute of Technology

Wednesday, August 21

10:00 am - 11:00 am
Investigation of lock exchange in a 3D valley configuration
Catherine Jones, University of California, San Diego

11:15 am - 12:15 pm
Modeling the evolution of a particle-rich layer in a double diffusive regime
Varvara Zemskova, University of North Carolina, Chapel Hill

1:30 pm - 2:30 pm
On the collision of sea breeze gravity currents
Karin van der Wiel, University of East Anglia

Thursday, August 22

10:00 am - 11:00 am
Granular flow in a rotating drum
Gregory Wagner, University of California, San Diego

11:15 am -12:15 pm
Induced mean flow of weakly nonlinear internal wave packets
Ton van den Bremer, University of Oxford

GFD 2013 Lecture 1: Introduction to Gravity Currents

Paul Linden; notes by Tobias Bischoff and Catherine Jones

June 17, 2013

1 Introduction

Gravity currents can be found in various contexts, including weather and climate (e.g. sea breezes, haboobs), pyroclastic flows and spills (e.g. Liquefied Natural Gas), and are perhaps most obvious upon opening the front door on a cold day (Fig. 1). This also explains why

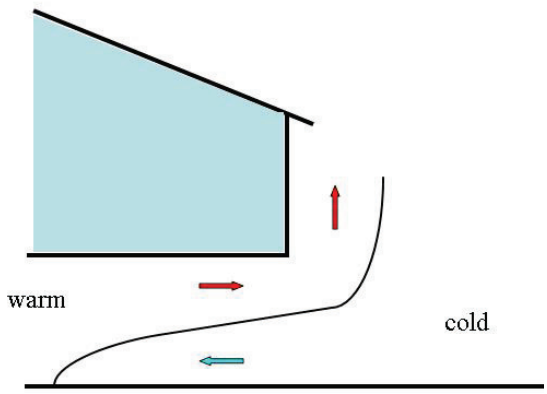

Figure 1: A sketch of a house after the door had been opened. The warm air escapes from the house through a gravity current along the ceiling, while cold air from the outside enters near the floor.

opening the door after taking a hot shower in order to clear the mirror is a futile attempt. The warm and moist air escapes near to the ceiling, so that the bottom half of the bathroom is clear, leaving the top part of the mirror unusable for shaving. A good understanding of gravity currents allows us to predict the speed of lava flows and haboobs, the strength of sea breezes, and many other useful properties of these phenomena. In addition, gravity currents have some important technical applications.

1.1 Lock exchange

Lock exchange is the classic experiment for studying gravity currents. One begins with a tank that is filled with two fluids of different densities that are separated by a barrier (see

Fig. 2). Upon removal of the barrier, the denser fluid flows along the bottom boundary into the lighter fluid, and there is a return flow in the lighter fluid. This process is driven by

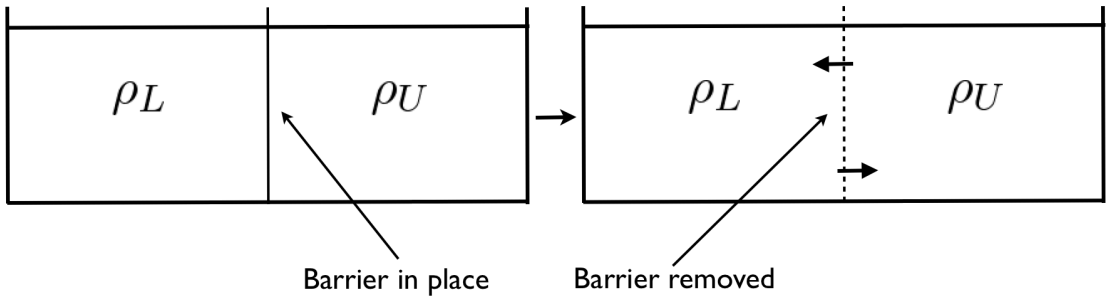

Figure 2: The two fluids are initially separated by a barrier. Once the barrier is removed, two gravity currents develop (arrows). In this setup, $\rho_U < \rho_L$.

a horizontal pressure gradient that arises from the density differences. Depending on the viscosities of the two fluids, the gravity current is subject to entrainment.

1.2 Reduced gravity

The buoyancy force acting on a body of density ρ_b that is immersed in a surrounding fluid of density ρ_f can be derived from Archimedes principle. This principle tells us that the force, $\mathcal{F}$, acting on the body is given by the gravity force acting on the body minus the gravitational force arising from the displacement of the surrounding fluid.

$$\mathcal{F} = -g(\rho_b - \rho_f) \tag{1}$$

If the density of the body is greater, the body will sink, and otherwise it will move upward. We can then define the effective gravitational constant, known as 'reduced gravity' as

$$g' = \frac{g\,(\rho_b - \rho_f)}{\rho_b}. \tag{2}$$

Switching to the variables used in the lock exchange experiment described earlier, we have

$$g' = \frac{g\,(\rho_L - \rho_U)}{\rho_L}. \tag{3}$$

This expression will be useful when we analyze the time evolution of gravity currents, because it is the gravitational acceleration used in defining the velocity scale.

1.3 Equations of motion

Below, we introduce the governing equations for most of the examples in these notes.

1.3.1 Navier-Stokes Equations

The governing equations for fluid in a box are found by enforcing mass and momentum conservation. They read

$$\frac{\partial \rho}{\partial t} + \nabla \cdot (\, \rho \mathbf{u}\,) = 0 \tag{4a}$$

$$\frac{\partial \mathbf{u}}{\partial t} + \mathbf{u} \cdot \nabla \mathbf{u} = -\frac{1}{\rho}\nabla p + \mathbf{g} + \nu \nabla^2 \mathbf{u}. \tag{4b}$$

Here, ρ is the density field, $\mathbf{u}$ is the velocity field, p is the pressure field, $\mathbf{g}$ is the gravitational acceleration, and ν is the kinematic viscosity of the fluid ($\nu \approx 10^{-6}$ m^2/s for water at 20 °C).

For most cases, we are going to assume incompressibility of the fluid under consideration, i.e.,

$$\frac{\mathrm{D}\rho}{\mathrm{D}t} = 0 \Leftrightarrow \nabla \cdot \mathbf{u} = 0. \tag{5}$$

Relation (5) together with Eq. (4b) are known as the incompressible Navier-Stokes equations.

1.3.2 Vorticity Equation

By taking the curl of Eq. (4b), we can recast the Navier-Stokes equations in vorticity form, in which $\boldsymbol{\omega} = \nabla \times \mathbf{u}$. Applying the identity $\mathbf{u} \cdot \nabla \mathbf{u} = \frac{1}{2}\nabla |\mathbf{u}|^2 - \mathbf{u} \times \boldsymbol{\omega}$ to this equation gives

$$\frac{\partial \boldsymbol{\omega}}{\partial t} + \mathbf{u} \cdot \nabla \boldsymbol{\omega} = \boldsymbol{\omega} \cdot \nabla \mathbf{u} + \underbrace{\frac{1}{\rho^2}\,(\,\nabla \rho \times \nabla p\,)}_{\text{baroclinic term}} + \nu \nabla^2 \boldsymbol{\omega}. \tag{6a}$$

The fluid is *barotropic* if the density is a function of pressure only, so that isocontours of pressure and density are aligned and the baroclinic term in Eq. (6a) vanishes. If pressure and density isocontours are not aligned, the baroclinic term is nonzero, the flow is *baroclinic*.

1.3.3 Boussinesq Approximation

The Boussinesq approximation neglects density differences in the momentum equations except where they multiply the gravitational acceleration. Mathematically speaking, this approximation is the first order correction in an expansion in the density difference between a background profile and the actual density profile. We decompose the density field into a constant density, ρ_0, and small spatio-temporal variations ρ^* so that

$$\rho(\mathbf{x}, t) = \rho_0 + \rho^*(\mathbf{x}, t) \tag{7a}$$

$$\rho^*(\mathbf{x}, t) = \overline{\rho}(z) + \rho'(\mathbf{x}, t). \tag{7b}$$

Here, we assumed that $\rho_0 = \text{const.}$ and $|\rho^*| \ll \rho_0$. Eq. (7b) defines a further decomposition of the small density variations ρ^* into a field $\overline{\rho}$ that varies only in the vertical and a field ρ', which is a function of both space and time. The pressure field can be decomposed in a similar way, giving

$$p(\mathbf{x}, t) = -\rho_0 g z + \overline{p}(z) + p'(\mathbf{x}, t), \tag{8}$$

where $\overline{p}(z)$ is defined via the hydrostatic relation

$$\frac{d\overline{p}}{dz} = -\overline{\rho}g \tag{9}$$

Combining Eq. (7b), (8), the gravity and pressure terms from Eq. (4b) can be expanded in ρ' and p' yielding

$$-\frac{1}{\rho}\nabla p + \mathbf{g} \approx -\frac{1}{\rho_0}\nabla p' - \mathbf{g}\frac{\rho'}{\rho_0}. \tag{10}$$

1.4 Frontogenesis

First, consider an inviscid fluid with a constant horizontal density gradient, $\rho_x = \rho_{x_0}$ (shown in Fig. 3a). From Eq. (5), we find

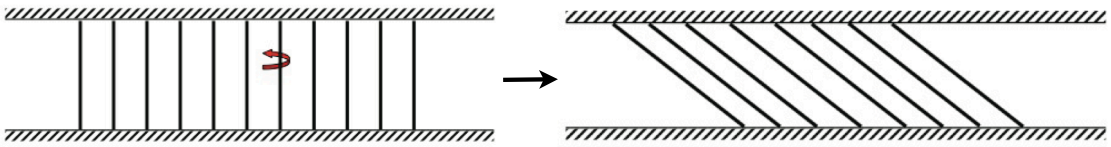

Figure 3: Lines of constant density for a) the initial state and b) at some later time. In both diagrams, the density is higher on the left than it is on the right.

$$\frac{\partial \rho}{\partial t} + u\frac{\partial \rho}{\partial x} = 0 \qquad t = 0. \tag{11}$$

Differentiating with respect to x gives

$$\left(\frac{\partial}{\partial t} + u\frac{\partial}{\partial x}\right)\frac{\partial \rho}{\partial x} = -\frac{\partial u}{\partial x}\frac{\partial \rho}{\partial x} = \frac{\partial w}{\partial z}\frac{\partial \rho}{\partial x}, \tag{12}$$

where the continuity condition, Eq. (5), was used to derive Eq. (12). Assuming a solution exists in which $w = 0$ and neglecting diffusivity, Eq. (4b) reduces to

$$u_t - \frac{1}{\rho_0}p_x = 0. \tag{13}$$

Using the hydrostatic condition, $p_z = -g\rho$, and integrating with respect to u and z whilst assuming ρ_x remains constant gives

$$u = \frac{g}{\rho_0}\rho_{x_0} z t. \tag{14}$$

This is equivalent to a linear shear in the flow that grows linearly with time. The final state of the fluid is shown in Fig. 3b. Now consider a case in which there is a region of small density gradient and a region of large density gradient, as in Fig. 4a. u grows faster in the region where $|\rho_x|$ is large than in the region where $|\rho_x|$ is small, so some fluid is

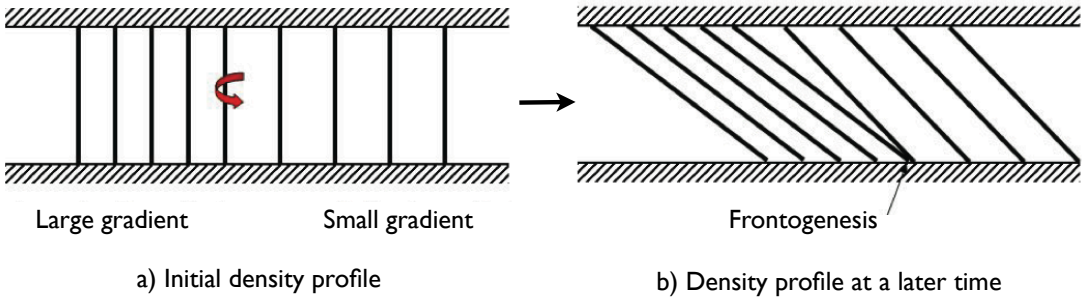

Figure 4: Lines of constant density. The horizontal density gradient on the left of each figure is larger than the density gradient on the right of each figure.

forced upwards between these two regions. w must be nonzero because u_x is nonzero. The Richardson number, Ri, where

$$\mathrm{Ri} = -\frac{g}{\rho_0}\frac{\partial \rho}{\partial z}\left(\frac{\partial u}{\partial z}\right)^{-2}, \tag{15}$$

can be easily derived from Eq. (12) and Eq. (14), giving Ri$= \frac{1}{2}$ for all time.

1.4.1 Rotating the tank

The results of this analysis were tested in an experiment by Simpson and Linden [1]. Setting up a horizontally stratified fluid like the one in Fig. 3a is difficult, and so they set up a fluid in which the isopycnals were already tilting, as in Fig. 3b. This was achieved by stratifying a long thin tank which was then rotated by 90°. The angle of the isopycnals that are produced in this process can be estimated by modeling the box as a long and thin ellipse and then solving Poisson's equation in a rotating reference frame. We start by moving from the laboratory frame to the rotating frame of the tank, giving an initial vorticity of -2Ω, where Ω is the rotation rate of the tank. Conserving vorticity, we can write Possion's equation for the stream function ψ,

$$\nabla^2 \psi = -2\Omega. \tag{16}$$

Modeling the tank as an ellipse with vanishing flow on the solid boundaries suggests a trial solution of

$$\psi = c\left(1 - \left(\frac{y}{b}\right)^2 - \left(\frac{x}{a}\right)^2\right), \tag{17}$$

where x and y are in the rotating reference frame and a and b are the axes of the ellipse. Eq. (17) can now be substituted into Eq. (16) to determine the constant value of c. Taking the limit $b \ll a$ (i.e. the limit of a long thin tank), gives

$$\psi \approx \Omega b^2\left(1 - \left(\frac{y}{b}\right)^2\right). \tag{18}$$

From Eq. (18), we calculate the velocity profile, and hence find the distance x a particle would travel in the flow field during the time Δt is

$$x = u\Delta t = 2\Omega y \Delta t. \tag{19}$$

Rotating the tank from a vertical initial position to the horizontal requires $\Omega \Delta t = \frac{\pi}{2}$, so that the angle between the isopycnals and the vertical is given by

$$\phi = \arctan\left(\frac{x}{y}\right) = \arctan(\pi) \approx 72^{\circ}. \tag{20}$$

1.5 Yih's Analysis (1947)

Yih [3] derived an expression for the velocity of gravity currents for the simple case of two fluids in a finite box separated by a barrier. Removing the perfect barrier instantaneously

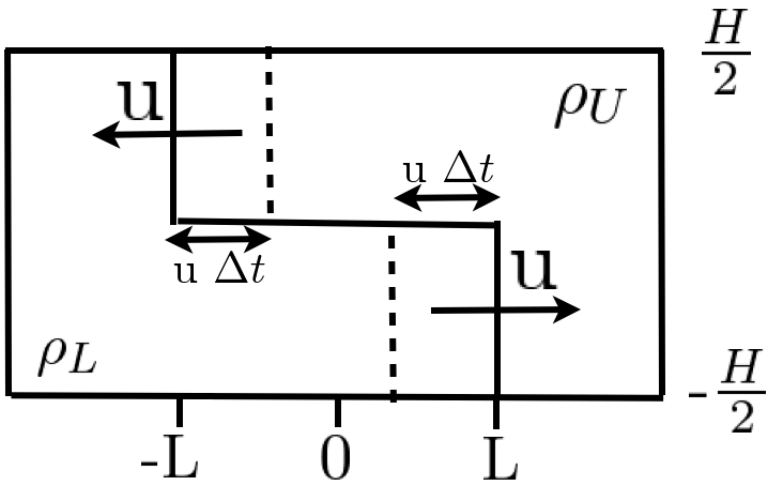

Figure 5: Schematic of Yih's model.

and neglecting frictional effects, the two gravity currents develop symmetrically, as in Fig. 5. Assuming that they travel at a velocity U and that they occupy half of the box height each, we can derive a simple expression for the change in potential energy over the infinitesimal time Δt, giving

$$\Delta \mathrm{PE} = \frac{1}{4} g' \rho_L H^2 U \Delta t. \tag{21}$$

At the same time, the kinetic energy of the system changes due to changes in both the velocity of the currents and the amount of mass in them

$$\Delta \mathrm{KE} = \frac{1}{2} \left(\rho_L + \rho_U \right) H U^3 \Delta t. \tag{22}$$

In the absence of energy loss, the change in potential energy must balance the change in kinetic energy, $\Delta \mathrm{PE} = \Delta \mathrm{KE}$. This allows us to derive an expression for U in terms of

densities ρ_U and ρ_L

$$U^2 = \frac{1}{4} g' H,\ g' = \frac{g(\rho_L - \rho_U)}{(\rho_L + \rho_U)}. \tag{23}$$

The dimensionless velocity or Froude number for this flow is

$$F_h = \frac{U}{\sqrt{g' H}} = \frac{1}{2}. \tag{24}$$

It is found to be about 0.46–0.47 in experiments with Yih's setup.

1.6 von Kármán's analysis (1940)

Von Kármán's [2] analysis differs from Yih's analysis in that the gravity current occurs in an infinite fluid. Assuming irrotational, inviscid fluid and a frame of reference in which the front is stationary, we get the setup shown in Fig. 6. Because we assume that the fluid is

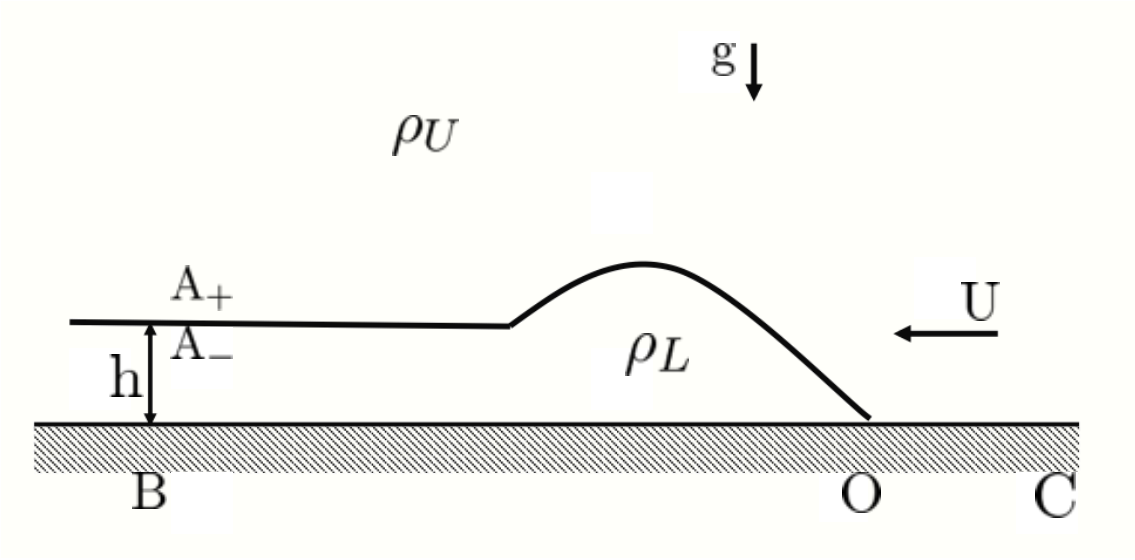

Figure 6: Sketch of the setup for von Kármán's analysis, in which the frame of reference is such that the front is stationary. U is the speed of the fluid. A is the position at the density interface where $\frac{\partial \rho}{\partial x} = 0$. B is below it A on the bottom boundary. O is the position at which the density interface intersects the boundary, and C is some distance away, again on the boundary.

irrotational, we can apply Bernoulli's equation along streamlines. Taking the streamline between O and A_+ gives

$$p_0 = p_A + g\rho_U h + \frac{1}{2}\rho_U U^2, \tag{25}$$

and taking the streamline between O and A_- gives

$$p_o = p_A + g\rho L h. \tag{26}$$

Subtracting Eq. (25) from Eq. (26), we can solve for U^2, giving

$$U^2 = \frac{2g\left(\rho_L - \rho_u\right)h}{\rho_U}. \tag{27}$$

Now we can redefine g' as

$$g' = \frac{g\left(\rho_L - \rho_U\right)}{\rho_L}, \tag{28}$$

giving a Froude number of

$$F_h = \frac{U}{\sqrt{g'h}} \tag{29a}$$

$$= \sqrt{\frac{2}{\gamma}}, \tag{29b}$$

where $\gamma = \frac{\rho_U}{\rho_L}$. As $\gamma \to 0$, F_h becomes infinite, because this equation only applies in the Boussinesq limit. If we take this limit (i.e. $\gamma = 1$), $F_h = \sqrt{2}$.

References

[1] J. E. Simpson and P. F. Linden, *Frontogenesis in a fluid with horizontal density gradients*, J. Fluid Mech., 202 (1989), pp. 1–16.

[2] von Kármán, *The engineer grapples with nonlinear problems*, Bull. Am. Math. Soc., 46 (1940), pp. 615 – 683.

[3] C. S. Yih, *A study of the characteristics of gravity waves at a liquid interface*, master's thesis, State University of Iowa, 1947.

GFD 2013 Lecture 2: Scaling Laws

Paul Linden; notes by Daniel Lecoanet and Karin van der Wiel

June 18, 2013

1 Introduction

These notes focus on scaling laws describing the evolution of a gravity current. For the moment, we will restrict our attention to a rectangular, finite volume release in a channel (see Figure 1). Given the reduced gravity of the released material, initially given by

$$g_0' = g\frac{\rho_L - \rho_U}{\frac{1}{2}(\rho_L + \rho_U)}, \tag{1}$$

the initial length L_0, and height D of the released material, we would like to describe the evolution of the reduced gravity g', length L, and height h as a function of time. We assume throughout the height of the ambient medium H is very large, and that we are in the Boussinesq approximation.

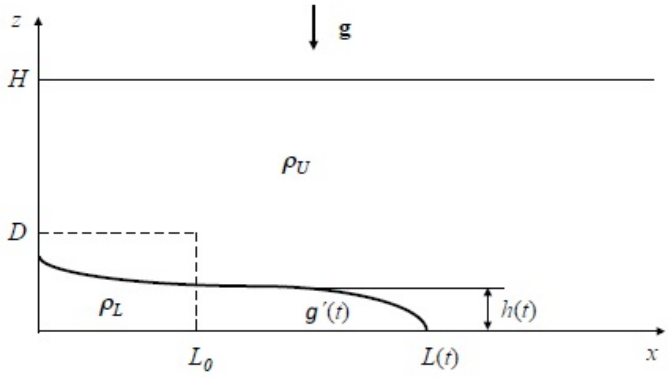

Figure 1: A schematic of the release of a finite volume of dense (ρ_L) fluid into a less dense (ρ_U) stationary environment of depth H. The dense fluid is initially held behind a lock gate at $x = L_0$, and the initial depth is D.

We will find that the gravity current evolution can be described by three different regimes: a constant velocity (or "slumping") regime, a "self-similar" regime, and a viscous regime. In both the constant velocity and self-similar regime, the buoyancy force is balanced by inertia. The initial wave propagation speed is $\sqrt{g_0' D}$, so it takes a time $\sim L_0/\sqrt{g_0' D}$ for the gravity current to realize it has finite extent. Before this time, the gravity current

spreads out with a constant velocity, but afterwards (during the self-similar regime) it spread more slowly due to only having finite buoyancy. At late times, the velocity can become small enough that viscosity becomes important. In this viscous regime, the spreading becomes even slower than in the self-similar regime.

In these notes, we describe these phenomena using three techniques. First, we will use dimensional analysis, along with insights from experiments, to describe these three regimes. Next, we note that experiments had measured constant Froude numbers in gravity currents prior to the viscous regime, and use this to derive the constant velocity and self-similar regimes. Lastly, we will describe the force balances in the three regimes.

Although we focus on finite volume release in a channel, this analysis can be easily extended to axisymmetric flows, and constant flux releases. These effects will alter the scaling laws, and sometimes even change the order or presence of different regimes of gravity current evolution. Finally, we will briefly mention some of the experimental results which support or refute these simple scaling laws.

2 Dimensional Arguments

We will begin by describing the constant velocity regime. Before waves can propagate the length L_0 of the gravity current, the flow does not know it has finite length. Thus, the only dimensional quantities in the problem are the initial reduced gravity, g_0', the initial layer depth D, and time t. Then we must have that the velocity of the gravity current $U = \dot{L}$ is

$$U = \left(g_0' D\right)^{1/2} F f\left(t/T_a\right), \tag{2}$$

where

$$T_a = \sqrt{\frac{D}{g_0'}}, \tag{3}$$

is a free-fall time, F is a dimensionless number, and f is some function. The experimental observation that U initially stays about constant suggests that $f(x) \to 1$ for $x \gg 1$. Then, we can identify F as the Froude number. Thus, for $t \gg T_a$, we have

$$U = \left(g_0' D\right)^{1/2} F, \tag{4}$$

$$L = L_0 + \left(g_0' D\right)^{1/2} F t. \tag{5}$$

We expect this to be valid on the intermediate timescale

$$T_a \ll t \ll T_V, \tag{6}$$

where T_V is defined below.

On the timescale

$$T_V = \frac{L_0}{\sqrt{g_0' D}} \tag{7}$$

several things change. First, this is the timescale on which waves will propagate along the layer, allowing communication along the entire length of the gravity current, adding a

new dimensional parameter L_0. Also, the length of the gravity current about doubles on this timescale. Whereas for $t \ll T_V$ we could approximate the gravity current as having height about D, for $t \gtrsim T_V$, the depth of the layer must change to conserve volume. By dimensional analysis, we now have that

$$U = \left(g_0' D\right)^{1/2} F f\left(t/T_a, t/T_V\right). \tag{8}$$

On timescales much longer than T_V (but much shorter than the viscous timescale T_ν defined below), we can posit that the only important dimensional quantities are the time and the total initial negative buoyancy,

$$B_0 = g_0' L_0 D. \tag{9}$$

Then, by dimensional analysis we have

$$U \sim \left(\frac{B_0}{t}\right)^{1/3} \tag{10}$$

$$L \sim B_0^{1/3} t^{2/3}. \tag{11}$$

On this intermediate timescale (between T_V and viscous timescale T_ν), the flow forgets its initial condition, i.e., this similarity solution is an attractor.

Finally, at very late times, viscosity becomes important. The viscous time T_ν is given by when the wave propagation time $L/\sqrt{g'h}$ equals the viscous time h^2/ν. Viscous evolution occurs for $t \gg T_\nu$. We assume that in the viscous regime g' does not change, i.e., stays equal to g_ν', so that the volume $V_\nu = hL$ stays constant. Thus, the viscous time is

$$T_\nu = \left(\frac{V_\nu^4}{g_\nu'^2 \nu^3}\right)^{1/7}. \tag{12}$$

It is also convenient to write this as

$$T_\nu = \frac{\nu L_\nu^2}{g_\nu' h_\nu^3}, \tag{13}$$

where $L_\nu = L(T_\nu)$ and $h_\nu = h(T_\nu)$, because we will later find that

$$t \sim \frac{\nu L^2}{g_\nu' h^3}, \tag{14}$$

although this cannot be derived via dimensional analysis.

3 Constant Froude Number

We will now exploit the experimental evidence that the Froude number stays about constant in the constant velocity and self-similar regimes. Thus, we assume that

$$F_h = \frac{U(t)}{\sqrt{g'(t)h(t)}} \tag{15}$$

stays constant. Furthermore, we assume that the buoyancy flux is constant,

$$g'(t)h(t)L(t) = c_B B_0, \tag{16}$$

where c_B is a geometrical factor which is equal to one for a rectangle. Implicit in this second expression is the assumption that g' is constant in space. Putting these together, we find

$$\frac{L(t)}{L_0} = \left[1 + \frac{3}{2} F_h \sqrt{c_B B_0} \frac{t}{T_V}\right]^{2/3}. \tag{17}$$

Now consider the limits of small or large t. If $t \ll T_V$, then we have

$$\frac{L}{L_0} \approx 1 + F_h c_B^{1/2} \frac{t}{T_V} \qquad t \ll T_V. \tag{18}$$

However, for large t, we have

$$\frac{L}{L_0} \approx \left[\frac{3}{2} F_h c_B^{1/2} \frac{t}{T_V}\right]^{2/3} \qquad t \gg T_V. \tag{19}$$

It is easy to check this is consistent with the results from the section of dimensional analysis.

4 Force Balance

If one considers the three forces that act on the fluid in the channel, expressions for the shifts between the three regimes will follow. Assume a channel where there is a constant source of fluid at $x = 0$, proportional to t^α. For $\alpha = 0$ this is the case of the finite volume release, $\alpha = 1$ describes the case of a constant volume flux into the channel (See Figure 2). Conservation of volume will give $hL \sim q_0 t^\alpha$ and the length of the current $L \sim Ut$. The total buoyancy is the reduced gravity times the input flux, $B = g'q$, with dimensions $[B] = L^3 T^{-3}$.

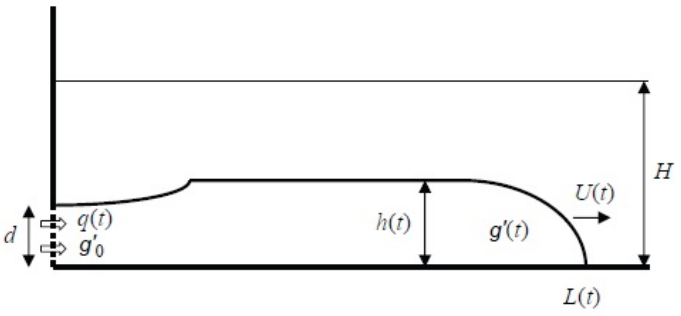

Figure 2: A schematic of a flux release in a channel of depth H. Fluid of reduced gravity g' is introduced at a rate of $q(t)$ at the end of the channel.

As mentioned, in both the constant velocity regime and the self-similar regime there is a balance between buoyancy and inertial forces. The force balance is thus between

$$F_b = \int \frac{\partial p}{\partial x} dV \sim \rho \frac{g'h}{L} q_0 t^\alpha \tag{20}$$

and

$$F_i = \rho \int u u_x dV \sim \rho \frac{L}{t^2} q_0 t^\alpha. \tag{21}$$

First consider the initial constant velocity regime, where $h \approx D$. In this case, equating F_b and F_i gives

$$L \sim \sqrt{g' D} t. \tag{22}$$

For the self-similar regime, we can take $hL \sim q_0 t^\alpha$, so the force balance implies

$$L \sim \left(g' q_0\right)^{1/3} t^{(\alpha+2)/3}. \tag{23}$$

For the finite volume release ($\alpha = 0$) $L \sim t^{2/3}$ which defines the self-similar regime. For the case of a constant volume flux into the channel ($\alpha = 1$) this describes the constant velocity regime as $L \sim t$.

Another possibility is a balance between buoyancy and viscous forces. With

$$F_\nu = \rho\nu \int \nabla^2 u dV \sim \rho\nu \frac{L}{th^2} q_0 t^\alpha \sim \rho\nu \frac{L^3}{q_0} L t^{-\alpha-1}, \tag{24}$$

this gives

$$L \sim \left(\frac{g' q_0^3}{\nu}\right)^{1/5} t^{(3\alpha+1)/5} \tag{25}$$

This describes the viscous regime for the finite volume release ($\alpha = 0$, $L \sim t^{1/5}$) and a decelerating flow for the constant volume flux case as $L \sim t^{4/5}$.

Next we find the time at which the system changes from the inertia–buoyancy balance to the viscosity–buoyancy balance. We divide the inertial force by the viscous force. Taking into account the different length scales for the two regimes (Equations 23 and 25), this gives:

$$\frac{F_i}{F_\nu} \sim \left[\left(\frac{q_0^4}{g'^2 \nu^3}\right)^3 t^{(4\alpha-7)/3}\right]^{2/3}. \tag{26}$$

So the time when all three forces are equal is

$$t_T = \left(\frac{q_0^4}{g'^2 \nu^3}\right)^{1/(4\alpha-7)} = J^{1/(4\alpha-7)}. \tag{27}$$

In Figure 3 the relative magnitude of inertial and viscous forces is plotted against time for four different cases. In the case where $J > 1$ the current starts in an inertial–buoyancy balance. If $\alpha > \alpha_c = 7/4$ (the upper curve), the increase in source flux maintains this balance for all times. When $\alpha < \alpha_c$ (the lower curve), the relative magnitude of the viscous force increases and the current enters a viscous–buoyancy balance for $t > t_1$. When $J < 1$ the current is initially in a viscous–buoyancy balance and remains there when $\alpha < \alpha_c$ (the lower curve), but becomes inertial if $\alpha > \alpha_c$ (the upper curve) for $t > t_2$.

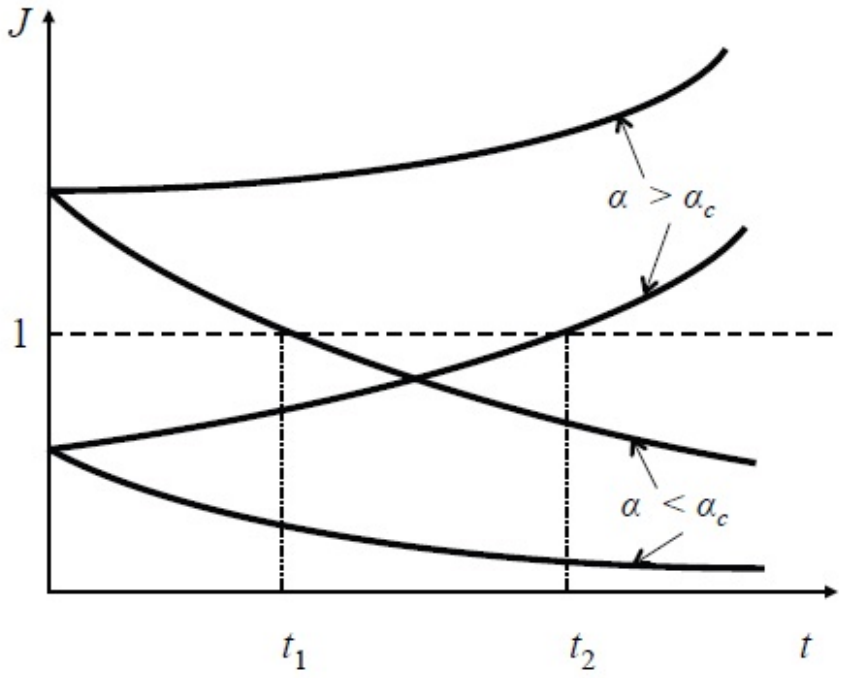

Figure 3: The relative magnitude of the inertia force F_i to the viscous force F_ν plotted against time.

5 Axisymmetric flow

For finite volume not in a channel one can consider the case of axisymmetric flow (See Figure 4). The initial buoyancy is $B_0 = g_0' D R_0^2 \pi$ with dimensions $L^4 T^{-2}$. It follows that

$$R(t) = B_0^{1/4} t^{1/2}, \tag{28}$$

which is the self-similar regime. Experiments have not given evidence for there being a constant velocity regime in the case of axisymmetric flow.

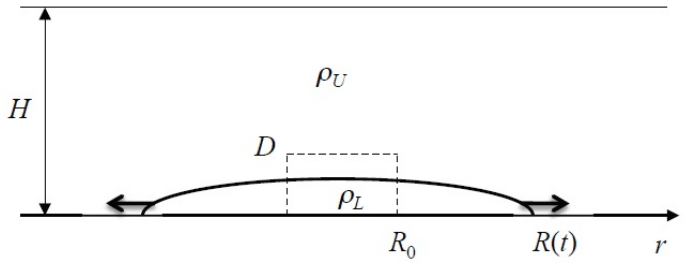

Figure 4: A schematic of the axisymmetric release of a finite volume of dense fluid into a less dense stationary environment of depth H. The dense fluid is initially held in a cylinder of radius R_0 and depth D.

6 Experimental results

Figure 5 shows the evolution in time of front positions from three lock release experiments (plotted dimensionlessly). One can see that at the start of all three experiments the front position scales linearly with time (i.e. $L \sim t$); this is the constant velocity regime. Two of the three experiments then go into a regime where $L \sim t^{2/3}$, the self-similar regime. Finally, all experiments end in the viscous regime as $L \sim t^{1/5}$.

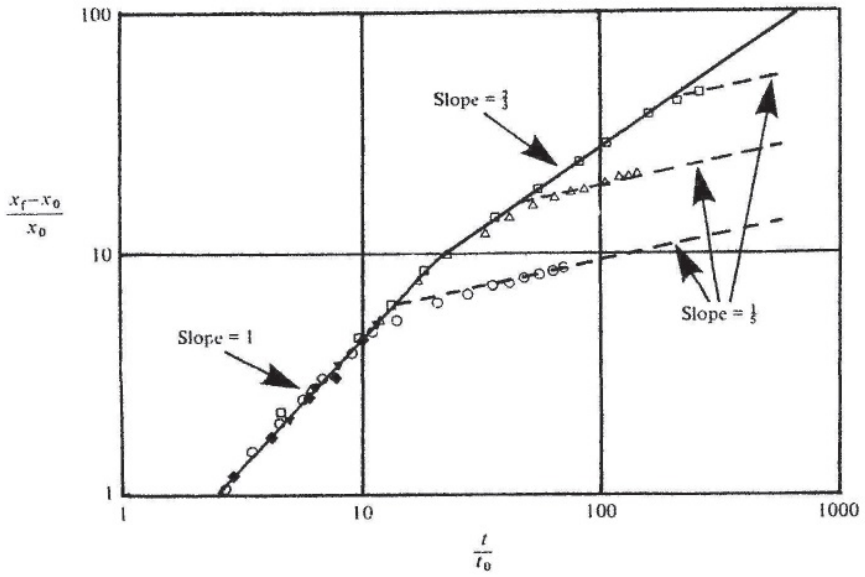

Figure 5: A log-log plot of dimensionless front positions against dimensionless time for 3 full-depth lock releases. Taken from [1].

References

[1] J. W. Rottman and J. E. Simpson, *Gravity currents produced by instantaneous release of a heavy fluid in a rectangular channel*, J. Fluid Mech., 135 (1983), pp. 95–110.

GFD 2013 Lecture 3: Hydraulic theories

Paul Linden; notes by Ton van den Bremer & Dhruv Balwada

June 19, 2013

1 Introduction

This lecture explores the use of hydraulic theories, theories that originated in the study of the behaviour of water in pipes or tube after the Greek words *hydro* for water and *aulis* for tube or pipe, to study gravity currents. It is exactly the motion of an air bubble in a pipe, illustrated in figure 1, that inspired the work by Benjamin [1] on gravity currents using the conservation laws of mass, momentum and energy that will be explored in this lecture.

2 Heavy current

Figure 2 gives a schematic representation of a dense flow with density ρ_L, the gravity current, protruding at the bottom of a two-dimensional horizontal channel filled with a lighter stagnant fluid of density ρ_U. We consider the problem in the reference frame in which the gravity current, which moves to the right relative to the channel with velocity U, is stationary. The depth of the 'downstream' (BE) end of the gravity current is h with the upper fluid moving at velocity u_U to the left (in the reference frame of the current), and the total depth of the channel is H. We assume a unit width throughout. In the reference frame of the current, there is a stagnation point at O.

Conservation of mass flux across the control volume $BCDE$ gives:

$$UH = u_U\big(H - h\big). \tag{1}$$

We further assume that the flow is horizontal, uniform across depth and that, accordingly, the pressure is hydrostatic. The vertical pressure distributions across BE and CD are therefore respectively given by:

$$BE: \quad p(z) = \begin{cases} p_B - g\rho_L z & 0 \le z \le h, \\ p_B - g\rho_L h - g\rho_U(z-h) & h \le z \le H, \end{cases} \tag{2}$$

$$CD: \quad p(z) = p_C - g\rho_U z, 0 \le z \le H \tag{3}$$

where z is measured from the bottom of the channel upwards, and gravity g acts in the negative z direction. Applying conservation of momentum across the control volume $BCDE$ ignoring the effects of the channel walls on the fluid through viscosity corresponds to:

$$\int_{z_C}^{z_D} (p + \rho u^2) dz = \int_{z_B}^{z_E} (p + \rho u^2) dz, \tag{4}$$

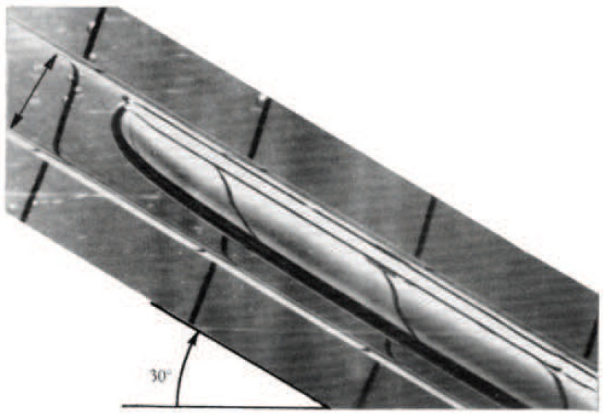

Figure 1: A bubble in an inclined closed tube from [3].

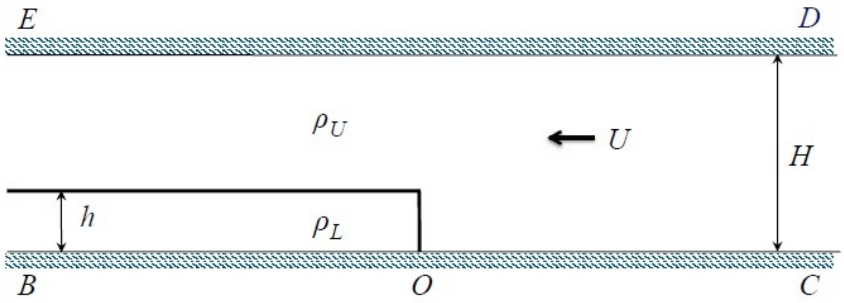

Figure 2: A schematic diagram of an idealized dense gravity current in a reference frame in which the current is at rest. In the laboratory reference frame, the current is propagating with constant speed U into an ambient fluid at rest. It is assumed that all the fluid within the current has the same speed.

which, in turn by simple rearranging and evaluation of the integrals, can be shown to correspond to:

$$p_B H + \frac{1}{2} g\big(\rho_L - \rho_U\big)h^2 - g\big(\rho_L - \rho_U\big)Hh + \rho_U u_U^2 (H-h) = p_C H + \rho_U U^2 H. \tag{5}$$

Equation (5) does not define the relationship between the pressures p_B and p_C that is required to close the problem. We apply Bernoulli along the lower boundary of the channel, which is evidently a streamline, from C to O and from O to B and obtain:

$$p_O = p_C + \frac{1}{2}\rho_U U^2 = p_B. \tag{6}$$

Substituting for u_U in terms of U from conservation of mass (1) and for the pressure difference $p_C - p_B$ from (6), equation (5) can be rewritten in the following form:

$$\frac{U^2}{g(1-\gamma)H} = \frac{1}{\gamma} f\Big(\frac{h}{H}\Big), \tag{7}$$

where $0 \leq \gamma = \rho_U/\rho_L, \leq 1$ and $f(h/H)$ is given by:

$$f\Big(\frac{h}{H}\Big) = f(\hat{h}) = \frac{\hat{h}(2-\hat{h})(1-\hat{h})}{1+\hat{h}}, \tag{8}$$

where $\hat{h} = h/H$. In the Boussinesq case, in which density difference are assumed to be small $\gamma \to 1$, the Froude number and the non-dimensional volume flux are then respectively given by:

$$F_H = \frac{U}{\sqrt{g'H}} = \sqrt{f(\hat{h})}, \quad \frac{Q}{\sqrt{g'H^3}} = \frac{Uh}{\sqrt{g'H^3}} = \hat{h}\sqrt{f(\hat{h})}. \tag{9}$$

Figure 3 shows both the Froude number F_H and the non-dimensional volume flux in (9) as a function of h/H. To find h itself, a further condition is needed.

2.1 The energy conserving case

Following Benjamin's [1] approach, we assume there are no energy losses, so that we can apply Bernoulli from E to D and obtain:

$$p_E + \frac{1}{2}\rho_U u_U^2 = p_D + \frac{1}{2}\rho_U U^2 \tag{10}$$

Combining (10) with conservation of mass (1), assuming there is a hydrostatic relationship between p_E and p_B and p_D and p_C, respectively, and that the relationship (6) between p_B and p_C still holds, we obtain:

$$\frac{U^2}{g(1-\gamma)H} = \frac{2}{\gamma}\frac{h\big(H-h\big)^2}{H^3}. \tag{11}$$

Equating (11) and the analogous expression derived without assuming zero energy losses (7) gives:

$$2\hat{h}(1-\hat{h})^2 = \frac{\hat{h}(2-\hat{h})(1-\hat{h})}{1+\hat{h}}, \tag{12}$$

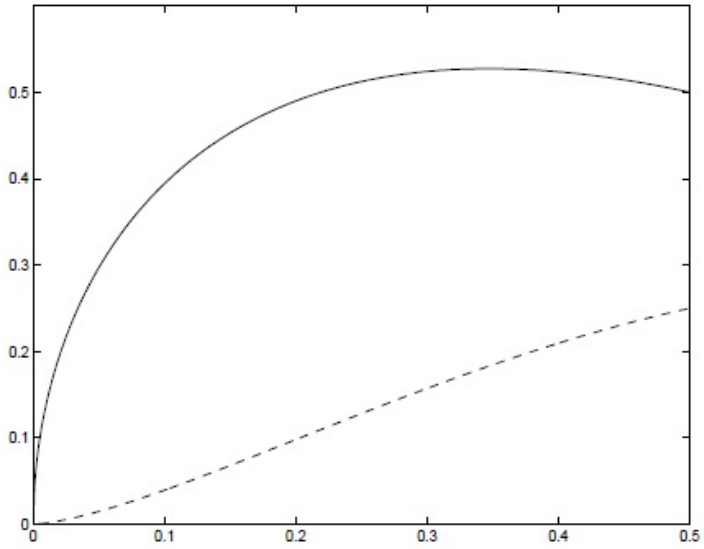

Figure 3: The Froude number F_H (continuous line) and the dimensionless volume flux $Q/\sqrt{g'H^3}$ (dashed line) as a function of the dimensionless gravity current depth $\hat{h} = h/H$.

where $\hat{h} = h/H$ as before. Equation (12) has three solutions: $\hat{h} = 0$, for which there is no gravity current, $\hat{h} = 1/2$ and $\hat{h} = 1$, for which the gravity current fills the entire channel. The only physically relevant solution is $h = H/2$ and, by substituting into (9) this can be shown to correspond to $F_H = 1/2$.

Now consider the Froude numbers based on the gravity current depth h for the energy conserving case $h = H/2$ and take the Boussinesq limit $\gamma \to 1$. From (11) we obtain:

$$F_h = \begin{cases} \frac{U}{\sqrt{g'h}} = \frac{U}{\sqrt{g'H}}\sqrt{\frac{H}{h}} = \frac{1}{\sqrt{2}} < 1 & \text{'upstream' (sub-critical),} \\ \frac{u_U}{\sqrt{g'h}} = \sqrt{2} > 1 & \text{'downstream' (super-critical),} \end{cases} \tag{13}$$

where 'upstream' and 'downstream' refer to the reference frame in which the current is stationary and we have used $u_U = 2U$ from mass conservation for $H = 2h$. In the downstream region of the control volume (the left-hand side) the flow is thus super-critical and waves cannot propagate faster than the speed of the gravity current. The sub-critical upstream region (the right-hand side) is left undisturbed until the arrival of the gravity current.

2.2 Energy losses

The energy flux $\dot{E}$ across a vertical plane is defined as follows:

$$\dot{E} = \int_0^H (p + \frac{1}{2}\rho u^2 + g\rho)u dz. \tag{14}$$

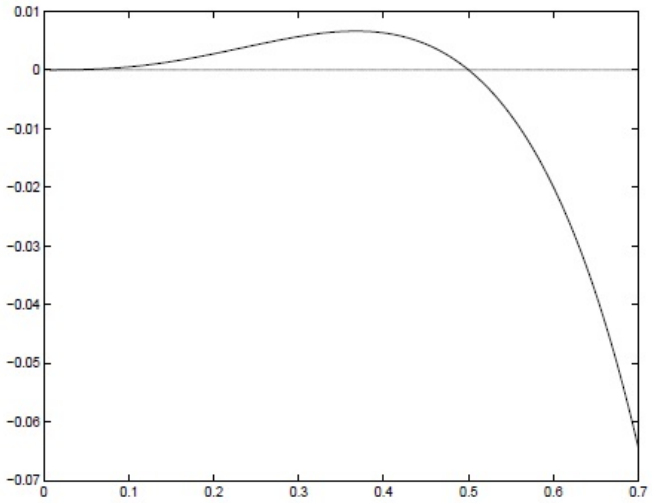

Figure 4: The dimensionless net energy loss flux $\Delta\dot{E}/gH^2U(\rho_L - \rho_U)$ as a function of the dimensionless gravity current depth $\hat{h} = h/H$.

Expressions for the energy fluxes at BE and CD are given by, respectively:

$$\dot{E}_{BE} = \Big(p_B - g(\rho_L - \rho_U)h + \frac{1}{2}\rho_U u_U^2\Big)u_U H, \tag{15}$$

$$\dot{E}_{CD} = \Big(p_C + \frac{1}{2}\rho_U U^2\Big)UH. \tag{16}$$

The energy loss flux is defined as $\Delta\dot{E} = \dot{E}_{CD} - \dot{E}_{BE}$. After substituting in for u_U from mass conservation (1) and momentum conservation (5) relating the pressures p_B and p_C by (6), the non-dimensional energy loss flux is defined by:

$$\frac{\Delta\dot{E}}{gH^2U\big(\rho_L - \rho_U\big)} = \frac{\hat{h} - \frac{1}{2}f(\hat{h})\frac{1}{(1-\hat{h})^2}}{1-\hat{h}}. \tag{17}$$

Figure 4, which shows the non-dimensional energy loss as a function of h/H, reveals there are only two solutions for which the energy losses described by (17) are zero: $h/H = 0$ and $h/H = 1/2$. It is evident from this figure that energy losses are only positive for $0 < h/H < 1/2$. For $h/H > 1/2$ energy needs to be input into the system. It is therefore impossible to maintain a gravity current with $h/H > 1/2$ unless the channel is tilted or energy is input into the flow in another way. In practical terms, such considerations are relevant for flushing pipeline applications, where it may hence not be possible to flush one liquid from the pipe entirely using another without tilting the pipe.

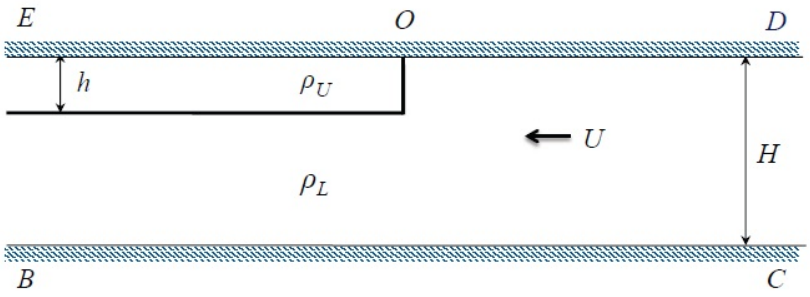

Figure 5: A schematic diagram of an idealized light gravity current in a reference frame in which the current is at rest. In the laboratory reference frame, the current is propagating with constant speed U into an ambient fluid at rest and it is assumed that all the fluid within the current has this same speed.

3 Light current

We now consider a light gravity current protruding into a heavy fluid at the top, as illustrated in figure 5. From conservation of mass we obtain:

$$u_L(H-h) = UH, \tag{18}$$

where u_L now denotes the horizontal velocity of the lower fluid at location BE in the reference frame of the gravity current. Assuming a hydrostatic pressure distribution, the pressure difference between BE and CD is given by:

$$\Delta p(z) = p_E - p_D + \begin{cases} (\rho_U - \rho_L)gz & 0 \le z \le h, \\ (\rho_U - \rho_L)gh & h \le z \le H, \end{cases} \tag{19}$$

where z is measured from the top of the channel down in the direction of gravitational acceleration g. Equating momentum fluxes across BE and CD gives:

$$\int_0^H \Delta p(z) + \rho_L u_L^2(H-h) - \rho_L U^2 = 0. \tag{20}$$

Integrating the pressure difference distribution (19), substituting for u_L from mass conservation (18) gives:

$$\frac{U^2}{g(1-\gamma)H} = f(\hat{h}), \tag{21}$$

where $\hat{h} = h/H$ and $f(\hat{h})$ is given by (8) as for the heavy gravity current. Comparison between (7) for a heavy current and (21) for a light current reveals a factor of $1/\gamma$. A heavy current moves faster than a light current ($\gamma < 1$).

4 Flow at the stagnation point

To understand the flow at the stagnation point and to find the local angle between the front and the edge of the current α (see figure 6), we solve for the potential flow field. We assume

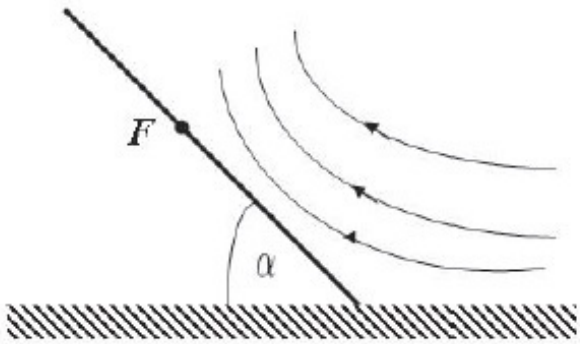

Figure 6: The flow in a corner representative of potential flow at the gravity current front.

uniform flow in the direction of the real axis of the complex domain w with corresponding complex potential $\Omega(w) = cw$, where c is a constant and for which the horizontal and vertical velocity are respectively given by $\mathrm{Re}[d\Omega(w)/dw] = c$ and $-\mathrm{Im}[d\Omega(w)/dw] = 0$. It is evident then that $\Omega(w)$ satisfies Laplace in the infinite half-space domain. We use a two-dimensional conformal mapping, to map to the space $z = r\exp(i\theta)$ in which the flow of the ambient fluid is confined by the gravity current (cf. figure 6 showing the flow field in z-space):

$$w = z^{\frac{\pi}{\pi-\alpha}} = r^{\frac{\pi}{\pi-\alpha}} e^{i\frac{\pi}{\pi-\alpha}\theta}. \tag{22}$$

The complex potential in z-coordinates is then given by:

$$\Omega(z) = \phi + i\psi = cz^{\frac{\pi}{\pi-\alpha}}. \tag{23}$$

The horizontal velocity can now be expressed as a function of the radial coordinate r:

$$q^2 = \frac{d\Omega}{dz}\frac{d\Omega^*}{dz} = c^2\Big(\frac{\pi-\alpha}{\phi}\Big)^2 r^{2\frac{\alpha}{\pi-\alpha}}, \tag{24}$$

where Ω^* is the complex conjugate of Ω. Applying Bernoulli along a streamline that takes a fluid particle from to the far right of the stagnation point elevating it and accelerating it to velocity q once it comes in the vicinity of the gravity current front, we obtain the equality:

$$\frac{1}{2}\rho q^2 = g\rho\sin(\alpha). \tag{25}$$

Substituting for q^2 from (24) into (25) and matching powers of r, we require $\alpha = \pi/3$ for the solution to Laplace to satisfy Bernoulli. For a current that flows down a slope of angle θ, $\sin(\alpha)$ in (25) is simply replaced by $\sin(\alpha+\theta)$. A maximum flow speed q then corresponds to $sin(\alpha+\theta) = 1$ and thus to $\theta = \pi/2 - \alpha = \pi/6$.

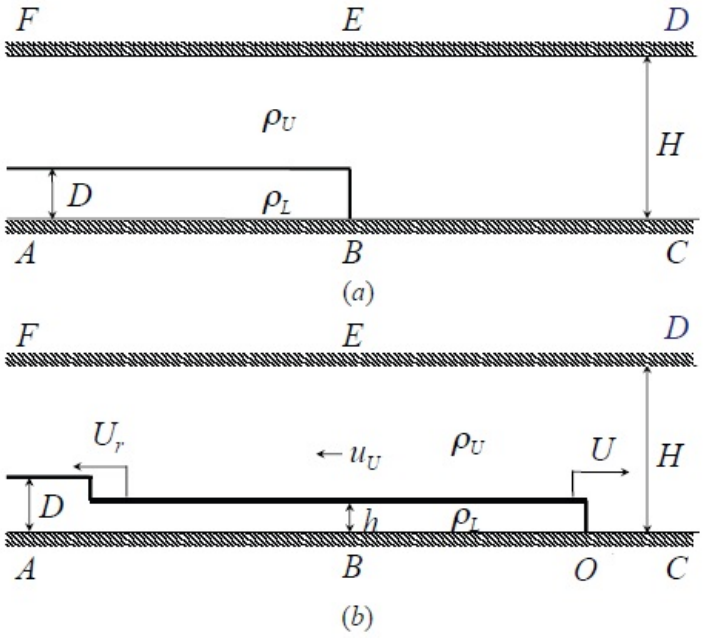

Figure 7: Schematic of a partial-depth lock release in a channel before release (a) and after release (b). Velocities are in the reference frame of the stationary channel.

5 Partial depth lock

Having only considered full-depth releases in a closed channel in the previous sections, figure 7 outlines what happens in the case of a partial depth lock release. In addition to a front travelling to the right with velocity U and depth h, there is a disturbance moving to the left with velocity U_r (both measured relative to the stationary closed channel) associated with a jump in fluid depth of h to D. At the far left hand side of the fluid (AF) the fluid is at rest (relative to the closed channel). Above the current of ρ_L, that is, to the right of the disturbance and to the left of the front, the upper fluid of density ρ_U moves to the left with speed u_U. Conservation of mass across the front is most easily considered in the reference frame in which the front is stationary:

$$UH = \big(U + u_U\big)\big(H - h\big) \rightarrow u_U = \frac{Uh}{H - h}. \tag{26}$$

Conservation of mass across the disturbance in the reference frame of the channel, gives a zero flux out on the left hand side and a positive flux out on the right hand side of magnitude Uh associated with the current moving to the right. This net outflux is balanced by a loss of total volume contained in the control volume of $U_r(D - h)$:

$$Uh = U_r(D - h) \rightarrow U_r = \frac{Uh}{D - h}. \tag{27}$$

We return to the reference frame of the stationary channel and consider a control volume just outside of both the left-travelling disturbance and the right-travelling gravity current

front. The distribution of the pressure difference between the left-hand side (AF) and the right-hand side is (CD):

$$\Delta p(z) = p_F - p_D \begin{cases} 0 & \leq z \leq H - D, \\ (\rho_L - \rho_U) g\Big(z - \big(H - D\big)\Big) & H - D \leq z \leq H, \end{cases} \tag{28}$$

where z is measured from the top of the channel down. Integrating (28) with respect to z across the depth of the channel gives net force applied to the control volume $ACDF$:

$$\dot{M} = \frac{1}{2} g(\rho_L - \rho_U) D^2 + (p_F - p_D) H. \tag{29}$$

Having considered the forces applied to the control volume, we consider the change in momentum that results. In the stationary reference frame we have for the lower fluid:

$$\dot{M}_L = \rho_L \Big(U + U_r\Big) U h \tag{30}$$

where the momentum per unit mass is U, and the rate of change of the volume that has this momentum is $dV/dt = h dL/dt = h(U + U_r)$. Here, the length scale L denotes the length of the gravity current. A unit width is assumed throughout this lecture. The upper fluid has momentum per unit mass $-u_U$:

$$\dot{M}_U = -\rho_U \Big(U + U_r\Big)(H - h) u_U, \tag{31}$$

where the rate of change of the volume that has momentum $-u_U$ is $dV/dt = (H-h) dL/dt = (H - h)(U + U_r)$. Here, again the length scale L denotes the length of the gravity current. Equating $\dot{M} = \dot{M}_L + \dot{M}_U$, where $\dot{M}$ is given by (29) and $\dot{M}_L$ and $\dot{M}_U$ by (30) and (31), respectively, gives:

$$(p_D - p_F) H = (\rho_L - \rho_U) \Big[U^2 \frac{Dh}{D - h} + \frac{1}{2} g D^2\Big]. \tag{32}$$

What remains to be found is the pressure difference $p_D - p_F$. Since with the two different velocities, U and U_r, a reference frame can no longer be found in which the problem is steady, we apply unsteady Bernoulli between D and F to find the pressure difference between these two points:

$$p_F + \rho_U \frac{\partial \phi_U}{\partial t}\Big|_F = p_D + \rho_U \frac{\partial \phi_U}{\partial t}\Big|_D, \tag{33}$$

where ϕ is the velocity potential. For (33) to hold, energy conservation in the top layer is assumed. Letting x_f denote the position of the front, x_r the position of the left travelling disturbance, the horizontal velocity in the top layer is given by:

$$u = \begin{cases} 0 & \text{for } x < x_r, \\ -u_U & \text{for } x_r < x < x_f, \\ 0 & \text{for } x > x_f. \end{cases} \tag{34}$$

Integrating (34) with respect to x gives the velocity potential:

$$\phi_U = \begin{cases} 0 & \text{for } x < x_r, \\ -u_U(x - x_r) & \text{for } x_r < x < x_f, \\ -u_U(x_f - x_r) & \text{for } x > x_f, \end{cases} \tag{35}$$

which is defined up to an arbitrary constant but does not include an arbitrary dependence on z, as the no-flow boundary condition requires $\partial\phi/\partial z = 0$ along the boundary of the channel. The pressure difference $p_D - p_F$ is then equal to:

$$p_D - p_F = \rho_U u_U\big(\dot{x}_f - \dot{x}_r\big) = \rho_U u_U\big(U + U_r\big). \tag{36}$$

Combining conservation of mass (26-27), momentum (32) and substituting for the pressure difference from (36) gives after some manipulation:

$$\frac{U^2}{gH} = \frac{(\rho_L - \rho_U)D(D-h)(H-h)}{2hH\big(\rho_L(H-h) + \rho_U h\big)}. \tag{37}$$

5.1 The energy conserving case

Finally, we assume energy is conserved to close the problem. There are no fluxes of energy into or out of the control volume $ACDF$. There is a decrease in potential energy associated with the loss in elevation of the interface position of the undisturbed fluid due to the disturbance travelling to the left and an increase in the potential energy associated with the increase in elevation due to the gravity current travelling to the right:

$$\dot{E}_P = -\frac{1}{2}g(\rho_L - \rho_U)U_r\Big(D^2 - h^2\Big) + \frac{1}{2}(\rho_L - \rho_U)Uh^2, \tag{38}$$

where $(1/2)g(\rho_L - \rho_U)(D^2 - h^2)$ and $(1/2)g(\rho_L - \rho_U)h^2$ are the potential energy per unit length associated with the disturbance and the gravity current, respectively. The rates of change of the respective length scales associated with these changes in potential energy are $dL/dt = -U_r$ for the disturbance and $dL/dt = U$ for the gravity current. The change in potential energy (38) is matched by an increase in kinetic energy of the current and the disturbance:

$$\dot{E}_K = \frac{1}{2}\rho_L U^2(U + U_r)h + \frac{1}{2}\rho_U u_U^2(H-h). \tag{39}$$

Equating $\dot{E}_P = \dot{E}_K$ from (38) and (39) and thereby assuming conservation of energy gives after some rearranging:

$$\frac{U^2}{gH} = \frac{(\rho_L - \rho_U)(D-h)(H-h)}{H\big(\rho_L(H-h) + \rho_U h\big)}. \tag{40}$$

Comparison of (40) and (37) reveals that the only solution that conserves energy thus has $h = D/2$ consistent with the analogous result for full-depth lock releases. Figure 8 compares this finding to the data providing support for the assumption of zero energy losses.

In the Boussinesq limit $\gamma \to 1$, (40) setting $h = D/2$ reduces to:

$$\frac{U^2}{g'H} = \frac{D(2H-D)}{4H^2}, \tag{41}$$

or in terms of a Froude number:

$$F_D = \frac{U}{\sqrt{g'D}} = \sqrt{\frac{1}{2} - \frac{1}{4}\frac{D}{H}}, \tag{42}$$

which is compared to experimental evidence in 9.

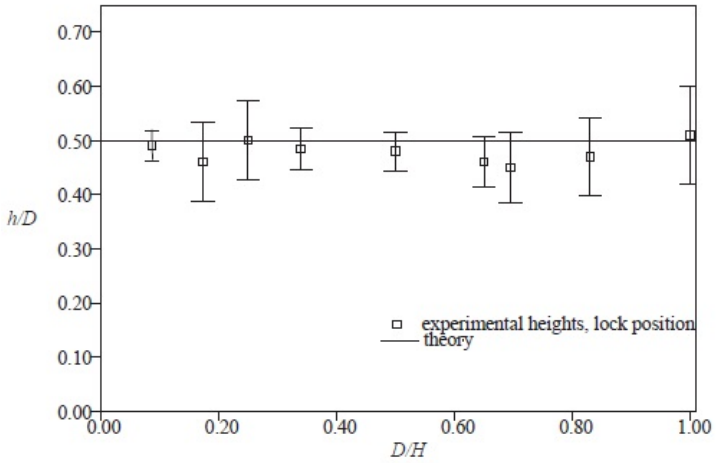

Figure 8: Comparison of measurements with the theoretical prediction (solid line) of the depth of the gravity current for partial-depth lock releases from [2].

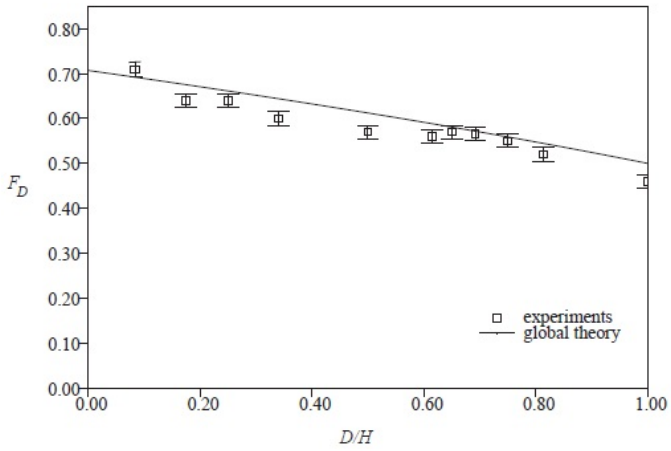

Figure 9: Comparison of measurements with the theoretical prediction (solid line) of the-gravity current speeds, expressed non-dimensionally as Froude numbers based on the depth of the lock D from [2].

5.2 Deep and shallow locks

In the limit of a full depth lock $D = H$, (41) reduces to $F_H = 1/2$, as for a full depth lock. In the shallow lock limit, we can write:

$$\frac{U^2}{g'h} = 1 - \frac{h}{H} \to 1 \quad \text{as } \frac{h}{H} \to 0. \tag{43}$$

5.3 Interfacial long waves

Finally, we compare the speed of the gravity current in a partial depth lock release to the phase speed of interfacial waves:

$$c_\pm = \frac{u_U h + u_L(H-h)}{H} \pm \frac{1}{H}\sqrt{h(H-h)\Big(g'H - (u_U - u_L)^2\Big)}, \tag{44}$$

which can be obtained from solving the linear long wave equation in a two-layer fluid, where the upper layer of depth $H - h$ has velocity u_U in the negative x-direction and the lower layer of depth h has velocity u_L in the positive x-direction. Normalisation of (44) by the solution for the horizontal front speed of the partial-depth lock release problem (41) and setting $U_L = U$ and $U_U = -Uh/(H-h)$ from mass conservation gives:

$$\frac{c_\pm}{U} = \frac{2(H-D)}{2H-D} \pm \sqrt{\frac{2(H-D)}{2H-D}}. \tag{45}$$

It is evident from (45) and from figure 10 that for shallow lock releases ($D/H < 0.76$) wave to the right travel faster than the current, whereas for deep enough locks the flow speed is super-critical ($c/U < 1$) even for the fast right-travelling waves. These waves are also evident in figure 11, in which they travel towards the front and accumulate there for the partial-depth release (figure 11a) and are stationary for the full-depth release (11b).

References

[1] T. B. Benjamin, *Gravity currents and related phenomena*, J. Fluid Mech., 31 (1968), pp. 209 – 248.

[2] J. O. Shin, S. B. Dalziel, and P. F. Linden, *Gravity currents produced by lock exchange*, J. Fluid Mech., 521 (2004), pp. 1–34.

[3] E. E. Zukoski, *Influence of viscosity, surface tension and inclination angle on the motion of long bubbles in closed tubes*, J. Fluid Mech., 25 (1966), pp. 821–840.

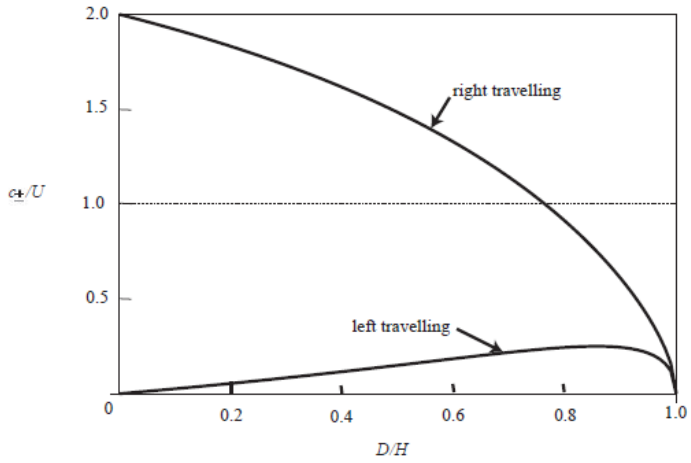

Figure 10: The speeds $c_{\pm}/U$ of waves on the top of the current as a function of the fractional depth D/H of the release. Waves travelling to the left are always slower than the current, while waves travelling to the right are faster for $D/H < 0.76$.

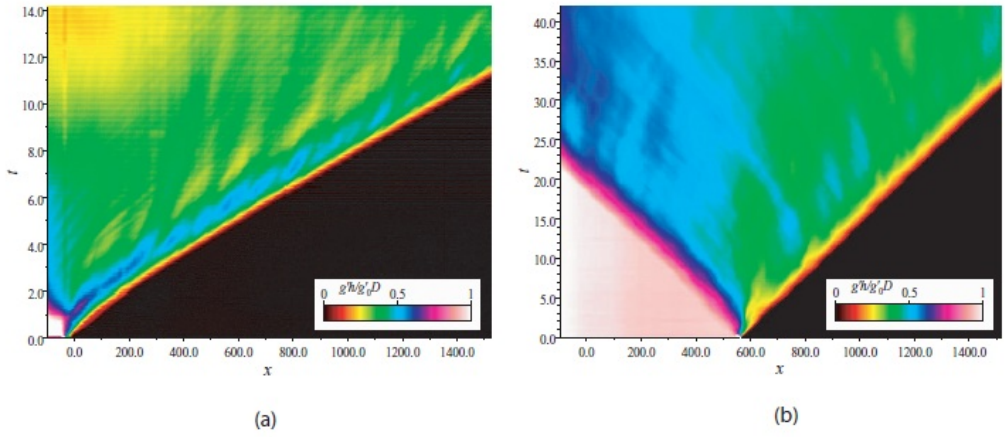

Figure 11: The buoyancy $g'h$ shown by the false colour plotted on an x-t plot for a partial-release $D/H = 0.21$ (a) and a full-depth release $D/H = 1$ in (b). The intensities are normalized by the initial buoyancy$g'_0 h$ in the lock. The front position at any time is the location at the edge of the black region, and the constant front speed is shown by the straight line fit to this shown in (a). The blue regions behind the front are elevated values of the buoyancy indicating deep regions of the current. They travel towards the front in (a), but are almost stationary in (b).

GFD 2013 Lecture 4: Shallow Water Theory

Paul Linden; notes by Kate Snow and Yuki Yasuda

June 20, 2014

1 Validity of the hydrostatic approximation

In this lecture, we extend the theory of gravity currents analysis by now applying the theory of the shallow water system. In the shallow water system, the hydrostatic approximation ($p_z = -\rho g$) and uniform motion with respect to height ($u_z = 0$) are assumed. Thus we have to check their validity.

First, in order to discuss the validity of the hydrostatic approximation, characteristic scales are introduced: L for horizontal length; U for horizontal velocity; H for vertical length; and W for vertical velocity. From the two dimensional incompressible condition $\frac{\partial u}{\partial x} + \frac{\partial w}{\partial z}$, $W \sim \epsilon U$ holds where $\epsilon := \frac{H}{L}$. By using the momentum equation in the x direction, the characteristic scale of pressure (P) can be estimated:

$$\underbrace{u_t}_{\frac{U}{T}} + \underbrace{uu_x + wu_z}_{\frac{U^2}{L}} = -\frac{1}{\rho}p_x, \tag{1}$$

$$P = \rho \ \max\left[\frac{UL}{T}, U^2\right]. \tag{2}$$

When the state is nearly steady [1], P is equal to ρU^2. Then the magnitude of each term in the vertical momentum equation can be estimated as follows:

$$\underbrace{uw_x + ww_z}_{\epsilon\frac{U^2}{L}} = \underbrace{-\frac{1}{\rho}p_z}_{\frac{U^2}{H}} - g. \tag{3}$$

Therefore, the magnitude of inertia terms are much smaller than that of the vertical pressure gradient, when the aspect ratio (ϵ) is small:

$$\frac{uw_x + ww_z}{-\frac{1}{\rho}p_z} = O(\epsilon^2). \tag{4}$$

This fact means that the hydrostatic balance holds with an accuracy of second order of ϵ.

Then it can be shown that the fluid layer moves uniformly in the z direction ($u_z = 0$) with the same accuracy. By differentiating (3) with respect to x, $p_{xz} = O(\epsilon^2)$ can be shown. Thus, if the fluid is initially uniform ($u_z|_{t=0} = 0$), uniformity also holds in later times with an accuracy of second order of ϵ.

[1] Or the time scale is equal to the advection time scale (L/U).

2 One layer shallow water equations

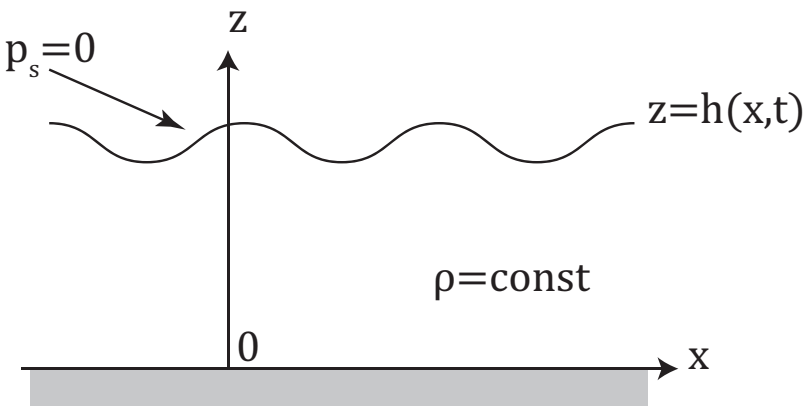

Figure 1: Two dimensional fluid system with a constant density. For simplicity, the pressure at the surface is taken to be zero.

We assume the following three things and then derive the one layer shallow water equations for the two dimensional fluid system with a constant density (Figure 1):

1. The hydrostatic balance holds.
2. Fluid moves uniformly with respect to height.
3. The aspect ratio is small.

Note that the third assumption is necessary for the validity of the other assumptions.

By the first assumption, p is equal to $\rho g\{h(x,t) - z\}$. By using the second assumption, the horizontal momentum equation becomes as follows:

$$u_t + uu_x = -gh_x. \tag{5}$$

By integrating the continuity equation and using the second assumption, the time evolution equation of h can be derived as follows:

$$\begin{aligned} w|_{z=h} &= -\int_0^h u_x dz, \\ \frac{Dh}{Dt} &= -hu_x. \end{aligned} \tag{6}$$

Note that the bottom boundary is flat, i.e., $w|_{z=0} = 0$, and the vertical variation of surface $\frac{Dh(x,t)}{Dt}$ is equal to $\frac{\partial h}{\partial t} + u\frac{\partial h}{\partial x}$. Thus (6) becomes

$$h_t = -\left(hu\right)_x. \tag{7}$$

The shallow water system consists of two equations (5), (7) and has two dependent variables $u(x,t), h(x,t)$.

When an axisymmetrical flow is considered, (7) becomes:

$$h_t + (uh)_r + \frac{uh}{r} = 0, \tag{8}$$

where r is radius, and u is radius velocity component. When the two layer stratified fluid [2] is considered as another extension, the interface of two layers is governed by (5) and (7), with g replaced by the reduced gravity (g').

3 Release in a channel

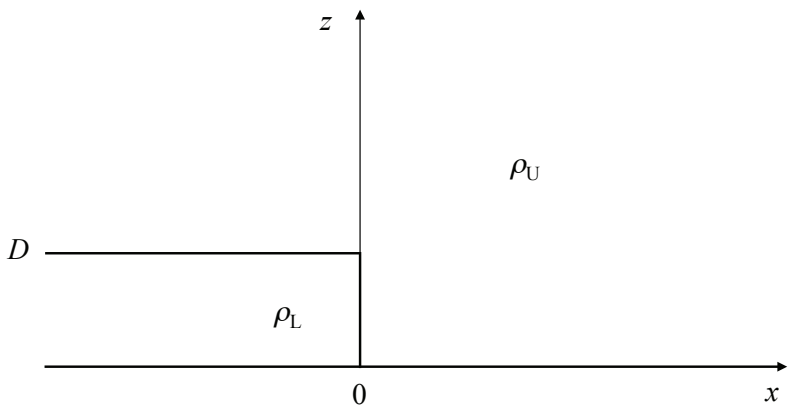

Figure 2: The initial state of gravity current.

Here, the gravity current is examined as an interface of the two layer shallow water system (Figure 2). Note that the mixing of the two different densities is not considered, and so g' is constant. The governing equations are the following:

$$u_t + uu_x + 2cc_x = 0, \tag{9}$$

$$(2c)_t + u(2c)_x + cu_x = 0, \tag{10}$$

where $c := \sqrt{g'h}$ is the phase speed of long waves. The initial conditions are then given by:

$$u(x,0) = 0(-\infty < x < \infty), \tag{11}$$

$$h(x,0) = \begin{cases} D & (x < 0), \\ 0 & (x > 0). \end{cases} \tag{12}$$

Further two conditions are necessary to specify the problem. The first condition is derived from the rear of the current:

$$u = 0, \quad \text{when} \quad h = D, \tag{13}$$

[2]The case of the rigid lid is considered.

and the second condition is derived from the front of the current:

$$u = F\sqrt{g'h}, \tag{14}$$

where F is a constant Froude number.

By adding (9) to (10) and subtracting (10) from (9), the governing equations are transformed into:

$$\{\partial_t + (u+c)\partial_x\}(u+2c) = 0, \tag{15}$$

$$\{\partial_t + (u-c)\partial_x\}(u-2c) = 0. \tag{16}$$

We solve this problem by using the method of characteristics. This method enables us to treat the PDE as an ODE. Characteristics are defined as $(t(s), x(s))$ where s is a parameter. Then the following relations are assumed:

$$\frac{dt}{ds} = 1, \quad \text{and} \quad \frac{dx}{ds} = u \pm c. \tag{17}$$

First, the case of positive characteristic (+ is chosen in (17)) is examined. Because of (15) and the following formula;

$$\frac{d}{ds} = \frac{\partial}{\partial t} + (u+c)\frac{\partial}{\partial x}, \tag{18}$$

$u + 2c$ is constant along the positive characteristic:

$$\frac{d(u+2c)}{ds} = 0. \tag{19}$$

By using the definition (17), the parameter s can be removed:

$$\frac{dx}{dt} = u + c. \tag{20}$$

The above equation describes the positive characteristic. In the same manner, $u - 2c$ is constant along the negative characteristic which is calculated by $\frac{dx}{dt} = u - c$.

Then we derive the specific solution of the situation shown in Figure 3. First, the case of $x < 0, t < 0$ is examined. From the initial conditions, $u = 0$ and $c = C := \sqrt{g'D}$. Then the characteristics are given by $\frac{dx}{dt} = \pm C$.

Second, the region of $x < 0, t > 0$ is examined. Here, there is a boundary line ($x = -Ct$) which represents the margin of the left propagating disturbance from the origin. So we have to consider separately the left and right regions from the boundary line. In the left region, by using the result of the region $x < 0, t < 0$, $u \pm 2c = \pm 2C$ along the positive and negative characteristics, respectively. Thus, $u = 0$ and $c = C$ holds in the left region from the boundary line.

On the other hand, in the right region, $u + 2c = 2C$ holds along the positive characteristics, and $u - 2c = A(\text{const})$ holds along the negative ones. At the origin, as there is a discontinuity of h in the initial condition, the wave speed can not be decided uniquely and then the negative characteristics intersect each other. From these equations, $2u = 2C + A$ and $c = \frac{2C-A}{4}$ hold. It is clear that the negative characteristics are straight lines, while the positive ones are curves due to the variation of A.

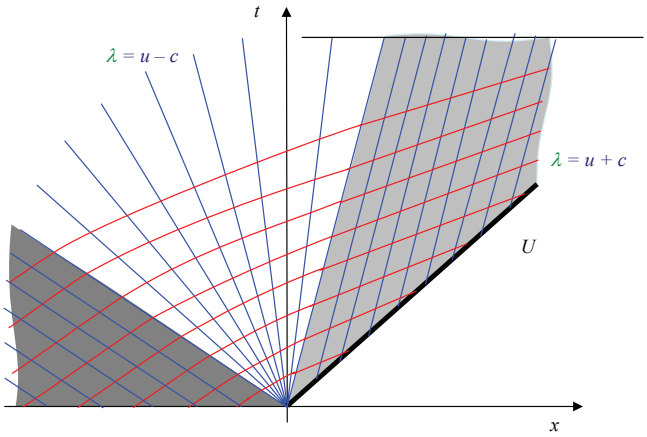

Figure 3: Characteristics for the problem of the gravity current. Positive (negative) characteristics are red (blue). The dark gray region corresponds to the left region from the boundary line which represents the margin of the left propagating disturbance from the origin. Figure kindly provided by Stuart Dalziel.

3.1 Front Velocity and Height

The front is initially at the origin and at rest. Then given that $u \pm 2c$ is conserved along the curve in equation (20), we may write:

$$u \pm 2c = u \pm 2\sqrt{g'h} = 0 \pm 2\sqrt{g'D} = \pm 2C,$$

where in this case $u = U$, the front velocity. We also know that $U = Fc$, and substituting c into the above equation gives:

$$U = \frac{2FC}{F+2}. \tag{21}$$

This is the solution for the front velocity, with the condition dependent on the choice of F.

The height of the front can also be determined based on the Froude number. This is calculated by substituting $U = cF$ into equation (21) giving:

$$cF = \frac{2FC}{F+2} \implies \sqrt{g'h_f}F = \frac{2F\sqrt{g'D}}{F+2},$$
$$\frac{h_f}{D} = \frac{4}{(F+2)^2}. \tag{22}$$

Again it is seen from equation (22) that the solution is dependant on the value of F. Figure 4 illustrates this further by providing the shape of the front for values of F from 1 to 3.

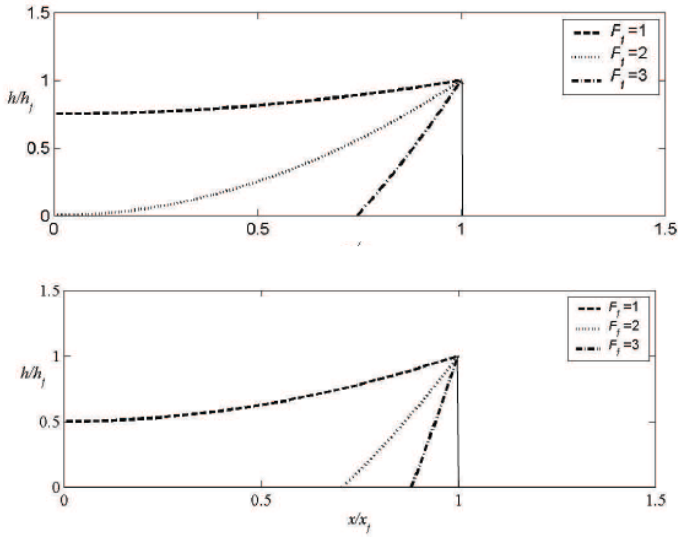

Figure 4: The shape of the front, x/x_f versus h/h_f, for varying values of the Froude number for both the channel (a) and axisymmetric current (b).

The full solution in the region $x > -Ct$ is given by the positive characteristic, $u + 2c = 2C$, and the negative characteristic, $\frac{dx}{dt} = u - c$, integrated to give $u - c = \frac{x}{t}$. Then solving these two equations simultaneously provides:

$$3c = 2C - \frac{x}{t} \implies 3\sqrt{g'h} = 2\sqrt{gD} - \frac{x}{t} \implies \sqrt{\frac{h}{D}} = \frac{2}{3} - \frac{x}{3Ct},$$

giving:

$$\frac{h}{D} = \frac{1}{9}(2 - \frac{x}{Ct})^2. \tag{23}$$

Equation (23) indicates the parabolic shape of the fluid height with x. We can also use this to obtain the position of the fluid by taking $h = h_f$ in (23) and equating this with (22) and rearranging:

$$\frac{x}{Ct} = \frac{2(F-1)}{F+2}. \tag{24}$$

Beyond the front position, the velocity and the depth remain constant as there is no fluid yet in this region, and this is indicated by the right hand non-shaded region in Figure 3.

The solutions provided above are clearly dependent on the value of F chosen. As an example, consider the case where $F = 1$ at time $Ct = 1$ shown in Figure 5. Substituting these values into equation (22), for an initial fluid depth $D = 1$, provides the front height as $h_f = 4/9$ and flow velocity $\frac{u}{C} = 2 - \frac{2c}{C} = \frac{2}{3}(1 + \frac{x}{Ct})$, which is indicated by the dashed line in the figure.

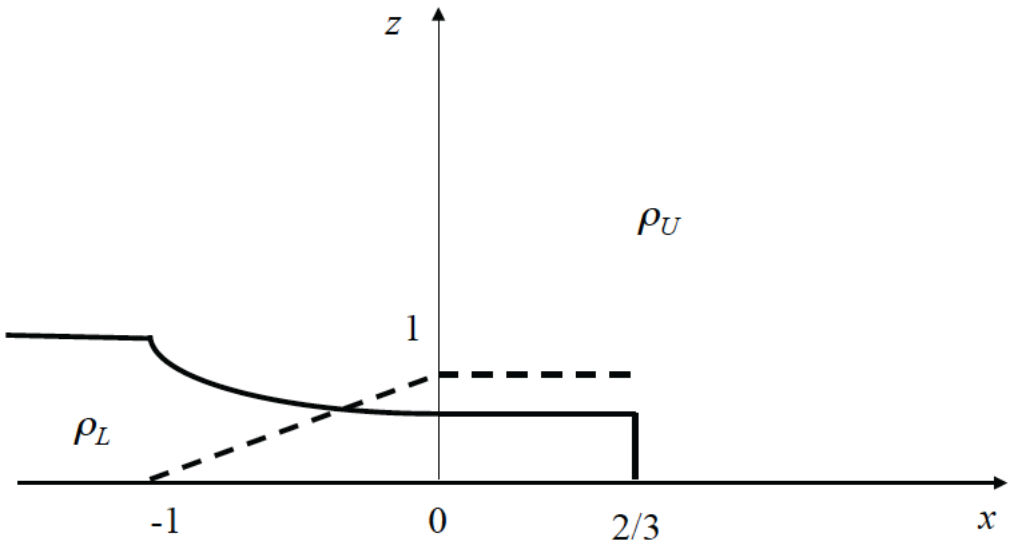

Figure 5: Distance versus height for the characteristic solution case of $Ct = 1$ and $F = 1$ showing the non dimensional depth of the fluid as the solid line and the non dimensional velocity as the dashed line.

3.2 Further Reading

For further reading on gravity currents, the reader is referred to the books and papers of John Simpson. His interest in the area was initiated from his time as a glider pilot, where he discovered the constant lift provided by uplifting sea breezes displaced by the lower outgoing land air that acted like a gravity current. His interest led to a number of books and influenced many to begin their own research in the area. As a couple of example references to his work, refer to [3], [4], [5] and [6].

4 Finite Volume Release

Consider now a one layer fluid, this time bounded in a finite volume (Figure 6).

We apply the same set of equations as previously, that is, the conservation of mass and momentum equations, and solve using dimensional analysis. The first step is to define the front velocity as:

$$u(x_f, t) = \dot{x_f}^2,$$

and apply the Froude condition:

$$F_f^2 g' h(x_f, t) = \dot{x_f}^2.$$

Now assuming conservation of volume (no mixing occurs within the system) we may write:

$$\int_0^{x_f} h(x, t) dx = V = DL_0.$$

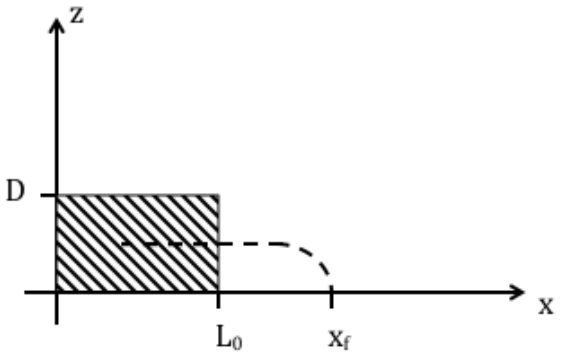

Figure 6: Two dimensional one layer fluid of finite volume, initial state (solid) and possible later state after lock release (dashed).

The flow can then seen to be defined by 5 governing parameters x, t, B, L_0 and F with two independent dimensions, length and time. Therefore, we make 3 dimensionless quantities and using the fact that $[B] = L^3T^{-2}$, define these quantities as:

$$\eta = \frac{x}{B^{\frac{1}{3}}t^{\frac{2}{3}}}, \qquad \tau = \frac{tB^{\frac{1}{2}}}{L_0^{\frac{3}{2}}}, \qquad F_f. \tag{25}$$

Applying dimensional analysis we therefore define:

$$u = \frac{x}{t}U(\eta, \tau, F_f), \tag{26}$$

$$g'h = \frac{x^2}{t^2}H(\eta, \tau, F_f), \tag{27}$$

$$x_f = xX(\eta, \tau, F_f), \tag{28}$$

where x_f is a function of x because the front velocity no longer travels at a constant speed with the finite volume case. We look for long time solutions, that is, solutions that are independent of the finite volume and so do not depend on L_0 (which is equivalent to saying the solution is independent of τ and so the above equations may be assumed to depend only on η and F). Applying the mass and momentum conservation equations in this situation we get:

$$\frac{\partial h}{\partial t} + \frac{\partial (uh)}{\partial x} = 0,$$

$$\frac{\partial}{\partial t}(\frac{x^2}{t^2}H) + \frac{\partial}{\partial x}(\frac{x^3}{t^3}UH) = 0,$$

$$-2\frac{x^2}{t^3}H + \frac{x^2}{t^2}\frac{\partial H}{\partial \tau}\frac{\partial \tau}{\partial t} + \frac{x^2}{t^2}\frac{\partial H}{\partial \eta}\frac{\partial \eta}{\partial t} + 3\frac{x^2}{t^3}UH + \frac{x^3}{t^3}\frac{\partial (UH)}{\partial \eta}\frac{\partial \eta}{\partial x}.$$

Since we've assumed the solution is now independent of τ then the $\frac{\partial H}{\partial \tau}$ goes to zero, and substituting $\frac{\partial \eta}{\partial x} = B^{-1/3}t^{-2/3}$ and $\frac{\partial \eta}{\partial t} = -\frac{2}{3}\frac{x}{B^{1/3}t^{5/3}}$ gives:

$$-2H - \frac{2}{3}H'\eta + 3UH + \eta(U'H + UH'),$$

which is rearranged and integrated:

$$\int \frac{dU}{U - \frac{2}{3}} = -\int \frac{dH}{H} - \int \frac{3}{\eta} d\eta,$$

providing:

$$U - \frac{2}{3} = \frac{k}{H\eta^3}, \tag{29}$$

where k is some constant of integration. Due to the conservation of the buoyancy, $g'h$ must always remain finite and so there is a discontinuity in (29) as x (and therefore η) approach zero. Hence, the only possible solution to (29) must be $k = 0$, producing the result $U = \frac{2}{3}$.

Now using conservation of momentum , equation (5), within the long time limit provides:

$$\frac{\partial}{\partial t}(\frac{x}{t}U) + \frac{x}{t}U\frac{\partial}{\partial x}(\frac{x}{t}U) = -\frac{\partial}{\partial x}(\frac{x^2}{t^2}H),$$
$$-\frac{x}{t^2}U + \frac{xU^2}{t^2} + \frac{Ux^2}{t^2}\frac{\partial U}{\partial \eta}\frac{\partial \eta}{\partial x} = -2\frac{x}{t^2}H - \frac{x^2}{t^2}\frac{\partial H}{\partial \eta}\frac{\partial \eta}{\partial x},$$

but since $U = \frac{2}{3}$ is a constant $\frac{\partial U}{\partial \eta} = 0$, then cancelling x and t terms and replacing with η we get:

$$\eta H' + 2H = U - U^2 = \frac{2}{9}. \tag{30}$$

Integrating equation (30):

$$H = \frac{1}{9} + \frac{K}{\eta^2}, \tag{31}$$

where K is a constant of integration. This the provides an expression for H where we must remove the unknown K term. To do, this return to the conservation of volume. Due to the constant g', conservation of buoyancy, which may be written as:

$$\int_0^{x_f} g'h(x,t)dx = B,$$

and:

$$\int_0^{x_f} g'h(x,t)dx = \int_0^{x_f} \frac{x^2}{t^2}Hdx = \int_0^{x_f} \frac{x^2}{t^2}(\frac{1}{9} + \frac{K}{\eta^2})dx.$$

Then replacing x with the equation for η the integral becomes:

$$x_f^3(\frac{1}{27} + \frac{K}{\eta_f^2}) = Bt^2. \tag{32}$$

Lastly we use the front condition on the Froude number:

$$u^2 = F^2 g' h \implies \dot{x_f^2} = F_f^2 g' h = F_f^2 \frac{x_f^2}{t^2} H = F_f^2 \frac{x_f^2}{t^2} (\frac{1}{9} + \frac{K}{\eta_f^2}),$$

and rearranging we can substitute the $K\eta_f^2$ term into (32) removing the K term and allowing the final governing equation to be found:

$$\dot{x_f^2} x_f = \frac{2}{27} F^2 \frac{x_f^3}{t^2} + F^2 B, \tag{33}$$

which has a solution of the form:

$$x_f = \Gamma t^{\frac{2}{3}}, \tag{34}$$

where $\Gamma = (\frac{27F^2B}{12-2F^2})^{\frac{1}{3}}$. The above results may also be put into dimensional terms:

$$x_f = (\frac{27F_f^2}{12 - 2F^2})^{\frac{1}{3}} B^{\frac{1}{3}} t^{\frac{2}{3}}, \tag{35}$$

$$\frac{h}{h_f} = 1 - \frac{1}{4} F^2 (1 - (\frac{x}{x_f})^2). \tag{36}$$

Hence, from the above results, it is found that the shape of the interface is parabolic in equation (36) and from equation (35) that the same $t^{\frac{2}{3}}$ time dependence occurs here as in the initial scaling analysis solution of the finite volume lock real case (the reader is referred to the second set of notes in this lecture series). Hence, we are seeing a similarity solution in each of the two cases. Figure 7 provides a comparison of the coefficient of the $t^{\frac{2}{3}}$ term in each case. In this figure, we see that as the Froude number is increased, the relative difference between the two solutions is also gradually increasing. Yet despite this difference, the insight given by the simplified box model still allows a result within approximately 20% of the shallow water model, displaying its usefulness as a tool for obtaining an approximate idea of the characteristics of the flow.

Figure 8 then provides the time evolution of the shape of the flow when initiated from a full depth lock. It is seen that after the initial sharp change, where the lock is released and there are large acceleration of the fluid, the head of the fluid flow remains at an approximately constant speed. At later times in the evolution this speed decelerates, as expected from the analysis and the similarity solution obtained. It is also noted that the head height reduces over time, this is due to the finite volume of the initial fluid and the flow left within the tail of current reduces the head volume.

Figure 9 shows the depth profiles for various similarity phases compared to the similarity solution case for three different Froude numbers. The similarity solutions do not extend to the furthest right of the profile at the front of the flow as the front region is very turbulent and the shallow water equations cannot be expected to represent this region. In the region prior to the front however, reasonable agreement can be observed between the theoretical and experimental cases with the larger value of the Froude number providing the closest agreement.

Looking also at the case of a partial depth release, Figure 10 indicates a longer, shallower tail region than in the full depth release case. This implies that a greater portion of the fluid

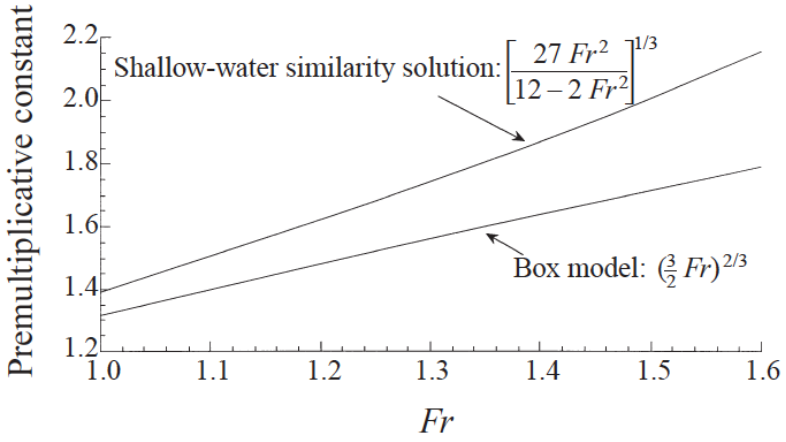

Figure 7: Coefficient of front distance for each of the cases in the similarity solution; the shallow water case derived in these notes and the box model in lecture two of this series.

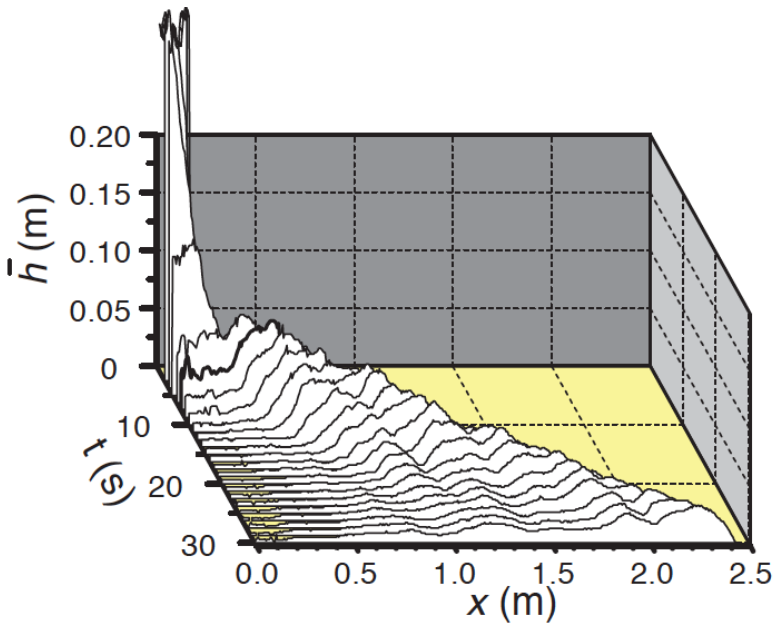

Figure 8: Height profiles at various stages of a full depth release flow with D/H=1 [1].

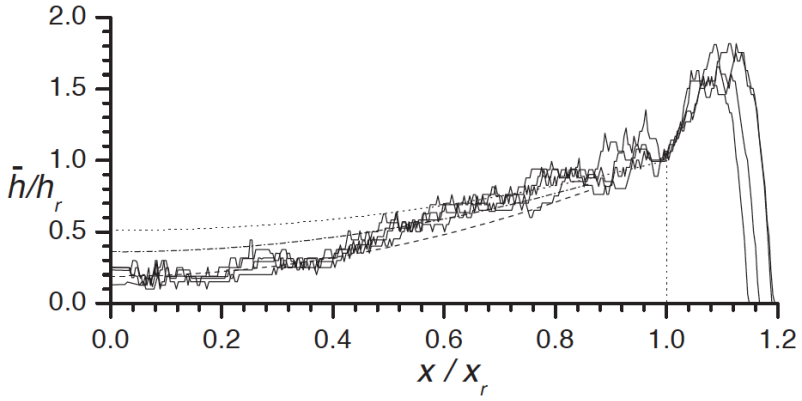

Figure 9: Equivalent height profiles for a full-depth with similarity phase values t/t_c =43.4, 46.9, 49.8 and 56.8. The profiles depicted by dotted, dash-dotted and dashed line profiles the similarity solutions to the shallow water equation for F_f =1.4, 1.6 and 1.8, respectively [1].

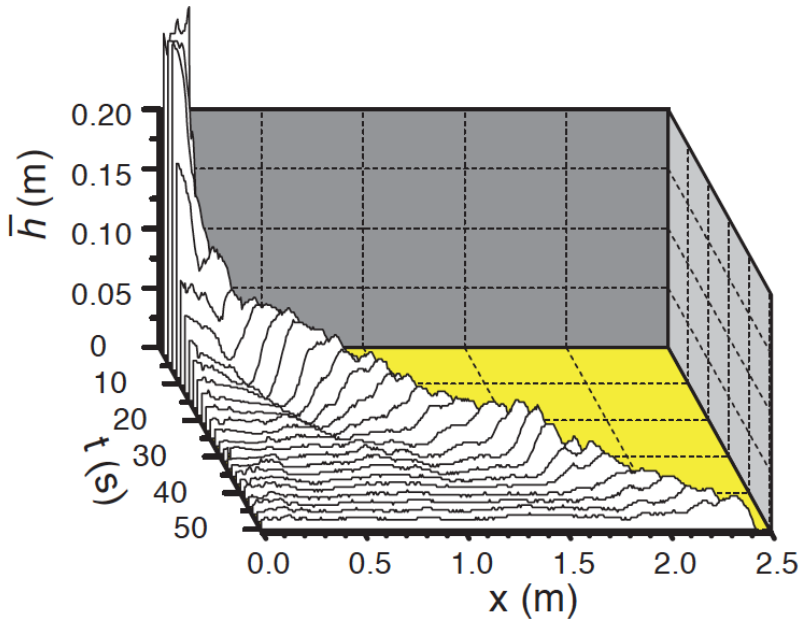

Figure 10: Height profiles at various stages of a partial depth release flow with D/H=0.675 [1].

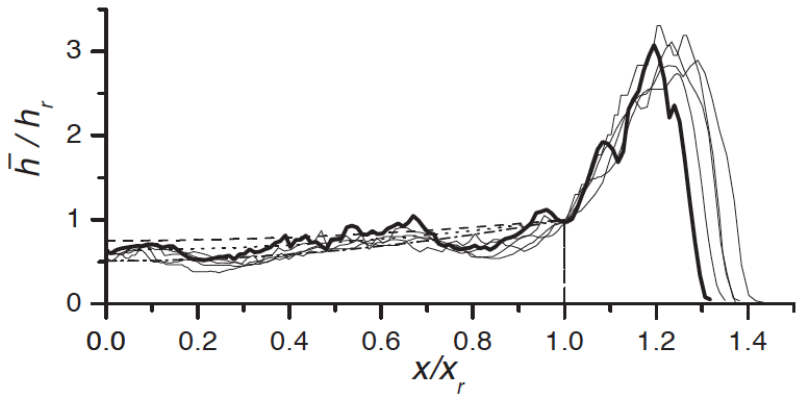

Figure 11: Equivalent height profiles for a partial-depth with similarity phase values t/t_c =43.4, 46.9, 49.8 and 56.8. The profiles depicted by dotted, dash-dotted and dashed line profiles the similarity solutions to the shallow water equation for F_f =1.4, 1.6 and 1.8, respectively [1].

is concentrated within the front region. The reader is referred to the paper of [2] for more details as here is provided an in depth analysis of the differences between the full and partial depth cases. In particular the main differences between the two cases can be attributed to the disturbances reflecting from the lock being closer to a bore case in higher initial depth locks and an expansion wave in shallower cases.

Figure 11 shows a comparison for the theoretical and experimental results of the similarity phase as in Figure 9 but now for the partial depth situation. Similar results are seen in this case as in Figure 9 with reasonable agreement between both sets of results, in particular when considering the error range of the experimental values.

Lastly lets consider alternatives for calculating the Froude number and where they are most relevant. Define F_D as the Froude number determined from the lock depth D; F_h as the Froude number evaluated from the maximum head height h and F_r as the Froude number determined from the height of the rear of the head. The definition of the rear of the head becomes rather difficult to precisely pin-point given the variation of profile shape over time and hence, as would be expected from such a definition, produces the greatest amount of scatter in the results (for full depth release see Figures 12 and partial depth release see Figure 13). Further, from the results in Figures 12 and 13, it is observed that the F_D definition provides the closest estimate to the constant velocity situation, where energy conserving theory may be applied, yet begins to diverge after the similarity phase is reached (this point is indicated by the vertical dashed lines). After the similarity phase, F_D decreases as expected for a Froude number defined in this manner. The F_h term however, remains fairly constant beyond the similarity phase, providing the best estimate of the speed in this region, despite the fact that it is derived from a non-hydrostatic region of the flow.

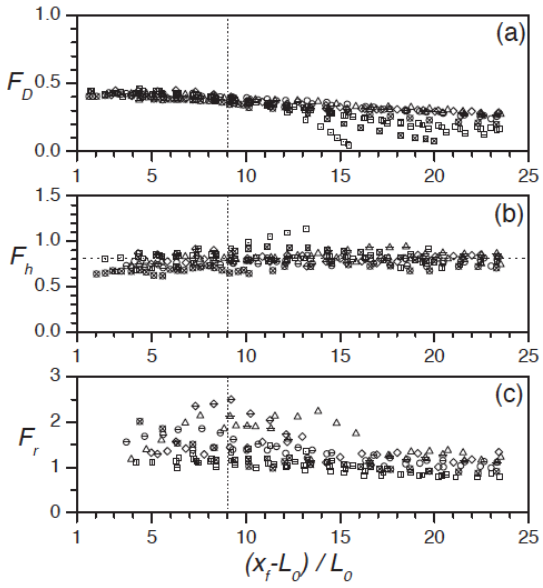

Figure 12: Evolution of the Froude number for the full-depth releases where F_f is determined from the lock height D, F_h from the maximum head height and F_r from the height of the rear of the head. The horizontal dashed line provides the average of the results while the vertical dashed lines indicates the area of departure from the constant-velocity phase situation. [1].

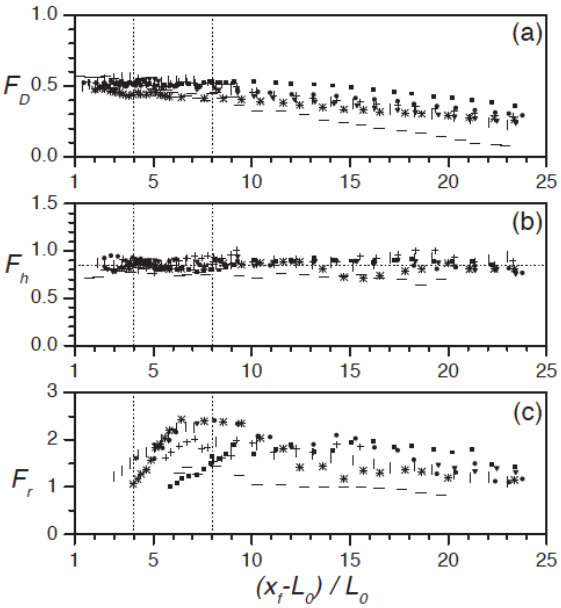

Figure 13: Evolution of the Froude number for the partial-depth releases where F_f is determined from the lock height D, F_h from the maximum head height and F_r from the height of the rear of the head. The horizontal dashed line provides the average of the results while the vertical dashed lines indicates the area of departure from the constant-velocity phase situation. [1].

References

[1] B. M. Marino, L. P. Thomas, and P. F. Linden, *The front condition for gravity currents*, J. Fluid Mech., 536 (2005), pp. 49–78.

[2] J. W. Rottman and J. E. Simpson, *Gravity currents produced by instantaneous release of a heavy fluid in a rectangular channel*, J. Fluid Mech., 135 (1983), pp. 95–110.

[3] J. E. Simpson, *A comparison between laboratory and atmospheric density currents*, Q. J. R. Met. Soc., 95 (1969), pp. 758–765.

[4] ——, *Effects of lower boundary on the head of a gravity current*, J. Fluid Mech., 53 (1972), pp. 759–768.

[5] ——, *Gravity currents in the environment and the laboratory*, Ellis Horwood, Chichester, 1987.

[6] ——, *Gravity Currents*, Cambridge University Press, 2nd ed., 1997.

GFD 2013 Lecture 5: Two-layer bores and non-Boussinesq gravity currents

Paul Linden; notes by Gregory Wagner and Barbara Zemskova

June 21, 2013

1 Introduction

A bore or hydraulic jump is a discontinuity like interfaces which occur between thin, fast moving layers of fluid and thicker, slower moving layers. Bores are commonly observed in everyday life; for example, when a stream of water from a tap strikes a horizontal surface and spreads radially it can be observed to spread at first in a thin layer until some radius at which the thickness of the fluid layer rapidly increases. Such "free-surface" bores also occur in some rivers due to the rising tide, in which case the bore propagates upstream. Two-layer bores are also possible in which a layer of heavy fluid flowing beneath a layer of lighter fluid forms a hydraulic jump; one example of such a bore can be observed over the Cape York peninsula in northern Queensland, Australia, where sea breezes generated off of the Pacific Ocean and the Gulf of Carpinteria collide, giving rise to a bore with a front which, given the correct atmospheric conditions, can form an impressive cylindrical cloud thousands of kilometers long.

Non-Boussinesq gravity currents are common and important: consider a mixture of air and water, whose densities differ by three orders of magnitude. Non-Boussinesq gravity currents exhibit significantly richer phenomena than Boussinesq gravity currents and are not completely understood. In particular, due to the high levels of turbulence associated with the few known experiments, it is unclear whether the current of heavier fluid develops a bore, causing a discontinuous decrease in the height of the layer, or whether the height of the fluid layer increases steadily upstream from the nose of the current.

2 Free-surface bores

A free-surface bore occurs in a layer of fluid flowing over a surface and through some infinite medium which by some mechanism downstream is required to decrease in speed. If the initial velocity of the flow is great enough, a bore will develop involving a sharp increase in the height of the layer and a rapid decrease in its velocity. Figures 1, 2 and 3 show a few examples of bores encountered in rivers, the atmosphere, experiments, and everyday life. In these notes we analyze the two-dimensional case sketched in Figure 4.

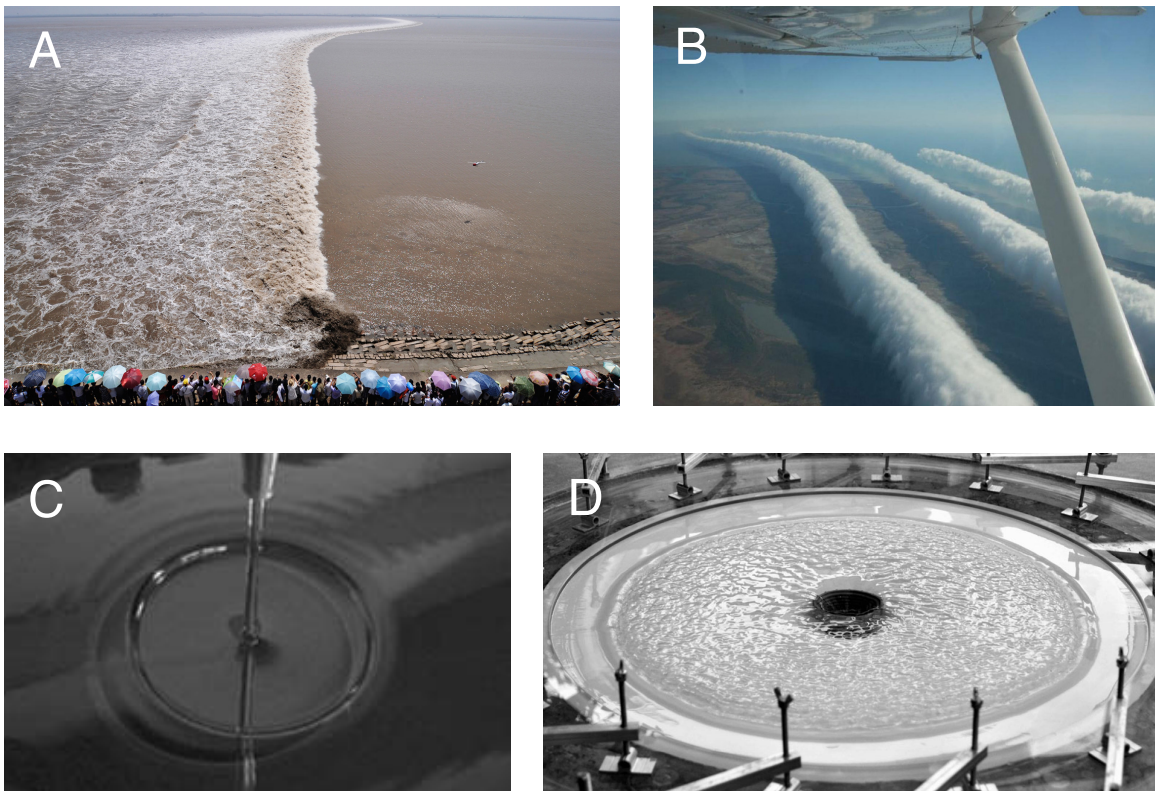

Figure 1: Examples of bores. (A) is a photograph of a tidal bore on Qiantong River in China. The front of the bore is turbulent but it also exhibits waves which can be seen downstream of the front. From `www.theatlantic.com/infocus/2011/10/21st-century-china/100174` (B) is a photograph taken of "Morning Glory" clouds which develop on the crests of an undular bore wave formed by the collision of sea breezes arising on either side of Cape York in northern Queensland. From `www.wikipedia.org/wiki/Morning_Glory_cloud` (C) is an image taken from [3] of a hydraulic jump of the kind observed in everyday life when water falling from a tap strikes a horizontal surface. (D) is an image of an experiment [5] where a hydraulic jump forms due to the radial inflow of water; the experiment is meant to serve as an analog for shocks which form in accretion disks during the formation of a neutron star.

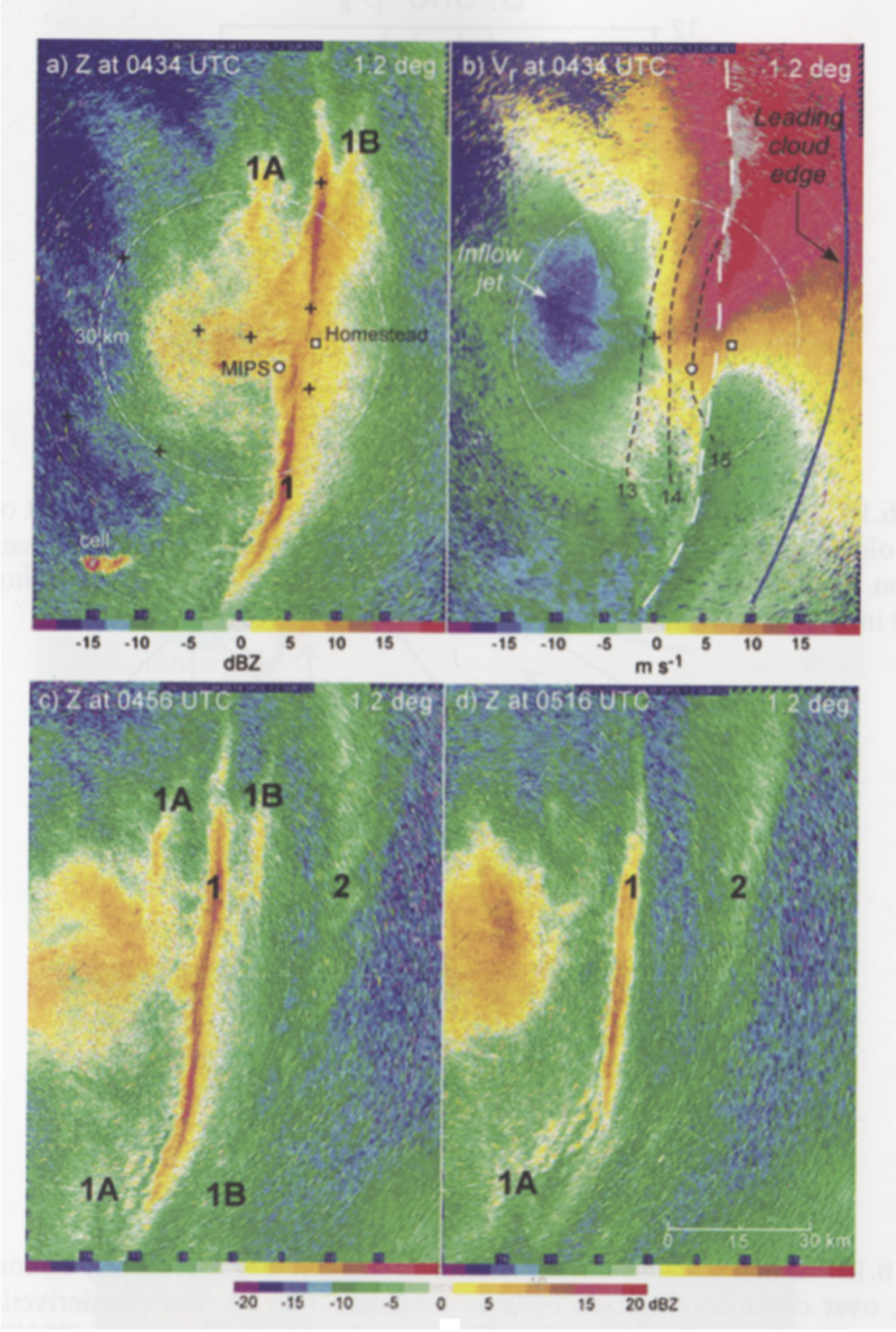

Figure 2: A bore observed in the atmosphere [12]

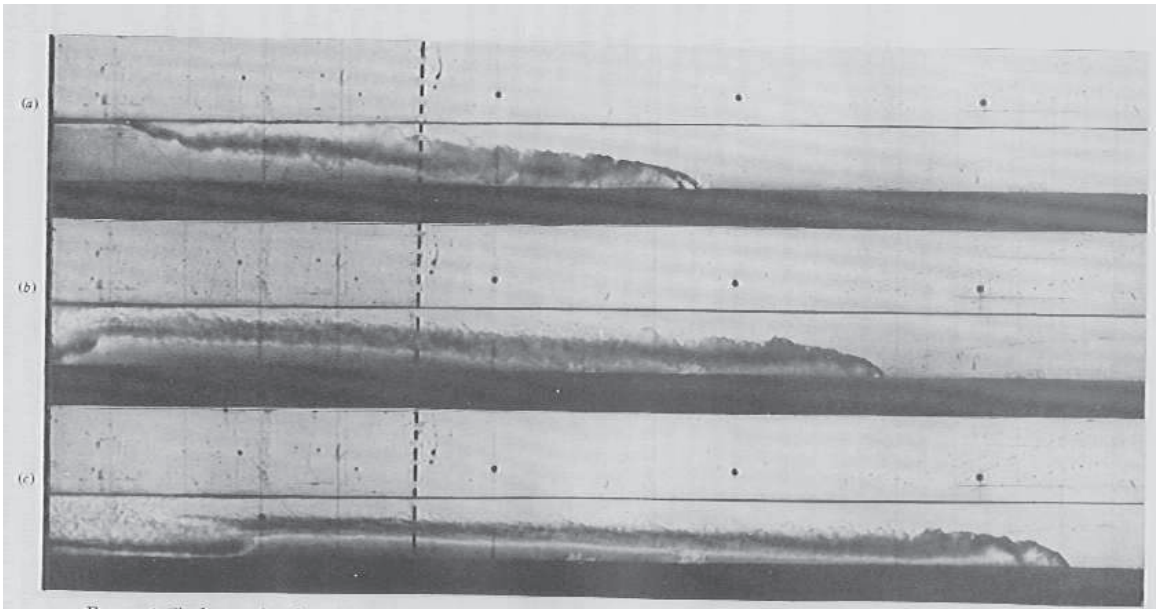

Figure 3: Shadowgraphs of a full-depth lock release. The location of the lock gate is shown by the vertical dotted line. In the top image a light surface current is propagating back into the lock. This reflects from the back wall of the lock and forms a bore, seen as the abrupt change in depth at the rear of the current in the second and third images. While the bore is behind the front, the front travels at a constant speed, as indicated by its position in the second and third images which are taken at equal time intervals. From [10].

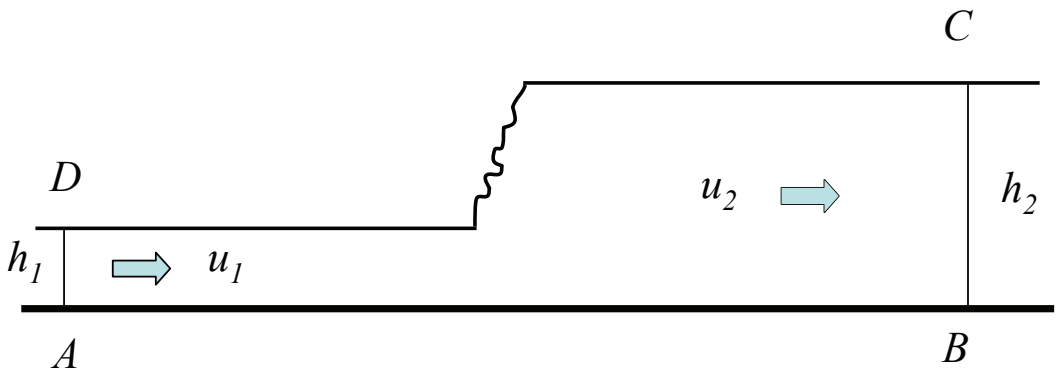

Figure 4: Schematic of a free-surface bore. The control volume affording easy analysis is the rectangle $ABCD$ (where D is properly taken to be at the same height as C). Applying conservation of mass to an accounting of energy flux shows that energy is dissipated only if $h_2 > h_1$. The nature of the front cannot be deduced from this simple analysis; but observations indicate a wave-like front is observed (an "undular bore") while for larger differences the front may become turbulent.

2.1 Analysis

Our approach is to use the same control volume analysis used extensively in the previous four lectures. To the boundaries of this control volume we apply the usual conservation principles for mass and momentum, which are simplified due to the assumption that the flow at each boundary is unidirectional and that pressure is hydrostatic. Conservation of mass implies

$$u_1 h_1 = u_2 h_2. \tag{1}$$

Conservation of momentum requires that the momentum flux, given in this case by

$$\int p + \rho u^2 \, \mathrm{d}z, \tag{2}$$

is equal for the inflow and outflow. If pressure is hydrostatic and given by $p_i = p_{\mathrm{atm}} + g\rho(h_i - z)$, where $i = 1, 2$. Conservation of momentum then implies

$$\frac{1}{2} g h_1 + u_1^2 h_1 = \frac{1}{2} g h_2^2 + u_2^2 h_2. \tag{3}$$

We may confirm the implication of the schematic that $h_2 > h_1$ by calculating the flux of energy through the control volume. The flux of energy through either AB or CD is given by

$$\int up + \frac{1}{2}\rho u^3 + \rho g u z \, \mathrm{d}z, \tag{4}$$

and therefore the flux of energy out of the control volume is

$$\Delta \dot{E} = \rho u_1 h_1 (h_1 - h_2) \left[g + \frac{1}{2} u_1^2 \left(\frac{h_1^2 + h_1 h_2 + h_2^2}{h_2^3} \right) \right]. \tag{5}$$

Therefore we see that because energy can only be removed from the control volume by viscous dissipation or the creation of surface gravity waves, we must have that $h_2 > h_1$. If we insert mass conservation into Equation 3 and solve for u_1 and u_2 we find

$$\begin{aligned} \frac{u_1^2}{g h_1} &= \frac{h_2(h_2 + h_1)}{2h_1^2} > 1, \\ \frac{u_2^2}{g h_2} &= \frac{h_1(h_2 + h_1)}{2h_2^2} < 1, \end{aligned} \tag{6}$$

where the inequalities follow from the fact that $h_2 > h_1$. Taken together these inequalities imply that surface waves generated either in the fluid layer upstream or downstream of the front cannot propagate towards the front, which implies that in the constructed scenario, a sharp continuity or hydraulic jump must exist at the interface between regions 1 and 2.

3 The two layer bore

A two-layer bore occurs when the fluid layer containing the hydraulic jump is overlain by a fluid of different density rather than simply a free surface. The free surface bore is actually a

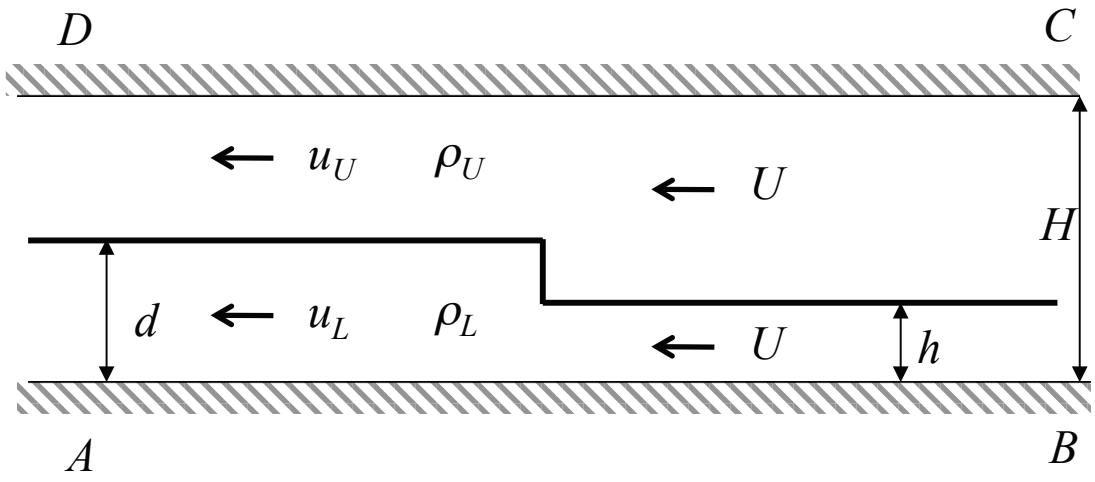

Figure 5: Schematic of a two-layer bore.

subset of this case, corresponding to the limit of vanishing upper layer density. A schematic of the two-dimensional problem is shown in Figure 5.

For the scenario we have two important limits in which we can test our results: the free-surface limit where $\rho_U/\rho_L \to 0$, and the gravity current limit where $h/H \to 0$. In this theory we assume that the flow is uniform, the pressure far from the bore is hydrostatic, and that the two fluids are similar in density such that they satisfy the Boussinesq approximation. The conservation of mass applied to each layer yields two equations,

$$\begin{aligned} u_U(H-d) &= U(H-h), \\ u_L d &= Uh, \end{aligned} \tag{7}$$

and the conservation of momentum along with the assumption that pressure along AB and CD is hydrostatic, yields

$$(p_D - p_C)\,H + \frac{1}{2}g\,(\rho_L - \rho_U)\left(d^2 - h^2\right) = U^2\,(d-h)\left(\rho_L \frac{h}{d} - \rho_U \frac{H-h}{H-d}\right). \tag{8}$$

In this case however we do not have a relation between p_D and p_C as we did in the free surface case when $p_D = p_C$. Because of this we need an additional condition to close the problem. Here we outline three approaches; two which invoke energy conservation in either the upper or lower layer, and a third approach proposed only recently in 2013 which uses a vortex sheet model to estimate vorticity flux of out the domain and thereby form a relation between the difference in velocities and the height of the layers.

3.1 Energy conservation in the upper layer

This approach was considered by Chu and Baddour in 1977 [4] and Wood and Simpson in 1984 [13]. If we presume that energy is conserved in the lighter upper fluid layer, we can alternatively conserve energy flux or apply Bernoulli's theorem between points C and D

(which is less algebraically intensive). Either of these give a relation between p_C and p_D, yielding

$$\frac{U^2}{g'H} = \frac{d(d+h)(H-d)^2}{H^2(2Hh+d^2-3dh)}. \tag{9}$$

Since energy is assumed to be conserved in the upper layer, this solution matches the free-surface solution in the limit $\rho_U \to 0$. However in the gravity current limit when $h/H \to 0$ we find that $U^2/g'H = (H-d)^2/H^2$, which does not match the gravity current solution except in the energy conserving case when $d/H = 1/2$ and $U^2/g'H = 1/4$.

3.2 Energy conservation in the lower layer

Klemp, Rottuno, and Skaworok in 1997 [8] observed that they obtained a closer match to experimental results by conserving energy in the heavier lower layer. Similar to the previous scenario we may either conserve energy flux in the layer or apply Bernouilli along the lower boundary between A and B, yielding

$$\frac{U^2}{g'H} = \frac{2d^2(H-d)^2}{H^2\left(2H(d+h)-2dh\right)}. \tag{10}$$

This solution fails in the free surface limit but produces a better match to experimental results overall.

3.3 Model for vorticity created in mixing layer

A third approach taken by Borden and Meiburg in 2013 [2] is to use the vorticity equation, which eliminates pressure and therefore requires only a model for the vorticity flux in the control volume to form a relationship between the velocities of each layer and their height. The steady, inviscid, 2D vorticity equation can be written

$$\mathbf{u} \cdot \nabla \omega = -g' \frac{\partial \rho^*}{\partial x}, \tag{11}$$

where $g' = g(\rho_U - \rho_L)/\rho_L$ is the reduced gravity and $\rho^* = (\rho - \rho_L)/(\rho_U - \rho_L)$ is a relative non-dimensional density. Integrating over the control volume and applying the divergence theorem yields

$$\oint \omega \left(\mathbf{u} \cdot \mathbf{n}\right) \mathrm{d}\ell = -\int g' \frac{\partial \rho^*}{\partial x} \, \mathrm{d}A. \tag{12}$$

If we presume that the density in the control volume is everywhere constant except for a very small region surrounding the front itself, the baroclinic term becomes

$$-\int g' \frac{\partial \rho^*}{\partial x} \, \mathrm{d}A = -g'(d-h). \tag{13}$$

For the integral of vorticity flux over the boundary, we assume that vorticity is zero along the boundary except at the interface between the two fluids downstream of the front. Here we estimate the vorticity with a vortex sheet model such that vorticity is concentrated in a

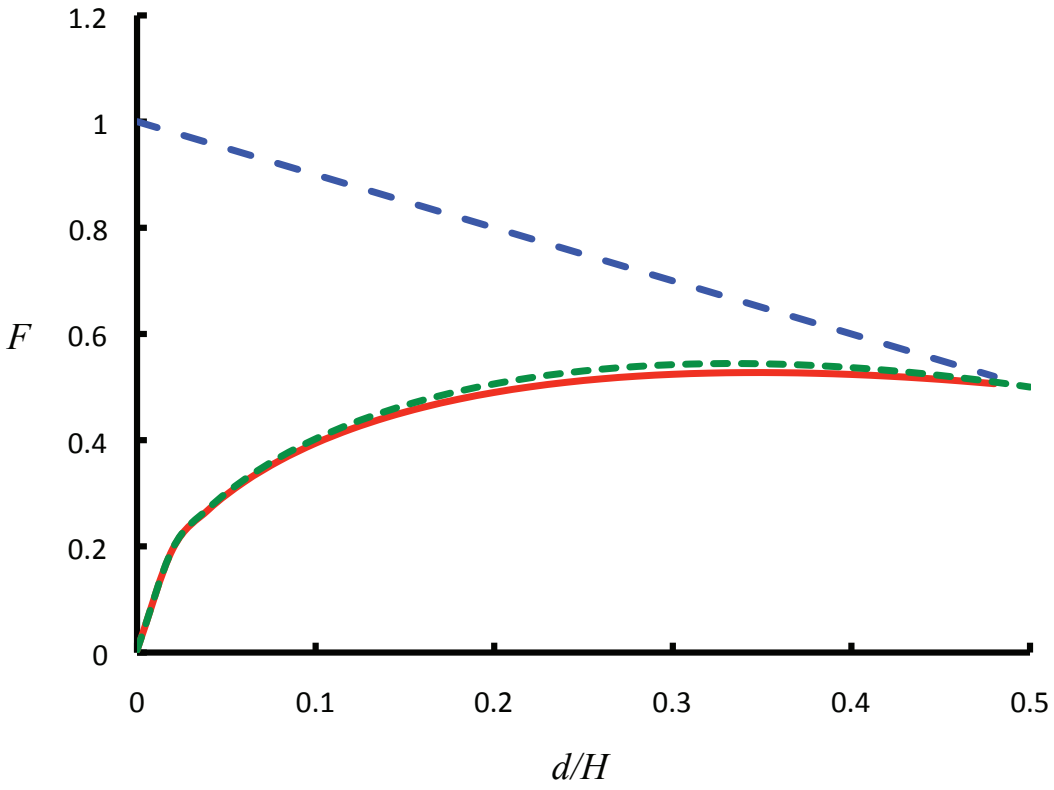

Figure 6: Gravity current speed derived from the limit $h/H \to 0$ for the theories of WS (dashed blue line) [13], KRS (dashed green line) [8] and Borden and Meiburg (solid red line) [2].

thin region on the interface between the two fluids where $\omega = u_U - u_L$ and $u = (u_U + u_L)/2$. These assumptions yield an relation between the velocities of the layers and their heights,

$$\frac{1}{2}\left(u_U^2 - u_L^2\right) = g'\left(d - h\right), \tag{14}$$

which implies

$$\frac{U^2}{g'H} = \frac{2d^2\left(H - d\right)^2}{hH\left(H\left(d + h\right) - 2dh\right)}. \tag{15}$$

It is interesting to note that this solution differs from the solution assuming conservation of energy in the lower, heavier layer only by a factor H/h. The solutions given by the three approaches are compared for the gravity current limit when $h/H \to 0$ in Figure 6, for the speed of the bore as a function of downstream depth d/H in Figure 7, and for the emerged dissipated across the bore in Figure 8.

Additional comparison can be made with two-dimensional numerical simulations carried about by [2]. These results are shown in Figure 9 where the vorticity predicted by a vortex sheet model $\Omega^* = (u_U - u_L)^2/2g'h$ for each method is compared with the vorticity calculated

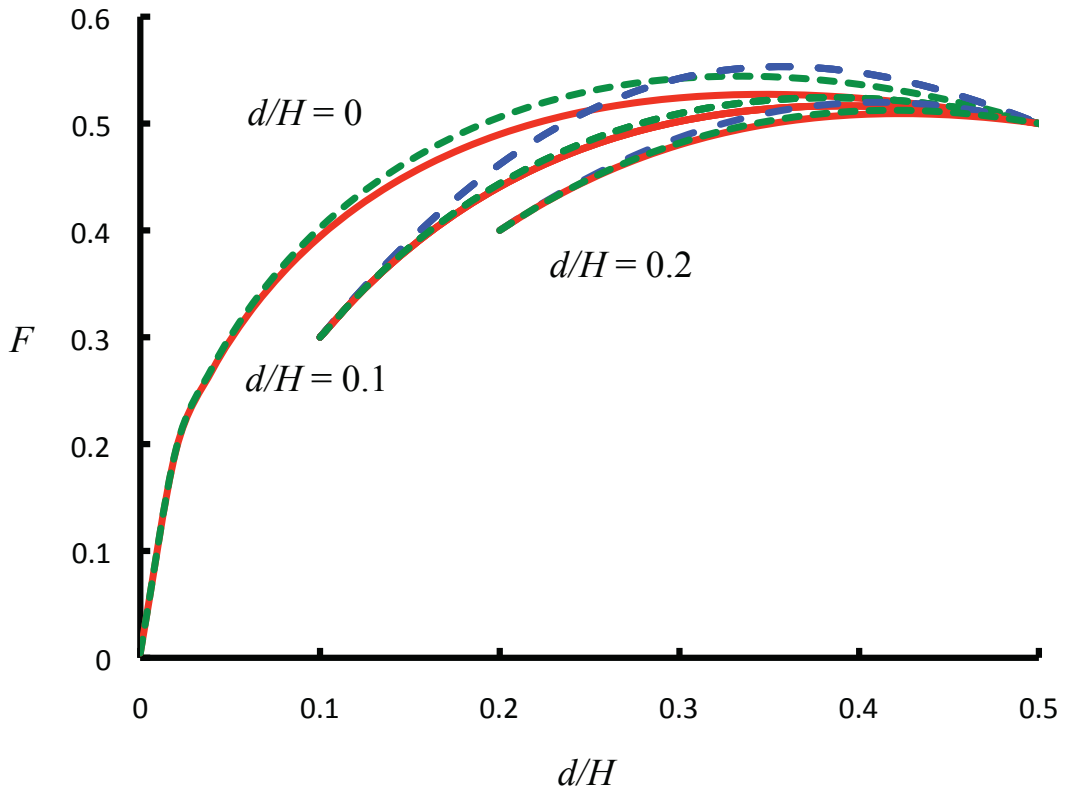

Figure 7: Bore speed as a function of downstream depth d/H for various h/H (erroneously denoted as d/H in center of the figure) for the theories of WS (dashed blue line) [13], KRS (dashed green line) [8] and Borden and Meiburg (solid red line) [2]

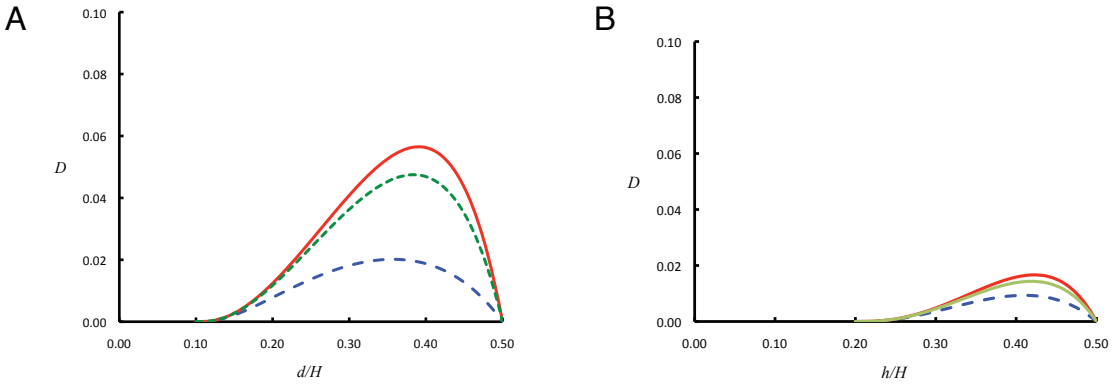

Figure 8: Dissipation across the bore as a function of (A) downstream height d/H and (B) upstream height h/H for the theories of WS (dashed blue line) [13], KRS (dashed green line) [8] and Borden and Meiburg (solid red line) [2].

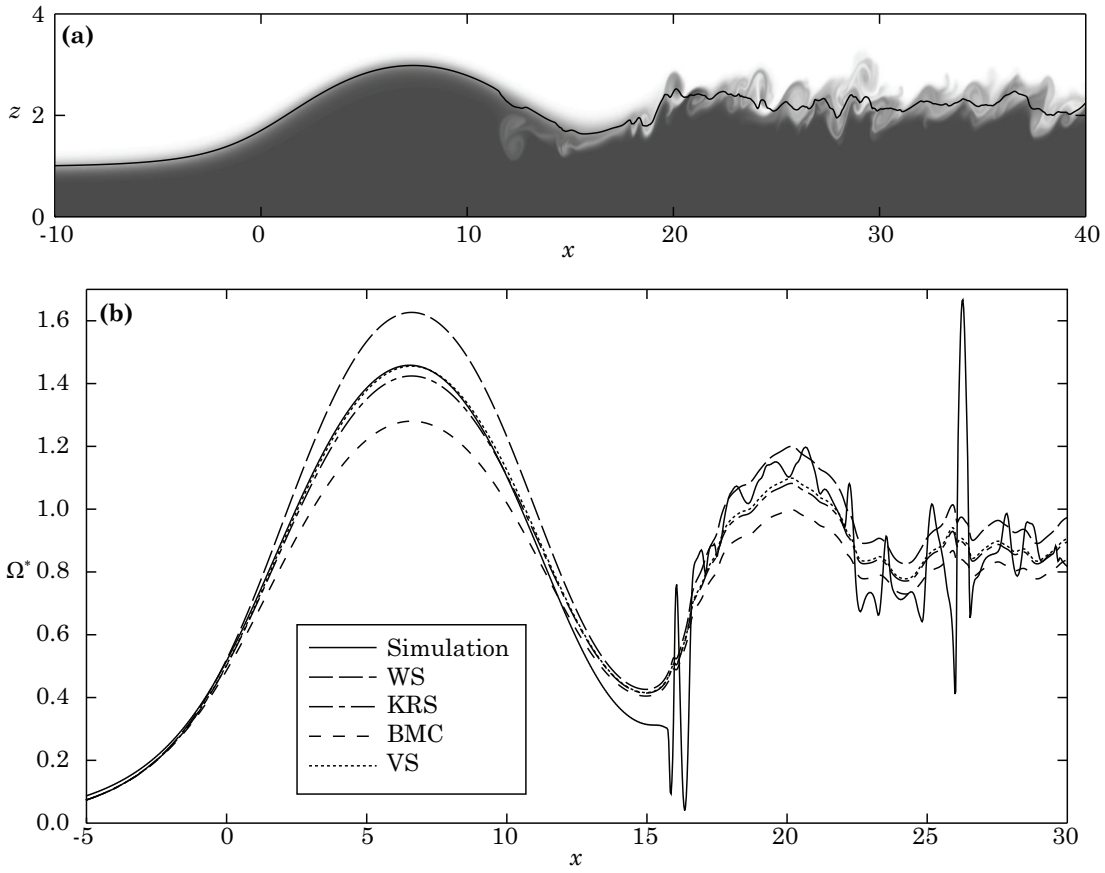

Figure 9: (a) Density field of a DNS simulated bore. (b) A comparison of measured and predicted vorticity from DNS simulations and theories. VS denotes the vortex sheet model proposed by Borden and Meiburg [2]. From [2].

in the simulations. In Figure 10 images taken from a lock exchange experiment are shown; the data from this experiment is shown in Figure 11.

4 Non-Boussinesq Gravity Currents

4.1 Non-Boussinesq Lock Exchange

As we have concluded from Benjamin's theory in Lecture 3, the Froude numbers for heavy and light currents in non-Boussinesq lock exchange are, respectively:

$$F_H = \frac{1}{\gamma} f\left(\frac{h}{H}\right), \tag{16}$$

and

$$F_H = f\left(\frac{h}{H}\right), \tag{17}$$

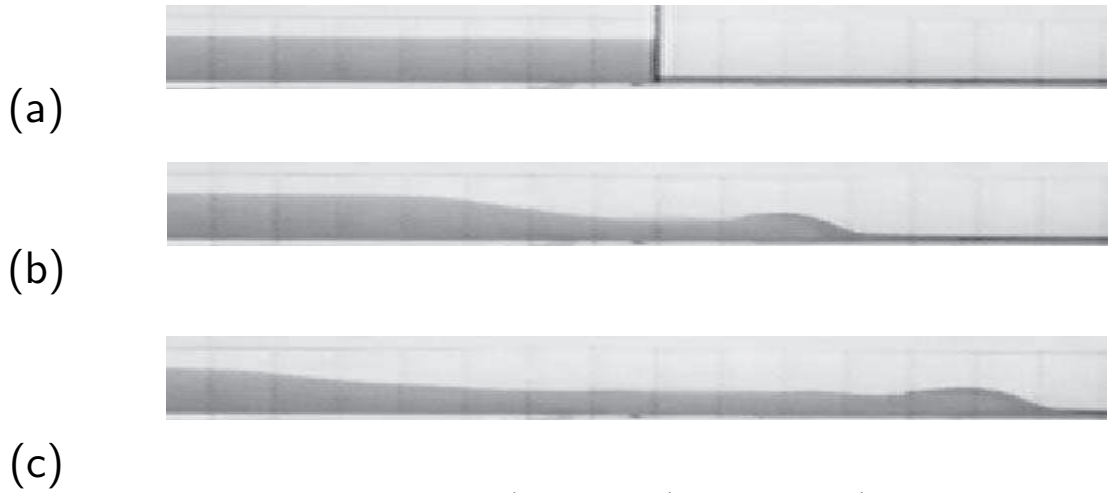

Figure 10: Lock exchange internal bore. (a) initial configuration $t^* = 0$, (b) $t* = 4.6$, and (c) $t^* = 9.5$, where the dimensionless time is $t^* = t\sqrt{H/g'}$. In the initial configuration fractional depths are $D/H = 0.79$ and $L/H = 0.25$. From [11].

where h is the depth of the current, H is the depth of the channel, $\gamma = \rho_U/\rho_L$ is the ratio of densities between the two fluids, and $f(h/H)$ is an unknown function. Since for the non-Boussinesq flows $\gamma < 1$, the heavier fluid travels faster than the lighter fluid. This phenomenon has also been observed in experiments; Figure 12(a) shows the movement of the heavy and light fronts over time after the lock has been removed for an experiment with $\gamma = 0.681$. As time progresses, the heavy front travels further than the lighter front, disturbing the symmetry about the lock observed in Boussinesq lock exchange experiments. This asymmetry becomes even more pronounced as the density difference between the two fluids increases, i.e. γ decreases. The difference in the position of each front relative to the lock is shown in Figure 12(b), with open circles for light front and filled circles for the heavy front. The plots are linear for both heavy and light front, as both are travelling at constant speed (constant velocity phase, see Lecture 2), but the heavier front travels at a greater velocity.

In addition to difference in flow velocities, the light fluid looks more like a Boussinesq flow in an energy conserving case (see Lecture 3): it is more stable and occupies about half of the total channel depth H, while the heavy fluid flow is more unstable and its depth is less uniform, not consistently occupying half of the total channel depth H. This difference is explained through flux imbalance in the schematic in Figure 13. Initially both currents occupy half of the channel depth, and since the heavier fluid is travelling at a greater velocity than the lighter fluid, $Q_1 < Q_2$. In the upper fluid layer, there is a greater supply of the light fluid coming in from the right of the lock than the amount of lighter fluid carried by the light front, creating enough pressure to sustain the upper fluid at half the channel depth. However, for the heavier fluid layer on the bottom, there is an insufficient supply of heavy fluid coming in from the left of the lock compared with the amount carried by the heavy front, so the heavy current eventually cannot be sustained at half the channel depth.

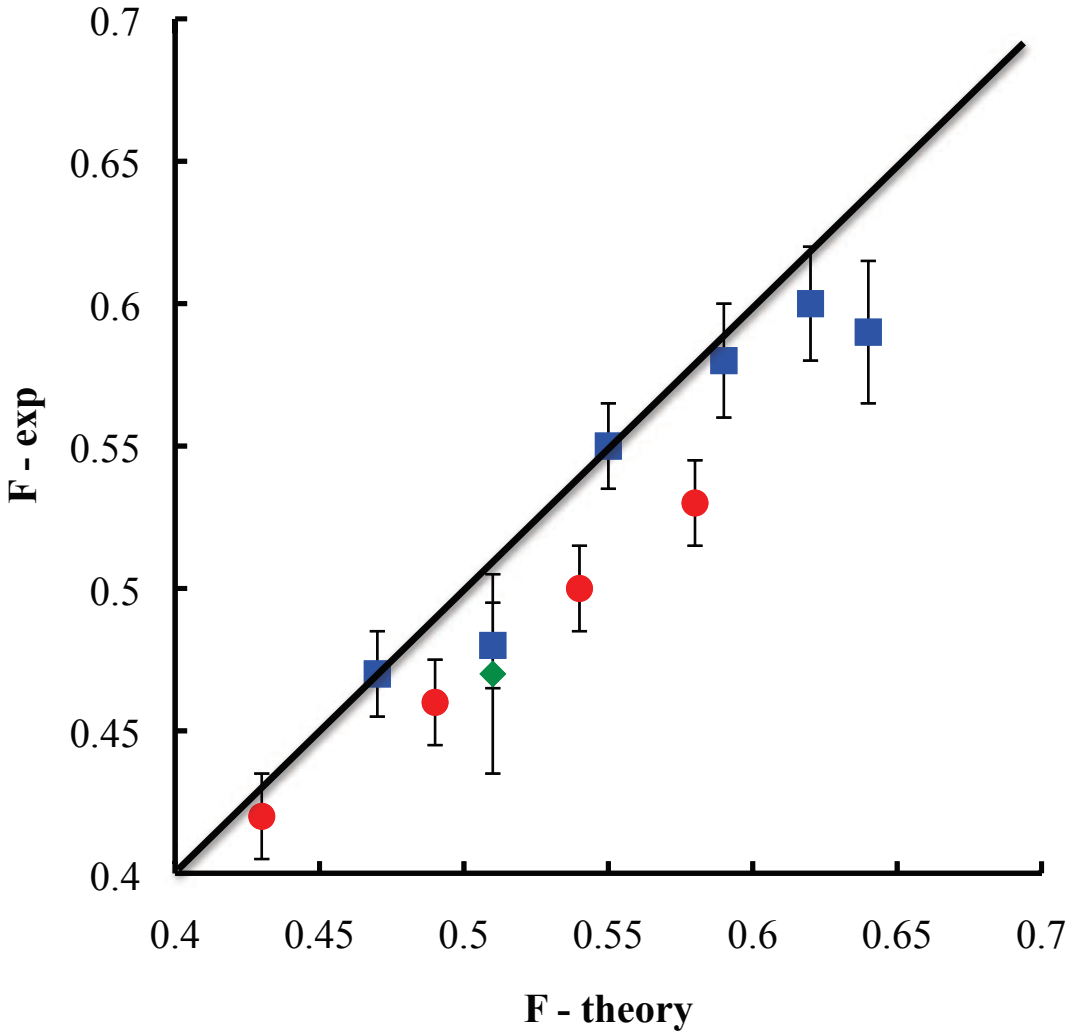

Figure 11: The speed of lock exchange internal bores expressed as Froude numbers. The data are coded according to the depth ahead of the current: squares are for $L/H = 0.1$; circles for $L/H = 0.25$ and diamonds for $L/H = 0.4$. Data from [11].

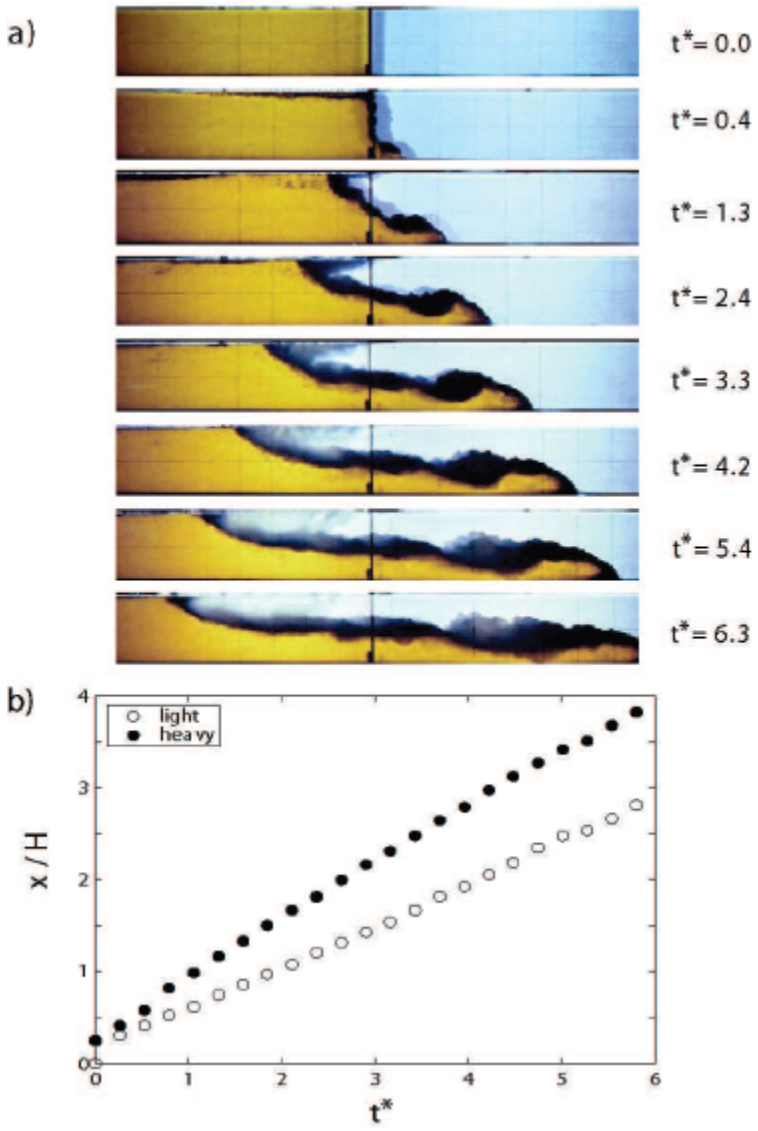

Figure 12: Non-Boussinesq lock exchange with $\gamma = 0.681$. (a) Sequence of shadowgraph images, (b) plot of horizontal position from the lock gate as a function of time; heavy front - filled circles, light front - open circles [9].

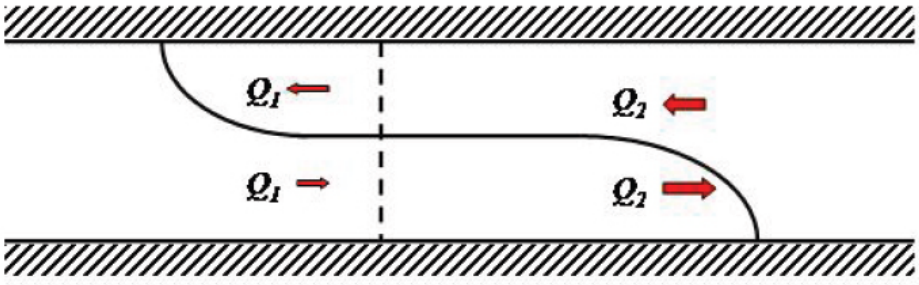

Figure 13: Schematic showing the flux imbalance in a non-Boussinesq lock exchange. $Q_1 < Q_2$ because the heavy current travels faster than the light current, and both currents occupy half the channel depth. As a result, there is enough pressure from the right to sustain the light current at half the channel depth, but not enough pressure to sustain the heavy current at half the channel depth.

4.2 Non-Boussinesq bores and expansion waves

Two possible schematics for non-Boussinesq flows are shown below in Figure (14). In the first scenario (Figure 14(a)), there are two energy-conserving currents that occupy half of channel depth each: left-propagating light current and right-propagating heavy current, which are connected by a long expansion wave and a bore. In the second scenario (Figure 14(b)), the energy-conserving light current, which propagates to the left, is connected by an expansion wave to a shallow dissipative heavy current, which propagates to the right. In Lecture 2, we have seen that a bore can travel faster than the heavy front, so once the bore catches up with the front, the flow schematic results in the second scenario.

The flow depth and the speed of the expansion wave can be obtained using shallow water theory for a 2-layer system by solving the following system of PDEs by the method of characteristics:

$$\begin{aligned} \frac{\partial h_L}{\partial t} + \frac{\partial}{\partial x}(h_L u_L) &= 0, \\ \frac{\partial u_L}{\partial t} + a\frac{\partial u_L}{\partial x} + b\frac{\partial h_L}{\partial x} &= 0, \end{aligned} \tag{18}$$

where $h_L(x,t)$ is the current depth, $u_L(x,t)$ is the current speed, and a is defined

$$a = \frac{u_L(h_U - \gamma h_L) + 2\gamma u_U h_L}{\gamma h_L + h_U}. \tag{19}$$

Figure 15 shows the speed u_L of the expansion wave in the lower fluid layer as a function of h/H for different γ values. As the lower fluid layer occupies closer to half of the channel depth, the velocities of the expansion waves roughly converge. However, as the flow becomes shallower (h/H decreases), the expansion wave travels faster for larger γ values.

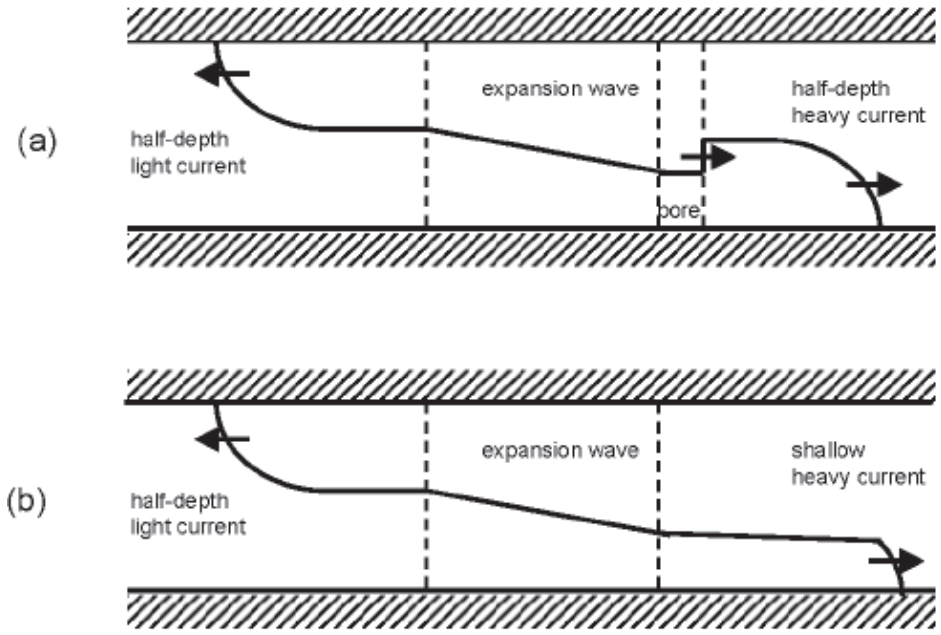

Figure 14: Diagram of two types of lock exchange flows: (a) left propagating energy-conserving light current, and right propagating energy conserving heavy current, connected by a long expansion wave and a bore; (b) left propagating energy-conserving light current, and right propagating dissipative heavy current connected by an expansion wave.

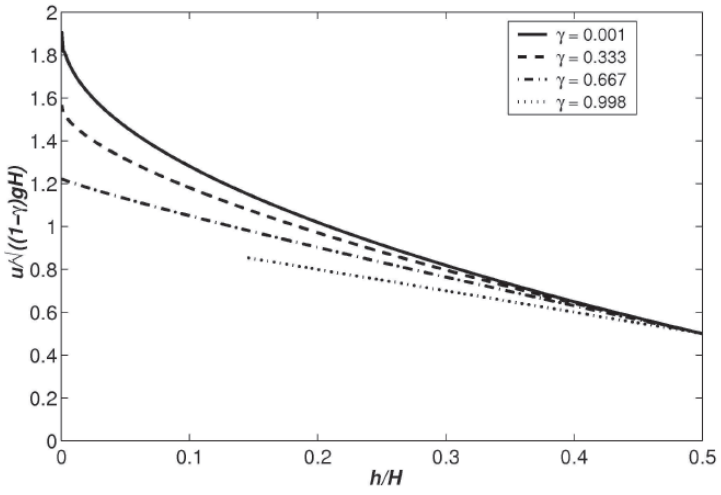

Figure 15: Speed u_L in the lower layer in the expansion wave as a function of lower layer depth h_L for different γ values.

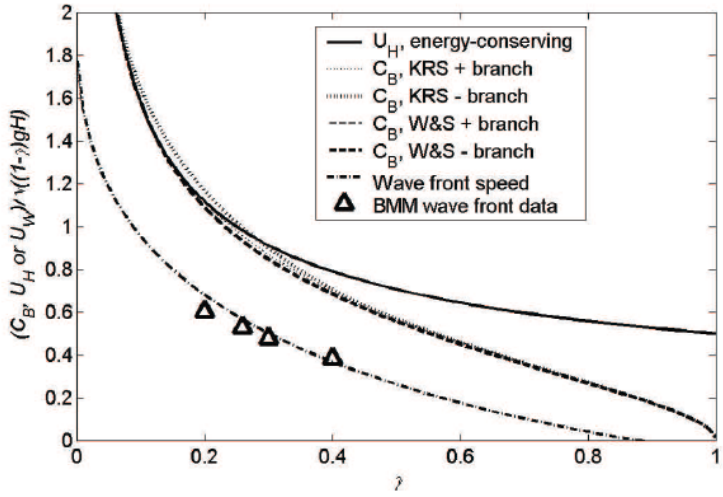

Figure 16: Bore speeds C_B computed using two theories, KRS (dotted lines) [8] and WS (dashed lines) [13] compared with U_H, the energy-conserving heavy gravity current speed (solid line) as a function of γ. The dash-dot line is the theoretical expansion wave front speed, which is lower than the bore speed for all γ values.

Furthermore, the bores speeds can be computed using either the Klemp, Rottuno, and Skamarock (KRS) model [8] or the Wood and Simpson (WS) model [13], both of which are not accurate in certain limits, as discussed in the first part of this lecture. Nonetheless, the bore speeds from these models (4 dashed lines) are compared with the flow velocity of energy-preserving right-propagating heavy front (solid line), and expansion wave velocity (dot-dashed line) for different γ values in Figure 16. This figure shows that for $\gamma > 0.3$, the bore travels slower than the energy-preserving heavy front, thus maintaining the schematic (a) in Figure 14. However, for γ values less than approximately 0.3, the bore velocity from positive branch of the KRS model is greater than the energy-preserving heavy front velocity, and the other bore velocities are very close to the energy-preserving heavy front velocity. Therefore, the bore can potentially travel faster than the heavy front for sufficiently small γ values, so that the flow schematic results in case (b) in Figure 14. Figure 16 also shows that the expansion wave speed is lower than that of a bore and of an energy-preserving heavy front, thus adhering to the schematics in Figure 14.

As for the velocity of the light front, both experimental and numerical results conclude that it travels roughly at the speed of the energy-preserving front, independent of the γ values. These results are shown in Figure 17, where the solid line is the theoretical speed of energy-preserving front, and triangles are numerical simulation results [1], and other markers are experimental results. These results also agree with energy-preserving scenario, since the front height is approximately half of the channel width, as predicted from the theoretical derivations, which is shown in Figure 18.

Unlike the light front, the velocity and the height of the heavy front cannot be predicted by the energy-preserving theory. Figure 19 shows the numerical (triangles) [1] and experi-

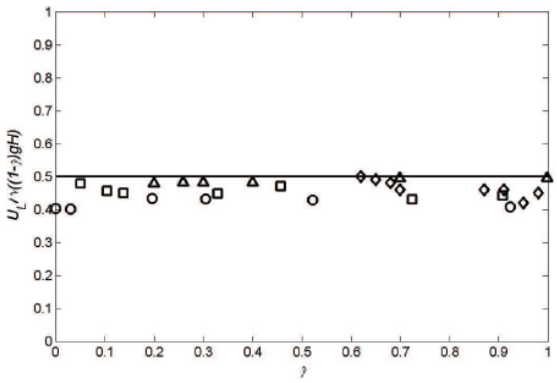

Figure 17: Light current speed: comparison of theoretical front speed (solid line) and numerical [1] and experimental measurements [6, 7] of U_L, as a function o γ.

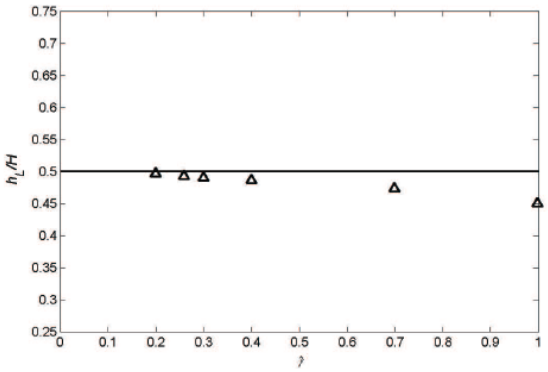

Figure 18: Light current speed: comparison of theoretical front height (solid line) and numerical measurements (triangles) of H_L [1], as a function of γ.

mental (other markers) [9, 6, 7] results for the heavy front velocities for different γ values compared with the energy-preserving front velocities (dashed line), front velocities for KRS bore model [8] (Figure 14(a) scenario, solid line), and front velocities for dissipative gravity current (Figure 14(b) scenario, dotted line). For $\gamma < 0.55$, the heavy front velocities are less than the ones predicted by the energy-preserving theory; and although the other two theories also overestimate the heavy front velocities, they produce better approximations than the energy-preserving theory. This fact is better illustrated in Figure 20, which shows the heavy front heights as a function of γ from the above theories and numerical and experimental results. The front height approaches $H/2$, value predicted by the energy-preserving theory, only when γ is very close to 1 (Boussinesq case). However, for smaller γ values the front height can be fairly well predicted by both the KRS bore theory (solid line) and the dissipative gravity current theory (dotted line), indicating that both configurations in Figure 14 are possible. In reality, in the experimental and numerical work, it is difficult to visually identify the presence of a bore. To illustrate this point, one can compare the outlines of a theoretical shape of the flow with a bore (top) and without a bore (bottom) overlaid on top of an outline (dotted) of the computed gravity current for $\gamma = 0.7$ in Figure 21.

4.3 Stability of non-Boussinesq gravity current

Using the linear stability theory, we can also calculate the wave number k for the interface between the heavy and the light gravity currents by solving:

$$\frac{\partial^2 \phi_i}{\partial x^2} + \frac{\partial^2 \phi_i}{\partial z^2} = 0, \tag{20}$$

where $i = 1$ for the upper lighter layer and $i = 2$ for the lower heavier layer, and the interface can be expressed as:

$$\phi = \hat{\phi}(z) e^{ik(x-ct)}. \tag{21}$$

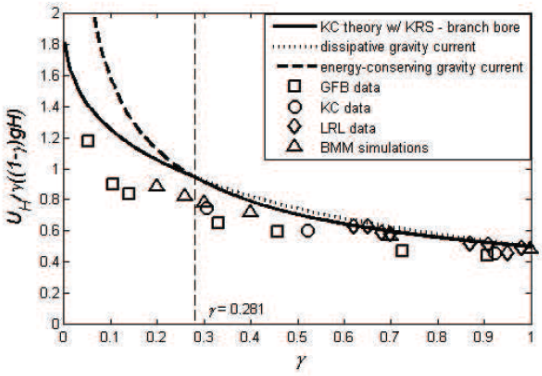

Figure 19: Heavy current speed: comparison of theoretical front speed (solid line) and numerical [1] and experimental [9, 6, 7] measurements of U_H, as a function o γ.Energy-conserving case is plotted as a line, bore-configuration theory is solid line [8], and dissipative gravity current (without a bore) is a dotted line.

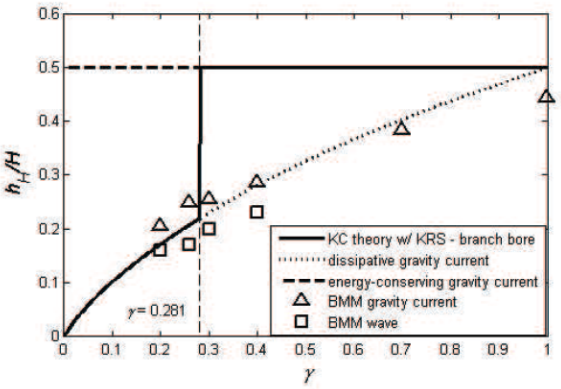

Figure 20: Heavy current speed: comparison of theoretical front height (solid line) and numerical measurements (triangles) of H_H, as a function of γ. Key is the same as in Figure 19.

Plugging Equation (21) into Equation (20), we obtain:

$$\frac{d^2\hat{\phi}_i}{dz^2} - k^2\hat{\phi}_i = 0, \tag{22}$$

which solving for ϕ_i yields $\hat{\phi}_i = A_i \cosh(kz) + B_i \sinh(kz)$. Now assuming that the depth of the upper layer is H_1 and of the lower layer is H_2 and that the interface is at $z = 0$, we apply the 4 boundary conditions to solve for the 4 unknown coefficients. First, at $z = H_1, H_2$

$$\frac{d\hat{\phi}_i}{dz} = 0, \tag{23}$$

such that

$$\frac{d\hat{\phi}_1}{dz} = kA_1 \sinh(H_1 k) + kB_1 \cosh(H_1 k) = 0, \tag{24}$$

and

$$\frac{d\hat{\phi}_2}{dz} = kA_2 \sinh(-H_2 k) + kB_2 \cosh(-H_2 k) = 0. \tag{25}$$

Next, at the interface ($z = 0$), it must hold that

$$\frac{d\hat{\phi}_1}{dz} = \frac{d\hat{\phi}_2}{dz}, \tag{26}$$

such that

$$kA_1 \sinh(0) + kB_1 \cosh(0) = kA_2 \sinh(0) + kB_2 \cosh(0),$$

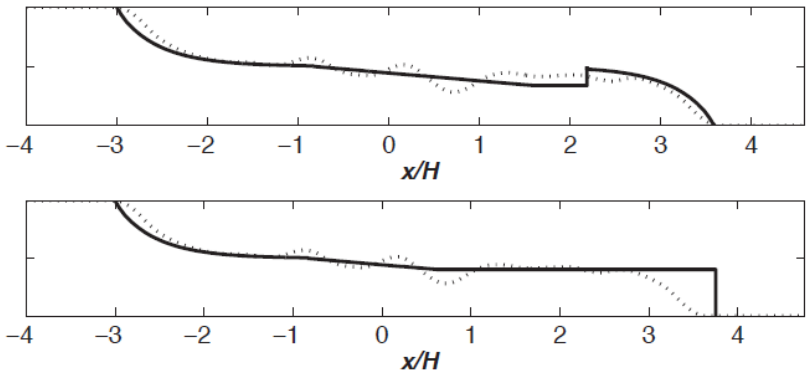

Figure 21: Theoretical interface shape (solid line) compared with computed shape (dotted line) from simulations with the top figure using theory with a bore (energy-preserving heavy gravity current), and the bottom figure using theory without a bore (dissipative heavy current).

yielding

$$B_1 = B_2. \tag{27}$$

Finally, the pressure at the interface also must be equal. In this case, the pressure is expressed as $p_i = g\rho_i z + \rho_i \frac{\partial \phi_i}{\partial t}$, so if $p_1 = p_2$ at $z = 0$, then

$$\begin{aligned} \rho_1 \hat{\phi_1}(0)(-ikc)e^{ik(x-ct)} &= \rho_2 \hat{\phi_2}(0)(-ikc)e^{ik(x-ct)}, \\ \implies \rho_1 \hat{\phi_1}(0) &= \rho_2 \hat{\phi_2}(0), \\ \implies \frac{\rho_1}{\rho_2} = \gamma &= \frac{\hat{\phi_1}(0)}{\hat{\phi_2}(0)} = \frac{A_1}{A_2}. \end{aligned} \tag{28}$$

Now, forming a linear system with 4 equations and 4 unknowns (A_1, B_1, A_2, B_2), we can find an expression such that the determinant of the coefficient matrix is equal to zero, yielding an expression that relates the wave number k and γ,

$$\tanh(kH_1) + \gamma \tanh(kH_2) = \frac{\gamma}{1-\gamma} \frac{(U_1 - U_2)^2}{g/k}. \tag{29}$$

Figure 22 shows the regions of stability for the light and heavy gravity currents for different γ and k values. The light gravity current has an increasingly greater stability region for smaller γ values, even at a high wave number.

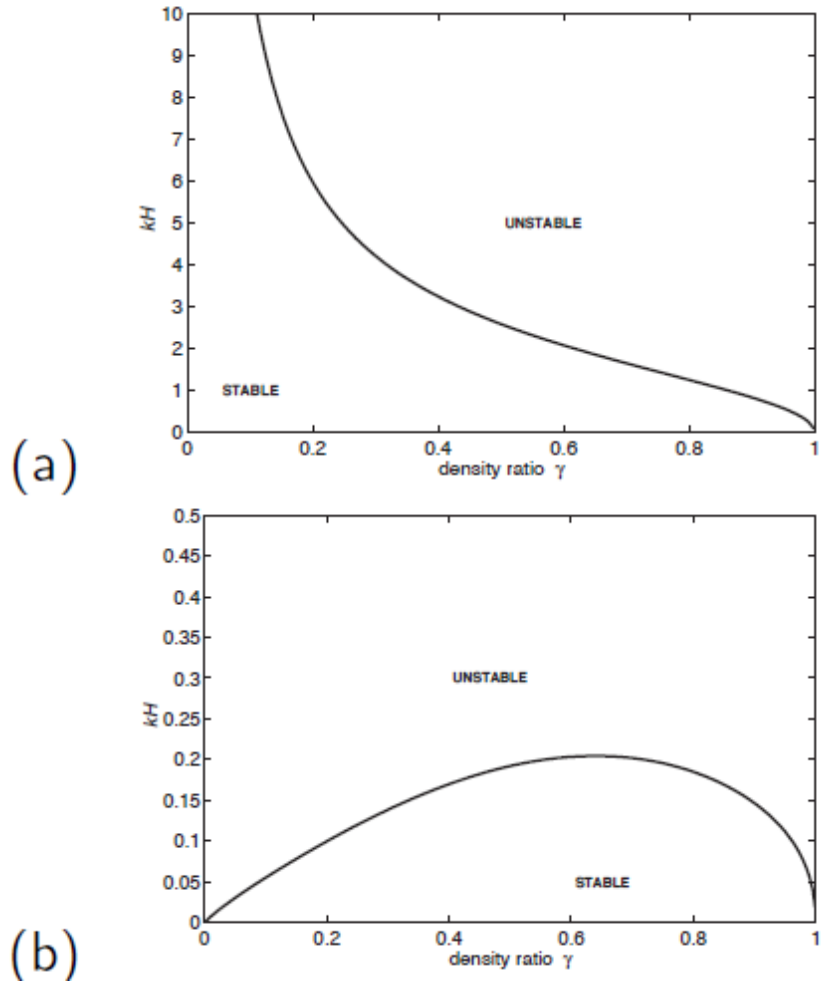

Figure 22: Wavenumber k as a function of γ for which the gravity current interface is neutrally stable according to linear stability theory; (a) light gravity current, (b) heavy gravity current.

References

[1] V. Birman, J.E. Martin, and E. Meiburg, *The non-boussinesq lock exchange problem. part 2. high resolution simulations.*, J. Fluid Mech., 537 (2005), pp. 125–144.

[2] Z Borden and E. H. Meiburg, *Circulation-based models for boussinesq internal bores*, J. Fluid Mech., 726, R1 (2013), pp. 1–11.

[3] J.W.M. Bush and J.M. Aristoff, *The influence of surface tension on the circular hydraulic jump*, J. Fluid Mech., 489 (2003), pp. 229–238.

[4] V. H. Chu and R. E. Baddour, *Surges, waves and mixing in two-layer density stratified flow*, in Proc. 17th Congr. I. A. H. R., vol. 1, 1977, pp. 303–310.

[5] T. Foglizzo, F. Masset, J. Guilet, and G. Durand, *Shallow water analogue of the standing accretion shock instability: Experimental demonstration and an two-dimensional model*, Phys. Rev. Lett., 108 (2012).

[6] H. P. Gröbelbauer, T. K. Fanneløp, and R. E. Britter, *The propagation of intrusion fronts of high density ratios*, J. Fluid Mech., 250 (1993), pp. 669–687.

[7] J. J. Keller and Y.-P. Chyou, *On the hydraulic lock exchange problem*, J. Appl. Math. Phys., 42 (1991), pp. 874–909.

[8] J. B. Klemp, R. Rottuno, and W. C. Skamarock, *On the propagation of internal bores*, J. Fluid Mech., 331 (1997), pp. 81–106.

[9] R. J. Lowe, J. W. Rottman, and P. F. Linden, *The non-Boussinesq lock exchange problem. Part 1. Theory and experiments*, J. Fluid Mech., 537 (2005), pp. 101–124.

[10] J. W. Rottman and J. E. Simpson, *Gravity currents produced by instantaneous release of a heavy fluid in a rectangular channel*, J. Fluid Mech., 135 (1983), pp. 95–110.

[11] J. O. Shin, *Colliding Gravity Currents*, PhD thesis, University of Cambridge, 2002.

[12] R. J. Trapp, *Mesoscale-convective processes in the atmosphere*, Cambridge University Press, 2013.

[13] I. R Wood and J. E. Simpson, *Jumps in layered miscible fluids*, J. Fluid Mech., 140 (1984), pp. 329 – 342.

GFD 2013 Lecture 6: Stratified Environments

Paul Linden; notes by Tobias Bischoff and Catherine Jones

June 24, 2013

1 Introduction

Buoyancy driven flows in stratified environments occur frequently in the real world. For example, when rivers flow into the ocean, the fresh river water floats and forms a gravity current within the stratified ocean. Another example the dust plume from the eruption of

Figure 1: The eruption of Eyjafjallajökull.

Eyjafjallajökull (Fig. 1), in which the hot, dust laden air rose until it reached the height of the air in the atmosphere with the same density and was then interleaved into the air column due to the stratification. This lecture explores the interleaving of intermediate density fluid into stratified fluid.

2 Intrusion in a two-layer fluid

As a simple example, we consider an intrusion in a two-layer fluid. Fig. 2 shows the conceptual setup. A layer of density ρ_i, where $\rho_U < \rho_i < \rho_L$, intrudes at the interface between the surface layer (density ρ_U) and the bottom layer (density ρ_L). Part of the intrusion flows in at a height above the two-layer interface and the other part penetrates below the interface.

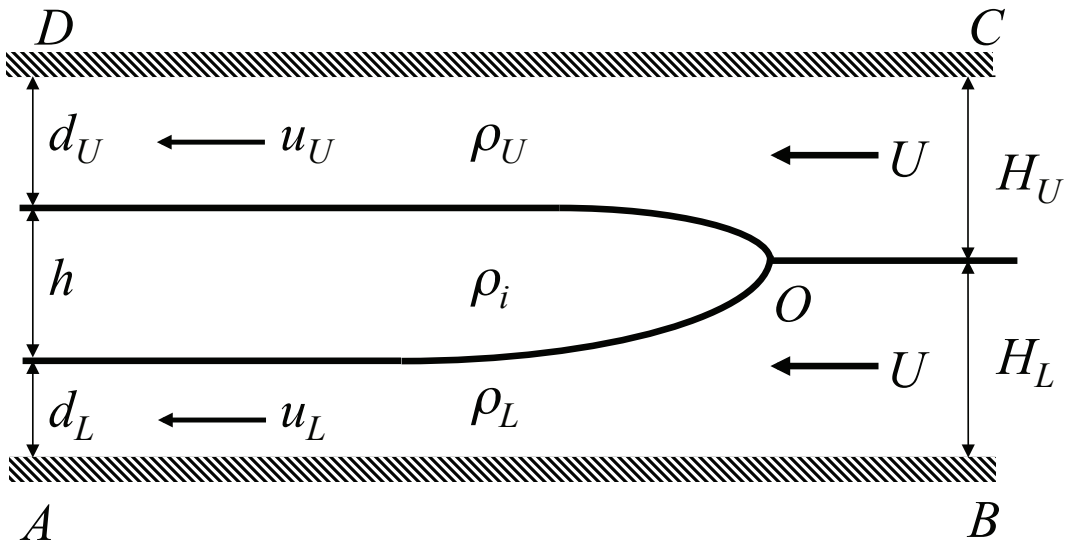

Figure 2: Schematic of an intrusion into a two-layer fluid. The density of the intrusion is ρ_i, where $\rho_U < \rho_i < \rho_L$, and in this frame of reference the intrusion is at rest.

In this example, it is useful to define three reduced gravities,

$$g'_{iU} = \frac{g\,(\rho_i - \rho_U)}{\rho_0} \tag{1a}$$

$$g'_{Li} = \frac{g\,(\rho_L - \rho_i)}{\rho_0} \tag{1b}$$

$$g'_{LU} = \frac{g\,(\rho_L - \rho_U)}{\rho_0} = g'_{iU} + g'_{Li}. \tag{1c}$$

These are reduced gravities for the three possible combination of the densities and are used in the following analysis.

2.1 The doubly symmetric case

The most obvious special case is a symmetric intrusion about the two-layer interface, where the intrusion density is the average of the layer densities. In this so-called doubly symmetric case we have

$$H_L = H_U = \frac{H}{2} \tag{2a}$$

$$\rho_i = \frac{\rho_U + \rho_L}{2}. \tag{2b}$$

This case is analogous to two gravity currents: a bottom current and a top current. Dimensional analysis yields that the front speed of the intrusion,

$$U = F\sqrt{\frac{g'_{iU}H}{2}} = \frac{1}{2}F\sqrt{g'_{LU}H}. \tag{3}$$

2.2 The general case

The general case is more complicated, with dimensional analysis giving

$$U = F\sqrt{g'_{iU}H}\, f\left(\frac{g'_{iU}}{g'_{Li}}, \frac{H_U}{H_L}\right), \tag{4}$$

where f is an arbitrary function of the dimensionless numbers $\frac{g'_{iU}}{g'_{Li}}$ and $\frac{H_U}{H_L}$. If we approach the problem from the viewpoint of Benjamin analysis and conserve mass, momentum and energy as in lecture 3, we can reduce the problem to two equations in two unknowns. They are nonlinear, and have multiple solutions. The equations and their solutions are described by Holyer and Huppert(1980) [1].

2.3 Equilibrium intrusions

We define equilibrium intrusions so that the fronts of the upper and lower component of the intrusion travel at the same speed, as in Fig. 2. We can construct an approximation for the relative heights of the layers and the density of the intrusion required for this situation to occur. Mass conservation requires

$$u_U d_U = U H_U \tag{5a}$$

$$u_L d_L = U H_L. \tag{5b}$$

Combining these with the equations of Holyer and Huppert gives

$$g'_{iU}\left(H_U - d_U\right) = g'_{Li}\left(H_L - d_L\right), \tag{6}$$

and

$$\frac{(H_U - d_U)}{H_U} = \frac{(H_L - d_L)}{H_L}. \tag{7}$$

We can use this simple constraint on the relative heights in the upper and lower part of the equilibrium intrusion problem to calculate a dynamical constraint on the intrusion density ρ_i. By resubstituting Eq. (7) into Eq. (6) we can obtain an equation that is linear in ρ_i so that

$$\rho_i = \frac{\rho_U H_U + \rho_L H_L}{H_U + H_L}. \tag{8}$$

This means that for equal velocities in the upper and lower part of the intrusion layer to be dynamically consistent with the density layering, we need to have an intrusion density that is the density layer height-weighted arithmetic mean of the upper and lower densities. Given the densities ρ_U, ρ_L and ρ_i, we can define h_E to satisfy Eq. (8) when $H_L = h_L$,

$$\hat{h}_E = \frac{h_E}{H} = \frac{g'_{iU}}{g'_{Li}}. \tag{9}$$

This definition can be used to introduce the nondimensional speeds for intrusions at the surface, U_H, the bottom, U_O and for equilibrium intrusions, U_E. We have

$$U_H = F\sqrt{1-\hat{h}_E} \tag{10a}$$

$$U_O = F\sqrt{\hat{h}_E} \tag{10b}$$

$$U_E = F\sqrt{\hat{h}_E(1-\hat{h}_E)} \tag{10c}$$

2.4 Minimization of Available Potential Energy

We can derive the speed at which the intrusion penetrates the layered stratification from simple energy conservation. In this case, we envision a lock release experiment of a fluid of density ρ_i into a two-layer stratification. After the system has equilibrated, and under the assumption that the fluids have stayed unmixed, we end up with a three-layer configuration. We consider the setup shown in Fig. 3a, in which the available potential energy, E_a is

$$E_a = \frac{1}{2}g\alpha\left(1-\alpha\right)\left(\left(H^2-2H_LH\right)\rho_i - \left(H-H_L\right)^2\rho_U\right). \tag{11}$$

We minimize the available potential energy with respect to H_L. This gives

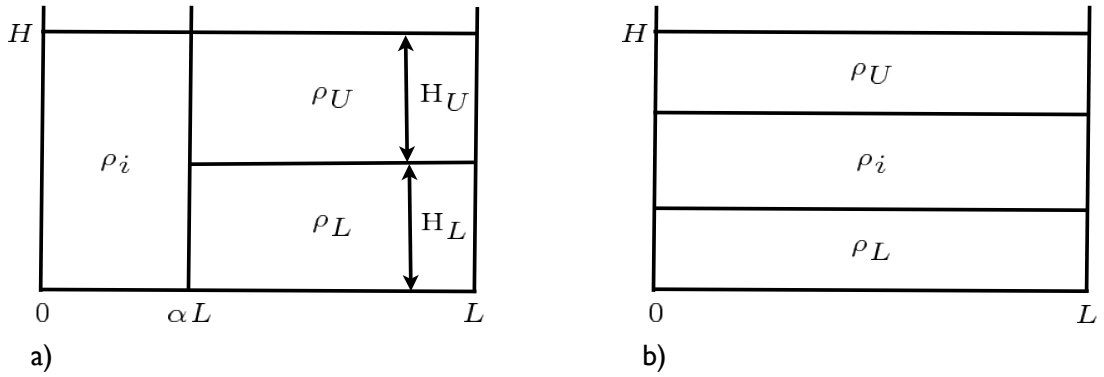

Figure 3: a) The initial setup and b) the final state.

$$\rho_i = \frac{\rho_U H_U + \rho_L H_L}{H}, \tag{12}$$

i.e. the equilibrium intrusion solution is identical to the case of minimum available potential energy. We turn again to the nondimensional velocity, which we define as an expansion in $\left(\hat{H_L} - \hat{h_E}\right)$ to second order,

$$\hat{U^2} = \hat{U_E}^2\left(a\left(\hat{H_L}-\hat{h_E}\right)^2 + b\left(\hat{H_L}-\hat{h_E}\right) + c\right). \tag{13}$$

When $\hat{H_L} = \hat{h_E}$, $\hat{U} = \hat{U_E}$, so $c = 1$. We can solve for a and b using Eq. (10a) when $\hat{H_L} = 1$ and Eq. (10b) when $\hat{H_L} = 0$. Expanding Eq. (13) gives

$$\hat{U} = F\sqrt{\hat{H_L}^2 - 2\hat{H_L}\hat{h_E} + \hat{h_E}}, \tag{14}$$

so when $H_L = \frac{1}{2}$, $\hat{U} = \frac{1}{2}F$, i.e., when $H_L = H_U$, the speed of the intrusion is the always same, no matter what its density is. An explanation for this can be found by looking at a

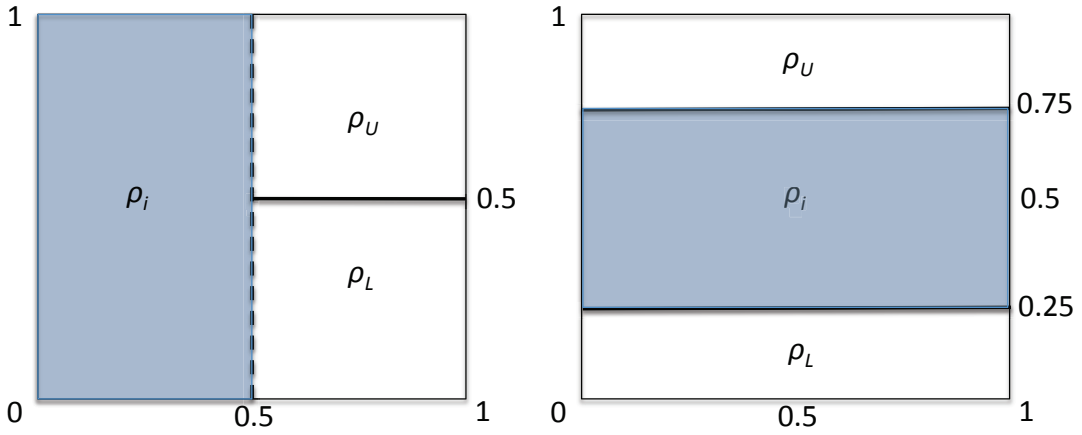

Figure 4: A special case of the setup shown above.

specific case of the setup, shown in Fig. 4 energy of the initial state is

$$\frac{1}{2}g\int_0^H \rho_i z \mathrm{d}z = \frac{1}{4}g\rho i H^2, \tag{15}$$

and the potential energy of the final state is

$$g\int_{\frac{H}{4}}^{\frac{3H}{4}} \rho_i z \mathrm{d}z = \frac{1}{4}g\rho i H^2, \tag{16}$$

i.e. the potential energy of the fluid in the intrusion does not change. This is equivalent to the height of the center of mass being conserved.

2.5 Multiple layer lock exchange

Let us consider the case of multiple layer lock exchange shown in Fig. 5. As before, we expect that

$$U \sim \sqrt{g'H}, \tag{17a}$$

$$\sim \sqrt{\delta\rho}, \tag{17b}$$

because this is just a multi-layer case of the interleaving flow discussed above. However, surprisingly, experiments yield

$$U \sim \frac{\delta\rho}{\Delta\rho}, \tag{18}$$

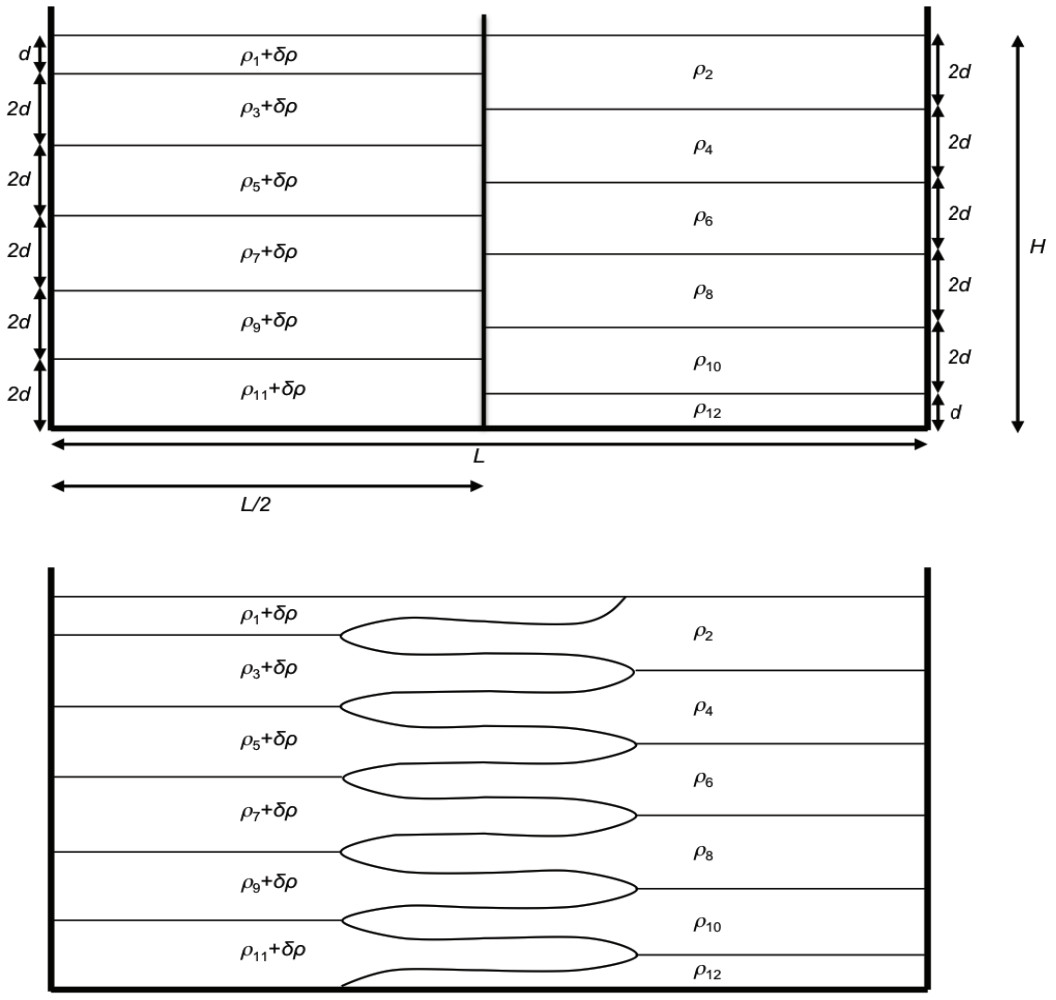

Figure 5: Schematic of intrusions in a stratified fluid. In this case, $\rho_i = \rho_{i-1} + \Delta\rho$ where $\Delta\rho$ is a constant. A small density difference is $\delta\rho < \frac{\Delta\rho}{2}$ is added to the densities on the left hand side. This provides an asymmetry, but all of the layers still interleave.

with no square root sign. If we calculate the available potential energy when $\delta\rho = 0$, we find that

$$E_a = \frac{1}{8} g \left(\rho_1 - \rho_N\right) d^2 \tag{19a}$$

$$= \frac{1}{8} g \left(N - 1\right) \Delta\rho d^2, \tag{19b}$$

where $2d$ is the depth of each layer and N is the number of layers. The available potential energy is equal to the kinetic energy of the whole system, so for each of the $N-1$ intrusions,

$$U_i \sim \sqrt{g\Delta\rho d}. \tag{20}$$

When $\delta\rho \neq 0$, there is extra potential energy from the asymmetry of the flow. The new available potential energy is

$$E_a = \frac{1}{8} g \left(\rho_1 - \rho_N\right) d^2 + \frac{1}{8} g\delta\rho d^2. \tag{21}$$

In this case, the available potential energy is again equal to the kinetic energy produced by the system, which can be divided into a shear component, where the shear velocity is U_s and a component from the velocity of the intrusions, U_i,

$$E_a \sim \left(\left(N - 1\right) U_i + U_s\right)^2. \tag{22}$$

If we assume that $U_s \ll U_i$, substitute in for U_i and expand, we find

$$U_s \sim \sqrt{gH} \sqrt{\frac{\delta\rho}{\rho_0}} \sqrt{\frac{\delta\rho}{\Delta\rho}} \sqrt{\frac{d}{H}}. \tag{23}$$

This explains Eq.(18), since $U_s \sim \delta\rho$.

References

[1] J. Y. Holyer and H. E. Huppert, *Gravity currents entering a two-layer fluid*, J. Fluid Mech., 100 (1980), pp. 739–767.

GFD 2013 Lecture 7: Continuously Stratified Ambient

Paul Linden; notes by Daniel Lecoanet and Karin van der Wiel

June 25, 2013

1 Introduction

In this lecture, we discuss the propagation of a gravity current into a continuously stratified medium, i.e., a background with a density $\rho(z)$, which is a continuous function of z. An important property of such a background is the buoyancy frequency (Brunt-Väisälä frequency)

$$N = \sqrt{-\frac{g}{\rho_0}\frac{d\rho}{dz}}, \tag{1}$$

which is the typical frequency of oscillation of a vertically displaced fluid element. Imagine a fluid element with volume V at an initial height z_i and density $\rho_i = \rho(z_i)$. If this fluid element is displaced to a position $z_i + s$, its density can be approximated by

$$\rho(z_i + s) \approx \rho(z_i) + \frac{d\rho}{dz}s. \tag{2}$$

Thus, Newton's second law gives

$$\rho(z_i)V\ddot{s} = -g\frac{d\rho}{dz}s, \tag{3}$$

which implies the fluid element oscillates at the buoyancy frequency (Equation 1). We will make the Boussinesq approximation, which implies that N is constant. This is only valid if $d\rho/dzL \ll \rho_0$, where L is the vertical length scale of the system, and ρ_0 is a typical density.

In these notes, we will mostly discuss the release of a fluid of constant density ρ_c into an ambient, stratified fluid with density $\rho(z)$. The behavior is very different depending on if there is a height h_N satisfying $\rho_c = \rho(h_N)$, or if instead ρ_c is either larger or smaller than $\rho(z)$ for all z in the domain. In the first case, there will be an intrusion at height $z = h_N$, where the fluid is locally neutrally buoyant. On the other hand, if ρ_c is larger (smaller) than $\rho(z)$, then then a gravity current forms on the bottom (top) of the domain. We will treat these cases separated. At the end of these notes, we will briefly mention the case of the release of a stratified fluid into a stratified ambient.

2 Gravity Current

To simplify our analysis, we will assume that ρ_c, the density of the released fluid, is larger than $\rho(z = 0) = \rho_B$, the density at the bottom of the ambient fluid (the case of $\rho_c < \rho_0$, the density at the top of the ambient fluid is likely similar). In this case, a gravity current forms at the bottom of the domain.

The driving force for the gravity current is a horizontal pressure jump between the released fluid and the ambient. In hydrostatic balance, the pressure is given by the integral of the density, i.e., an average density. Thus, to lowest order, we would expect the gravity current to be equivalent to one released into a constant density ambient with density ρ_E, where this density is given by the average of ρ over the height of the current, i.e., $\rho_E = \rho(h/2)$ for Boussinesq stratification (see Figure 1). For an energy-conserving gravity current from a lock of depth D, we have $h = D/2$, so

$$\rho_E = \rho(D/4) = \rho_B - \frac{\rho_0}{4g} N^2 D. \tag{4}$$

We have

$$g'_E = g'_N + \frac{1}{4} N^2 D, \tag{5}$$

where

$$g'_N = g \frac{\rho_c - \rho_B}{\rho_0} \tag{6}$$

is the strength of the gravity current in terms of background stratification.

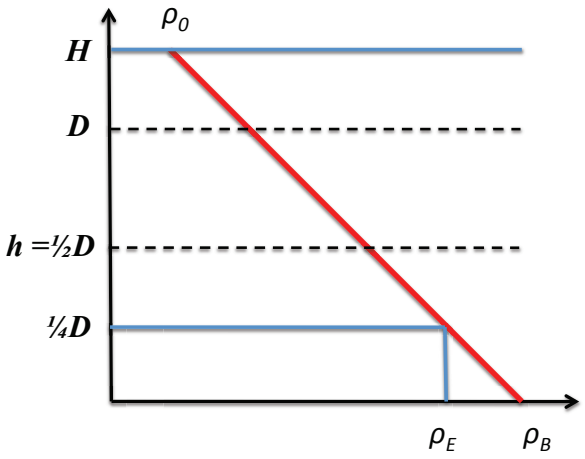

Figure 1: A schematic depicting the equivalent density ρ_E. This is the average density of the ambient stratified fluid over the bottom half of the domain. The simplest prediction for a gravity current with density $\rho_c > \rho_B$ released into a stratified fluid is that the gravity current acts as if it was released into a fluid with constant density ρ_E.

Recall that a gravity current released into a fluid of constant density has a Froude number

$$\frac{U}{\sqrt{g'D}} = \frac{1}{2}\sqrt{2 - D/H}. \tag{7}$$

If the gravity current is equivalent to one released into an ambient fluid with constant density, then this relation should still hold, with g' replaced by g'_E. This makes the prediction

$$F_N = \frac{1}{2}, \tag{8}$$

where

$$F_N \equiv \frac{U}{\sqrt{\left(g'_N D + \frac{1}{4}N^2 D\right)\left(2 - \frac{D}{H}\right)}}. \tag{9}$$

This prediction was tested experimentally and numerically for various values of ρ_c and stratifications. We introduce the stratification parameter

$$S \equiv \frac{\rho_B - \rho_0}{\rho_c - \rho_0}, \tag{10}$$

[5] recalling that ρ_0 is the density at the top of the domain. Thus, $S = 0$ for an unstratified ambient fluid, $S = 1$ if $\rho_c = \rho_B$, and $S > 1$ if there is an intrusion. Figure 2 shows F_N as a function of S. We note that there appears to be a critical S_C above which the Froude number deviates from one half.

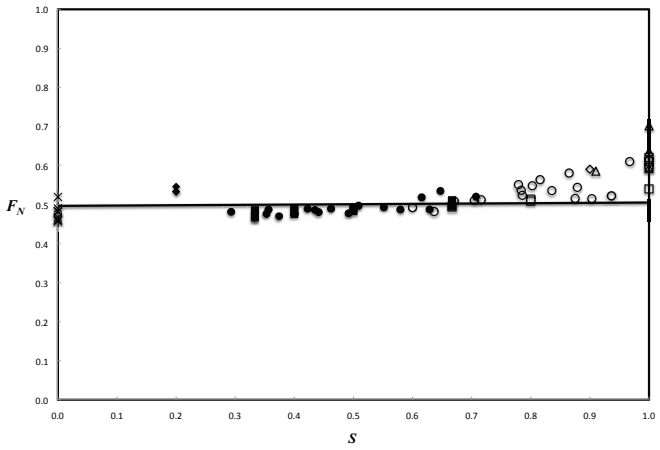

Figure 2: Froude number F_N as a function of the stratification parameter S for experiments and simulations from [2, 4, 3, 6]. Subcritical currents are depicted with open symbols and supercritical currents are depicted with filled symbols.

To understand the deviations from the $F_N = 1/2$, we must discuss internal waves. Internal waves are a generalization of the vertical oscillation of a fluid parcel in a stratified

background. The momentum equation and buoyancy equation can be manipulated into the following equation for the vertical velocity w,

$$(\partial_x^2 + \partial_z^2)\partial_t^2 w + N^2 \partial_x^2 w = 0, \tag{11}$$

where we assume 2D flow. Assuming we can Fourier decompose w as

$$w = \hat{w} \exp(i(kx + mz - \omega t)), \tag{12}$$

we have the dispersion relation for internal waves

$$\frac{\omega^2}{N^2} = \frac{k^2}{k^2 + m^2}. \tag{13}$$

For long waves satisfying $m \gg k$, we have that the phase and group velocity are both given by

$$\frac{\omega}{k} = \pm \frac{N}{m}. \tag{14}$$

Now we will impose that the boundary conditions that $w = 0$ on the top ($z = H$) and bottom ($z = 0$). This implies

$$w \propto sin\left(\frac{n\pi z}{H}\right), \tag{15}$$

where n is an integer. This implies m is quantized

$$m = \frac{n\pi}{H}, \tag{16}$$

and the wave velocity is

$$c = \pm \frac{NH}{n\pi}. \tag{17}$$

The fastest wave speed is

$$c_{\max} = \frac{NH}{\pi}. \tag{18}$$

If the gravity current travels faster than this velocity, it is supercritical and cannot launch internal waves. However, for gravity current velocities smaller than $c_{\max}$, the current is subcritical and it radiates internal waves (see Figure 3). These internal waves change the upstream condition, and speed up the gravity current. The case $U = c_{\max}$ defines the critical stratification S_C. The curve S_C as a function of D/H is given in Figure 4. This is roughly consistent with the experimental results (Figure 2). Note that S_C can never be higher than ≈ 0.85.

There has been some work to apply hydraulic theory (i.e., an analysis similar to Benjamin) to the release of constant density fluid into a stratified ambient. However, this work has assumed that ρ becomes constant above the current, which is not the case. This approach requires a description of the flow which cannot be predicted by the theory.

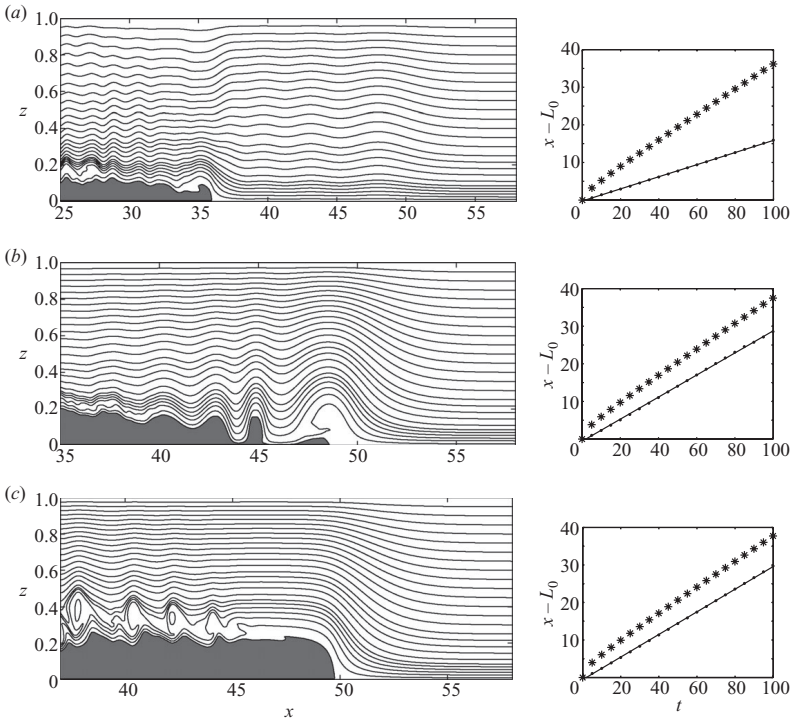

Figure 3: Numerical simulations of constant density gravity currents released into stratified ambient fluid. (a) & (b) show upstream propagating internal waves, whereas (c) does not [6].

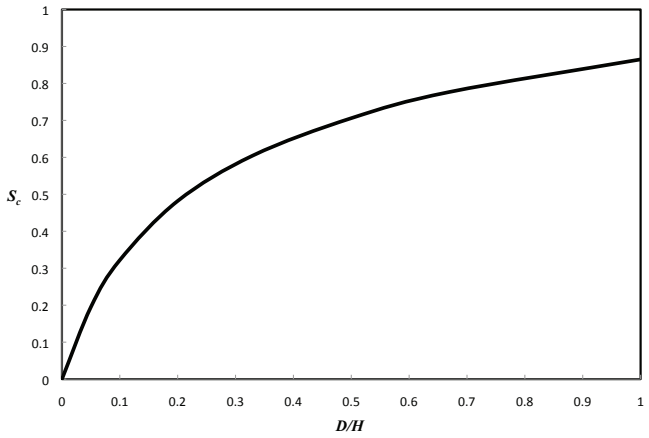

Figure 4: Curve of critical stratification parameter S_C as a function of D/H. For $S < S_C$, the gravity current is supercritical and does not emit upstream propagating internal waves, and the current evolves as if it is expanding into a medium of uniform density ρ_E. For $S > S_C$, the gravity current is subcritical and emits upstream propagating internal waves, influencing the upstream condition, and increase propagation speed of the current.

3 Intrusion Currents

As before we will consider the release of a finite volume of well-mixed fluid (ρ_i) into a linearly stratified channel (constant N^2). However, now we will consider the case where $\rho_u < \rho_i < \rho_l$. In this case a gravity intrusion current will form, propagating within the ambient fluid (see Figure 5). Assume the depth of the lock D is equal to the depth of the channel H.

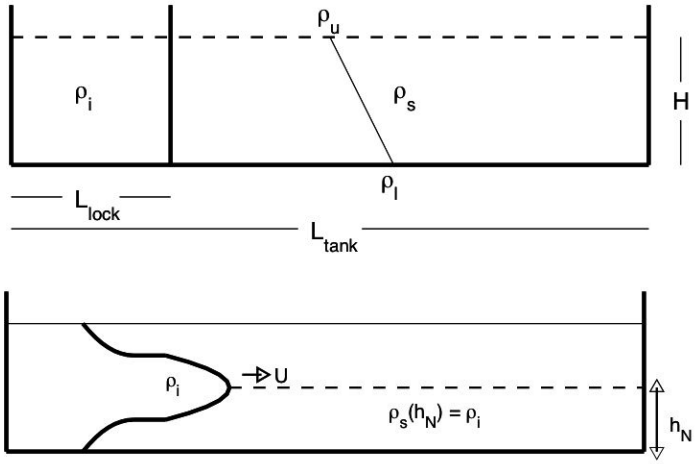

Figure 5: Top: A sketch of the initial setup for the intrusion where $\rho_u < \rho_i < \rho_l$. Bottom: A sketch of an intruding current with $\rho_i = 1/2(\rho_u + \rho_l)$ after the lock has been removed. In this case the neutral buoyancy level is at $h_N = H/2$.

The level of neutral buoyancy (h_N) is the level at which the density of the intrusion is equal to the density of the ambient fluid $\rho_i = \rho_s(h_N)$. This is the level along which the gravity current will propagate. Let us start with the special case where the density of the intrusion fluid is equal to the average density of the ambient fluid in the channel ($\rho_i = 1/2(\rho_u + \rho_l)$). The level of neutral buoyancy will be $h_N = H/2$. As before we use the Froude number to describe the flow and use the equivalent reduced gravity in place of g' (Equations 8 and 9). The strength of the gravity current in terms of the background stratification at $h = h_N$ is

$$g'_N = g\frac{(\rho_i - \rho_s(h_N))}{\rho_0} = 0. \tag{19}$$

With $H = D$ we find:

$$F_N = \frac{U}{1/2NH} = 1/2 \tag{20}$$

$$U = 1/4NH \tag{21}$$

The mid-depth current travels at half the speed of a gravity current along the bottom of a channel in a stratified fluid.

The total Available Potential Energy (APE) for the intrusion current is:

$$APE = g\int_{h_N}^{0}(\rho_s(z)-\rho_i)zdz + g\int_{0}^{H-h_N}(\rho_i-\rho_s(z))zdz \quad (22)$$

$$= \frac{g}{3}\left((\rho_l-\rho_i)h_N^2+(\rho_i-\rho_u)(H-h_n)^2\right). \quad (23)$$

The level h_N for which this has a minimum (differentiate with respect to h_N) is:

$$h_N = \frac{H}{2}. \quad (24)$$

In Figure 6 images of an intrusion gravity current are shown. The top panel shows the initial setup, with dye marking isopycnal surfaces. For this experiment N was chosen to be 1 s^{-1} and $h_N = 0.8$. In the next panels the evolution in time is shown, a gravity current develops. Note that in front of the current the isopycnal surfaces are deflected downwards, indicating waves are able to travel faster than the current and change the conditions of the ambient fluid. The flow is thus subcritical to at least one long wave mode.

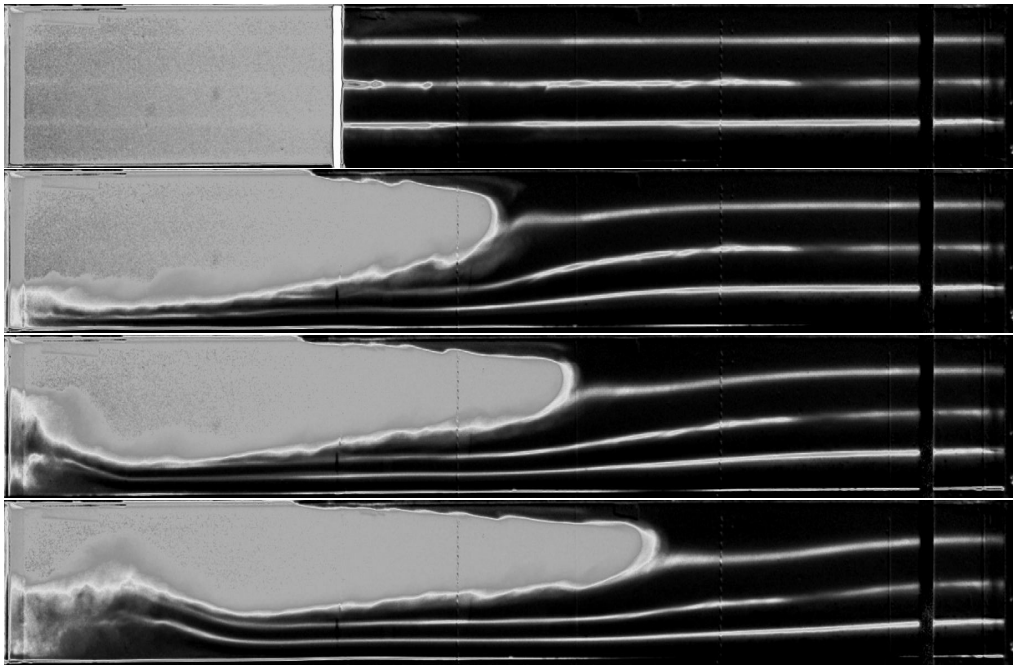

Figure 6: Images of an intrusion gravity current from experiments. In this case $N = 1$ and $h_N = 0.8$.

Figure 7 shows the dimensionless intrusion current velocity for different values of h_N. The minimum is the discussed special case of $h = 1/2H$, where $U = 1/2F_N NH$. At the boundaries where the current flows along the bottom and top ($h = 0$, $h = 1$) we find double the velocity ($U = F_N NH$). The dashed, horizontal grey lines in the figure show the speed of the first three modes of long waves. The grey line near the top of the plot is the first long wave mode. Its nondimensional speed is larger than the nondimensional current speed for

all h and thus these flows are always subcritical to the first long wave mode. The second long wave mode is the middle grey line plotted. Depending on the value of h the flow is either subcritical (small and large h) or supercritical (mid-level currents) to this mode. The third long wave mode is too slow to make an impact for all h, so is unable to transmit information ahead of the intrusion current.

Based on these numbers it can be concluded that the experiment in Figure 6 is subcritical to the first mode of long waves only and thus it must be these waves that cause the deflections of the isopycnal surfaces in the ambient fluid ahead of the current.

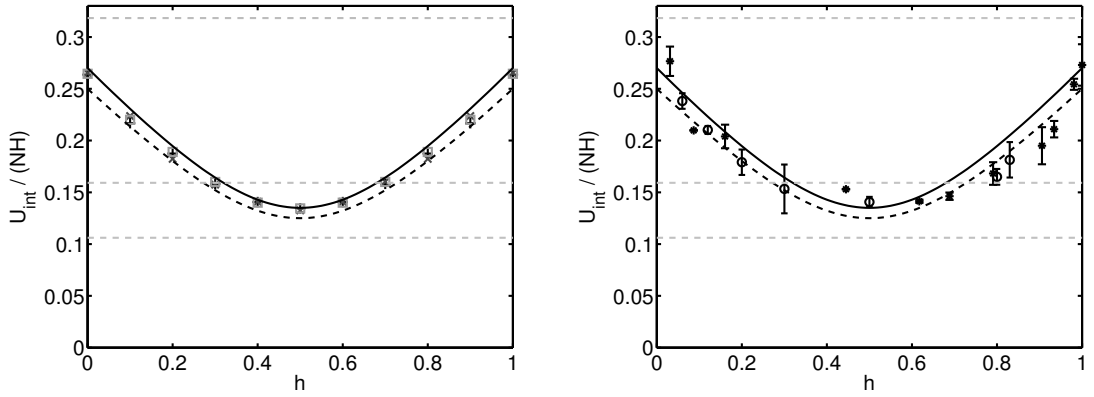

Figure 7: Comparison of dimensionless intrusion velocity ($U/(NH)$) for numerical simulations (left) and experiments (right) to model predictions. The dashed line shows the theoretical $F = 0.25$, the solid line $F = 0.266$. The light grey horizontal dashed lines on each plot represent from top to bottom the first, second and third mode long wave speed respectively.

4 Adjacent stratified regions

Finally, we consider the case of a lock exchange between two differently linear stratisfied fluids (Figure 8). The fluid in the left lock has a constant buoyancy frequency equal to N_i, the right lock has a constant buoyancy frequency N_a. Let us define the stratification ratio S as the ratio between the buoyancy frequency in the two locks:

$$S = \frac{N_i^2}{N_a^2}. \tag{25}$$

From previous lectures and the considerations above we already know the intrusion current speed for some cases.

- Equal stratification in the two locks, i.e. $N_i = N_a$ and thus $S = 1$. In this case there is no horizontal density gradient in the channel and thus no gravity current: $U = 0$.
- No stratification in the left lock, i.e. $N_i = 0$, $S = 0$. This is the case described in section 3, of a well-mixed fluid, propagating as an intrusion into a linearly stratisfied fluid, $U = 1/8NH$.

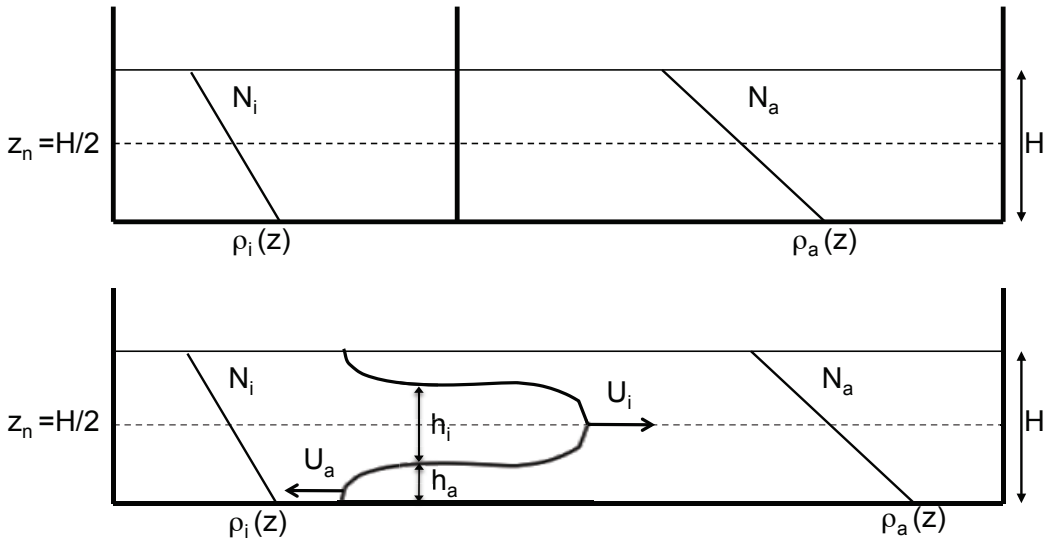

Figure 8: Schematic showing the initial conditions of lock-release of a linearly stratified intruding fluid of N_i, into a linearly stratified ambient fluid of N_a, where the average densities of both fluids are equal. From [1].

The cases where $0 \leq S \leq 1$, the intrusion current speed is a function of the stratification ratio: $U = 1/4NHf(S)$. Because N_i is smaller than N_a the intrusion current will travel from the left lock into the right fluid.

Figures 9 and 10 show experiments and numerical simulations respectively for two different stratification cases. On the left $S \simeq 0.2$, a relatively fast intrusion current, and on the right a slower current of $S \simeq 0.8$.

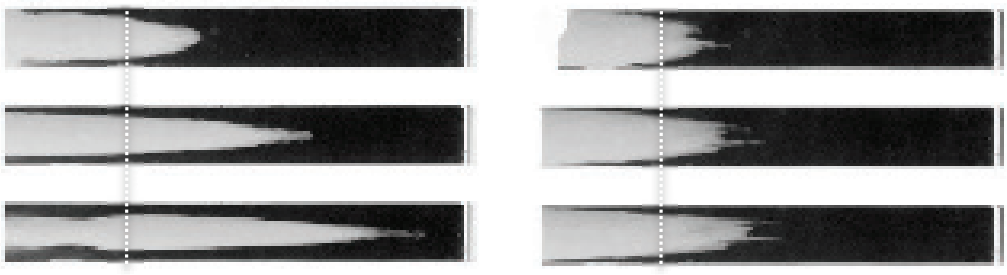

Figure 9: Snapshots of the laboratory experiments for $S = 0.23$ (left) and $S = 0.77$ (right) for $N_a = 1.5$ s^{-1} at the dimensionless times $Nat = 10$, 20 and 30. The dashed white line denotes the initial position of the gate. The intrusion fluid is visualized with dye.

References

[1] B. D. Maurer, D. T. Bolster, and P. F. Linden, *Intrusive gravity currents between two stably stratified fluids*, J. Fluid Mech., 647 (2010), pp. 53–69.

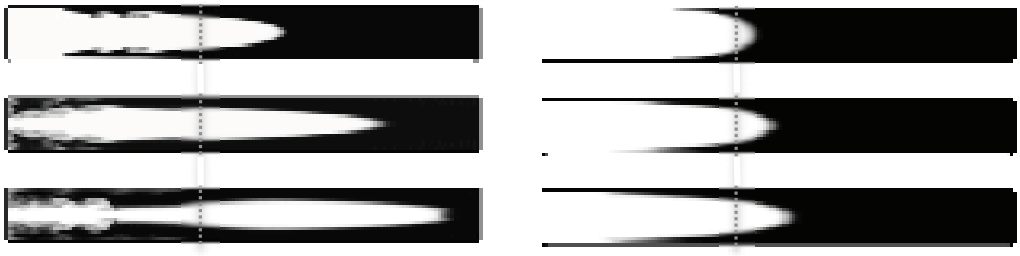

Figure 10: Snapshots of the numerical simulations for $S = 0.20$ (left) and $S = 0.80$ (right) for $N_a = 1\ \mathrm{s}^{-1}$ at the same dimensionless times as Figure 9. The dashed gray line denotes the initial position of the gate. The motion of the lock fluid is visualized using a passive tracer.

[2] T. Maxworthy, J. Leilich, J. E. Simpson, and E. H. Meiburg, *The propagation of a gravity current into a linearly stratified fluid*, J. Fluid Mech., 453 (2002), pp. 371–394.

[3] E. H. Meiburg, V. K. Birman, and M. Ungarish, *On gravity currents in stratified ambients*, Phys. Fluids., 19 (2007).

[4] J. O. Shin, S. B. Dalziel, and P. F. Linden, *Gravity currents produced by lock exchange*, J. Fluid Mech., 521 (2004), pp. 1–34.

[5] M. Ungarish and H. E. Huppert, *On gravity currents propagating at the base of a stratified ambient*, J. Fluid Mech., 458 (2002), pp. 283–301.

[6] B. L. White and K. R. Helfrich, *Gravity currents and internal waves in a stratified fluid*, J. Fluid Mech., 616 (2008), pp. 327–356.

GFD 2013 Lecture 8: Rotating currents

Paul Linden; notes by Dhruv Balwada & Ton van den Bremer

June 26, 2013

1 Introduction

Figure 1 shows two examples of gravity currents occurring on the earth's surface in the direct vicinity of boundaries. Rotation has the important effect of adding a Coriolis force to the momentum equations in the non-inertial rotating frame of reference. Under the influence of the Coriolis force, currents travelling to the North on the Northern hemisphere will deviate to the east, as will currents travelling to the South on the Southern hemisphere. These currents will follow or even curve around the land boundaries they meet on their paths. In this lecture, the effect of the Coriolis force on light gravity currents is explored in the context of shallow water theory.

Figure 2 shows an example from a lab experiment. A shallow cylindrical lens of light water is released at the centre of a rotating tank on top of a thick layer of dense water. The tank rotates in the clockwise direction. As some of the light fluid spreads radially upon release, it must start rotating in the anti-clockwise direction to conserve angular momentum to simulate the effect of a land boundary. A solid radial boundary is then introduced that prevents flow in the azimuthal direction across the entire depth of the fluid. The presence of the radial boundary blocks the azimuthal flow, and the current propagates along the radial boundary in the radially outward direction under the influence of the Coriolis force in the same way as gravity currents observed in real life might do along a coastline (cf. figure 1).

2 Light boundary currents: shallow water theory

We consider a gravity current with thickness h in a reference frame rotating around the z axis, the axis along which gravity g acts in the negative direction, at angular velocity Ω, as illustrated in figure 3. Its dynamics are described by shallow water theory, and conservation of momentum in the x, y and z direction give:

$$u_t + uu_x + vu_y - fv = -\frac{1}{\rho_0}p_x, \tag{1}$$

$$v_t + uv_x + vv_y + fu = -\frac{1}{\rho_0}p_y, \tag{2}$$

$$0 = -\frac{1}{\rho_0}p_z - \frac{g\rho}{\rho_0}, \tag{3}$$

a 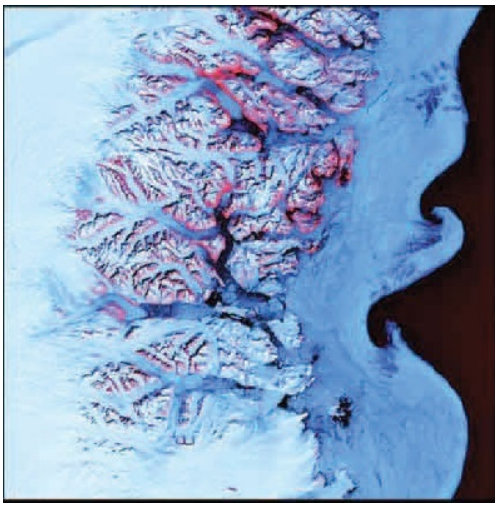 b 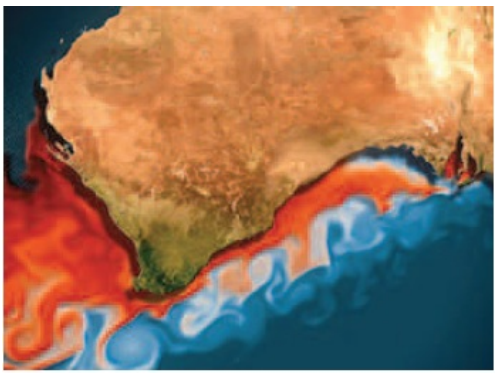

Figure 1: Two real-life examples of the effect of the Coriolis force on currents: the East Greenland current flowing in the northerly direction on the Northern hemisphere (a) and the Leeuwin current flowing in the southerly direction near the coast of western coast of Australia on the Southern hemisphere.

where we have assumed that there is no motion in the z direction, that is, we have made the shallow water approximation. The magnitude of the Coriolis force is denoted by $f = 2\Omega$. Conservation of volume is given by:

$$h_t + (uh)_x + (vh)_y = 0. \tag{4}$$

It can be shown (see appendix A) that (1-4) are consistent with the conservation of (shallow water) potential vorticity:

$$q = \frac{f+\zeta}{h} \quad \text{and} \quad \frac{D}{Dt}(q) = 0, \tag{5}$$

where ζ, the relative vorticity, is defined as:

$$\zeta = v_x - u_y. \tag{6}$$

Making the usual hydrostatic assumption, the pressure in the fluid $p(z)$ can be written as:

$$p(z) = \begin{cases} g\rho_U(\eta - z) & -h \le z \le \eta, \\ g\rho_U(h+\eta) - g\rho_L(z+h) & z \le -h, \end{cases} \tag{7}$$

where $\eta = \eta(x, y)$ is the free surface elevation. We are in interested in solutions that are steady. We thus ignore the $\partial/\partial t$ term in addition to the non-linear advective momentum terms in (2), as part of a small-amplitude approximation, and obtain the equation for geostrophic balance between the Coriolis force and the pressure gradient in the direction normal to the axis of rotation:

$$fu = -\frac{1}{\rho_0} p_y. \tag{8}$$

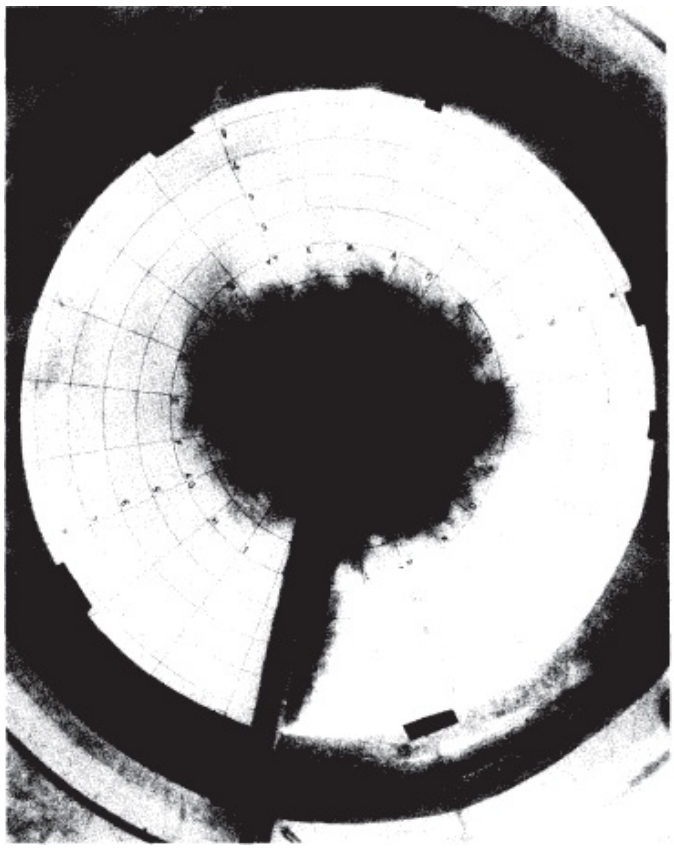

Figure 2: Plan view of a buoyant region of fluid adjusting geostrophically next to a side boundary from [3].

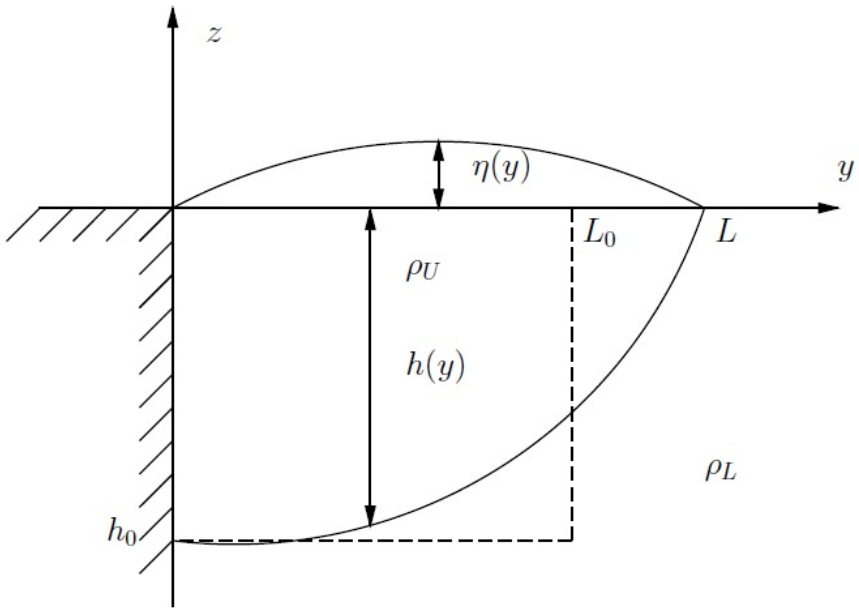

Figure 3: A schematic diagram of an idealized dense gravity current in a rotating reference frame.

Combining (7) and (8) gives:

$$\rho_0 f u = \begin{cases} -g\rho_U \frac{\partial \eta}{\partial y} & -h \le z \le \eta, \\ -g\rho_U \frac{\partial \eta}{\partial y} + g(\rho_L - \rho_U)\frac{\partial h}{\partial y} & z \le -h. \end{cases} \tag{9}$$

Now suppose that the lower layer is deep, so that it can be considered passive and its velocity can be ignored. We have from the lower layer part ($z \le -h$) of (9):

$$-g\rho_U \frac{\partial \eta}{\partial y} + g(\rho_L - \rho_U)\frac{\partial h}{\partial y} = 0. \tag{10}$$

Substituting from (10), the upper layer part ($-h \le z \le \eta$) of (9), can now be rewritten as:

$$fu = -g' \frac{\partial h}{\partial y}, \tag{11}$$

where $g' = g(\rho_L - \rho_U)/\rho_0$. Equation (11) holds for the fluid inside the gravity current. From conservation of potential vorticity (5), we have:

$$q = \frac{f}{h_0} = \frac{f - \frac{\partial u}{\partial y}}{h}, \tag{12}$$

where $\partial v/\partial x = 0$, since we ignore all variation in the x-direction, the direction of propagation of the gravity current. Combination of (11) and (12) gives a second-order ordinary differential equation in h

$$\frac{\partial^2 h}{\partial y^2} - \frac{1}{R_D^2} h = -\frac{f^2}{g'}, \tag{13}$$

where $R_D = \frac{\sqrt{g'h_0}}{f}$ is the so-called Rossby deformation radius. Physically, this represents the length scale over which the flow starts to experience the effects of rotation.

We can solve the ordinary differential equation (13) assuming the boundary condition $h = 0$ at $y = L$, the right hand side boundary of the gravity current, and $u = 0$ at $y = 0$. The second boundary condition derives from the no-flow boundary condition at the wall ($v = 0$) and from neglecting pressure variations in the x-direction ($\partial p/\partial x = 0$). These conditions along with the momentum equation in the x direction (1) imply $\partial u\ \partial t = 0$. If the current is initially at rest at the boundary ($u(t = 0) = 0$), its horizontal velocity at that location will remain zero. The solution to (13) subject to these boundary conditions is then:

$$\frac{h}{h_0} = 1 - \frac{\cosh\left(y/R_D\right)}{\cosh\left(L/R_D\right)}, \tag{14}$$

or in terms of the horizontal velocity in the x-direction:

$$u = \sqrt{g'h_0}\frac{\sinh\left(y/R_D\right)}{\sinh\left(L/R_D\right)}. \tag{15}$$

Finally, conservation of volume gives the steady-state extent of the current in the y-direction L:

$$\int_0^L h(y)dy = h_0L_0 \rightarrow \frac{L}{R_D} - tanh\frac{L}{R_D} = \frac{L_0}{R_D}. \tag{16}$$

Figure (4) shows the relationship in (16) and its asymptotic behaviour $L \propto L_0$ for large L_0 ($L_0/R_D \gg 1$).

3 Baroclinic instability

Figures 5 and 6 show the set-up and results for a laboratory experiment exploring the dynamics of a coastal current and the onset of baroclinic instability in these currents. Figure 5 shows a rotating tank with a layer of light fluid initially held in place by an annular lock. The outer wall of the annulus is then removed, and the fluid starts to spread radially, which leads to the formation of an anticyclonic (clockwise) current. Figure 6 shows a top view of the current with the light fluid being dyed. The sequence of figures shows the growth of a baroclinic instability.

Baroclinic instability is a mechanism by which available potential energy is released and converted to kinetic energy. Consider a system shown in figure 7. The solid lines are isopycnals and the dashed lines are geopotentials. There is also a current out of the plane that decreases with height and is thus sheared. The system is in a steady state: the tendency of the isopycnals to become horizontal is balanced by the Coriolis force associated with the shear flow. By differentiating the equation for geostrophic balance (8) with respect to the vertical coordinate z keeping the rate of rotation f constant combined with hydrostatic pressure variation from (3), we obtain:

$$f\frac{\partial u}{\partial z} = +\frac{g}{\rho_0}\frac{\partial \rho}{\partial y}. \tag{17}$$

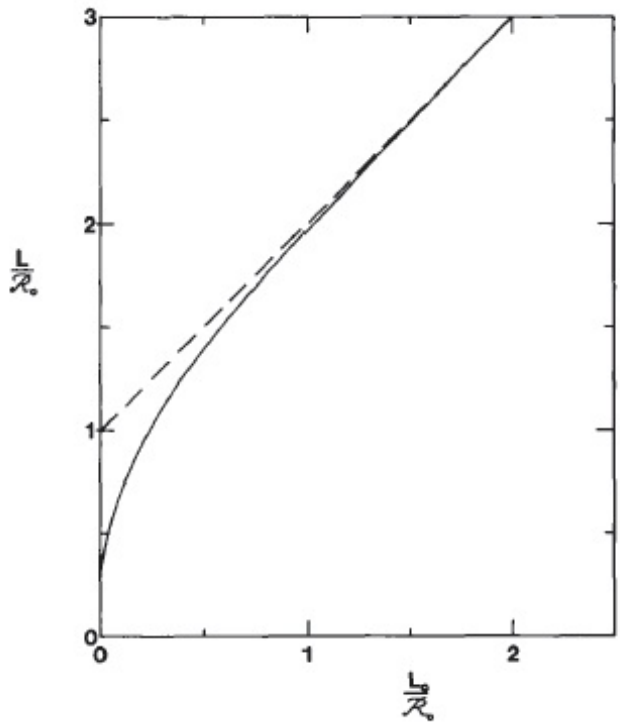

Figure 4: The relationship between the initial width L_0 of the upper layer inside the annulus and the final width L in quasi-geostrophic balance. The solid line is given by (16), while the dashed straight line assumes that the edge of the upper layer is directly proportional to L_0. From [1].

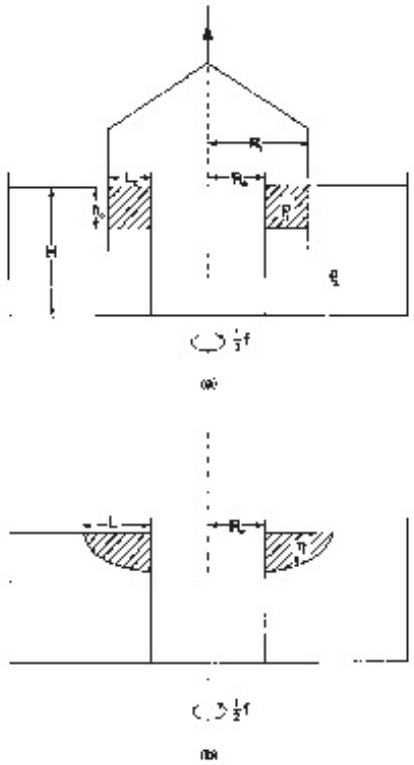

Figure 5: Diagrams of the baroclinic instability experiment before the outer wall of the annulus is withdrawn (a) and after the two layers have adjusted to a quasi-geostrophic balance (b).

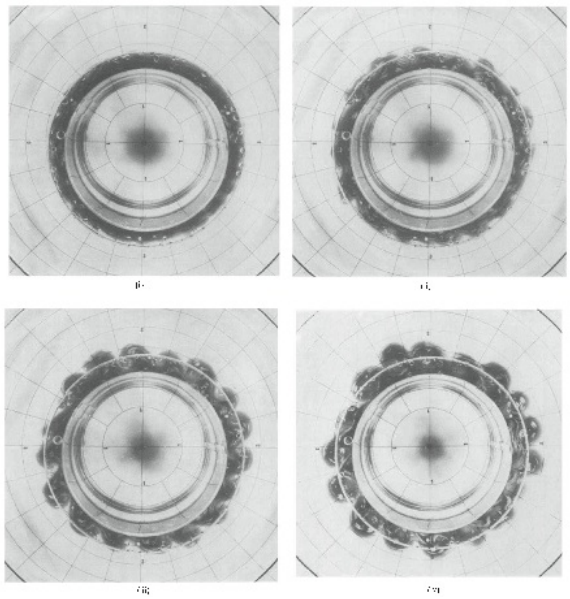

Figure 6: The top view of the baroclinic instability experiment. The panels show the time evolution of the experiment after the outer wall of the annulus is removed. The light fluid is dyed.

The vertical shear is required to satisfy the so-called thermal wind relation (17), in which vertical shear balances horizontal density gradients.

We now examine the stability of this equilibrium to perturbations using figure 7 by considering the available potential energy of the system. We consider three different perturbations. If a parcel of fluid is moved vertically down, it will be surrounded by denser fluid and be restored to its original position by its own buoyancy. If the same parcel is displaced horizontally, buoyancy forces will not act to return the parcel to its initial position, but no potential energy will be released. The perturbation that does release potential energy and does not result in the parcel of fluid being restored to its initial position, is one in which the particle is moved both vertical and horizontally, as illustrated by the arrow in figure 7. This perturbation will grow in size and is called a baroclinic instability. We note that in the figure the vertical scale is exaggerated. In reality the angle between isopycnals and geopotentials is very small, and fluid parcels need to move great horizontal distances to reduce convert their available potential energy into kinetic energy. Consequently, the horizontal scale of baroclinic instabilities is large.

4 Rotating lock exchange

Figure (8) shows the behaviour of a gravity current, as discussed in the previous lectures, but now under the influence of rotation. For each panel (I, II), the subsequent sub-panels (a-

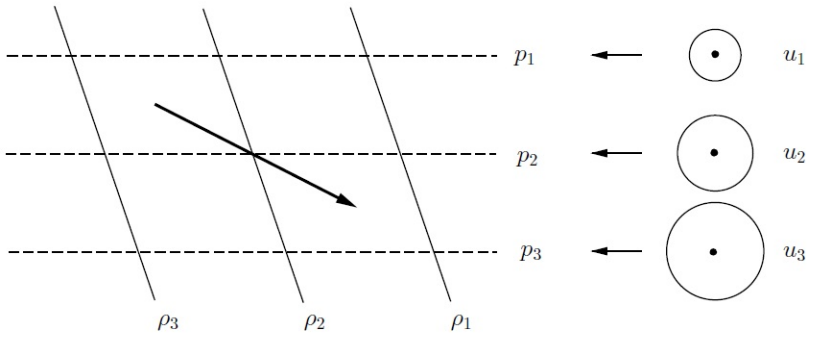

Figure 7: A schematic diagram of baroclinic instability in a continuously stratified fluid. The horizontal (dashed) lines denote surfaces of constant pressure (or geopotential) surfaces, where $p_3 > p_2 > p_2$, and the inclined (continuous lines) denote lines of constant density (or isopycnal) surfaces, where $\rho_3 > \rho_2 > \rho_1$. The velocity out of the plane increases with depth ($u_3 > u_2 > u_1$) denoted by circles of increasing radius, and the corresponding shear results in a horizontal torque that is in equilibrium with the horizontal density gradient.

e) show the time evolution of the experiments. The rotation rate is zero in panel I and large for panel II. As the rotation is increased we can see the effect of the Coriolis force, which turns the flow to its right. The flow moves along the right hand side wall of the channel (as seen from the direction of propagation of the current). As the Coriolis is pushing the fluid towards the side wall, it is not able to escape and form a strong front in the same wave a gravity current unaffected by rotation would. The fluid gets trapped in the initial release and can only escape along the wall and forms a boundary current.

A Conservation of potential vorticity in shallow water

To derive conservation of potential vorticity in shallow water making use of the Boussinesq approximation, start with the momentum equations in vector form:

$$\frac{D\mathbf{u}}{Dt} + \mathbf{f} \times \mathbf{u} = \frac{1}{\rho_0}\nabla p - \mathbf{g}\frac{\rho}{\rho_0}, \tag{18}$$

where $\mathbf{f} = f\hat{\mathbf{k}} = 2\Omega\hat{\mathbf{k}}$ and $\mathbf{u} = (u, v, w)$. In Cartesian coordinates (18) takes the form:

$$u_t + uu_x + vu_y - fv = -\frac{1}{\rho_0}p_x, \tag{19}$$

$$v_t + uv_x + vv_y + fu = -\frac{1}{\rho_0}p_y, \tag{20}$$

$$0 = -\frac{1}{\rho_0}p_z - \frac{g\rho}{\rho_0}, \tag{21}$$

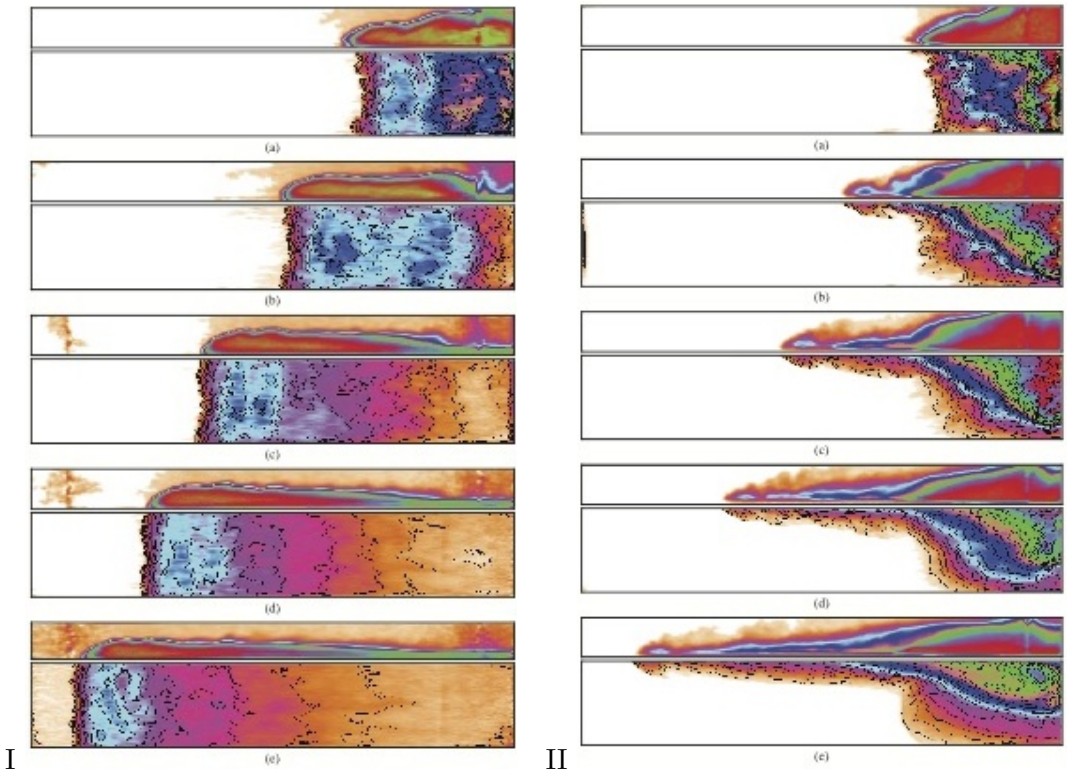

Figure 8: Results from two lock-exchange experiments one without rotation (I) and one with strong rotation (II). For each panel (I, II), the sub-panels (a-e) show the time evolution of the experiments. Within each sub-panel, the narrow top section shows the side view and the bottom section shows the top view. From [2].

where it has been assumed that the motion is always in the horizontal plane and thence $w = 0$. Taking the curl of (18) gives the following vector for the right hand side:

$$\Big(- \frac{g}{\rho_0}\frac{\partial \rho}{\partial y}, \frac{g}{\rho_0}\frac{\partial p}{\partial x}, 0\Big) \tag{22}$$

For the z-component we thus have for the left hand side:

$$\frac{\partial}{\partial x}\Big[v_t + uv_x + vv_y + fu\Big] - \frac{\partial}{\partial y}\Big[u_t + uu_x + vu_y - fv\Big] = 0. \tag{23}$$

We define relative vorticity ζ as follows:

$$\zeta = v_x - u_y. \tag{24}$$

Without making further assumptions, equation (23) can now be simplified to:

$$\frac{\partial \zeta}{\partial t} + \mathbf{u} \cdot (\nabla^* \zeta + f) + (f + \zeta)\nabla^* \cdot \mathbf{u} = 0, \tag{25}$$

which can be written in terms of a material derivative:

$$\frac{D}{Dt}(f + \zeta) + (f + \zeta)\nabla^* \cdot \mathbf{u} = 0. \tag{26}$$

where we have let ∇^* denote the vector differential operator in the x and the y coordinate only: $\nabla^* = \hat{\mathbf{i}}\partial/\partial x + \hat{\mathbf{j}}\partial/\partial y$. From conservation of volume we have:

$$\frac{Dh}{Dt} + h\nabla^* \cdot \mathbf{u} = 0, \tag{27}$$

where h is the depth of fluid. Combining conservation of volume (27) and (26) gives, after multiplication by h, the conserved quantity known as potential vorticity $(f + \zeta)/h$:

$$\frac{D}{Dt}\Big(\frac{f + \zeta}{h}\Big). \tag{28}$$

References

[1] R. W. Griffiths and P.F. Linden, *Laboratory experiments on fronts*, Geophys. Astrophys. Fluid Dyn., 19 (1982), pp. 159–187.

[2] J. Hacker, *Gravity currents in rotating channels*, PhD thesis, University of Cambridge, 1996.

[3] P. Wadhams, A. E. Gill, and P. F. Linden, *Transects by submarine of the East Greenland Polar Front*, Deep-Sea Research, 26A (1979), pp. 1311–1327.

GFD 2013 Lecture 9: Mass Loss Currents

Paul Linden; notes by Yuki Yasuda and Kate Snow

June 27, 2013

1 Introduction

Previous lectures have investigated the flow of gravity currents where the driving buoyancy is a result of temperature or salinity differences creating a difference in density or stratification between the current and ambient fluid. Another form of gravity current is that in which the difference in density is produced due to suspension of particles in the fluid. The density of the gravity current is then produced from the addition of the fluid and particle densities. Examples of this form of flow include avalanche and pyroclastic flow. For an informative presentation on avalanche flow and a laboratory model set up using sand as the representative particle of the flow, the reader is directed to the website:

http://www.youtube.com/watch?v=lpjcla-8XNQ

As a specific example, Figure 1 shows the pyroclastic plume from the 1991 eruption of Mount Pinatubo. Soon after the photo was taken, enough of the particles in the flow had settled out that the hot air of the plume became buoyant enough to rise, allowing the occupants of the vehicle to survive.

Another situation where understanding of this type of flow is important is in industry, for example, water quality and treatment and understanding the removal of unwanted particles in water through sedimentation.

Figure 1: Pyroclastic flow of 1991 Mount Pinatubo eruption.

2 Particle Driven Currents

We will now set up a simple model of a particle driven current which in effect takes the classical gravity current model, but allows for the current density to change due to the deposition of particles. Suppose we have solid particles of density ρ_p suspended in an interstitial fluid of density ρ_i. Assume that $\rho_p > \rho_i$, then it is expected that the particles will fall through the fluid where the falling rate is defined by the Stokes velocity V_s. The Stokes velocity is the terminal velocity at which a sphere of density ρ_p will fall through a fluid of density ρ_i and is dependent on the viscosity, the density difference, gravity g and the size of the particles. In this analysis we assume that all the particles are of the same size and are non-cohesive allowing for a constant V_s to be taken along the length of the current. Further assumptions include:

- The suspension of particles is dilute, which implies there is no hindered settling of the particles.
- The particles are well mixed and only fall out at the lower boundary where the vertical velocity is zero.
- No resuspension occurs.
- The current density and ambient fluid density are similar.

The second assumption is arguable since if it were well mixed, then the flow would be turbulent and detrainment would occur at the top of the fluid. Yet many similar models apply this condition and still provide insightful representations of the flow and little work has been done to verify this assumption for or against. The final assumption given above is suitable for many situation, such as sedimentation or avalanche flow, however fails for cases such as a pyroclastic flow where the hot air of the current is very different from the surrounding ambient. The final assumption also allows the reduced gravity of the current to be defined as:

$$g'_c = \frac{g(\rho_c - \rho_0)}{\rho_0}, \tag{1}$$

where ρ_0 is the density of the ambient and the current density ρ_c is given by:

$$\rho_c = \rho_i + \phi(\rho_p - \rho_i),$$

where ϕ is the volume fraction of particles. Then in the limiting case where $\rho_i = \rho_0$ we get $g'_c = \phi g'_p$ where:

$$g'_p = \frac{g(\rho_p - \rho_0)}{\rho_0}.$$

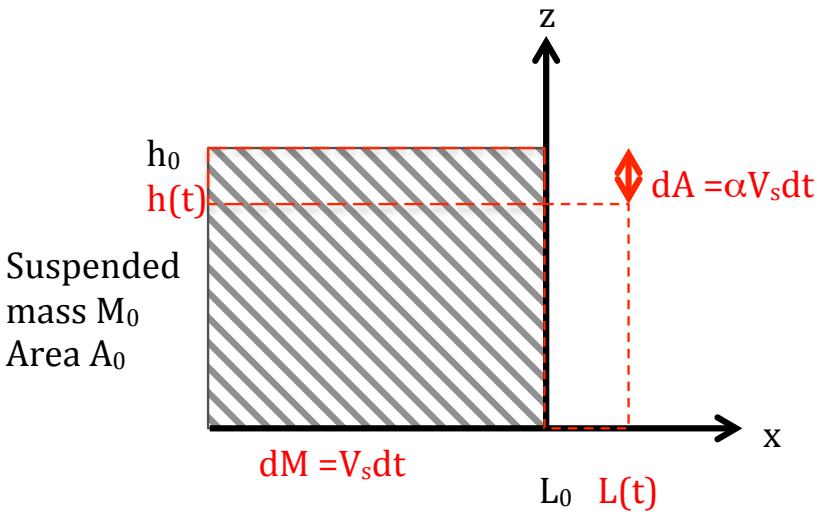

Figure 2: Constant volume release of particle current area A_0, mass M_0 into ambient fluid.

2.1 Constant Volume Release

We consider the case now of a constant volume release with values defined similarly to previous lectures with the particle current defined over a length $L(t)$ and height $h(t)$ (see Figure 2). We take both the current velocity U and g_c' to be uniform in space and perform the analysis per unit width where width = 1. Then the area of the current is $A = Lh$ and taking M as the suspended mass, the rate of change of mass is given by:

$$dM = -\frac{M}{h}V_s dt = -\frac{M}{A}LV_s dt. \tag{2}$$

To allow for possible entrainment or detrainment at the upper boundary of the current, we also define the rate of change of area of the current:

$$dA = -\alpha L V_s dt, \tag{3}$$

where α defines the degree of entrainment. So if $\alpha = 0$ there is no entrainment and the current remains at a constant volume, if $\alpha > 0$ detrainment of the interstitial fluid occurs and the current volumes decrease and if $\alpha < 0$ entrainment of the ambient fluid occurs increasing the volume of the current. Based on the results of the analysis in previous lectures we also assume here that the propagation occurs with a constant Froude number:

$$dL = F_h(g_c' h)^{\frac{1}{2}} dt. \tag{4}$$

However, though the Froude number is constant, g_c' is not constant but changes with time as particles settle out and so the propagation speed is not constant. In fact, we expect to see the current decelerate with time as particles settle out and g_c' approaches zero. Replacing h with $\frac{A}{L} = \frac{M}{L\rho_p\phi}$ and $g_c' = \phi g_p'$ gives:

$$dL = F_h \left(\frac{g'_p}{\rho_p} \frac{M}{L} \right)^{\frac{1}{2}} dt. \tag{5}$$

Taking the initial state as occurring at $L = 0$, $M = M_0$ and $A = A_0$ at $t = 0$, that is, defining the z-axis to be at the initial point of the front of the current, we can use integration of various values to obtain information about the current. So first, divide equation (3) by (2):

$$\frac{dA}{dM} = \alpha \frac{A}{M},$$

which integrates to give:

$$\frac{A}{A_0} = \left(\frac{M}{M_0} \right)^{\alpha}. \tag{6}$$

Equation (6) indicates the intuitive result that if there is no entrainment ($\alpha = 0$), then the area remains as A_0 but as the entrainment or detrainment increases, the area increases or reduces dependent on the mass and the degree of entrainment. Now to obtain an expression of the length of the flow divide equation (5) with (2):

$$\frac{dL}{dM} = -\frac{F_h}{V_s} \left(\frac{g'_p}{\rho_p} \frac{M}{L} \right)^{\frac{1}{2}} \frac{A}{ML},$$

which may be rewritten as:

$$\frac{dL}{dM} = -\frac{F_h}{V_s} \left(\frac{g'_p}{\rho_p} \right)^{\frac{1}{2}} L^{-\frac{3}{2}} M^{-\frac{1}{2}} \left(\frac{M}{M_0} \right)^{\alpha} A_0, \tag{7}$$

and simplifying:

$$L^{\frac{3}{2}} dL = -cM^{\alpha - \frac{1}{2}} dM, \tag{8}$$

where $c = \frac{F_h}{V_s} \frac{A_0}{M_0^{\alpha}} \left(\frac{g'_p}{\rho_p} \right)^{\frac{1}{2}}$ is a constant. We now integrate (8) to get:

$$\left[\frac{2}{5} L^{\frac{5}{2}} \right]_0^L = -c \left[\frac{M^{\alpha + \frac{1}{2}}}{\alpha + \frac{1}{2}} \right]_{M_0}^M,$$

and putting c back:

$$\frac{2}{5} L^{\frac{5}{2}} = -\frac{F_h}{V_s} \frac{A_0}{M_0^{\alpha}} \left(\frac{g'_p}{\rho_p} \right)^{\frac{1}{2}} \frac{1}{\alpha + \frac{1}{2}} \left(M^{\alpha + \frac{1}{2}} - M_0^{\alpha + \frac{1}{2}} \right),$$

and rearranging:

$$(2\alpha + 1) L^{\frac{5}{2}} = -\frac{5F_h}{V_s} A_0^{\frac{3}{2}} \left(\frac{g'_p M_0}{\rho_p A_0} \right)^{\frac{1}{2}} \left(\frac{M^{\alpha + \frac{1}{2}}}{M_0^{\alpha + \frac{1}{2}}} - \frac{M_0^{\alpha + \frac{1}{2}}}{M_0^{\alpha + \frac{1}{2}}} \right),$$

which gives:

$$\left(\frac{M}{M_0}\right)^{\alpha+\frac{1}{2}} = 1-(1+2\alpha)\left(\frac{L}{L_f}\right)^{\frac{5}{2}}, \tag{9}$$

where we have defined $L_f = \left(\frac{5F_h}{V_s}A_0^{\frac{3}{2}}(g_0')^{\frac{1}{2}}\right)^{\frac{2}{5}}$ and $g_0' = \frac{g_p' M_0}{\rho_p A_0}$. But the above equation is only true if $\alpha \neq -1/2$. If $\alpha = -1/2$ we instead get:

$$\frac{M}{M_0} = e^{(-L/\lambda)^{\frac{5}{2}}}, \tag{10}$$

where $\lambda = \left(\frac{5}{2}\frac{F_h}{V_s}A_0^{\frac{3}{2}}(g_0')^{\frac{1}{2}}\right)^{\frac{2}{5}}$. In this case, since $\alpha < 0$ we have an entraining situation, yet there is no defined limit to this situation, it is seen from equation (10) that the current may go on forever reaching infinite length as the mass becomes smaller and smaller. Clearly this is not a purely realistic situation, yet the results based on the assumptions used are still insightful into the nature of the flow. For example, now consider the case where $\alpha > -1/2$ as defined by equation (9). Simple states for equation (9) would be the $\alpha = 0$ case. Here, the mass becomes zero when $L = L_f$ and we call L_f the run-out length. In other words the current will continue to flow but now only to a finite length defined by L_f. We can also see the dependence of L_f on V_s, indicating that the faster the particles settle out the sooner the current will reach its run-out length.

Now consider the case for $\alpha > 0$. In this case, $(1+2\alpha) > 1$, which is effectively equivalent to saying that L_f is smaller as it is an inverse factor in equation (9). In this regime, particles are settling out in addition to loss of volume at the top due to detrainment. This effectively slows down the flow more rapidly.

Figure 3 plots the propagation of the sediment of the non-dimensional time τ, this is the time it would take the flow to reach L_f if no mass were being lost by the current. In the early stages of the flow, the results are equivalent even for the varying amounts of detrainment. One reason for this is that in the early stages of the flow, relatively small amounts of particles have settled out allowing the buoyancy force to be relatively unaffected. However, as the flow continues, more fluid is detrained from the current for the higher values of α, increasing the relative concentration of the particles and so increasing the sediment rate, producing a shorter run-out length, as seen in Figure 3.

The distribution of the sedimentation can also be determined. This is calculated by defining a value $D(x)$ that gives the thickness of the deposit at each distance x along the length of the current. That is:

$$D(x) = -\int_{t_x}^{\infty} \frac{dM}{dt}\frac{1}{L}dt = -\int_{x}^{L_f} \frac{dM}{dL}\frac{1}{L}dt, \tag{11}$$

where t_x is the time at which the current reaches x. The non-dimensional deposit thickness versus current length are given in Figure 4 for varying values of α. It is seen from this figure, that as the detrainment of the fluid increases, allowing an increased sedimentation rate, the thickness is greater at shorter length but the relative change between values of α is small.

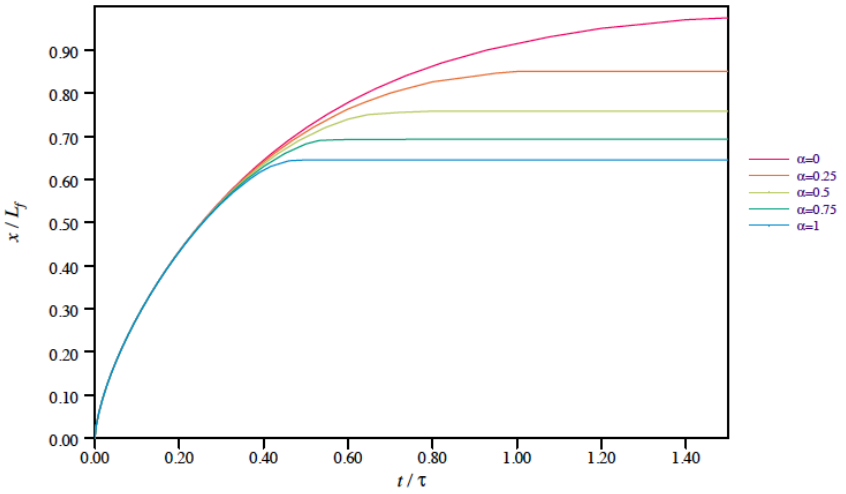

Figure 3: The propagation of the sediment versus time for varying values of α, where time has been non-dimensionalised by $\tau = L_f^{\frac{3}{2}}(g_0' A_0)^{\frac{1}{2}}$, [3].

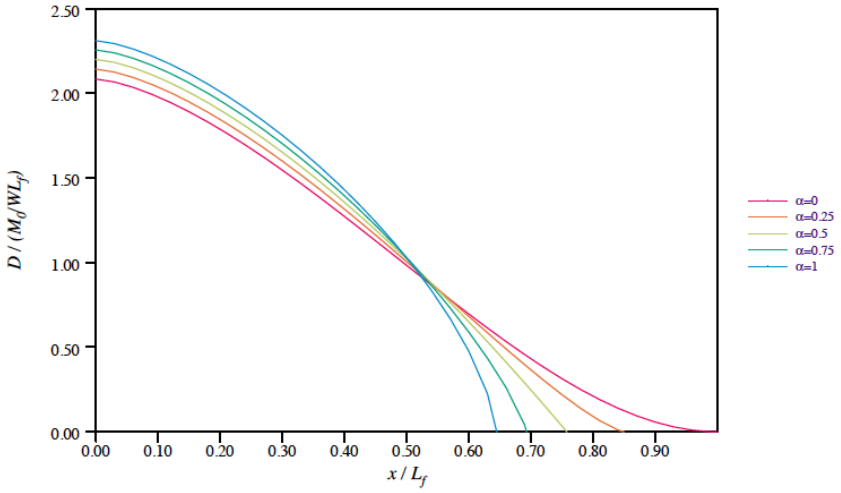

Figure 4: The final sediment distribution versus distance for varying values of α, [3].

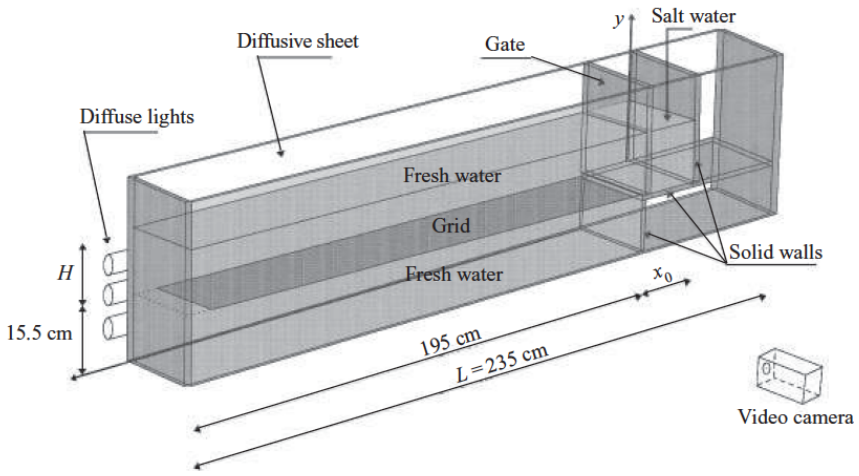

Figure 5: Experimental set-up for the analysis of a gravity current flow over a porous media.

3 Porous Boundary

Another important gravity current situation is the flow over a porous boundary. This may be considered to be similar to the particle-laden fluid current, as the porous boundary acts as a continuous loss of buoyancy of the fluid in a similar manner to the parcel sedimentation of the particle laden fluid. In this case, the flow reduces in density as it flows simply because the denser current is being absorbed by the porous boundary. A representation of the possible experimental set-up of a porous boundary gravity current is given in Figure 5. Further details of this case will refer the reader to [5] and [6].

4 Boundary Currents: Experimentation

In this section, we examine the experimental results of particle-laden gravity currents which are instantaneously released into the homogeneous ambient fluid. This section is based on [3].

4.1 Method to Measure the Thickness of the Sedimentation

For examining the particle-laden gravity currents, it is necessary to measure the sediment layer thickness instantaneously and locally. Here, the thickness of the layer is measured with the use of its electrical resistance. The thicker the sediment layer is, the higher its electrical resistance is. By using this fact, the experimental tank in Figure 6 is used to measure the thickness of the gravity current.

4.2 Results of the Boundary Currents

Experiments of a lock-release gravity currents were performed for various lock aspect ratios (R). Initially, Silicon-Carbide particles were suspended by the water in the lock, and then released instantaneously. Figures 7 shows the time evolution of the gravity current with

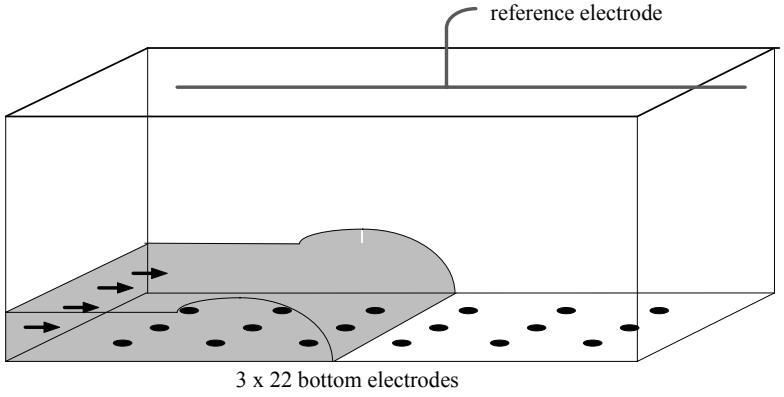

Figure 6: Illustration of the experimental tank to measure sediment thickness. The gray image represents the propagating gravity current.

$R = 0.65$ (low aspect ratio). Each figure shows the image of the current and the plot of the deposit thickness $D(x)$ (defined in (11)).

It is found in this case, that the current has a long tail and the particles are suspended for a long time. Actually, the height of the tail and the magnitude of $D(x)$ are nearly constant until 35 s. After that, a slight maximum can be found near the head of the current.

For the case of the current with the high aspect ratio, instead of the long tail, the current has a short core near the head, and the particles are suspended for a shorter time (not shown).

Figure 8 shows the non-dimensional lengths of currents in the experiments of the four different aspect ratios and the theoretical integral models. Distance and time are non-dimensionalized by using L_f and τ, respectively. The result of the standard integral model corresponds to the experimental data when $R \leq 1.3$. Furthermore, when the dependence of F_h on the current depth is considered, the theoretical prediction becomes closer to the experimental data. However, Figure 8 shows that the current with the highest aspect ratio ($R = 2.6$) is fastest, and the differences between its data and the theoretical predictions grow in time. [4] suggested that the standard integral model underestimates the final length of the current by a factor of 1.6. However, the prediction of this adjusted integral model well corresponds to the experimental data for only $R = 2.6$. The prediction of the integral model with the moving trailing edge ([2]) also well corresponds to the experimental data for $R = 2.6$. This model contains the adjustable parameter C_S, which is set to 1.5, in order to obtain the best fit with the experimental data for $R = 2.6$.

Figure 9a-d show the final sediment distributions for $R = 2.6, 1.3, 0.87$, and 0.65, respectively. The cases of $R = 1.3, 0.87$, and 0.65 are similar (Figure 9b-d). The large sediment layer thicknesses are observed near the locks, and they decrease monotonically. Their distributions have inflection points and local minimums. However, the case of $R = 2.6$ (Figure 9a) is different from the others. The local minimum is observed near the lock, and the local maximum follows it.

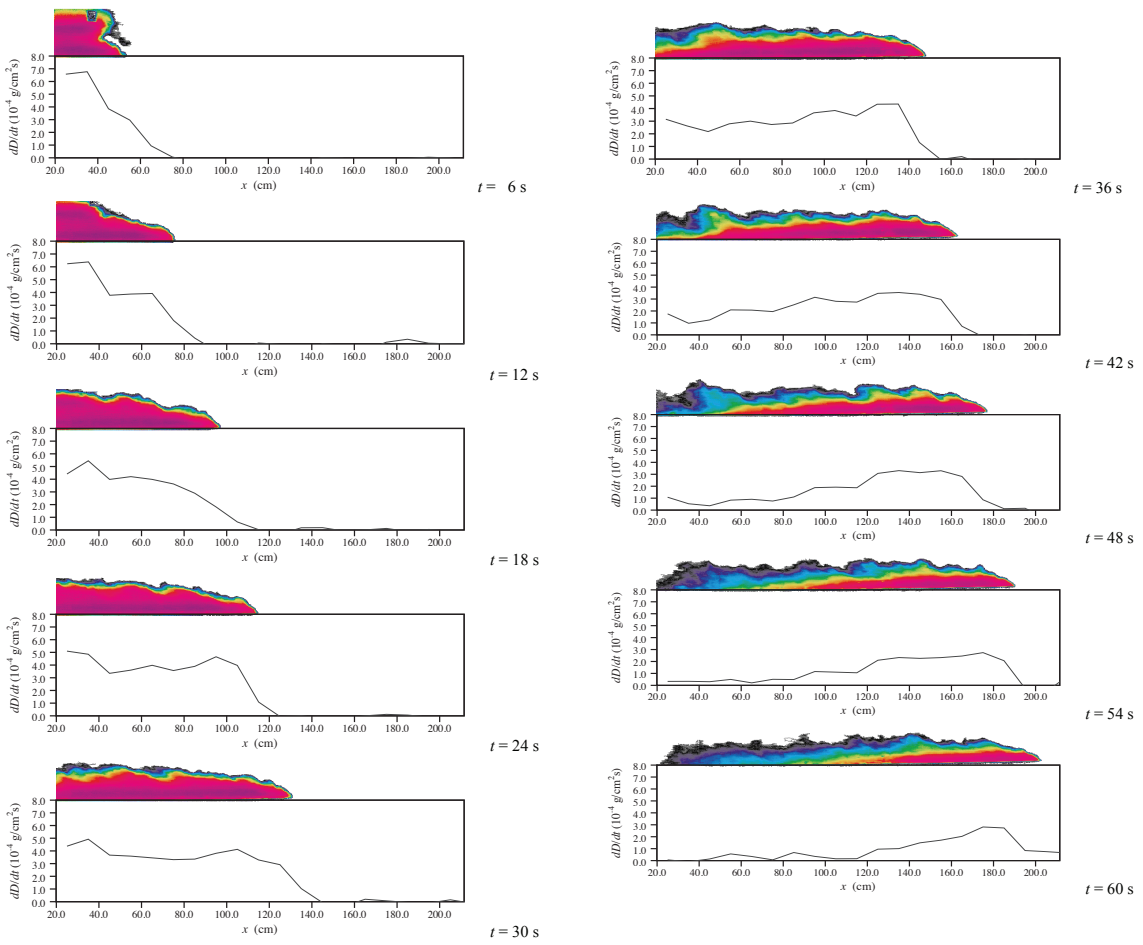

Figure 7: The images of the lock-release particle-laden gravity currents and the plots of its deposit thicknesses $D(x)$. The definition of $D(x)$ is in (11).

Figure 9a-d also show several theoretical predictions. It is found that the result of the standard integral model well corresponds to the experimental data for $R \leq 1.3$ (Figure 9b-d), but not for $R = 2.6$ (Figure 9a). The curve of "shallow water model" is obtained by using the numerical approximation proposed by [1]. Every theoretical model can not predict the local maximum of the current with $R = 2.6$. The only exception is the modified integral model proposed by [2] with the adjustable parameter $C_S = 1.5$ as Figure 8. However, this model has just the local maximum, and its prediction does not correspond to the experimental data (Figure 9a).

The mechanism at which the particles maintaining the initial concentrations reach the front, and then they are deposited is proposed from the following two facts. Firstly, the settling time of the particles ($\frac{h}{V_S}$) is much longer than the speed of the current propagation ($\frac{L_0}{\sqrt{g'h}}$). Secondly, the magnitude of the turbulent velocity for mixing the particles is much smaller than that of the propagation speed. This mechanism is confirmed by using the experimental data. Figure 10a-d show the plots of the deposition rate ($\frac{dD}{dt}$) at various times.

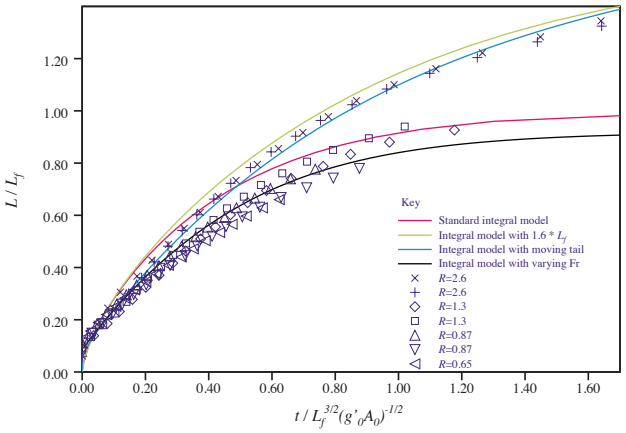

Figure 8: The non-dimensional lengths of the currents for lock-release particle-laden currents. The symbols and curves represent the experimental data and the theoretical predictions, respectively.

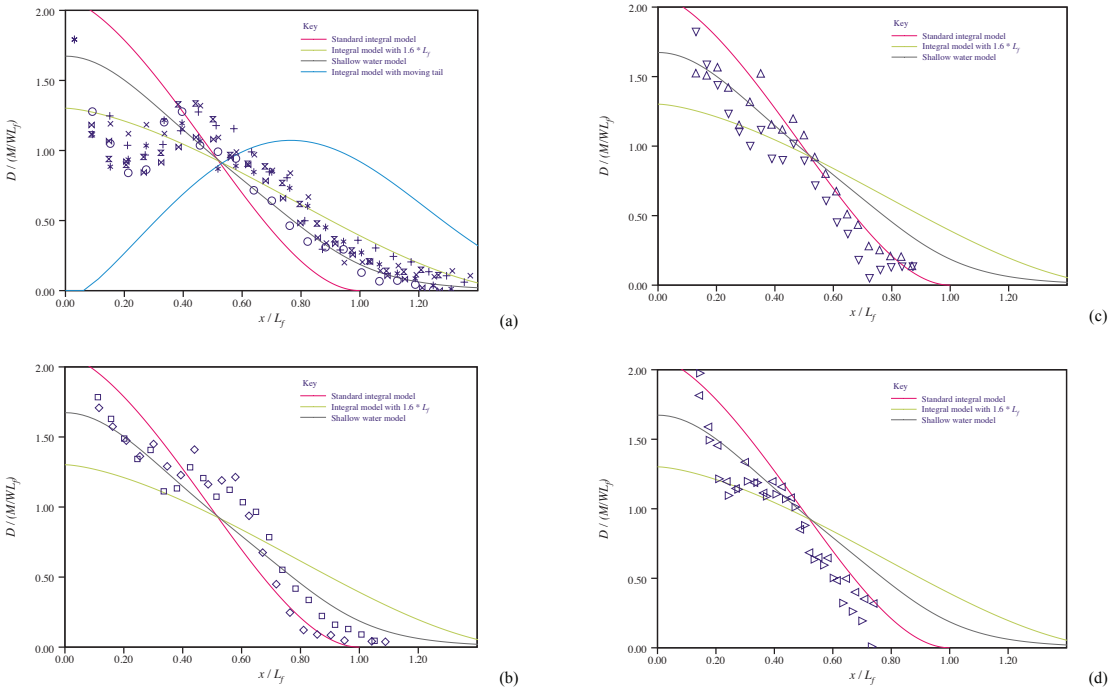

Figure 9: The final sediment distributions for (a) $R = 2.6$, (b) $R = 1.3$, (c) $R = 0.87$, and (d) $R = 0.65$. The symbols and curves represent the experimental data and theoretical predictions, respectively. The deposit thickness and distance are non-dimensionalized.

The purple line represents the expected maximum of the deposition rate from the front

position and above mechanism. It is found that the purple lines well correspond to the instantaneous maximums of the deposition rate.

The integral model with $\alpha = 1$ can express the imperfect turbulent mixing, and then can predict the position $(\frac{L_f}{(2\alpha+1)^{2/5}})$ where the deposition is finished. In Figure 10a-d, the ticks at the top represent these positions. The difference between the experimental data and model predictions is attributed to two facts. First, the location where the magnitude of the deposition begins to decrease is closer to the release position for the experiments than for the models, and second, the models predict abrupt ends of depositing.

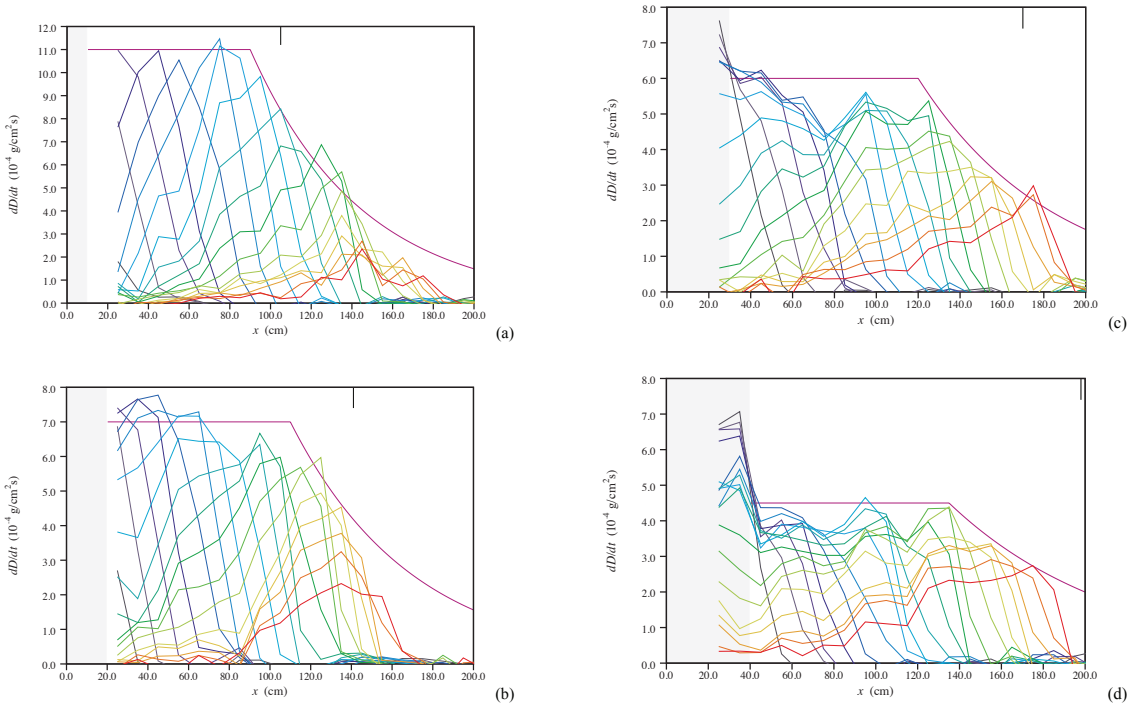

Figure 10: The distributions of the deposition rate $(\frac{dD}{dt})$ at various times for (a) $R = 2.6$, (b) $R = 1.3$, (c) $R = 0.87$, and (d) $R = 0.65$. The time interval is 3 s. The purple line represents the expected maximum of the deposition rate. The tick at the top represents the expected position by the integral model ($\alpha = 1$) where the deposition is finished.

5 Constant-Flux Boundary Currents

In this section, the boundary currents with a continuous release of the particle-laden fluid is examined. Instantaneous deposition were measured by using the system of Section 4.1, as in the preceding experiments. This section is also based on [3].

5.1 Method to Supply Particle-Laden Fluid Continuously

First, we explain how to supply particle-laden fluid continuously. The following system (Figure 11) was used. This system has a particle hopper and a conveyor belt with a scraper, and a constant head tank, which supply the Silicon-Carbide particles and water into the mixing tank at a constant rate, respectively. The particle concentration can be changed by adjusting the speed of the conveyor and the height of the scraper. Fluid is well mixed in the tank, and then supplied into the experimental tank.

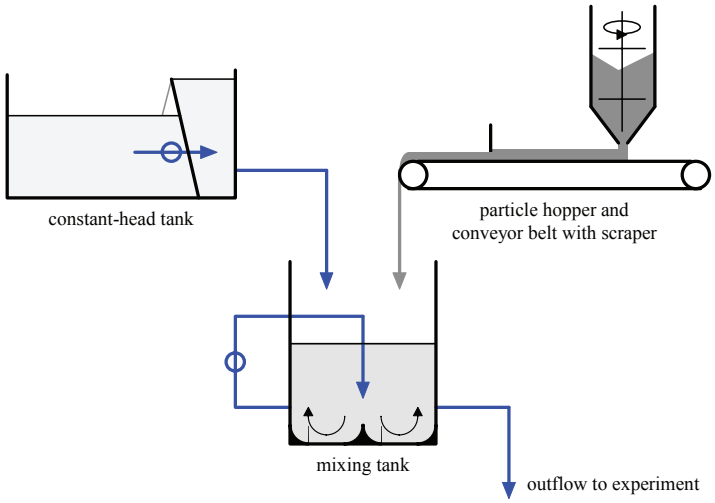

Figure 11: The system supplying the particle-laden fluid continuously.

5.2 Results of the Constant-Flux Boundary Currents

Figures 12 shows the images of the constant-flux particle-laden fluid currents. The color represents the particle concentration. Initially (Figure 12a-f), the front of the current is developed. The concentration near the front gradually decreases due to the deposition, while the concentration near the tail is nearly constant due to the fluid supply. At later time (Figure 12g), the front disappears and the current becomes nearly in steady state. The particle-laden fluid supply maintains the tail in which the particle concentration decreases gradually along the bottom. In addition, the height of the tail is nearly constant in time.

Initially, as the cumulative effects of deposition are small, the buoyancy flux $B = g'Q$ is nearly constant, where $Q(= uh)$ is the volume flux. As the buoyancy drives the current, the speed of the current is also nearly constant (Figure 13). Thus the initial velocity is scaled by $B^{1/3}$. At later time, as the particles are deposited, B decreases. This fact leads to a decrease of the front speed.

Figure 14 shows the plots of the deposition rate. The horizontal extent of the deposition layer increases, as the front propagates further. At later time, as the speed of the front decrease, the curve at each time becomes closer. Figure 14 also shows the plot of the average deposition rate during the steady state. At most locations, the initial deposition

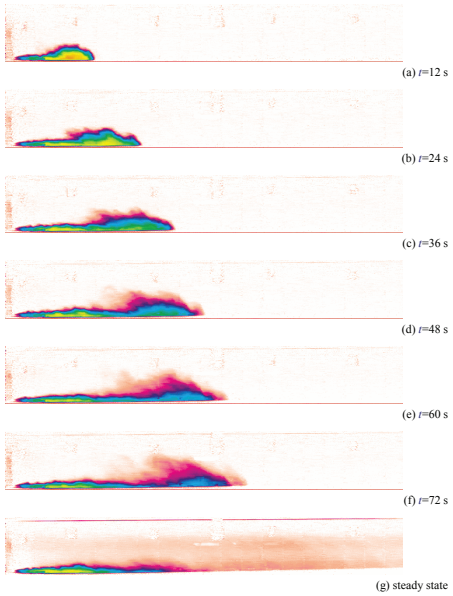

Figure 12: The images of the constant-flux particle-laden fluid currents. The color represents the particle concentration. The time interval is 12 s. (g) shows the current in the first 10 minutes after the start.

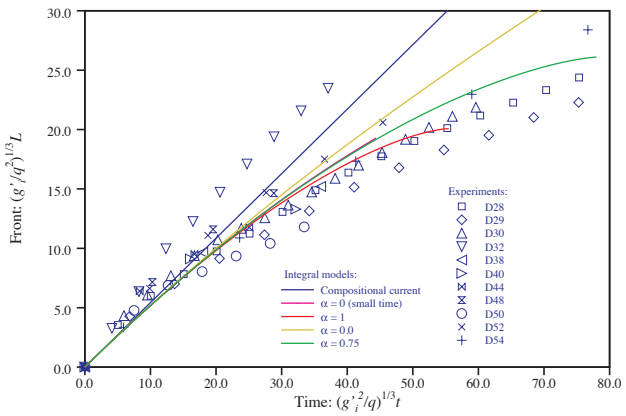

Figure 13: The positions of the fronts plotted against time. The symbols and curves represent the experimental data and model predictions. Distance and time are non-dimensionalized.

rates are higher than the average one. This means that the initial current carries more particles than the steady one.

Finally, we examine the steady state. The steady current can be divided into three zones (Figure 15a). In zone I, the entrainment of the ambient fluid occurs. In zone II, the current

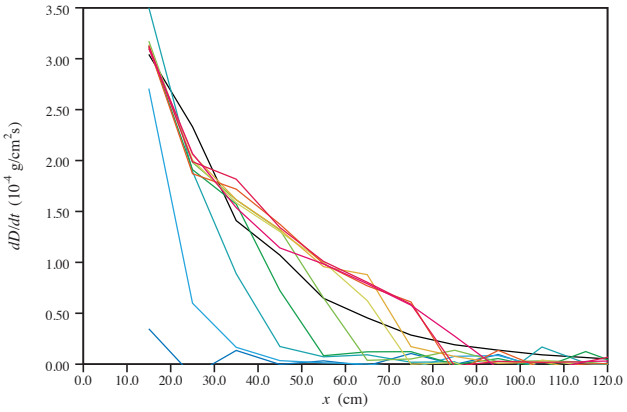

Figure 14: The deposition rates plotted against the horizontal distance for the constant-flux particle-laden fluid currents. The curves are at 12 s intervals. The black curve shows the deposition rate averaged over 5 minutes in the steady state.

has the nearly constant height, and this zone is the longest. Zone III is the extremity of the current, and the height and concentration become zero.

As shown later, the characteristic length scale of zone II depends on the volume flux at the end of zone I ($Q_{\rm C}$). Firstly, in order to estimate $Q_{\rm C}$, the momentum flux ($F.F.$) at the start and end of zone I is calculated;

$$F.F. := \rho_0 \int_0^h \left(u^2 + g'z\right)\, dz = \rho_0 \left(\frac{Q^2}{h} + \frac{Bh^2}{2Q}\right). \tag{12}$$

Here, the four assumptions were made: (1) Boussinesq approximation; (2) the uniformity of the fluid motion in the layer; (3) the hydrostatic balance because of the approximate horizontality of the fluid motion at the start and end of zone I; and (4) the quite small effects by the ambient fluid ($z = h$ to H).

The entrainment into the layer is characterized by the layer Richardson number (Ri);

$$\mathrm{Ri} := \frac{g'h}{u^2} = \frac{BH^3}{Q^3}. \tag{13}$$

Ri represents the ratio of the magnitude stratification to that of the velocity. (12) can be expressed in terms of Ri;

$$\frac{F.F.}{\rho_0 B^{1/3}} = Q\left(\mathrm{Ri}^{-1/3} + \frac{1}{2}\mathrm{Ri}^{2/3}\right). \tag{14}$$

This quantity is the same at the start and end of zone I. [7] showed that Ri is nearly at unity where the entrainment ceases, i.e., at the end of zone I. Thus, the volume flux at the end of zone I ($Q_{\rm C}$) can be expressed as follows;

$$Q_{\rm C} = Q_{\rm I}\frac{2 + \mathrm{Ri_I}}{\mathrm{Ri_I}^{1/2}}, \tag{15}$$

where Q_{I} and Ri_{I} are the volume flux and Richardson number at the start of zone I, respectively.

By using Q_{C}, we can estimate the characteristic decay length scale of the particle concentration in zone II. From the observation, h is nearly constant in zone II. This fact suggests that volume flux in zone II is nearly constant and equal to Q_{C}, and then the horizontal velocity of the current $U(=\frac{Q_{\mathrm{C}}}{h})$ is also nearly constant. In addition, from the visual observation, it is assumed that the current is well mixed and concentration (ϕ) is independent of the height. Thus, we can express the rate of the loss of the particles through the layer as follows;

$$\begin{aligned} h\, d\phi &= -\phi V_{\mathrm{S}} dt, \\ \frac{d\phi}{dx} &= -\phi \frac{V_{\mathrm{S}}}{Q_{\mathrm{C}}}, \end{aligned} \tag{16}$$

where $U = \frac{dx}{dt}$ is used. From this differential equation, it can be shown that ϕ exponentially decays with a decay length scale $\frac{Q_{\mathrm{C}}}{V_{\mathrm{S}}}$. In Figure 16, the typical decay length scales (λ_{mean}) obtained by the experiments are plotted against the theoretical one $\frac{Q_{\mathrm{C}}}{V_{\mathrm{S}}}$. It can be confirmed that $\frac{Q_{\mathrm{C}}}{V_{\mathrm{S}}}$ represents the typical decay length scale.

In zone II, Ri is between 0.6 and 1.0. This means that the layer is strongly stratified and has a sharp boundary against the ambient fluid. Thus, instability occurs there, which looks like Holmboe shear instability. In Figure 15b, there are waves near the top boundary of zone II corresponding with this instability.

In zone III, as the particle concentration becomes very low, it is difficult to make clear observations. The flow velocity is believed to be too low to maintain the well-mixed current. Thus the steady wedge-shaped extremity is formed. The angle of the wedge (θ) may be calculated from $\theta = \frac{V_{\mathrm{S}}}{U}$, however, we have no experimental data to confirm this.

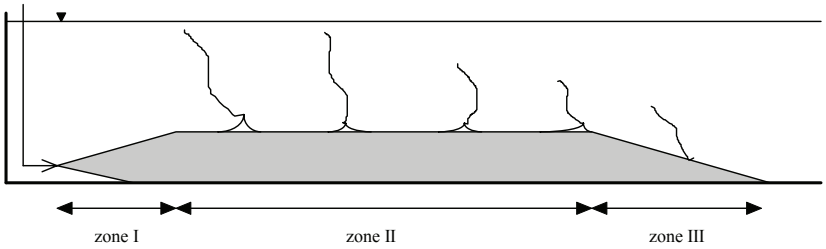

Figure 6.6. Sketch of the steady state reached with a constant flux of particle-laden fluid. The characteristics of the three zones are described in the text.

(a) Figure 15a

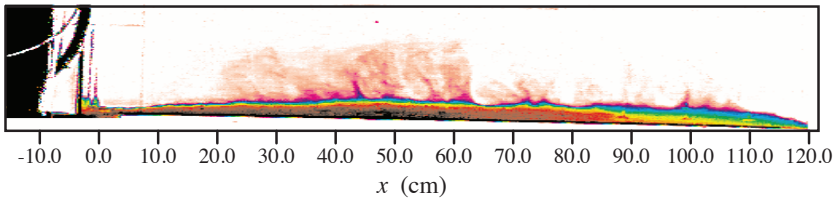

(b) Figure 15b

Figure 15: (a) The conceptual illustration for the steady current corresponding to (b). (b) the image of the final steady states. Color represents the particle concentration, and combined dye which is added to visualize Holmboe-like instability near the top of the current.

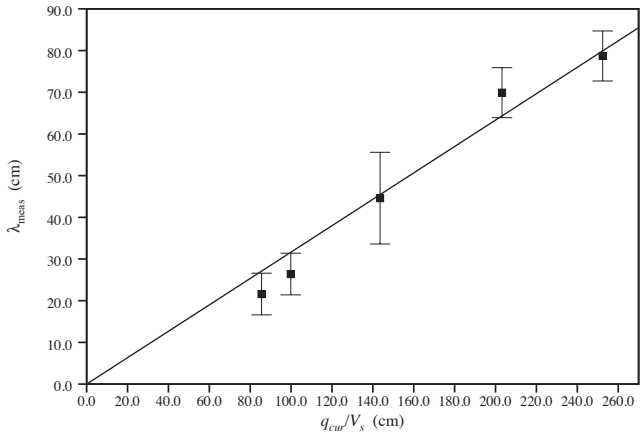

Figure 16: The typical decay length scales (λ_{mean}) obtained by the experiments plotted against theoretical one ($\frac{Q_C}{V_S}$).

References

[1] R. T. Bonnecaze, H.E. Huppert, and J.R. Lister, *Patterns of sedimentation from*

polydisperse turbidity currents, Proc. Roy. Soc. London A, 452 (1996), pp. 2247–2261.

[2] W.B. Dade and H.E. Huppert, *Runout and fine-sediment deposits of axisymmetric turbidity currents*, J. Geophys. Res., 100 (1995), pp. 18597–18609.

[3] F. de Rooij, *Sedimenting particle-laden flows in confined geometries*, PhD thesis, University of Cambridge, 1999.

[4] H.E. Huppert, *Quantitative modelling of granular suspension flows*, Phil. Trans. R. Soc. Lond. A, 356 (1998), pp. 2471–2496.

[5] L. P. Thomas, B. M. Marino, and P. F. Linden, *Gravity currents over porous substrates*, J. Fluid Mech., 366 (1998), pp. 239–258.

[6] ——, *Lock-release inertial gravity currents over a thick porous layer*, J. Fluid Mech., 503 (2004), pp. 299–319.

[7] D.L. Wilkinson and I.R. Wood, *A rapidly varied flow phenomenon in a two-layer flow*, J. Fluid Mech., 47 (1971), pp. 241–256.

GFD 2013 Lecture 10: Gravity currents on slopes and in turbulent environments

Paul Linden; notes by Gregory Wagner and Barbara Zemskova

June 28, 2013

1 Introduction

Natural gravity currents are often found flowing down slopes. Examples include the flow of hot ash down the flank of a volcano, to snow avalanches down the sides of mountains, to the flow of dense water from saline seas or silty rivers into the ocean and down a continental slope. The tilting of a gravity current down a slope adds new physics to the problem, in particular the process of entrainment of ambient fluid into the current can be important (which in flows on flat surfaces in largely suppressed by density stratification).

2 Gravity currents on slopes

2.1 Finite volume current

A finite volume gravity current can be studied with an experimental apparatus involving the sudden release of a fixed volume of dense fluid into a lighter fluid. A diagram of an experimental apparatus is shown in Figure 1. Images from a finite volume release experiment on six different slopes is shown in Figure 2, and streak photos showing the fluid motion within the current for an experiment on a 20° slope are shown in Figure 3.

The relevant parameters in a finite volume release and their dimensions are

g'	reduced gravity (without taking slope angle into account)	$[L/T^2]$;
Q_0	current volume / width	$[L^2]$;
θ	slope angle	no units.

The only combinations of parameters which give the correct units for velocity, length, and height of the current are then

$$\begin{aligned} U &= \left(g'\right)^{1/2} Q_0^{1/4} f_0(\theta), \\ \{L, h\} &= Q_0^{1/2} f_{1,2}(\theta). \end{aligned} \tag{1}$$

We also expect the entrainment, which we characterize by a "rate of entrainment" velocity u_e to scale with the velocity of the flow such that

$$u_e \sim U, \tag{2}$$

where in the regime we are interested in, U is constant. We can then conclude that

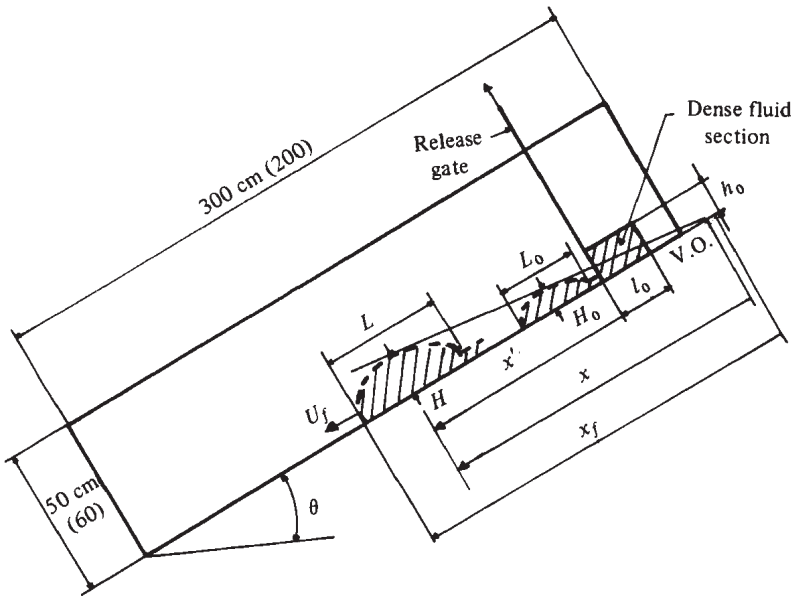

Figure 1: Diagram of experimental apparatus for finite volume release of dense fluid on a slope [1].

1. the volume of the current increases linearly in time, and therefore
2. both L and h increase linearly in time because the shape of current is self-similar.

One particularly interesting point is that due to the flow structure within the current, most of the fluid entrained from the ambient environment enters at the rear of the flow. This is particularly apparent in the low Reynolds number limit for the 90° angle current, where the falling dense fluid is simply a negatively buoyant vortex ring. The scaling of the height and length of the current with time are plotted in Figure 4, and the increase in the height of the current as a function of the slope angle (which we denoted $f_2(\theta)$) is plotted in Figure 5. A plot of the dimensionless front velocity is shown as a function of distance in Figure 6 – note that the range of velocities is small even for a large range of slope angles.

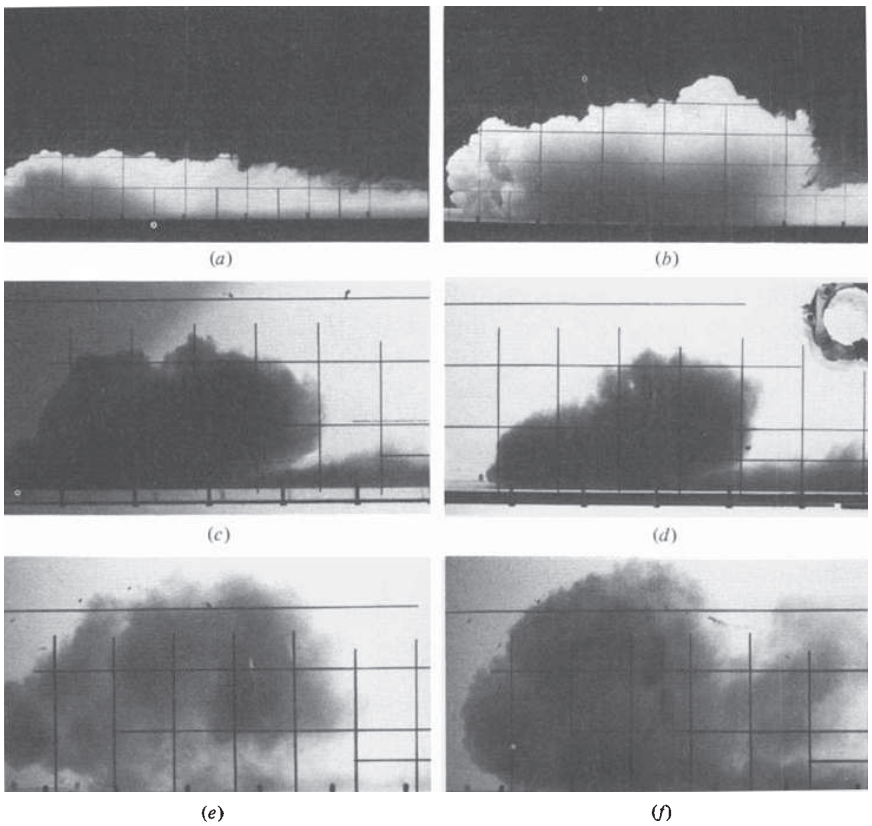

Figure 2: Finite volume release of dense fluid on a slopes angled at 5, 15, 45, 60, and 90° (images a–f respectively). [1].

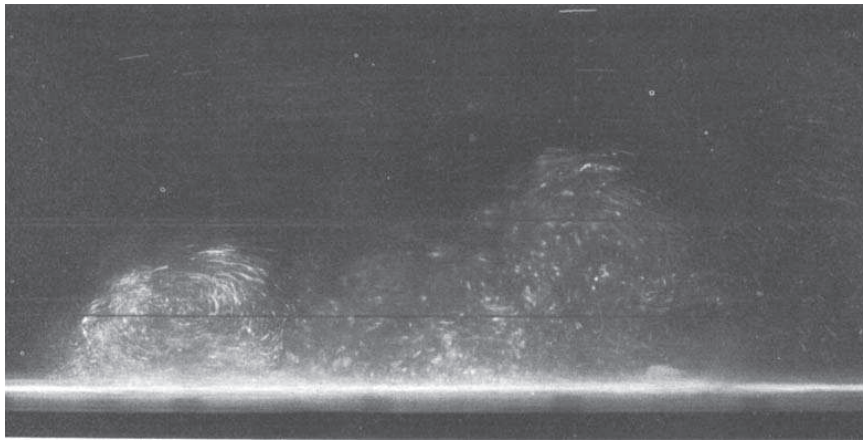

(a)

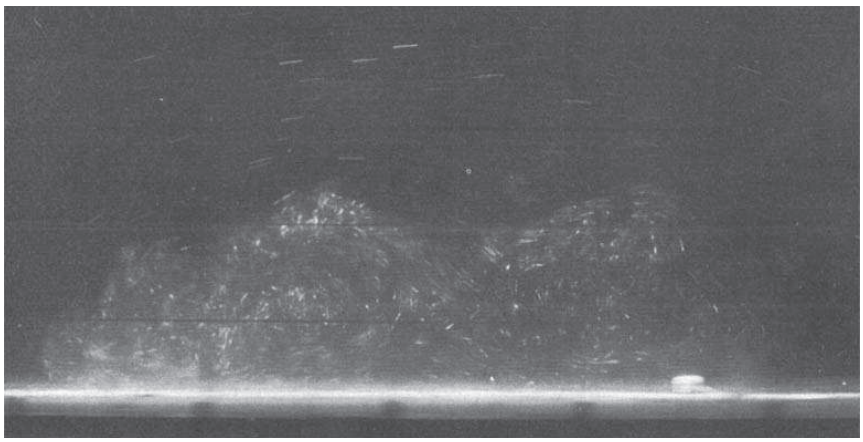

Figure 3: Streak photos of finite volume release of dense fluid on a 20° slope [1].

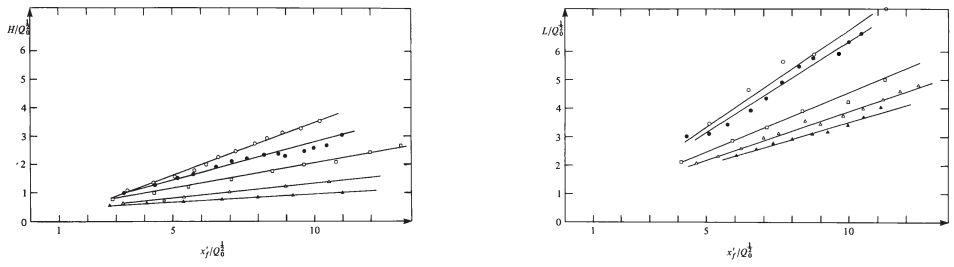

Figure 4: Dimensionless current height and length on slopes 5° (▲), 15° (△), 45° (), 60° (●), and 90° (○). From [1].

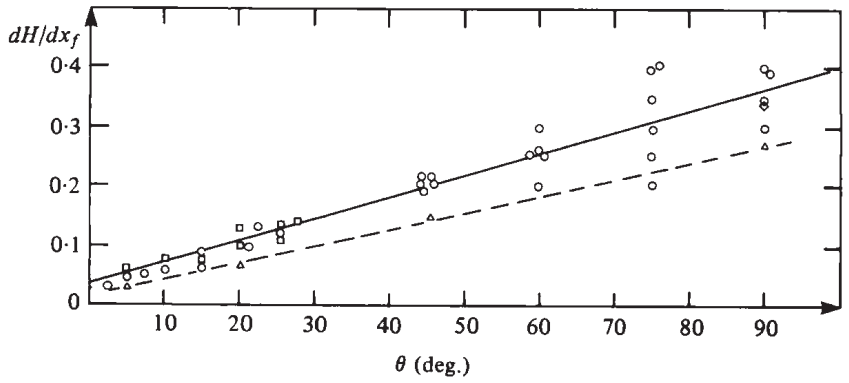

Figure 5: Increase in height as a function of slope. The dashed line is the current head measured by [3]. From [1].

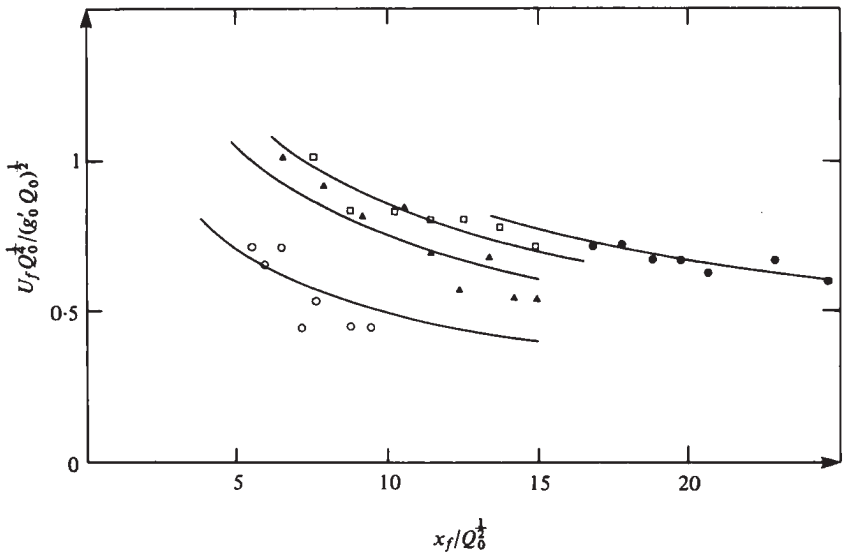

Figure 6: Dimensionless front velocity as a function of distance for slopes of 5° (•), 15° (), 45° (▲), and 60° (○). From [1].

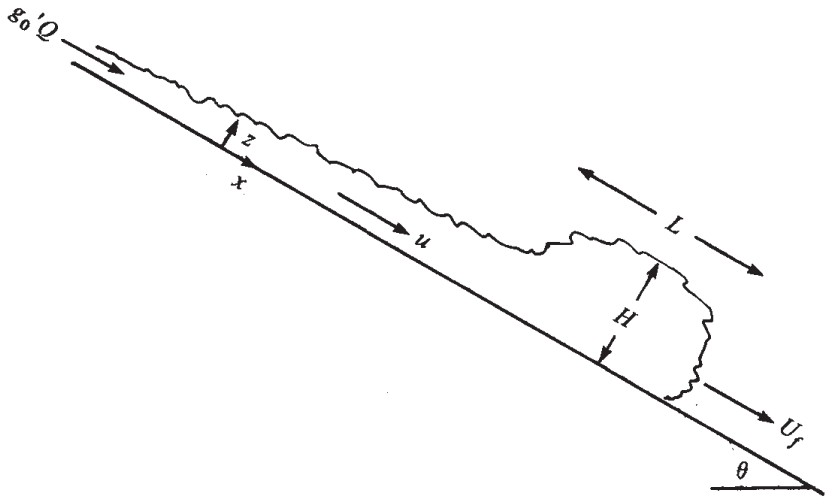

Figure 7: Schematic of a constant flux gravity current down a slope. From [3].

2.2 Constant flux current

In a constant flux gravity current the rate at which volume is released down the slope is fixed. In this case the current usually exhibits a "head" at it's front, which can be characterized by dimensions L and H, followed by a long, thinner tail. A schematic of a constant flux current is shown in Figure 7 and images from an experiment are shown in Figure 8.

The relevant parameters in a constant flux current and their dimensions are

g'	reduced gravity (without taking slope angle into account)	$[L/T^2]$;
Q	volume flux / unit width	$[L^2/T]$;
θ	slope angle	no units.

Dimensionally then the velocity U of the current must be

$$U = \left(g'Q\right)^{1/3} f(\theta). \tag{3}$$

A plot the front position of a gravity current in time and a plot of U versus $(g'Q)^{1/3}$ showing the validity of this scaling are shown in Figure 9. A plot of the quantity $U/\left(g'Q\right)^{1/3}$ versus slope angle is shown in Figure 10 in an attempt to extract $f(\theta)$. While the data in Figure 10 is scattered, an examination of a similar plot for the speed of a cavity propagating in a fluid-filled tube, which perhaps represents the positive buoyancy case of a gravity current on a slope is shown in Figure 11, demonstrating well developed curves for $f(\theta)$. The growth rate of the height of the head at the front of the gravity current is plotted against slope angle in Figure 12. The entrainment rate as a function of slope and Richardson number is plotted in Figure 13. One interesting observation for the vertical current is that the entrainment and current shape is identical to a falling or rising plume which has been divided in half.

A persistent problem with the constant flux experiments is that it is difficult to obtain a high Reynolds number for the low angle flows in the lab such that the loss of momentum

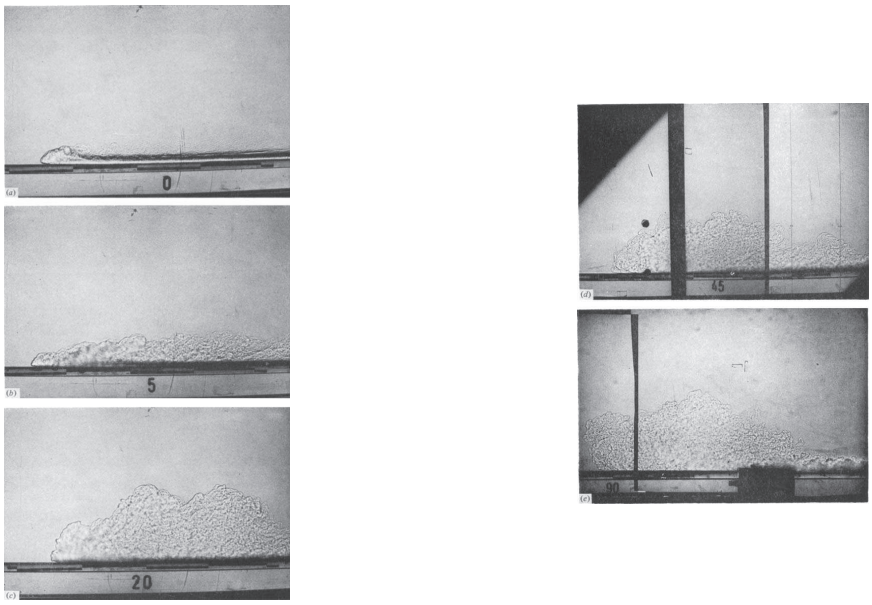

Figure 8: A constant flux gravity current flowing from right to left on slopes of 0, 5, 20, 45, and 90°. From [3].

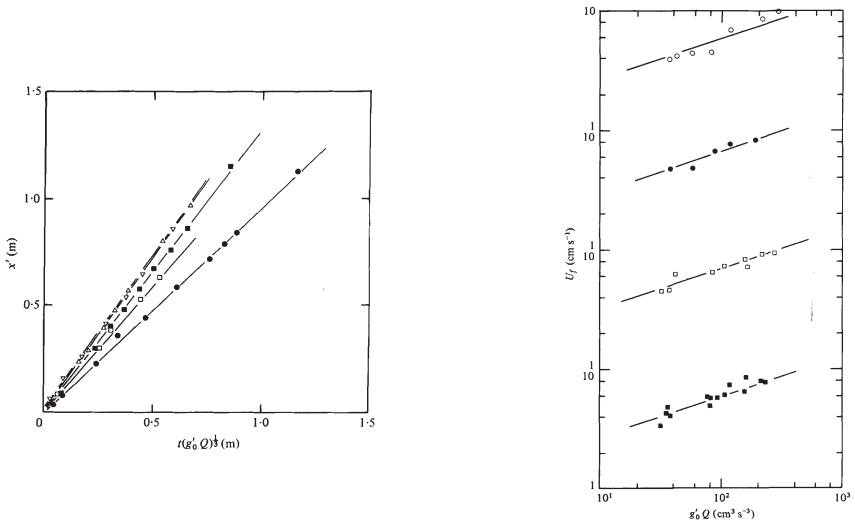

Figure 9: The front position of a gravity current on slopes of 0° (•), 5° (□), 20° (■), 45° (△), and 90° (▽). From [3].

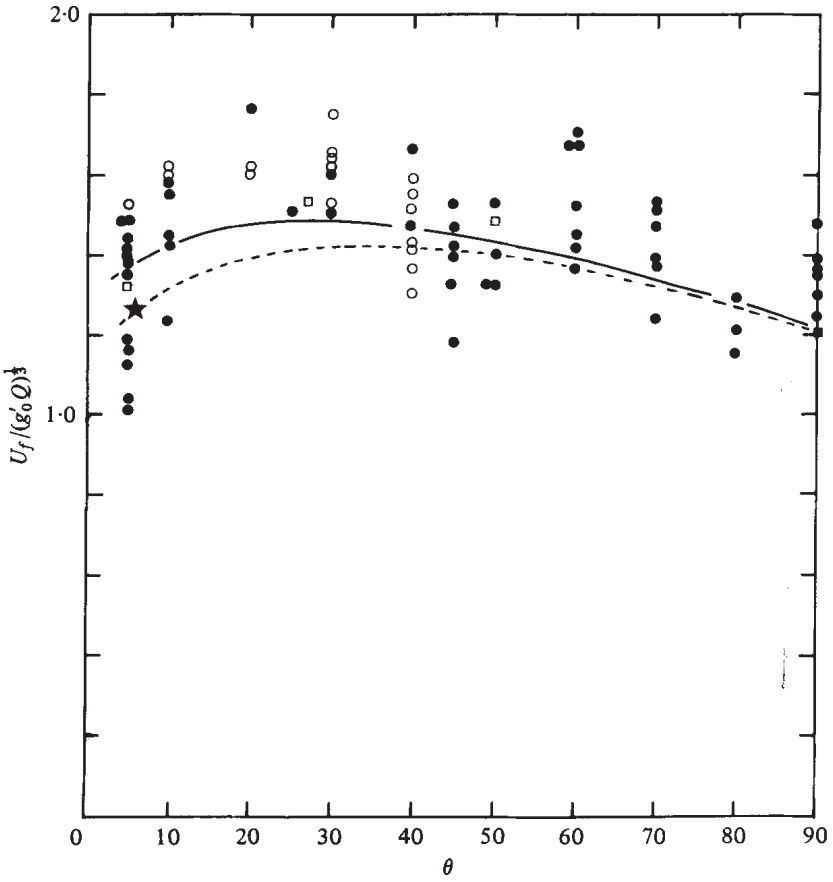

Figure 10: Non-dimensional front velocity $U/\left(g'Q\right)^{1/3}$ plotted against slope. $\star$ [5], [9], ■ [8], ○ [7], • [3]. From [3].

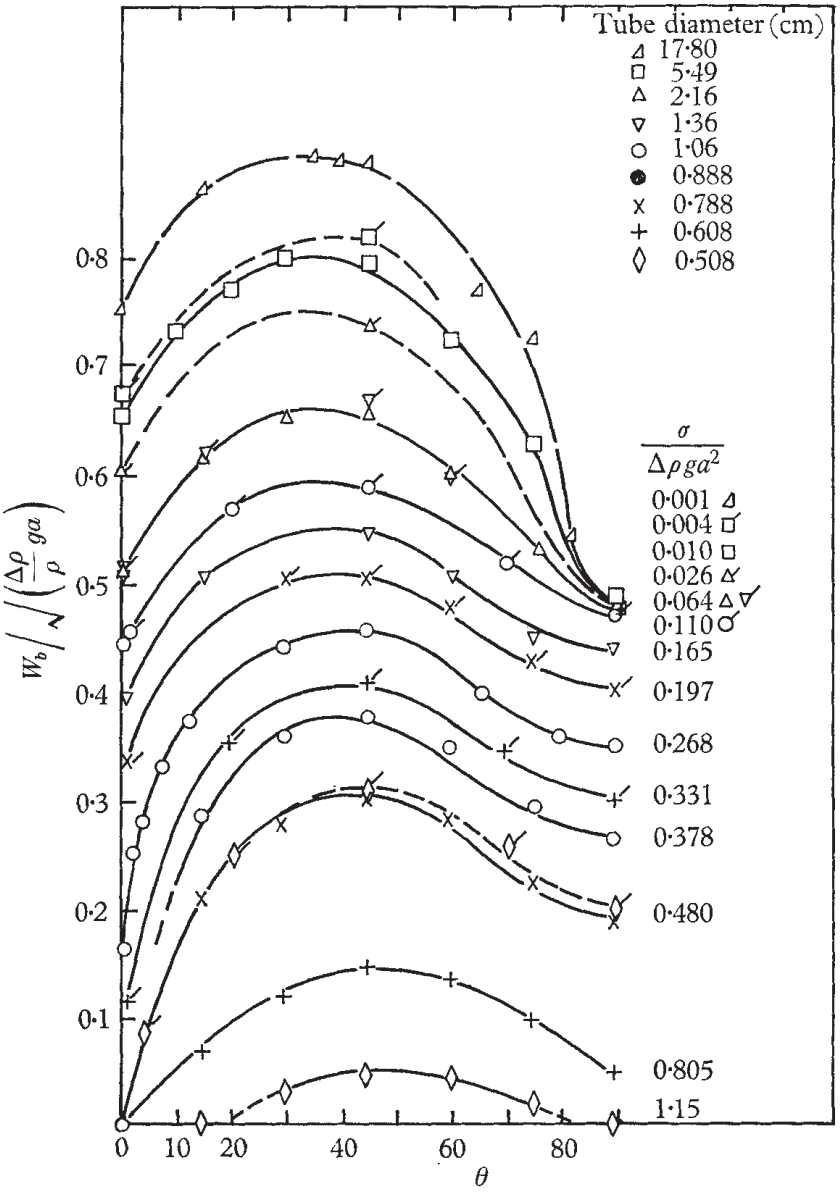

Figure 11: The speed of a cavity propagating along an emptying tube as a function of the angle of the tube axis to the horizontal. The speeds are expressed in terms of Froude numbers and the differences result from the effects of surface tension. In every case the maximum speed is at an inclination of 30° [10]

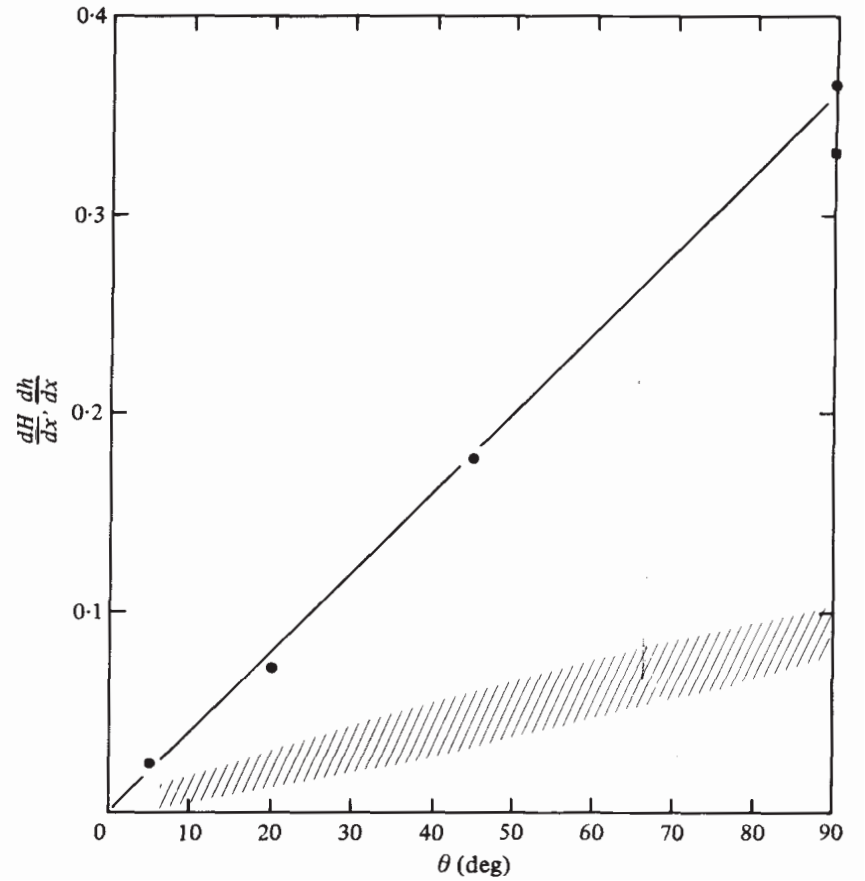

Figure 12: Growth rate of the head $\mathrm{d}H/\mathrm{d}x$ plotted against slope. The height of the following thinner layer is also shown by the shaded region (from [4]). From [3].

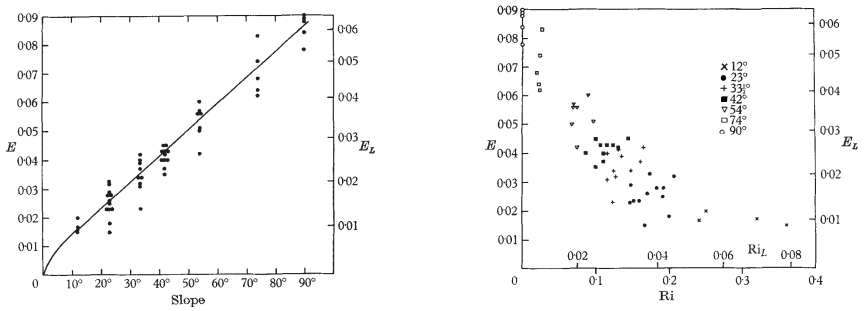

Figure 13: The entrainment rate measured in a continuous downslope flow as a function of slope angle and Richardson number Ri. From [4].

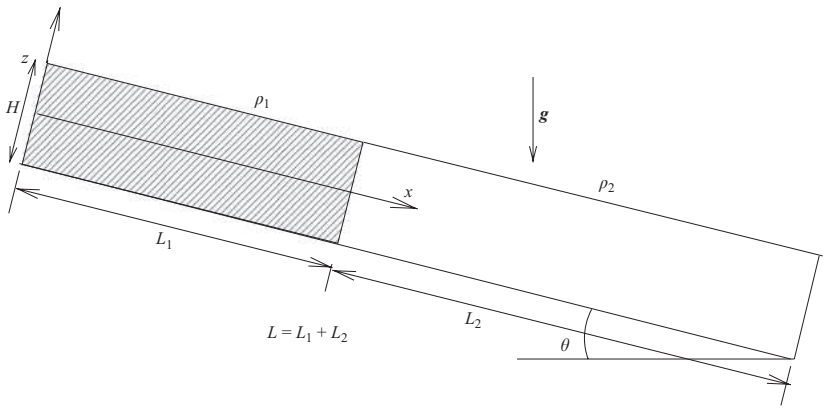

Figure 14: Lock exchange in a sloping channel [2].

due to bottom drag is not important. In many flows, additionally, we might expect a transition at some critical slope angle in the dominant factor controlling the velocity of the flow, from bottom drag to the loss of momentum due to the entrainment of ambient fluid. Additionally, because of the entrainment of ambient fluid, the velocity of the current is only a weak function of θ.

2.3 Lock exchange

We may also consider lock exchange in a sloping channel, which differs from the gravity currents considered above because of the addition of an upper boundary. A schematic of lock exchange in a sloping channel is shown in Figure 14. Similar to unconfined gravity currents on slopes, one of the most important differences induced by the slope is to make overturning and turbulent mixing more energetically favorable on the boundary between the two fluids. This is demonstrated by simulations (Figure 15) and experiments (Figure 16) and is especially evident at later times when the current becomes well-developed.

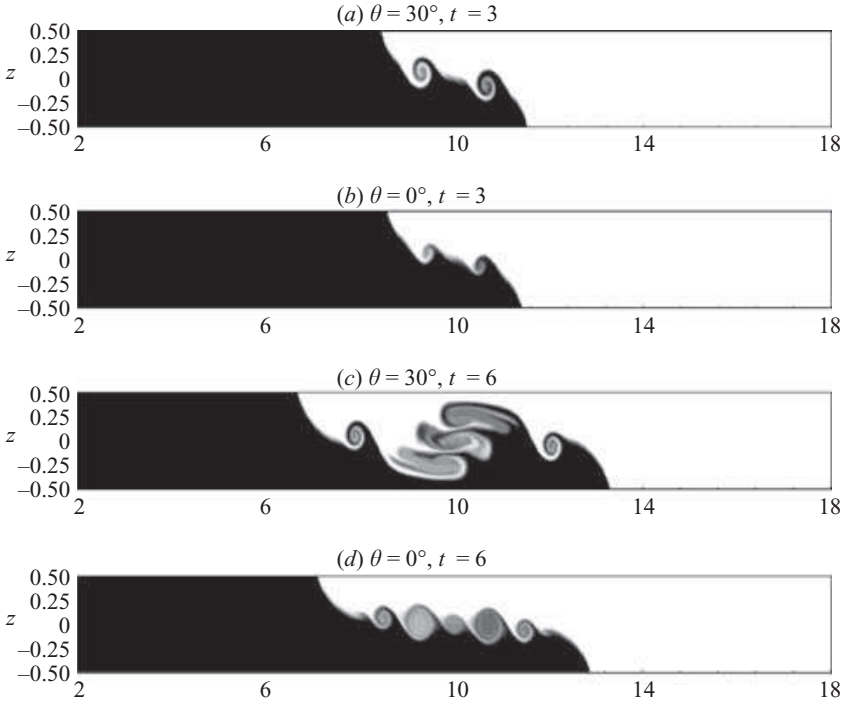

Figure 15: 2D DNS simulation of a Boussinesq sloping lock exchange for $\rho_1/\rho_2 = 0.98$ (where ρ_1 is on the right and ρ_2 is on the left) and $\Re = 4,000$ [2].

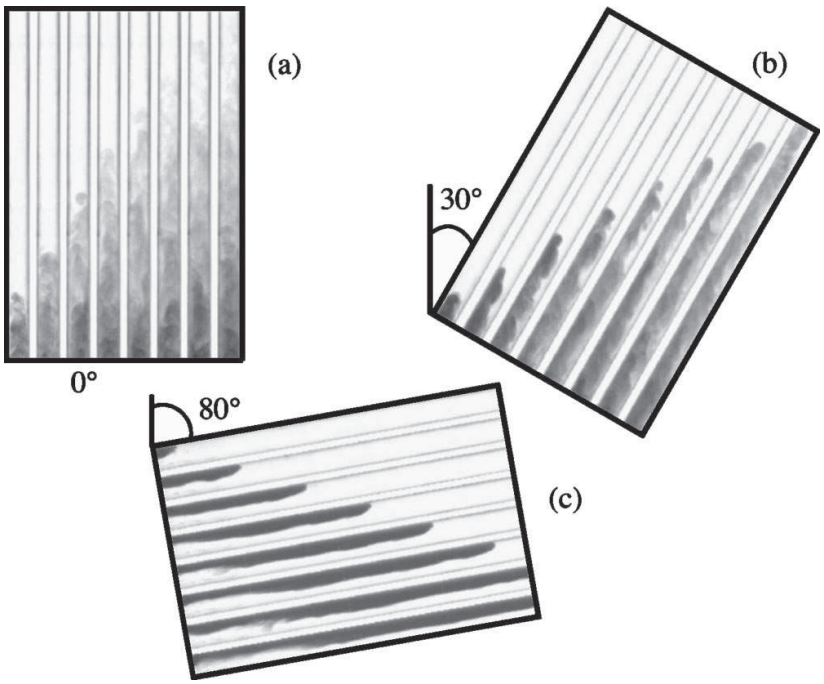

Figure 16: Images of sloping lock exchange at various angles for $\rho_1/\rho_2 = 0.992$. Note that $\theta = 90° - \alpha$, where θ is defined in the schematic in Figure 14 and α is the angle denoted in the images. From [6].

References

[1] P. Beghin, E. J. Hopfinger, and R. E. Britter, *Gravitational convection from instantaneous sources on inclined boundaries*, J. Fluid Mech., 107 (1981), pp. 407–422.

[2] V.K Birman, B.A. Battandier, E. Meiburg, and P.F. Linden, *Lock-exchange flows in sloping channels*, J. Fluid Mech., 577 (2007), pp. 53–77.

[3] R. E. Britter and P. F. Linden, *The motion of the front of a gravity current travelling down an incline*, J. Fluid Mech., 99 (1980), pp. 531–543.

[4] T. H. Ellison and J. S. Turner, *Turbulent entrainment in stratified flows*, J. Fluid Mech., 6 (1959), pp. 423–448.

[5] E. H. M. Georgeson, *The free streaming of gasses in sloping galleries*, Proc. Roy. Soc. A, 180 (1942), pp. 484–493.

[6] T. Séon, D. Hulin, J.-P.and Salin, B. Perrin, and E. J. Hinch, *Buoyant mixing of miscible fluids in tilted tubes*, Phys. Fluids, 16 (2004), pp. L103–L106.

[7] ——, *Buoyancy driven miscible front dynamics in tilted tubes*, Phys. Fluids, 17 (2005), pp. –31702.

[8] G. Tsang and I. R. Wood, *Motion of a two-dimensional starting plume*, J. Engng. Mech. Div. A.S.C.E., EM6 (1968), pp. 1547–1561.

[9] I. R. Wood, *Studies in unsteady self-preserving turbulent flows*, Tech. Report 81, University of New South Wales, Water Research Lab., 1965.

[10] E. E. Zukoski, *Influence of viscosity, surface tension and inclination angle on the motion of long bubbles in closed tubes*, J. Fluid Mech., 25 (1966), pp. 821–840.

Response of Thermohaline Circulation to Changes in Precipitation

Yuki Yasuda

October 1, 2013

1 Introduction

The oceanic thermohaline circulation has important roles in the global heat transport and hydrological cycle by transporting heat from low latitudes to high latitudes and by transporting freshwater from high latitude to low latitude. Especially, the marginal sea (e.g., Labrador and Greenland Seas) is important for the thermohaline circulation, because it is one of a few origins of the deep ocean water [4] and because waters such as Labrador Sea water spread widely [9]. However, its dynamics is not very clear.

One method for analyzing a complicated system is to use the reduced system in which the degree of freedom is lower than in the original system. [8] proposed the idealized two-dimensional dynamical system (DS) for the thermohaline circulation, i.e., two-box model. In this model, the exchange between the boxes is due to the mean flow directly driven by the pressure gradient. However, large-scale flow in the ocean is approximately geostrophically balanced, and hence, the assumption used for the two-box model is not valid.

[5, 7] derived the new two-dimensional DS. He considered the idealized marginal sea (Fig. 1). The boundary current is geostrophically balanced, which flows along the topographic contours because of the potential vorticity conservation and the pressure gradient between the boundary current and the interior region. On the other hand, in the interior region, the sea water is cooled by the atmosphere and becomes fresh by the precipitation. Thus, it is considered that baroclinic instability occurs due to the density difference between the boundary current (warm and salty) and the interior region (cold and fresh). The heat and salt transports are driven by these baroclinic eddies.

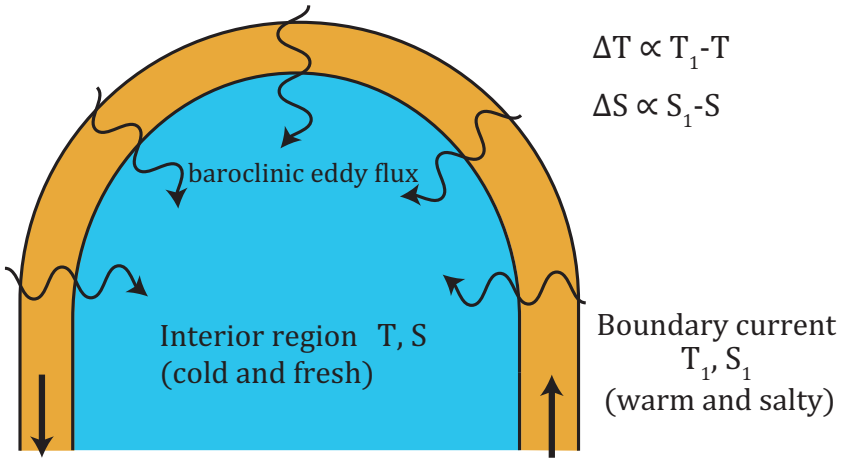

Figure 1: Schematic picture of the idealized marginal sea.

It is easy to understand the physics in the reduced DS, however, it is not clear whether this DS describes the correct physics inherent in the original system. [5, 7] compared the steady-state solutions obtained by the DS with those obtained by the numerical model in which mesoscale eddies are explicitly resolved. He showed that the derived DS well predicts the behaviors of the numerical model for the steady states.

In this study, we extend the DS proposed by [7] to the case with time-dependent precipitation and examine its behavior. After that, in order to confirm the validity of the DS, results by the DS are compared with those by the numerical model.

The structure of this report is as follows. In Section 2, we extend the DS and review its properties under the steady precipitation. In Section 3, the DS with periodic precipitation is examined. It is shown that there are three kinds of limit cycle. In Section 4, the results obtained by the DS in Section 3 are compared with results of the numerical model. It is shown that the DS qualitatively well describes the behaviors of the numerical model. In Section 5, the DS with step function precipitation is examined, and especially, transition time between the fixed points is analyzed. In Section 6, it is shown that the DS qualitatively well describes the behaviors of the numerical model also in the case of the step function precipitation. In Section 7, causes for the quantitative disagreement between the DS and

the numerical model are discussed. In Section 8, summary is made.

2 Two-dimensional non-autonomous dynamical system

2.1 Governing equations

The most important quantities for the idealized marginal sea (Fig. 1) are temperature and salinity, because the other quantities (e.g., baroclinic velocity and strength of the meridional overturning circulation) can be deduced from them. Thus, we consider the following fundamental equations for temperature and salinity:

$$\frac{\partial \overline{T}}{\partial t} + \boldsymbol{\nabla} \cdot (\overline{\boldsymbol{u}}\overline{T}) = -\boldsymbol{\nabla}(\overline{\boldsymbol{u}'T'}) + Q_T, \tag{1}$$

$$\frac{\partial \overline{S}}{\partial t} + \boldsymbol{\nabla} \cdot (\overline{\boldsymbol{u}}\overline{S}) = -\boldsymbol{\nabla}(\overline{\boldsymbol{u}'S'}) + Q_S, \tag{2}$$

where a bar represents the time average, and Q_T and Q_S represent non-conservative forcings (e.g, atmospheric cooling and precipitation). In the marginal sea, the time scale of baroclinic eddy is determined mainly by the relaxation time of the atmospheric cooling, because eddies are considered to run away from the baroclinic region. In this case, it is enough to take three-month average.

Four assumptions are made following [7] for deriving the reduced DS:

1. Temperature T_1 and salinity S_1 of the boundary current are constant.
2. Interior region is well-mixed, and temperature T and salinity S are constant there.
3. The magnitude of eddy flux is much larger than that of mean flux.
4. Integrated eddy fluxes are parametrized as follows:
   $\int \overline{\boldsymbol{u}'T'}\,\mathrm{d}S = \alpha V \Delta T = \alpha\beta|\Delta T - \Delta S|\Delta T$, and
   $\int \overline{\boldsymbol{u}'S'}\,\mathrm{d}S = \alpha V \Delta S = \alpha\beta|\Delta T - \Delta S|\Delta S$.

The first assumption is made for simplicity. The second assumption is based on the fact that the interior region is well-mixed when the deep convection occurs there. The third assumption is based on the fact that the mean boundary current flows approximately along the topographic contours. The fourth assumption is made for closing the governing equations. In the above

parameterization, α and β are the constants given by the characteristic values of topography, Coriolis parameter, basic density, and thermal and haline expansion coefficients [7]. ΔT and ΔS are the differences of mean temperature and mean salinity between in the boundary current and in the interior region.

The two-dimensional non-autonomous DS is obtained from (1) and (2) as follows:

$$\frac{\mathrm{d}\Delta T}{\mathrm{d}t} = -\Delta T\,|\Delta T - \Delta S| + \frac{2\mu}{\epsilon}(1 - \Delta T), \tag{3}$$

$$\frac{\mathrm{d}\Delta S}{\mathrm{d}t} = -\Delta S\,|\Delta T - \Delta S| - \frac{\gamma_0}{4\epsilon} - \frac{\gamma'(t)}{4\epsilon}, \tag{4}$$

where each quantity is non-dimensionalized and the non-dimensional numbers (ϵ, μ and γ_0) are introduced following [7]. The first terms in the right hand sides (RHS) of (3) and (4) represent the baroclinic eddy fluxes which are down gradient. The second term in the RHS of (3) represents the atmospheric cooling, which forces ΔT to be 1. The relaxation time is determined by μ[1]. The second and the third terms in the RHS of (4) represent the constant basic and the time-dependent nets evaporation minus precipitation, respectively. Precipitation is basically dominant at high latitudes, meaning the negative γ_0. In this study, $\epsilon = 0.15$, $\frac{\mu}{\epsilon} = 0.05$, and $\frac{\gamma_0}{\epsilon} = -0.1$ are taken unless otherwise specified. These values are considered to be close to those for Labrador Sea [7].

It should be emphasized here that the first assumption is not critical and can be removed easily by adding the tendencies of T_1 and S_1 to the RHS of (3) and (4), respectively. Especially, γ' can be considered to contain the tendency of S_1, i.e., $\frac{\mathrm{d}S_1}{\mathrm{d}t}$.

The system (3) and (4) can be regard as the following three-dimensional "autonomous" DS:

$$\frac{\mathrm{d}\Delta T}{\mathrm{d}t} = -\Delta T\,|\Delta T - \Delta S| + \frac{2\mu}{\epsilon}(1 - \Delta T), \tag{5}$$

$$\frac{\mathrm{d}\Delta S}{\mathrm{d}t} = -\Delta S\,|\Delta T - \Delta S| - \frac{\gamma}{4\epsilon} - \frac{\gamma'(\Theta)}{4\epsilon}, \tag{6}$$

$$\frac{\mathrm{d}\Theta}{\mathrm{d}t} = \omega. \tag{7}$$

Note that the phase space is $\mathbb{R}^2 \times \mathrm{S}^1$. We treat the two-dimensional non-autonomous DS unless otherwise specified.

[1] ϵ is the geometrical parameter, and hence, is not related to the thermodynamical properties of the ocean.

2.2 General properties

It can be shown that ΔT and ΔS are not divergent in time when $\gamma'(t)$ is finite. In other words, the trajectory remains in the finite region of the phase space. $\frac{\mathrm{d}\Delta T}{\mathrm{d}t}$ is positive at $\Delta T = 0$ and negative at $\Delta T = 1$. This means that $0 < \Delta T < 1$ when the initial value of ΔT is between 0 and 1. Note that taking the initial value between 0 and 1 is physically reasonable, and if it is taken outside this region, ΔT enters $(0, 1)$ quickly. The same argument can be made for ΔS. Note that the volume of the above finite region in the phase space depends on the maximum and the minimum of $\gamma'(t)$.

At almost all positions, the volume in the phase space is contracted, because the divergence of the velocity $(\frac{\mathrm{d}\Delta T}{\mathrm{d}t}, \frac{\mathrm{d}\Delta S}{\mathrm{d}t})$ is negative. This fact suggests that phase points asymptotically reach a set whose volume is zero. In other words, there are not repelling fixed points or repelling closed orbits. All fixed points are sinks or saddles, and all closed orbits are stable or saddle-like. Therefore, phase points are considered to be attracted to either fixed points, limit cycles, tori or strange attractors. Note that the above statements related to contraction are not mathematically exact, because the velocity $(\frac{\mathrm{d}\Delta T}{\mathrm{d}t}, \frac{\mathrm{d}\Delta S}{\mathrm{d}t})$ is not smooth on the line of $\Delta T = \Delta S$ and the divergence of the velocity can not be defined there.

2.3 Case of the steady precipitation

For preparation, we examine (3) and (4) when $\gamma'(t) = 0$. Figure 2(a) shows the vector field in the phase space. Note that all vectors are normalized at unity. The solid (dashed) curves represent the nullclines where $\frac{\mathrm{d}\Delta T}{\mathrm{d}t}(\frac{\mathrm{d}\Delta S}{\mathrm{d}t}) = 0$. It is found that there are three fixed points: stable spiral (haline mode), saddle (unstable thermal mode), and stable node (stable thermal mode).

Figure 2(b) shows the vector field in which $\frac{\gamma_0}{\epsilon} = 0.1$, i.e., evaporation is stronger than precipitation. This fact is reflected in the only one fixed point at which sea water is more salty in the interior region than in the boundary current (i.e., ΔS is negative).

Figure 3 shows the bifurcation diagrams for ΔT and ΔS against γ_0/ϵ. When γ_0 is positive, it is found that the saddle-node bifurcation occurs and the (stable) thermal mode disappears at the critical value $\gamma^{\mathrm{critical}}$, while the haline mode always exists. Interestingly, the bifurcation also occurs at $\gamma_0 = 0$, in which the haline mode disappears. The (stable) thermal mode only exists when γ_0 is negative.

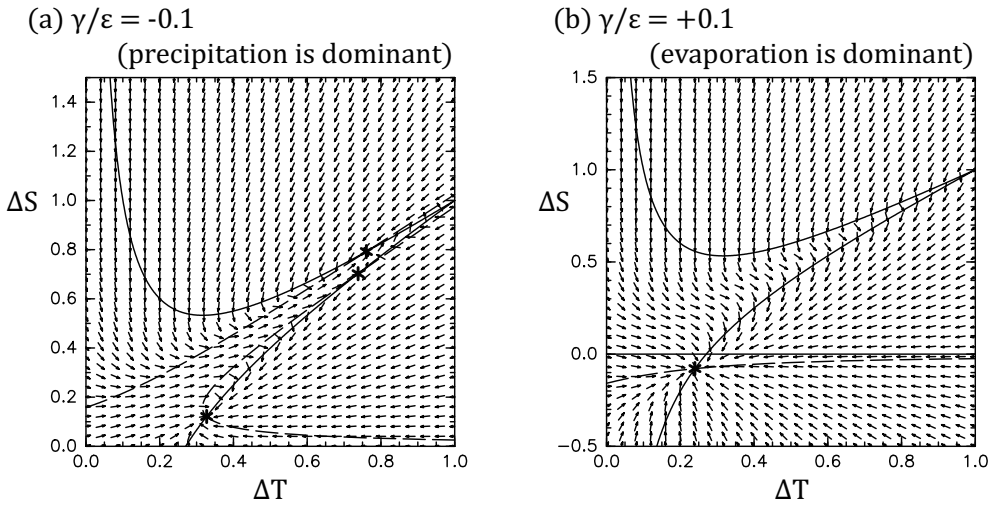

Figure 2: Vector fields, nullclines, and fixed points in the phase space. All vectors are normalized at unity. The solid (dashed) curves represent the nullclines where $\frac{\mathrm{d}\Delta T}{\mathrm{d}t}(\frac{\mathrm{d}\Delta S}{\mathrm{d}t}) = 0$.

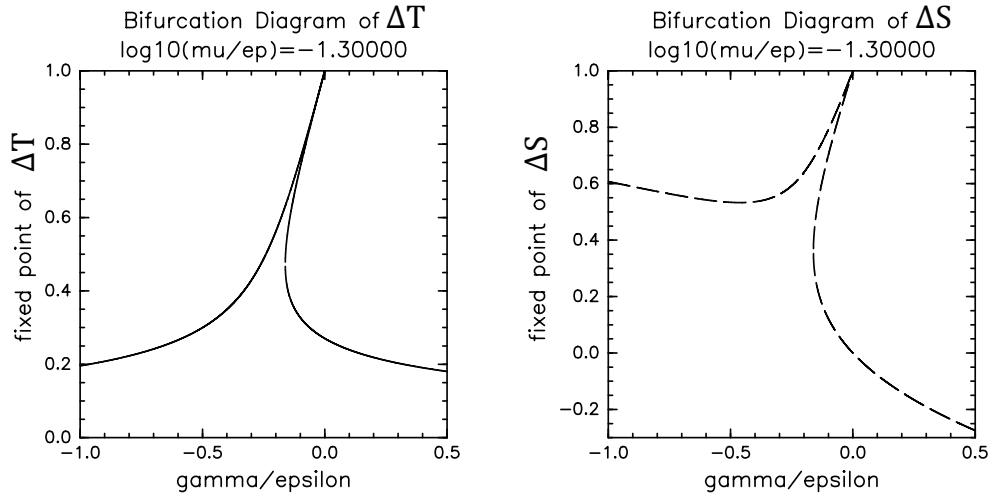

Figure 3: Bifurcation diagrams for ΔT and ΔS against γ_0/ϵ.

3 Examination of the case of periodic precipitation by the dynamical system

In this section, we examine the DS with the periodic precipitation: $\gamma'(t) = A\sin(\omega t)$ where A is the "negative" constant, ω is the positive constant. Equations (3) and (4) become

$$\frac{\mathrm{d}\Delta T}{\mathrm{d}t} = -\Delta T\,|\Delta T - \Delta S| + \frac{2\mu}{\epsilon}(1 - \Delta T), \tag{8}$$

$$\frac{\mathrm{d}\Delta S}{\mathrm{d}t} = -\Delta S\,|\Delta T - \Delta S| - \frac{1}{4\epsilon}\left\{\gamma_0 + A\sin(\omega t)\right\}. \tag{9}$$

Here the initial values are taken to be the steady solution without the periodic precipitation.

3.1 Small amplitude forcing

First, we examine the case of the small amplitude of γ'. It is expected that the (regular) perturbation method is valid. We derived the perturbation solution by assuming that the nonlinear terms are small enough.

The zeroth-order solution $(\Delta T_0, \Delta S_0)$ is the steady solution without γ'. The first-order solution $(\Delta T_1, \Delta S_1)$ consists of $\sin\omega t$ and $\cos\omega t$. The second-order solution $(\Delta T_2, \Delta S_2)$ consists of constant values, $\sin 2\omega t$, and $\cos 2\omega t$, because of nonlinear terms composed of ΔT_1 and ΔS_1.

Figure 4(a) shows the phase differences between ΔT and γ' (solid curves), or ΔS and γ' (dashed curves). For each curve, the black (red) curve represents the result obtained by numerical calculation (perturbation solution). It is found that the phase differences are well predicted by the perturbation theory. Figure 4(b) shows the time averaged second-order quantities. It is found that each quantity is well predicted by the perturbation theory when $\omega > 10^{-1}$, while its variation is qualitatively predicted when $\omega \leq 10^{-1}$. The value of A in Fig. 4 is -0.05, while $\gamma^{\mathrm{critical}} - \gamma_0$ is -0.0615. This fact means that the minimum of the total gamma is very close to the critical value. It should be emphasized here that the differences between the perturbation solution and the numerical solution can hardly be recognized when $A = -0.01$.

3.2 Arbitrary amplitude forcing

Figure 5 shows the ratios of the time-averaged values obtained by numerical calculations to the steady solutions without the periodic precipitation

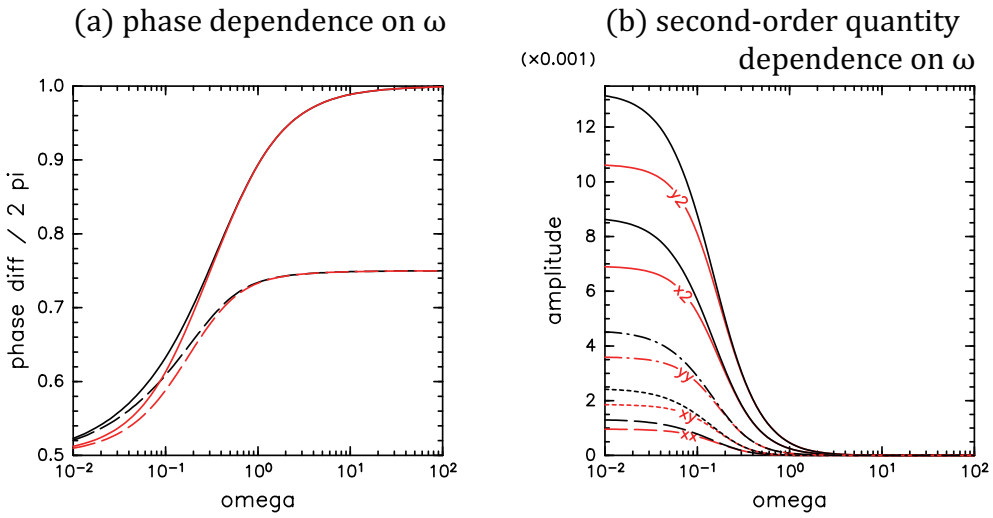

Figure 4: (a) Phase differences divided by 2π between ΔT and γ' (solid curves), or ΔS and γ' (dashed curves) plotted against ω. (b) Time averaged second-order quantities plotted against ω: $x_2 = \overline{\Delta T_2}$; $y_2 = \overline{\Delta S_2}$; $xx = \overline{\Delta T_1\ \Delta T_1}$; $xy = \overline{\Delta T_1\ \Delta S_1}$; and $yy = \overline{\Delta S_1\ \Delta S_1}$. In both figures, the black (red) curve represents the result obtained by numerical calculation (perturbation solution).

(i.e., $\overline{\Delta T}/\Delta T_0$ and $\overline{\Delta S}/\Delta S_0$). It is found that the ratios are near unity when the amplitude of γ' (A) is small. This means that the perturbation solution is valid. Interestingly, even when A is not small enough, the ratios are near unity when ω is high enough. Actually, the perturbation solution is also valid in this case. This is because the equations (8) and (9) are approximately uncoupled when $\omega \gg \max(\Delta T_0, \Delta S_0)$ and $\frac{A}{4\epsilon} \leq \omega \cdot \max(\Delta T_0, \Delta S_0)$. This fact can be shown by the scale analysis (see Appendix A).

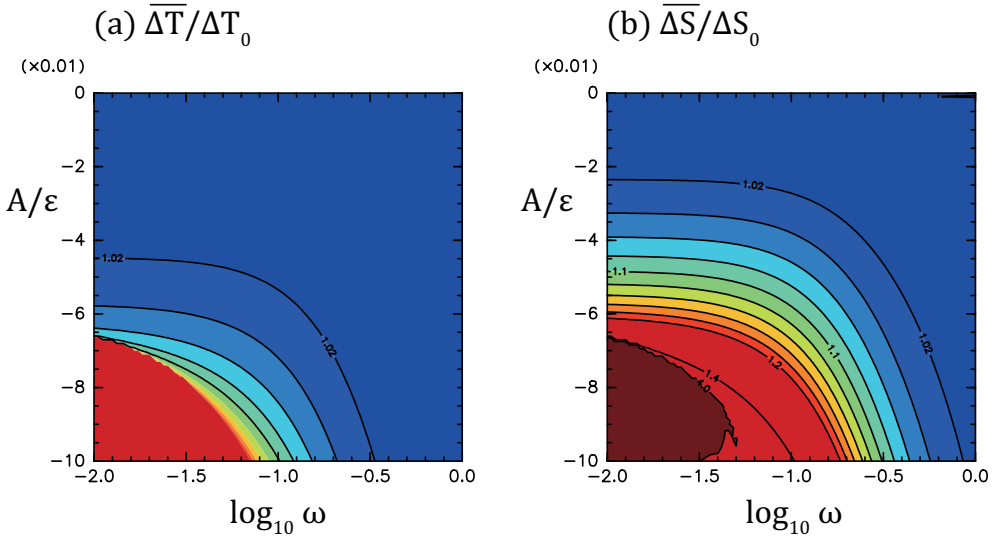

Figure 5: Ratios of the time-averaged values obtained by numerical calculations to the steady solutions without the periodic precipitation, i.e., (a) $\overline{\Delta T}/\Delta T_0$ and (b) $\overline{\Delta S}/\Delta S_0$.

In order to examine shapes of trajectories in the parameter region where ω is not high enough or the perturbation solution is not valid, the magnitude of ΔT is compared with that of ΔS. Figure 6 shows that the shapes of trajectories can be divided into three groups: ΔT (ΔS) is always greater than ΔS (ΔT) in the blue (green) region, while trajectories pass the line of $\Delta T = \Delta S$ in the red region. Note that the perturbation solution is valid in almost all blue regions by the scale analysis (see Appendix A).

The case of low ω is discussed, in which solutions can be regarded as the quasi-steady solutions. The behaviors of trajectories can be understood by

using the bifurcation diagrams (Fig. 3). In Fig. 6, the cross on the vertical axis represents $A = \gamma^{\text{critical}} - \gamma_0$. At this value, the saddle-node bifurcation occurs at the minimum of the total gamma, and hence, the state becomes the haline mode ($\Delta S > \Delta T$) even when the initial values are in the region of $\Delta T > \Delta S$. It is found that the border between the blue (thermal limit cycle) and the green (haline limit cycle) regions is very close to the cross on the vertical axis. In addition to that, the maximum of the total gamma is zero when $A/\epsilon = \gamma_0/\epsilon = -0.1$. At this value, the haline mode disappears, and the thermal mode only exists (Fig. 3). This corresponds to the border between the green and the red regions.

In the parameter region of $A/\epsilon < -0.1$, i.e., red region, the phase point passes the line of $\Delta T = \Delta S$. This is explained as follows. When the total gamma is the critical value (γ^{critical}), the saddle-node bifurcation occurs and the mode changes from the thermal mode to the haline mode. After that, the phase point moves very slowly with keeping the haline mode as the total gamma varies. However, when the total gamma is zero, the haline mode disappears and the mode changes to the thermal mode. After that, the phase point moves very slowly with keeping the thermal mode as the total gamma varies. When the total gamma is the critical value (γ^{critical}), the saddle-node bifurcation occurs again and the mode changes again from the thermal mode to the haline mode. This cycle is repeated.

So far, we have discussed the cases of low and high ω. Figure 6 shows that an interesting thing happens when ω is an intermediate value. Even when the maximum of the total gamma is negative, the trajectory can pass the line of $\Delta T = \Delta S$ around $\log_{10}\omega = -1.3$. Figure 7 shows trajectories when $A/\epsilon = -0.095$ (the maximum of the total γ/ϵ is -0.005). It is found that the trajectory is always in the region of $\Delta S > \Delta T$ ($\Delta T > \Delta S$) when ω is quite low (high), however, the trajectory passes the line of $\Delta T = \Delta S$ and looks like "8" when $\log_{10}\omega = -1.33333$. As shown in the next subsection, these three kinds of trajectories are limit cycle. Hereafter, we call the limit cycles always in the region of $\Delta T > \Delta S$ and $\Delta S > \Delta T$ thermal limit cycle (TLC) and haline limit cycle (HLC), respectively. The other limit cycle is called mixed limit cycle (MLC). The parameter region, in which each limit cycle exists, corresponds to the region in Fig. 6 as follows: TLC to blue; HLC to green; and MLC to red.

3.3 Limit cycles

In this subsection, we examine TLC, HLC, and MLC. It is confirmed that these three trajectories are limit cycles by calculating Floquet multipliers [2].

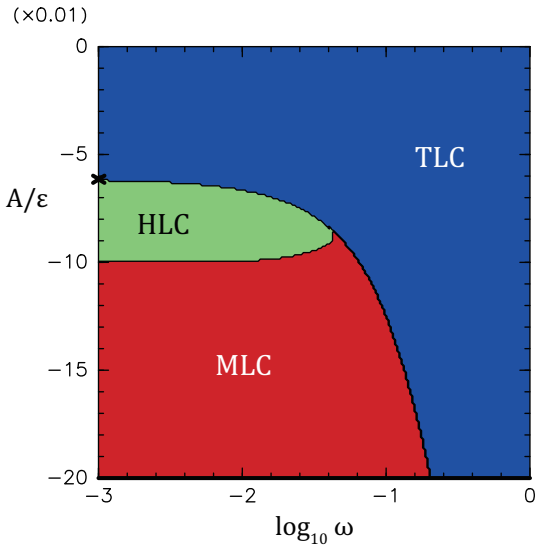

Figure 6: Parameter regions where three kinds of limit cycle exist. The cross on the vertical axis represents $A = \gamma^{\text{critical}} - \gamma_0$.

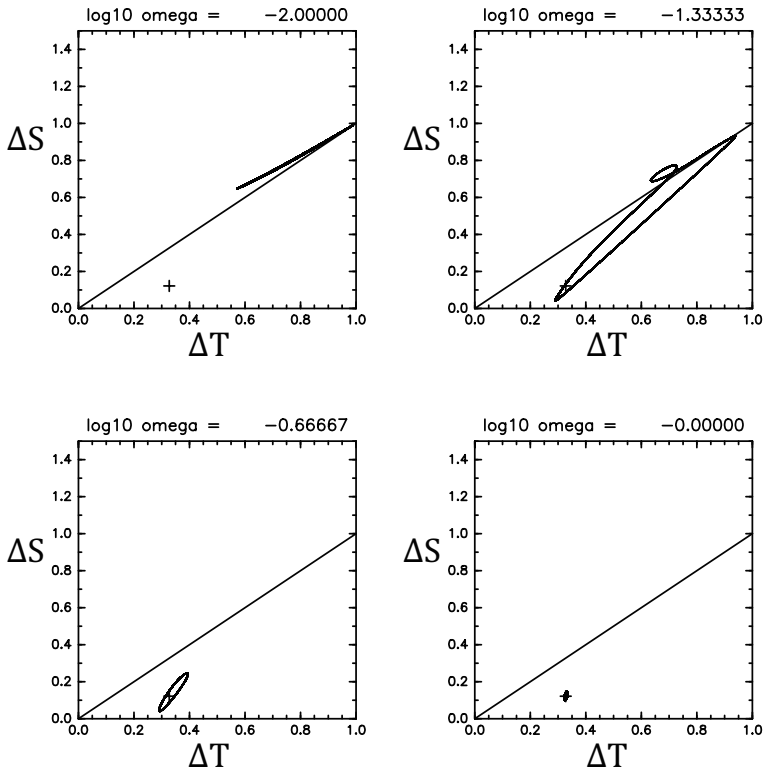

Figure 7: Trajectories when $A/\epsilon = -0.095$ (the maximum of the total γ/ϵ is -0.005). Crosses represent the initial positions.

In other words, these trajectories attract nearby points exponentially.

Figure 8 shows time cross-sections for TLC: ΔT (solid); ΔS (long dashed); $\Delta T - \Delta S$ (short dashed); and γ' (thick dashed-dotted). Note that γ' is only normalized. Figure 8(a) (ω is quite low) shows that the phase difference between ΔT (ΔS) and γ' is about 180°, while that between $\Delta T - \Delta S$ and γ' is about 0°. Figure 8(b) (ω is quite high) shows that the phase difference between ΔT and γ' is about 0°, while that between ΔS and γ' is about $-90°$. The sea water becomes fresh by the strong precipitation behind 90°. This leads to reduce the baroclinicity, and hence reduce the eddy flux of temperature. Thus, the sea water becomes cold by the atmospheric cooling more behind 90°. This process occurs nearly simultaneously when the precipitation period is very long (Fig. 8(a)), while it occurs in order when the period is not very long (Fig. 8(b)).

This phase relation can also be understood by using the following first-order equations for high ω:

$$\frac{\mathrm{d}\Delta T_1}{\mathrm{d}t} \approx \Delta T_0 \Delta S_1 = \frac{\Delta T_0}{4\omega\epsilon} A \cos \omega t, \tag{10}$$

$$\frac{\mathrm{d}\Delta S_1}{\mathrm{d}t} \approx -\frac{\gamma'(t)}{4\epsilon} = -\frac{1}{4\epsilon} A \sin \omega t. \tag{11}$$

Here the leading terms are only left. It is clear that the magnitudes of time-derivative terms become large as ω increases. This means that the amplitudes of ΔT_1 and ΔS_1 decrease as ω increases. This fact is reflected in decreasing the second-order quantities (Fig. 4(b)) and high accuracy of the perturbation solution when ω is high enough and A is not small enough (Figs. 5 and 6).

Figure 9 shows time cross-section for HLC: ΔT (solid); ΔS (long dashed); $\Delta T - \Delta S$ (short dashed); and γ' (thick dashed-dotted). Note that γ' is only normalized. Each parameter is the same as in Fig. 8. Figure 9(a) (ω is quite low) shows that the phase difference between ΔT (ΔS) and γ' is about 0°, while that between γ' and the "magnitude" of $\Delta T - \Delta S$ ($= |\Delta T - \Delta S|$) is about 180°. Note that $|\Delta T - \Delta S|$ is maximum when γ' is minimum. These phase relations mean that the sea water is warm and salty when precipitation is strong, because of the strong eddy flux (i.e., large baroclinicity). However, these relations are changed as ω increases.

Figure 9(b) (ω is quite high) shows that the phase difference between ΔT and γ' is about 180°, while that between ΔS and γ' is about $-90°$. In this case, the sea water becomes "fresh" by the strong precipitation behind 90°. This leads to increase the baroclinicity, and hence increase the eddy flux of temperature. Thus, the sea water becomes "warm" more behind 90°.

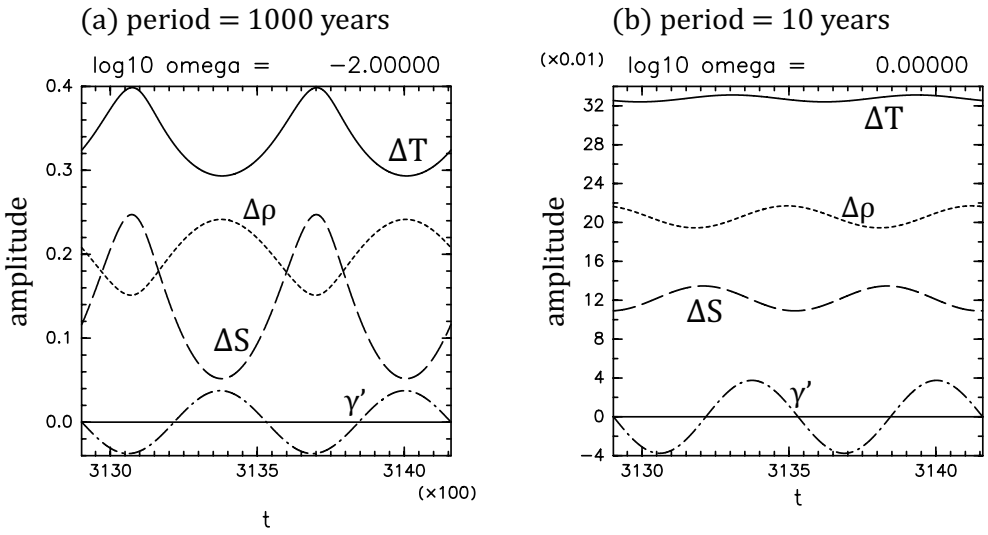

Figure 8: Time cross-sections for TLC: ΔT (solid); ΔS (long dashed); $\Delta T - \Delta S$ (short dashed); and γ' (thick dashed-dotted). γ' is only normalized.

It should be emphasized here that the effect of the fresh sea water on the baroclinicity is opposite to the case of the TLC, in which the fresh sea water reduces the baroclinicity, leading to reduce the eddy flux of temperature. The reason for the difference is that the baroclinicity (the density difference) is $\Delta T - \Delta S$ in the TLC, while that is $\Delta S - \Delta T$ in the HLC.

There is another interesting point about the phase relations between the TLC and the HLC. Examining (9) and Figs. 8 and 9, it is found that the dominant term in the eddy flux of salinity ($-\Delta S|\Delta T - \Delta S|$) is different even when its whole value is the same. For the TLC, ΔS is maximum when $|\Delta T - \Delta S|$ is minimum, while for the HLC, ΔS is minimum when $|\Delta T - \Delta S|$ is maximum. This phase-relation difference means that rotational directions of trajectories are also different: for the TLC, the direction is clockwise, while for the HLC, it is counter-clockwise.

The MLC is examined finally. Figure 10 shows the trajectory and the time cross-section of each term in (8) and (9). The atmospheric cooling and the precipitation terms are dominant when ΔT and ΔS increase, while the eddy flux terms are dominant when ΔT and ΔS decrease. This cycle is repeated only once for the TLC and the HLC, however, twice for the MLC. This is because the trajectory passes the line of $\Delta T = \Delta S$ and the eddy flux terms are proportional to $|\Delta T - \Delta S|$. When ΔT and ΔS increase

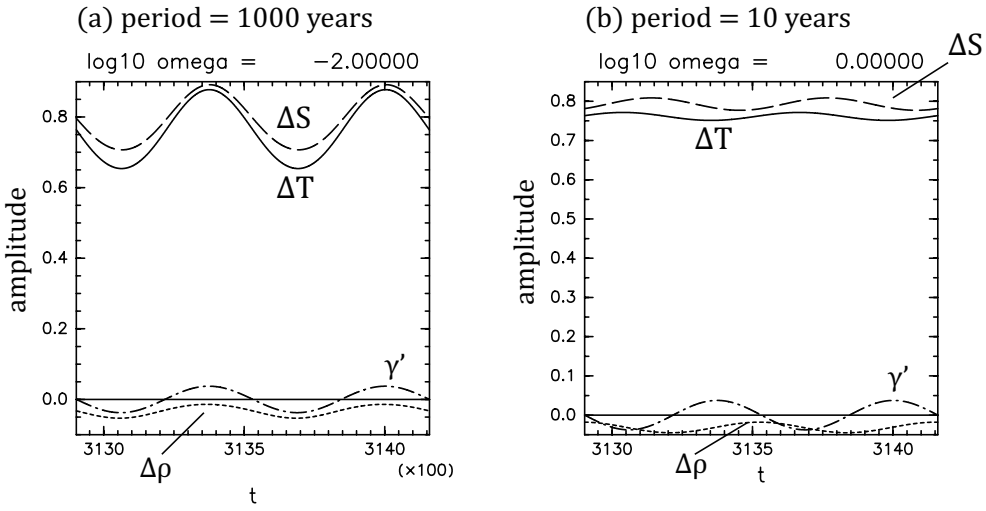

Figure 9: Time cross-sections for HLC: ΔT (solid); ΔS (long dashed); $\Delta T - \Delta S$ (short dashed); and γ' (thick dashed-dotted). γ' is only normalized.

enough after passing the line of $\Delta T = \Delta S$, the eddy flux terms reduce them. Thus, ΔT and ΔS approach the line of $\Delta T = \Delta S$ again. After that, the atmospheric cooling and the precipitation terms increase ΔT and ΔS again. If $|\Delta T - \Delta S|$ is replaced with $\Delta T - \Delta S$, ΔT and ΔS are divergent. It is considered that MLC is a limit cycle which is a mixture of the TLC and the HLC, because the rotational direction is clockwise (counter-clockwise) in the region $\Delta T > \Delta S$ ($\Delta S > \Delta T$) as the TLC (HLC).

The existence of the MLC can be discussed from a view point of an unstable limit cycle. Figures 2 and 3 show there are three fixed points for the DS without the periodic precipitation. It is considered that the thermal mode (stable node) corresponds to the TLC, while the haline mode (stable spiral) corresponds to the HLC. Thus, it is expected that an unstable limit cycle corresponding to the "unstable" thermal mode (saddle) exists. By using the single-point shooting method [2], it has been shown that the unstable limit cycle exists in some parameter regions, and that all of three limit cycles (i.e., TLC, HLC, and unstable limit cycle) expand as $|A|$ increases or ω decreases (Fig. 11). These results suggest that the unstable limit cycle helps join the TLC to the HLC as $|A|$ increases or ω decreases, because it repels nearby points. However, we have not examined the exis-

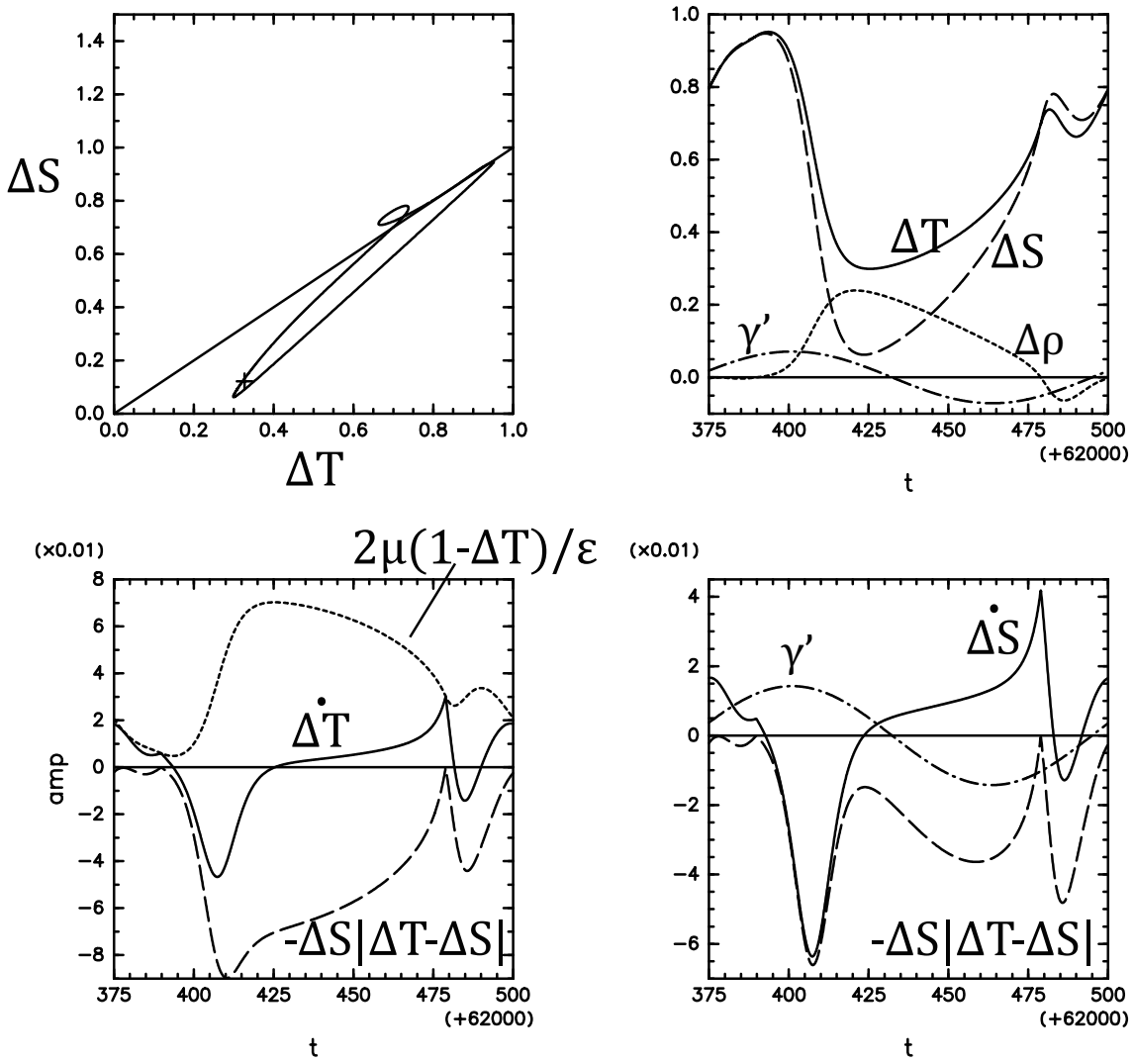

Figure 10: Top left: trajectory with the initial position (cross). Top right: ΔT (solid); ΔS (long dashed); $\Delta T - \Delta S$ (short dashed); and γ' (thick dashed-dotted). Bottom left: $\dot{\Delta T} = \frac{\mathrm{d}\Delta T}{\mathrm{d}t}$ (solid); $-\Delta T|\Delta T - \Delta S|$ (long dashed); and $\frac{2\mu}{\epsilon}(1 - \Delta T)$ (short dashed). Bottom right: $\dot{\Delta S} = \frac{\mathrm{d}\Delta S}{\mathrm{d}t}$ (solid); $-\Delta S|\Delta T - \Delta S|$ (long dashed); and γ' (thick dashed-dotted). γ' is only normalized.

tence of the unstable limit cycle in the parameter region where the MLC exists. In these parameter regions, the calculations for the unstable limit cycles are very unstable because of too large Floquet multipliers. Thus, it is necessary to use the multipoint shooting method [2] instead of the single one. In addition to that, we have to discuss the closeness of the orbits in the "three-dimensional" phase space ((5), (6), and (7)) because all of the limit cycles are trajectories in the three-dimensional phase space. The relation between the MLC and the unstable limit cycle is one of our future works.

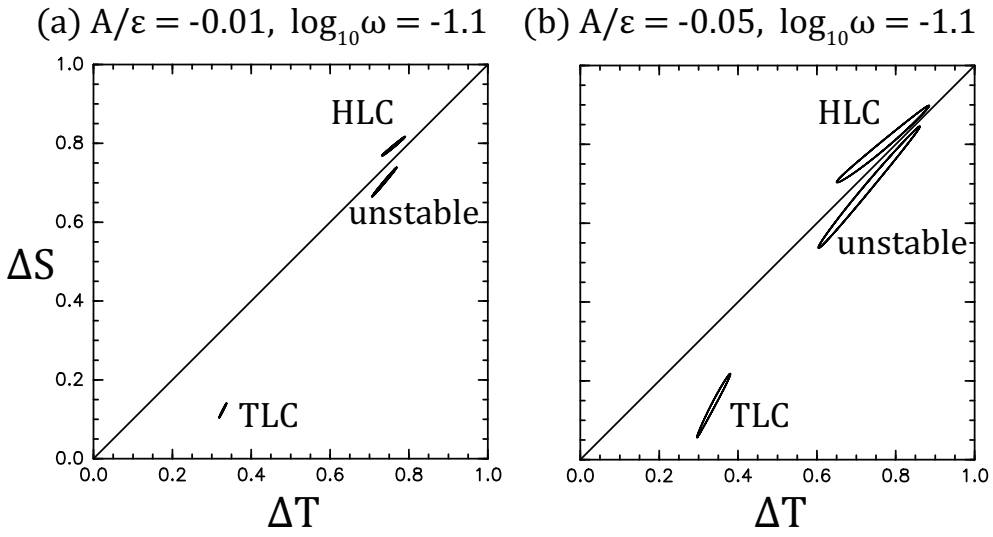

Figure 11: TLC, HLC, and unstable limit cycle in the phase space.

3.4 Dependence of limit cycles on the initial values

The dependence of TLC, HLC, and MLC on the initial values is examined. The phase constant α is introduced in the periodic precipitation: $\gamma' = A\sin(\omega t + \alpha)$. The initial values are taken to be the steady solutions of the system (8) and (9) with $t = 0$. In other words, the initial values are determined only by α. The initial values that $\Delta S > \Delta T$ are excluded in order to examine the cases where the initial states are the thermal modes.

TLC, HLC, and MLC do not depend on the initial values except for near

the boundary between the parameter regions of the HLC and the TLC (not shown), i.e., between the green and the blue regions in Fig. 6. This result means that each limit cycle has the large basin. On that boundary of the parameter space, some points are attracted to the HLC ($\Delta S > \Delta T$) even when $\Delta T > \Delta S$ initially, meaning that the basin of the HLC includes the region of $\Delta T > \Delta S$.

3.5 Chaotic behavior

At some parameters, the DS ((8) and (9)) shows chaotic behavior. Figure 12 shows two trajectories, in which the differences between their initial values are 10^{-13} for both ΔT and ΔS. Here $\frac{\mu}{\epsilon} = 0.1$, $\frac{\gamma_0}{\epsilon} = -0.2$, $\frac{A}{\epsilon} = -0.18$, $\omega = 0.2$ and $\alpha = \pi/2$ are taken. The bottom figures show the time cross-sections for the differences of ΔT and ΔS. Clearly the Lyapunov exponent is positive.

4 Examination of the case of periodic precipitation by MITgcm

In order to confirm the validity of the DS with the periodic precipitation, the oceanic circulation in the idealized marginal sea is simulated by using the numerical model. If the validity is shown, the physical understandings obtained by the DS in Section 3 can be applied to the more general oceanic circulation. The numerical model used in this study is the Massachusetts Institute of Technology General Circulation Model (MITgcm; [3]). The configuration is the same as in [6, 7] except the periodic precipitation, in which $\epsilon = 0.15$, $\frac{\mu}{\epsilon} = 0.05$, and $\frac{\gamma_0}{\epsilon} = -0.1$ as in the DS. It should be emphasized here that the MITgcm with the setting in [6, 7] explicitly resolves mesoscale eddies.

4.1 Model setting and initial value

The model domain and the forcing are shown in Fig. 13(a). The white contours show the height of the bottom topography. The region north of the sill at 1200 km latitude corresponds to the marginal sea, while the region between 1200 km and 200 km latitudes corresponds to the subpolar gyre. The other region south of 200 km latitude corresponds to the rest of the World Ocean [6], where the full depth restoring forces the state to be the uniform stratification and be the constant salinity.

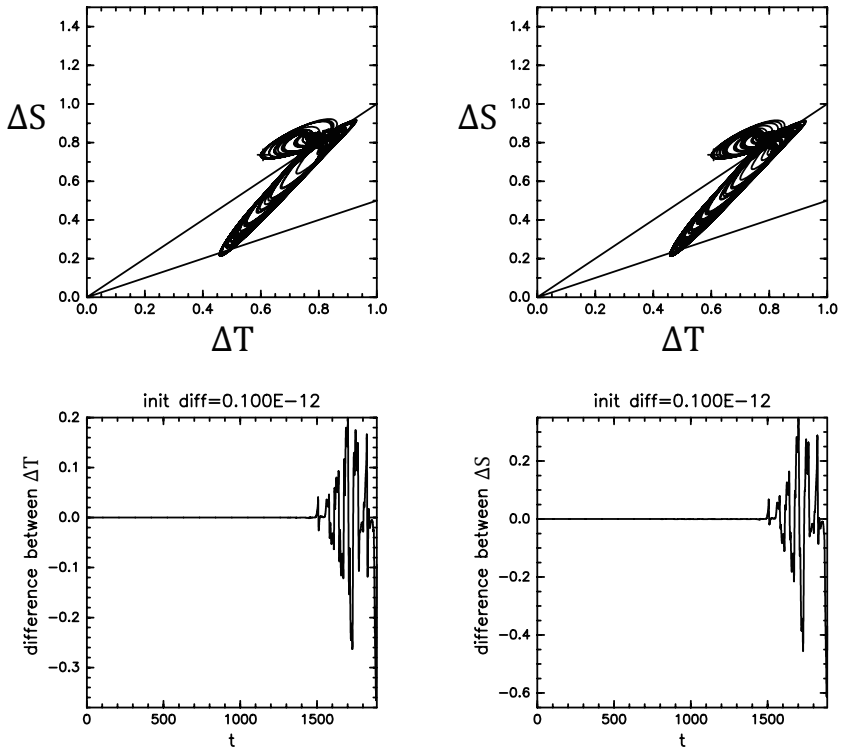

Figure 12: Top figures: two trajectories, in which the differences between their initial values are 10^{-13} for both ΔT and ΔS. Bottom figures: time cross-sections for the differences of ΔT and ΔS.

The model is run for a period of 24 years in order to obtain the initial value which can be regarded as the steady state with the steady precipitation. Figures 13(b) and 13(c) show temperature and salinity at the sea surface. The vectors in Fig. 13(c) show the horizontal velocity at the sea surface. It is found that there is a boundary current along the bottom topography, however, it is fluctuated by mesoscale eddies.

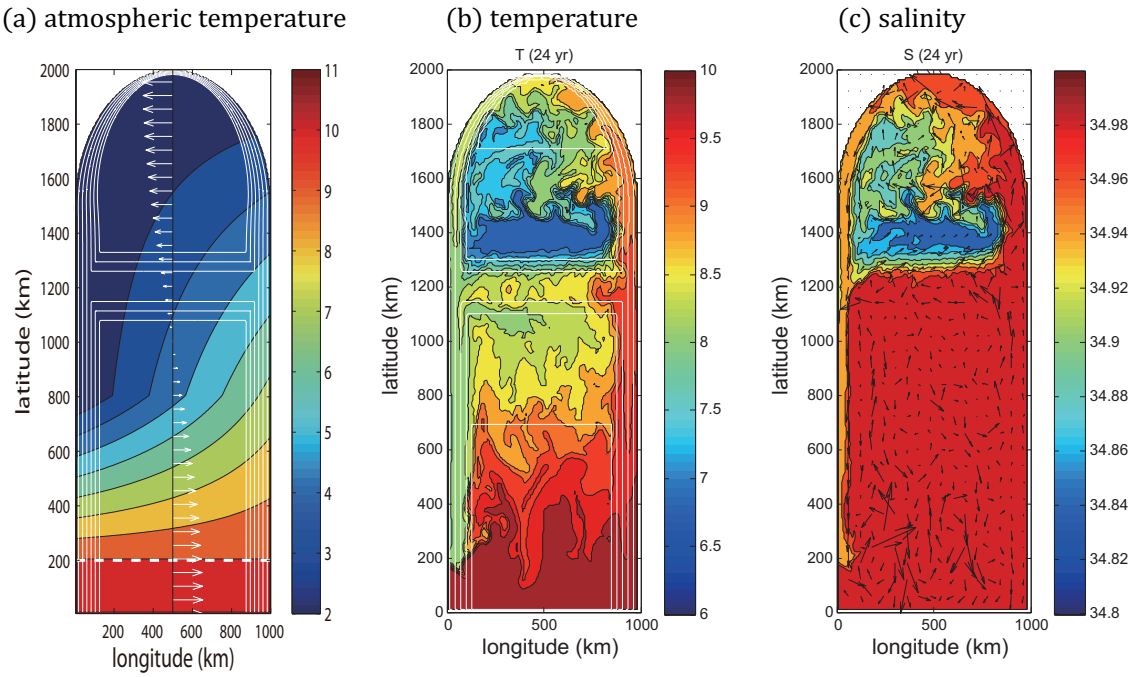

Figure 13: (a) Model domain, bottom topography (white contours; CI=300 m), wind stress (vectors), and atmospheric temperature (color). (b) Temperature at the sea surface (color). (c) Salinity (color) and horizontal velocity (vectors) at the sea surface.

After the initial spinup, the model is run with the periodic precipitation which is only in the marginal sea. The time range of integration is taken to be the doubled period of the precipitation.

4.2 Time evolutions of ΔT and ΔS

Figures 14(a) and 14(b) show the time cross-sections of ΔT, ΔS, and γ' where the periods of the precipitation are 10 and 80 years, respectively.

Here $A/\epsilon = \gamma_0/\epsilon = -0.1$ is taken for both cases. In each figure, dashed curve is obtained by the DS, while solid curve is obtained by the MITgcm. Red curves show the components having frequencies lower than or equal to the frequencies of the precipitation. It has been confirmed that these low frequency components are dominant by calculating the spectrum densities of ΔT and ΔS (not shown).

It is found that the phase relations of the DS results between ΔT, ΔS, and γ' qualitatively well correspond to those of the MITgcm results, while the amplitudes of ΔT and ΔS are much larger in the DS than in the MITgcm. These results suggest that the DS qualitatively describes the behaviors of the MITgcm, while it does not quantitatively.

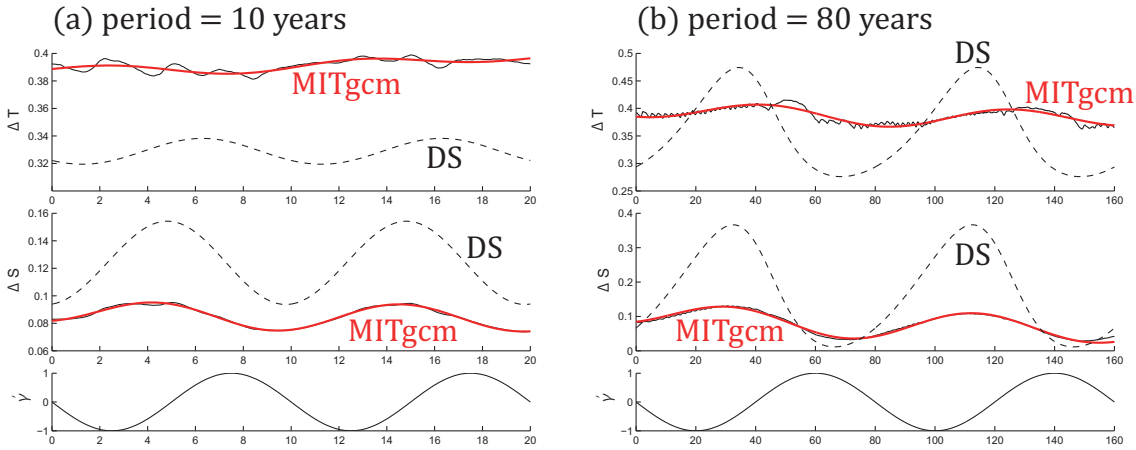

Figure 14: Time cross-sections of ΔT, ΔS, and γ' where the periods of the precipitation are (a) 10 years and (b) 80 years. In both cases, $A/\epsilon = \gamma_0/\epsilon = -0.1$ is taken. See text for details.

4.3 Quantitative evaluation of the dynamical system

In order to show the qualitative agreement between the behaviors of the DS and the MITgcm, correlation coefficients between their results are calculated. Figure 15 shows the scatter plots for the phases and the amplitudes of ΔT and ΔS. In each figure, the lateral axis shows a quantity obtained by the DS, while the vertical axis shows that obtained by the MITgcm. Here the phase at the initial time is defined as 0 rad. It is suggested that the DS qualitatively well describes the behaviors of the MITgcm.

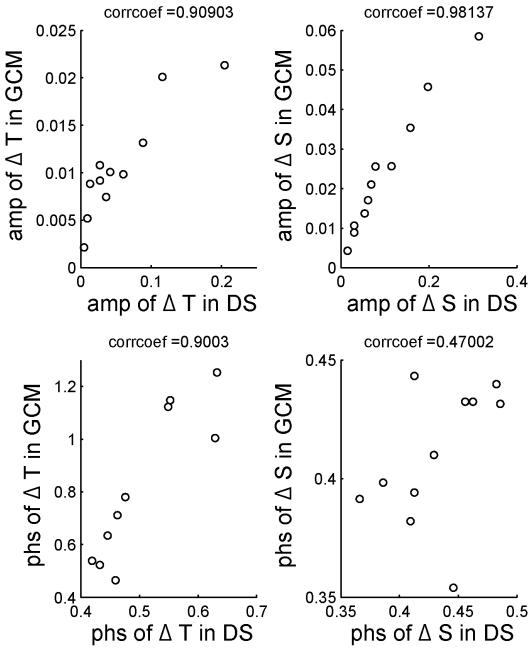

Figure 15: Scatter plots and correlation coefficients for the phases and the amplitudes of ΔT and ΔS.

One of causes for the quantitative disagreement is the difference of the transition time between in the DS and in the MITgcm. If the transition time is much longer in the MITgcm, it may take more time to increase (decrease) the amplitudes of ΔT and ΔS when the precipitation becomes strong (weak). Thus, we examine the DS with the step function precipitation in Section 5, and compare the result with that obtained by MITgcm in Section 6.

5 Examination of the case of step function forcing by the dynamical system

In this section, we examine the DS with the step function precipitation:

$$\gamma'(t) = \begin{cases} \Delta\gamma & (t \geq 0), \\ 0 & (t < 0). \end{cases} \tag{12}$$

The initial values are taken to be the steady solution without the step function precipitation. Transitions between thermal modes are only examined.

5.1 Trajectory

The fixed point instantly changes to the new one as the precipitation changes. Figure 16(a) shows the trajectories in the phase space where the cross (triangle) is the old (new) thermal mode. Figure 16(b) shows the correspondent time cross-section: ΔT (solid) and ΔS (dashed). It is found that the sea water becomes fresh and cold because the precipitation becomes strong. On the other hand, when the precipitation becomes instantly weak, the sea water becomes salty and warm (not shown).

5.2 Transition time

Transition times for ΔT and ΔS are defined as the minimum values t such that $\frac{|\Delta T(\infty)-\Delta T(t)|}{|\Delta T(\infty)-\Delta T(0)|} < 10^{-1}$ and $\frac{|\Delta S(\infty)-\Delta S(t)|}{|\Delta S(\infty)-\Delta S(0)|} < 10^{-1}$, respectively, where $(\Delta T(0), \Delta S(0))$ represents the old fixed point and $(\Delta T(\infty), \Delta S(\infty))$ represents the new one. The transition time is obtained as the average between those for ΔT and ΔS.

Figure 17 shows the transition time plotted against $\frac{\Delta\gamma}{\epsilon}$. The black curve is obtained by the numerical calculations, while the red curve is obtained by the asymptotic solutions described below. It is found that the transition

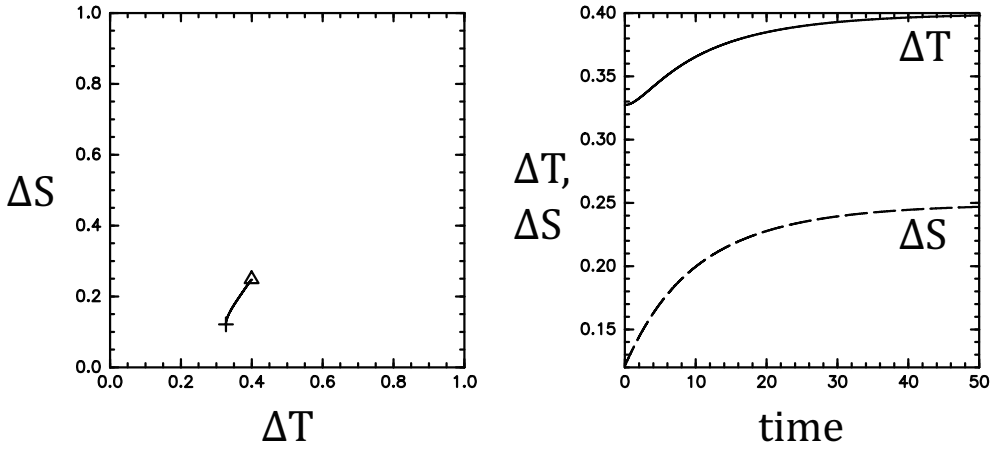

Figure 16: (a) Trajectory. The cross (triangle) is the old (new) thermal mode. (b) time cross-sections of ΔT (solid) and ΔS (dashed).

time is asymmetrical about $\frac{\Delta\gamma}{\epsilon}$. It takes more time to transition when the precipitation becomes instantly strong ($\Delta\gamma < 0$).

In order to understand the above asymmetry, the asymptotic solution is obtained by using the renormalization group method [1]. The renormalization group method is one of singular perturbation methods, which has the following features. (i) Many singular perturbation methods for ordinary differential equations (e.g., boundary layer method, WKB method, and multiple scale method) can be regarded as the renormalization group method. (ii) Particular preparations, such as the proper introduction of multiple time-scale in the multiple scale method, are not necessary. (iii) The solution is sometimes more accurate than those obtained by using other methods such as the boundary layer method.

The dependent variables are expanded as $\Delta T = \Delta T_0 + \sigma\Delta T_1 + \sigma^2\Delta T_2$ and $\Delta S = \Delta S_0 + \sigma\Delta S_1 + \sigma^2\Delta S_2$ where σ is considered as the small parameter and $\frac{\Delta\gamma}{4\epsilon}$ is also considered to be $O(\sigma)$. After obtaining the first-order solution, σ is taken to be unity. It is found from Fig. 17 that the transition time by the asymptotic solution well corresponds to that by the numerical solution when $|\Delta\gamma/\epsilon|$ is small, while the asymptotic solution well represents the asymmetry of the transition time about $\Delta\gamma$ in the wide range of $\frac{\Delta\gamma}{\epsilon}$.

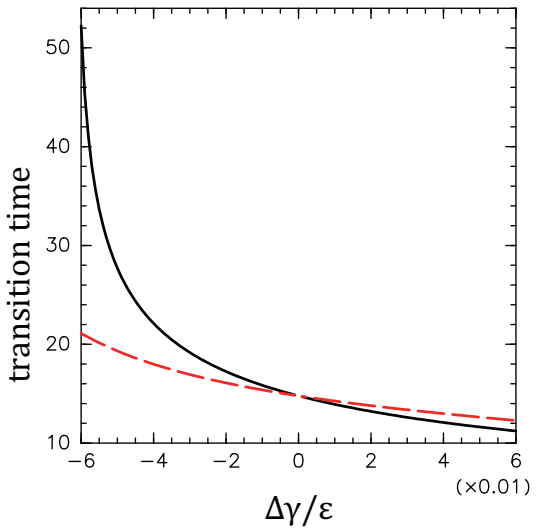

Figure 17: Transition time plotted against $\frac{\Delta\gamma}{\epsilon}$. The black curve is obtained by the numerical calculations, while the red curve is obtained by the asymptotic solutions.

It can be found from the case of the small $|\frac{\Delta\gamma}{\epsilon}|$ that the asymmetry of the transition time in the asymptotic solution is due to the asymmetry of the eigenvalues for the new thermal mode. In fact, the magnitudes of the eigenvalues for the stable thermal mode monotonically increase as gamma increases, i.e., the precipitation becomes weak. This means that the new thermal mode starts attracting nearby points more strongly as $\frac{\Delta\gamma}{\epsilon}$ increases.

From the above discussion, the asymmetry of the transition time in the numerical solution of Fig. 17 can be explained as follows. When $\frac{\Delta\gamma}{\epsilon}$ is positive (negative), the baroclinicity of the new thermal mode is larger (smaller) than that of the old thermal mode because of the strong (weak) atmospheric cooling. This fact leads that the magnitudes of the eddy fluxes increase (decrease) as the state approaches the new thermal modes. Thus, it takes more time to transition in the case of the negative $\frac{\Delta\gamma}{\epsilon}$.

6 Examination of the case of step function forcing by MITgcm

In order to confirm the difference between the transition times in the DS and the MITgcm, the ocean circulation under the step function precipitation is simulated by using the MITgcm. The setting and the initial condition are the same as in the cases of the periodic precipitation (Section 4.1). In this section, the time range of integration is taken to be 40 years.

6.1 Time evolutions of ΔT and ΔS

Figure 18 shows the time cross-sections of ΔT and ΔS. Red curves are obtained by the second-degree-polynomial-curve fitting. Figures 18(a) and 18(b) show the cases of $\Delta\gamma = 0.4\gamma_0 < 0$, and $\Delta\gamma = -0.4\gamma_0 > 0$, respectively. It is found that the sea water becomes fresh and cold (warm and salty) when $\Delta\gamma$ is negative (positive). It is seen that ΔS approaches the new steady state, while ΔT is fluctuated. The transition time for the MITgcm is calculated only by using the data of ΔS. Here, $\Delta S(\infty)$ in the MITgcm is considered to be the value of ΔS at 40 years (the end of the numerical integration).

6.2 Quantitative evaluation of the dynamical system

Figure 19(a) shows the transition time against $\Delta\gamma/\epsilon$ in the DS (solid curve) and the MITgcm (dots). It is found that the dependence of the transition time on $\Delta\gamma$ in the MITgcm is well described by the DS, however,

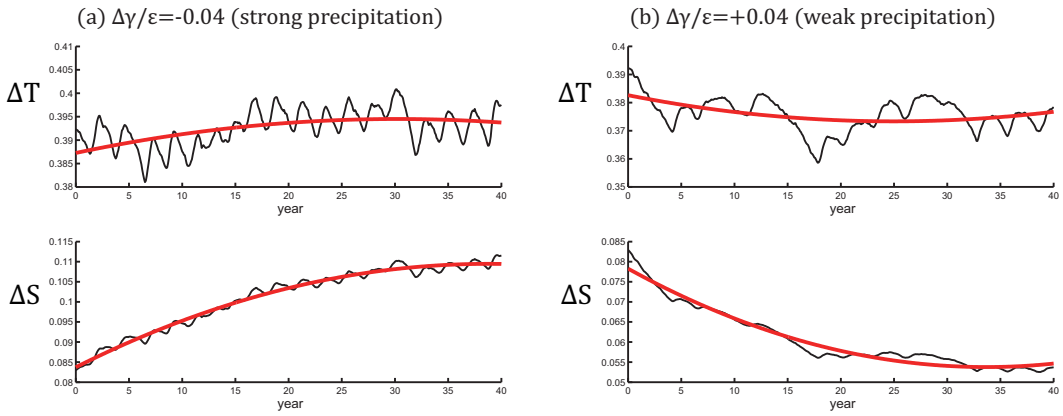

Figure 18: Time cross-sections of ΔT and ΔS in the case of step function precipitation. Red curves are obtained by the second-degree-polynomial-curve fitting.

it takes more time to transition in the MITgcm. Figures 19(b) and 19(c) show ΔT and ΔS at the end of the integration, respectively. It is clear that the DS qualitatively well describes the behaviors of the MITgcm, while it does not quantitatively.

7 Discussion

In this section, we discuss causes for the quantitative disagreement between the results of the DS and the MITgcm. In Sections 5 and 6, we have compared the transition time in the DS with that in the MITgcm. As expected before, it takes more time to transition in the MITgcm. However, this fact is not considered to be the main cause for the quantitative disagreement. In the DS with the step functional case, ΔT and ΔS change to the new equilibrium values within the "same" time-scales. Figure 19(c) shows that ΔS in the DS is very close to that in the MITgcm when $\frac{\Delta\gamma}{\epsilon} = 0.04$. Note that the transition time is shorter when $\Delta\gamma > 0$. Thus, ΔT in the DS should be also very close to that in the MITgcm, even if the transition time in the MITgcm is longer than that in the DS. However, ΔT in the DS is much smaller than that in the MITgcm when $\frac{\Delta\gamma}{\epsilon} = 0.04$. The transition time for ΔT might be longer than that for ΔS in the MITgcm, differently from in the DS.

At least, there are three possible causes for the quantitative disagree-

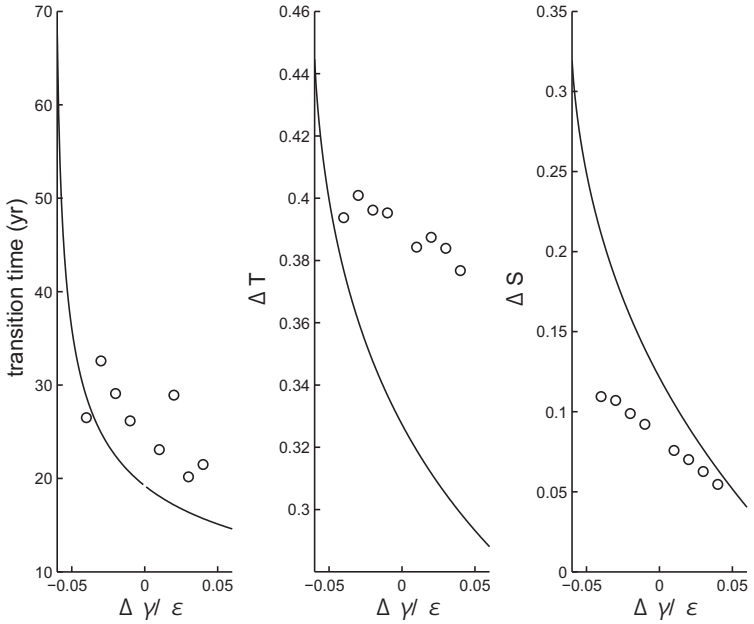

Figure 19: (a) Transition time against $\Delta\gamma/\epsilon$, (b) ΔT and (c) ΔS at the end of the integration in the DS (solid curve) and the MITgcm (dots).

ment:

1. Sensitivity of the DS to the parameters, i.e., $\epsilon, \mu, \gamma_0, A, \omega$, and $\Delta\gamma$.
   The determination of the parameters have a lot of uncertainty. Thus, it may be possible to get better quantitative agreement by choosing other parameter values within the reasonable ranges.

2. Parametric resonance for the baroclinic flow.
   The parameterization in the fourth assumption of Section 2 is based on the Eady problem. However, the parametric resonance may occur when the basic baroclinic flow is time-periodic. Thus, the parameterization used for the DS might not be valid.

3. Effect of changes in the spatial structure.
   In the DS, changes in the spatial structures of the boundary current and the eddy are ignored, resulting from the reduction of the original system. It is possible that changes in the spatial structures affect ΔT and ΔS obtained by the spatial integration.

One of the most important future works is to compare the eddy and the mean fluxes in the DS with those in the MITgcm. Note that the mean fluxes are taken to be zero in the DS by the third assumption of Section 2. Only the eddy and the mean flux are originated in the nonlinear effects, while the atmospheric cooling and the precipitation can be regarded as the external forcings. It is expected that we can estimate the main cause for the quantitative disagreement by this comparison.

8 Summary

We extended the two-dimensional dynamical system (DS) for the idealized marginal sea proposed by [7] to the case with time-dependent precipitation.

In the case of the periodic precipitation, the DS had three kinds of limit cycle: thermal limit cycle (TLC), haline limit cycle (HLC), and mixed limit cycle (MLC). The physics of the TLC and the HLC could be understood by the regular perturbation solution. It was weakly suggested that the existence of the MLC was related to the unstable limit cycle correspondent to the saddle in the DS with the steady precipitation.

In the case of the step function precipitation, the transition time is asymmetrical about the gap of the precipitation. It takes more time to transition

when the precipitation becomes strong instantly. This asymmetry can be explained by the asymmetry of the baroclinicity in the new equilibrium state.

By comparing with results by the numerical model simulations following [7], it was shown that the DS qualitatively well described the behaviors of the numerical model, while it did not quantitatively.

Acknowledgments

I am deeply grateful to Michael Spall for proposing this project, having a lot of discussion with me, and guiding me through the summer. He also let me use his computers and kindly helped me to run the MITgcm. I am deeply grateful to Predrag Cvitanović for telling me how to analyze the periodic orbit and having a lot of discussion with me. I am grateful to Edward Spiegel for introducing me to Predrag and telling me a lot of interesting things about an application of dynamical system. I am grateful to Joseph Pedlosky and Pascale Garaud for giving helpful comments. I am grateful to Oliver Bühler for answering my questions about wave-mean flow interaction. I am deeply grateful to the coordinators of this GFD program, Claudia Cenedese, Eric Chassignet, and Stefan Llewellyn Smith for giving helpful supports. I am also grateful to Woods Hole Oceanographic Institution. I am grateful to Paul Linden for giving the principal lecture about the gravity current. I am grateful to all staff for having many interesting lectures. Finally, I would like to thank all the fellows for the great time we had in Walsh Cottage, housings, softball field, beautiful beaches, and many good restaurants and bars in Woods Hole and Falmouth. I enjoyed summer very much and learned many things.

A Scale analysis of the DS with the periodic precipitation

We separated ΔT and ΔS as $\Delta T_{\rm S} + \Delta T'$ and $\Delta S_{\rm S} + \Delta S'$, respectively, where $(\Delta T_{\rm S}, \Delta S_{\rm S})$ is the steady solution without the periodic precipitation. Here we consider that $\Delta T > \Delta S$. The same scale analysis can be made for $\Delta S > \Delta T$. The DS ((8) and (9)) is transformed as follows:

$$\frac{{\rm d}\Delta T'}{{\rm d}t} = m\Delta T' + n\Delta T' - \Delta T'^2 + \Delta T'\Delta S', \tag{13}$$

$$\frac{{\rm d}\Delta S'}{{\rm d}t} = k\Delta T' + l\Delta T' + \Delta S'^2 - \Delta T'\Delta S' + f\sin\omega t. \tag{14}$$

Here m, n, k, l and f are the following constant numbers: $m = -2\Delta T_{\rm S} + \Delta S_{\rm S} - \frac{2\mu}{\epsilon}$; $n = \Delta T_{\rm S}$; $k = -\Delta S_{\rm S}$; $l = 2\Delta S_{\rm S} - \Delta T_{\rm S}$; and $f = \frac{A}{4\epsilon}$. We rescale time as $\tau = \omega t$, and coefficients (m, n, k, l) as $(m, n, k, l) = c(M, N, K, L)$ where $M, N, K, L = O(1)$. In addition to that, we introduce the new dependent variables as $x \equiv c\Delta T'/f$ and $y \equiv c\Delta S'/f$. Finally, we introduce two non-dimensional numbers $\Omega = \omega/c$ and $F = f/c^2$. Thus, equations (13) and (14) become

$$\Omega\frac{{\rm d}x}{{\rm d}\tau} = Mx + Ny - Fx^2 + Fxy, \tag{15}$$

$$\Omega\frac{{\rm d}y}{{\rm d}\tau} = Kx + Ly + Fy^2 - Fxy + \sin\tau. \tag{16}$$

There are nine cases for Ω and F. In some cases, the leading equations are linear as follows.

Table 1: The linearity/non-linearity of the leading equation

	$\Omega \ll 1$	$\Omega \sim 1$	$\Omega \gg 1$
$F \ll \Omega$	linear	linear	linear (uncouple)
$F \sim \Omega$	linear	non-linear	linear (uncouple)
$F \gg \Omega$	non-linear	non-linear	non-linear

The term "uncouple" means that the leading equations are (10) and (11). These uncoupled cases correspond to the case where $\omega \gg \max(\Delta T_{\rm S}, \Delta S_{\rm S})$ and $\frac{A}{4\epsilon} \leq \omega \cdot \max(\Delta T_{\rm S}, \Delta S_{\rm S})$, because of $O(c) = \max(\Delta T_{\rm S}, \Delta S_{\rm S})$.

References

[1] Lin-Yuan Chen, Nigel Goldenfeld, and Y. Oono, *Renormalization group and singular perturbations: Multiple scales, boundary layers, and reductive perturbation theory*, Phys. Rev. E, 54 (1996), pp. 376–394.

[2] P. Cvitanović, R. Artuso, R. Mainieri, G. Tanner, and G. Vattay, *Chaos: Classical and Quantum*, Niels Bohr Institute, Copenhagen, 2012.

[3] J. Marshall, C. Hill, L. Perelman, and A. Adcroft, *Hydrostatic,quasi-hydrostatic, and non-hydrostatic ocean modeling*, J. Geophys. Res., 102 (1997), p. 57335752.

[4] J. Marshall and F. Schott, *Open-ocean convection: Observations, theory, and models*, Rev. Geophys., 37 (1999), pp. 1–64.

[5] Michael A. Spall, *Boundary currents and water mass transformation in marginal seas*, J. Phys. Oceanogr., 34 (2004), pp. 1197–1213.

[6] ——, *On the role of eddies and surface forcing in the heat transport and overturning circulation in marginal sea*, J. Climate, 24 (2011), p. 48444858.

[7] ——, *Influences of precipitation on water mass transformation and deep convection*, J. Phys. Oceanogr., 42 (2012), pp. 1684–1700.

[8] H. Stommel, *Thermohaline convection with two stable regimes of flow*, Tellus, 13 (1961), p. 224230.

[9] L. D. Talley and M. S. McCartney, *Distribution and circulation of Labrador Sea water*, J. Phys. Oceanogr., 12 (1982), pp. 1189–1205.

Particle Driven Flow down an Incline into a Linear Stratification

Kate Snow
Australian National University

October 1, 2013

1 Introduction

1.1 Motivation

Particle driven gravity currents occur commonly in nature; pyroclastic plumes in the atmospheric setting; turbidity currents in the ocean and the dumping of particle-rich pollutants from industrial means. But the most common form of particle laden currents is that of the turbidity current, sediment laden flows where the sediment suspension is due to the turbulent nature of the flow. These currents occur at the outflow of rivers into the ocean [22, 23], are generated by storm waves impacting the coast [28] and occur in regions of submarine landslides or due to tectonic activity [18]. Turbidity currents are also responsible for the transportation of sediment on a global scale [20], defining the main mechanism that allows sediment to be transported to the deeper ocean [20, 31, 24, 17, 11, 16]. Because of their impacts in global sediment transport, identifying where such currents are dominant and their flow characteristics is an important consideration in understanding the effects of outflowing sediment rich rivers into ocean and their role in erosion and deposition over continental slopes and submarine canyons. Such knowledge is also important in identifying regions of hydrocarbon reservoirs [17, 27], and of paramount importance in consideration of engineering construction and infrastructure near river mouths [22, 23] and on continental shelves [6, 17].

It is not only important to consider where the sediment may be deposited, it is also important to consider at what depth the turbidity current will intrude if it were hyperpycnal, that is, has a density greater than the surface ambient and hence flows below the surface. For example, if a particle pollutant were to intrude at the surface of the ocean, there is important consideration that must be taken into account when considering the effects the pollutant will have on coastal flora and fauna, whereas if the pollutant were to intrude at depth, its removal becomes more difficult and the environmental effects potentially less clear. Risk assessments of a spill therefore would be aided by knowing the intrusion depth of particle laden gravity currents.

A further motivation for knowing the intrusion depth and characteristics of particle laden currents is provided through the work of Clark et al . [8]. In this paper, the extreme cooling event of the Holocene Climate 8.2 kya is investigated, where the believed cause of

the cooling was due to a fresh water flux at the surface of the North Atlantic after the catastrophic drainage of two super lakes. But if this were the case, then why was the constant flux of fresh water occurring prior to the flood over a course of roughly 100 yrs not causing a change in the overturning and hence a similar cooling? Clark et al .[8] argues that the reason there is no change in the overturning prior to the flood is due to the outflowing waters being sufficiently turbid to become particle laden and so descend beneath the surface. To be able to understand such processes more precisely it becomes important to develop an increased understanding of the outflow characteristics and intrusion of a particle laden gravity current.

1.2 Previous Studies

Only limited observational records exist for the occurrence and flow of turbidity currents. This is due to the difficulty in predicting the time and frequency of turbidity currents as well as the destructive nature of such sediment laden currents [32, 26]. Due to the lack of observations, it is increasingly important that properties of turbidity currents are analysed in both the experimental and theoretical fields to allow for an increased understanding of the properties and interactions of such currents.

Many previous studies exist that investigate the nature of turbidity currents, the majority of which only apply to the case where the ambient fluid is of a constant density. Such studies include the numerical study of Hurzeler et al. [15] which considers a flat bottom set-up and experimental and theoretical analyses[12, 13, 4, 30] which again all consider only flat bottom cases.

Cases where the bottom is sloping are considered in, for example Parson et al. [25], where they investigate the production of hyperpycnal plumes on a sloping bottom from the convective instabilities produced from a hypopycnal plume. Bonnecaze et al. [5] also looks at flows of particle laden currents on sloping bottoms. In this case they consider an experimental and theoretical perspective where the current flows into a constant density ambient. The only experimental and theoretical study to consider the effects the of stratification of the ambient fluid for a propagating particle laden current is that of de Rooji [9]. In this study they investigate the settling process, the ambient density and the production of internal waves. However, the set-up is flat bottom and investigates an intrusive current rather than a flow initially propagating along the bottom, such as would occur for hyperpycnal turbidity currents flowing out from rivers and is the main consideration of this report.

1.3 Outline

None of the studies outlined in Section 1.2 include both the effects of slope and stratification as has been performed for studies of saline gravity currents [21, 1, 2, 34, 7]. But to capture the characteristics of a turbidity current flowing into the ocean, both the continental slope and the ocean stratification must be taken into account. This means there is a clear gap within the current studies of turbidity currents and hence a gap in attaining a complete understanding of the features of particle laden, their flow characteristics and their sediment transport properties. Hence, the study reported here provides the initial steps and means to fill the research gap by combining both the effects of slope and ambient stratification in the investigation of particle laden flows. This is done through laboratory experiments, the

set-up of which is outlined in Section 2, and scaling theory presented in Section 3. Results and an example application of the theory are presented in Section 4 and Section 5 with final conclusions in Section 6.

2 Experimental Set-up

Experiments were conducted in a rectangular tank of dimensions, $L = 120.8$ cm, $H = 8.5$ cm and $W = 4.5$ cm . The tank was raised at one end to produce the sloping bottom, where two slope angles were considered, that of $\theta = 8.4^\circ$ and $\theta = 4.4^\circ$, the largest value being the greatest angle possible to allow the entire bottom of the tank to act as a sloping boundary. A Perspex gate edged with foam seal provided the means to produce the lock in which the interstitial fresh water and particle mixture was created. The interstitial fluid density was always that of fresh water (0.998 g cm^{-3}) and the particles were always glass spheres of density 2.5 g cm^{-3}. The diameter of the particles, d, varied between experiments with the particles taking five possible values of 1-38 μm, 13-45 μm, 38-53 μm, 53-75 μm and 63-90 μm. In addition, a few salt solution gravity currents were considered, in which case no particles are used, rather the salt solutions experiments provided a base case to compare the particle currents to.

The ambient fluid was created using the double bucket method of producing a linear stratification. To take into account the slope at the bottom of the tank however, the method was modified so that the salty bucket contains half the volume of the fresh water bucket, the density of the flow out of the salt water bucket changes quadratically in time, and thus the stratification in the triangular domain changes linearly with depth. The stratification values used were approximately $N = 0$, 1.12, 1.9 and 3.0 s^{-1} where N is the buoyancy frequency and the stratification was measured after the tank was filled using six densitometer measurements taken evenly with height at the deepest end of the tank. Figure 1 provides a summary of the key characteristics of the experimental set-up.

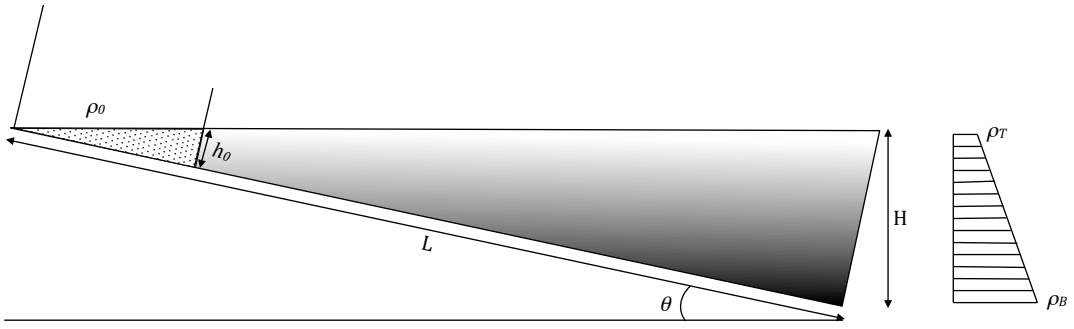

Figure 1: Summary of the experimental setup used in this study.

The height of the lock, h_0, which defines the downslope velocity speed, was varied by changing the position of the lock along the slope so that it may be in deeper or shallower water. The lock heights considered are 3, 4.5 and 6 cm. The density of the particle laden fluid within the lock, ρ_0, was then determined by the mass of particles added to the given volume of fresh water within the lock, with the final lock densities ranging from 1.02 g

cm^{-3} to 1.21 g cm^{-3}. Coloured dye was added to the lock fluid, and after vigorous mixing to ensure the particles are uniformly distributed, the lock was pulled and the flow of the current recorded using a digital camera. Image analysis techniques of the footage of the flow and the progression of the front allows for both down speed velocities and intrusion depth are determined. The intrusion depth here is defined as the point at which the current front first lifts up off the slope and is quantified by the depth z at which this occurs. This depth and the progression of the flow down the slope is indicated in Figure 2.

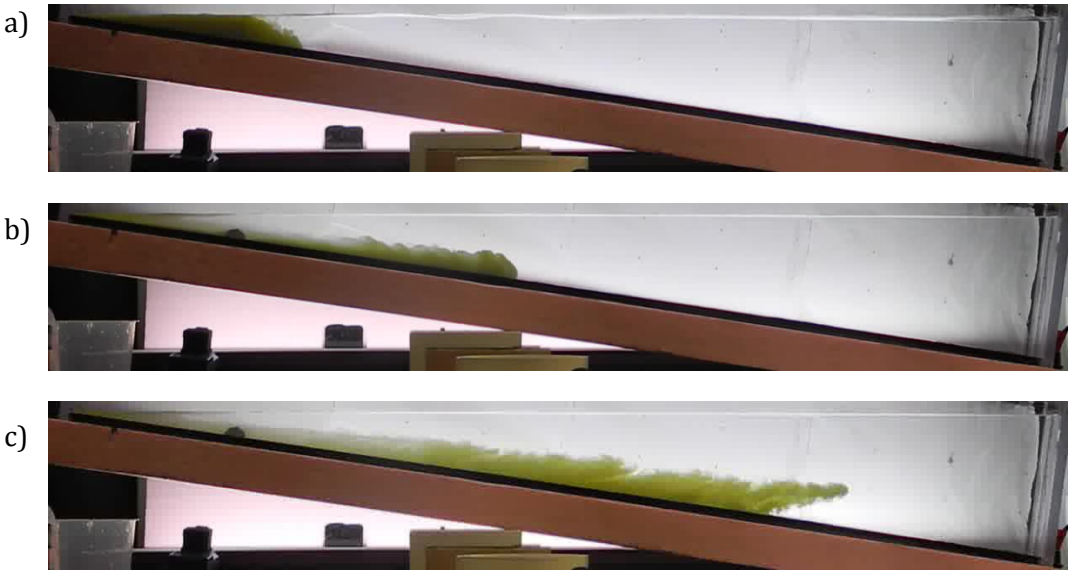

Figure 2: Illustration of the progression of the current a) after the lock is pulled, b) as it flows down the slope and c) after the points of intrusion z, where in this case $N = 1.1$ s^{-1}, $h_0 = 3.3$ cm, $\rho_0 = 1.02$ g cm^{-3} and $d = 1 - 38$ μm.

3 Scaling Theory

Scaling theory is applied to the situation defined in the experimental set-up to produce a theoretical expression for the intrusion depth of a particle laden current. Firstly, consider a particle laden gravity current made up particles of density ρ_P and an interstitial fluid density, ρ_i, flowing down a slope, S, into an ambient fluid that has a constant stratification, N. Then since N is constant, it may be defined by the bottom density, ρ_B, and the density at the top of the tank, ρ_T:

$$N^2 = \frac{g}{\rho_{00}} \frac{d\rho}{dz} = g \frac{\rho_B - \rho_T}{\rho_T H}, \tag{1}$$

where H is the height of the fluid at the deepest end of the tank, g is the gravitational constant, and we have chosen the reference density, ρ_{00} to be ρ_T as we apply the Boussinesq approximation.

With the addition of the slope into the system, the driving force can no longer be assumed to be only buoyancy and inertial forces; now both entrainment and bottom friction need to be considered. However, the effects of friction may be ignored if the Reynolds number is high and hence the flow is within the turbulent regime. The Reynolds number is given by:

$$Re = \frac{Uh_0}{\nu} \tag{2}$$

where ν is the kinematic viscosity of the fluid (for fresh water ν 10^{-6}), U is the speed of the current ($0.05 - 0.1$ m/s for the majority of the flow before the intrusion depth is reached), h_c is the height of the current (0.03 at the head) and θ is the angle of the slope ($4 - 8°$). Hence, given the approximate values for each term, it is verified that for all cases the Reynolds number for the flow is of the order of 1500-3000 meaning the flow is always within the turbulent regime and the effects of friction may be ignored.

3.1 Flow Separation

In a uniformly stratified fluid, the velocity of the gravity current at the front is dependent on the stratification:

$$U = F_N N h_0 \tag{3}$$

where F_N is the Froude number for stratified ambients and expected to be of the order of 0.266 [19] to 0.25 [33].

For a uniform ambient however, we expect the constant front velocity to depend on the reduced gravity, taking the form:

$$U = F_0 \sqrt{g' h_0} \tag{4}$$

where now the Froude number, F_0 for a constant density ambient is of order 0.5 based on theory [3], but is often closer to 0.48 in experiments [29]. We have assumed that the slope is small so that the the effects of the slope on the front velocity may be ignored, an assumption that is verified by [7] where they show that there is little dependence on the front velocity with slope. Hence, assuming that the initial flow is large enough that viscous forces are unimportant (as expected for the high Reynolds number situation considered here) and the size of the lock is unseen by the flow in the initial stages, the initial front velocity U may be defined in terms of the $\beta = \frac{Nh_0}{\sqrt{g' h_0}}$:

$$U = \sqrt{g' h_0} f(\beta) \tag{5}$$

where g'_0 is the initial reduced gravity and f is a function representing the change in the Froude number when going from uniform ambient to a uniformly stratified fluid, i.e. $f(0)$ approaches 0.5 and decreases to 0.25 when $Nh_0 = \sqrt{g' h_0}$, i.e. $f(1) = 0.25$. The trend of f is found experimentally and given in Figure 7. After initial experimental results (refer to Section 4.1), it is found that the majority of the flow before the intrusion depth is reached occurs at a constant velocity. Therefore, to a first approximation, we are going to assume that U is constant.

3.1.1 Dilution of Interstitial Fluid

In order to determine the intrusion depth, all the factors that effect the density of the current with time must be considered. The key characteristics of particle laden currents that change the overall density are; the entrainment of the interstitial fluid with the ambient fluid, and the settling of the particles as the current progresses down the slope. Firstly considering the entrainment of the interstitial fluid, we assume that it occurs independently of the particles settling out.

Due to the thinness of the tank, there is assumed to be no cross-slope velocity and effectively the flow is represented as a 2D flow. A box model set-up is then applied to the interstitial fluid flow as shown in Figure 3, where h_c is the height of the current, l_c is the front position down the slope, $V = h_c l_c$ is the volume of the interstitial and ρ_a is the ambient density. The vertical coordinate is taken to be perpendicular to the slope and defined as h and the horizontal co-ordinate is taken perpendicular to the slope, defined as l.

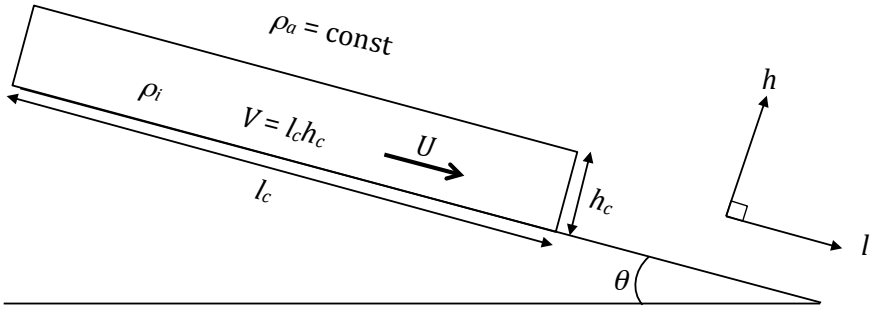

Figure 3: Summary of the box model set-up for the interstitial fluid flow down the slope.

The entrainment is assumed to be a function of the speed of the flow and an entrainment coefficient defined here as $E = 0.08$ and taken to be constant. The change in volume of the 2D current may then be written as:

$$\frac{dV}{dt} = U_e l \tag{6}$$

where U is the front velocity, $U_e = EU$ is the entrainment velocity, and dt is the change in time. Since the velocity of the current may be assumed constant from section 3.1 and the entrainment coefficient is constant, the change in volume may be defined from (6) as:

$$dV = EU(l_0 + Ut)dt \tag{7}$$

where $l_c = l_0 + Ut$. Hence, the change in density of the interstitial $d\rho_i$ is given through the change in volume dV by:

$$\rho_i + d\rho_i = \frac{\rho_i V_0 + \rho_a EU(l_0 + Ut)dt}{V_0 + EU(l_0 + Ut)dt} \tag{8}$$

where l_0 is the initial lock length, V_0 is the initial lock volume and ρ_a is the density of the ambient. The Boussinesq approximation is applied for the ambient density allowing ρ_a to

be a constant. Such an approach is necessary to avoid numerical solutions for this simple scaling theory approach.

Since dt is small, the denominator of (8) can be expanded through a Taylor series leading to, at the first order approximation:

$$d\rho_i = (\rho_a - \rho_i)\left(\frac{EUl_0}{V_0} + \frac{EU^2}{V_0}t\right)dt = \frac{(\rho_a - \rho_i)}{V_0}dV \tag{9}$$

which is integrated to give:

$$\rho_i = \rho_a - (\rho_a - \rho_{i0})e^{-\frac{V}{V_0}+1} \tag{10}$$

where ρ_{i0} is the initial density of the interstitial fluid, i.e. the density of fresh water. Hence, an equation representing the change in density of the interstitial fluid due to entrainment is given.

3.1.2 Particle Settling

The second effect that must be considered for the change in density of the particle laden current is the settling of the particles. The particles being used in this experiment are that of glass spheres and are assumed to not flocculate within the current. Suitably low concentrations of the particles are also used (volume fractions < 0.15) so it is assumed that there is no hindrance to settling of the particles as they travel with the current. It is further assumed that the flow is sufficiently turbulent that the particles are uniformly mixed through the current, yet none are lost through the top. This is the most common approach to defining the sedimentation process [14, 4]. Hence, to a first approximation, the change in concentration of the particles within the current is defined through the Stokes settling velocity, U_s, acting at the lower boundary of the current. Though the particles may vary in size in a particular experiment through a small range (e.g. d = 38-53 μm), the variation of U_s is considered negligible and a constant settling velocity is taken for a single particle type.

The Stokes settling U_s defining the speed at which the particles settle out of the interstitial fluid is given by:

$$U_s = \frac{gd^2(\rho_P - \rho_i)}{18\mu} \tag{11}$$

where μ is the dynamic viscosity ($\mu = 1 * 10^{-6}$Pas for fresh water) and d is the diameter of the particles. Hence, the change in mass of the particles dm_p within the current is given by:

$$dm_p = -\frac{m_p}{h_c}U_s dt = -\frac{m_p l_c U_s}{V}dt \tag{12}$$

Dividing both sides of (12) by (7) gives an equation in terms of V and m_p which when integrated yields:

$$m_p = m_{p0}\left(\frac{V}{V_0} - 1\right)^{-\gamma} \tag{13}$$

where $\gamma = \frac{U_s}{U_e}$, is the ratio of the settling velocity to the entrainment velocity.

Applying a change of variables so that (13) may be written in terms of the volumes fraction of particles, ϕ, where $m_p = \rho_P V \phi$ gives:

$$\phi = \phi_0 \left(\frac{V}{V_0} - 1 \right)^{-\gamma - 1} \tag{14}$$

Hence, we now too have an equation defining the change in the volume fraction of the particles with time. Combing this with the change in the density of the interstitial fluid will then provide the overall change in density of the particle laden current.

3.1.3 Separation Depth

With both the effects of entrainment and particle settling accounted for, the depth of the intrusion or separation of the fluid may be defined. This occurs when the density of the current ρ_c equals the density of the ambient along the slope ρ_s, where ρ_s is a function of position due to the linear stratification of the ambient. Hence, solving for $\rho_c = \rho_s$ where $\rho_c = \rho_i + \phi(\rho_P - \rho_i)$ gives:

$$\rho_a + (\rho_{i0} - \rho_a) e^{-\frac{V}{V_0} + 1} + \phi_0 \left(\frac{V}{V_0} - 1 \right)^{-\gamma - 1} \left(\rho_P - \rho_a - (\rho_{i0} - \rho_a) e^{-\frac{V}{V_0} + 1} \right)$$

$$= (\rho_B - \rho_T) \frac{l_0 + Ut}{L} + \rho_T$$

Substituting for V and again applying the Boussinesq approximation, assume that $\rho_{i0} = \rho_a = \rho_T$ giving:

$$\phi_0 \left(\frac{V}{V_0} + 1 \right)^{-\gamma - 1} (\rho_P - \rho_T) = (\rho_B - \rho_T) \frac{l_0 + Ut}{L} \tag{15}$$

which can be written as:

$$\phi_0 \left(1 + \frac{EU}{l_0^2 S} (t l_0 + t^2 U/2) \right)^{-\gamma - 1} (\rho_P - \rho_T) = (\rho_B - \rho_T) \frac{l_0 + Ut}{L} \tag{16}$$

where S is the slope. Equation (16) may be solved implicitly in time to determine the points of intrusion, or limits in time may be taken.

3.2 Asymptotic Limits

3.2.1 Time limit $t >> \frac{l_0}{U}$

The first limit to consider is the case where the current flows further than one lock length, that is $t >> \frac{l_0}{U}$. Then $\frac{t^2 U}{2} >> t l_0$ and in (16):

$$t l_0 + \frac{t^2 U}{2} \approx \frac{t^2 U}{2} \tag{17}$$

With this limit, the remaining time dependence is given by $1 + \frac{U_e}{V_0} \frac{t^2 U}{2}$ which may be further simplified.

Case 1. If $\frac{U_e}{V_0}\frac{t^2U}{2} >> 1$ then it is necessary that $t^2 >> \frac{2V_0}{EU^2} = \frac{l_0^2 h_0}{EU^2 l_0} = \frac{l_0^2}{U^2}\frac{S}{E}$ which implies $t >> \frac{l_0}{U}\sqrt{\frac{S}{E}}$. But it has already been noted in this case that $t >> \frac{l_0}{U}$, so this limit simply requires $\sqrt{\frac{S}{E}}$ isn't much less than 1. Considering we expect $E < 0.1$, then we are left with the same limit for anything but slopes that approach 0. Hence, in this limit (16) becomes:

$$\phi_0 \left(\frac{EU^2}{2V_0}\right)^{-\gamma-1} t^{-2\gamma-2} = \frac{(\rho_B - \rho_T)}{(\rho_P - \rho_T)}\frac{Ut}{L} \tag{18}$$

which may be written as:

$$\frac{t}{\tau} = \left(\frac{N^2 \rho_T \sin(\theta)}{g\phi_0(\rho_P - \rho_T)}\sqrt{\frac{2V_0}{E}}\right)^{\frac{-1}{2\gamma+3}} \tag{19}$$

where $\tau = \sqrt{\frac{2V_0}{EU^2}}$. Putting (19) in terms of the intrusion depth z where $z = l_c/\sin(\theta)$ and $l_c = l_0 + Ut$ at the point of intrusion gives the final result:

$$\frac{z}{h_0} = \left(\frac{g_0'}{N^2 h_0}\right)^{\left(\frac{1}{2\gamma+3}\right)} \left(\frac{S}{E}\right)^{\left(\frac{\gamma+1}{2\gamma+3}\right)} \tag{20}$$

where g_0' is the initial reduced gravity. It is seen from (20) that the defining parameter of the system is γ, the ratio of the settling and entrainment velocities.

Case 2. The second option in the limit $t >> \frac{l_0}{U}$ is that $t << \frac{l_0}{U}\sqrt{\frac{S}{E}}$ in which case (16) may be written as:

$$\phi_0 \,(1)^{-\gamma-1} \,(\rho_P - \rho_T) = (\rho_B - \rho_T)\frac{l_0 + Ut}{L} \tag{21}$$

rearranged gives the result:

$$\frac{l}{L} = \frac{\phi_0(\rho_P - \rho_T)}{\rho_B - \rho_T} \tag{22}$$

and substituting for z and $L\sin(\theta) = H$ gives:

$$\frac{z}{H} = \frac{\phi_0(\rho_P - \rho_T)}{\rho_B - \rho_T} \tag{23}$$

which may be written as:

$$\frac{z}{h_0} = \frac{g_0'}{N^2 h_0} \tag{24}$$

The result of (24) shows no dependence on the γ parameter and hence, the entrainment or settling velocity. So effectively, (24) represents the case where the flow travels such a short distance or there is such minimal settling over the period before intruding that these effects have minimal impact on the density of the current before it intrudes.

3.2.2 Time limit $t << \frac{l_0}{U}$

Now consider the opposite case to the previous section, i.e. $t << \frac{l_0}{U}$, the current intrudes less than one lock length along the slope. Then it is clear that $tl_0 + \frac{t^2U}{2} \approx tl_0$ and we must now consider how the term $1 + \frac{U_e}{V_0}tl_0$ evolves with time.

Case 3. First take $t << \frac{V_0}{U_e l_0} = \frac{l_0}{U}\frac{S}{E}$, which is true for anything but where the entrainment approaches zero. In these experiments the entrainment parameter E is found to be approximately 0.08 and the slope ranges from 0.07 to 0.15, hence this limit is valid for all the experiments performed here that intrude at less than one lock length. The result of applying these limits then provides the same results as was found in Case 2 for equation (24).

Case 4. In this case $t << \frac{l_0}{U}$, but assume now that the slope approaches zero so that $t >> \frac{l_0}{U}\frac{S}{E}$. Then from (16) this gives:

$$\phi_0 \left(\frac{U_e}{h_0}t\right)^{-\gamma-1} (\rho_P - \rho_T) = (\rho_B - \rho_T)\frac{l_0}{L} \tag{25}$$

which can be written as:

$$\frac{Ut}{h_0} = E\left(\frac{g_0'}{N^2 h_0}\right)^{\frac{1}{\gamma+1}} \tag{26}$$

Writing (26) in terms of z gives the intrusion depth as:

$$\frac{z}{h_0} = ES\left(\frac{g_0'}{N^2 h_0}\right)^{\frac{1}{\gamma+1}} \tag{27}$$

again providing the dependence of the intrusion depth to the parameter γ.

3.3 Particle Concentration at Intrusion

It is often useful to provide an indication of the quantity of particles that have settled out along the slope and the amount that continue to be transported with the intruded fluid. This provides an indication of where the particles will end up and at what depth. The amount of particles remaining within the intrusion can then be determined by knowing the density of the interstitial fluid at the point of intrusion and the total current density at intrusion. Both of these can be found by knowing the intrusion point z. The interstitial density (10) in terms of the intrusion depth z is given by:

$$\rho_i = \rho_a - (\rho_a - \rho_{i0})e^{-\frac{E}{S}\frac{z^2}{h_0^2}} \tag{28}$$

where:

$$\rho_a = \frac{\rho_s(z) + \rho_T}{2} = \frac{N^2\rho_T z}{2g} \tag{29}$$

is the mean density of the ambient fluid over the depth of intrusion z. Hence, solving $\rho_c = \rho_i + \phi(\rho_P - \rho_i)$ for ϕ will provide the volume fraction of particles at the point of intrusion, ϕ_i, and is found to be represented by:

$$\phi_i = \frac{\frac{N^2 \rho_{00} z}{g} + \rho_T - \rho_{i0} + (\rho_a - \rho_{i0})\, e^{-\frac{E}{S}\frac{z^2}{h_0^2}}}{\rho_P - \rho_a + (\rho_a - \rho_{i0})\, e^{-\frac{E}{S}\frac{z^2}{h_0^2}}} \tag{30}$$

Applying the Boussinesq approximation so that $\rho_T = \rho_{i0} = \rho_a$ then gives:

$$\phi_i = \frac{h_0 N^2 \frac{z}{h_0}}{g\left(\frac{\rho_P}{\rho_{i0}} - 1\right)} \tag{31}$$

Hence, (31) provides an indication of the amount of particles deposited down the slope and the amount continuing to intrude into the ambient fluid. If we also assume that there is no entrainment after the current intrudes and the only change in density of the current is due to the settling of the particles, then the settling of the particles over time may be defined through:

$$\phi = \phi_i e^{-\frac{U_s}{h_c} t} \tag{32}$$

This leads to a representation of where the particles will end up over the entire course of the current flow and settling process.

3.4 Fingering

One dominant feature of the flow is the presence of smaller intrusions or fingers prior to the current reaching the final intrusion depth. These fingers are seen also in the saline solution gravity currents and have been noted previously as a double outflow effect [2] and a similar effect is found when a time varying density enters a continuous stratification [10]. This fingering is illustrated in Figures 4 and 5:

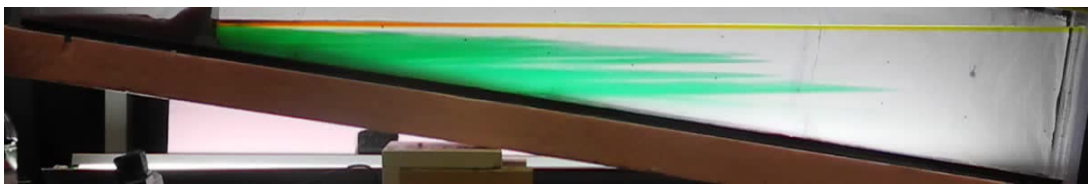

Figure 4: Fingering intrusion observed for $N = 1.9$, $\rho_0 = 1.2$, $\theta = 8.4$, $d = 13 - 45$ μm and $h_0 = 3$ cm (green dye). Note: the red and yellow dye are previous lock exchange experiments run in the same tank set-up, but have not affected the overall startification of the ambient and so do not affect the results presented here.

The only difference in the runs of Figures 4 and 5 is the height of the lock used, and therefore, the speed of the current. In Figure 5, the current speed is greater than that of Figure 4 and it is also noted that the average spacing between fingers appears to be larger. Hence, it would appear, to first order, that the fingering spacing is a result of the degree of stratification N and the speed of the current as it flows down the slope U. Dimensional analysis therefore would indicate that the spacing of the fingers is of the order of U/N.

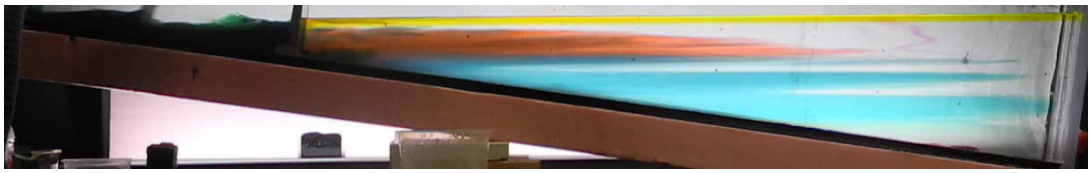

Figure 5: Fingering intrusion observed for $N = 1.9$, $\rho_0 = 1.2$, $\theta = 8.4$, $d = 13 - 45$ μm and $h_0 = 6$ cm (blue dye). Note: the red and yellow dye are previous lock exchange experiments run in the same tank set-up, but have not affected the overall startification of the ambient and so do not affect the results presented here.

4 Results

4.1 Front Velocity

The experimental studies provide a clear observation of the flow processes and characteristics. After the gate is released, the gravity current front is quickly set-up and flows down the slope until it either hits the end of the tank or reaches the point of intrusion. As it flows, the turbulent nature of the current is clear and entrainment occurs at the upper edge boundary and head of the current. Once the current intrudes, if it is still heavily laden with particles, some further particle settling is observed to occur.

Measurements of the front position as it travels down the slope are taken against time using image analysis tools in Matlab. An example of such results are shown in Figure 6 where the position of currents of density 1.02, 1.1 and 1.2 g cm^{-1} are given. It is seen from Figure 6, that a constant slope of position versus time is maintained from the initial set-up of the current nearly all the way to the intrusion point where the slope position becomes a maximum. This constant slope gives the speed of the current front as it travels.

It may also be noted that there are some oscillations of the position on the slope after the first intrusion in Figure 6. These oscillations are due to the effects of rebounding internal waves off the back wall to the tank, however such internal waves initiated by the flow do not affect the current until after the intrusion point has been reached and so are ignored in this study.

With the front velocities measured for each case, the dependence of the velocity to the stratification can be determined as explained in Section 3.1 and (5) and the results of front velocity for changing stratification is shown in Figure 7. It can be seen from Figure 7, that for zero stratification, the non-dimensional front velocity approaches a value of 0.5, that is, the expected value of Froude number for a constant density ambient. As the stratification increases however, the non-dimensional frontal velocity decreases until the point at which $Nh_0 = \sqrt{g_0' h_0}$ and $\beta = 1$ where the non dimensional frontal velocity is approaching 0.25. This is again the approximate value expected for this case and so further verifies the trend provided in Figure 7 indicating the effects of increasing stratification to front velocity.

4.2 Intrusion Depth

The depth of intrusion z is determined as the depth at which the head first lifts up off the slope, meaning experimentally it is measured as the maximum position of the front along the

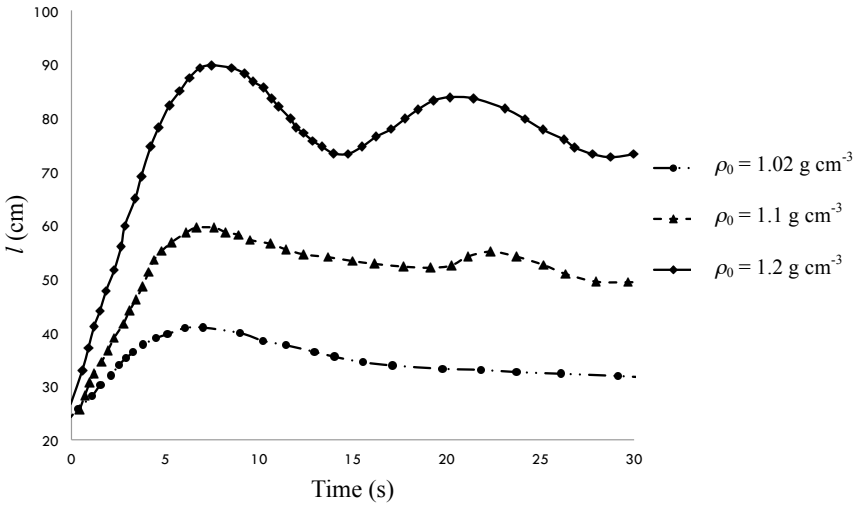

Figure 6: Slope position of gravity current front for $\rho_0 = 1.02$, 1.1 and 1.2 g cm^{-1}, $d = 13-45$ μm, $\theta = 8.4°$, $N = 3.0$ s^{-1} and $h_0 = 3$ cm.

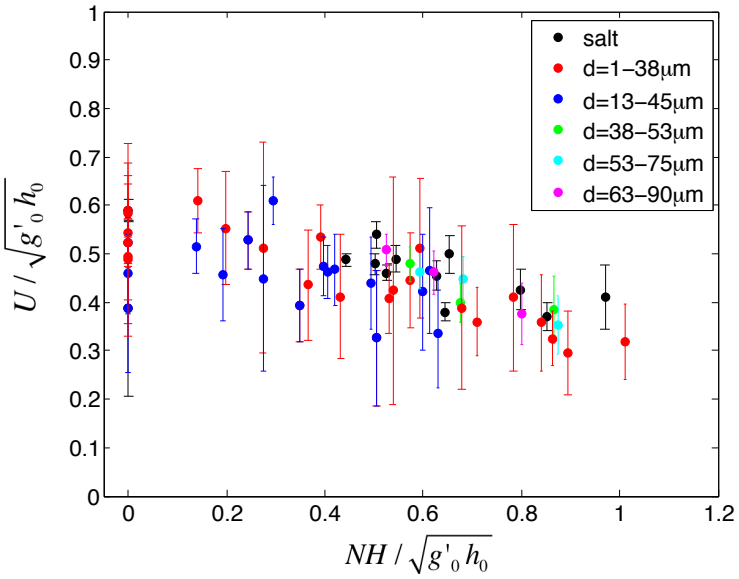

Figure 7: Non-dimensionalized front velocity U versus the ratio of the effects of stratification N and initial buoyancy determined from the reduced gravity g_0'.

slope as may be observed in Figure 6. The measured z/h_0 values are then plotted against the theoretical value of z/h_0 given by case 1, (20), for currents that intrude less than one lock length down the slope and case 3, (24), for currents that travel more than one lock length and the results presented in Figure 8.

It is seen from Figure 8a) that values for z/h_0 less than one do not fit the theoretical results well. This is to be expected as the theory in this case is within the time limit where

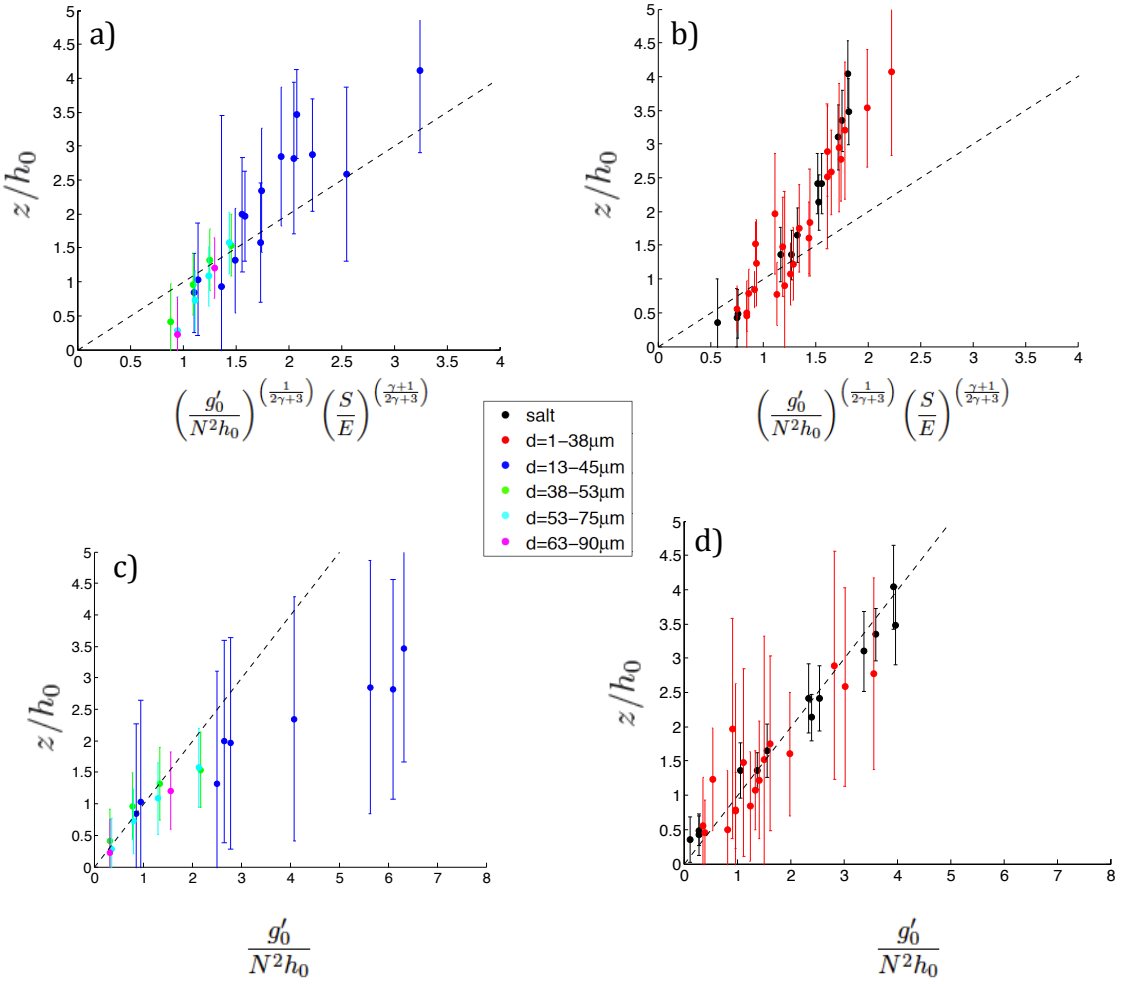

Figure 8: Non-dimensional intrusion depth versus theoretical intrusion depth for currents that intrude greater than one lock length a) and b) and less than one lock length c) and d), where a) and c) show the larger particles intrusions and b) and d) only the smallest particle and salt solution intrusions.

the current is assumed to flow more than one lock length. Yet there is good agreement in Figure 8a) for currents travelling greater than one lock length for these larger particle cases, verifying the theory. However, for Figure 8b), the same agreement is not seen between the theory and the smallest particle size and the salt solution experiments. Yet it is noted that, despite the theory being within the less than one lock length limit for Figure 8d), all the experiments, whether travelling less than or more than one lock length, match the theoretical prediction in this case. What this indicates is that essentially, the dependence of these flows on the γ parameter is not present and so the dependence of the flow on the settling velocity to entrainment velocity is absent. This is expected for the saline solution as in that case, with no particles, $\gamma = 0$, and for the smallest particle cases where $d = 1 - 38$ μm, the settling velocity is so small that it does not play a dominant role in affecting the

intrusion depth of the flow. If a longer tank had been used and the flow permitted to travel over a longer distance then potentially the effect of settling would play a more dominant role for the smallest particle currents, but over the short distances allowed, the settling was too slow to have a large impact on the density of the current.

There is close match between experiments and theory when z/h_0 is less than one in Figure 8c) where the theory is within the less than one lock length limit, again verifying the theory for the larger particle currents. It is also noted from Figure 8c), that the further from the one lock length limit the current has intruded, the further the deviation of the experimental results to the theory. This indicates the necessity of having both the case 1 and case 3 theories in defining the characteristics of the flow for the larger particles cases and hence, the importance of the γ parameter in defining particle laden currents where the particles play a dominant role.

4.3 Intrusion Fingers

One dominant characteristics of the particle current is the presence of intrusion fingers. Comparing the saline current fingers to that of the particle laden currents, it is noted that the fingering appears to be more distinct in the particle currents. This is potentially due to the shallower tail region of the flow which leads to increased settling as indicated from (12) for a smaller value of h_c. Hence, some fluid intrudes at shallower depths than would occur in a saline current, leading to a clearer and wider range of fingering.

Applying the scaling analysis of Section 3.4, the theoretical values of U/N is plot against the mean measured finger spacing z_f, where z_f is determined with the application of Matlab image analysis tools. The results of z_f versus U/N are shown in Figure 9.

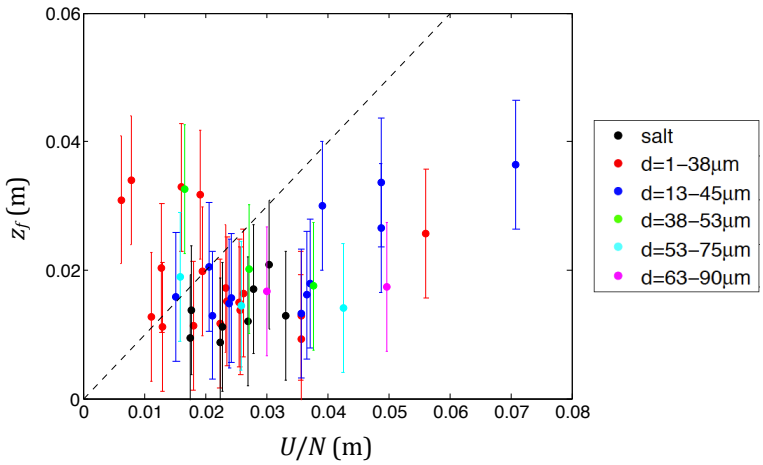

Figure 9: Mean measured distance between fingers z_f versus U/N.

From Figure 9, no clear trend is seen in the data given. It is also possible that not all the fingers being produced were fully discernible due to the spreading width of the fingers, two fingers may have merged and so the simple method of searching the image for finger positions may not have been robust enough to capture the full fingering effects. Such fingering however, could potentially impact the transport and outflow properties of particle

laden plumes as they travel down a slope into a stratified fluid and so would be of benefit to investigate further.

5 Application

The study of Clark et al. [8], uses shallow water equations solved numerically to provide an indication of the properties of the outflowing water entering the North Atlantic prior to the 8.2 kya extreme cooling event. The main limitation of their model however, was that they did not have a suitable indication of the concentration of particles required to cause the water to sink below the surface. The only condition at hand was that of a threshold value for hyperpycnal plumes, that is, calculating the fraction of particles required so that the density of the outflowing water is greater than the density of the ambient. Under this assumption, it means that there must be a volume fraction of particles of 0.0206. Clark et al. [8] also note that under such conditions, the particle levels are quite large but not impossibly high for glacial meltwaters.

A comparison between the value of Clark et al. [8] and a value determined from the theoretical analysis presented in this study could provide an indication of a more suitable condition for the outflowing meltwaters to become hyperpycnal and flow below the surface. Such knowledge will provide an increased understanding of the properties of the outflowing water and the events prior to the extreme event of the Holocene Climate 8.2 kya. To apply the theory presented here, relevant parameters must be chosen to determine the volume fraction of particles needed for the intrusion to sink below the surface. In particular, rather than simply looking at what densities would be required to allow the current to sink just below the surface where it is highly likely that some surface fresh-water fluxes would indeed occur, rather it is more relevant to determine values of particles fractions that would mean no fresh water flux reached the surface even some time after the intrusion. Hence, consider the case where the outflowing water intrudes below the thermocline where the stratification of the overlaying waters would inhibit the rise of any remaining fresh water. Further, if the water did intrude to depths of say 100 m, the approximate thermocline depth, then the entrainment that occurs as it descends would remove the majority of the fresh water from the North Atlantic. Hence, taking $z = 100$ m, we also then define the density of the ambient as that of salt water $\rho_a = 1.035$ g cm^{-3}, the density of the particles is $\rho_P = 2.700$ g cm^{-3}, [8] and the interstitial density is taken as $\rho_{i0} = 1.00$ g cm^{-3}, that of cold fresh water. The slope then is taken as a typical shallow ocean shelf slope, $S = 0.01$, and the height of the lock is assumed to be $h_0 = 40$ m based on an approximate value from the outflowing river height in Clark et al. [8]. Finally, the entrainment parameter is kept fixed at 0.08 and the stratification is taken as a mean value for the pycnocline range $N = 0.001$ s^{-1}. From these values, the volume fraction of particles required to cause the flow to intrude to 100 m may be calculated, taking a range of particles sizes, $d = 2, 5, 20, 50$ μm, which are the diameters of fine clay, clay, silt and sand respectively, the main sediment expected to be picked up by the flow.

In all cases of particles sizes, the volume fraction of particles required for the outflowing water to sink below 100 m is of the order of 0.0209. This is only slightly larger than that predicted by Clark et al. [8] using the simple threshold method, however it provides a more robust indication of the particle concentrations required to allow the flow to intrude at

depth. Hence, the results here potentially allow for a more complete picture of the nature of the outflowing waters prior to the extreme event and also provides a reasonable value compared to possible particle concentration levels for glacial metlwaters.

5.1 Convective Instabilities

A further note of Clark et al. [8] is that potentially a hyperpycnal plume can be produced at much lower sediment concentration [25]. Parso et al. [25] looks at the development of a hyperpycnal plume from the convective instability produced from a hypopycnal plume as the particles settle out. In their study however, their experimental set-up considered only the case of a constant density ambient, and while the production of a hyperpycnal plume from a hypopycnal plume was also observed in the constant ambient experiments of this report, (refer to Figure 10) the continued settling of particles later led to the interstitial fluid of the hyperpycnal plume to become negatively buoyant and return to the surface as shown seen in Figure 10e) meaning for the case of Clark et al. [8], the fresh water flux may still have occurred at the surface. Further, such convective instabilities were not observed in any of the cases where the ambient was stratified. Figure 11 shows the settling of particles after the intrusion occurs within a lineally stratified ambient. It is observed that the particles separate from the flow and settle at a rate proportional to the settling velocity with no convective instabilities developed. It seems then that the presence of the stratification hinders the production of the convective instabilities and so prevents any further descent of the interstitial fluid. Hence, when considering an intrusion into the ocean where stratification plays an important role, in order to maintain the fresh water flux intruding at depth and not returning to the surface, particle concentrations must be of the order such that the plume is initially hyperpycnal and intrudes at depth.

6 Conclusion

In this study, laboratory experiments were undertaken to investigate the effects of both slope and stratification on particle-driven gravity currents. The slope velocity, intrusion depth and the effects of fingering were all measured. As with studies on saline gravity currents, an initial constant velocity is set-up that may be defined through the initial reduced gravity of the flow and the stratification through the Froude number. The effects of the variation of the front velocity and Froude number to increasing stratification is presented and provides an indication of the dependence of the front velocity to the effect of stratification.

The stratification of the ambient is also found to lead to a fingering effect with multiple intrusions occurring along the slope. This effect has been observed previously only as double intrusion of a saline gravity current [1] and in changing density currents entering a stratified fluid [10]. Quantifying this effect however, has proven to be more difficult than expected. The dependence of the distance between fingers on the front velocity is presented leading to a clear scaling term of U/N, however experiments were unable to verify this results, potentially due to the method of analysis used to calculate the distance between fingers, as some fingers may merge and so not be picked up.

The intrusion depth of the flow is represented through theoretical scaling analysis equations incorporating all the key effects of the flow, in particular that of of the entrainment of

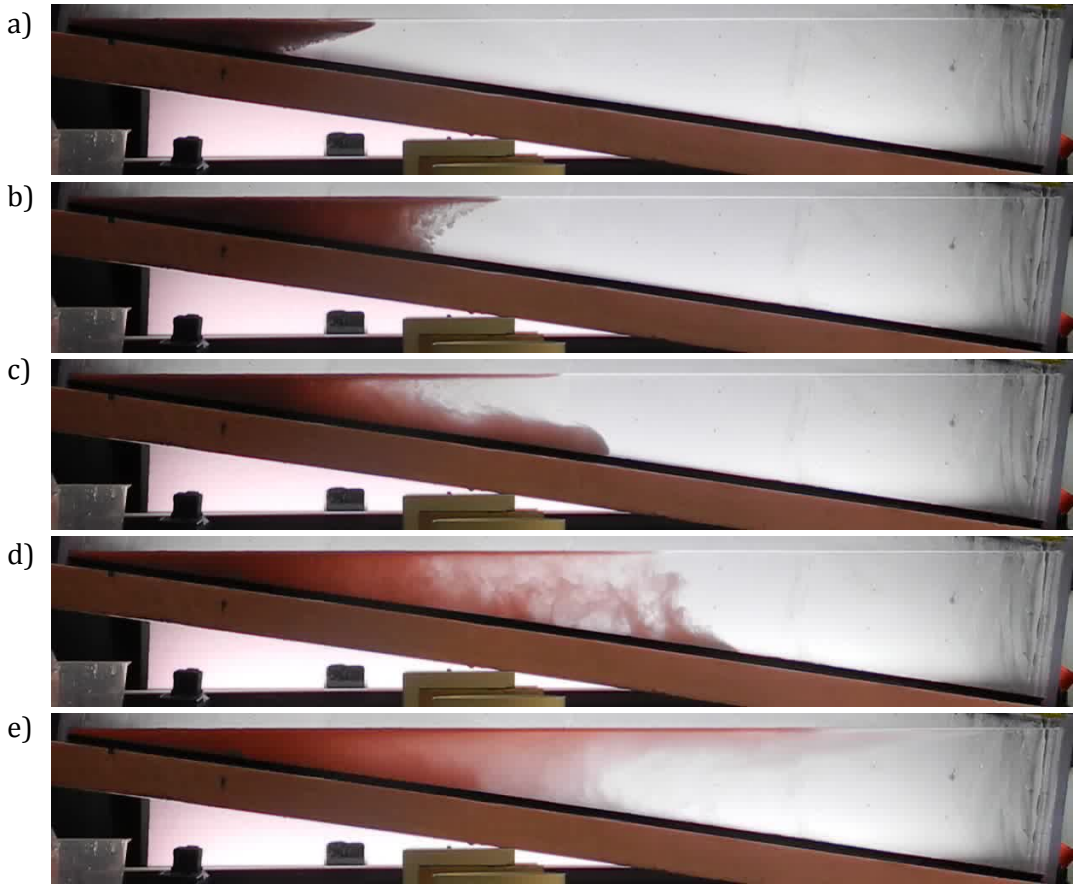

Figure 10: Flow of a particle laden current in a stratified ambient $N = 3.0$ s^{-1}, $\rho_0 = 1.12$ g cm^{-3} with interstitial fluid density 0.998 g cm^{-3}, $d = 13 - 45$ μm and $h_0 = 3$ cm where a) the initial hypopcyanl plume is shown. Instabilities develop b) that lead to the production of a hyperpycnal plume c) which after further settling of particles within the hyperpycnal plume leads to the reversing buoyancy of the interstitial d) and the fluid returning to the surface e) as hypopycnal.

the interstitial fluid and the settling of the particles. These theoretical results are verified by the application of experimental results performed with varying particle sizes, stratifications and particle volume fractions. From these results it is found that one of the key parameters defining the flow is the γ parameter, defining the ratio of settling velocity to entrainment velocity. This parameter becomes increasingly important for larger particles where the settling velocity is greater, while for decreasing particle size, where the current approaches a nature more comparable to that of a dense salt solution, the dependence on this term is no longer present. In the saline and small particle gravity currents, it is instead found that the intrusion depth of the flow may be represented by a simple scaling term dependent on the initial buoyancy of the flow, the lock height and the stratification of the ambient.

With the verification of the theory to the experiments, the theory is applied to the

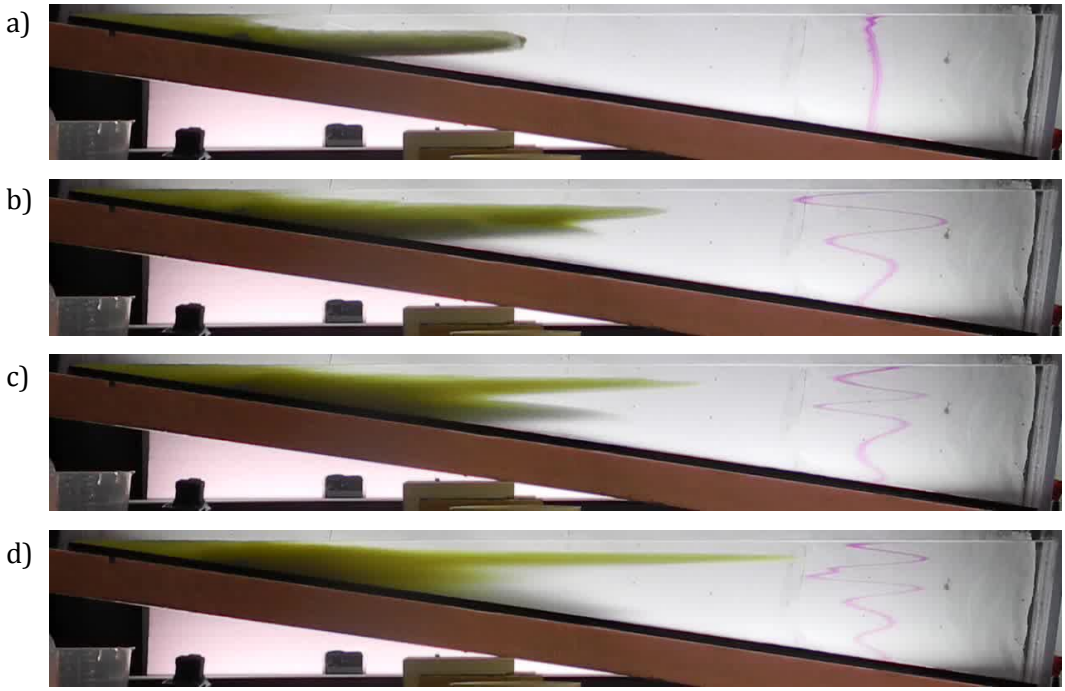

Figure 11: Flow of a particle laden current in constant density ambient of density 1.07 g cm^{-3}, $\rho_0 = 1.18$ g cm^{-3} with interstitial fluid density 0.998 g cm^{-3}, $d = 1 - 38$ μm and $h_0 = 3$ cm where a) the initial intrusion carries the particles within it until they slowly separate from the flow in b) and a distinct particle layer develops in c) slowly settling to the bottom at the settling velocity and carrying no more than marginal amounts of interstitial to lower depths d).

situation presented in [8], providing a means to determine the required particle concentration for a hyperpycnal plume to intrude at a certain depth. The results provide a more robust indication of the particle concentrations required to allow the flow to not return to the surface and indicate the simple applicability of the scaling theory to the real world. Further, the effect of the stratification to inhibit the presence of convective instabilities produced from the settling particles indicates the necessity to incorporate the key characteristics of both slope and stratification in order to more fully understand and represent the nature of particle laden currents. Hence, overall, by incorporating both these terms, the main effects influencing outflowing turbidity entering the ocean are represented and as such, a more complete picture of the nature of such flows is found.

7 Acknowledgement

I would like to thank Bruce Sutherland, whose guidance and input allowed my project to be possible and to progress as it did. I would also like to thank the organiser of the summer school for putting together such an amazing program and Paul Linden for teaching us so

much in those initial days. Thanks also go to George Veronis for giving his time to force us away from our work and inspiring us to have fun together and even, somehow, win a few softball games. And lastly of course I would like to thank the fellows for all the fun times and adventures we shared.

References

[1] P. G. Baines, *Mixing in downslope flows in the ocean Ð plumes versus gravity currents*, J. Fluid Mech., 443 (2001), pp. 237–270.

[2] ——, *Mixing in flows down gentle slopes into stratified environments*, Atmos.-Ocean, 46 (2008), pp. 405–419.

[3] T. B. Benjamin, *Gravity currents and related phenomena*, J. Fluid Mech., 31 (1968), pp. 209–248.

[4] R. T. Bonnecaze, H.E. Huppert, and J.R. Lister, *Particle-driven gravity currents*, J. Fluid Mech., 250 (1993), pp. 339–369.

[5] R. T. Bonnecaze and J. R. Lister, *Particle-driven gravity currents down planar slopes*, J. Fluid Mech., 390 (1999), pp. 75–91.

[6] S. F. Bradford, *Numerical Modelling of Turbidity Current Hydrodynamics and Sedimentation*, PhD thesis, University of Michigan, 1996.

[7] R. E. Britter and P. F. Linden, *The motion of the front of a gravity current travelling down an incline*, J. Fluid Mech., 99 (1980), pp. 531–543.

[8] G. K. C. Clark, A. B. G. Bush, and J. W. M. Bush, *Freshwater discharge, sediment transport, and modeled climate impacts of the final drainage of glacial lake agassiz*, J. Climate, 22 (2009), pp. 2161–2180.

[9] F. de. Rooij, *Sedimenting particle-laden flows in confined geometries*, PhD thesis, University of Cambridge, 1999.

[10] R. Fernandez and J. Imberger, *Time-varying underflow into a continuous stratification with bottom slope*, J. Hydraul. Eng., 134 (2008), pp. 1191–1198.

[11] M. Garcia and G. Parker, *Experiments on the entrainment of sediment into suspension by a dense bottom current*, J. Geophys. Res., 98 (1993), pp. 4793–4807.

[12] A. J. Hogg, H. E. Huppert, and M. A. Hallworth, *Reversing buoyancy of particle-driven gravity current*, Phys. Fluids, 11 (1999), pp. 2891–2900.

[13] ——, *Particle-driven gravity currents: asymptotic and box model solutions*, Eur. J. Mech. B Fluids, 19 (2000), pp. 139–165.

[14] H. E. Huppert, *Gravity currents: a personal perspective*, J. Fluid Mech., 554 (2006), pp. 299–322.

[15] B. E. Hurzeler, G. N. Ivey, and J. Imberger, *Spreading model for a turbidity current with reversing buoyancy from a constant-volume release*, Mar./ Freshwater/ Res., 46 (1995), pp. 393–408.

[16] B. Kneller and C. Buckee, *The structure and fluid mechanics of turbidity currents: a review of some recent studies and their geological implications*, Sedimentology, 47 (2000), pp. 62–94.

[17] A. A. Lawrence, W. D. McCaffrey, and P. J. Talling, *Special issue introduction: Sediment gravity flows Ð recent insights into their dynamic and stratified/composite nature*, Marine and Petroleum Geology, 26 (2009), pp. 1897–1899.

[18] D. G. Masson, R. G. Arzola, R. B. Wynn, J. E. Hunt, and P. P. E. Weaver, *Seismic triggering of landslides and turbidity currents offshore portugal*, Geochemistry, Geophysics, Geosystems, 12 (2011).

[19] T. Maxworthy, J. Leilich, J. E. Simpson, and E. H. Meiburg, *The propagation of a gravity current into a linearly stratified fluid*, J. Fluid Mech., 453 (2002), pp. 371–394.

[20] E. Meiburg and B. Kneller, *Turbidity currents and their deposits*, Annu. Rev. Fluid Mech., 42 (2010), pp. 135–156.

[21] J. J. Monahgan, R. A. F. Cas, A. M. Kos, and M. Hallworth, *Gravity currents descending a ramp in a stratified tank*, J. Fluid Mech., 379 (1999), pp. 39–69.

[22] T. Mulder and J. P. M. Syvitski, *Gravity currents descending a ramp in a stratified tank*, Journal of Geology, 103 (1995), pp. 285–299.

[23] T. Mulder, J. P. M. Syvitski, S. Migeon, J. C. Faugeres, and B. Savoye, *Marine hyperpycnal flows: initial, behaviour and related deposits. a review*, Marine and Petroleum Geology, 20 (2003), pp. 861–882.

[24] G. Parker, Y. Fukushima, and H. M. Pantin, *Self accelerating turbidity currents*, J. Fluid Mech., 171 (1986), pp. 145–181.

[25] J. P. Parson, J. W. M. Bush, and J. P. M. Syvitski, *Hyperpycnal plume formation from riverine outflows with small sediment concentration*, Sedimentology, 48 (2001), pp. 465–478.

[26] C. K. Paull, W. Ussler III, H. G. Greene, R. Keaten, P. Mitts, and J. Barry, *Caught in the act: the 20 december 2001 gravity flow event in monterey canyon*, Geo-Mar Lett, 22 (2003), pp. 227–232.

[27] C. Primez and J. Irman, *Reconstruction of turbidity currents in amazon channel*, Marine and Petroleum Geology, 20 (2003), pp. 823–849.

[28] F. P. Shepard, P. A. McLoughlin, N. F. Marshall, and G. G. Sullivan, *Current-meter recordings of low-speed turbidity currents*, Geology, 5 (2013), pp. 297–301.

[29] J. O. Shin, S. B. Dalziel, and P. F. Linden, *Gravity currents produced by lock exchange*, J. Fluid Mech., 521 (2004), pp. 1–34.

[30] R. S. J. Sparks, R. T. Bonnecaze, H. E. Huppert, J. R. Lister, M. A. Hallworth, H. Mader, and J. Phillips, *Sediment-laden gravity currents with reversing buoyancy*, Earth and Planetary Science Letters, 114 (1993), pp. 243–257.

[31] D. A. V. Stow, *Deep sea processes of sediment transport and deposition*, in Sediment Transport and Depositional Processes, K. Pye, ed., Blackwell Scientific Publications, Oxford, Boston, 1994, pp. 257–293.

[32] K. M. Straub, *Quantifying Turbidity Current Interaction with Topogrpahy*, PhD thesis, Massachusetts Institute of Technology, 2007.

[33] M. Ungarish, *On gravity currents in a linearly stratified ambient: a generalization of benjamin's steady-state propagation results*, J. Fluid Mech., 548 (2006), pp. 49–68.

[34] M. Wells and P. Nadarajah, *The intrusion depth of density currents flowing into stratified water bodies*, J. Phys. Oceanogr., 39 (2009), pp. 1935–1947.

Nonlinear Optimal Perturbations

Daniel Lecoanet

October 1, 2013

1 Introduction

In this report, I will describe a series of calculations employing nonlinear optimal perturbations. This technique was used by [4] to study transition to turbulence in shear flows. They searched for the lowest energy perturbation to the laminar state that would yield turbulence at late time. Since the kinetic energy of the perturbation is higher in the turbulent state than in the laminar state (where it is zero), they tried to maximize the perturbation kinetic energy at some late time T. This maximization was subject to the constraint that the initial condition has a given perturbation kinetic energy E_0. For E_0 lower than some threshold energy, E_c, they found that the optimization procedure was not able to find a turbulent state. However, for E_0 greater than E_c, the optimization procedure was able to find initial perturbations which evolved into turbulence. This suggests that E_c is the minimum energy required to trigger turbulence, and the perturbation with this energy that yields turbulence is referred to as the minimum seed.

To illustrate this technique, I will describe the nonlinear optimization procedure for a much simpler system: a system of 2 ODEs. The ODEs are

$$\partial_t x_1 = -x_1 + 10x_2 \tag{1}$$
$$\partial_t x_2 = x_2(x_2 - 1)\left(10\exp(-x_1^2/100) - x_2\right). \tag{2}$$

This system has two stable fixed points, one at $\boldsymbol{x} = \boldsymbol{x}_l \equiv \boldsymbol{0}$, and the other at $\boldsymbol{x} = \boldsymbol{x}_t \approx (14.0174, 1.40174)$. To make an analogy to the transition to turbulence problem, the former can be thought of as the laminar state, and the latter as the turbulent state. It is straightforward to check that the basin of attraction of the laminar state is the region with $x_2 < 1$, and the basin of attraction of the turbulent state is the region with $x_2 > 1$. The analogous problem to finding the minimum seed is then to maximize x_2 at some late time T, subject to the constraint that the initial perturbation from $\boldsymbol{0}$ has norm $|\boldsymbol{x}|^2 = E_0$. I will now describe how to perform this optimization.

Consider the functional $\mathcal{L}$ given by

$$\mathcal{L} = x_2(T) + \alpha\left(|\boldsymbol{x}(0)|^2 - E_0\right) + \int_0^T dt\ \boldsymbol{\nu}(t)\cdot\left(\partial_t\boldsymbol{x}(t) - \boldsymbol{f}(\boldsymbol{x}(t))\right), \tag{3}$$

where α and $\boldsymbol{\nu}(t)$ are Lagrange multipliers imposing the constraints that $\boldsymbol{x}(0)^2 = E_0$ and that $\boldsymbol{x}(t)$ satisfies the system of ODEs (1 & 2). $\boldsymbol{\nu}(t)$ are referred to as the adjoint variables.

Varying $\mathcal{L}$ yields

$$\begin{aligned}\delta\mathcal{L} = \quad & \delta x_2(T) + \delta\alpha\left(|\boldsymbol{x}(0)|^2 - E_0\right) + 2\alpha\boldsymbol{x}(0)\cdot\delta\boldsymbol{x}(0) \\ & + \int_0^T dt\ \delta\boldsymbol{\nu}(t)\cdot\left(\partial_t\boldsymbol{x}(t) - \boldsymbol{f}(\boldsymbol{x}(t))\right) \\ & + \int_0^T dt\ \boldsymbol{\nu}(t)\cdot\left(\partial_t\delta\boldsymbol{x}(t) - \frac{\partial\boldsymbol{f}}{\partial\boldsymbol{x}}\cdot\delta\boldsymbol{x}(t)\right). \end{aligned} \tag{4}$$

The partial derivatives of $\mathcal{L}$ are thus

$$\frac{\delta\mathcal{L}}{\delta\alpha} = |\boldsymbol{x}(0)|^2 - E_0, \tag{5}$$

$$\frac{\delta\mathcal{L}}{\delta\boldsymbol{\nu}(t)} = \partial_t\boldsymbol{x}(t) - \boldsymbol{f}(\boldsymbol{x}(t)), \tag{6}$$

$$\frac{\delta\mathcal{L}}{\delta\boldsymbol{x}(T)} = (0,1) + \boldsymbol{\nu}(T), \tag{7}$$

$$\frac{\delta\mathcal{L}}{\delta\boldsymbol{x}(t)} = -\partial_t\boldsymbol{\nu}(t) - \boldsymbol{\nu}\cdot\frac{\partial\boldsymbol{f}}{\partial\boldsymbol{x}}, \tag{8}$$

$$\frac{\delta\mathcal{L}}{\delta\boldsymbol{x}(0)} = 2\alpha\boldsymbol{x}(0) - \boldsymbol{\nu}(0). \tag{9}$$

If all these conditions are satisfied, then $\boldsymbol{x}(0)$ maximizes $x_2(T)$ subject to $|\boldsymbol{x}(0)|^2 = E_0$. (8) is an evolution equation (backward in time) for the adjoint variables, and is referred to as the adjoint equation.

The optimization procedure is an iterative algorithm which uses the above expressions to update a guess for $\boldsymbol{x}(0)$, call it $\boldsymbol{x}^{(0)}(0)$, to another initial condition, $\boldsymbol{x}^{(1)}(0)$, which has a larger $x_2(T)$ than the first guess.

First, pick $\boldsymbol{x}^{(0)}(0)$ which satisfies $|\boldsymbol{x}^{(0)}(0)| = E_0$ (5). Then use (6) to integrate $\boldsymbol{x}(t)$ from $t = 0$ to $t = T$. Then use (7) to set $\boldsymbol{\nu}(T)$, which in this case is always equal to $(0,-1)$, but in general will depend on $\boldsymbol{x}(T)$. Next, (8) is integrated backward in time to get $\boldsymbol{\nu}(0)$. Finally, if $\boldsymbol{\nu}(0)$ is parallel to $\boldsymbol{x}^{(0)}(0)$, (9) shows that $\boldsymbol{x}^{(0)}(0)$ maximizes $x_2(T)$. If $\boldsymbol{\nu}(0)$ is not parallel to $\boldsymbol{x}^{(0)}(0)$, then use (9) to update to a new initial perturbation using steepest ascent,

$$\boldsymbol{x}^{(1)}(0) = \boldsymbol{x}^{(0)}(0) + \epsilon\frac{\delta\mathcal{L}}{\delta\boldsymbol{x}(0)}, \tag{10}$$

where ϵ sets the size of the update. For sufficiently small ϵ, the initial condition $\boldsymbol{x}^{(1)}(0)$ will lead to a larger $x_2(T)$ than $\boldsymbol{x}^{(0)}(0)$. Note that for arbitrary ϵ and α, $\boldsymbol{x}^{(1)}(0)$ does not satisfy the norm constraint (5) $|\boldsymbol{x}^{(1)}(0)|^2 = E_0$. Rather, α must be chosen to satisfy this constraint.

In the remainder of this report, I will apply this technique to two new problems. The first is an extension of the optimization procedure to allow for multiple perturbations, instead

of just a single perturbation at $t = 0$. The second is an application of the optimization to the Vlasov-Poisson equations.

2 Multiple Perturbations

For simplicity, I will consider the multiple perturbation problem only in the context of 2D ODE systems. However, the approach is easily generalized to more complicated ODE or PDE systems.

To be general, assume that I will maximize the quantity $\phi(\boldsymbol{x}(T))$, for some function ϕ. I want to derive a procedure for finding the set of perturbations $\boldsymbol{\xi}_i$, $0 \leq i \leq n-1$, which act on $\boldsymbol{x}$ at

$$0 = T_0 < T_1 < \cdots < T_{n-1}, \tag{11}$$

with $T_{n-1} < T = T_n$, which maximize $\phi(\boldsymbol{x}(T))$. I will also limit the size of the perturbations $\boldsymbol{\xi}_i$ using some constraint $N(\boldsymbol{\xi}_i) = 0$, e.g., $N(\boldsymbol{\xi}_i) = \sum |\boldsymbol{\xi}_i|^2 - E_0$. This is a generalization of the single perturbation case, in which $n = 1$.

To perform the optimization analysis, I will also split the dependent variable $\boldsymbol{x}$ into n parts, $\boldsymbol{x}_i(t)$ with $0 \leq i \leq n-1$, where $\boldsymbol{x}_i(t)$ is defined between $T_i \leq t \leq T_{i+1}$. I take $\boldsymbol{x}_0(T_0) = \boldsymbol{\xi}_0$, and for $1 \leq i \leq n-1$, $\boldsymbol{x}_i(T_i) = \boldsymbol{x}_{i-1}(T_i) + \boldsymbol{\xi}_i$. Thus, I am maximizing $\phi(\boldsymbol{x}_{n-1}(T)) = \phi(\boldsymbol{x}_{n-1}(T_n))$. To simplify the equations, I will define $\boldsymbol{x}_{-1}(T_0) = \boldsymbol{x}_s$.

The optimization will follow from extremizing

$$\begin{aligned}
\mathcal{L} &= \phi(\boldsymbol{x}_{n-1}(T_n)) + \alpha N(\boldsymbol{\xi}_i) \\
&+ \sum_{i=0}^{n-1} \boldsymbol{\beta}_i \cdot (\boldsymbol{x}_i(T_i) - \boldsymbol{x}_{i-1}(T_i) - \boldsymbol{\xi}_i) \\
&+ \sum_{i=0}^{n-1} \int_{T_i}^{T_{i+1}} dt\ \boldsymbol{\nu}_i(t) \cdot (\partial_t \boldsymbol{x}_i - \boldsymbol{f}(\boldsymbol{x}_i))\,.
\end{aligned} \tag{12}$$

The variation of $\mathcal{L}$ is

$$\begin{aligned}\delta\mathcal{L} = \quad & \frac{\partial\phi}{\partial \boldsymbol{x}} \cdot \delta\boldsymbol{x}_{n-1}(T) + \delta\alpha N(\boldsymbol{\xi}_i) + \alpha \sum_{i=0}^{n-1} \frac{\partial N}{\partial \boldsymbol{\xi_i}} \cdot \delta\boldsymbol{\xi}_i \\ & + \sum_{i=0}^{n-1} \delta\boldsymbol{\beta}_i \cdot (\boldsymbol{x}_i(T_i) - \boldsymbol{x}_{i-1}(T_i) - \boldsymbol{\xi}_i) \\ & + \sum_{i=0}^{n-1} \boldsymbol{\beta}_i \cdot (\delta\boldsymbol{x}_i(T_i) - \delta\boldsymbol{x}_{i-1}(T_i) - \delta\boldsymbol{\xi}_i) \\ & + \sum_{i=0}^{n-1} \int_{T_i}^{T_{i+1}} dt\ \delta\boldsymbol{\nu}_i(t) \cdot (\partial_t \boldsymbol{x}_i - \boldsymbol{f}(\boldsymbol{x}_i)) \\ & + \sum_{i=0}^{n-1} \int_{T_i}^{T_{i+1}} dt\ \boldsymbol{\nu}_i(t) \cdot \left(\partial_t \delta\boldsymbol{x}_i - \frac{\partial \boldsymbol{f}}{\partial \boldsymbol{x}_i} \cdot \delta\boldsymbol{x}_i\right). \end{aligned} \tag{13}$$

Thus, the partial derivatives are

$$\frac{\delta\mathcal{L}}{\delta\alpha} = N(\boldsymbol{\xi}_i), \tag{14}$$

$$\frac{\delta\mathcal{L}}{\delta\boldsymbol{\nu}_i(t)} = \partial_t \boldsymbol{x}_i - \boldsymbol{f}(\boldsymbol{x}_i), \tag{15}$$

$$\frac{\delta\mathcal{L}}{\delta\boldsymbol{\beta}_i} = \boldsymbol{x}_i(T_i) - \boldsymbol{x}_{i-1}(T_i) - \boldsymbol{\xi}_i, \tag{16}$$

$$\frac{\delta\mathcal{L}}{\delta\boldsymbol{x}_{n-1}(T)} = \frac{\partial\phi(\boldsymbol{x}_{n-1}(T))}{\partial\boldsymbol{x}_{n-1}(T)} + \boldsymbol{\nu}_{n-1}(T), \tag{17}$$

$$\frac{\delta\mathcal{L}}{\delta\boldsymbol{x}_i(t)} = -\partial_t\boldsymbol{\nu}_i(t) - \boldsymbol{\nu}_i \cdot \frac{\partial\boldsymbol{f}}{\partial\boldsymbol{x}_i}, \tag{18}$$

$$\frac{\delta\mathcal{L}}{\delta\boldsymbol{x}_{i-1}(T_i)} = -\boldsymbol{\beta}_i + \boldsymbol{\nu}_{i-1}(T_i), \tag{19}$$

$$\frac{\delta\mathcal{L}}{\delta\boldsymbol{x}_i(T_i)} = \boldsymbol{\beta}_i - \boldsymbol{\nu}_i(T_i), \tag{20}$$

$$\frac{\delta\mathcal{L}}{\delta\boldsymbol{\xi}_i} = \alpha\frac{\partial N}{\partial\boldsymbol{\xi}_i} + \boldsymbol{\beta}_i. \tag{21}$$

The optimization algorithm now follows from these partial derivatives. As before, start with an initial set of perturbations $\boldsymbol{\xi}_i^{(0)}$ satisfying the norm condition (14). Integrate $\boldsymbol{x}(t)$ (for simplicity, I drop the subscripts) forward in time using (15), adding in the perturbations at the times T_i according to (16). Set $\boldsymbol{\nu}(T)$ using (17) and $\boldsymbol{x}(T)$. Then integrate $\boldsymbol{\nu}$ back in time to $t = 0$ using (18). (19) and (20) imply that $\boldsymbol{\nu}(t)$ is continuous at T_i. To update $\boldsymbol{\xi}_i$, I use steepest ascent along with (21), identifying $\boldsymbol{\beta}_i$ with $\boldsymbol{\nu}(T_i)$ (20).

2.1 Changing the times of the perturbations, T_i

I also change T_i for $1 \leq i \leq n-1$ to better optimize the functional. The variation of $\mathcal{L}$ with T_i is

$$\frac{\delta \mathcal{L}}{\delta T_i} = \boldsymbol{\beta}_i \cdot \left(\left. \frac{\partial \boldsymbol{x}_i}{\partial t} \right|_{T_i} - \left. \frac{\partial \boldsymbol{x}_{i-1}}{\partial t} \right|_{T_i} \right), \tag{22}$$

or,

$$\frac{\delta \mathcal{L}}{\delta T_i} = \boldsymbol{\beta}_i \cdot \left(\boldsymbol{f}(\boldsymbol{x}_i) - \boldsymbol{f}(\boldsymbol{x}_{i-1}) \right). \tag{23}$$

T_i is updated using steepest ascent.

2.2 Numerical Experiments

I found nonlinear optimal sets of perturbations for two systems of second order ODEs. The first set are (1 & 2). The optimal perturbation for these equations is $\boldsymbol{x} = (0, 1+\epsilon)$. The optimization algorithm has no difficulty in finding this optimal perturbation. When considering multiple perturbations, it is important to pick the current norm for describing the size of the set of perturbations. A naive choice would be to use the sum of magnitudes, i.e.,

$$N(\boldsymbol{\xi}_i) = \sum_i |\boldsymbol{\xi}_i|^2. \tag{24}$$

However, this norm has the flaw that $N(\{(0,1)\}) = 1$, but $N(\{(0,\frac{1}{2}),(0,\frac{1}{2})\}) = \frac{1}{2}$, where $\{\boldsymbol{\xi}_i\}$ denotes the set of perturbations. That is to say, having multiple perturbations that act at the same time and in the same direction is more efficient than a single perturbation. To avoid this issue, I use the magnitude of sum norm,

$$N(\boldsymbol{\xi}_i) = \left| \sum_i \boldsymbol{\xi}_i \right|^2. \tag{25}$$

Using this norm, I find that having more than one perturbation does not change the minimum norm required to perturb the system into the attractor of the second fixed point $\boldsymbol{x}_t$. The minimum seed is the single perturbation $(0, 1+\epsilon)$, which has energy $1+2\epsilon$.

The reason that multiple perturbations do not help the system transition to the second fixed point $\boldsymbol{x}_t$ is that $\partial_t x_2 < 0$ between $0 < x_2 < 1$ near $\mathbf{0}$ – $\partial_t x_2$ only becomes positive for $0 < x_2 < 1$ when $|x_1| \gtrsim 15.17$. This implies that the ODE flows downwards near $\mathbf{0}$. Having multiple perturbations is thus not efficient, because the perturbations have to fight against the ODE flow. Thus, putting all the energy into one big perturbation is the most efficient way of pushing the system into the attractor of the second fixed point $\boldsymbol{x}_t$.

With this in mind, I have also investigated the related ODE system,

$$\partial_t x_1 = -x_1 + 10x_2 \tag{26}$$

$$\partial_t x_2 = x_2(x_2-1)\left(20\exp(-(x_1-7)^2/14) - 10x_2\right). \tag{27}$$

As for (1 & 2), these ODEs also possess two linearly stable fixed points, one at $\boldsymbol{x} = \boldsymbol{x}_l \equiv \mathbf{0}$, and the other at $\boldsymbol{x} = \boldsymbol{x}_t \approx (10.094, 1.0094)$. As before, the boundary between the basins of attraction of the two fixed points is $x_2 = 1$. This ODE system was chosen such that there is a region with $x_2 > 0$ and $|\boldsymbol{x}|^2 < 1$ which has $\partial_t x_2 > 0$, i.e., the ODE can flow the system toward the boundary at $x_2 = 1$.

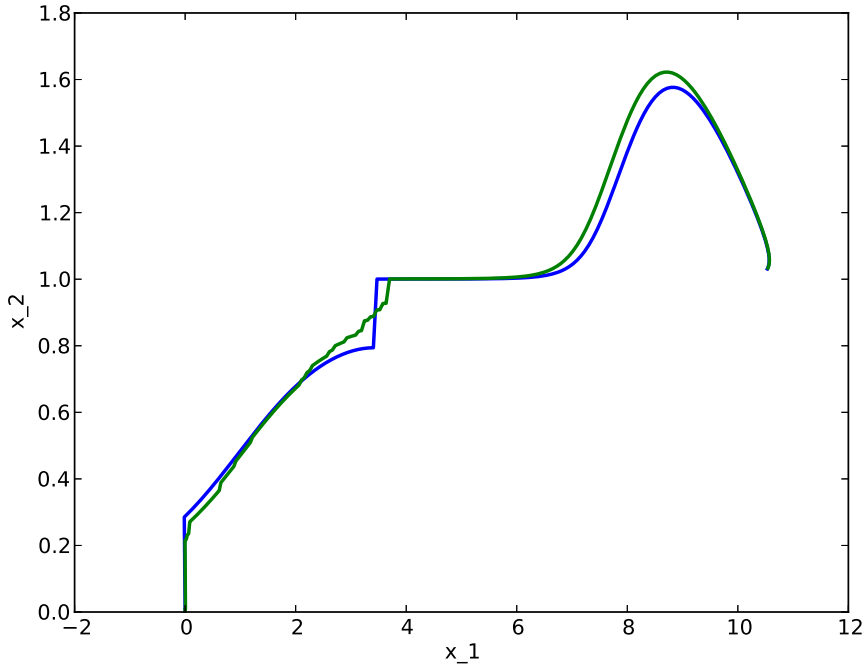

Figure 1: Trajectories for optimal sets of perturbations for ODEs (26 & 27), for two perturbations (blue) and fifty perturbations (green).

As before, optimizing over one perturbation yields a minimum seed of $(0, 1+\epsilon)$, having energy of $1 + 2\epsilon$. However, optimizing over two perturbations allows the system to take advantage of the upwards flow of the ODE. In Figure 1, I have plotted the trajectories of the optimal set of perturbations, for both two and fifty perturbations. The (mostly vertical) discontinuities are the perturbations. Looking at the blue curve, there is an initial perturbation upwards from $\boldsymbol{x} = \mathbf{0}$. This is followed by allowing the ODE flow to the point where $\partial_t x_2 = 0$, at which point a second perturbation is used to push the system above $x_2 = 1$. Once $x_2 > 0$, the system is in the basin of attraction of the second fixed point $\boldsymbol{x}_t$, and flows into this fixed point. This set of perturbations has a "magnitude of sum" norm of 0.485, about a factor of two smaller than the single perturbation optimal.

Interestingly, the optimal set of perturbations for fifty perturbations is similar to the optimal set for two perturbations. As before, there is a large perturbation near $\boldsymbol{x} = \mathbf{0}$ to push the system into the region of phase space where $\partial_t x_2 > 0$. This is followed by perturbations near the point at which $\partial_t x_2 = 0$ that push the system above $x_2 = 1$. Furthermore, the "magnitude of sum" norm of this set of perturbations is also 0.485, i.e.,

it does no better than two perturbations. For this system of ODEs, two perturbations is enough to realize the minimum seed. Presumably, one could cook up a slightly more complicated ODE system which has two disconnected regions where $\partial_t x_2 > 0$ between $x_2 = 0$ and $x_2 = 1$ – in this case, optimal sets of perturbations would require at least three perturbations: the first perturbing the system from $\boldsymbol{x} = \mathbf{0}$ to the first region where $\partial_t x_2 > 0$, the second moving the system from the first region where $\partial_t x_2 > 0$ to the second such region, and then the third perturbation pushing the system above $x_2 = 1$. In a real fluids system, this would correspond to using several distinct mechanisms to amplify the energy of a perturbation sufficiently to access a new nonlinear state.

2.3 Stochastic Forcing

In experiments, systems are rarely perturbed by the optimal perturbation. A more relevant perturbation might be small amplitude random noise. I will analyze how easily an ODE system can switch between stable equilibria under small amplitude random noise using the mean exit time from the attractor of the fixed point at $\boldsymbol{x} = \mathbf{0}$. It turns out that the mean exit time is related to the energy of the minimum seed (allowing for multiple perturbations). This is because, in the limit of low amplitude noise, the randomly perturbed system leaves the attractor of the fixed point at $\boldsymbol{x} = \mathbf{0}$ only when the random perturbations almost coincide with the minimum seed. This is related to Large something-something theory [1].

I determine the mean exit time using two approaches. First, I integrate the stochastic differential equations (SDEs)

$$\partial_t x_i = f_i(\boldsymbol{x}) + \sqrt{2\sigma_i}\partial_t W_{ti}, \tag{28}$$

where W_{ti} are Weiner processes, and $\boldsymbol{\sigma}$ is a constant. To integrate this SDE system, I integrate the ODE system (ignoring the noise), applying a forcing $\sqrt{2\sigma_i}\Delta W_i$ at each time step, where ΔW_i are iid normally distributed random variables with expected value zero and variance Δt, the time step.

As an example, consider the SDE where $\boldsymbol{f}(\boldsymbol{x})$ given by (1 & 2), and with $\sigma_1 = 0.1$, $\sigma_2 = 0.4$. In Figure 2, I plot three trajectories generated from this SDE, starting at $\boldsymbol{x} = \mathbf{0}$ at $t = 0$ and integrated to $t = 20$. The green trajectory never leaves the basin of attraction of the fixed point at $\boldsymbol{x} = \mathbf{0}$. The red trajectory makes it to the basin of attraction of the second fixed point, $\boldsymbol{x}_t$. However, the most interesting trajectory is the blue trajectory, which makes it to the basin of attraction second fixed point at $\boldsymbol{x}_t$, but eventually is perturbed back into the basin of attraction of the fixed point at $\mathbf{0}$.

Second, I evolve the probability distribution function (pdf), $F(\boldsymbol{x}, t)$, for the state of the system as a function of time. Integrating $F(\boldsymbol{x}, t)$ in the neighborhood of $\boldsymbol{x}_0$ gives the probability that $\boldsymbol{x} = \boldsymbol{x}_0$ at the time t. $F(\boldsymbol{x}, t)$ satisfies a modified diffusion equation known as a Fokker-Planck equation,

$$\partial_t F = -\boldsymbol{\nabla} \cdot (F\boldsymbol{f}(\boldsymbol{x})) + \partial^2_{x_i}(\sigma_i F). \tag{29}$$

I integrate the Fokker-Planck equation forward in time, using a sharply peaked Gaussian centered at $\boldsymbol{x} = \mathbf{0}$ as the initial condition. I set $F(\boldsymbol{x}, t) = 0$ on the outer edge of the domain in $\boldsymbol{x}$-space – this is a good approximation provided that the domain is large enough (I test

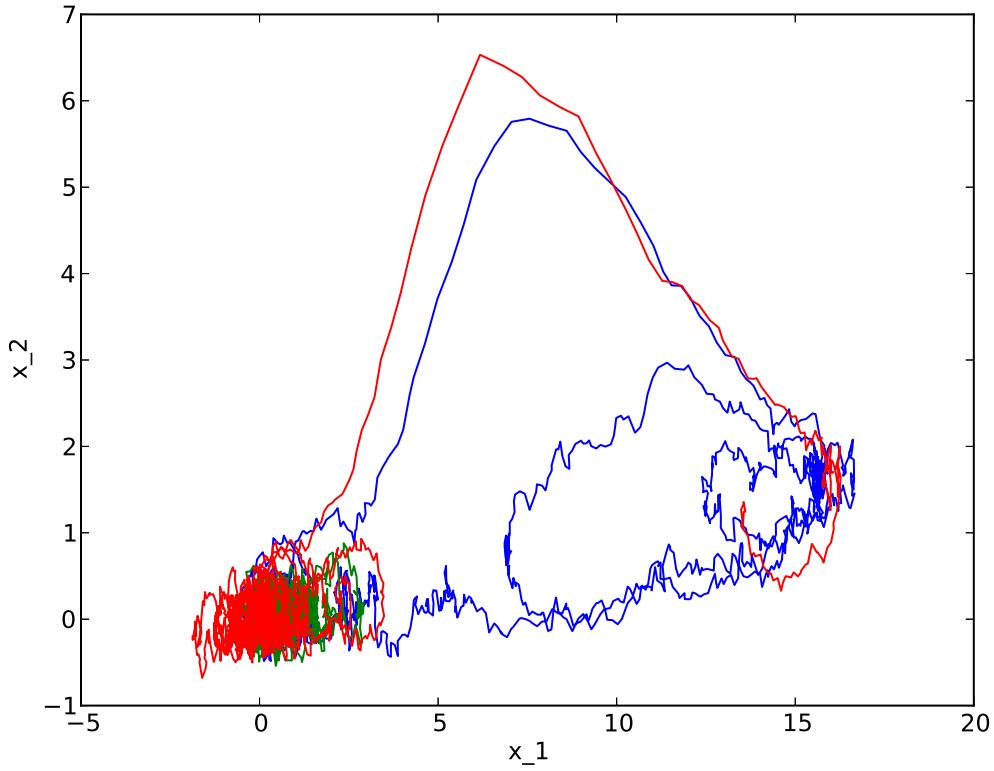

Figure 2: Three trajectories from the SDEs corresponding to (1 & 2), for $\sigma_1 = 0.1$ and $\sigma_2 = 0.4$, integrated to $t = 20$.

this by confirming that the solution is insensitive to the domain size). I found that explicit integration schemes have stability problems, so I integrate the Fokker-Planck equation using the forward Euler scheme.

For example, Figure 3 shows $F(\boldsymbol{x}, 10)$ for when $\boldsymbol{f}(\boldsymbol{x})$ is given by (1 & 2), and $\sigma_1 = 0.1$, $\sigma_2 = 0.4$. Note the similarities between the pdf and the trajectories in Figure 2.

The outer-most contour in Figure 3 shows the typical trajectory between the two fixed points. Going from the fixed point at $\boldsymbol{x} = \boldsymbol{0}$ to the fixed point at $\boldsymbol{x}_t$, the system typically crosses $x_2 = 1$ at around $x_1 \approx 2 - 3$, goes up to $\boldsymbol{x} \approx (6, 7)$, and then approaches $\boldsymbol{x}_t$, staying near $\boldsymbol{x} = (16, 2)$. This has larger x_1 and x_2 than $\boldsymbol{x}_t \approx (14, 4)$. I assume this is because the pull of the ODE back to the fixed point is stronger in the southwest direction than in the northeast direction. However, the system is often kicked out of the attractor of this fixed point. These features occur in both the trajectories and in the pdf.

As t increases, the pdf $F(\boldsymbol{x}, t)$ approaches a steady distribution. One could in principle find this distribution by setting the $\partial_t F$ term in the Fokker-Planck equation equal to zero, and then solving the corresponding elliptic equation. I have not done this, because one would presumably need to be careful about the boundary conditions. However, if one integrates the Fokker-Planck equation in time long enough, one can verify that the distribution function

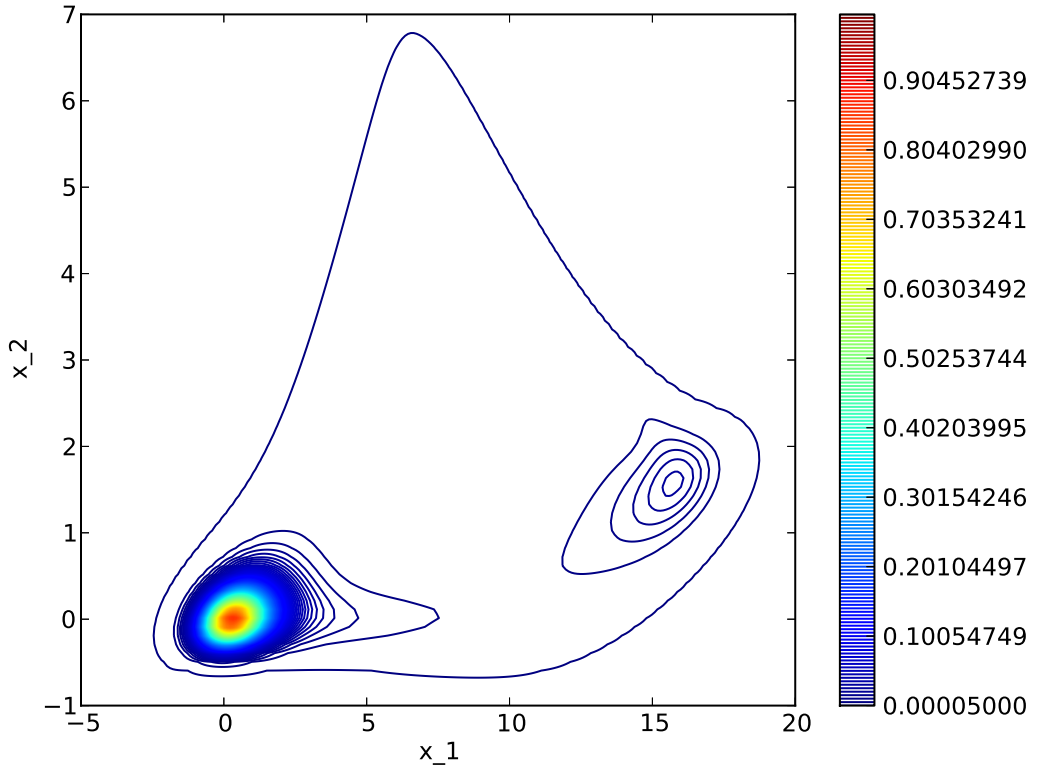

Figure 3: Contours of the probability density, as derived from the Fokker-Planck equation, for the ODEs (1 & 2), using $\sigma_1 = 0.1$, $\sigma_2 = 0.4$, and integrating to $t = 10$.

converges. For instance, in this example,

$$\frac{\int d^2\boldsymbol{x}\,|F(\boldsymbol{x},15) - F(\boldsymbol{x},10)|}{\int d^2\boldsymbol{x} F(\boldsymbol{x},15)} \approx 0.01, \tag{30}$$

and the analogous change between $t = 15$ and $t = 20$ is 0.002. Thus, it seems that $F(\boldsymbol{x}, t)$ has reached the a steady state distribution.

Another comparison is to consider an ensemble average of many integrations of the SDEs. I have integrated 20,000 instances of the SDEs to $t = 10$, and calculated a pdf of the states (Figure 4). In the limit of the SDEs being integrated infinitely many times, the pdf of the system states should converge to the result of the pdf given by the Fokker-Planck equation. Indeed, Figure 4 agrees well with Figure 3. Presumably, including even more integrations of the SDEs would improve the agreement.

3 Vlasov-Poisson

The Vlasov-Poisson equations describe a collision less electrostatic plasma. I will consider the case of an electron plasma, with a uniform and stationary background of ions. Then

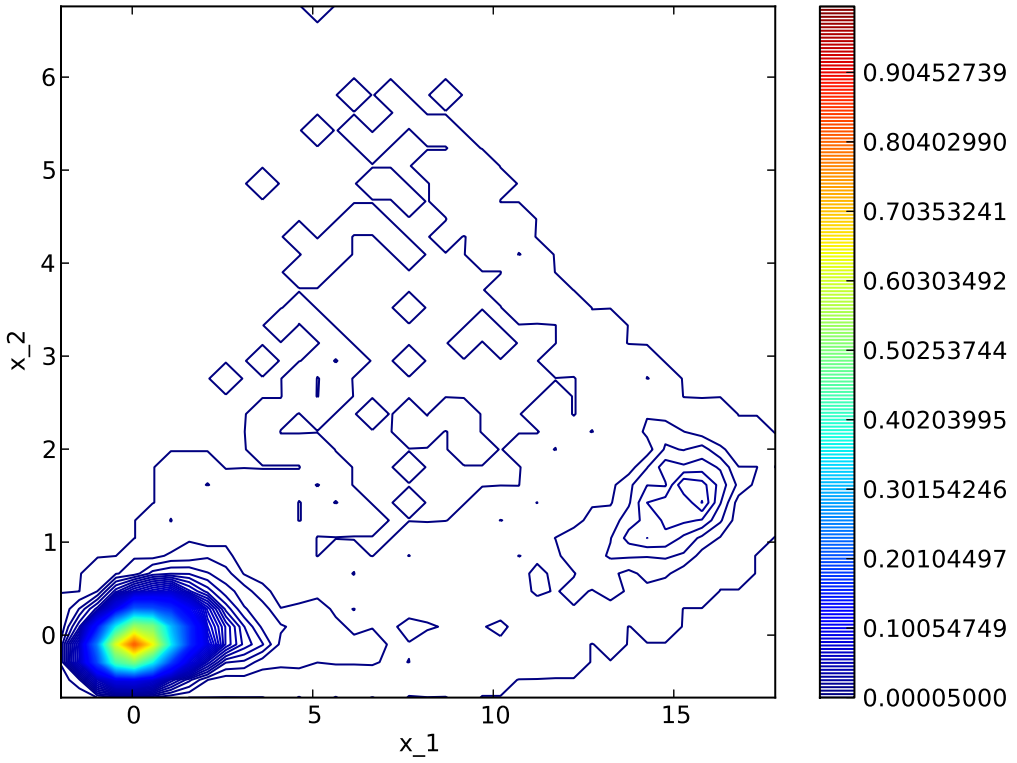

Figure 4: Contours of the probability density from 20,000 integrations of the SDEs corresponding to (1 & 2), using $\sigma_1 = 0.1$, $\sigma_2 = 0.4$, and integrating to $t = 10$.

the electron distribution function, $f(x, v, t)$, satisfies

$$\partial_t f(x, v, t) + v\partial_x f(x, v, t) - \frac{e}{m_e} E(x, t)\partial_v f(x, v, t) = 0, \tag{31}$$

$$\epsilon_0 \partial_x E(x, t) = e n_e - e \int_{-\infty}^{+\infty} dv \; f(x, v, t), \tag{32}$$

where e is the electron charge, m_e is the electron mass, n_e is proton number density (which equals the average electron number density), and ϵ_0 is the vacuum permittivity. The natural frequency scale is the electron plasma frequency,

$$\omega_{pe} = \sqrt{\frac{n_e e^2}{m_e \epsilon_0}}. \tag{33}$$

For simplicity, I assume that the plasma is periodic in the x direction with periodicity L. Non-dimensionalizing according to

$$\begin{aligned} x &\rightarrow xL, \\ t &\rightarrow t/\omega_{pe}, \\ v &\rightarrow vL\omega_{pe}, \\ f &\rightarrow fn_e/(L\omega_{pe}), \\ E &\rightarrow ELen_e/\epsilon_0, \end{aligned} \tag{34}$$

the Vlasov-Poisson equations become

$$\partial_t f(x,v,t) + v\partial_x f(x,v,t) - E(x,t)\partial_v f(x,v,t) = 0, \tag{35}$$

$$\partial_x E(x,t) = 1 - \int_{-\infty}^{+\infty} dv\ f(x,v,t). \tag{36}$$

An alternative form of (36) is

$$\partial_t \partial_x E(x,t) = \int_{-\infty}^{+\infty} dv\ v\partial_x f(x,v,t) \tag{37}$$

It has been observed through experiments and numerical simulation (e.g., [2] and references therein) that some perturbations to a spatially uniform electron plasma decay to zero in time, whereas others lead to non-linear states analogous to BGK waves, in which the electric field stays finite as $t \rightarrow \infty$. I am interested in finding the smallest perturbation to the distribution function which will generate an electric field which stays finite as $t \rightarrow \infty$. There are many ways to perturb the distribution function, but I will limit myself to perturbations which change the electron density as a function of x, but which do not change the velocity dependence of the distribution function.

The variational problem is as follows. The optimization is over the electric field at $t = 0$. I want to maximize

$$\int_0^L dx\ E(x,T)^2. \tag{38}$$

To limit the size of the perturbation, I fix

$$\int_0^L dx\ |\partial_x E(x,0)|^2 = N_0. \tag{39}$$

Recall that the velocity-averaged distribution function is given by $\partial_x E$. Furthermore, for $E(x,0)$ to be representable as the derivative of a periodic potential, it must have zero mean. Thus,

$$\int_0^L dx\ E(x,0) = 0. \tag{40}$$

The initial distribution function must be consistent with $E(x,0)$, so I impose

$$f(x,v,0) = F(v)(1 - \partial_x E(x,0)), \tag{41}$$

where $F(v)$ is the initial velocity-space structure of the distribution function, which is assumed to integrate to one. For instance, one could take,

$$F(v) = \frac{1}{\sqrt{2\pi}} \exp(-v^2/2). \tag{42}$$

The optimization is based on the initial electric field, rather than the full distribution function, because it is one dimensional. It would be possible to introduce additional degrees of freedom regarding the velocity distribution. For instance, one could take

$$f(x,v,0) = F(v) - \partial_x E(x,0) G(v), \tag{43}$$

where $G(v)$ integrates to one. If $G(v)$ is assumed to be a Gaussian with width σ centered at v_0, then it would be possible to optimize over σ and v_0 as well as $E(x,0)$.

3.1 Variational Problem

The functional I want to maximize is

$$\begin{aligned}
\mathcal{L} = \quad & \int_0^L dx\ E(x,T)^2 \\
& + \lambda \left(\int_0^L dx\ |\partial_x E(x,0)|^2 - N_0 \right) + \gamma \left(\int_0^L dx E(x,0) \right) \\
& + \iint dx dv\ \beta(x,v) \left[f(x,v,0) - F(v)(1 - \partial_x E(x,0)) \right] \\
& + \int dt \int_0^L dx\ \nu(x,t) \left(\partial_t \partial_x E(x,t) - \int_{-\infty}^{+\infty} dv\ v \partial_x f(x,v,t) \right) \\
& + \int dt \iint dx dv\ \mu(x,v,t) \left(\partial_t f(x,v,t) + v \partial_x f(x,v,t) \right. \\
& \qquad \left. - E(x,t) \partial_v f(x,v,t) \right).
\end{aligned} \tag{44}$$

Varying $\mathcal{L}$ yields

$$\begin{aligned}
\delta\mathcal{L} = \quad & \int_0^L dx\ 2\delta E(x,T)E(x,T) + \delta\gamma\int_0^L dx E(x,0) + \gamma\int_0^L dx\delta E(x,0) \\
& + \delta\lambda\left(\int_0^L dx\ |\partial_x E(x,0)|^2 - N_0\right) + \lambda\int_0^L dx\ 2\partial_x\delta E(x,0)\partial_x E(x,0) \\
& + \iint dxdv\ \delta\beta(x,v)\left[f(x,v,0) - F(v)(1-\partial_x E(x,0))\right] \\
& + \iint dxdv\ \beta(x,v)\left[\delta f(x,v,0) + F(v)\partial_x\delta E(x,0)\right] \\
& + \int dt\int_0^L dx\ \delta\nu(x,t)\left(\partial_t\partial_x E(x,t) - \int_{-\infty}^{+\infty} dv\ v\partial_x f(x,v,t)\right) \\
& + \int dt\int_0^L dx\ \nu(x,t)\left(\partial_t\partial_x\delta E(x,t) - \int_{-\infty}^{+\infty} dv\ v\partial_x\delta f(x,v,t)\right) \\
& + \int dt\iint dxdv\ \delta\mu(x,v,t)\left(\partial_t f(x,v,t) + v\partial_x f(x,v,t)\right. \\
& \qquad\qquad \left. - E(x,t)\partial_v f(x,v,t)\right) \\
& + \int dt\iint dxdv\ \mu(x,v,t)\left(\partial_t\delta f(x,v,t) + v\partial_x\delta f(x,v,t)\right. \\
& \qquad \left. - \delta E(x,t)\partial_v f(x,v,t) - E(x,t)\partial_v\delta f(x,v,t)\right). \qquad (45)
\end{aligned}$$

Thus, the partial derivatives are

$$\frac{\delta \mathcal{L}}{\delta \lambda} = \int_0^L dx\ |\partial_x E(x,0)|^2 - N_0, \tag{46}$$

$$\frac{\delta \mathcal{L}}{\delta \beta(x,v)} = f(x,v,0) - F(v)(1 - \partial_x E(x,0)), \tag{47}$$

$$\frac{\delta \mathcal{L}}{\delta \gamma} = \int_0^L dx\ E(x,0), \tag{48}$$

$$\frac{\delta \mathcal{L}}{\delta \nu(x,t)} = \partial_t \partial_x E(x,t) - \int_{-\infty}^{+\infty} dv\ v \partial_x f(x,v,t), \tag{49}$$

$$\frac{\delta \mathcal{L}}{\delta \mu(x,v,t)} = \partial_t f(x,v,t) + v\partial_x f(x,v,t) - E(x,t)\partial_v f(x,v,t), \tag{50}$$

$$\frac{\delta \mathcal{L}}{\delta E(x,T)} = 2E(x,T) - \partial_x \nu(x,T), \tag{51}$$

$$\frac{\delta \mathcal{L}}{\delta E(x,0)} = -2\lambda \partial_x^2 E(x,0) + \partial_x \nu(x,0) + \gamma - \int dv\ \partial_x \beta(x,v) F(v), \tag{52}$$

$$\frac{\delta \mathcal{L}}{\delta f(x,v,T)} = \mu(x,v,T), \tag{53}$$

$$\frac{\delta \mathcal{L}}{\delta f(x,v,0)} = -\mu(x,v,0) + \beta(x,v), \tag{54}$$

$$\frac{\delta \mathcal{L}}{\delta f(x,v,t)} = v\partial_x \nu(x,t) - \partial_t \mu(x,v,t) - v\partial_x \mu(x,v,t) + E(x,t)\partial_v \mu(x,v,t), \tag{55}$$

$$\frac{\delta \mathcal{L}}{\delta E(x,t)} = \partial_t \partial_x \nu(x,t) - \int dv\ \mu(x,v,t)\partial_v f(x,v,t). \tag{56}$$

The nonlinear optimization algorithm is as follows: First, make a guess $E^{(0)}(x,0)$. Then integrate the Vlasov-Poisson equations to $t = T$. Then solve for the adjoint variables at $t = T$ using

$$\rho(x,T) = 2E(x,T), \tag{57}$$

$$\mu(x,v,T) = 0, \tag{58}$$

where I define $\rho(x,t) = \partial_x \nu(x,t)$. Integrate the adjoint equations back to $t = 0$ using

$$\partial_t \rho(x,t) = \int dv\ \mu(x,v,t)\partial_v f(x,v,t), \tag{59}$$

$$\partial_t \mu(x,v,t) + v\partial_x \mu(x,v,t) - E(x,t)\partial_v \mu(x,v,t) = v\rho(x,t). \tag{60}$$

Finally, update the guess to $E^{(1)}(x,0)$ by

$$E^{(1)}(x,0) = E^{(0)}(x,0) + \epsilon \frac{\delta \mathcal{L}}{\delta E(x,0)}, \tag{61}$$

where

$$\frac{\delta \mathcal{L}}{\delta E(x,0)} = -2\lambda \partial_x^2 E^{(0)}(x,0) + \rho(x,0) - \int dv\ \partial_x \beta(x,v) F(v) + \gamma. \tag{62}$$

At this stage λ, γ, and $\beta(x,v)$ are all still unknown. They must be chosen to satisfy

$$\int_0^L dx\ |\partial_x E(x,0)|^2 = N_0, \tag{63}$$

$$\int_0^L dx\ E(x,0) = 0, \tag{64}$$

$$\frac{\delta \mathcal{L}}{\delta f(x,v,0)} = \beta(x,v) - \mu(x,v,0) = F(v)\partial_x \left(\frac{\delta \mathcal{L}}{\delta E(x,0)} \right). \tag{65}$$

The last condition implies

$$\beta(x,v) = F(v)\partial_x \left(\frac{\delta \mathcal{L}}{\delta E(x,0)} \right) + \mu(x,v,0), \tag{66}$$

and thus

$$\begin{aligned} \frac{\delta \mathcal{L}}{\delta E(x,0)} = \quad & -2\lambda \partial_x^2 E^{(0)}(x,0) + \rho(x) + \gamma - \int dv\ \partial_x \mu(x,v,0) F(v) \\ & -\partial_x^2 \left(\frac{\delta \mathcal{L}}{\delta E(x,0)} \right) \int dv\ F(v)^2. \end{aligned} \tag{67}$$

Putting the $\delta \mathcal{L}/\delta E$ terms on the LHS yields

$$\left(1 + \int dv\ F(v)^2 \partial_x^2 \right) \frac{\delta \mathcal{L}}{\delta E(x,0)} = -2\lambda \partial_x^2 E^{(0)}(x,0) + \hat{\rho}(x), \tag{68}$$

where

$$\hat{\rho}(x) = \rho(x) - \int dv\ \partial_x \mu(x,v,0) F(v) + \gamma. \tag{69}$$

To solve for λ, first calculate $\hat{\rho}(x)$, picking γ such that $\hat{\rho}(x)$ has zero mean. Then Fourier transform the equations, and invert the derivative operator acting on $\delta \mathcal{L}/\delta E$,

$$\frac{\delta \mathcal{L}}{\delta E(k)} = \frac{2\lambda k^2 E^{(0)}(k) + \hat{\rho}(k)}{1 - k^2 \int dv\ F(v)^2}, \tag{70}$$

where k denotes the wavenumber. Then (61) becomes

$$E^{(1)}(k) = 2\lambda\epsilon \frac{k^2 E^{(0)}(k)}{1 - k^2 \int dv\ F(v)^2} + E^{(0)}(k) + \frac{\epsilon\hat{\rho}(k)}{1 - k^2 \int dv\ F(v)^2}. \tag{71}$$

Multiplying this equation by its complex conjugate times k^2 and then integrating over k yields

$$\begin{aligned} N_0 &= 4\lambda^2\epsilon^2 \int dk\ \frac{k^6 |E^{(0)}(k)|^2}{(1 - k^2 \int dv\ F(v)^2)^2} \\ &\quad + 4\lambda\epsilon \int dk\ \frac{k^4}{1 - k^2 \int dv\ F(v)^2} \times \\ &\qquad \Re\left[E^{(0)}(k) \left(E^{(0)}(k)^* + \frac{\epsilon\hat{\rho}(k)^*}{1 - k^2 \int dv\ F(v)^2} \right) \right] \\ &\quad + \int dk\ k^2 \left| E^{(0)}(k) + \frac{\epsilon\hat{\rho}(k)}{1 - k^2 \int dv\ F(v)^2} \right|^2. \end{aligned} \tag{72}$$

Solving this quadratic equation for λ specifies $\delta\mathcal{L}/\delta E$ (70), allowing $E^{(0)}$ to be updated to $E^{(1)}$. For sufficiently small ϵ, this update will increase $\int dx E(x,T)^2$. To find a NLOP, $E(x,0)$ is updated in this way until a local maximum is found.

3.2 Numerical Method

Stefan and Neil have provided a code that solves the Vlasov-Poisson system (35-36). The code uses operator splitting, separately solving

$$\partial_t f(x,v,t) + v\partial_x f(x,v,t) = 0, \tag{73}$$

and

$$\partial_t f(x,v,t) - E(x,t)\partial_v f(x,v,t) = 0. \tag{74}$$

These can be solved by shifting the x and v coordinates of $f(x,v,t)$ appropriately.

The code input is $f(x,v,t_n)$ in Fourier space (in x). To evolve to $f(x,v,t_{n+1})$, where $t_{n+1} = t_n + \Delta t$, the code does the following:

1. Shift x by an amount $-v\Delta t/2$:

$$f(x,v,t_{n+1/2}) = f(x - v\Delta t/2, v, t_n). \tag{75}$$

2. Solve the Poisson equation (36) for $E(x,t_{n+1/2})$ using $f(x,v,t_{n+1/2})$.

3. Transform to real space (in x).

4. Shift v by an amount $E(x,t_{n+1/2})\Delta t$:

$$f^*(x,v,t_{n+1/2}) = f(x, v + E(x,t_{n+1/2})\Delta t, t_{n+1/2}). \tag{76}$$

5. Transform to Fourier space (in x).

6. Shift x by an amount $-v\Delta t/2$:

$$f(x, v, t_{n+1}) = f^*(x - v\Delta t/2, v, t_{n+1/2}). \tag{77}$$

If this procedure is repeated many times, steps (6) and (1) can be done simultaneously (i.e., shift x by $-v\Delta t$).

The adjoint equations (59 & 60), have rather different structure. In particular, there is a source term for μ (the variable adjoint to f). This is important, given that μ is initialized to zero. Furthermore, ρ (adjoint to E) now satisfies a hyperbolic equation, rather than an elliptic equation.

My method for solving the adjoint equations is essentially a generalization of the operator splitting algorithm above. The adjoint equations evolve backward in time, so start with $\rho(x, t_{n+1/2})$ (in real space) and $\mu(x, v, t_n)$ (in Fourier space). In the following, $\Delta t > 0$.

1. Shift x by an amount $v\Delta t/2$ in μ:

$$\mu^*(x, v, t_{n-1/2}) = \mu(x + v\Delta t/2, v, t_n). \tag{78}$$

2. Transform $\mu^*(x, v, t_{n-1/2})$ to real space (in x).

3. Shift v by an amount $-E(x, t_{n-1/2})\Delta t/2$ in μ^*:

$$\mu^{**}(x, v, t_{n-1/2}) = \mu^*(x, v - E(x, t_{n-1/2})\Delta t/2, t_{n+1/2}). \tag{79}$$

4. Update ρ using the implicit step

$$\begin{aligned}\rho(x, t_{n-1/2}) \left(1 + \frac{\Delta t^2}{2} \int dv f(x, v, t_{n-1/2})\right) = \rho(x, t_{n+1/2}) \\ -\frac{\Delta t}{2} \int dv\ \mu(x, v, t_{n+1/2}) \partial_v f(x, v, t_{n+1/2}) \\ -\frac{\Delta t}{2} \int dv\ \mu^{**}(x, v, t_{n-1/2}) \partial_v f(x, v, t_{n-1/2}).\end{aligned} \tag{80}$$

5. Update μ^{**} using $\rho(x, t_{n-1/2})$:

$$\mu(x, v, t_{n-1/2}) = \mu^{**}(x, v, t_{n-1/2}) + v\Delta t \rho_{n-1/2}. \tag{81}$$

6. Shift v by an amount $-E(x, t_{n-1/2})\Delta t/2$ in μ

$$\tilde{\mu}(x, v, t_{n-1/2}) = \mu(x, v - E(x, t_{n-1/2})\Delta t/2, t_{n-1/2}). \tag{82}$$

7. Transform $\tilde{\mu}(x, v, t_{n-1/2})$ to Fourier space (in x).

8. Shift x by an amount $v\Delta t/2$ in $\tilde{\mu}$:

$$\mu(x, v, t_{n-1}) = \tilde{\mu}(x + v\Delta t/2, v, t_{n-1/2}). \tag{83}$$

When repeating the algorithm, steps steps (8) & (1) are combined.

3.3 Numerical Results

The goal for the optimization problem is to start with an initial distribution function for which the electric field decays to zero, and then find a different distribution function with an initial electric field of the same size for which the electric field does not decay to zero. I will start with initial distribution functions similar to those studied in [2, 3]. They considered

$$f(x, v, 0) = \frac{0.1}{\sqrt{2\pi}} \exp(-(v/0.1)^2/2) \times (1 + \epsilon \cos(8\pi x)), \tag{84}$$

i.e., a Gaussian with width 0.1, with a sinusoidal perturbation with a wavelength one fourth the box size, with strength ϵ.

It is nontrivial to determine the critical ϵ^* such that if $\epsilon > \epsilon^*$ the electric field will stay finite as $t \to \infty$, but if $\epsilon < \epsilon^*$, the electric field will decay to zero as $t \to \infty$. This is because numerically, the electric field can never decay to zero, only to the limits of the accuracy of the calculation (e.g., double point precision). For this problem, the typical evolution of the electric field is as follows (see Figure 5). The electric field strength is always oscillatory in time, but I will discuss the behavior of the envelop of this oscillation. First, linear Landau damping causes the electric field to decay. If $\epsilon > \epsilon^*$, then at a time $t_{\min}$, the electric field reaches a minimum value $E_{\min}$, and begins to grow. This sort of instability then saturates, and the electric field has a local maximum at $t_{\max}$, with field strength $E_{\max}$. After this point, the electric field oscillates near $E_{\max}$.

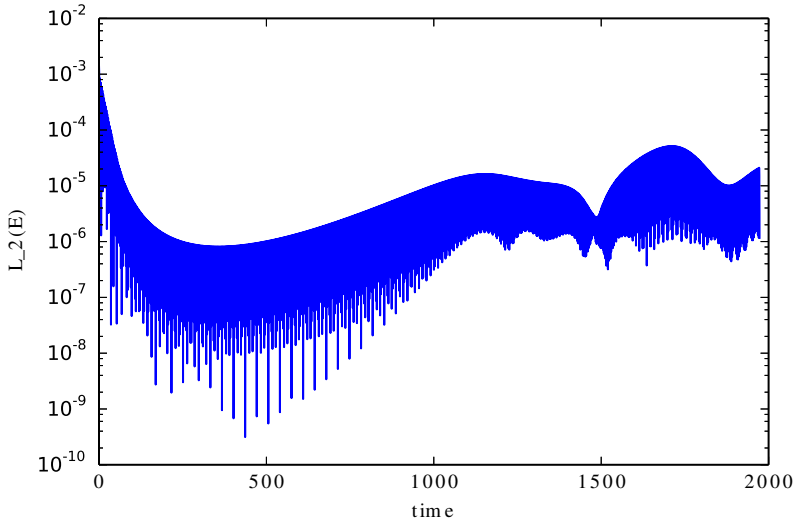

Figure 5: The L_2 norm of the electric field as a function of time, using the initial distribution function (84), for $\epsilon = 0.011$.

[3] found that as ϵ approaches ϵ^* from above, $t_{\min}$ and $t_{\max}$ go to infinity, and $E_{\min}$ and $E_{\max}$ go to zero as power-laws in $(\epsilon - \epsilon^*)$. This can be seen in the electric field traces in Figure 6. The five highest curves (blue, green, red, cyan, and purple) all have $\epsilon > \epsilon^*$, and have electric field minima which occur later and at lower electric field strengths as ϵ

decreases. The spikes occurring at e.g., $t \approx 1100$ and 1400 are numerical artifacts – they diminish in strength or disappear when the v resolution increases. Note that the electric field for $\epsilon < \epsilon^*$ does level off. This corresponds to reaching the numerical precision of the simulation.

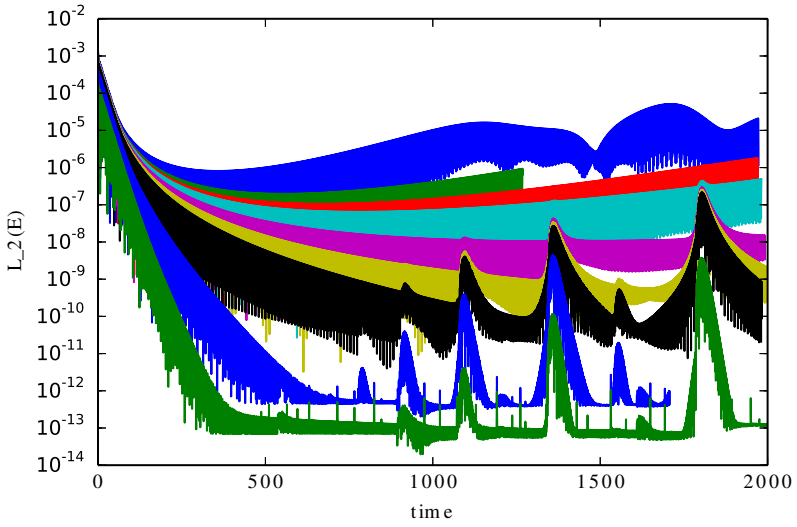

Figure 6: The L_2 norm of the electric field as a function of time, using the initial distribution function (84), for (from top to bottom) ϵ equal to 0.011, 0.01, 0.0097, 0.0095, 0.009, 0.0085, 0.008, 0.005, 0.002.

In [3], ϵ^* is determined by finding the best fit of the different quantities (e.g., $t_{\min}$) to the curve $A(\epsilon - \epsilon^*)^\alpha$. They found that the best fits for all four quantities $t_{\min}$, $t_{\max}$, $E_{\min}$, and $E_{\max}$ had ϵ^* very close to 0.0084, although they each had different power law indices α. I have reproduced their calculations, and also find that assuming $\epsilon^* = 0.0084$, the $t_{\min}$ and $E_{\min}$ are power-laws in $(\epsilon - \epsilon^*)$. This is compelling evidence that $\epsilon^* = 0.0084$ for this problem.

Now that the threshold amplitude has been established, I can run the optimization procedure starting from an initial electric field corresponding to $\epsilon = 0.008$, which is less than the threshold amplitude. I did this by maximizing the L_2 norm of the electric field at $T = 50$, in the way described in section 3.1. I also limited the initial electric field to only consist of the first ten Fourier components. After many iterations of the algorithm, I find that the electric field in Figure 7 has a large electric field at $T = 50$. Note that the electric field remains dominated by the fourth Fourier mode, but also has a non-negligible component from the first Fourier mode.

In Figure 8, I plot the electric field strength versus time for the initial distribution function given in (84) for $\varepsilon = 0.008$, as well as for the initial distribution function corresponding to the electric field plotted in Figure 7. The electric field is much larger at late times for the electric field derived by the optimization procedure, indicating that the algorithm has worked. Furthermore, rather than decaying to zero, the electric field seems to have saturated at a relatively high amplitude. I also believe this to be a numerically converged result

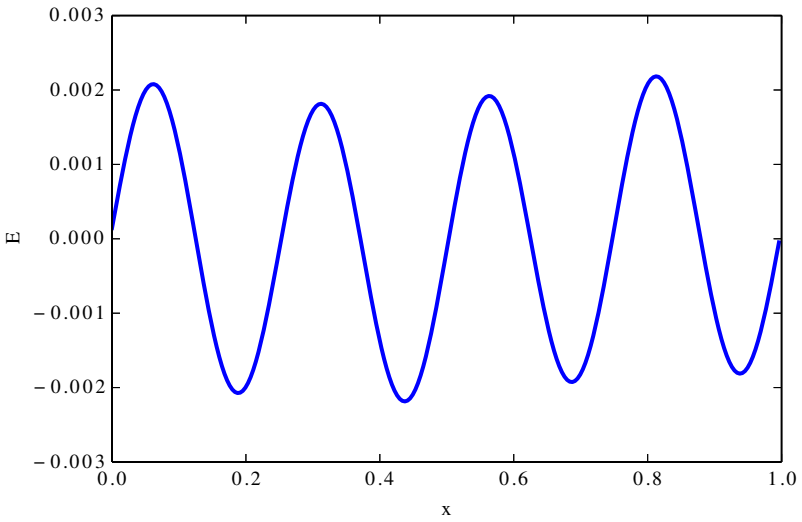

Figure 7: The initial electric field after many iteration of the optimization procedure for the L_2 norm of the electric field at $T = 50$.

– increasing the x, v, t resolution, as well as increasing $v_{\max}$, all have no effect on the electric field. Thus, the algorithm has successfully started from an electric field which decays to zero, and then find a different electric field of the same size which appears to remain finite for all time.

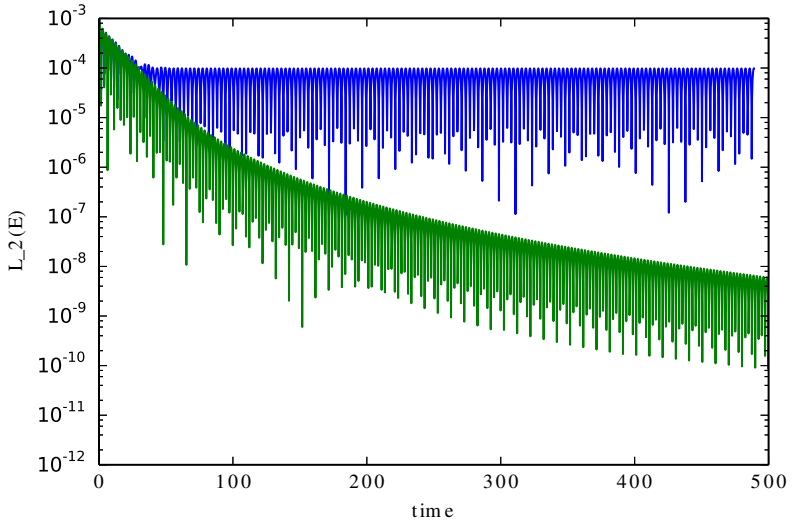

Figure 8: The L_2 norm of the electric field for the initial distribution function given in (84) for $\varepsilon = 0.008$ (green), and for the initial distribution function corresponding to the electric field plotted in Figure 7 (blue).

4 Further Work

In this report, I have described the application of nonlinear perturbation theory to two problems: low dimensional systems of ODEs, and the 1D Vlasov-Poisson equations. In both cases, I derived an algorithm for updating perturbations to increase a desirable quantity at late times. And in both cases, the numerical implementation of the algorithms seems to have been successful.

However, for the Vlasov-Poisson problem, there still remain many open questions. It is unclear what property of the initial electric field in Figure 7 allows the system to maintain a strong electric field. The distribution function at late times does not have any characteristics (e.g., a cat's eye pattern) that would suggest a mechanism for maintaining the electric field. Also, it is surprising that even when $\epsilon > \epsilon^*$ that the electric field can decay by many orders of magnitude before beginning to grow again and produce a cat's eye pattern. Both of these issues are likely amiable to analytic investigation.

These Vlasov-Poisson calculations were possible because I was able to parallelize the algorithm described above using MPI to efficiently run on about 32 processors. However, the algorithm uses global x and v interpolation techniques, which requires all-to-all communication calls. If a sufficiently accurate local interpolation scheme was implemented in the v direction, then the parallelization would be significantly more efficient.

5 Acknowledgements

First, I would like to thank my advisors, Rich Kerswell, Neil Balmforth, and Stefan Llewellyn Smith for proposing and shaping the project, and providing assistance and direction throughout the summer and beyond. Claudia Cenedese, Eric Chassignet, and Stefan Llewellyn Smith also deserve thanks for organizing a great summer. Most importantly, I would like to thank the other eight fellows for all the dinners at Quick's Hole (I got it; somehow?). I was partially supported over the summer by a Hertz Foundation Fellowship, and a National Science Foundation Graduate Research Fellowship under grant No. DGE 1106400.

References

[1] F. Bouchet, J. Laurie, and O. Zaboronski, *Control and instanton trajectories for random transitions in turbulent flows*, Journal of Physics Conference Series, 318 (2011), p. 022041.

[2] M. Brunetti, F. Califano, and F. Pegoraro, *Asymptotic evolution of nonlinear Landau damping*, Physical Review E, 62 (2000), pp. 4109–4114.

[3] A. V. Ivanov, I. H. Cairns, and P. A. Robinson, *Wave damping as a critical phenomenon*, Physics of Plasmas, 11 (2004), pp. 4649–4661.

[4] C. C. T. Pringle and R. R. Kerswell, *Using Nonlinear Transient Growth to Construct the Minimal Seed for Shear Flow Turbulence*, Physical Review Letters, 105 (2010), p. 154502.

Energy Stability and Mixing Efficiency in Forced Stratified Shear Flows

Tobias Bischoff
supervised by Pascale Garaud and Basile Gallet

April 16, 2014

1 Introduction

Stratified flows are ubiquitous in nature. They occur in oceans, atmospheres and in the interiors of planets and stars. The density stratification in these systems can be caused by thermal gradients, i.e., the system is warm on one side and cold on the other, or by compositional gradients, such as induced by salt in the ocean (or other materials that impact the density of a fluid parcel). Stably stratified fluids are fluids in which the density gradient acts to stabilize the system against mixing. It is then often of interest to understand when mixing and transport can occur in the direction of the density gradient and how much transport can theoretically occur depending on the strength of the stratification. Turbulent properties such as the total heat and compositional fluxes, the total dissipation in the system, can be investigated using bounding techniques and direct numerical simulations.

In this report, we investigate simple stratified shear flows that are driven by an external body-force. Unlike flows that are driven on the boundaries, the forcing applies everywhere in the fluid. We investigate their energy stability properties and show that energy stability can be achieved in the case of strong stratifications for certain classes of stratified flows. We show how, at least in two dimensions, bounds for the viscous dissipation of the system can be extended from the unstratified case to the stratified case for any strength of the stratification. We then show that there exists a parameter regime in which the transport efficiency, i.e., the ratio of energy dissipation by vertical transport of heat to the total energy input per time, approaches one. This is confirmed by 2D direct numerical simulations.

We then further use direct numerical simulations to determine the dependence of the heat transport on the stratification. We find that there exist at least three regimes: For very strong stratification the laminar solution of the system is linearly stable and the heat transport is zero. In the regime of intermediate stratification, the system displays a bursting behavior, i.e., we observe mixing events followed by longer periods of episodic relaminarization of the flow. In the regime of weak stratifications the flow is fully chaotic. In two dimensions, we find that the flow field is dominated by large vortices at the forcing length scale, that advect the temperature field and dominate heat transport.

1.1 General Setup

The governing equations are the Boussinesq equations, in which density fluctuations are neglected except in the buoyancy force. In addition, we decompose the temperature field into a steady mean field with constant gradient T_{0z}, and a fluctuating field T so that the full set of equations reads

$$\frac{\partial \mathbf{u}}{\partial t} + \mathbf{u}\cdot\nabla\mathbf{u} = -\nabla p + \alpha g T \mathbf{e}_z + \nu\nabla^2\mathbf{u} + \mathcal{F}_0 f(kz)\mathbf{e}_x, \tag{1a}$$

$$\frac{\partial T}{\partial t} + \mathbf{u}\cdot\nabla T + wT_{0z} = \kappa_T\nabla^2 T, \tag{1b}$$

$$\nabla\cdot\mathbf{u} = 0, \tag{1c}$$

where

$$\frac{\rho}{\rho_0} = -\alpha T \tag{2}$$

defines the thermal expansion coefficient α. The other input parameters for this system are the gravitational constant g, the thermal diffusivity κ_T, the kinematic viscosity ν, the forcing amplitude $\mathcal{F}_0$ (with dimensions of an acceleration), and the forcing length scale k. Using the scales $[U] = (\mathcal{F}_0/k)^{1/2}$, $[t] = (k\mathcal{F}_0)^{-1/2}$, $[L] = k^{-1}$, and $[T] = T_{0z}/k$, we can nondimensionalize the governing equations (1a) to (1c). In addition, we assume that the perturbation equations are periodic in all directions so the nondimensional forcing profile $f(kz)$ must be a periodic function of the vertical coordinate. We also assume without loss of generality that $f(kz)$ is an odd function. After nondimensionalization, the governing equations become

$$\frac{\partial \mathbf{u}}{\partial t} + \mathbf{u}\cdot\nabla\mathbf{u} = -\nabla p + \mathrm{Ri} T\mathbf{e}_z + \frac{1}{\mathrm{Gr}_u^{1/2}}\nabla^2\mathbf{u} + f(z)\mathbf{e}_x, \tag{3a}$$

$$\frac{\partial T}{\partial t} + \mathbf{u}\cdot\nabla T + w = \frac{1}{\mathrm{Gr}_T^{1/2}}\nabla^2 T, \tag{3b}$$

$$\nabla\cdot\mathbf{u} = 0, \tag{3c}$$

where all quantitaties are nondimensional and where we introduced three nondimensional numbers that are based on the forcing amplitude $\mathcal{F}_0$. These nondimensional numbers are given by

$$\mathrm{Ri} = \frac{\alpha g T_{0z}}{k\mathcal{F}_0},\ \mathrm{Gr}_u^{1/2} = \frac{\mathcal{F}_0}{\nu^2 k^3} \text{ and } \mathrm{Gr}_T^{1/2} = \frac{\mathcal{F}_0}{\kappa_T^2 k^3} = \mathrm{Pr}^2\mathrm{Gr}_u^{1/2}, \tag{4}$$

where $\mathrm{Pr} = \nu/\kappa_T$ is the Prandtl number. The nondimensional number $\mathrm{Gr}_u^{1/2}$ is equivalent to a Reynolds number, but is based on the forcing amplitude and therefore usually called Grashof number. Equivalently, $\mathrm{Gr}_T^{1/2}$ corresponds to the Péclet number, but is based on the forcing amplitude.

The laminar solution of the system can be expressed in terms of the forcing function $f(z)$ and $\mathrm{Gr}_u^{1/2}$ with no background temperature fluctuations

$$\mathbf{u}_L = -\mathrm{Gr}_u^{1/2}\left(\partial_z^{-2} f(z)\right)\mathbf{e}_x, \tag{5a}$$

$$T_0 = 0. \tag{5b}$$

In the case of a Kolmogorov flow, the forcing profile $f(z)$ is given by $\sin(z)$ and the velocity field of the laminar solution is

$$\mathbf{u}_L = \mathrm{Gr}_u^{1/2} \sin(z)\mathbf{e}_x. \tag{6}$$

2 Energy stability of stratified shear flows

In this section we introduce the concept of energy stability to investigate some of the nonlinear stability properties of forced stratified shear flows. The first half of this section deals with the general case, where temperature perturbations can evolve freely. The second half of this section deals with the low Péclet number approximation and how it impacts energy stability. We find in the latter case that because the temperature perturbations are slaved to the perturbations in vertical velocity, we can derive a Richardson number criterion for energy stability, whereas we cannot derive such a result easily for the general case.

2.1 Energy stability theory

In this subsection, we investigate the energy stability of viscous stratified shear flows in two dimensions and apply it to the system introduced in the previous section. This is done by investigating the time evolution of an energy-like functional for perturbations to the laminar solution in Eq. (5a). We begin by letting $\mathbf{u} = \mathbf{u}_L + \tilde{\mathbf{u}}$, where $\tilde{\mathbf{u}} = (\tilde{u}, \tilde{w})$ is the perturbation velocity field. The governing equations then become

$$\frac{\partial \tilde{\mathbf{u}}}{\partial t} + \mathbf{u}_L \cdot \nabla \tilde{\mathbf{u}} + \tilde{\mathbf{u}} \cdot \nabla \mathbf{u}_L + \tilde{\mathbf{u}} \cdot \nabla \tilde{\mathbf{u}} = -\nabla p + \mathrm{Ri} T \mathbf{e}_z + \frac{1}{\mathrm{Gr}_u^{1/2}} \nabla^2 \tilde{\mathbf{u}} + f(z)\mathbf{e}_x, \tag{7a}$$

$$\frac{\partial T}{\partial t} + \mathbf{u}_L \cdot \nabla T + \tilde{\mathbf{u}} \cdot \nabla T + \tilde{w} = \frac{1}{\mathrm{Gr}_T^{1/2}} \nabla^2 T, \tag{7b}$$

$$\nabla \cdot \tilde{\mathbf{u}} = 0, \tag{7c}$$

and the "energy" equation for the perturbation velocity field $\tilde{\mathbf{u}}$ and the perturbation temperature field T takes the form

$$\frac{1}{2}\langle \tilde{\mathbf{u}}^2 + \gamma^2 T^2 \rangle_t = \left(\mathrm{Ri} - \gamma^2\right) \langle \tilde{w} T \rangle + \mathrm{Gr}_u^{1/2} \langle \tilde{u}\tilde{w}\partial_z^{-1} f \rangle - \frac{1}{\mathrm{Gr}_u^{1/2}} \langle |\nabla \tilde{\mathbf{u}}|^2 \rangle - \frac{\gamma^2}{\mathrm{Gr}_T^{1/2}} \langle |\nabla T|^2 \rangle, \tag{8a}$$

$$= (\Gamma - 1) \left(\frac{1}{\mathrm{Gr}_u^{1/2}} \langle |\nabla \tilde{\mathbf{u}}|^2 \rangle + \frac{\gamma^2}{\mathrm{Gr}_T^{1/2}} \langle |\nabla T|^2 \rangle \right), \tag{8b}$$

where

$$\Gamma = \frac{\left(\mathrm{Ri} - \gamma^2\right) \langle \tilde{w} T \rangle + \mathrm{Gr}_u^{1/2} \langle \left(\partial_z^{-1} f\right) \tilde{u}\tilde{w} \rangle}{\frac{1}{\mathrm{Gr}_u^{1/2}} \langle |\nabla \tilde{\mathbf{u}}|^2 \rangle + \frac{\gamma^2}{\mathrm{Gr}_T^{1/2}} \langle |\nabla T|^2 \rangle}. \tag{9}$$

Here, the inverse derivative in the vertical of the forcing function is given by $(\partial^{-1} f)(z) = -\mathrm{Gr}_u^{1/2} \partial_z u_L$ and is a measure of the shear applied to the flow. The angled brackets $\langle (.) \rangle$ denote the domain average (defined in the appendix). Since the second term in parentheses on the right hand side of (8b) is positive, this equation tells us that, for the energy to decay

in time, Γ needs to be less than 1. We are therefore interested in the maximum of Γ over all possible divergence-free flow fields, and over all possible temperature fields. This can be rexpressed as a maximization problem for the constrained Lagrangian

$$\mathcal{L} = \frac{\left(\mathrm{Ri} - \gamma^2\right)\langle \tilde{w}T\rangle + \mathrm{Gr}_u^{1/2}\langle\left(\partial_z^{-1} f\right)\tilde{u}\tilde{w}\rangle + \langle p\nabla\cdot\tilde{\mathbf{u}}\rangle}{\frac{1}{\mathrm{Gr}_u^{1/2}}\langle|\nabla\tilde{\mathbf{u}}|^2\rangle + \frac{\gamma^2}{\mathrm{Gr}_T^{1/2}}\langle|\nabla T|^2\rangle}, \tag{10}$$

where the divergence term in the numerator was introduced to satisfy the divergence-free constraint. The field p serves as the associated Lagrange multiplier. We need to find the maximum of the functional $\mathcal{L}$ with respect to the dynamical fields and the minimum with respect to the optimization constant γ^2. This can be done via the associated Euler-Lagrange equations derived from the first variation of $\mathcal{L}$. The Euler-Lagrange equations in two dimensions are given by the following four equations

$$\mathrm{Gr}_u^{1/2}\left(\partial_z^{-1} f\right)\tilde{w} - \partial_x p + \frac{2\Gamma}{\mathrm{Gr}_u^{1/2}}\nabla^2\tilde{u} = 0, \tag{11a}$$

$$\left(\mathrm{Ri} - \gamma^2\right)T + \mathrm{Gr}_u^{1/2}\left(\partial_z^{-1} f\right)\tilde{u} - \partial_z p + \frac{2\Gamma}{\mathrm{Gr}_u^{1/2}}\nabla^2\tilde{w} = 0, \tag{11b}$$

$$\left(\mathrm{Ri} - \gamma^2\right)\tilde{w} + \frac{2\Gamma\gamma^2}{\mathrm{Gr}_T^{1/2}}\nabla^2 T = 0, \tag{11c}$$

$$\nabla\cdot\tilde{\mathbf{u}} = 0, \tag{11d}$$

where the first one comes from the variation of $\mathcal{L}$ with respect to $\tilde{u}$, the second one comes from the variation of $\mathcal{L}$ with respect to $\tilde{w}$, the third one comes from the variation of $\mathcal{L}$ with respect to T and the last one comes from the variation of $\mathcal{L}$ with respect to p. Here, Γ is now treated as an eigenvalue of these PDEs. If $\Gamma < 1$ then $\min_{\gamma^2}\max_{\mathbf{u},T,p}\mathcal{L} < 1$ and the perturbations decay at least exponentially (apply Poincaré's inequality to equation (8b)). We now seek to solve the previous set of equations in order to determine the part of the parameter space for which the laminar solution is energy stable and the flow remains laminar for arbitrary perturbations. The equations can be simplified by taking the curl of the first two equations to remove the Lagrange multiplier. This leaves us with the following simplified set of equations

$$-\left(\mathrm{Ri} - \gamma^2\right)\partial_x T + \mathrm{Gr}_u^{1/2} f\tilde{w} - \mathrm{Gr}_u^{1/2}\left(\partial_z^{-1} f\right)\left(\partial_x\tilde{u} - \partial_z\tilde{w}\right) = -\frac{2\Gamma}{\mathrm{Gr}_u^{1/2}}\nabla^2\left(\partial_z\tilde{u} - \partial_x\tilde{w}\right), \tag{12a}$$

$$\left(\mathrm{Ri} - \gamma^2\right)\tilde{w} = -\frac{2\Gamma\gamma^2}{\mathrm{Gr}_T^{1/2}}\nabla^2 T, \tag{12b}$$

$$\nabla\cdot\tilde{\mathbf{u}} = 0, \tag{12c}$$

which can be simplified further by introducing the stream function ϕ for the components of the velocity field, i.e., $\tilde{u} = \partial_z\phi$ and $\tilde{w} = -\partial_x\phi$. This automatically satisfies the incompressibility constraint and allows us to rewrite the problem in terms of a system of linear

partial differential equations for two unknown fields only:

$$-\left(\mathrm{Ri}-\gamma^2\right)\partial_x T-\mathrm{Gr}_u^{1/2} f\partial_x\phi-2\mathrm{Gr}_u^{1/2}\left(\partial_z^{-1}f\right)\partial_{xz}\phi=-\frac{2\Gamma}{\mathrm{Gr}_u^{1/2}}\nabla^4\phi, \tag{13a}$$

$$-\frac{\left(\mathrm{Ri}-\gamma^2\right)}{\gamma^2}\partial_x\phi=-\frac{2\Gamma}{\mathrm{Gr}_T^{1/2}}\nabla^2 T. \tag{13b}$$

Finally, taking the Laplacian of the first equation and using the second one to replace the temperature field leaves a single partial differential equation for the stream function

$$-\frac{\mathrm{Gr}_T^{1/2}}{2\Gamma}\frac{\left(\mathrm{Ri}-\gamma^2\right)^2}{\gamma^2}\partial_{xx}\phi-\nabla^2(\mathrm{Gr}_u^{1/2} f\partial_x\phi+2\mathrm{Gr}_u^{1/2}\left(\partial_z^{-1}f\right)\partial_{xz}\phi)=-\frac{2\Gamma}{\mathrm{Gr}_u^{1/2}}\nabla^6\phi. \tag{14}$$

Expanding all fields in Fourier series (see appendix) in the x-direction results in a set of linear ordinary differential equations for the Fourier coefficients in the z-direction

$$\frac{\mathrm{Gr}_T^{1/2}}{2\Gamma}\frac{\left(\mathrm{Ri}-\gamma^2\right)^2}{\gamma^2}k_x^2\hat{\phi}-ik_x\left(\partial_{zz}-k_x^2\right)(\mathrm{Gr}_u^{1/2} f\hat{\phi}+2\mathrm{Gr}_u^{1/2}\left(\partial_z^{-1}f\right)\partial_z\hat{\phi})+\frac{2\Gamma}{\mathrm{Gr}_u^{1/2}}\left(\partial_{zz}-k_x^2\right)^3\hat{\phi}=0, \tag{15}$$

where $\hat{\phi}$ is the Fourier transform of the stream function and k_x is the horizontal wavenumber. This is a periodic boundary value problem in the vertical direction, which can either be solved using finite differences or by rewriting all z-dependent fields in terms of Fourier series as well, and then solving for the determinant of the resulting infinite dimensional matrix.

2.2 Example: Constant vertical shear

In this section, we investigate the energy stability of a flow field with constant vertical shear ($\partial_z u_L = S$). In this case, we do not need a forcing term as $\langle\nabla^2\mathbf{u}_L\rangle = 0$. We therefore set $f = 0$. While the total flow field $\mathbf{u}_L + \tilde{\mathbf{u}}$ is no longer periodic in z in this case, we can still assume that the perturbation field $\tilde{\mathbf{u}}$ is periodic. Also note that because there is no external forcing, we need to define the nondimensional parameters slightly differently. Given a constant shear profile $\mathbf{u}_L = Sz$, where S is the shear, we define the velocity scale $U = SL$, where L is the vertical extent of the domain. Length scales are normalized by L. The governing equations then look essentially the same as for the forced case with only the nondimensional numbers defined differently

$$\frac{\partial\mathbf{u}}{\partial t}+\mathbf{u}\cdot\nabla\mathbf{u}=-\nabla p+\mathrm{Ri}T\mathbf{e}_z+\frac{1}{\mathrm{Re}}\nabla^2\mathbf{u}, \tag{16a}$$

$$\frac{\partial T}{\partial t}+\mathbf{u}\cdot\nabla T+w=\frac{1}{\mathrm{Pe}}\nabla^2 T, \tag{16b}$$

$$\nabla\cdot\mathbf{u}=0. \tag{16c}$$

The nondimensional numbers based on the new length scale and velocity scale are given by

$$\mathrm{Ri}=\frac{\alpha g T_{0z}}{S^2},\ \mathrm{Re}=\frac{SL^2}{\nu}\text{ and }\mathrm{Pe}=\frac{SL^2}{\kappa_T}. \tag{17}$$

In this case, the analog of Eq. (15) (with Re, Pe instead of $\mathrm{Gr}_u^{1/2}$ and $\mathrm{Gr}_T^{1/2}$), with nondimensionalized laminar solution $u_L = z$, reduces to a set of algebraic equations in Fourier space (essentially setting $\mathrm{Gr}_u^{1/2}\left(\partial_z^{-1} f\right) = -1$ in Eq. (15)). Requiring nontrivial solutions allows us to determine the eigenvalues Γ. In this constant shear case there is no coupling of the Fourier modes and we have

$$\frac{\mathrm{Pe}}{2\Gamma\gamma^2}\left(\mathrm{Ri}-\gamma^2\right)^2 k_x^2\hat{\phi} + 2k_xk_z\left(k_x^2+k_z^2\right)\hat{\phi} - \frac{2\Gamma}{\mathrm{Re}}\left(k_x^2+k_z^2\right)^3\hat{\phi} = 0, \tag{18a}$$

$$\Rightarrow \left(\Gamma^2 - \mathrm{Re}\Gamma\frac{k_xk_z}{\left(k_x^2+k_z^2\right)^2} - \mathrm{PeRe}\frac{\left(\mathrm{Ri}-\gamma^2\right)^2}{4\gamma^2}\frac{k_x^2}{\left(k_x^2+k_z^2\right)^3}\right)\hat{\phi} = 0. \tag{18b}$$

The term in parentheses in Eq. (18b) needs to be 0. In order for this equation to have nontrivial solutions, the eigenvalues Γ need to satisfy

$$\Gamma = \frac{\mathrm{Re}k_xk_z}{2\left(k_x^2+k_z^2\right)^2} \pm \sqrt{\frac{\mathrm{Re}^2k_x^2k_z^2}{4\left(k_x^2+k_z^2\right)^4} + \mathrm{PeRe}\frac{\left(\mathrm{Ri}-\gamma^2\right)^2}{4\gamma^2}\frac{k_x^2}{\left(k_x^2+k_z^2\right)^3}}, \tag{19a}$$

$$= \frac{\mathrm{Re}k_xk_z}{2\left(k_x^2+k_z^2\right)^2}\left(1 \pm \sqrt{1+\frac{\mathrm{Pe}}{\mathrm{Re}}\frac{\left(\mathrm{Ri}-\gamma^2\right)^2}{\gamma^2}\frac{\left(k_x^2+k_z^2\right)}{k_z^2}}\right). \tag{19b}$$

The term involving the Richardson number under the square root is minimal for $\gamma^2 = \mathrm{Ri}$. Therefore, we have the case $\Gamma = 0$ and the case

$$\min_{\gamma^2}\Gamma = \frac{\mathrm{Re}k_xk_z}{\left(k_x^2+k_z^2\right)^2}. \tag{20}$$

Here, Γ is positive if k_x and k_z are either both positive or both negative. Without loss of generality, we assume positivity. Maximizing Γ with respect to k_x gives

$$\min_{\gamma^2}\max_{k_x}\Gamma = \mathrm{Re}\frac{3\sqrt{3}}{16}\frac{1}{k_z^2}, \tag{21}$$

for $k_x = k_z/\sqrt{3}$. The smallest (nondimensional) vertical wavenumber is given by 2π (see appendix Fourier transform) which maximizes Γ:

$$\min_{\gamma^2}\max_{k_z,k_x}\Gamma = \mathrm{Re}\frac{3\sqrt{3}}{64\pi^2}. \tag{22}$$

We require the maximum Γ to be less than 1 for energy stability. Hence, we arrive at a Reynolds number criterion for energy stability:

$$\mathrm{Re} < \frac{64\pi^2}{3\sqrt{3}}. \tag{23}$$

This implies that there is a critical Re above which the system will not be energy stable. Unfortunately, the critical Re is independent of the Richardson number, i.e, energy stability cannot be guaranteed for any Ri since there is always a value of Re above which the flow is not energy stable. In other words, even for very large Richardson numbers, the system is not energy stable and insight into the nonlinear evolution of arbitrary perturbations cannot be gained this way.

2.3 Example: Kolmogorov flow

In this section, we explore the first steps of the forced case for $f = \sin(z)$. The laminar solution is of Kolmogorov type and the governing equations are given by Eqs. (3). Taking Eq. (15) and expanding $\hat{\phi}$ in a Fourier series (see appendix) in the z-direction as

$$\hat{\phi}_{k_x}(z) = \sum_{k_z} \tilde{\phi}_{k_x,k_z} \exp(ik_z z). \tag{24}$$

This leaves us with terms of the form

$$f^{(q)}\hat{\phi}^{(p)}_{k_x} = i^p \sum_{k_z} {k_z}^p \tilde{\phi}_{k_x,k_z} f^{(q)} e^{ik_z z}, \tag{25}$$

where $f^{(q)}$ denotes the q-th derivative of f and $\hat{\phi}^{(p)}$ denotes the p-th derivative of $\hat{\phi}$. This determines the degree of mode coupling due to the presence of the shear forcing f. In the case of a Kolmogorov flow with $f = \sin(z)$, the derivatives $f^{(q)}$ are given by

$$f^{(q)} = \frac{1}{2} i^{q-1} \left(e^{iz} + (-1)^{q+1} e^{-iz} \right). \tag{26}$$

Taking the Fourier transform of the derivatives of the stream function ϕ into account, the quadratic coupling terms take the simple form

$$\left(f^{(q)}(z)\hat{\phi}^{(p)}_{k_x} \right)_{k_z} = \frac{1}{2} i^{p+q-1} \left((k_z - 1)^p \tilde{\phi}_{k_x,k_z-1} + (-1)^{q+1}(k_z + 1)^p \tilde{\phi}_{k_x,k_z+1} \right). \tag{27}$$

Here, the subscript k_z denotes the Fourier coefficient associated with the vertical wavenumber k_z. This relation allows us to rewrite Eq. (15) in terms of Fourier components, i.e., construct a simple matrix equation in wavenumber space

$$\frac{\Gamma}{\mathrm{Gr}_u^{1/2}} \tilde{\phi}_{k_x,k_z} = \Gamma^{-1} a(k_x,k_z)\tilde{\phi}_{k_x,k_z} + \mathrm{Gr}_u^{1/2} b(k_x,k_z)\tilde{\phi}_{k_x,k_z-1} + \mathrm{Gr}_u^{1/2} c(k_x,k_z)\tilde{\phi}_{k_x,k_z+1}. \tag{28}$$

Setting $\Gamma = 1$ implies that the critical Grashof number, at a given horizontal wavenumber k_x, at which instability occurs, is given by the solution of

$$a(k_x,k_z)\tilde{\phi}_{k_x,k_z} + \mathrm{Gr}_u^{1/2} b(k_x,k_z)\tilde{\phi}_{k_x,k_z-1} + \mathrm{Gr}_u^{1/2} c(k_x,k_z)\tilde{\phi}_{k_x,k_z+1} - \frac{1}{\mathrm{Gr}_u^{1/2}} \tilde{\phi}_{k_x,k_z} = 0. \tag{29}$$

The k_x and k_z-dependent coefficients define a matrix with

$$a(k_x,k_z) = \frac{\mathrm{Gr}_T^{1/2} \left(\mathrm{Ri} - \gamma^2 \right)^2 {k_x}^2}{4\gamma^2 \left({k_x}^2 + {k_z}^2 \right)}, \tag{30a}$$

$$b(k_x,k_z) = \frac{k_x {k_z}^2 (2k_z - 1) - {k_x}^3 (1 - 2k_z)}{2 \left({k_x}^2 + {k_z}^2 \right)^3}, \tag{30b}$$

$$c(k_x,k_z) = \frac{k_x {k_z}^2 (2k_z + 1) + {k_x}^3 (1 + 2k_z)}{2 \left({k_x}^2 + {k_z}^2 \right)^3}. \tag{30c}$$

We can find the critical Grashof number by determining for which $\mathrm{Gr}_u^{1/2}$ the determinant of this matrix is zero. Because the determinant defines a function of $\mathrm{Gr}_u^{1/2}$, this problem can be solved with a root-finding algorithm. However, these last steps will be subject of future work.

2.4 The low Péclet number approximation

In this section we derive the low thermal Grashof number equations from the forced Boussinesq equations (3). This is equivalent to what is usually called the "low Péclet number approximation", an approximation commonly made in the context of astrophysics [7, 8, 10]. It holds for very low Prandtl numbers. At the same time, we require the Richardson number to be large. In fact, we require it to be of order $1/\mathrm{Gr}_T^{1/2}$. In order to derive this approximation, we write the dynamical fields formally as asymptotic expansions in the $\mathrm{Gr}_T^{1/2}$

$$\mathbf{u} = \mathbf{u}_0 + \mathrm{Gr}_T^{1/2}\,\mathbf{u}_1 + \dots, \tag{31a}$$

$$T = T_0 + \mathrm{Gr}_T^{1/2}\,T_1 + \dots . \tag{31b}$$

The governing equations at order $\mathrm{Gr}_T^{1/2}$ reduce to Laplace's equation for the zeroth order temperature fluctuation

$$\nabla^2 T_0 = 0, \tag{32}$$

which, in the case of a periodic domain, requires $T_0 = 0$. At the next order, the governing equations read

$$\frac{\partial \mathbf{u}_0}{\partial t} + \mathbf{u}_0 \cdot \nabla \mathbf{u}_0 = -\nabla p_0 + \tilde{\mathrm{Ri}} T_1 \mathbf{e}_z + \frac{1}{\mathrm{Gr}_u^{1/2}} \nabla^2 \mathbf{u}_0 + f(z)\mathbf{e}_x, \tag{33a}$$

$$w_0 = \nabla^2 T_1, \tag{33b}$$

$$\nabla \cdot \mathbf{u}_0 = 0, \tag{33c}$$

where we replaced Ri by $\mathrm{Ri} = \tilde{\mathrm{Ri}}/\mathrm{Gr}_T^{1/2}$ and assumed $\tilde{\mathrm{Ri}} = \mathcal{O}(1)$. This can be combined to give a more compact set of integro-differential equations:

$$\frac{\partial \mathbf{u}_0}{\partial t} + \mathbf{u}_0 \cdot \nabla \mathbf{u}_0 = -\nabla p_0 + \tilde{\mathrm{Ri}} \nabla^{-2} w_0 \mathbf{e}_z + \frac{1}{\mathrm{Gr}_u^{1/2}} \nabla^2 \mathbf{u}_0 + f(z)\mathbf{e}_x, \tag{34a}$$

$$\nabla \cdot \mathbf{u}_0 = 0. \tag{34b}$$

From this perspective, we see that the important nondimensional parameter that controls the importance of the stratification is $\mathrm{RiGr}_T^{1/2} = \tilde{\mathrm{Ri}}$. We also see that T drops out entirely so that the energy stability can now be investigated simply by analyzing the time evolution of the kinetic energy in the perturbation field.

2.5 Energy Stability in the low Péclet number limit: Bounds

In this section, we derive a Richardson number criterion for the energy stability of the laminar solution of a forced stratified shear flow in the low Péclet/low thermal Grashof number limit. We proceed as before, but this time we begin with the kinetic energy equation for arbitrary perturbation to the laminar solution. With $\mathbf{u} = \mathbf{u}_L + \tilde{\mathbf{u}}$, we have

$$\frac{1}{2}\langle \tilde{\mathbf{u}}^2 \rangle_t = \mathcal{H}\left[\tilde{\mathbf{u}}\right] = \tilde{\mathrm{Ri}} \langle \tilde{w} \nabla^{-2} \tilde{w} \rangle + \mathrm{Gr}_u^{1/2} \langle \left(\partial_z^{-1} f\right) \tilde{w}\tilde{u} \rangle - \frac{1}{\mathrm{Gr}_u^{1/2}} \langle |\nabla \tilde{\mathbf{u}}|^2 \rangle. \tag{35}$$

Here, $\mathcal{H}[\tilde{\mathbf{u}}]$ is a quadratic form of the velocity perturbations only. The task at hand is to show that for all parameters of the system there exists a value of the Richardson number so that the quadratic form is negative semi-definite. Such a criterion defines the region of parameter space in which the system is energy stable. We approach the problem using simple bounding methods instead of the optimization technique used in the previous sections. We start with a conventional estimate for the triple term involving the shear term

$$|\langle\left(\partial_z^{-1} f\right)\tilde{w}\tilde{u}\rangle| \leq ||\partial_z^{-1} f||_\infty \langle\tilde{w}\tilde{u}\rangle \leq \frac{||\partial_z^{-1} f||_\infty}{2}\left(\frac{1}{a}\langle\tilde{w}^2\rangle + a\langle\tilde{u}^2\rangle\right). \tag{36}$$

Here, we used the Young's inequality $|ab| < 1/2(a^2+b^2)$ (see appendix). Of course, this gives a very crude estimate, because the right hand side is positive and we want to estimate a potentially negative term. The free parameter a introduced will give some freedom in the rest of the derivation. Using the estimate (36) to bound the quadratic form from above, we get

$$\mathcal{H}[\tilde{\mathbf{u}}] \leq -\tilde{\mathrm{Ri}}\langle(\nabla^{-1}\tilde{w})^2\rangle + \frac{\mathrm{Gr}_u^{1/2}}{2}||\partial_z^{-1} f||_\infty\left(\frac{1}{a}\langle\tilde{w}^2\rangle + a\langle\tilde{u}^2\rangle\right) - \frac{1}{\mathrm{Gr}_u^{1/2}}\langle|\nabla\tilde{\mathbf{u}}|^2\rangle, \tag{37a}$$

$$\leq \sum_{\mathbf{k}} \frac{\mathrm{Gr}_u^{1/2}}{2}||\partial_z^{-1} f||_\infty\left(\frac{1}{a}|\tilde{w}_{\mathbf{k}}|^2 + a|\tilde{u}_{\mathbf{k}}|^2\right) - \frac{\tilde{\mathrm{Ri}}}{\mathbf{k}^2}|\tilde{w}_{\mathbf{k}}|^2 - \frac{\mathbf{k}^2}{\mathrm{Gr}_u^{1/2}}\left(|\tilde{u}_{\mathbf{k}}|^2 + |\tilde{w}_{\mathbf{k}}|^2\right), \tag{37b}$$

$$\leq \sum_{\mathbf{k}}\left(\frac{\mathrm{Gr}_u^{1/2}}{2a}||\partial_z^{-1} f||_\infty - \frac{\tilde{\mathrm{Ri}}}{\mathbf{k}^2} - \frac{\mathbf{k}^2}{\mathrm{Gr}_u^{1/2}}\right)|\tilde{w}_{\mathbf{k}}|^2 + \left(a - \frac{1}{\mathrm{Gr}_u^{1/2} L_{\max}^2}\right)|\tilde{u}_{\mathbf{k}}|^2, \tag{37c}$$

where we used the periodicity of the system to write all fields in terms of their Fourier expansions (see appendix) and made use of the finite size of the system with largest length scale $L_{\max}$. In the second line, we also replaced the Fourier coefficients of the temperature field in terms of the Fourier coefficients of the vertical velocity. A sufficient criterion for energy stability can be obtained by requiring that the expressions in the parentheses are negative. The first parenthesis is of the form

$$F(X) = A - BX^{-2} - CX^2, \tag{38}$$

which has a maximum as

$$F_{\max} = A - 2\sqrt{BC}. \tag{39}$$

Therefore, we can estimate the quadratic form from above by using the maximum of F(X) for the worst-case-scenario:

$$\mathcal{H}[\tilde{\mathbf{u}}] \leq \sum_{\mathbf{k}}\left(\frac{\mathrm{Gr}_u^{1/2}}{2a}||\partial_z^{-1} f||_\infty - 2\left(\frac{\tilde{\mathrm{Ri}}}{\mathrm{Gr}_u^{1/2}}\right)^{\frac{1}{2}}\right)|\tilde{w}_{\mathbf{k}}|^2 + \left(a - \frac{1}{\mathrm{Gr}_u^{1/2} L_{\max}^2}\right)|\tilde{u}_{\mathbf{k}}|^2. \tag{40}$$

We want the $1/a$ term in the first parenthesis to be as small as possible provided that the second parenthesis remains negative. Hence, a suitable a is $a = 1/(2\mathrm{Gr}_u^{1/2} L_{\max}^2)$. Inserting this into the previous estimate, we arrive at

$$\mathcal{H}[\tilde{\mathbf{u}}] \leq \left(\mathrm{Gr}_u L_{\max}^2||\partial_z^{-1} f||_\infty - 2\left(\frac{\tilde{\mathrm{Ri}}}{\mathrm{Gr}_u^{1/2}}\right)^{\frac{1}{2}}\right)\langle\tilde{w}^2\rangle - \frac{1}{2\mathrm{Gr}_u^{1/2} L_{\max}^2}\langle\tilde{u}^2\rangle < 0. \tag{41}$$

We can then pick a Richardson number to let the expression in the first parenthesis remain negative for all other system parameters, i.e.,

$$\tilde{\mathrm{Ri}} > \frac{L_{\max}^4}{2} ||\partial_z^{-1} f||_\infty^2 \, \mathrm{Gr}_u^{5/2}. \tag{42}$$

We see that the Richardson number needs to be very large when $\mathrm{Gr}_u^{1/2}$ is large or when the size of the domain itself is very large. Interestingly, it depends on the shear only through the maximum value of $\partial_z^{-1} f$ and the "shape" of f does not enter. In contrast to the general case, we now have a stability criterion that does indeed depend on Ri through $\tilde{\mathrm{Ri}}$, i.e., the strength of the stratification. This is a direct consequence of the fact that the temperature field is completely determined by the vertical velocity, a key assumption of this approximation.

2.6 Energy Stability in the low Péclet number limit: Analysis

We now want to investigate the full energy stability similar to what was done in section 2.1. For that we start in the same fashion, i.e., by using the perturbation energy equation. From there, we can straightforwardly derive the Euler-Lagrange equations for the problem and understand the differences to the full problem. The kinetic energy equation in the low $\mathrm{Gr}_T^{1/2}$ limit is given by Eq. (35). From this, we can define a quadratic form $\mathcal{H}[\mathbf{u}]$ that can be written in a similar way as before

$$\mathcal{H}[\tilde{\mathbf{u}}] = -\tilde{\mathrm{Ri}} \langle |\nabla^{-1} \tilde{w}|^2 \rangle + \mathrm{Gr}_u^{1/2} \langle \left(\partial_z^{-1} f\right) \tilde{w} \tilde{u} \rangle - \frac{1}{\mathrm{Gr}_u^{1/2}} \langle |\nabla \tilde{\mathbf{u}}|^2 \rangle, \tag{43a}$$

$$= \frac{1}{\mathrm{Gr}_u^{1/2}} \langle |\nabla \tilde{\mathbf{u}}|^2 \rangle \left(\frac{-\tilde{\mathrm{Ri}} \langle |\nabla^{-1} \tilde{w}|^2 \rangle + \mathrm{Gr}_u^{1/2} \langle \left(\partial_z^{-1} f\right) \tilde{w} \tilde{u} \rangle}{\frac{1}{\mathrm{Gr}_u^{1/2}} \langle |\nabla \tilde{\mathbf{u}}|^2 \rangle} - 1 \right), \tag{43b}$$

$$= \frac{1}{\mathrm{Gr}_u^{1/2}} \langle |\nabla \tilde{\mathbf{u}}|^2 \rangle \left(\Gamma - 1 \right), \tag{43c}$$

$$\tag{43d}$$

where

$$\Gamma = \frac{-\tilde{\mathrm{Ri}} \langle |\nabla^{-1} \tilde{w}|^2 \rangle + \mathrm{Gr}_u^{1/2} \langle \left(\partial_z^{-1} f\right) \tilde{w} \tilde{u} \rangle}{\frac{1}{\mathrm{Gr}_u^{1/2}} \langle |\nabla \tilde{\mathbf{u}}|^2 \rangle}. \tag{44}$$

We need to determine the maximum of Γ over all divergence-free vector fields $\tilde{\mathbf{u}}$ as before. This leads to an equivalent maximization problem for the Lagrangian

$$\mathcal{L} = \left(\frac{-\tilde{\mathrm{Ri}} \langle |\nabla^{-1} \tilde{w}|^2 \rangle + \mathrm{Gr}_u^{1/2} \langle \left(\partial_z^{-1} f\right) \tilde{w} \tilde{u} \rangle + \langle p \nabla \cdot \tilde{\mathbf{u}} \rangle}{\frac{1}{\mathrm{Gr}_u^{1/2}} \langle |\nabla \tilde{\mathbf{u}}|^2 \rangle} \right). \tag{45}$$

Analogously, the maximum has to solve the following Euler-Lagrange equations in two dimensions

$$\mathrm{Gr}_u^{1/2}\left(\partial_z^{-1} f\right)\tilde{w} + \frac{2\Gamma}{\mathrm{Gr}_u^{1/2}}\nabla^2\tilde{u} - \partial_x p = 0, \tag{46a}$$

$$2\tilde{\mathrm{Ri}}\nabla^{-2}\tilde{w} + \mathrm{Gr}_u^{1/2}\left(\partial_z^{-1} f\right)\tilde{u} + \frac{2\Gamma}{\mathrm{Gr}_u^{1/2}} - \partial_z p = 0. \tag{46b}$$

These are similar to the ones for the general case, but now include a nonlocal term in the second equation that helps to control the vertical component of the perturbation velocity field. Again, taking the curl and introducing a stream function ϕ yields the following integro-partial differential equation

$$2\tilde{\mathrm{Ri}}\partial_x\left(\nabla^{-2}\partial_x\phi\right) - \mathrm{Gr}_u^{1/2} f\partial_x\phi - 2\mathrm{Gr}_u^{1/2}\left(\partial_z^{-1} f\right)\partial_{xz}\phi = -\frac{2\Gamma}{\mathrm{Gr}_u^{1/2}}\nabla^4\phi. \tag{47}$$

As an example, although slightly artificial, we consider again the constant shear case, i.e., we investigate the energy stability of the solution $\mathbf{u}_L = Sz$ with respect to spatially periodic perturbations $\tilde{\mathbf{u}}$. Just like in Section 2.2, we consider the system to be unforced and the velocity scale to be SL, with L being the vertical domain size (i.e, we consider Re, Pe instead of $\mathrm{Gr}_u^{1/2}$ and $\mathrm{Gr}_T^{1/2}$). Otherwise, we can proceed as outlined and we again expand ϕ in a Fourier series (essentially setting $\mathrm{Gr}_u^{1/2}\left(\partial_z^{-1} f\right) = -1$ in Eq. (47)) to obtain

$$\frac{\tilde{\mathrm{Ri}}k_x^2}{k_x^2 + k_z^2}\hat{\phi} - k_x k_z\hat{\phi} + \frac{\Gamma}{\mathrm{Re}}\left(k_x^2 + k_y^2\right)^2\hat{\phi} = 0, \tag{48}$$

which allows for nontrivial solutions only if Γ is

$$\Gamma = \frac{\mathrm{Re}k_x k_z}{\left(k_x^2 + k_z^2\right)^2} - \frac{\mathrm{Re}\tilde{\mathrm{Ri}}k_x^2}{\left(k_x^2 + k_z^2\right)^3}. \tag{49}$$

The maximum value of Γ over all wavenumbers k_x and k_z therefore can be calculated by the point in wavenumber space where the gradient of Γ with respect to k_x, k_z is zero (this can be done quickly using polar coordinates). This gives

$$\Gamma_{\max} = \frac{\mathrm{Re}}{4\tilde{\mathrm{Ri}}}. \tag{50}$$

The Richardson number criterion for energy stability is given by $\Gamma_{\max} \leq 1$, i.e.,

$$\tilde{\mathrm{Ri}} \geq \frac{1}{4}\mathrm{Re}. \tag{51}$$

This criterion differs from the one obtained in the previous section in that the power-law dependence on Re is more advantageous. This of course stems from the fact that before we have used relatively crude estimates, whereas here, we calculated the optimal bound.

As we have seen now, in the limit of low Péclet numbers, energy stability can be achieved for large enough $\tilde{\mathrm{Ri}}$, because the temperature perturbation drops out of the equations. It is this slaving of the temperature perturbation to the vertical velocity perturbation that constitutes the main difference between the low Péclet number limit and the general case.

3 Exact upper bounds for body-forced stratified flows

In this section we develop some exact upper bounds for body-forced stratified shear flows in two-dimensional doubly periodic domains. Bounds for energy injection and dissipation in body-forced flows have been investigated in the unstratified case by [5, 1] and for stratified boundary-forced flows by [4, 11]. In [5] the authors derive general bounds on the energy injection in the three-dimensional case, whereas the authors of [1] derive bounds on the energy dissipation in two dimensions using the enstrophy budget. Here, we apply similar mathematical arguments to body-forced stratified flows and show that the arguments used for the unstratified case still hold in the stratified case.

For convenience, the calculations in this section are based on the dimensional momentum equation (1a). The system is assumed to be two dimensional. We start by defining the viscous energy dissipation ϵ and enstrophy dissipation χ as

$$\epsilon = \nu\langle\overline{|\nabla\mathbf{u}|^2}\rangle = \nu\langle\overline{|\omega^2|^2}\rangle, \tag{52a}$$

$$\chi = \nu\langle\overline{|\nabla\omega|^2}\rangle = \nu\langle\overline{|\nabla^2\mathbf{u}|^2}\rangle, \tag{52b}$$

where $\omega = \nabla\times\mathbf{u}$ is the vorticity (a scalar in two dimensions) of the flow field and the overbar denotes a long time average (defined in appendix). Using these two definitions and the Cauchy-Schwarz inequality (see appendix), we can bound the viscous energy dissipation in terms of the root-mean-square velocity U and the enstrophy dissipation

$$\epsilon^2 = \nu^2\langle\overline{|\omega^2|^2}\rangle^2 \leq \nu^2U^2\langle\overline{|\nabla\omega|^2}\rangle = \nu U^2\chi. \tag{53}$$

By bounding the enstrophy dissipation χ, we can therefore simultaneously find a bound for the viscous energy dissipation ϵ. The enstrophy equation can be obtained by taking the curl in two dimensions of Eq. (1a), multiplying by ω and integrating over the entire volume and taking a long time average. This yields

$$\chi = \langle\overline{\psi\omega}\rangle - \alpha g\langle\overline{\omega\partial_x T}\rangle, \tag{54}$$

where $\psi = \nabla\times\mathcal{F}_0 f(kz)\mathbf{e}_x$ is the curl of the forcing. In the calculations that follow, we will also need the total energy and temperature equations, which can be obtained by taking the dot product of the momentum equation with the velocity field and integrating over space and time:

$$-\alpha g\langle\overline{wT}\rangle + \epsilon = \langle\overline{\mathcal{F}_0 f(kz)u}\rangle. \tag{55}$$

Similarly, multiplying Eq. (1b) by T and integrating over the entire volume and time gives the temperature equation

$$\langle\overline{wT}\rangle = -\frac{\kappa_T}{T_{0z}}\langle\overline{|\nabla T|^2}\rangle. \tag{56}$$

The first term in Eq. (54) is treated in [1] and bounded as

$$\langle\overline{\psi\omega}\rangle \leq k_f^2 U\langle\overline{|\mathcal{F}_0 f(kz)|^2}\rangle^{1/2} \tag{57}$$

by integration by parts and Cauchy-Schwarz inequality. Here, $k_f^2 = \langle|\nabla^2 f|^2\rangle^{1/2}/\langle|f|^2\rangle^{1/2}$ is a forcing length scale that is equal to k for Kolmogorov-type forcings. The second term on

the right hand side can be bounded using Young's and the Cauchy-Schwarz inequality (see appendix)

$$|-\alpha g\langle\overline{\omega\partial_x T}\rangle| \le \alpha g\langle\overline{|\omega|^2}\rangle^{1/2}\langle\overline{|\nabla T|^2}\rangle^{1/2} = \frac{\alpha g}{\nu^{1/2}}\epsilon^{1/2}\langle\overline{|\nabla T|^2}\rangle^{1/2}, \tag{58a}$$

$$= \left(\frac{\alpha g T_{0z}}{\nu\kappa_T}\right)^{1/2}\epsilon^{1/2}\left(\frac{\alpha g\kappa_T}{T_{0z}}\langle\overline{|\nabla T|^2}\rangle\right)^{1/2}, \tag{58b}$$

$$\le \frac{1}{2}\left(\frac{\alpha g T_{0z}}{\nu\kappa_T}\right)^{1/2}\left(\epsilon + \frac{\alpha g\kappa_T}{T_{0z}}\langle\overline{|\nabla T|^2}\rangle\right), \tag{58c}$$

$$= \frac{1}{2}\left(\frac{\alpha g T_{0z}}{\nu\kappa_T}\right)^{1/2}\left(\epsilon - \alpha g\langle\overline{wT}\rangle\right) = \frac{1}{2}\left(\frac{\alpha g T_{0z}}{\nu\kappa_T}\right)^{1/2}\left(\langle\overline{u\mathcal{F}_0 f(kz)}\rangle\right), \tag{58d}$$

$$\le \frac{1}{2}\left(\mathrm{RiPeRe}\right)^{1/2} k_f^2 U\langle\overline{|\mathcal{F}_0 f(kz)|^2}\rangle^{1/2}, \tag{58e}$$

where we made use of energy and temperature equations. Here, the three nondimensional numbers are defined in terms of the root-mean-square velocity U

$$\mathrm{Ri} = \frac{\alpha g T_{0z}}{U^2 k_f^2},\ \mathrm{Re} = \frac{U}{\nu k_f} \text{ and } \mathrm{Pe} = \frac{U}{\kappa_T k_f}. \tag{59}$$

We therefore obtain the following bound for the enstrophy dissipation χ:

$$\chi \le k_f^3 U^3 \frac{\langle\overline{|\mathcal{F}_0 f(kz)|^2}\rangle^{1/2}}{k_f U^2}\left(1 + \frac{1}{2}\left(\mathrm{RiPeRe}\right)^{1/2}\right). \tag{60}$$

In order to complete the calculation, we also need to find a bound for $\langle\overline{|\mathcal{F}_0 f(kz)|^2}\rangle^{1/2}/k_f U^2$. This can be done by multiplying the x-momentum equation with $\mathcal{F}_0 f(kz)$ and averaging over the entire volume and time (see [1] for the details) to get

$$\langle\overline{|\mathcal{F}_0 f(kz)|^2}\rangle^{1/2} \le k_f U^2\left(c_1 + \frac{c_2}{\mathrm{Re}}\right), \tag{61}$$

where c_1 and c_2 are constants that depend only on the shape of the forcing function f. Using Eq. (61) we finally obtain

$$\chi \le k_f^3 U^3\left(c_1 + \frac{c_2}{\mathrm{Re}}\right)\left(1 + \frac{1}{2}\left(\mathrm{RiPeRe}\right)^{1/2}\right). \tag{62}$$

This bound for the enstrophy dissipation can be used to bound the energy dissipation. Using Eq. (53), we find a bound for the nondimensional viscous energy dissipation $\epsilon/k_f U^3$ in terms of Ri, Re and Pe

$$\frac{\epsilon}{k_f U^3} \le \frac{1}{\mathrm{Re}^{1/2}}\left(c_1 + \frac{c_2}{\mathrm{Re}}\right)^{1/2}\left(1 + \frac{1}{2}\left(\mathrm{RiPeRe}\right)^{1/2}\right)^{1/2}. \tag{63}$$

This bound illustrates nicely that in two dimensions, the nondimensional viscous energy dissipation approaches 0 asymptotically as $\mathrm{Re}^{-1/4}$. This is different in the unstratified case, where it approaches 0 asymptotically as $\mathrm{Re}^{-1/2}$ (see [1]), but our result reduces to that of [1] when $\mathrm{Ri} = 0$. In both cases however, the viscous energy dissipation approaches 0 as the Reynolds number approaches infinity. This is consistent with turbulence phenomenology where the viscous dissipation is zero for infinite Re in two dimensions.

4 Numerical experiments

In this section, we test some of our theoretical results with direct numerical simulations, and present additional results that relate the heat flux through the fluid to input parameters.

4.1 Model setup

In all that follows, we present two-dimensional simulations in a doubly-periodic box of dimensions $5\pi \times 2\pi$. The resolution varies from 64 to 256 Fourier modes in the vertical and from 364 to 512 modes in the horizontal. The forcing is of Kolmogorov type, with $f(z) = \sin(z)$. In addition, we explore the scaling behavior of vertical heat transport for a variety of $\mathrm{Gr}_u^{1/2}$, $\mathrm{Gr}_T^{1/2}$ and Ri. The code used is pseudo-spectral and uses Fast Fourier Transforms in horizontal and vertical directions.

4.2 Typical results

Typical realizations of the simulations are shown in Figs. 2 and 3 for small and large Ri respectively. We find that, given $\mathrm{Gr}_u^{1/2}$ and $\mathrm{Gr}_T^{1/2}$, for strong stratifications (large Ri), the system systematically displays a bursting behavior, i.e., with periodic relaminarization interrupted by bursts of mixing. For weak stratifications (small Ri) the system displays a quasi-stationary turbulent behavior and the flow field is large scale, with vortices on the same scale as the forcing. We calculate time-averaged quantities by running the simulations for a sufficiently long time and then begin the averaging process after the transient period is over.

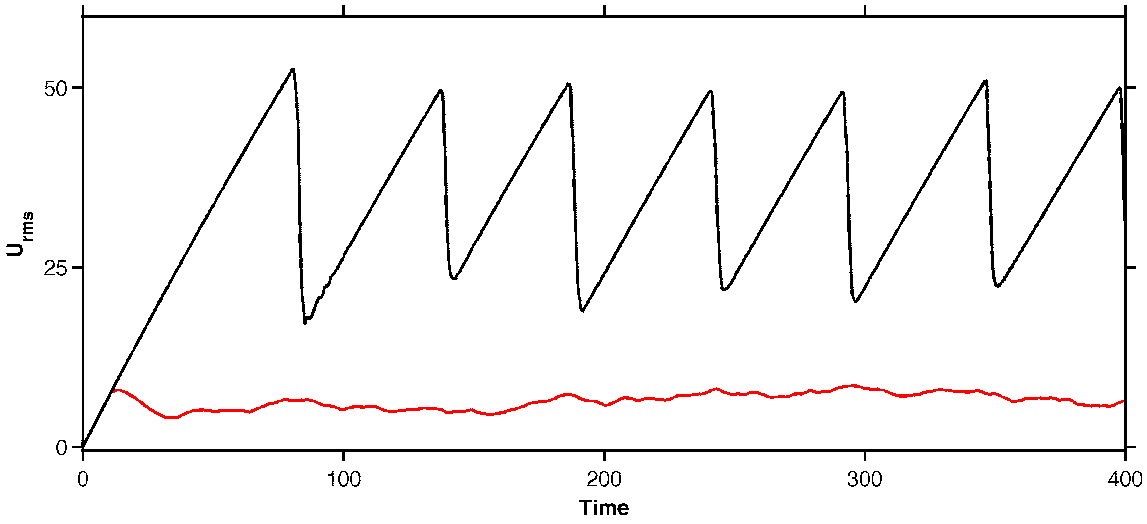

Figure 1: This figure shows two example time series for the large Ri case presented in Fig. 3 (black line) and the low Ri case presented in Fig. 2 (red line). In the case of strong stratification (large Ri) the root-mean-square velocity grows linearly with time until shear instabilities cause mixing. This happens on a quasi-periodic basis. The lower Ri case by contrast, exhibits stationary turbulent flows.

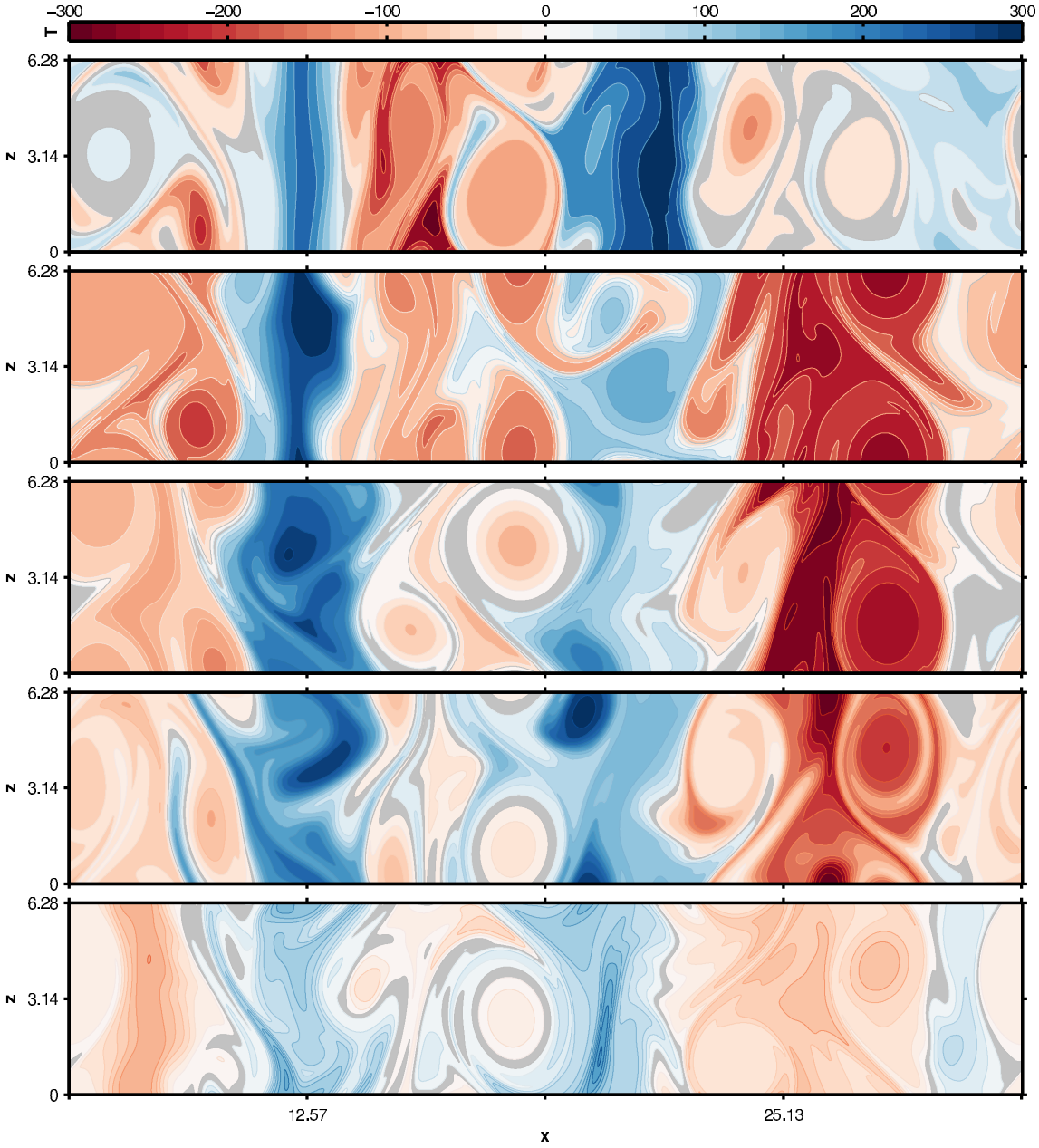

Figure 2: This figure shows a series of typical snapshots of the temperature field for a simulation at $\mathrm{Gr}_T^{1/2} = 100, \mathrm{Ri} = 0.001, \mathrm{Gr}_u^{1/2} = 500$. The flow is dominated by large scale vortices that lead to filamentation of the temperature field and hence to sharp gradients in the temperature field.

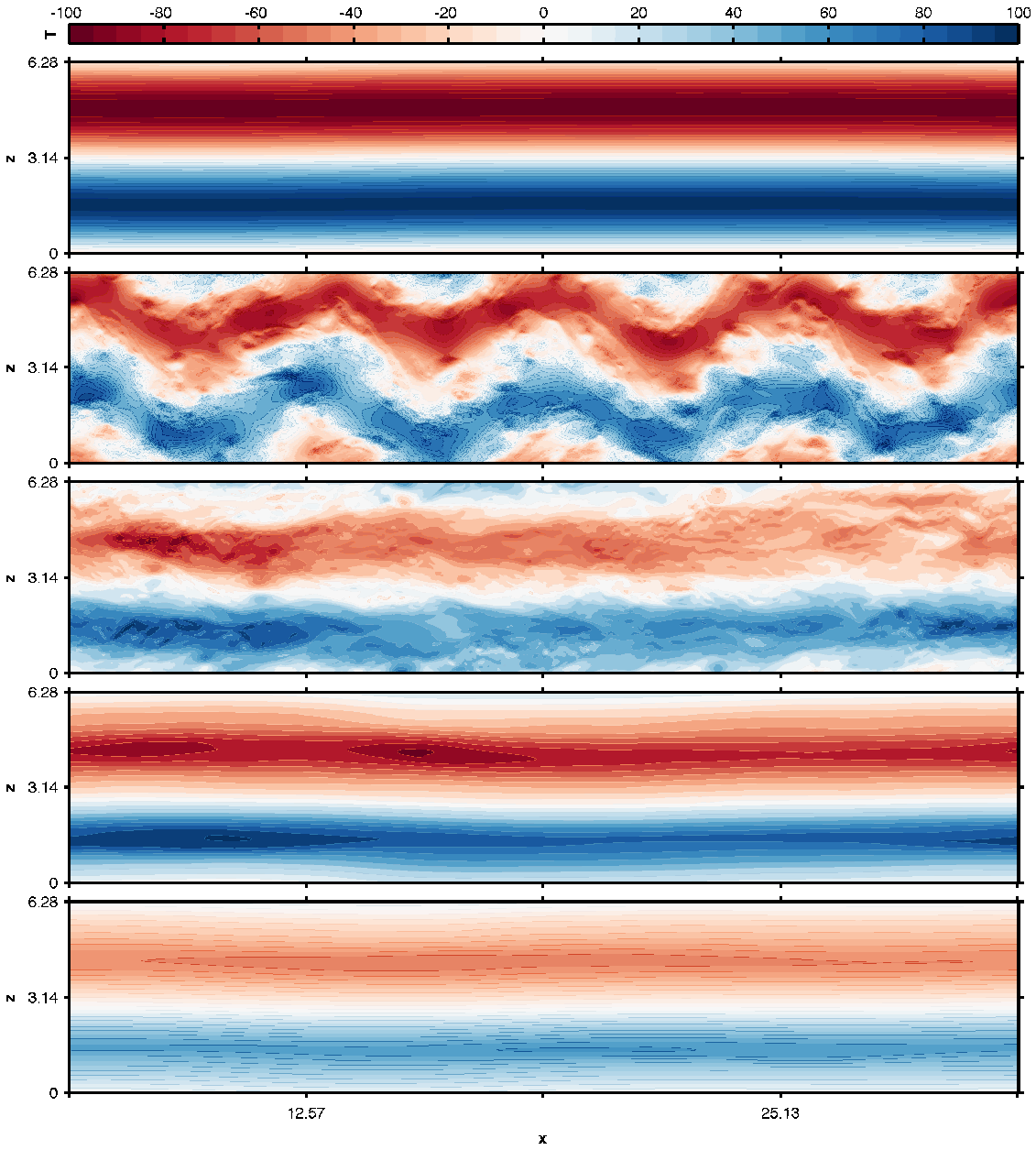

Figure 3: This figure shows a series of snapshots of the horizontal velocity for a bursting simulation at $\mathrm{Gr}_T^{1/2} = 100, \mathrm{Ri} = 1000, \mathrm{Gr}_u^{1/2} = 500$. One can see how the flow goes unstable and then relaminarizes.

4.3 Transport efficiency

An important quantity characterizing a system with stratification is the transport efficiency. It is the ratio of the potential energy used for vertical buoyancy transport to the total energy input into the system, i.e, how much of the injected energy is used for transporting heat compared to being dissipated by viscosity? This efficiency is thus defined as

$$\eta = \frac{-\mathrm{Ri}\langle\overline{wT}\rangle}{\langle\overline{fu}\rangle} = \frac{-\mathrm{Ri}\langle\overline{wT}\rangle}{-\mathrm{Ri}\langle\overline{wT}\rangle + \epsilon}. \tag{64}$$

On phenomenological grounds, one can argue that, at least in two dimensions, the viscous dissipation ϵ tends to zero in the limit of $\mathrm{Gr}_u^{1/2} \to \infty$. This is true if $\mathrm{Gr}_T^{1/2}$ is fixed as $\mathrm{Gr}_u^{1/2}$ increases, because the viscous dissipation approaches zero as long as the root-mean square velocity approaches a constant, while the transport of heat reaches a fixed value. This is equivalent to saying that the transport efficiency η tends to 1 for large $\mathrm{Gr}_u^{1/2}$. We can use the nondimensional temperature equation (essentially Eq. (56)) to replace the vertical transport term in the definition of η and we arrive at

$$\eta = \frac{\frac{\mathrm{Ri}}{\mathrm{Gr}_T^{1/2}}\langle\overline{|\nabla T|^2}\rangle}{\frac{\mathrm{Ri}}{\mathrm{Gr}_T^{1/2}}\langle\overline{|\nabla T|^2}\rangle + \frac{1}{\mathrm{Gr}_u^{1/2}}\langle\overline{|\nabla \mathbf{u}|^2}\rangle}. \tag{65}$$

The phenomenological argument goes as follows: The energy of the velocity field cascades to large scales in two dimensions, which leads to weak gradients. Meanwhile the T field is advected by the velocity field and develops sharp gradients as a result, regardless of Ri. Hence, the transport efficiency therefore approaches 1 in two dimensions. In three dimensions, the situation is generally more complicated, because the viscous dissipation might not approach 0 for large $\mathrm{Gr}_u^{1/2}$. The tracer field might cascade to small scales, but the velocity field is dominated by small scales as well. As $\mathrm{Gr}_u^{1/2}$ approaches infinity (again typically equivalent to the large Reynolds number limit), the viscous dissipation does not approach zero but approaches a finite value. We expect that the transport efficiency will approach a value smaller than 1 which then may depend on the Prandtl number.

We first calculated the transport efficiency for various $\mathrm{Gr}_T^{1/2}$ and Ri, and varying $\mathrm{Gr}_u^{1/2}$, to show that the transport efficiency approaches 1 as $\mathrm{Gr}_u^{1/2}$ increases. We also wish to determine at which point $\eta \approx 1$. Fig. 4 shows the transport efficiency, heat transport and root-mean-square velocity as functions of $\mathrm{Gr}_u^{1/2}$ for different parameter pairs $(\mathrm{Ri}, \mathrm{Gr}_T^{1/2})$ and $(\mathrm{Ri}, \mathrm{Pr})$. We find that the heat transport approaches a constant value as $\mathrm{Gr}_u^{1/2}$ increases, in agreement with a temperature field that is dominated on small scales. As expected, the root-mean-square velocity of the flow does not diverge as $\mathrm{Gr}_u^{1/2}$, but instead also appears to converge to a constant. We find that $\eta \longrightarrow 1$ as predicted, although the rate of convergence seems to depend on the Prandtl and Richardson numbers.

4.4 A scaling for the heat transport based on the Richardson number

In this section, we derive simple scaling laws for the heat flux $\langle\overline{wT}\rangle$ of the flow, based on numerical simulations and heuristic arguments.

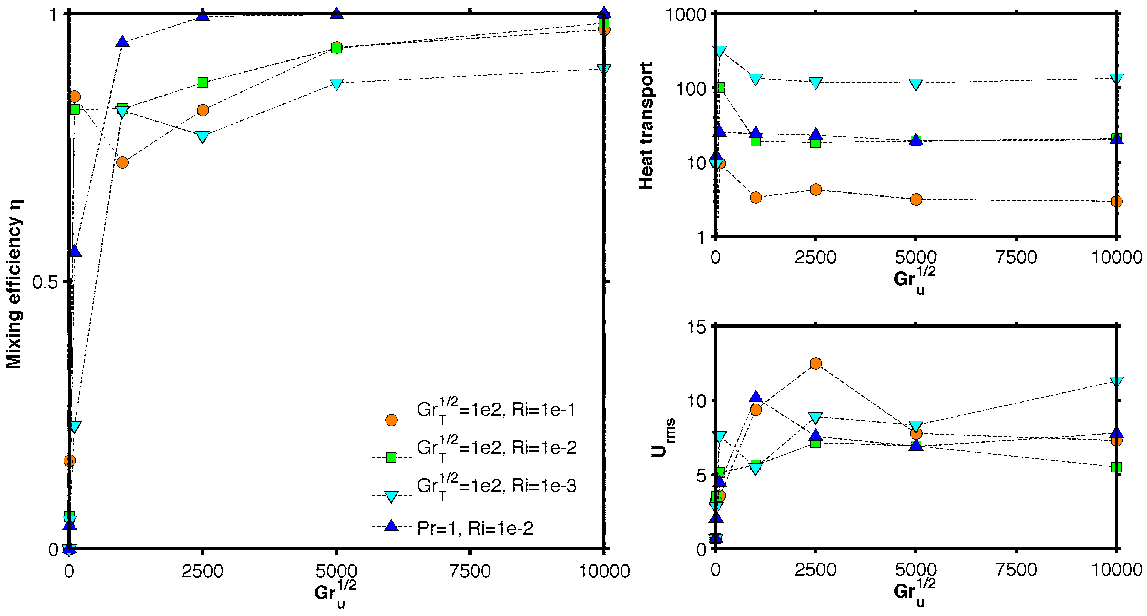

Figure 4: The left panel shows transport efficiency vs $\mathrm{Gr}_u^{1/2}$. Top right panel shows the heat transport vs $\mathrm{Gr}_u^{1/2}$ and the bottom right panel shows the root-mean-square velocity vs $\mathrm{Gr}_u^{1/2}$. As expected, the transport efficiency approaches 1 for large $\mathrm{Gr}_u^{1/2}$ and the root-mean-square velocity remains finite.

4.4.1 The gradient Richardson number

We define a gradient Richardson number in terms of the horizontally-averaged (indicated here as $[(.)]$) temperature and velocity fields as

$$\mathcal{J} = \mathrm{Ri}\frac{1+\partial_z[T]}{(\partial_z[u])^2}. \tag{66}$$

The linear stability of stratified shear flows has been studied at length in [9, 6, 12, 3, 2], and reveals $\mathcal{J}$ to be a critical parameter. At high $\mathrm{Gr}_T^{1/2}$, the flow is linearly unstable, provided $\mathcal{J}$ is less than an $\mathcal{O}(1)$ constant, whose exact value depends on the forcing selected. At low $\mathrm{Gr}_T^{1/2}$, high Ri flows can also be unstable as shown in [7].

4.4.2 Small Richardson numbers, Ri < 1

For low Richardson numbers ($\mathrm{Ri} < 1$), our simulations suggest that $\langle\overline{wT}\rangle \propto 1/\mathrm{Ri}$. We also find that the horizontally-averaged flow projects onto the forcing with

$$\langle\overline{fu}\rangle \sim \mathcal{O}(1). \tag{67}$$

For constant $\mathrm{Gr}_T^{1/2}$, $\mathrm{Gr}_u^{1/2}$, this projection remains of order 1 regardless of the Richardson number as long as $\mathrm{Ri} < 1$. Balancing the heat transport in the energy equation for large

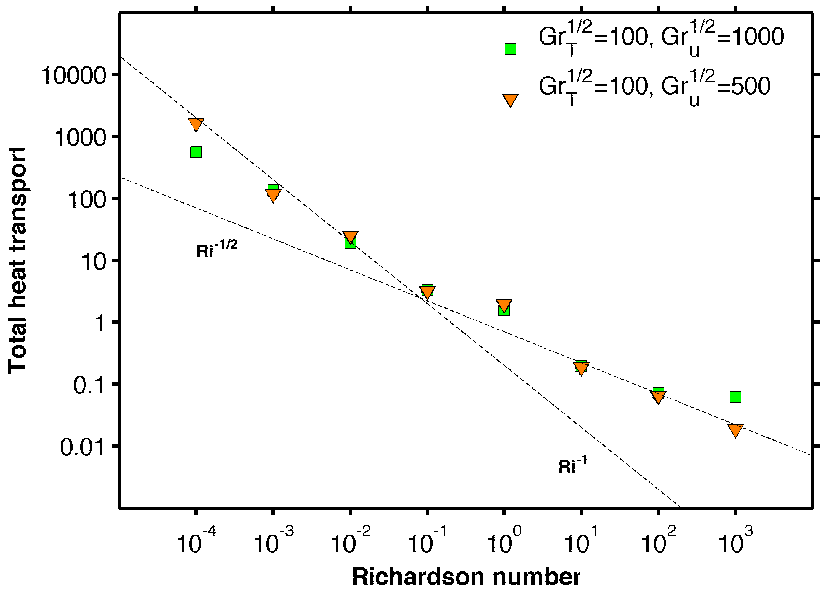

Figure 5: This figure shows the total heat flux through the system $\langle \overline{wT} \rangle$, as a function of the Richardson number. There appear to be two scaling regimes. For low Ri, the flow field is dominated by large vortices that advect the temperature field; we find that $\langle \overline{wT} \rangle \propto \mathrm{Ri}^{-1}$. For high Ri, the system displays a bursting behavior with periods of relaminarization; we find that $\langle \overline{wT} \rangle \propto \mathrm{Ri}^{-1/2}$.

$\mathrm{Gr}_u^{1/2}$ (viscous dissipation approaches 0) then yields

$$\mathrm{Ri}\langle \overline{wT} \rangle \sim \langle \overline{fu} \rangle \sim \mathcal{O}(1) \Leftrightarrow \langle \overline{wT} \rangle \sim \frac{1}{\mathrm{Ri}}, \tag{68}$$

which qualitatively explains the scaling behavior of the heat transport for low Richardson numbers. However, detailed investigations would be necessary to confirm that this scaling holds unambiguously since there is no apriori reason for why $\langle \overline{fu} \rangle \sim \mathcal{O}(1)$ independently of the Richardson number. Furthermore, it will be interesting to determine whether the prefactor depends on other quantities, such as the Prandtl number, for instance in the limit $\mathrm{Gr}_u^{1/2} \longrightarrow \infty$.

4.4.3 Large Richardson numbers, $\mathbf{Gr}_u^{1/2} > \mathbf{Ri} > 1$

At large Richardson numbers, the flow shows a "bursting" behavior (see Fig. 6) which is characterized by times during which the flow field is laminar, with a form $[u](z) \approx a(t)\sin(z)$, where $a(t)$ is a linearly growing function of time. This is halted when the gradient Richardson number drops roughly below 1 (see Fig. 7), at which point the shear goes linearly unstable. The perturbation energy decays again, and the process starts over. This can be used to estimate the heat flux. Indeed, assuming weak temperature gradients as in the laminar solution, we have that a sinusoidal horizontally-averaged horizontal velocity

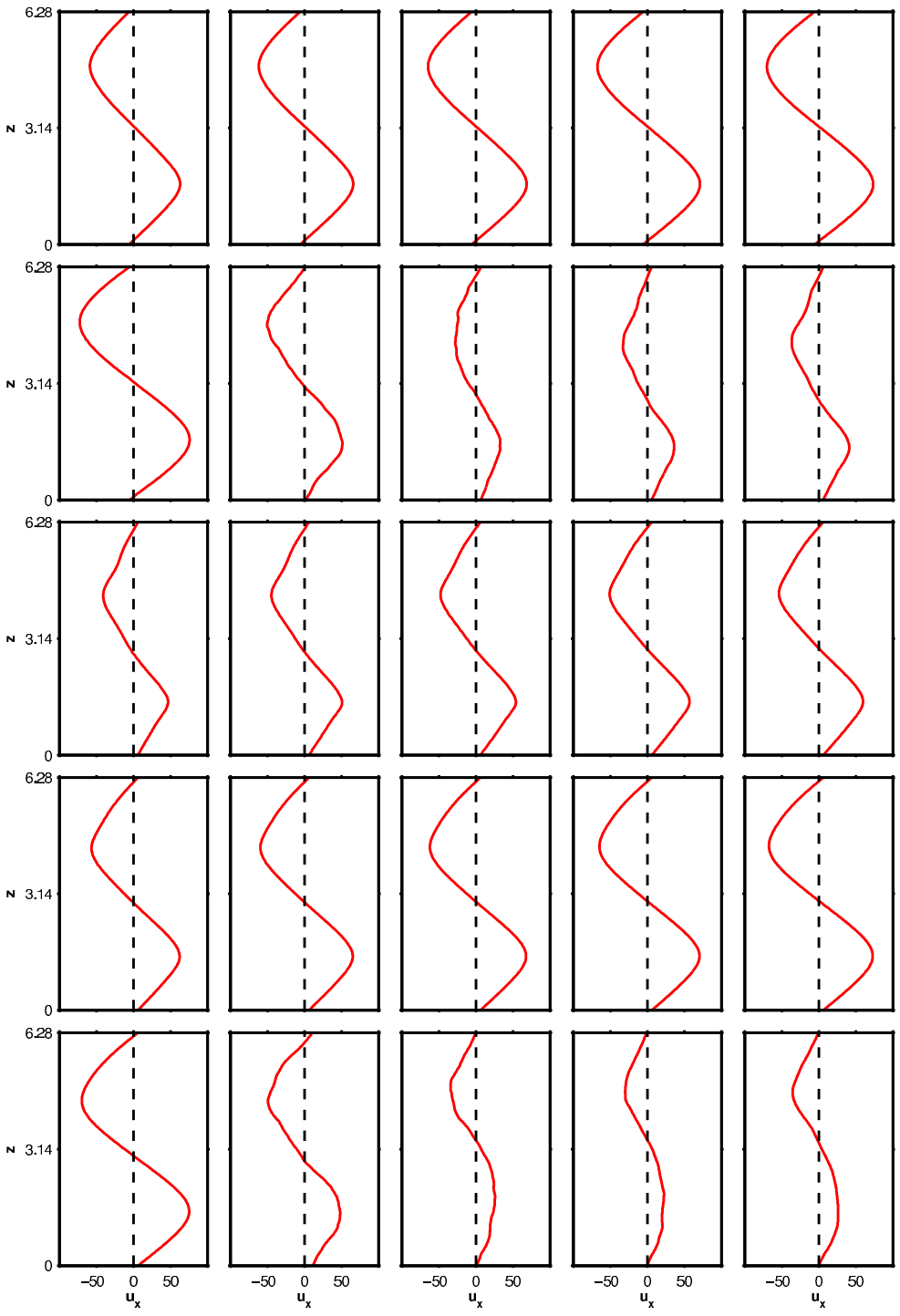

Figure 6: This figure shows, from top left to bottom right, an example of a series of horizontally averaged horizontal velocity profiles from the numerical simulation for $\mathrm{Gr}_T^{1/2} = 100, \mathrm{Ri} = 1000, \mathrm{Gr}_u^{1/2} = 500$. It illustrates that the averaged flow projects strongly onto the laminar solution.

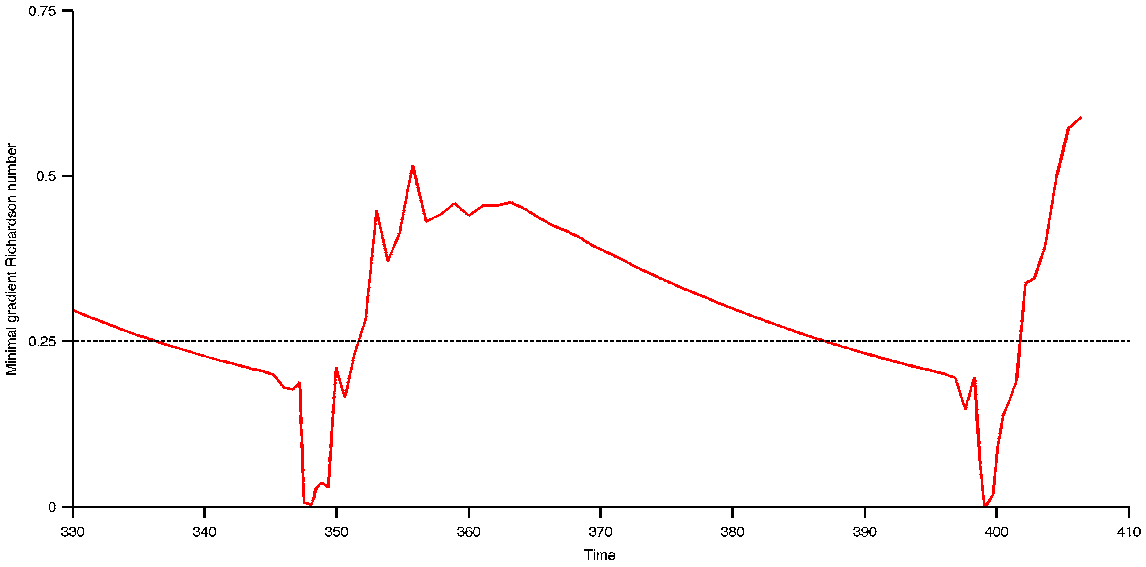

Figure 7: This figure shows a time series for the minimal gradient Richardson number of the flow field for a simulation with $\mathrm{Gr}_T^{1/2} = 100, \mathrm{Ri} = 1000, \mathrm{Gr}_u^{1/2} = 500$. As $\mathcal{J}$ drops below a value of about 0.2 the flow becomes linearly unstable.

profile, $[u] = a(t)\sin(z)$, is linearly unstable if

$$\mathcal{J} \sim \mathcal{O}(1) \Rightarrow \mathcal{O}(1) \sim \frac{\mathrm{Ri}}{a(t)^2 \max_z \{\sin(z)^2\}} \Rightarrow a(t)^2 \propto \mathrm{Ri}. \tag{69}$$

This then implies that $\langle \overline{fu} \rangle \sim \sqrt{\mathrm{Ri}}$. For large values of $\mathrm{Gr}_u^{1/2}$, as previously seen, the viscous dissipation term approaches zero, which then leads to the following balance in the energy equation

$$\mathrm{Ri}\langle \overline{wT} \rangle \sim \langle \overline{fu} \rangle \sim \sqrt{\mathrm{Ri}} \Leftrightarrow \langle \overline{wT} \rangle \sim \frac{1}{\sqrt{\mathrm{Ri}}}. \tag{70}$$

4.4.4 Very large Richardson numbers, $\mathbf{Ri} \gtrsim \mathbf{Gr}_u^{1/2}$

For very large Richardson numbers, the laminar solution is itself linearly stable as shown by [12, 3, 2]. We can estimate the region of the parameter space where the laminar solution is linearly stable using the Miles-Howard criterion for linear stability of stratified shear flows in the inviscid limit [9, 6]. Using our nondimensionalization, we find that the flow is stable provided

$$\mathcal{J} \sim \mathcal{O}(1) \Rightarrow \mathcal{O}(1) \sim \frac{\mathrm{Ri}}{\mathrm{Gr}_u^{1/2}} \Rightarrow \mathrm{Ri} \propto \mathrm{Gr}_u^{1/2}. \tag{71}$$

Because the laminar solution is stable, we have no vertical heat transport as $T = 0$ in this case,

$$\langle \overline{wT} \rangle = 0. \tag{72}$$

Our simulations show that this limit is indeed attained provided $\mathrm{Ri} \gtrsim \mathrm{Gr}_u^{1/2}$.

5 Conclusion and Summary

We have shown that energy stability for stratified shear flows can be achieved for large enough Richardson numbers in the limit of small $\mathrm{Gr}_T^{1/2}$ (similar to a small Péclet number limit). In the general case, the same approach is unsuccessful, in the sense that we find that the energy stability is independent of Ri. In two dimensions, bounds for the viscous dissipation of the system can be extended from the unstratified case to the stratified case. We have shown that standard bounding techniques for forced flows can be applied in much the same way for all values of the Richardson number.

We also argued (at least for the two dimensional case) that the transport efficiency (or mixing efficiency), i.e., the ratio of energy dissipation by vertical transport of heat to the total energy input per unit time approaches 1 in the limit of large $\mathrm{Gr}_u^{1/2}$. This is because energy cascades to large scales in two dimension, whereas the temperature field remains filamented. The dependence of the heat transport on the Richardson number was investigated for constant $\mathrm{Gr}_T^{1/2}$. We found that there are at least three regimes. For $\mathrm{Ri} \gtrsim \mathrm{Gr}_u^{1/2}$ the laminar solution is linearly stable. In the regime of large $\mathrm{Gr}_u^{1/2} > \mathrm{Ri} > 1$, the system displays a bursting behavior. The bursting can be explained by a mean flow profile that strongly projects onto the forcing with an amplitude that periodically grows trying to approach the laminar solution. Because the amplitude of the laminar solution is proportional to $\mathrm{Gr}_u^{1/2}$, it is not linearly stable in this regime, and the system becomes linearly unstable when the amplitude reaches a critical value. In the regime of small Ri the flow is fully chaotic, i.e., the flow field is dominated by large vortices at the forcing length scale that advect the temperature field. The heat transport is no longer achieved by episodic bursts, but is now achieved by the transport induced by these large scale vortices.

6 Acknowledgements

First and foremost, I would like to thank Pascale Garaud and Basile Gallet for their guidance on this project and Charles Doering for helpful discussions on bounding methods and Jacuzzis. I would also like to thank the organizers of this summer school for their efforts in creating an intellectually stimulating environment. However, most importantly, I would like to thank the fellows of the 2013 Woods Hole GFD Summer Program for a wonderful summer, many stimulating discussions and 8 new friendships.

A Averages

We define the volume average in n-dimensions as

$$\langle (.) \rangle = \frac{1}{V} \int (.) \, \mathrm{d}\Omega, \tag{73}$$

where V is the Volume of the domain and $\mathrm{d}\Omega$ is the volume element. We define the long time average $\overline{(.)}$ as

$$\overline{(.)} = \lim_{T \to \infty} \left(\frac{1}{T} \int_0^T (.) \, \mathrm{d}t \right), \tag{74}$$

and the horizontal average $[(.)]$ as

$$[(.)] = \frac{1}{L_x} \int_0^{L_x} (.)\, \mathrm{d}x, \tag{75}$$

where L_x is the horizontal domain size.

B Fourier series

We define the Fourier series of a real-valued zero-mean function $f(\mathbf{x})$ on the periodic domain $[0, L_1] \times \ldots \times [0, L_d]$ as follows:

$$f(\mathbf{x}) = \sum_{\mathbf{k}} \exp(i\mathbf{k} \cdot \mathbf{x})\, \hat{f}_{\mathbf{k}}, \tag{76}$$

for $\mathbf{k} = 2\pi\mathbf{n}$, where $\mathbf{n} = (n_1/L_1, \ldots, n_d/L_d)$ with positive and negative integers n_i. Here, L_i denotes the domain size in the i-th direction and $\hat{f}_{\mathbf{k}}$ is the potentially complex Fourier coefficient associated with the wavenumber vector $\mathbf{k}$. The largest domain size is given by $L_{\max} = \max(L_1, \ldots, L_d)$ and the total volume is given by $V = L_1 \cdot \ldots \cdot L_d$. We define the norm of the wavenumber vector to be $k = |\mathbf{k}|$ with $k \geq 2\pi/L_{\max}$.

C Basic Inequalitites

C.1 Young's inequality

Young's inequalities can be derived from first principles in the following way:

$$(a+b)^2 = a^2 + 2ab + b^2, \tag{77a}$$

$$(a-b)^2 = a^2 - 2ab + b^2, \tag{77b}$$

$$\Rightarrow -\frac{1}{2}\left(a^2 + b^2\right) \leq ab \leq \frac{1}{2}\left(a^2 + b^2\right). \tag{77c}$$

Therefore, the product $2ab$ can be sandwiched between the sum of the squares. This is useful when it comes to estimating products, since sums greatly simplify the treatment of integrals (compared to products).

C.2 Hoelder's inequality

We prove a simple form of Hoelder's inequality for scalar functions [5]. Given two function f and g, where we only need that g is bounded and f is integrable, we have that at every point

$$f(x)g(x) \leq |f(x)g(x)| \leq \sup_y [|g(y)|]\, |f(x)|. \tag{78}$$

Now, we can use this under the integral so that we arrive at the integral inequality

$$\int f(x)g(x)\, \mathrm{d}x \leq \sup_y [|g(y)|] \int |f(x)|\, \mathrm{d}x. \tag{79}$$

This can be used when information on shape or the boundedness of function is available.

C.3 Poincaré's inequality

Poincaré's inequality can be used to estimate norms of zero-mean functions in terms of the norm of their derivative (or gradient) [5]. We restrict ourselves to finite periodic domains ω of dimension d with largest extent $L_{\max}$. Using Parseval's theorem, we have

$$\int |\nabla f|^2 \,\mathrm{d}\Omega = V \sum_{\mathbf{k}} \mathbf{k}^2 f_k^2 \geq V \sum_{\mathbf{k}} \frac{4\pi^2}{L_{\max}^2} f_k^2 = \frac{4\pi^2}{L_{\max}^2} \int |f|^2 \mathrm{d}\Omega. \tag{80}$$

This allows for useful estimates when dissipation rate terms are involved, i.e., terms of the form $\langle |\nabla u|^2 \rangle$.

C.4 Cauchy-Schwarz inequality

The Cauchy-Schwarz inequality is useful when dealing with product of functions under an integral [5]. If f and g are square integrable scalar functions

$$\left| \int f(x) g(x) \,\mathrm{d}x \right|^2 \leq \int |f|^2 \,\mathrm{d}x \int |g|^2 \,\mathrm{d}x. \tag{81}$$

References

[1] Al Alexakis and C R Doering, *Energy and enstrophy dissipation in steady state 2D turbulence*, Physics Letters A, 359 (2006), pp. 652–657.

[2] NJ Balmforth and Y-N Young, *Stratified Kolmogorov flow. Part 2*, Journal of Fluid Mechanics, 528 (2005), pp. 23–42.

[3] N J Balmforth and Y-N Young, *Stratified Kolmogorov flow*, Journal of Fluid Mechanics, 450 (2002), pp. 131–168.

[4] C P Caulfield and R R Kerswell, *Maximal mixing rate in turbulent stably stratified shear flow*, Physics of Fluids, 13 (2001), pp. 894–900.

[5] C R Doering and C Foias, *Energy dissipation in body-forced turbulence*, Journal of Fluid Mechanics, 467 (2002), pp. 289–306.

[6] L N Howard, *Note on a paper of John W Miles*, Journal of Fluid Mechanics, 10 (1961), pp. 509–512.

[7] F Lignières, *The small-Péclet-number approximation in stellar radiative zones*, Astronomy and Astrophysics, 348 (1999), pp. 933–939.

[8] F Lignières, F Califano, and A Mangeney, *Shear layer instability in a highly diffusive stably stratied atmospheres*, Astronomy and Astrophysics, 349 (1999), pp. 1027–1036.

[9] J W Miles, *On the stability of heterogeneous shear flows*, Journal of Fluid Mechanics, 10 (1961), pp. 496–508.

[10] V Prat and F Lignières, *Turbulent transport in radiative zones of stars*, Astronomy and Astrophysics, 551 (2013), p. L3.

[11] W Tang, C P Caulfield, and R R Kerswell, *A prediction for the optimal stratification for turbulent mixing*, Journal of Fluid Mechanics, 634 (2009), pp. 487–497.

[12] Y-N Young and N J Balmforth, *On stratified Kolmogorov flow*, Stirring and mixing: 1999 Program of Summer Study in Geophysical Fluid Dynamics, (2000), p. 97.

Investigation of lock release gravity currents in an upslope valley

Catherine Jones

October 1, 2013

1 Introduction

The sun heats the land faster than it heats the ocean, causing the air to be warmer over land than over the sea during the day. Convection over land keeps these air masses apart. However, as convection weakens in the afternoon and evening, a pressure gradient causes the cold dense air over the ocean to flow under the warm air on the land in a "sea breeze." In areas where sea breezes occur, they cool the region of land adjacent to the ocean and bring in moisture. In the Santa Barbara region, where valleys penetrate into coastal mountain ranges, sea breezes propagate to high inland plateaus, enabling grapes to be grown; in the absence of sea breezes, the climate would otherwise be too hot and dry. In general, it is of interest to study the flow of dense fluids into valleys and up hills. The results presented here may be applicable not only to coastal agriculture, but also to tidal flows in submarine canyons and estuaries.

Sea breezes are a type of gravity current, and gravity currents are often studied by performing lock-release experiments. This is the approach we take here. A dense fluid is held at one end of the tank by a gate, and the rest of the tank is filled with a lighter fluid. When the gate is removed, the dense fluid, driven by the pressure gradient, flows under the lighter fluid as a gravity current.

The experiments, numerics, and theory in this manuscript explore full-depth lock-release at high Reynolds numbers in the parameter range available when a tank is tilted in the x and y directions, as shown in Figure 1. The aim is to look at the behaviour of gravity currents up slopes and in symmetric and asymmetric V-shaped valleys, and in particular to measure the speed, the time-dependence, and the shape of the currents we observe. We wish to understand what factors control these parameters in order to make general predictions for the initial speed and time dependence of a gravity current in a valley. The timescale of sea breezes is much shorter than one day, and so we do not expect the rotation of the Earth to be important.

In Section 2 of this manuscript we describe previous work on gravity currents, particularly those in valleys and up slopes. In Section 3, we extend Benjamin's analysis to predict the speed and height of a gravity current in a V-shaped valley. A prediction for the speed of upslope flow as a function of slope is also made based on local water depth at the front. In Section 4, we perform laboratory experiments to explore the speed and time dependence

of a gravity current when the tank is tilted in the x and y directions. In Section 5, numerical experiments using the HYbrid Coordinate Ocean Model (HYCOM) are used to shed more light on the experimental results. All of the results are summarised and discussed in Section 6.

2 Background

Lock-release gravity currents with a flat bottom in a rectangular domain are well understood. The initial speed of an energy conserving gravity current, U, is predicted fairly well by Benjamin's analysis, which conserves mass, momentum and energy across the front of the gravity current [1]. It is found that

$$U = \frac{\sqrt{g'H_0}}{2}\,, \tag{1}$$

where H_0 is the height of the fluid at the lock and g' is the reduced gravity for the two fluids. For a flat bottom gravity current, it is understood that there are three phases: the constant speed phase, where the speed of the front is constant, the self-similar phase, where the position of the front X depends on time t as $X(t) \sim t^{\frac{2}{3}}$ and the viscous phase where $X \sim t^{\alpha}$where $\alpha < 1$ and depends on the geometry and set-up [7].

The important parameter for studying the speed of a gravity current is the Froude number, which can be defined in two different ways: one based on the local tank height, H_0 and the other based on h, the height of the gravity current far away from the front:

$$\mathrm{Fr}_H = \frac{U}{\sqrt{g'H_0}}\,, \tag{2a}$$

$$\mathrm{Fr}_h = \frac{U}{\sqrt{g'h}}\,. \tag{2b}$$

Benjamin's analysis predicts that $\mathrm{Fr}_H = \frac{1}{2}$ and $\mathrm{Fr}_h = \sqrt{2}$ for full-depth, flat bottom lock-release.

Downslope gravity currents in rectangular channels are also well understood, both for constant flux down the slope [4] and for a lock release [2]. In both cases, downslope flows have a quasi-constant speed that is a function of slope angle. Experiments show that the nondimensional velocity is maximum at an angle of around 40°. Birman et al. [2] find that for a downslope lock release, Fr_H fits the parabolic curve

$$\mathrm{Fr}_H(\theta < 0) = -0.1924\theta^2 + 0.2781\theta + 0.4871\,, \tag{3}$$

where θ is expressed in radians. This means that for small θ, $\mathrm{Fr}_H(\theta)$ depends approximately linearly on θ. Britter and Linden [4] find that for angles less than 0.5°, downslope flow is no longer quasi-steady, but rather decelerates after the initial constant velocity phase.

Except for a recent study by Ottolenghi et al. [11], upslope gravity currents have received far less attention than downslope gravity currents. Ottolenghi et al. use both experiments and numerics to show that a current decelerates more as the upslope angle increases. They also find that for upslope flow the initial speed of the current does not depend on the slope. Ottolenghi et al. are constrained by the length of their tank, and are only able to achieve

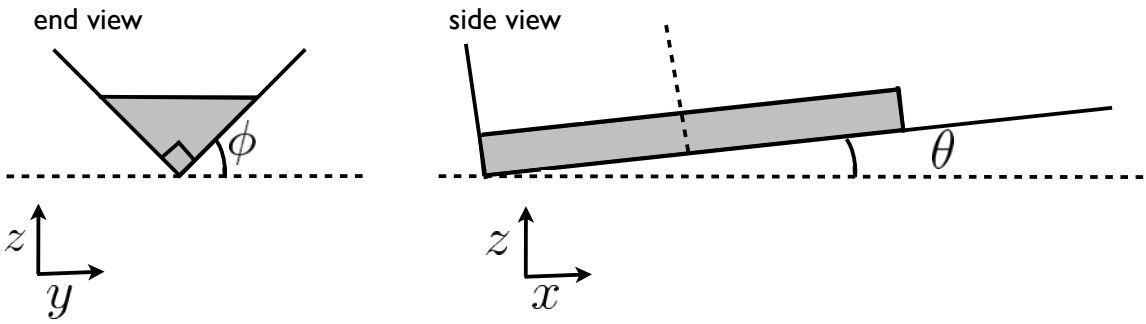

Figure 1: θ and ϕ are the angles that define the orientation of the tank.

slope angles of up to 1.8° in their experiments, and of up to 5° in their numerics. We extend this range to about 8° in both our experiments and our numerics. We also consider upslope flow in V-shaped valleys.

Lock-release flows in symmetric V-shaped valleys have been studied theoretically and experimentally by Monaghan et al. [10] and Marino and Thomas [9]. Monaghan et al. [10] observe that these sorts of currents have a self-similar, parabolic shape and therefore they take a similarity solution approach, assuming a constant value for Fr_h. They predict that the front position X is dependent on time t as $X(t) \sim t^{\frac{4}{5}}$, and they find that their experiments agree with this prediction. Zemach and Ungarish [14] also study flow in a V-shaped valley using shallow water theory, and compare their results to the similarity solution described above. They find good agreement and are able to extend their model to asymmetric basins.

The inital speed of a gravity current in a V-shaped valley has not been predicted analytically in previous work, so we extend Benjamin's analysis for this purpose. We also investigate the effects of tilting a V-shaped valley in the x-z plane, so that the current is flowing up slope. To the best of our knowledge, this experiment has never been done before.

3 Theory

Henceforth, variation in θ is called *rise*, and the variation in ϕ is called *tilt*. These angles are illustrated in Figure 1. They are measured in degrees in the remainder of this manuscript.

3.1 Extension of Benjamin's analysis for $\phi = 45°$

Following Benjamin (1968) [1], we apply conservation of mass, conservation of momentum, and the Bernoulli equation along the free surface and bottom boundary, to find the height and speed of the gravity current. The set-up is shown in Figure 2, in which the frame of reference has been changed so that the front and the dense fluid behind it are stationary. The dense fluid has density ρ_l and the light fluid has density ρ_u. We define the reduced gravity for the two fluids to be

$$g' = \frac{g(\rho_l - \rho_u)}{\rho_u}\,. \tag{4}$$

There are a number of assumptions associated with this approach. It is assumed that gravity waves on the free surface are too fast to affect the speed of the gravity current. It is also assumed that the speed of each layer is relatively uniform, which means that we neglect the effects of viscous boundary layers. Applying Bernoulli along the top and bottom boundaries assumes that there is a streamline along the bottom corner of the tank (at $y = 0$, $z = 0$) and along the free surface (at $y = H$, $z = 0$). This is justified by symmetry considerations in the $\phi = 45°$ case. It is also assumed that energy is conserved along these lines, which is not strictly true, but a good approximation.

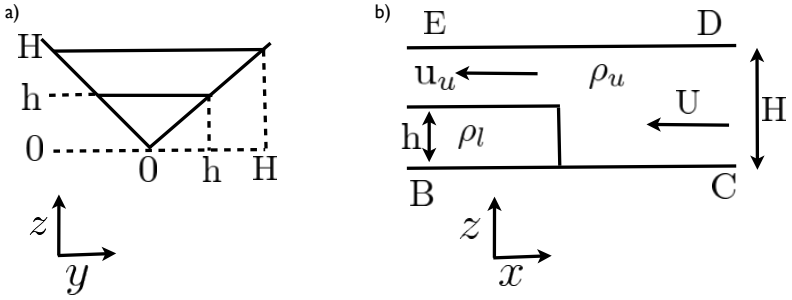

Figure 2: Schematic of the $\phi = 45^0$, $\theta = 0^0$ setup. a) shows a cross section view at BE and b) shows a section along the tank at $y = 0$.

The mass flowing through the cross section at BE must equal the mass flowing through the cross section at DC, so

$$H^2 U = \left(H^2 - h^2\right) u_u \,. \tag{5}$$

Then applying Bernoulli along BC and ED gives

$$p_B = p_C + \frac{\rho_u U^2}{2} \,, \tag{6a}$$

$$p_E + \frac{\rho_u u_u^2}{2} = p_D + \frac{\rho_u U^2}{2} \,. \tag{6b}$$

Integrating the hydrostatic equation, $\frac{dp}{dz} = -\rho g$, we find that the pressure in the cross-section at BE is

$$p = \begin{cases} p_B - \rho_l g z & \text{if } z < h; \\ p_B - \rho_l g h - \rho_u g \left(z - h\right) & \text{if } z > h. \end{cases} \tag{7}$$

and the pressure in the cross-section at CD is

$$p = p_C - \rho_u g z. \tag{8}$$

Now we conserve the flux of momentum through the tank. The flux of momentum through the cross section at BE must be equal to the flux of momentum through the cross section at CD. We consider only the positive half of the domain, because symmetry dictates that

flow in the negative half behaves identically. Conserving momentum,

$$\int_0^h \int_y^h p_B - \rho_l g z \,\mathrm{d}z\mathrm{d}y + \int_0^h \int_h^H p_B - \rho_l g h - \rho_u g\,(z-h) + \rho_u u_u^2 \,\mathrm{d}z\mathrm{d}y + \int_h^H \int_y^H p_B - \rho_l g h - \rho_u g\,(z-h) + \rho_u u_u^2 \,\mathrm{d}z\mathrm{d}y = \int_0^H \int_y^H p_C - \rho_u g z + \rho_u U^2 \mathrm{d}z\mathrm{d}y\,. \tag{9}$$

Integrating with respect to z yields

$$\begin{aligned}\int_0^h p_B\,(h-y) - \rho_l g\left(\frac{h^2}{2} - \frac{y^2}{2}\right)\,\mathrm{d}y \\ + \int_0^h \left(p_B - \rho_l g h + \rho_u g h + \rho_u u_u^2\right)(H-h) - \rho_u g\left(\frac{H^2}{2} - \frac{h^2}{2}\right)\mathrm{d}y \\ + \int_h^H \left(p_B - \rho_l g h + \rho_u g h + \rho_u u_u^2\right)(H-y) - \rho_u g\left(\frac{H^2}{2} - \frac{y^2}{2}\right)\mathrm{d}y \\ = \int_0^H p_C\,(H-y) - \rho_u g\left(\frac{H^2}{2} - \frac{y^2}{2}\right) + \rho_u U^2\,(H-y)\,\mathrm{d}y\,.\end{aligned} \tag{10}$$

Rearranging, and then integrating with respect to y gives

$$\begin{aligned}&\left(p_B - \rho_l g h + \rho_u g h + \rho_u u_u^2\right)\left(\frac{H^2}{2} - \frac{h^2}{2}\right) \\ &+ p_B\left(h^2 - \frac{h^2}{2}\right) - \rho_l g\left(\frac{h^3}{2} - \frac{h^3}{6}\right) + \frac{\rho_u g}{2}\left(h^3 - H^3\right) + \rho_u g\left(\frac{H^3}{6} - \frac{h^3}{6}\right) \\ &= p_C\left(H^2 - \frac{H^2}{2}\right) - \rho_u g\left(\frac{H^3}{2} - \frac{H^3}{6}\right) + \rho_u U^2\left(H^2 - \frac{H^2}{2}\right).\end{aligned} \tag{11}$$

Then substituting in for p_C using equation Eq. (6a), and expressing $g(\rho_l - \rho_u)/\rho_u$ as g',

$$g'\frac{h^3}{6} - g' h \frac{H^2}{2} + U^2\frac{H^2}{4} + u_u^2\left(\frac{H^2}{2} - \frac{h^2}{2}\right) = U^2\frac{H^2}{2}\,. \tag{12}$$

into which we can substitute for u_u using Eq. (5), giving

$$g'\frac{h^3}{6} - g' h \frac{H^2}{2} = \frac{U^2 H^2}{2}\left(\frac{1}{2} - \frac{H^2}{(H^2 - h^2)}\right). \tag{13}$$

Again using the hydrostatic equation, the pressures at B, C, D and E are related by

$$p_E = p_B - \rho_l g h - \rho_u g\,(H-h) \tag{14a}$$

$$p_D = p_C - \rho_u g H\,. \tag{14b}$$

Using the above expression and Eq. (6a), Eq. (6b) can be rewritten as

$$\frac{u_u^2}{2} = g' h\,. \tag{15}$$

Applying mass conservation (Eq. (5)),

$$\frac{\left(H^2-h^2\right)^2 g'h}{H^2} = \frac{H^2U^2}{2}\,, \tag{16}$$

which relates the speed of the current U to its height h. We can substitute Eq. (16) into Eq. (13) to give an expression for the height of the current h in terms of the total height of the tank H,

$$h^2 = \frac{H^2}{3}\,. \tag{17}$$

This means that in a symmetric V-shaped valley, the height of the gravity current is $H/\sqrt{3}$, which is taller than $H/2$, the height of a gravity current in a rectangular channel. We can obtain the speed of the current by substituting Eq. (17) back into Eq. (16) and rearranging, giving

$$U^2 = 2g'\left(\frac{2}{3}\right)^2\sqrt{\frac{1}{3}}H\,. \tag{18}$$

Therefore the predicted Froude number for a V-shaped valley with $\phi = 45^\circ$ is

$$\begin{aligned}\mathrm{Fr}_H(\phi=45^\circ) = \frac{U}{\sqrt{g'H}} &= \sqrt{\frac{8}{9\sqrt{3}}} \\ &\approx 0.72\,.\end{aligned} \tag{19}$$

This is significantly larger than the prediction $\mathrm{Fr}_H(\phi = 0^\circ) = \frac{1}{2}$ for a gravity current in a rectangular channel. Qualitatively, this result can be explained using conservation of mass. Because the tank is wider at the top in the valley case, the gravity current can be taller than $H/2$ without restricting the return flow, which has a speed $u_u - U$. A taller gravity current is usually associated with a faster front speed, because it leads to a higher difference in pressure at the front. Even though the front is taller in the $\phi = 45^\circ$ case, the return flow is still slower than the gravity current.

3.2 Extension of Benjamin's analysis for general ϕ

Here we extend the Benjamin's analysis above for general ϕ. A schematic of the set-up is shown in Fig. 3. Again, conservation of mass gives

$$H^2U = \left(H^2-h^2\right)u_u\,. \tag{20}$$

We then apply Bernoulli along BC and ED. It is important to note that applying Bernoulli at the corner of the tank is a very strong assumption. A streamline along the bottom corner of the tank may not exist, because the valley is no longer symmetric. Bernoulli yields

$$p_B = p_C + \frac{\rho_u U^2}{2}\,, \tag{21a}$$

$$p_E + \frac{\rho_u u_u^2}{2} = p_D + \frac{\rho_u U^2}{2}\,. \tag{21b}$$

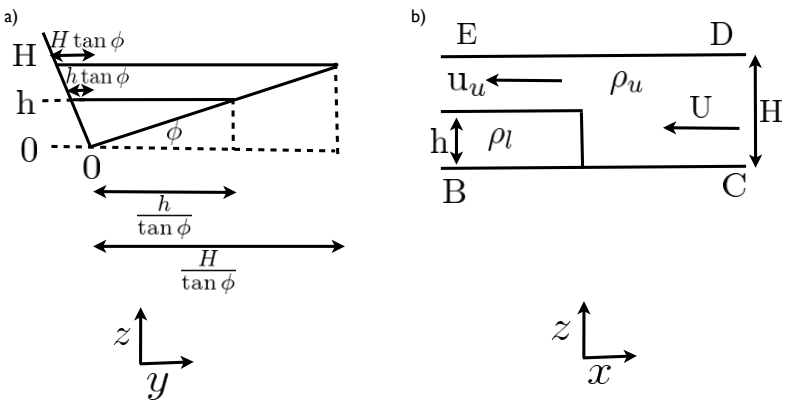

Figure 3: Schematic of the $\theta = 0$ setup for general ϕ. a) shows a cross section view at BE and b) shows a section along the tank at $y = 0$.

Integrating the hydrostatic equation, $\frac{dp}{dz} = -\rho g$, we find that the pressure in the cross-section at BE is

$$p = \begin{cases} p_B - \rho_l g z & \text{if } z < h; \\ p_B - \rho_l g h - \rho_u g\,(z-h) & \text{if } z > h. \end{cases} \tag{22}$$

and the pressure in the cross-section at DC is

$$p = p_C - \rho_u g z. \tag{23}$$

Now we conserve momentum flux, which can be expressed as a sum of the flux of momentum in the positive section of the domain and the flux of momentum in the negative section of the domain,

$$\sum_{i=1,2}\left(\int_0^{\mu_i h}\int_{y/\mu_i}^{h} p_B - \rho_l g z\,\mathrm{d}z\mathrm{d}y + \int_0^{\mu_i h}\int_h^H p_B - \rho_l g h - \rho_u g\,(z-h) + \rho_u u_u^2\,\mathrm{d}z\mathrm{d}y + \right.$$
$$\left.\int_{\mu_i h}^{\mu_i H}\int_{y/\mu_i}^{H} p_B - \rho_l g h - \rho_u g\,(z-h) + \rho_u u_u^2\,\mathrm{d}z\mathrm{d}y = \int_0^{\mu_i H}\int_{y/\mu_i}^{H} p_C - \rho_u g z + \rho_u U^2 \mathrm{d}z\mathrm{d}y\right), \tag{24}$$

where $\mu_1 = \tan\phi$ and $\mu_2 = 1/\tan\phi$. In what follows, the summation is implied by the subscript i. We integrate with respect to z first to give

$$\begin{aligned}
&\int_0^{\mu_i h} p_B\left(h - \frac{y}{\mu_i}\right) - \rho_l g\left(\frac{h^2}{2} - \frac{y^2}{2\mu_i^2}\right)\mathrm{d}y \\
&\qquad + \int_0^{\mu_i h}\left(p_B - \rho_l g h + \rho_u g h + \rho_u u_u^2\right)(H-h) - \rho_u g\left(\frac{H^2}{2} - \frac{h^2}{2}\right)\mathrm{d}y \\
&\qquad + \int_{\mu_i h}^{\mu_i H}\left(p_B - \rho_l g h + \rho_u g h + \rho_u u_u^2\right)\left(H - \frac{y}{\mu_i}\right) - \rho_u g\left(\frac{H^2}{2} - \frac{y^2}{2\mu_i^2}\right)\mathrm{d}y \\
&\qquad = \int_0^{\mu_i H} p_C\left(H - \frac{y}{\mu_i}\right) - \rho_u g\left(\frac{H^2}{2} - \frac{y^2}{2\mu_i^2}\right) + \rho_u U^2\left(H - \frac{y}{\mu_i}\right)\mathrm{d}y\,.
\end{aligned} \tag{25}$$

We then integrate with respect to y to give

$$\begin{aligned}
&p_B\left(\mu_i h^2 - \frac{\mu_i h^2}{2}\right) - \rho_l g\left(\frac{\mu_i h^3}{2} - \frac{\mu_i h^3}{6}\right) + \mu_i h\left(p_B - \rho_l g h + \rho_u g h + \rho_u u_u^2\right)(H-h) \\
&\quad - \mu_i h \rho_u g\left(\frac{H^2}{2} - \frac{h^2}{2}\right) + \left(p_B - \rho_l g h + \rho_u g h + \rho_u u_u^2\right)\left(\mu_i H^2 - \mu_i h H - \frac{\mu_i H^2}{2} + \frac{\mu_i h^2}{2}\right) \\
&\quad - \rho_u g\left(\frac{\mu_i H^3}{2} - \frac{\mu_i H^2 h}{2} - \frac{\mu_i H^3}{6} + \frac{\mu_i h^3}{6}\right) \\
&\quad = p_C\left(\mu_i H^2 - \frac{\mu_i H^2}{2}\right) - \rho_u g\left(\frac{\mu_i H^3}{2} - \frac{\mu_i H^3}{6}\right) + \rho_u U^2\left(\mu_i H^2 - \frac{\mu_i H^2}{2}\right).
\end{aligned} \tag{26}$$

At this point, we can divide through by μ_i to give Eq. 11, meaning that the predictions of Benjamin's theory in an asymmetric valley are the same as those in a symmetric valley, i.e.

$$h^2 = \frac{H^2}{3}. \tag{27}$$

and

$$\begin{aligned}
\mathrm{Fr}_H(\phi) = \frac{U}{\sqrt{g'H}} &= \sqrt{\frac{8}{9\sqrt{3}}} \\
&\approx 0.72.
\end{aligned} \tag{28}$$

Surprisingly, the results are independent of ϕ. It seems likely that this does not reflect the effects of changing ϕ in the real world, and is instead a consequence of the strong assumption that there is a streamline along the bottom corner of the tank. In the symmetric ($\phi = 45°$) case, the streamline must follow the bottom corner of the tank, because the flow must be symmetric (this assertion will be validated by the laboratory experiments). However, in the asymmetric case, it is unlikely that a streamline exists along the bottom corner, because flow down the walls will occur at different speeds. It is possible that a streamline exists somewher on the wall, and this may be something we investigate in future. That $\mathrm{Fr}_H(\phi)$ does not approach $\frac{1}{2}$ as $\phi \to 0°$ may reflect the importance of having both left and right boundaries in a channel flow.

3.3 Prediction of deceleration in the upslope, no tilt case.

One way to predict the deceleration of upslope flow on a flat bottom is to assume a constant Froude number, Fr_H, and therefore assume that the speed of the current is only dependent on local water depth at the front. First we express the speed of the current U in terms of the Froude number, reduced gravity and local water depth, which is a function of distance along the tank.

$$U = \mathrm{Fr}\sqrt{g'H(x)}. \tag{29}$$

If $s = \tan\theta$ is the slope and H_0 is the height of the water at the lock, U can be expressed in terms of the distance of the front from the lock x to give

$$U = \mathrm{Fr}\sqrt{g'H_0}\sqrt{1 - \frac{sx}{H_0}}. \tag{30}$$

Defining $U_0 = \mathrm{Fr}\sqrt{g'H_0}$ yields the differential equation

$$\frac{dx}{dt} = U_0\sqrt{1 - \frac{sx}{H_0}}\,. \tag{31}$$

When we solve this differential equation, we get

$$X = x_0 + U_0 t - \frac{U_0^2 t^2 s}{4H_0}\,. \tag{32}$$

This result was separately derived in the study of shoaling surface gravity currents passing over an underlying slope [8]. For large values of H_0 or small values of s, we expect that the effect of the local water depth will no longer dominate, and other effects like energy conservation will become important. However, for the shallow water in our experiments, the effect of water depth may dominate over these other effects.

4 Laboratory experiments

We first explore the validity of the extended Benjamin results and the predictions for upslope flow by comparing them to the results of laboratory experiments. The experiments explore the parameter range shown in Table 1, where θ and ϕ are defined as in Figure 1.

The tank is 148cm long, 19.8cm wide and 28.7cm tall, and the lock is 36.7cm long, occupying approximately a quarter of the total volume of the tank. The short length of the tank allows us to explore a larger range of θ than in previous studies [11]. For the majority of experiments the tilt is either $\phi = 0°$ or $\phi = 45°$, although $\phi = 15°$ and $\phi = 30°$ cases are also considered.

The density of the fluid in the lock is increased by adding salt, and colored food dye is also added in order to make the current visible. The reduced gravity g' for each experiment is around 6 cm/s^2, although it varies slightly due to inaccuracies in measuring the volume of the tank and the amount of salt added. This should not affect the results, which are nondimensionalized using the particular value of g' for each experiment.

The experiments are recorded in black and white so that the shape and location of the front can be tracked. The camera position varies with experiment (see Figure 4), and a mirror is placed at 45° to the side of the tank in order to give another view of the current. In the $\phi = 0°$ case the mirror shows the shape of the front, and the top view shows the amount of three-dimensionality in the current. In the $\phi \neq 0°$ cases, the mirror allows us to see how symmetric the current is and to check that the top edge of the tank does not obstruct too much of the current.

In the case where $\phi = 0°$ the current is approximately two-dimensional, but a small amount of three-dimensionality occurs due to instabilities and asymmetry in the removal of the gate. In order to quantify the error due to three-dimensional instabilies, three time series of the current are taken at five centimeter intervals across the tank (shown in Figure 5).

One of these time series with $\theta = 6.2°$ is shown in Figure 6. A threshold brightness is chosen to define the front, and a series of points is generated giving the position of the front in each frame. Points are not taken in the first few seconds after the gate is pulled, because there is a short period of readjustment when the gate is removed and the location of the

$\phi(^\circ)$	$\theta(^\circ)$	g' (m/s^2)
0	0	6.6
0	1	6.6
0	1.9	6.4
0	2.9	6.1
0	3.9	6.7
0	4.8	6.8
0	6.2	6.2
0	7.0	6.7
0	8.1	7.4
45	0	5.9
45	0.9	6.0
45	1.9	5.3
45	2.9	6.6
45	3.8	6.2
45	5.2	6.1
45	6.2	6.2
45	6.6	6.3
45	8.0	6.7
15	0	6.7
15	6.2	6.1
30	0	6.2
30	6.2	6.5

Table 1: The parameter range of the experiments.

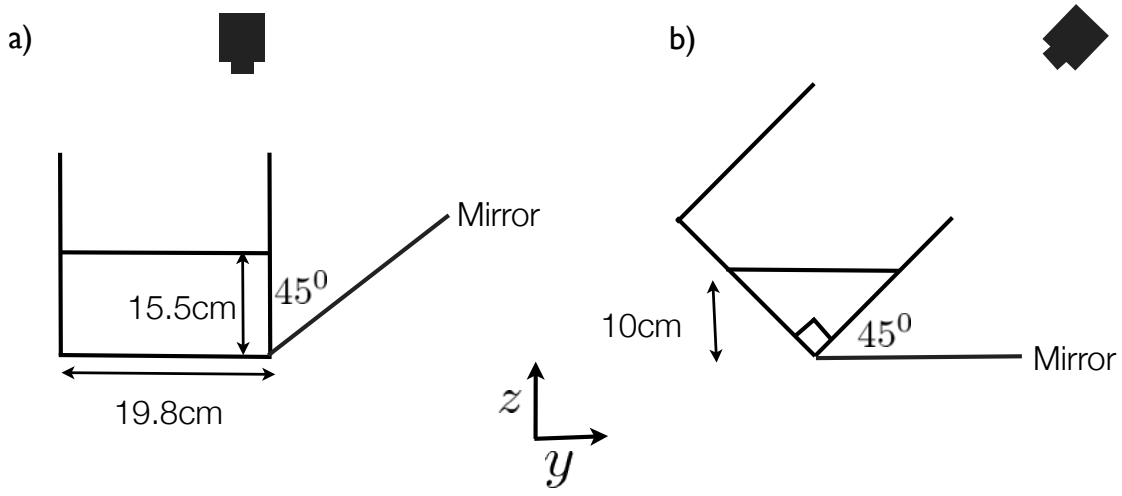

Figure 4: The location of the camera with respect to the tank when a) $\phi = 0°$, and b) $\phi = 45°$.

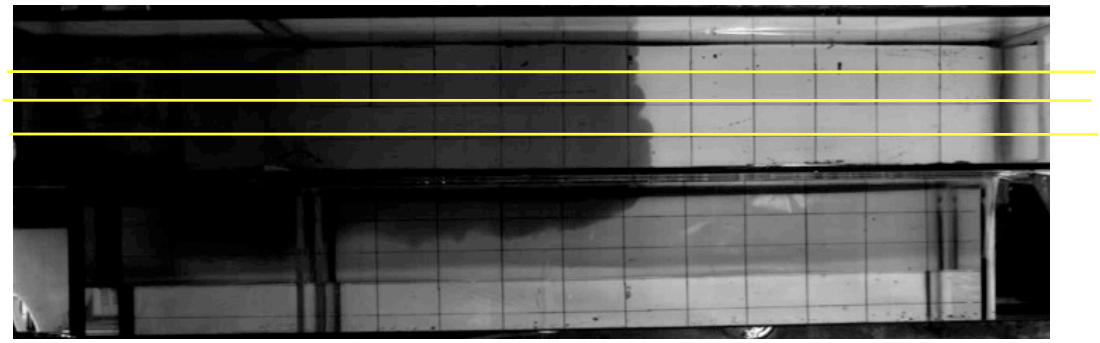

Figure 5: When $\phi = 0°$, three time series are taken at 5cm intervals across the tank.

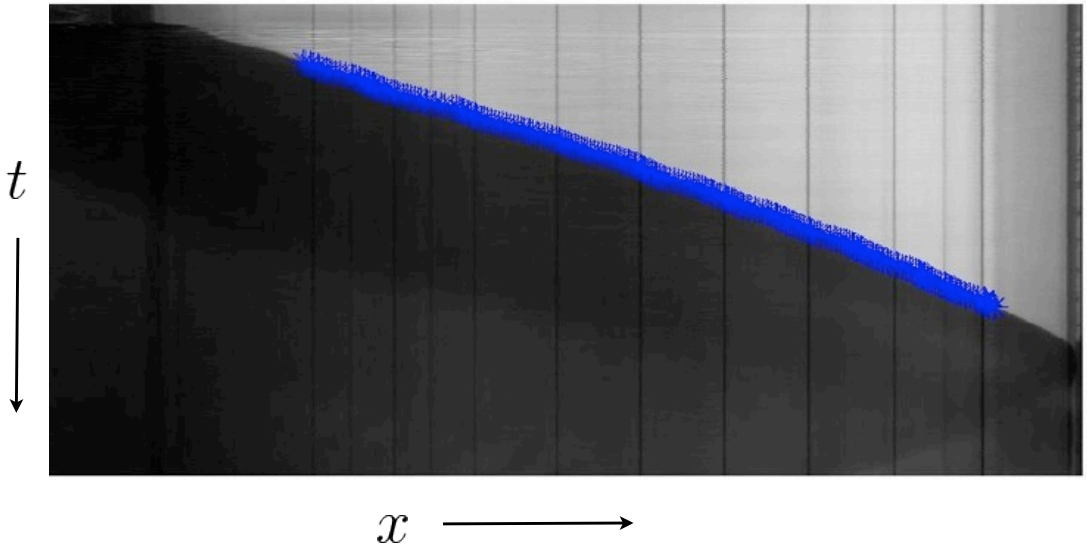

Figure 6: Time series taken when $\theta = 6.2°$ (black and white image) and points showing the loaction of the front away from the initial readjustment.

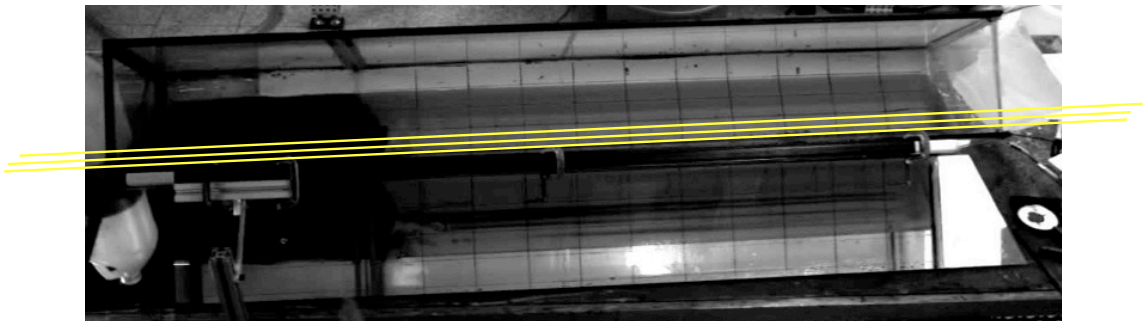

Figure 7: When $\phi = 45°$, ten time series are taken at 1 pixel intervals starting at the tank edge and moving upward.

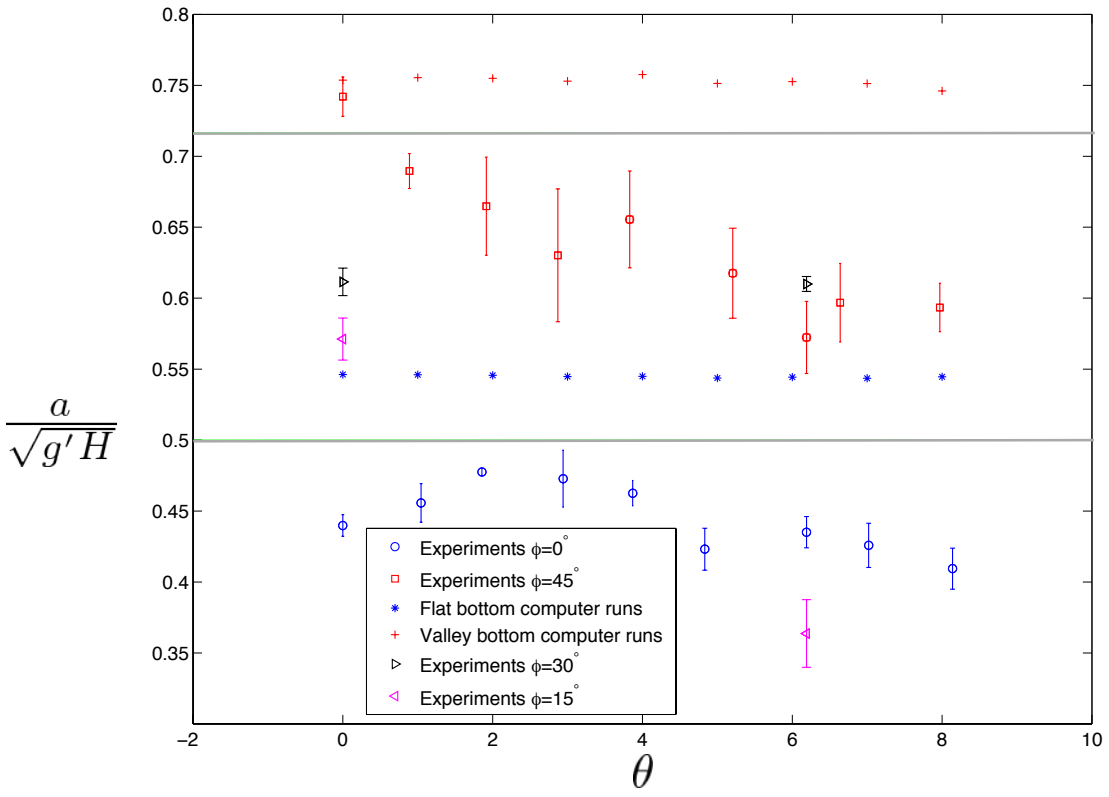

Figure 8: Initial gravity current speed a for the experimental data and numerical simulations, when front position is fitted with the line $X(t) = x_0 + at + bt^2$. The grey lines indicate the theoretical results.

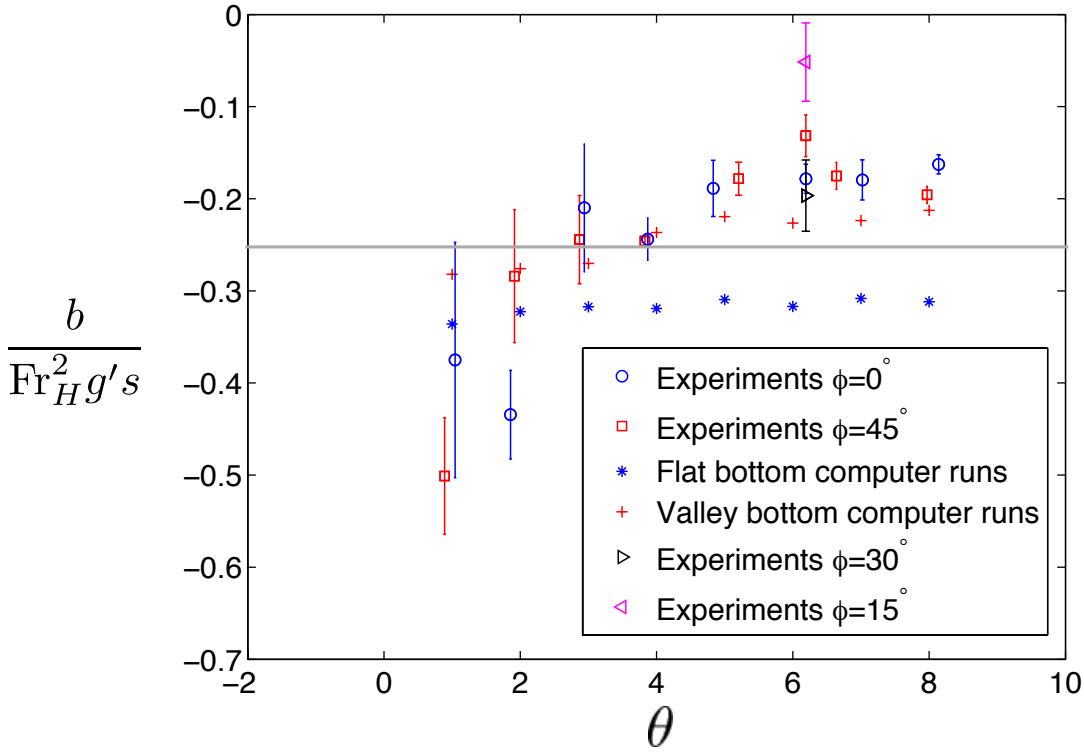

Figure 9: Relative double-acceleration, b for the experimental data and numerical simulations, normalized using $U_0 = \mathrm{Fr}_H\sqrt{g'H_0}$, where Fr_H from the $\theta = 0°$ case is taken as a prediction of Fr_H for all θ when front position is fitted with the line $X(t) = x_0 + at + bt^2$. The grey line indicates the theoretical result.

front is unclear because of the turbulence generated. However, the time at which the gate is pulled is recorded as $t = 0$. Because the theory predicts that $x = x_0 + U_0 t - \frac{U_0^2 t^2 s}{4H_0}$, a quadratic of the form $X(t) = x_0 + at + bt^2$ is fitted to the points for each of the three time series, and then the mean values of a and b are taken. Error bars are generated based on the spread of the three values.

In the case where $\phi \neq 0°$, the current is three-dimensional, and the main source of error is that the time series is not taken in the fastest part of the current (which is at the corner of the tank). In order to mitigate for this, ten time series are taken, starting at the edge of the tank and moving upwards by one pixel for each new time series (see Figure 7). The clearest three to five are used. This is necessary because some of the lines chosen overlap with the edge of the tank, while others are too far from the center line and therefore do not exhibit a well-defined front due to turbulence.

The results of the laboratory experiments are shown in Figures 8, 9 and 10. In all cases $X(t) = x_0 + at + bt^2$ is a good fit to the data. It is likely that the error bars on a and b for $\phi = 45°$ are too small, probably because the lines chosen for time series are not completely parallel to the centerline of the current. If a time series is taken at an angle to the centerline

of the current, both the initial speed a and the relative double-acceleration b are likely to be too small.

In the $\phi = 0°$ case, $\mathrm{Fr}_H(t=0) = \frac{a}{\sqrt{g'H_0}}$ is 10 to 20% less than the predicted value of 0.5. This is typical for the results of lock exchange experiment [13], and is probably because energy conservation is an approximation. While the Benjamin result strictly only applies in the $\theta = 0°$ case, there is no reason why the initial speed should change when $\theta \neq 0°$, and the results show that a remains relatively constant with changing θ. This is consistent with the results of Ottolenghi et al. [11], who also found that the initial speed does not change with rise for a gravity current in a rectangular channel.

In the $\phi = 45°$ case, the inital speed a decreases with increasing rise θ. This is a surprise, and is not yet understood. We hypothesize that the initial velocity of the front in the upslope case is slowed by turbulent momentum transport from the sides of the valley. The flow at the sides of the valley is slower than the flow in the middle, and so any momentum transport from there would cause a slowing of the gravity current.

The normalized deceleration $\frac{b}{\mathrm{Fr}_H g' s}$ is plotted in Figure 9. Given that we expect that $X(t) = x_0 + U_0 t - \frac{U_0^2 t^2 s}{4H_0}$, if a were independent of rise and $U_0 = \mathrm{Fr}_H\sqrt{g'H_0}$ where Fr_H is predicted by the theory for the zero slope case, then

$$\frac{b}{Fr_H^2 g' s} = \frac{1}{4}\,. \tag{33}$$

The data does not fit Eq. (33) very well because a does not fit the theoretical result very well. If we do not assume that Benjamin theory and its extension holds, we expect that

$$\frac{bH_0}{a^2 s} = \frac{1}{4}\,. \tag{34}$$

The data fits Eq. (34) except at small angles, where s is small, causing errors to be magnified (see Figure 10). It is also possible that for small rise, other effects are important for decelerating the flow, for example, energy conservation or viscosity. In fact, it is surprising that our predictions hold so well for the majority of the angles studied.

For the asymmetric valley cases, the results do not agree well with Benjamin's analysis. This is probably because the assumption of a streamline along the bottom of the domain is incorrect. In particular, the case $\theta = 6.2°$, $\phi = 15°$ is very far from the expected value for $\mathrm{Fr}_H(\phi = 15°) = \frac{a}{\sqrt{g'H}}$ of 0.72. However, in these cases b still fits well with Eq. 34, suggesting that the dependence of deceleration on changing water depth still holds. More experiments are needed in order to say anything further about the effects of asymmetry.

5 Numerical experiments

The HYbrid Coordinate Ocean Model (HYCOM) [3], [5], [6] is a hydrostatic model that solves the shallow water equations. We use a two layer set up in the same geometry as the experiments, and with a grid spacing of 0.5cm. g' is approximately the same as the experiments, but the computational Reynolds number is 1200, lower than the experimental Reynolds number of 7000. Varying viscosity does not produce major changes in the model output, so the difference in Reynolds number is not likely to affect the results very

Parameter	Descripton	Value
visco2	deformation-dependent Laplacian viscosity factor	0.05
visco4	deformation-dependent biharmonic viscosity factor	0
veldf2	diffusion velocity (m/s) for Laplacian momentum dissipation	0.01
veldf4	diffusion velocity (m/s) for biharmonic momentum dissipation	0.01
thkdf2	diffusion velocity (m/s) for Laplacian thickness diffusion	0.001
thkdf4	diffusion velocity (m/s) for biharmonic thickness diffusion	0

Table 2: Parameters for diffusion of momentum in the HYCOM model. These parameters aim to compensate for the lack of turbulence in the model. However, our results are fairly robust and small changes to these parameters do not affect the speed and time dependence of the current (though they do change the shape of the front).

much. Further parameters used in HYCOM are shown in Table 2. These parameters were tuned until the shape of the front resembled the laboratory experiments. Changes in these parameters do not affect a and b noticably.

In the numerical model, the front is defined as the first location at which the bottom layer is thicker than 0.5cm. As in the laboratory, $X(t) = x_0 + at + bt^2$ is fitted to a time series of front position.

Figure 11 shows a comparison between the shape of the gravity current in the model and in the laboratory. Away from the front, the height of the current is similar in both cases, but shape of the head of the current in the model is very different from the shape of the head of the current in the experiment. This difference is probably because the model is hydrostatic and the processes at the front are non-hydrostatic. Benjamin analysis requires the assumption that the height of the current tends to a constant value far away from the front. We can see from Figure 11 that this is a valid assumption.

In the numerical simulation, there are a lot more waves at the interface in the valley case than in zero tilt case. The experiments are also a little more irregular, consistent with observations by Monaghan et al. [10]. This might perhaps be due to the two speeds involved in the valley case: the speed of the current along the tank (in the x-direction) and the speed at which the fluid collapses into the middle of the tank (in the y-direction). The irregularity may be more pronounced in the model because it does not allow turbulence so the waves cannot dissipate their energy so easily.

HYCOM allows us to look at the cross-section of the current, something that is difficult to do in the laboratory experiment. In cross-section it is observed that far away from the front, the interface is flat, as one would expect, but near to the front the height of the interface varies in the y-direction, and the center of the current is higher than the edges.

Figures 8, 9 and 10 show the results of both the numerical simulations and laboratory experiments. In the numerical experiments, $\mathrm{Fr}_H(t=0) = \frac{a}{\sqrt{g' H_0}}$ is higher than the predictions of Benjamin's analysis and its extension. This is unsurprising because in the model, Bernoulli does not necessarily apply along the top and bottom boundaries and because the model is hydrostatic, it does not conserve momentum exactly. Faster speeds are often available when this sort of condition is relaxed [12].

In the HYCOM model, the initial speed a is independent of θ. It is hypothesized

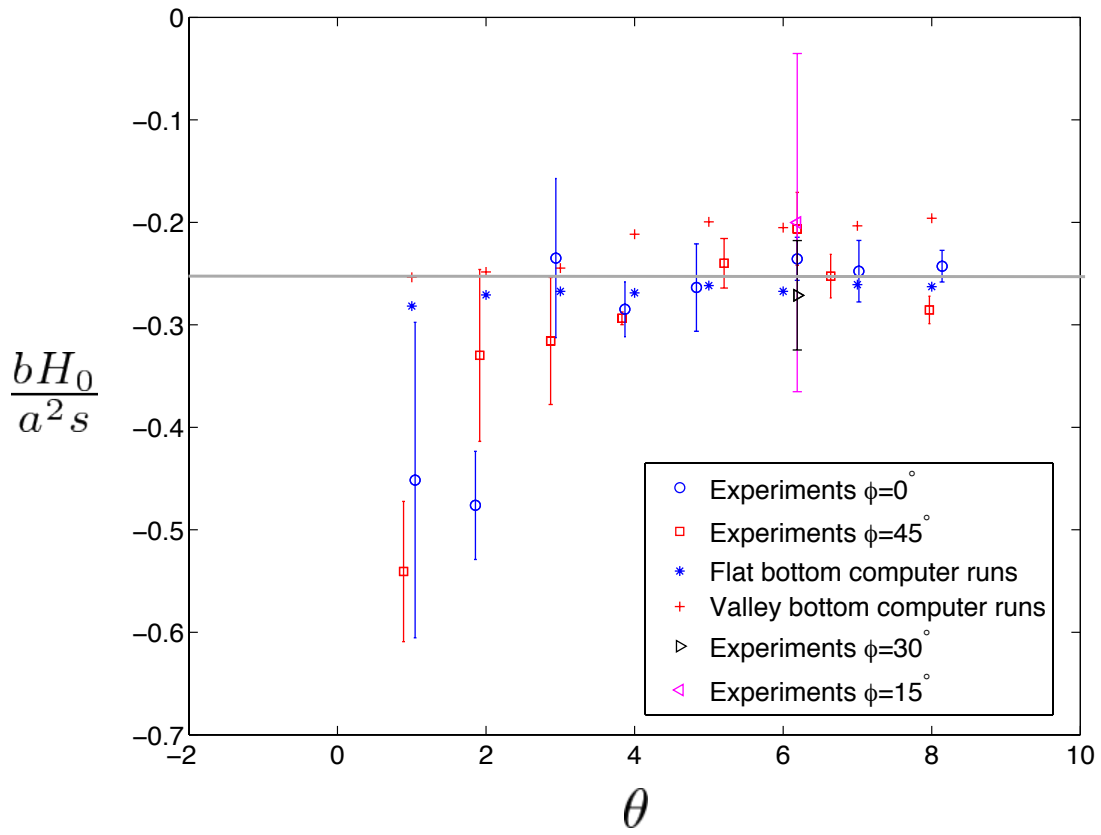

Figure 10: Relative double-acceleration b for the experimental data and numerical simulations, normalized using the measured initial speed a when front position is fitted with the line $X(t) = x_0 + at + bt^2$. The grey line indicates the theoretical results.

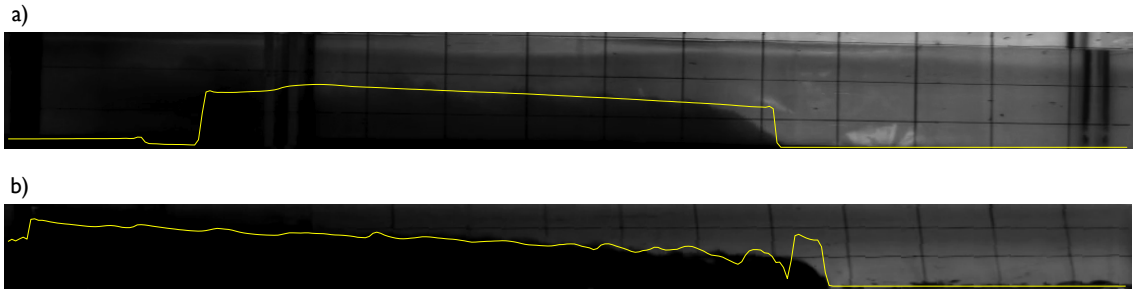

Figure 11: Comparison of head shape between the numerical model (yellow line) and the experiments for the case a) $\phi = 0°$, $\theta = 0°$ and b) $\phi = 45°$, $\theta = 0°$.

that turbulent momentum transport from the sides of the valley is responsible for the slower current in the laboratory. This fits well with the numerical results because turbulent momentum transport does not occur in the HYCOM model, so it is expected that a should be independent of θ in the model.

6 Summary and Discussion

Theory, experiments and numerics agree that a gravity current in a valley is faster than a gravity current in a rectangular channel, and specifically that $\mathrm{Fr}_H = 0.72$ for a symmetric valley where $\phi = 45°$. While theory, experiments and numerics differ slightly, this is not unexpected, because the theory makes assumptions about conservation of energy that are not necessarily followed in the experiments or numerics.

Laboratory experiments show that, unlike in the $\phi = 0°$ case, the initial speed of the gravity current in the $\phi = 45°$ case decreases as θ increases and it is unclear what causes this. However, we hypothesize that lateral turbulent momentum transport moves momentum away from the fast moving center of the current into the slower moving edges where the depth is much shallower.

To first order, the upslope flow speed seems to be controlled by the local depth of the fluid in the parameter range explored here. Gravitational acceleration, bottom drag, and viscosity are secondary effects, and the role of these need further investigation, since in currents with bigger H_0, smaller s or smaller g', the role of these effects will probably be larger. This is likely to be the case in real-world applications like sea breezes up valleys, where H_0 is not clearly defined. For small slopes, the predictions based on local fluid depth do not fit the data well, and this is likely to be because some of these other effects are important.

In an attempt to compare our results with Monaghan et al. [10]'s prediction for the time dependence of front position, a fit to a log-log plot of the front position in the zero slope cases of both the laboratory and numerical experiments was taken. However, in both cases it was found that front position $X \sim t$ rather than $X \sim t^{\frac{4}{5}}$. It may be that the time series taken in our experiments and numerics was not long enough. Monaghan et al. used a tank that was more than fifteen lock lengths long, whereas our tank was only about four lock lengths long. It is also possible that the assumption of self-similarity in Monaghan et al.'s theory is invalid in our flow, but this seems unlikely since the current has the same self-similar shape as Monaghan et al. describe.

More investigation is needed into why the initial speed predicted by the model differs from the initial speed measured in the laboratory. This could be done by simulating the flow in a Direct Numerical Simulation that includes lateral momentum transfer via turbulence. Alternatively, an experiment in which the viscosity of the flow was increased (so that turbulence was surpressed) could be performed, though this would introduce viscous boundary layer effects.

There are still many questions to be answered in understanding how topography steers gravity currents. It would be interesting to look at the effect of changing the angle inside the valley, since the sides of most valleys in the real world slope less than those in my experiment. We would also like to look at the transfer between kinetic and potential energy

in the numerical model, because it is surprising that this does not appear to play a role in the upslope speed of a gravity current.

7 Acknowledgements

I would like to thank my advisors, Eric Chassignet, Bruce Sutherland, Claudia Cenedese and Paul Linden. I would also like to thank Flavien Gouillon and Alexandra Bozec for their help in setting up the HYCOM model.

References

[1] T. B. Benjamin, *Gravity currents and related phenomena*, J. Fluid Mech., 31 (1968), pp. 209 – 248.

[2] V.K. Birman, E. Meiburg, and M. Ungarish, *On gravity currents in stratified ambients*, Phys. Fluids., 19 (2007).

[3] R Bleck, *An oceanic general circulation model framed in hybrid isopycnic? cartesian coordinates.*, Ocean Modeling, 4 (2002), pp. 55–88.

[4] R. E. Britter and P. F. Linden, *The motion of the front of a gravity current travelling down an incline*, J. Fluid Mech., 99 (1980), pp. 531–543.

[5] E.P. Chassignet, LT Smith, GR Halliwell, and R Bleck, *North atlantic simulations with the hybrid coordinate ocean model (hycom): Impact of the vertical coordinate choice, reference density, and thermobaricity*, J. Phys Oceanogr., 33 (2003), pp. 2504–2526.

[6] GR Halliwell, *Evaluation of vertical coordinate and vertical mixing algorithms in the hybrid-coordinate ocean model (hycom)*, Ocean Modeling, 7 (2004), pp. 285–322.

[7] H.E. Huppert, *The propagation of two-dimensional and axisymmetric viscous gravity currents over a rigid horizontal surface*, J. Fluid Mech., 121 (1982), pp. 43–58.

[8] G. H. Keulegan, *The motion of saline fronts in still water*, Natl Bur. Stnd. Rep., 5813 (1958).

[9] B. M. Marino and L. P. Thomas, *Dam-break release of a gravity current in a power-law channel section*, J. Phys.: Conf. Ser., 296 (2011), pp. 1–10.

[10] J.J. Monaghan, C.A. Meriaux, H.E. Huppert, and J.M. Monaghan, *High reynolds number gravity currents along v-shaped valleys*, European Journal of Mechanics - B/Fluids, 28 (2009), pp. 651 – 659.

[11] L. Ottolenghi, C. Adduce, V. Armenio, R. Inghilesi, and F. Roman, *Large eddy simulation of lock-exchange gravity currents moving on upsloping beds.* Unpublished manuscript.

[12] J. O. Shin, S. B. Dalziel, and P. F. Linden, *Gravity currents produced by lock exchange*, J. Fluid Mech., 521 (2004), pp. 1–34.

[13] B.R. Sutherland, D Polet, and M. Campbell, *Gravity currents shoaling on a slope*, Phys. Fluids., 25 (2013).

[14] T Zemach and M Ungarish, *Gravity currents in non-rectangular cross-section channels: Analytical and numerical solutions of the one-layer shallow-water model for high-reynolds-number propagation*, Physics of Fluids, 5 (2012), p. 026601.

Modelling the Evolution of an Iron-Rich Layer in a Double Diffusive Regime

Barbara Zemskova
University of North Carolina at Chapel Hill

September 22, 2013

1 Introduction

1.1 Problem Background

Thanks to the recent success of the astroseismology component of the Kepler mission, renewed attention has been given to the mechanism that causes time-varying luminosity, or pulsations, in β-Cepheid stars. The pulsation mechanism for regular Cepheids is well-understood in terms of the kappa-mechanism. The pulsations are dependent on the opacity κ of the ionized layers of a star. This opacity is controlled by radiative processes, namely the absorption and re-emission of photons as they move away from the stellar core. However, the electrons in an ionized layer block photons and prevent radiative heat transport through the layer. From Kramer's Law, the opacity of an outer layer is found by: $\kappa = \rho/T^{3.5}$, where ρ is the density in the layer and T is the temperature. If the outward pressure beneath the layer decreases, then the layer contracts inwards, and its volume decreases. The energy that is released upon contraction of the layer partially ionizes the helium atoms, rather than increases the temperature of the layer, thus increasing the opacity. Heat is then transported through the layer less efficiently, so pressure builds up beneath the layer. This pressure is eventually enough to push the layer outward, thus increasing its volume. As the layer expands, the electrons recombine with the ions, and the density within the layer drops, such that the opacity consequently decreases, allowing greater heat transport through the layer. Eventually the pressure beneath the layer drops again, and the cycle repeats, resulting in periodic variations in the star's luminosity [3, 9].

However, the role of helium partial ionization zones, as presented in the standard kappa mechanism, is sensitively dependent on the temperature of the star. For a hot star with effective temperature greater than 7500 K, the partial ionization zones are located too close to the star's outer surface, and they are unable to drive significant pulsations. For cooler stars with effective temperature less than 5500 K, the partial ionization zones are too close to stellar core, and heat can be transported by convection rather than by radiation, and does not build up beneath the partial ionization zones. The regular Cepheids, which are located on the instability strip, are within the perfect temperature range to exhibit these pulsations described by the kappa mechanism. The β-Cepheids, on the other hand, have too high temperatures to have helium partial ionization zones, so one would not expect them

to pulsate. However, these stars do exhibit pulsations. It has been recently thought that they may have iron partial ionization zones that could explain their periodic pulsations in a similar way [4]. These stars are larger and brighter than regular Cepheids, so it is important to understand the mechanism that drives their pulsations for other astrophysical applications as well.

If such iron partial ionization layers could be responsible for pulsations in β-Cepheids, how can these layers form and is there evidence that such iron layers exist in stars? To see how iron layers may form, note that there are two opposing forces that act on atoms: radiative levitation and gravitational settling. The radiative levitation acts away from the stellar core due to the upward momentum on atoms exerted by photons that are emitted from the core, while the gravitational settling acts toward the stellar core. The total settling velocity, V, of an atom can be expressed as:

$$V = (g_{rad} - g)\frac{mD}{kT} \tag{1}$$

where g_{rad} is radiative acceleration (away from the core), g is the gravitational acceleration (toward the core), m is the element mass, D is the molecular diffusion coefficient, k is the Boltzman constant, and T is the stellar temperature [8]. The force balance is element-dependent, not only because of the element mass, but also because the radiative acceleration depends on the chemical species in question. Therefore, the sign of the total settling velocity, which is determined by the sign of $g_{rad} - g$, is element-dependent. This dependency is illustrated in the work of [7], where profiles for selected chemical species are shown (see Figure (1)). For each element, Figure (1) shows $\log(g_{rad}/g)$ as a function of the distance away from the stellar core, such that -6 on the x-axis indicates outer layers, and 0 indicates proximity to the stellar core. For certain elements, such as Mg, $\log(g_{rad}/g) < 0$ in all regions, so the radiative levitation is less than the gravitational settling, and the total settling velocity is always toward the core. For other elements, such as Mn, Ca, and Fe, there are regions where the radiative levitation exceeds the gravitational settling. The case of iron is particularly interesting because there is a region where $\log(g_{rad}/g) > 0$, with regions where $\log(g_{rad}/g) < 0$ both above and below it. As a result, there is a zone where the iron atoms converge in a "pinched layer", as shown in Figure (2). It is due to this mechanism that iron layers could exist near a stellar photosphere.

In this study, we attempt to describe several characteristics of iron "pinched layer", such as the thickness of the layer, iron profile, and maximum iron concentration. Additionally, we show that depending on the system parameters and the mass of iron, the layer may be either double diffusively or fully convectively unstable, which would alter the iron concentration profile. Note that the analysis in this project is not specific to iron atoms, and the results can be generalized to any system that fits the formulation described above.

1.2 Governing Equations

Here, we consider a domain that is thin compared with the local system scaleheight and assume that both the background temperature and adiabatic temperature gradients are constant within that region. In astrophysical systems, the background temperature decreases away from the stellar core toward the outer layers, thus the background temperature gradient is negative. However, because the fluid is not incompressible, the adiabatic temperature

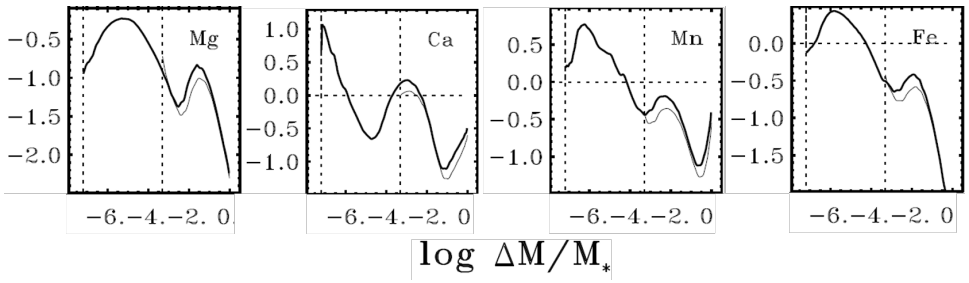

Figure 1: Profiles of radiative acceleration of selected elements normalized with respect to local gravity as a function of distance from the stellar core for a main sequence star. For certain elements like Mg, gravitational settling exceeds the radiative levitation. For some other elements, there are layers where radiative levitation exceeds gravitational settling [7]).

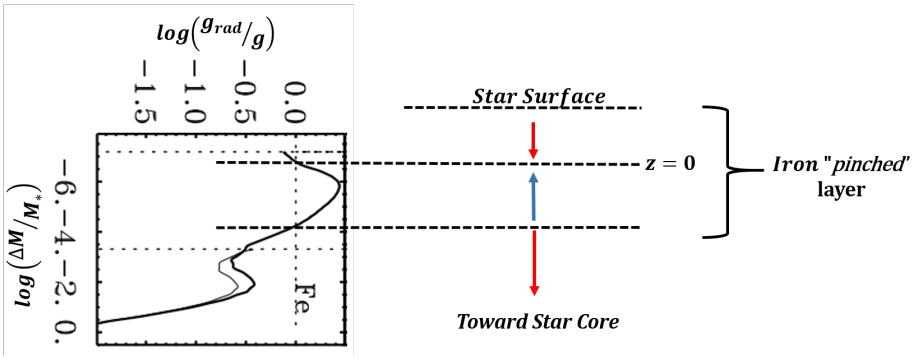

Figure 2: Model of a system with an iron converging zone based on a profile from Figure (1). In this "pinched" layer, total settling velocity is positive (radiative levitation exceeds gravitational settling) for $z < 0$, and total settling velocity is negative (gravitational settling exceeds radiative levitation) for $z > 0$.

gradient is nonzero. Since the difference between background and adiabatic temperature gradients is positive, the combined effect of the temperature gradients makes the fluid stably stratified . The governing equations for the system are ([5]):

$$\frac{\partial \vec{u}}{\partial t} + \vec{u} \cdot \nabla \vec{u} = -(1/\rho_0)(\nabla p - \rho \vec{g}) + \nu \nabla^2 \vec{u}, \tag{2}$$

$$\frac{\partial T}{\partial t} + \vec{u} \cdot \nabla T + w \left(\frac{\partial \bar{T}_{back}}{\partial z} - \frac{\partial \bar{T}_{adiab}}{\partial z} \right) = \kappa_T \nabla^2 T, \tag{3}$$

$$\frac{\partial C}{\partial t} + \vec{u} \cdot \nabla C + \frac{\partial}{\partial z}(V_s C) = \kappa_C \nabla^2 C, \tag{4}$$

$$\nabla \cdot \vec{u} = 0 \tag{5}$$

where $\vec{u} = (u, v, w)$ is the velocity field, T is the temperature, C is the iron concentration, p is the pressure, κ_T is the thermal diffusivity, κ_C is the diffusivity of the iron atoms, ν is the molecular viscosity, $\bar{T}_{back}$ is the background temperature and $\bar{T}_{adiab}$ is the adiabatic temperature. The only change to the original advection-diffusion equations is the added "settling" velocity term V_s for the iron, which depends on the vertical position z. These equations are then non-dimensionalized with the following length and time scales, as described in [6]:

$$d = [l] = \left(\frac{\kappa_T \nu}{g \alpha \bar{T}_z} \right)^{1/4}, \tag{6}$$

$$[t] = \frac{d^2}{\kappa_T}, \tag{7}$$

$$[u] = \frac{\kappa_T}{d}, \tag{8}$$

$$[T] = \bar{T}_z d, \tag{9}$$

$$[C] = \frac{\alpha \bar{T}_z d}{\beta}. \tag{10}$$

where we have defined for simplicity $\bar{T}_z = \frac{\partial \bar{T}_{back}}{\partial z} - \frac{\partial \bar{T}_{adiab}}{\partial z}$, α is the thermal expansion coefficient, and β is the compositional contraction coefficient. In this non-dimensionalization, the length scale d corresponds to the typical horizontal length scale of a finger, and the time scale is the thermal diffusion time scale. From non-dimensionalization, the governing equations can be re-written as follows with 2 non-dimensional parameters:

$$\frac{1}{\mathrm{Pr}}\left(\frac{\partial \vec{u}}{\partial t} + \vec{u} \cdot \nabla \vec{u}\right) = -\nabla p + (T - S)\hat{k} + \nabla^2 \vec{u}, \tag{11}$$

$$\frac{\partial T}{\partial t} + \vec{u} \cdot \nabla \vec{T} + w = \nabla^2 T, \tag{12}$$

$$\frac{\partial C}{\partial t} + \vec{u} \cdot \nabla \vec{C} + \frac{\partial}{\partial z}(V_s C) = \tau \nabla^2 C, \tag{13}$$

$$\nabla \cdot \vec{u} = 0 \tag{14}$$

where Pr is the Prandtl number, defined as $\mathrm{Pr} = \nu/\kappa_\mathrm{T}$, and $\tau = \kappa_C/\kappa_T$ is the ratio of the diffusion coefficients. Here, $V_s(z)$ is the non-dimensionalized settling velocity. For double diffusive convection to occur, it is important that $\tau \ll 1$. When a warm fluid parcel with

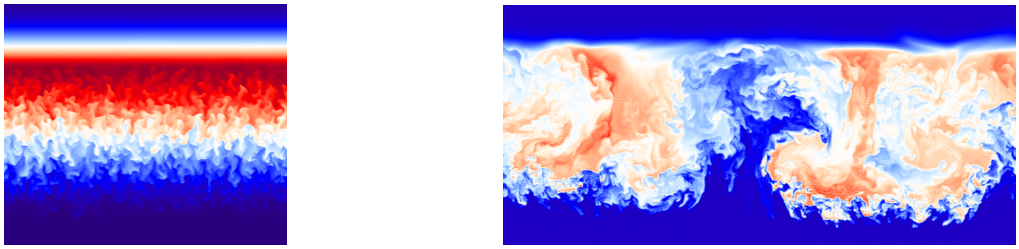

Figure 3: An example of fingering convection, a type of double diffusive instability (left) for a system with $\tau = \text{Pr} = 0.1$, $s = 0.001$, $C_0 = 466$, and an example of full convection (right) with $\tau = \text{Pr} = 0.1$, $s = 0.01$, $C_0 = 4500$. Warm colors show fluid parcels with higher iron concentration, cooler colors with lower concentration. Fingers with higher iron concentration extend downward, and the ones with lower iron concentration extend upward.

high compositional concentration is moved downward into cooler ambient fliud, it naturally rises because it is more buoyant. However, if the thermal diffusion time scale is less than the amount of time it takes the parcel to move back to its original position, then the fluid parcel loses its heat, but retains its concentration. As a result, it becomes heavier than the ambient and sinks, forming a downward finger. Equally, a cool parcel with low composition concentration would form an upward extending finger when perturbed into a warm layer. The result of such double diffusive instability is fingering convection, an example of which is shown in Figure (3). An example of a fully-convective system is shown to the right for comparison.

2 Evolution of the Background Profiles

We begin our investigation by considering the evolution of the iron concentration, assuming there is no fluid motion. Thus, we seek solution to a one-dimensional advection-diffusion equation with respect to the iron concentration C:

$$\frac{\partial C}{\partial t} + \frac{\partial}{\partial z}(V_s C) = \tau \frac{\partial^2 C}{\partial z^2}. \tag{15}$$

Here $V_s(z)$ is the iron settling/levitation velocity, defined as $V_s = -sz$ where s is a constant. Indeed, from the schematic of the iron "pinched layer" in Figure (2), we see that we can approximate $V_s(z)$ near the center of this layer ($z = 0$) with a linear function. We model $V_s(z)$ such that the downward gravitational settling dominates in the upper half of the domain ($z > 0$), and the upward radiative levitation dominates in the lower half of the domain ($z < 0$). Therefore we choose $V_s = -sz$ with $s > 0$.
An analytical solution to this equation is a Gaussian in the form:

$$C(z,t) = \frac{C_0}{\sqrt{2\pi f(t)}} e^{-\frac{z^2}{2f(t)}}, \tag{16}$$

where $\sqrt{f(t)}$ is the width of the Gaussian at time t. C_0 is a non-dimensional term that is related to total column density of iron, such that $C_{dim} = C_0[C]$ and $\int C_{dim} dz$ is the column

density of iron in the layer,Σ_0. This implies that $C_0 = \frac{\alpha \bar{T}_z}{\beta \Sigma_0} d$.
Plugging in (16) into (15), we can solve for $f(t)$:

$$f = \frac{\tau + \tilde{b} e^{-2st}}{s}, \tag{17}$$

where $\tilde{b}$ is some initial width of the Gaussian at time t_0. Note that $f(t) \to \tau/s = f_\infty$ as $t \to \infty$. Therefore, in absence of instabilities the ultimate laminar steady state concentration profile is in the form:

$$C(z) = \frac{C_0}{\sqrt{2\pi f_\infty}} e^{-\frac{z^2}{2f_\infty}}. \tag{18}$$

3 Stability of Double Diffusive Convection with Particle Settling

As the width of the Gaussian decreases and the iron concentration in the "pinched layer" increases, the concentration profile becomes steeper and steeper at a certain place in the layer, and the system may eventually become double diffusively unstable. In order to study the stability of the iron layer to double diffusive convection one must analyze the problem allowing a spatially-varying background that also evolves in time. However, as such formulation is not trivial, we begin by approaching the problem in a simpler way.

3.1 Stability of a system with linear gradients

The Gaussian concentration profile from (16) has maximum gradient at the inflection points that occur at $z = \pm\sqrt{f}$. Further, it is most unstable where the maximum concentration gradient is positive, at $z = -\sqrt{f}$. In this approach, we perform a local stability analysis near this most unstable point $z = -\sqrt{f}$ to determine whether the system becomes double diffusively unstable or not. Near this point, the background temperature and concentration profiles can be approximated by linear functions with constant gradients $\bar{T}_z = \frac{\partial \bar{T}_{back}}{\partial z} - \frac{\partial \bar{T}_{adiab}}{\partial z}$ and $\frac{\partial \bar{C}_{back}}{\partial z}$. We also assume that the time scale for the development of the instabilities is much less than the time scale for the evolution of the background. We can then apply the "frozen-in" approximation, which assumes that the background temperature and concentration gradients are constant not only in space, but also in time. These simplifications recover the approach from [1], but the equations contain an additional settling term in the iron concentration equation. We then apply the linear stability theory by linearizing the

governing equations, such that:

$$\frac{1}{\mathrm{Pr}}\frac{\partial u}{\partial t} = -\frac{\partial p}{\partial x} + \nabla^2 u, \tag{19}$$

$$\frac{1}{\mathrm{Pr}}\frac{\partial v}{\partial t} = -\frac{\partial p}{\partial y} + \nabla^2 v, \tag{20}$$

$$\frac{1}{\mathrm{Pr}}\frac{\partial w}{\partial t} = -\frac{\partial p}{\partial z} + (T - C) + \nabla^2 w, \tag{21}$$

$$\frac{\partial T}{\partial t} + w = \nabla^2 T, \tag{22}$$

$$\frac{\partial C}{\partial t} + \frac{w}{R_0} + V\frac{\partial C}{\partial z} = \tau\nabla^2 C, \tag{23}$$

$$\frac{\partial u}{\partial x} + \frac{\partial v}{\partial y} + \frac{\partial w}{\partial z} = 0. \tag{24}$$

Here, we have defined another nondimensional parameter, $R_0 = 1/(\partial\bar{C}/\partial z)$, where $\partial\bar{C}/\partial z$ is the non-dimensional gradient of iron concentration at $z = -\sqrt{f}$. In the dimensional sense, R_0 is the ratio of the stabilizing temperature gradient to the destabilizing compositional gradient, such that ${R_0}^{dim} = (\alpha {\bar{T}_z}^{dim})/(\beta {\bar{C}_z}^{dim})$. At the point where the Gaussian is most unstable ($z = -\sqrt{f}$), $\bar{C}_z$ is maximum and R_0 is minimum, so we have:

$$\bar{C}_z = \frac{C_0}{f\sqrt{2\pi e}}, \tag{25}$$

and

$$R_0 = \frac{f\sqrt{2\pi e}}{C_0}. \tag{26}$$

Note how in the linearized equation for particle concentration, we have also assumed that the settling velocity is locally constant at value V. Expressing the quantities u, w, p, T, C in the form $Q = \hat{Q}e^{ilx+ikz+\lambda t}$, where $\hat{Q}$ represents the mean quantity, we obtained a cubic for the growth rate λ, which is similar to the original cubic of [1], but has additional imaginary terms in the coefficients that are associated with the particle settling.

$$\lambda^3 + a_2\lambda^2 + a_1\lambda + a_0 = 0, \text{ where} \tag{27}$$

$$a_2 = ikV + K^2(\tau + 1 + \mathrm{Pr}) \tag{28}$$

$$a_1 = K^2(ikV)(\mathrm{Pr} + 1) + \mathrm{K}^4(\tau\mathrm{Pr} + \tau + \mathrm{Pr}) + \frac{\mathrm{Pr}(\mathrm{m}^2 + \mathrm{l}^2)}{\mathrm{K}^2}(1 - \frac{1}{\mathrm{R}_0}) \tag{29}$$

$$a_0 = \frac{\mathrm{Pr}}{K^2}(ikV)(K^6 + (m^2 + l^2)) + K^6\mathrm{Pr}\tau + \frac{\mathrm{Pr}(\mathrm{m}^2 + \mathrm{l}^2)}{\mathrm{K}^2}(\tau - \frac{1}{\mathrm{R}_0}) \tag{30}$$

$$\tag{31}$$

where $K^2 = l^2 + m^2 + k^2$. However, after examining the solutions to the cubic for different l and k values, we find that the fastest growing mode is still $k = 0$, as in the case without settling. This means that the added settling term, ikV, does not impact the initial development of the instabilities.

Given the nondimensional parameters Pr, τ, and R_0 of the system, one can determine the maximum growth rate of the instability λ_{max} and its associated horizontal wave number l_{max}. We then take $k = 0$ and maximize λ with respect to l, resulting in a quadratic:

$$b_2\lambda^2 + b_1\lambda + b_0 = 0, \text{ where} \tag{32}$$

$$b_2 = 1 + \mathrm{Pr} + \tau \tag{33}$$

$$b_1 = 2l^2(\tau + \mathrm{Pr} + \tau\mathrm{Pr}) \tag{34}$$

$$b_0 = 3\tau\mathrm{Prl}^4 + \mathrm{Pr}(\tau - \frac{1}{\mathrm{R_0}}); \tag{35}$$

λ_{max} and and l_{max} can be found by solving (27) and (32) simultaneously, using a Newton method for instance.

3.2 Estimation of width of the Gaussian at the onset of instability

[1] showed that the stability of the system depends on R_0. A system is double diffusively unstable when $1 < R_0 < 1/\tau$. If $R_0 > 1/\tau$, then the system is stable, and as R_0 becomes less than 1, the system becomes fully convective. We can therefore use these criteria to determine whether an iron layer is stable, double diffusively unstable, or fully convective. In the early stages of the evolution the iron layer is mostly likely stable, but as the Gaussian concentration profile contracts with time, $\bar{C}_z$ increases and R_0 decreases at the point of maximum instability, $z = -\sqrt{f}$. We can then estimate the width of the Gaussian profile when a system first becomes marginally unstable to double diffusion. This happens when $R_0 = 1/\tau$, which from (26) corresponds to:

$$f(t^*) = f_{crit} = \frac{C_0}{\tau\sqrt{2\pi e}}. \tag{36}$$

We see that whether an iron layer, with given input parameters τ, Pr, and s, ever becomes unstable and at which width the instabilities occur, depends on the total surface density of the system. Figure (4) shows $\sqrt{f_{crit}/f_\infty}$ as a function of C_0. If $f_{crit} < f_\infty$, the evolving concentration profile would reach a steady state laminar solution before attaining the width at which double diffusive instabilities appear. However, if $f_{crit} > f_\infty$, then double diffusive instabilities appear when the concentration profile reaches the width $\sqrt{f_{crit}}$. We define C_{crit} as the input mass for which $f_{crit} = f_\infty$: $C_{crit} = \frac{\tau^2\sqrt{2\pi e}}{s}$. For systems with $C_0 < C_{crit}$, double diffusive instabilities are not predicted to occur, and the concentration profile should relax to a laminar solution. Conversely, for systems with $C_0 > C_{crit}$, the system is predicted to be double diffusively unstable. The subsequent evolution of the concentration profiles for such systems are analyzed in the next section.

4 Simplified model for the long-term evolution of the system

In order to study the evolution of layers that become double diffusively unstable, we need to consider the turbulent transport of iron in addition to diffusion and to the settling/levitation

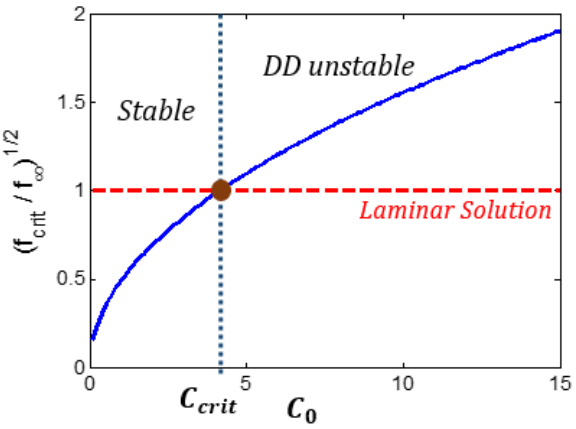

Figure 4: Diagram of stable regions and double diffusively unstable regions with respect to input mass C_0. The system is stable if $f_{crit}/f_\infty \leq 1$. Therefore, if $C_0 < C_{crit}$ and the initial concentration profile has width greater than $\sqrt{f_\infty}$, the steady state concentration profile will converge to a laminar Gaussian solution of (18) and the system is stable. However, if $C_0 < C_{crit}$, double diffusive instabilities will develop before the system converges to a laminar solution.

balance. The 1D advection-diffusion equation used contains an additional term to model this effect:

$$\frac{\partial C}{\partial t} + \frac{\partial F_s}{\partial z} + \frac{\partial}{\partial z}(V_s C) = \tau \frac{\partial^2 C}{\partial z^2}, \tag{37}$$

where F_s is the turbulent flux, which can be defined in terms of a Nusselt number, Nu as:

$$F_s = -\tau \frac{\partial C}{\partial z}(\mathrm{Nu} - 1). \tag{38}$$

Therefore, (37) can be re-written as:

$$\frac{\partial C}{\partial t} + \frac{\partial}{\partial z}(V_s C) = \tau \frac{\partial}{\partial z}\left(\frac{\partial C}{\partial z}\mathrm{Nu}\right). \tag{39}$$

[2] proposed a new turbulent transport parametrization for double diffusive convection, which takes the form:

$$\mathrm{Nu} = 1 + \hat{\mathrm{C}}^2 \frac{\lambda^2}{\tau \mathrm{l}^2(\lambda + \tau \mathrm{l}^2)} \tag{40}$$

where $\hat{C} = 7$ is an empirical constant, and where λ and l, the growth rate and the wavenumber of the fastest growing mode respectively, are found from the linear stability analysis described in Section 3.1. Note that if the layer is stable and $\lambda = 0$, Nu $= 1$, so Equation (39) recovers the original advection-diffusion equation (15).
At steady state, we must solve:

$$V_s C = -szC = \tau \mathrm{Nu} \frac{\partial \mathrm{C}}{\partial \mathrm{z}}. \tag{41}$$

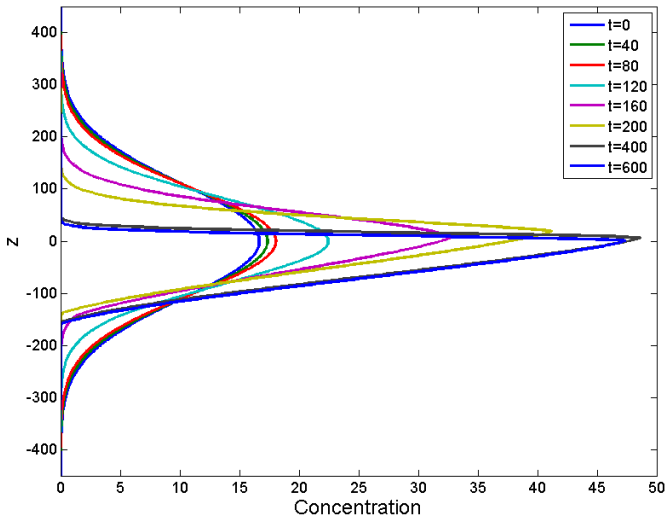

Figure 5: Time evolution of the iron concentration from numerical solution with the following parameters: $\tau = \mathrm{Pr} = 0.1$, $s = 0.001$, and $C_0 = 466$. The concentration profile is initially stable, but becomes double diffusively unstable after contraction, and is no longer of Gaussian form.

We wish to find an analytical expression for this steady-state solution. The difficulty arises because Nu is a function of λ and l, which depend on $R_0 = 1/C_z$, so Nu is a function of $\bar{C}_z$ as well.

We first solve (39) numerically to observe the time evolution of the iron concentration. Figure (5) shows the iron concentration profiles in the layer at different time steps. The concentration profile initially takes a stable Gaussian form, but eventually contracts enough to become double diffusively unstable. Once this happens, Nu becomes larger than 1 and turbulent fluxes become significant. After a while, we observe that the concentration converges to a steady-state, but it is no longer Gaussian. Figure(6) shows $\frac{\partial C}{\partial z}$ as a function of z in this steady-state solution. The profile has 3 parts: above z_1 and below z_2, $C_z < \tau$, so the system is stable to double diffusion and $\mathrm{Nu} = 1$. Between z_1 and z_2, $\tau < C_z < 1$, so the layer is double diffusively unstable. Since at z_1 and z_2 the instabilities are just triggered, $\lambda = 0$ and $\mathrm{Nu} = 1$, the steady-state at those two points implies (see Equation (41)):

$$-sz_1 C(z_1) = \tau C_z(z_1) = \tau^2, \tag{42}$$

$$-sz_2 C(z_2) = \tau C_z(z_2) = \tau^2. \tag{43}$$

Here we find that $C(z_1) = -f_\infty \tau / z_1$ and $C(z_2) = -f_\infty \tau / z_2$. For $z > z_1$ and for $z < z_2$, the system is stable and the concentration profile is Gaussian. Therefore, these parts of the

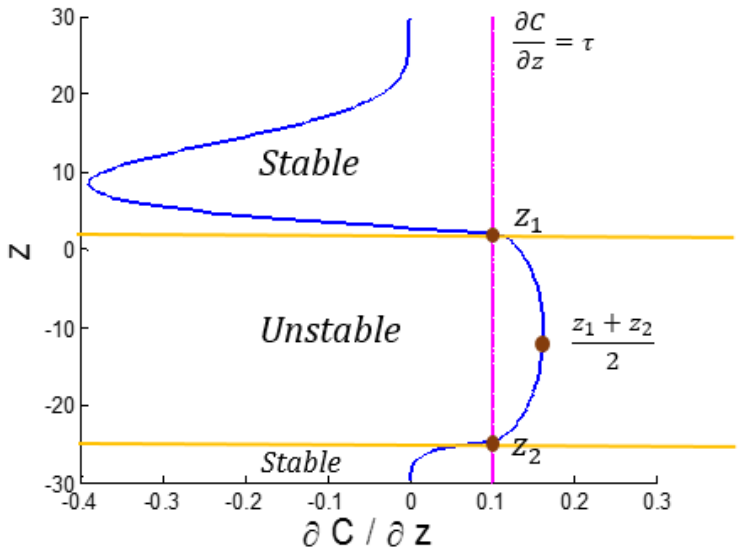

Figure 6: Schematic of the theoretical approach to a steady state concentration profile. The plot shows the derivative of steady state concentration profile from 1D simulation, $\frac{\partial C}{\partial z}$. The parts where $\frac{\partial C}{\partial z} < \tau$ are stable, while the parts where $\frac{\partial C}{\partial z} > \tau$ are double diffusively unstable. The two points, z_1 and z_2 are located where $\frac{\partial C}{\partial z} = \tau$.

concentration profile are expressed as:

$$C(z \geq z_1) = \frac{C_u}{\sqrt{2\pi f_\infty}} e^{-\frac{z^2}{2f_\infty}}, \tag{44}$$

$$C(z \leq z_2) = \frac{C_L}{\sqrt{2\pi f_\infty}} e^{-\frac{z^2}{2f_\infty}}. \tag{45}$$

where C_u and C_L are two constants to be determined. Using the expressions for $C(z_1)$ and $C(z_2)$, C_u and C_L can be expressed as:

$$C_u = -\sqrt{2\pi f_\infty} e^{\frac{{z_1}^2}{2f_\infty}} \frac{f_\infty \tau}{z_1}, \tag{46}$$

$$C_L = -\sqrt{2\pi f_\infty} e^{\frac{{z_2}^2}{2f_\infty}} \frac{f_\infty \tau}{z_2}. \tag{47}$$

In the region where $z_2 < z < z_1$, $C_z > \tau$. We approximate C_z using a parabola: $C_z = \tau + k(z_1 - z)(z - z_2)$ for some value k. The concentration profile in this region is then approximately:

$$C(z_2 < z < z_1) = C(z_2) + \int_{z_2}^{z} (\tau + k(z_1 - z)(z - z_2))\, dz =$$
$$C(z_2) + \tau(z - z_2) + \frac{k}{2}(z_1 - z_2)(z - z_2)^2 - \frac{k}{3}(z - z_2)^3. \tag{48}$$

Plugging in z_1 for z and the fact that $C(z_1) = -f_\infty \tau / z_1$, we obtain an equation relating k, z_1, and z_2.

Finally, we assume that at $\hat{z} = (z_1 + z_2)/2$ there is a balance between the advective flux $V_s C$ and turbulent flux F_s, such that:

$$-s\hat{z}C(\hat{z}) = \tau \mathrm{Nu}(\mathrm{C_z}(\hat{z}))\mathrm{C_z}(\hat{z}). \tag{49}$$

As a result of these assumptions, we obtain 3 equations for 3 unknowns: k, z_1, and z_2. Equation (50) is obtained from mass conservation by integrating the piecewise concentration profile. Equation (51)is found from plugging in z_1 for z in the cubic equation for $C(z_2 < z < z_1)$. Equation (52) incorporates the advective and turbulent fluxes at $\hat{z}$.

$$C_0 + \frac{\tau f_\infty}{z_1} e^{\frac{{z_1}^2}{2f_\infty}} \sqrt{\frac{\pi f_\infty}{2}} \left[1 - \mathrm{erf}\left(\frac{\mathrm{z_1}}{\sqrt{2\mathrm{f_\infty}}}\right)\right] + \frac{\tau f_\infty}{z_2} e^{\frac{{z_2}^2}{2f_\infty}} \sqrt{\frac{\pi f_\infty}{2}} \left[1 + \mathrm{erf}\left(\frac{\mathrm{z_2}}{\sqrt{2\mathrm{f_\infty}}}\right)\right] = 0 \tag{50}$$

$$f_\infty \tau - z_1 z_2 \left[\tau + \frac{k}{6}(z_1 - z_2)^2\right] = 0 \tag{51}$$

$$\frac{(\tau z_1 + z_2)^2}{4 z_1 z_2} - \mathrm{Nu}(\mathrm{C_z}(\hat{\mathrm{z}})) \left[\tau + \frac{\mathrm{k}(\mathrm{z_1} - \mathrm{z_2})^2}{4}\right] = 0 \tag{52}$$

These 3 equations can be solved for k, z_1, and z_2 using Newton's method for a given set of input parameters: τ, Pr, s, and C_0. Once these are known, piecewise steady state concentration profile $C(z)$ is:

$$C(z > z_1) = -\frac{f_\infty \tau}{z_1} e^{-\frac{z^2 - {z_1}^2}{2f_\infty}}, \tag{53}$$

$$C(z_2 \geq z \leq z_1) = -\frac{f_\infty \tau}{z_2} + \tau(z - z_2) + \frac{k}{2}(z_1 - z_2)(z - z_2)^2 - \frac{k}{3}(z - z_2)^3, \tag{54}$$

$$C(z < z_2) = -\frac{f_\infty \tau}{z_2} e^{-\frac{z^2 - {z_2}^2}{2f_\infty}}. \tag{55}$$

For example using $\tau = \mathrm{Pr} = 0.1$, $s = 0.01$, $f_\infty = 10$, Figure (7) shows the solutions for z_1, z_2, and k as functions of C_0. The value for z_1 approaches zero as C_0 increases, while z_2 decreases nonlinearly. The value of k decreases sharply and approaches a constant. These patterns are true for any choice of different input parameters of τ, Pr and s.

Furthermore, in Section 3.1 we defined $R_0 = 1/C_z$ and stated that double diffusive instabilites occur for $1 < R_0 < 1/\tau$. For $R_0 < 1$, the system is predicted to become fully-convective. In the unstable region $z_2 < z < z_1$, we approximated C_z as a parabola, which has a maximum at $\hat{z} = (z_1 + z_2)/2$, such that $C_{zmax} = \tau + (k/4)(z_1 - z_2)^2$. From $R_{0min} = 1/C_{zmax}$, for a given set of τ, Pr, s, we can find C_{conv}, the value of C_0 above which the layer is predicted to become fully convective. Figure (8) shows an example for a system with $\tau = \mathrm{Pr} = 0.1$, $s = 0.01$, $f_\infty = 10$. For this example, the theory predicts that the system will be fully convective if $C_0 > C_{conv} = 4600$.

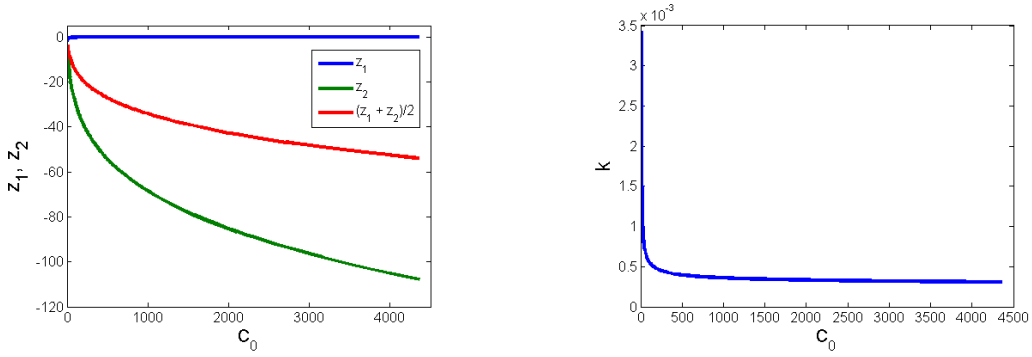

Figure 7: Plot on the left shows z_1 and z_2 as functions of input mass C_0; z_1 approaches zero, z_2 decreases nonlinearly as C_0 increases. Plot of the right shows k as a function of C_0; k rapidly decreases and approaches a constant as C_0 increases. Both of the plots are examples for a system with input parameters: $\tau = Pr = 0.1$, $s = 0.01$, $f_\infty = 10$.

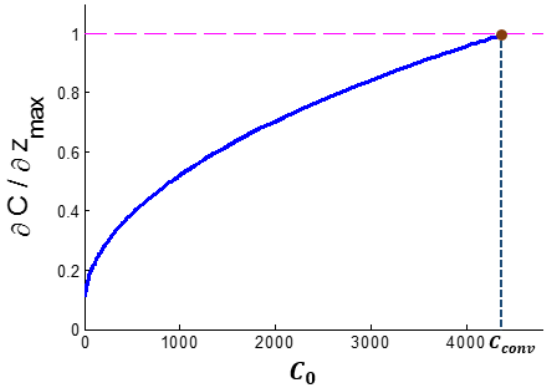

Figure 8: A plot of maximum $\frac{\partial C}{\partial z}$ as a function of C_0 for a system with $\tau = Pr = 0.1$, $s = 0.01$, $f_\infty = 10$. The piecewise steady state theory predicts C_{conv}, the input mass enough to make the system fully convective for which maximum $\frac{\partial C}{\partial z} = 1$.

5 Results of Numerical Simulations

In order to evaluate the theoretical predictions for the onset of the double diffusive instabilities, the steady state concentration profiles, and the surface densities above which double diffusive instabilites or full convection may occur, we have ran several 3-D numerical simulations.

5.1 Set-up of the 3D code

Our code solves equations (11) - (14) in a triply-periodic domain. The temperature perturbations are initialized with random noise. The initial concentration profile is a Gaussian of a form:

$$C_{init}(z) = \frac{C_0}{2\pi f_{init}} \tag{56}$$

where $f_{init} > f_{crit}$, chosen such that the iron layer is initially stable. This way we can determine whether the concentration profile will converge to a laminar solution, or whether double diffusive instabilites or full convection develop. To save computational time, f_{init} was typically taken to be $1.1 - 2f_{crit}$, where f_{crit} is given in Equation (36).

The typical width of a double diffusive finger being $7 - 10d$, the width of the domain (x-direction) was chosen as $100d$ to allow at least 10 fingers to develop in the system. From preliminary computations in a 2-dimensional domain, we have also that found artificial shear develop in the solutions. Therefore, we ran 3D simulations in a domain with a depth of $15d$ which is thick enough to allow the fluid motions to be 3-dimensional (to avoid this problem), but also thin enough to decrease the computational cost of the simulations.

The height of the domain (z direction) depended on the input parameters of the simulation. For most of the simulations, the vertical velocity was prescribed as a sine function of the form $V(z) = -K\sin((2\pi z)/\Gamma_z)$, where Γ_z is the height of the domain and $K = (s\Gamma_z)/(2\pi)$. Note that $V(z)$ must be a periodic function in order to maintain the periodicity of the domain. However, since we have assumed that vertical velocity decreases linearly with height in the system, the initial Gaussian profile had to be contained within the linear part of the sine function as shown in Figure (9a). Therefore, the height of the domain had to be chosen large enough. The vertical extent of the domain was on the order of $1000d$, and had to be increased with higher C_0 since f_{crit} increases with C_0. To reduce the computational cost, some of the later simulations at very high C_0 were performed with a high-order polynomial function for settling velocity of the form $V = -sz(m^{20} - z^{20})/(m^{20})$, where $m = \Gamma_z/2$. This formulations allowed the vertical extent of the domain to be smaller, since the linear part of this function encompasses a greater fraction of the domain than that of the sine function. Figure (9) shows the comparison of the proportion of the linear part of two functions with respect to an initial concentration profile. The polynomial formulation can reduce the required height of the domain by a half.

5.2 Low input mass regime

This section compares the theoretical predictions of the concentration profile to the 3D numerical simulations. From the analytical analysis, it is predicted that a system with $C_0 < C_{crit}$ will converge to a laminar steady state solution given by Equation (18). However,

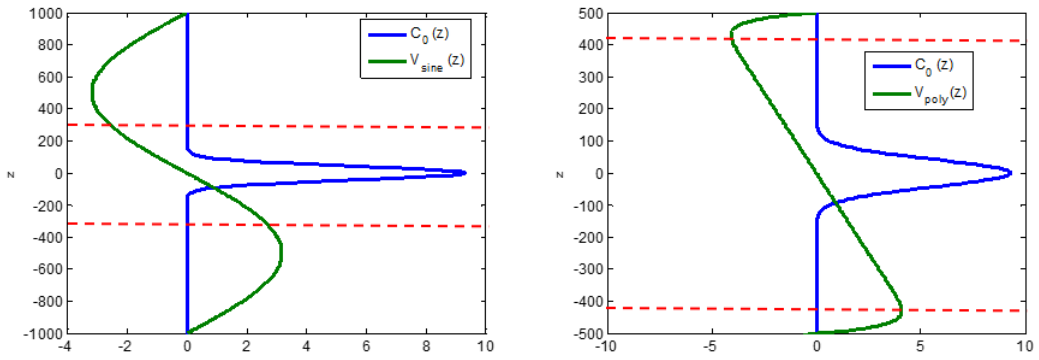

Figure 9: Initial condition $C_{init}(z)$ and two expressions for settling velocity: sinusoidal (left) and polynomial (right). The red dashed lines indicate the region where the settling velocity functions are linear. The polynomial function is linear for a greater fraction of the domain than the sinusoidal function.

for a system with an input mass $C_{crit} < C_0 < C_{conv}$, then the system is predicted to develop double diffusive instabilities, and a steady state profile can be, in theory, approximated by the piecewise profile from Equations (53) - (55). In this study, we fixed $\tau = \Pr = 0.1$ and varied f_∞ from 10 to 100 (corresponding to settling velocity gradients $s = 0.01$ and 0.001 respectively). We examined systems with $C_0 = 0.5C_{crit}$ and $C_0 = 2C_{crit}$ to determine whether the double diffusive instabilities occured. For the system with $f_\infty = 10$, we find that $C_{crit} = 4$ and for $f_\infty = 100$, $C_{crit} = 46$. Figure (10) shows horizontally-averaged concentration profiles $C_{init}(z)$ at steady state, with $f_\infty = 10$ in the upper panel and $f_\infty = 100$ in the lower panel. The systems with $C_0 = 0.5C_{crit}$ are on the left side, and the systems with $C_0 = 2C_{crit}$ are on the right side. Each plot shows the theoretical prediction for the steady state profile from piecewise theory in blue, using a laminar Gaussian solution in green, and finally, the actual 3D horizonatally-averaged concentration profile in red dots. When $C_0 < C_{crit}$, the theory predicts that the system should be stable. The results from 3D simulations and the theoretical prediction overlay the laminar Gaussian steady state solution, showing that the system is indeed stable. When $C_0 > C_{crit}$, the theory predicts that double diffusive instabilities will develop. The 3D simulation results deviate from the laminar Gaussian steady state solution due to the effects of double diffusive instabilities in the region where $z < 0$. Furthermore, the steady state concentration profiles calculated from (53)-(55) fit the 3D simulation results extremely well. This shows that our estimates of the steady state profile of low-mass iron-rich layers are good predictors of the actual results.

5.3 Higher input mass regime

We have also investigated whether the theoretical approximations are valid for systems with higher input C_0. For $\tau = \Pr = 0.1$ and $f_\infty = 10, 100$, we ran simulations for $C_0 = 100C_{crit}$. To verify that the theory is valid for different values of τ, we also ran a simulation with $\tau = 1/30$, $\Pr = 0.1$, $f_\infty = 10$, $s = 1/300$. Figure (11) shows the concentration profiles $C(z)$ for $\tau = 0.1$, $f_\infty = 10$ on the left and $f_\infty = 100$ on the right, and the simulation with $\tau = 1/30$

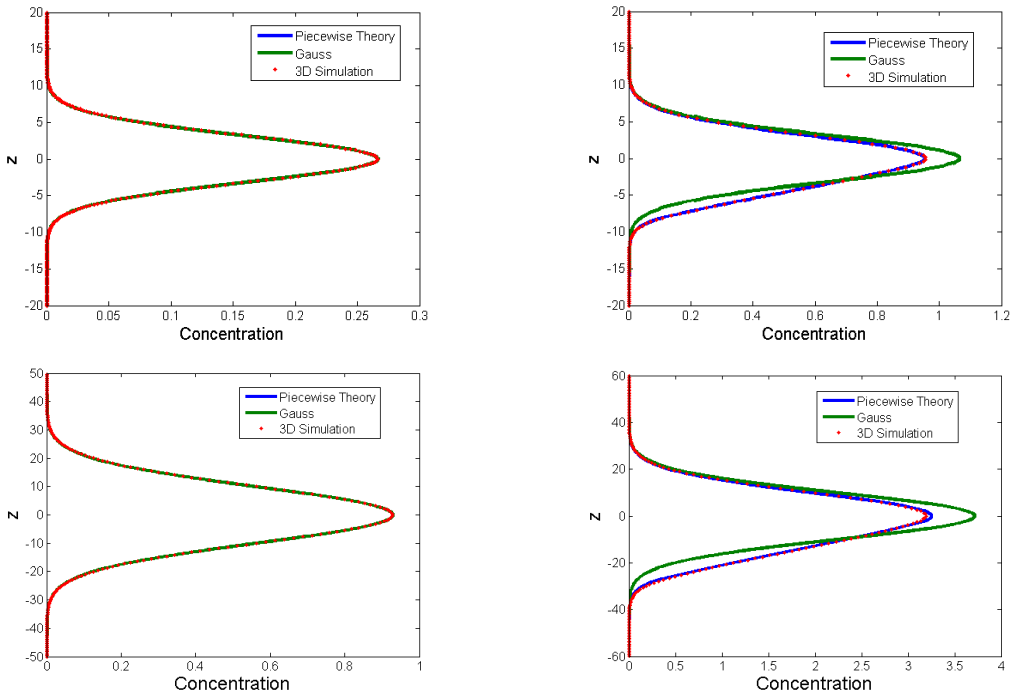

Figure 10: Steady state concentration profiles as a function of z-direction for systems with low input mass. The figures in the upper panels are from simulations with $f_\infty = 10$, and the figures in the lower panels with $f_\infty = 100$. The figures on the left side are from simulations with input mass below C_{crit}, such that $C_0 = 0.5C_{crit}$, and the figures input mass above C_{crit}, such that $C_0 = 2C_{crit}$. The blue line indicates concentration profile from piecewise analytical theory, green line is Gaussian laminar solution, and red dots show horizontally-averaged concentration from 3D simulations.

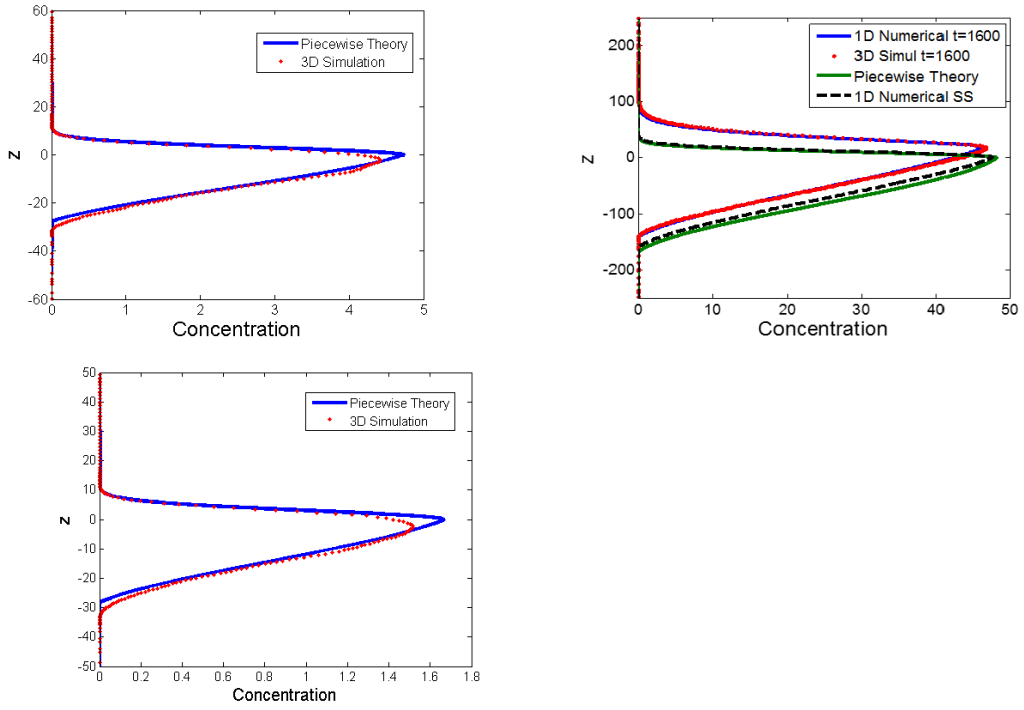

Figure 11: Concentration profiles as a function of z-direction for systems with higher input $C_0 = 100C_{crit}$. The figure on the left is from simulations with $f_\infty = 10$, $\tau = 0.1$, the figure on the right has $f_\infty = 100$, $\tau = 0.1$, and the figure on the bottom has $f_\infty = 10$, $\tau = 1/30$.

on the bottom. In the first two cases, the 3D simulation results and theoretical piecewise concentration profile agree very well. The last 3D simulation took a long time, and we were unable to reach a steady state in a given time frame. Therefore, for the $f_\infty = 100$ simulation, a 1D simulation based on Equation (39) with the same input parameters was run to steady state, and the results from the 1D simulation were compared with the results from the 3D simulations as well as the theoretical piecewise steady state concentration profile. The figure shows an agreement between 1D simulation and 3D horizontally-averaged simulation results at the same time $t = 1600$, and an agreement between the steady state concentration profiles from 1D simulation and the piecewise analytical formula. Therefore, the transient solutions of the 3D problem can be well-approximated by solving Equation (39), and the steady state concentration profiles are given by analytical piecewise approximation (53)-(55) even for systems with higher input mass.

5.4 Fully-convective regime

Finally, we tested the theoretical prediction for the input mass criteria for the transition from double diffusively unstable to the fully convective regime. Because the simulations with high input mass and large f_∞ values are computationally expensive, we ran simulations with $f_\infty = 10$, $\tau = \mathrm{Pr} = 0.1$, $s = 0.01$. For these input parameters, $C_{conv} = 4400$, so we ran simulations with greater input mass, $C_0 = 4500$, for which the system is predicted to be fully

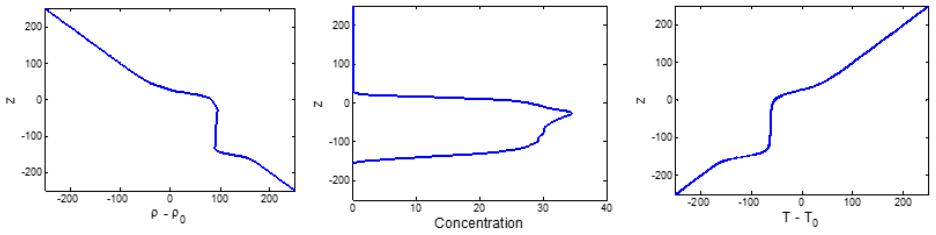

Figure 12: Vertical profiles of density deviations from background density, compositional concentration, and temperature deviations from background temperature for a fully convective simulation with input parameters: $f_\infty = 10$, $\tau = \mathrm{Pr} = 0.1$, $s = 0.01$, $C_0 = 4500$. The density and temperature profiles appear fully mixed within the convective layer.

convective, and with lower input mass, $C_0 = 4000$ and $C_0 = 3500$, which are predicted to be only double diffusively convective. However, the results from the 3D simulations showed that all three systems were fully convective, making the prediction for C_{conv} inaccurate. Such results may be due to the limitation of the validity of assumptions in the theory for the prediction of a steady state profile, as described in Section 4. A better estimate for C_{conv} needs to be derived in the future.

Figure (12) shows the vertical profiles of the density deviations away from background density ρ_0, from the compositional concentration, and the temperature deviations away from the background temperature T_0, from the simulation with $C_0 = 4500$. Both density and temperature profiles appear to be well-mixed in the fully convective region, while the concentration profile is not as well mixed by convection. As a system becomes closer to being fully convective, the background temperature gradient is no longer maintained constant, violating one of the assumptions of the piecewise theory. What determines the thickness of the fully convective layer as a function of C_0, τ, Pr, and s remains to be determined. In addition, we observed gravity waves generated in 3D simulations with high input mass, which could also alter the transport in and out of the "pinched" layer. The generation of the waves can be observed from the horizontal velocity field, as shown in Figure (13).

6 Discussion

In this work, we modelled the distribution of iron in the outer layer of a star, assuming that it settles from the top and is levitated from the bottom. We found that the laminar steady state solution, in absence of convective instabilities in the system, approaches a Gaussian distribution, which is dependent on 3 parameters: the total amount of iron, the ratio of thermal diffusivity to particle diffusivity, and the slope of the settling velocity profile.

We also studied the iron concentration profiles in systems which become double diffusively unstable. In particular, we found an analytical prediction for total mass of iron in the system, for a given Prandtl number, diffusivity ratio, and settling velocity slope, above which the system becomes double diffusively unstable rather than approach the laminar steady state solution. We also developed a semi-analytical piecewise concentration profile that approximates the steady state solution for systems that are double diffusively unsta-

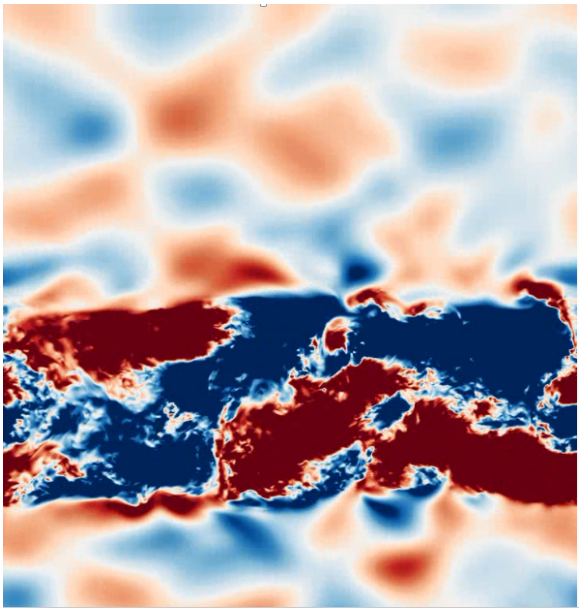

Figure 13: Horizontal velocity field for xz-plane from a fully convective 3D simulation. Positive velocity is in warm colors, negative in cool colors. The 45-degree alternative pattern of velocity field indicates gravity waves travelling toward the "pinched layer" (super-saturated region).

ble. Our theoretical predictions agreed well with the vertical concentration profiles from 3D simulation runs for several values of input masses, Prandl numbers, diffusivity ratios and settling velocity slopes. In addition, we found that the transient concentration profiles obtained from a 1D code that solves (39) agree with the vertical concentration profiles from 3D simulations at the same time steps. These conclusions are important for the development of the stellar evolution models, especially if iron layers do play a role in the pulsations of certain stars. These models are complex, and the incorporation of a 1D approximation or a piecewise theoretical solution into the model is more suitable than running a full 3D simulation for the double diffusive process.

Since this work developed tools to approximate steady state and transient solutions for systems that are either stable or double-diffusively unstable, the next step is to develop a theoretical model for the concentration profiles in a fully convective system. However, as the system becomes fully convective, the underlying assumption of constant background temperature gradient is violated. In addition, as the fluid is continuously mixed in such system, defining a steady state or reaching a steady state through simulations may be difficult. In the 3D simulations with full convection, we observed gravity waves that transport material into and out of convective layer. The influence of these waves most likely also needs to be taken into consideration when developing a model for a fully convective layer.

7 Acknowledgements

I would like to thank my advisor, Pascale Garaud, for her invaluable guidance and continuous supervision throughout the summer and help with revising this report. I am also thankful to the directors for organizing a smooth program, and to all of the faculty members and summer participants for insightful discussions and a memorable summer.

References

[1] P.G. Baines and A.E. Gill, *On thermohaline convection with linear gradients*, J. of Fluid Mechanics, 37 (1969), pp. 289–306.

[2] J.M. Brown, P. Garaud, and S. Stellmach, *Chemical transport and spontaneous layer formation in fingering convection in astrophysics*, Astrophysical Journal, 768 (2013), pp. 34–95.

[3] J. P. Cox, *On second helium ionization as a cause of pulsation instability in stars*, Astrophysical Journal, 138 (1963), pp. 487–536.

[4] M. Kiriakidis, M.F. El Eid, and W.Glatzel, *Heavy element opacities and the pulsations of beta cepheid stars*, Monthly Notices of the Royal Astronomical Society, 255 (1991), pp. 1–5.

[5] E.A. Spiegel and G. Veronis, *On the boussinesq approximation for a compressible fluid*, Astrophysical Journal, 131 (1960), pp. 442–447.

[6] A. Traxler, S. Stellmach, P. Garaud, T. Radko, and N. Brummell, *Dynamics of fingering convection i: Small-scale fluxes and large-scale instabilities*, J. of Fluid Mechanics, 677 (2011), pp. 530–553.

[7] S. Turcotte, J. Richer, and G. Michaud, *Consistent evolution of f. stars: Diffusion, radiative accelerations, and abundance anomalies*, Astrophysical Journal, 504 (1998), pp. 559–572.

[8] S. Vauclair and G. Vauclair, *Element segregation in stellar outer layers*, Ann. Rev. Astronomy and Astrophysics, 20 (1982), pp. 37–60.

[9] S.A. Zhevakin, Russ. Astrophysical Journal, 30 (1953), pp. 161–170.

On the Collision of Sea Breeze Gravity Currents

Karin van der Wiel

September 30, 2013

1 Introduction

The diurnal cycle of solar heating often generates sea and land breezes in coastal regions. Differences in heating over land and sea create horizontal density differences that set up the sea/land breeze front. The horizontal extent of these circulations have been shown to depend strongly on latitude [12, 22, 1]. In England (50°N) sea breeze fronts have been observed 100 km inland [20]; in southern Australia (32°S) fronts travel as far as 400 km [6].

The large horizontal extent implies that for narrow peninsulas, islands or seas, converging sea breezes from opposing shorelines can meet. Horizontal convergence of sea breezes may be responsible for direct initiation of deep convection [4]. Examples of this include, southern Florida where the convergence of sea breezes is one of the dominating controls of the location of thunderstorm complexes [3, 15]; the Cape York Peninsula (Australia) where the North Australian Cloud Line is linked to double sea breezes [13]; and the Hector thunderstorms over the Tiwi Islands (Australia) which get part of their convective strength from the convergence generated by two nearby coastlines [4, 8]. Over bodies of water not wider than 500 km convergence of two land breezes can be expected [10, 9].

Converging sea breezes have been studied using observational data and numerical simulations. These studies have focused on different aspects of the collision. For example, vertical velocities were found to be maximum if the sea breezes were to collide between 14:00 and 17:00 local time [21], given a sea breeze propagation rate across an island the optimal width of the island resulting in maximum vertical velocities can thus be computed. The sea breeze fronts that collided before or after this time window were slightly weaker and therefore generated weaker vertical motions in the numerical simulations performed in [21]. The height of the sea breeze front is influenced by both the direction of the surface wind and the direction of low-level shear. Depending on whether those point in the same direction the effects on meeting currents can be one of two: either the gravity current height remains unchanged on both shores or at one shore the height might be enhanced while it is being surpressed at the other shore, increasing the height difference during collision [11]. Finally, [7] discusses the formation of atmospheric undular bores by the rising of cool, moist sea breeze air into a warmer environment.

Sea breeze fronts are one practical example of gravity currents. Gravity currents, sometimes referred to as density or buoyancy currents, are flows driven by horizontal density differences. The study of converging gravity currents is also relevant in situations other than sea breezes. Another example of meteorological gravity currents are the cold downdrafts from thunderstorms, these are fronts of cold air that can interact with other downdraft fronts

or other pre-existing fronts. Other natural examples of gravity currents include the spreading of oil slicks in the ocean, avalanches and volcanic pyroclastic flows [18]. In industry gravity currents provide a description of the spreading of dense gases into the environment [16]. In the unfortunate case of an accident it is important to have accurate predictions of the spreading and any interactions that might follow.

In the laboratory, 'lock-exchange' experiments can be used to create gravity currents. Few experimental studies of colliding gravity currents have been published. A lab experiment discussed in [18, p. 196-197] shows the emergence of two bores traveling in opposite directions. This result was confirmed in a numerical simulation [14]. A more extensive discussion of colliding gravity currents can be found in [16], which presents experimental results based on collisions of currents of equal density but different heights. The study also develops a global theory for the propagation speed of the incoming gravity currents and resulting bores based on momentum and energy conservation.

Before the collision takes places, there are two horizontal propagating gravity currents. After the lock-release there is a short period of acceleration, after which the current enters the constant-speed regime. There exist multiple theories of what this speed should be and all are based on the non-dimensional Froude number:

$$U_1 = F_H \sqrt{g_1' H_1}, \tag{1}$$

where U_1 is the propagation speed, F_H is a dimensionless Froude number, g_1' is the reduced gravity and H_1 is the lock height [18]. The reduced gravity is based on the density difference between the gravity current (ρ_1) and the ambient fluid (ρ_0):

$$g_1' = \frac{\rho_1 - \rho_0}{\rho_1} g. \tag{2}$$

Different authors have presented different theories for what the Froude number should be. In this study the Froude number as defined in [17] will be used throughout:

$$F_H = \frac{\sqrt{2 - H_1/H_0}}{2}, \tag{3}$$

with H_0 the total depth of the fluid.

The objective of this study is to investigate what happens during the collision of two sea breeze fronts. Laboratory experiments of two colliding gravity currents in a rectangular channel are presented. These experiments have been designed to test the influence of differences in density, height and speed of two meeting gravity currents on the collision. In the remainder of this report different aspects of these collisions are discussed. Section 2 gives a description of the experimental setup and the experiments performed. Experimental results are presented in Section 3, some theoretical consideration is mentioned in Section 4. A final discussion is given in Section 5.

2 Experimental setup

All experiments were carried out in a horizontal rectangular channel. The tank used in this study was made of glass, 150 cm long and 15.5 cm deep. In all cases the tank was filled to

a depth of $H_0 = 20$ cm. The tank was lit from the back using a light sheet that was the same size as the back wall of the tank. Experiments were filmed using a video camera at approximately 2 m distance.

At both ends of the tank a separate section, a 'lock', was made using a vertical barrier, the 'lock gate'. The locks were 20 cm long. In the locks salt (NaCl) was added to the water to increase the density and thus create the horizontal density differences needed for the gravity currents. Yellow and blue food dye was added to distinguish the denser fluids from the transparent, fresh, ambient fluid after lock release. Densities were measured using a density meter with a precision of 10^{-4} g cm^{-3}. A schemetic of the experimental setup is shown in Figure 1.

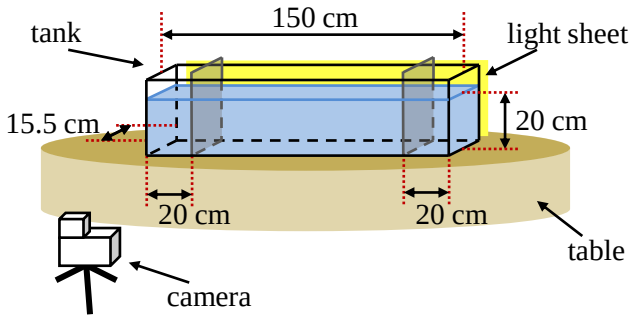

Figure 1: Experimental setup.

Two sets of experiments were performed. The first set was designed to study the influence of (relative) differences in reduced gravity on the collision. This set of experiments will be referred to as 'full-depth' lock exchanges or 'full-depth' experiments. Both locks were filled to the top with dense fluid, i.e. $H_1 = H_2 = H_0$ (Figure 2a), where H_0 is the total depth of the fluid and H_1 and H_2 are the height of denser fluid in the two locks. In total eighteen experiments were done; these are mapped out in parameter space in the lower panels of Figure 2. The ratio of the reduced gravities ranged from $0.22 < r_g < 0.99$, where r_g is defined as

$$r_g = \frac{g'_{light}}{g'_{heavy}}. \tag{4}$$

In the second set of experiments the depth of one of the locks was half of the total depth ($H_1 = H_0$, $H_2 = \frac{1}{2}H_0$, Figure 3a). A second independent parameter, gravity current height, has been introduced to the problem this way. These experiments are a more realistic representation of the environmental sea breeze convergence, as for those both the density and height of the meeting fronts might be different. In total fourteen half-depth experiments were done.

Finally, four additional partial-depth experiments were done for different ratios of the lock height. The $g'_1 H_1$ and $g'_2 H_2$ values for the meeting gravity currents were kept constant at approximately 100 cm^2 s^{-2}, but different combinations of g' and H were used. An overview of the initial conditions of all experiments is given in Appendix A.

At the start of the experiments the lock gates were pulled up vertically. There was always a short period of acceleration, but soon after the release the gravity currents entered

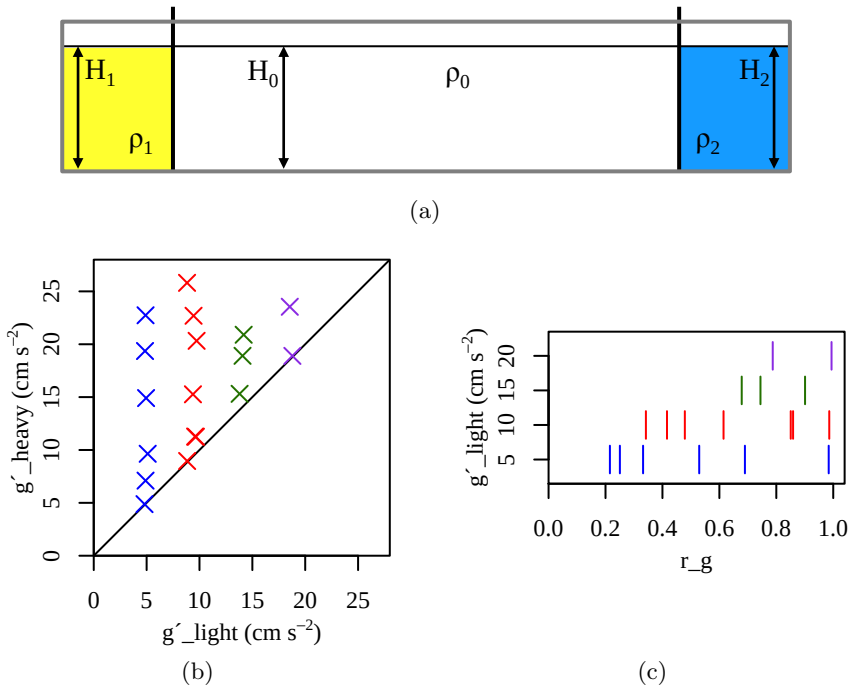

Figure 2: (a) Schematic of the initial setup for the full-depth experiments. (b,c) Position in parameter space of all full-depth experiments performed.

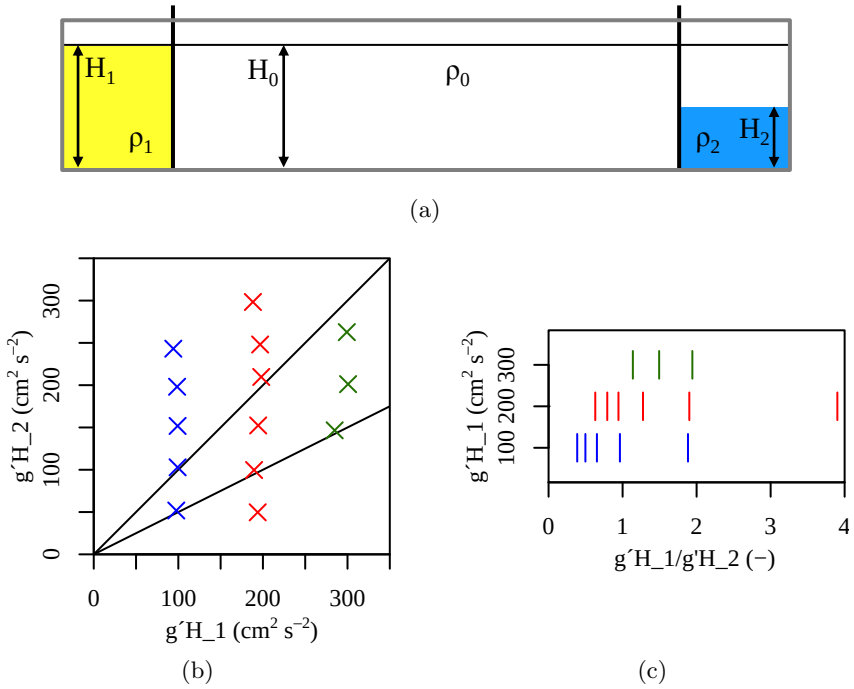

Figure 3: (a) Schematic of the initial setup for the half-depth experiments. (b,c) Position in parameter space of all half-depth experiments performed.

the constant-speed regime. The collision event always happened within this regime. Viscous effects do not play a role as the Reynolds numbers based on gravity current height (h) and speed (U),

$$Re = \frac{Uh}{\nu}, \tag{5}$$

was always above 3500, well above the critical value of a 1000 [18, p.141]. At the end of most experiments water samples from different depths in the tank were analyzed using the density meter to create a density profile. In the bottom half of the tank two samples were taken every centimeter water depth, in the top half every five centimeters. These data were then used to compute mixing efficiency data.

3 Experimental results

Snapshots from two full-depth experiments are shown in Figure 4. The left column shows a symmetric case, where g'_1 was equal to g'_2 ($r_g = 0.99$); the right column is an asymmetric case with heavier blue fluid ($r_g = 0.33$).

Different aspects of these experiments will be discussed in this section of the report. In Section 3.1 the propagation speed of the gravity currents before collision (Figures 4a and 4b) will be discussed and compared to the theoretical predictions. The collision will be analyzed in more detail in Section 3.2, which considers both the initial collision angle

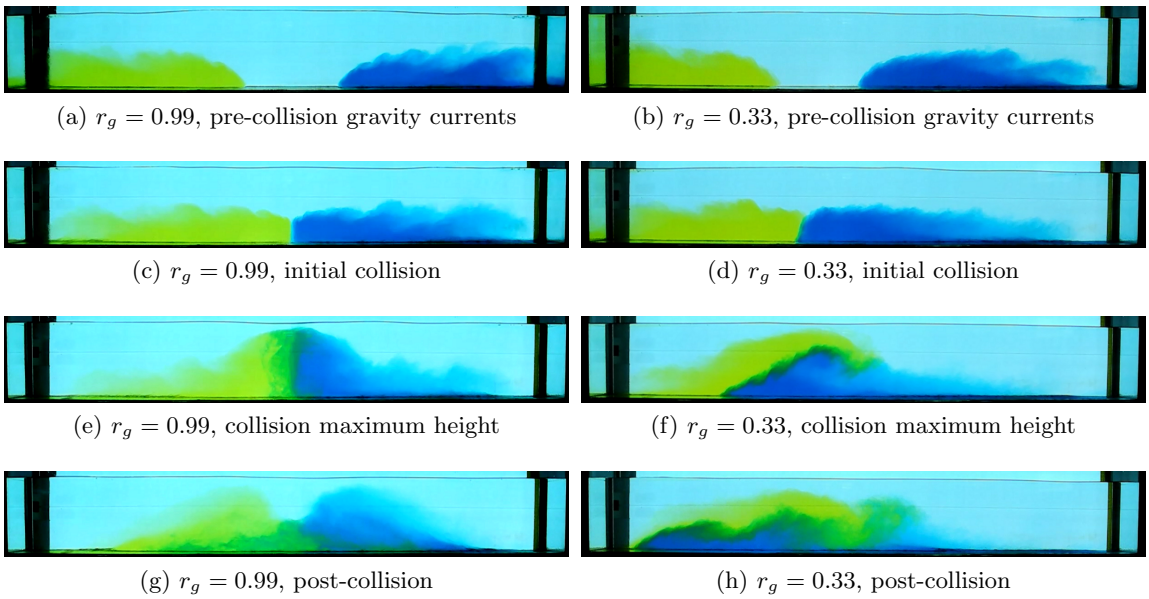

(a) $r_g = 0.99$, pre-collision gravity currents

(b) $r_g = 0.33$, pre-collision gravity currents

(c) $r_g = 0.99$, initial collision

(d) $r_g = 0.33$, initial collision

(e) $r_g = 0.99$, collision maximum height

(f) $r_g = 0.33$, collision maximum height

(g) $r_g = 0.99$, post-collision

(h) $r_g = 0.33$, post-collision

Figure 4: Snapshots of two experiments at different times. Note that the time difference between different panels is not the same for the two experiments. Times shown: (a,b) pre-collision gravity currents, (c,d) initial collision, (e,f) collision maximum height, (g,h) post-collision. Experiments shown: (a,c,e,g) symmetric case with $r_g = 0.99$, (b,d,f,h) asymmetric case with $r_g = 0.33$.

(Figures 4c and 4d) and the maximum height (Figures 4e and 4f). Last, total mixing in the tank will be discussed in Section 3.3.

3.1 Pre-collision gravity currents

Figure 5 compares measured propagation speeds and Froude numbers of the experimental gravity currents with theoretical prediction using Equations 1 and 3. For clarity only currents from full-depth (53 currents) and half-depth (16 currents) locks are shown. Theoretical curves are plotted for both lock heights. Lower lock heights create slower propagating gravity currents with a higher Froude number. For all currents except one, the measured speeds are lower than the theory predicts. This can be explained by assumptions made in the derivation of the equations. The theory assumes no energy loss due to friction, mixing or viscosity. The Reynolds numbers in the experiments were sufficiently high to meet the last criterion, but effects from friction and mixing cannot be neglected.

Froude numbers are about 15% lower than the theoretical value, independent of the value of g' or the height H_1 of fluid in the lock. For the full-depth experiments we find a mean Froude number of 0.42 instead of the 0.5 from theory. The mean Froude number for the half-depth lock experiments is 0.53, where theory predicted 0.61. These values are slightly lower than the Froude numbers found in [17], these were 0.46±0.015 and 0.57±0.015 for full-depth and half-depth lock exchanges respectively.

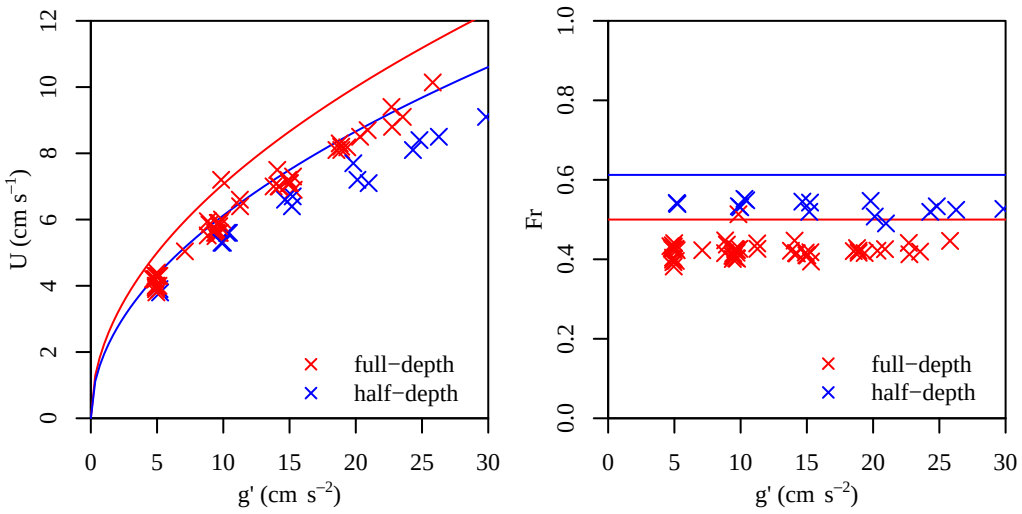

(a) Gravity current speed (b) Froude numbers

Figure 5: (a) Gravity current propagation speed versus reduced gravity. (b) Froude numbers versus reduced gravity. In both panels the marks are all individual experiments, lines are the theoretical values based on Equations 1 and 3. The red marks and line correspond to the full-depth lock experiments, blue symbols mark the half-depth experiments.

3.2 Collision

Figure 6 shows the first second of a collision event in more detail. Frames from the experimental videos were analyzed to find the position of the fronts in time. Both sequences start at time = 0, which is the first frame at which the fronts collide. The next frames are 5 frames ≈ 165 ms apart, up to frame 30 ≈ 1 s after first collision. The plots show a short period spanning around what was shown in Figures 4c and 4d.

In the symmetric case of equal g' (Figure 6a) the shape of the fronts is similar and the collision front is vertical. In time this front extends in height and remains vertical, and mixing occurs on the front line. This can also be seen in Figures 4c and 4e. The asymmetric case is different (Figure 6b). Before colliding, the fronts are already changing shape and therefore have different steepness upon collision. The collision front develops at an angle with the heavier fluid (blue) pushing underneath the lighter fluid. The front shape is not steady in time, after a while (in this case half a second, 15 frames) a new gravity current forms at the bottom and Kelvin-Helmholtz billows develop at the top. The front transforms from an initial straight line at an angle to an 'S' shaped front that changes shape to being more horizontal in time.

The initial angle changes for different experiments. This angle is defined as the angle θ between the front and the vertical, positive clockwise with denser fluid to the right. To clarify, in Figures 4c and 6a this angle is 0°, in Figures 4d and 6b (frames 5 and 10) the angle is about 16°. The initial collision angles for all experiments performed are plotted in Figure 7 against r_g. The three colours mark the different sets of experiments. However

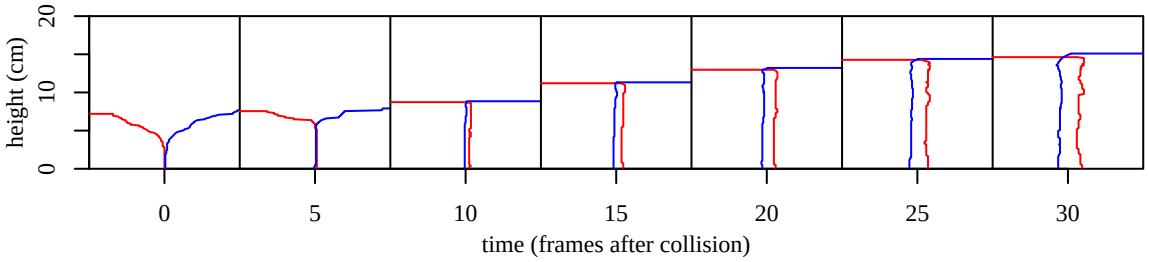

(a) $r_g = 0.99$

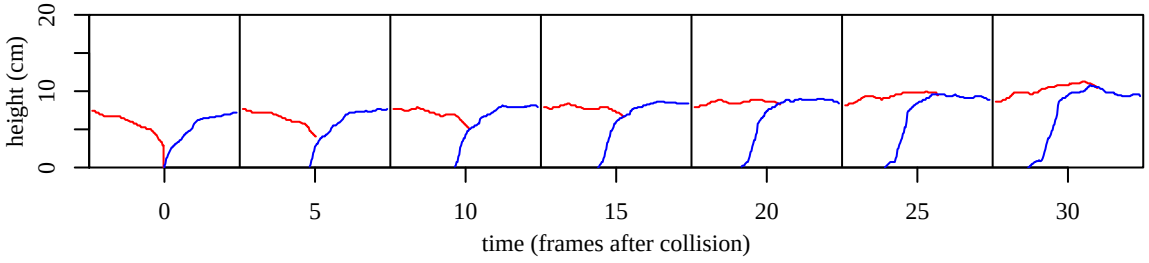

(b) $r_g = 0.33$

Figure 6: Analyzed front positions at and after collision for two different experiments. Along the horizontal different time frames in the experimental videos are shown, one frame corresponds to 33 ms. Experiments shown: (a) $r_g = 0.99$ (b) $r_g = 0.33$, these are the same experiments as shown in Figure 4.

the data are not clustered by these sets, and the height of the incoming gravity currents seems not to affect the initial collision angle. The relation between the collision angle and the ratio of g', r_g, is clear from the data. For near-symmetric experiments ($r_g \approx 1.0$) the angle is small and the collision front is almost vertical. For increasingly asymmetric cases the front tilts, with the heavier fluid sitting underneath the lighter fluid. The collision angle increases from 0° for $r_g = 1.0$ to about 20° for $r_g = 0.2$. The slope of the linear regression line is $-25.53 \pm 2.55°$.

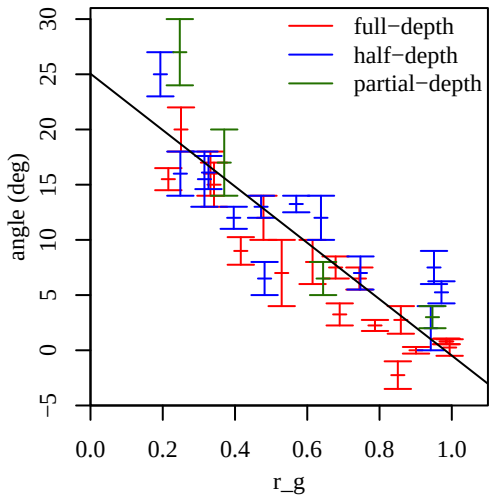

Figure 7: Initial collision angle set against ratio r_g. The red marks correspond to the full-depth lock experiments, blue marks correspond to the half-depth experiments, green marks are the final four partial-depth experiments. The black line is the linear fit to all data.

In addition to the angle of the collision front, temporal changes in the height of the front are also of interest. The heights of the moving gravity currents and the maximum height of the colored fluid were measured in each experiment. For the full-depth lock releases, energy-conservation theory predicts that the height of the gravity current is half the total water depth [2]. The full-depth lock release gravity currents presented here have a similar value (see Figure 8). In the full-depth experiments, Figure 8a, the maximum height after collision is approximately 0.90 of the total water depth independent of r_g. This height is not reached after a constant time difference after the collision event, as can be seen in Figure 6. The colored fluid in the experiment shown in Figure 6a reaches 15 cm after one second (frame 30), in the asymmmetric case it only goes up to 11 cm after the first second. Preliminary analysis on the speed of this rise seems to point to a dependence on the propagation speeds of the incoming gravity currents. However it is difficult to quantify the exact vertical speed from the current experimental setup. The half-depth experiments (coloured marks in Figure 8b) show more variation in collision height with r_g, though the spread is large.

In the partial-depth experiments (black in Figure 8b) we have a symmetric case of two half-depth locks ($r_g \approx 1.0$). The maximum height reached in this experiment was 0.75 of the total water depth, higher than the initial lock heights. Based on this result, a hypothesis can

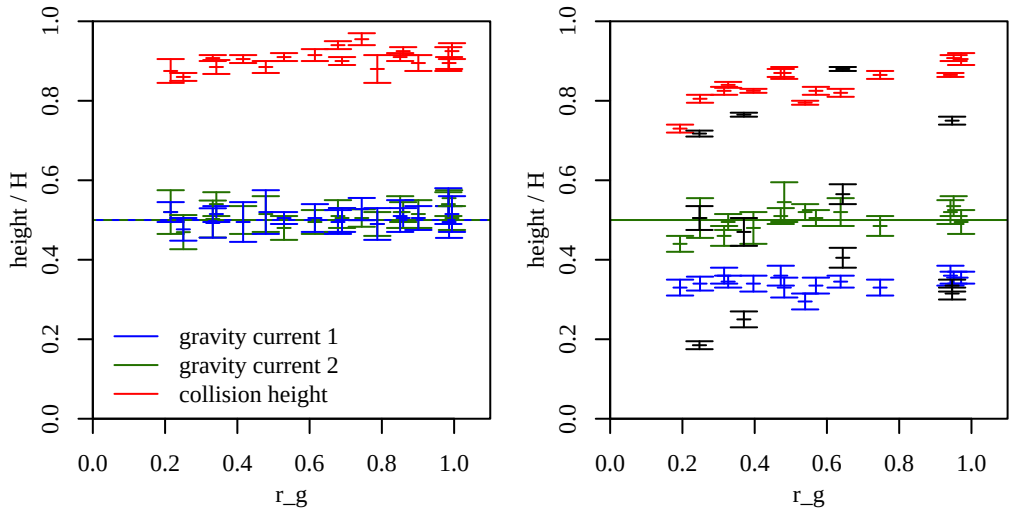

(a) Full-depth experiments (b) Half- and partial-depth experiments

Figure 8: Pre-collision gravity current heights and maximum height reached after collision against ratio r_g. All heights are normalized by the total water depth, H_0. The horizontal lines show the theoretical, energy conserving value for the height of a gravity current from a full-depth lock. (a) Full-depth experiments, (b) half-depth experiments in the same colours as (a) and partial-depth experiments in black.

be formed that different processes near the water surface (at H_0) might have influenced or ultimately stopped the rise of colored fluid in the full-depth experiments. Motivated by the different results of the collision of two symmetric currents from full-depth lock-exchanges and the collision of two currents from symmetric half-depth experiments.

3.3 Post-collision mixing

As a measure of mixing in the tank we use mixing efficiency. This is defined as fraction of energy lost from the total Potential Energy (PE) during the experiment:

$$E_M = 1 - \frac{PE_{t=0} - PE_{profile}}{PE_{t=0} - PE_{rearranged}}, \tag{6}$$

where $PE_{t=0}$ is the potential energy in the initial set up before lock release, $PE_{profile}$ the potential energy in the measured density profile at the end of the experiments and $PE_{rearranged}$ is the minimum potential energy in the theoretical case of no mixing. This rearranged profile is therefore the densest fluid at the bottom and lightest fluid on top, in a stepfunction like profile. PE is computed through:

$$PE = \int_0^{H_0} \rho g z \, \mathrm{d}z. \tag{7}$$

The mixing data for the full-depth experiments is plotted against the mean Reynolds number in Figure 9a. The mean Reynolds number is the geometric mean of the Reynolds

numbers of the two incoming gravity currents before collision (Equation 5). There is enhanced energy loss due to mixing with increasing Reynolds number. This was also found in previous experiments [5]. No relationship was found with r_g. The mixing data of the half-depth lock experiments do not exhibit this relation with Reynolds number (Figure 9a).

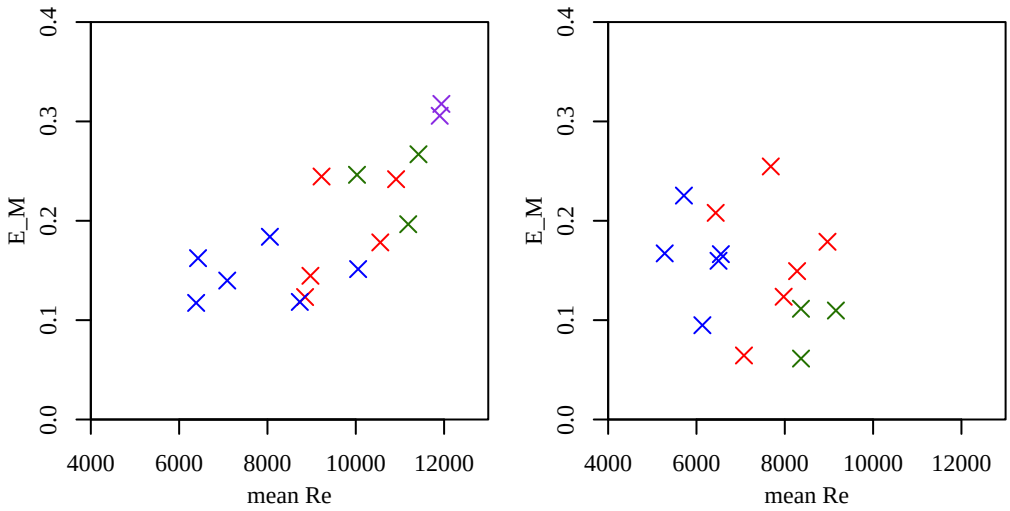

(a) Full-depth experiments

(b) Half-depth experiments

Figure 9: Mixing efficiency against mean Reynolds number of the two incoming gravity currents. (a) Full-depth experiments, (b) half-depth experiments. Colors as in Figures 2b and 3b.

4 Theoretical considerations

Two different models will be presented as an attempt to predict the initial collision angle based on knowledge of two incoming asymmetrical gravity currents. The first model is a steady state model, based on conservation of mass and horizontal momentum. It has some similarities with existing theories for colliding jets. The second model is not steady and is based on the generation of a shear flow from horizontal density gradients [19].

4.1 Momentum conservation

Consider two gravity currents (ρ_1, U_1, h_1 and ρ_2, U_2, h_2) propagating towards each other and colliding at stagnation point O. At collision the two fluids rise under angle θ to a height D. The ambient fluid has density ρ_0 and height H_0, atmospheric pressure at the top is considered to be zero. Figure 10 shows a schematic of this flow.

We will consider the angle in a frame of reference where the stagnation point is at rest. Hence:

$$U_1 - \Delta U = U_2 + \Delta U = U_{in}. \tag{8}$$

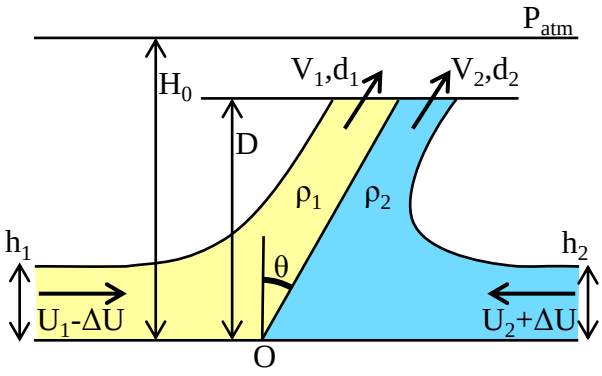

Figure 10: Schematic of collision in a frame of reference where the stagnation point O is at rest.

Rearranging, we find for the incoming gravity current speeds:

$$U_{in} = \frac{U_1 + U_2}{2} \tag{9}$$

and

$$\Delta U = \frac{U_1 - U_2}{2}. \tag{10}$$

Mass conservation for the two fluids gives:

$$h_1 U_{in} = d_1 V_1 \cos\theta, \tag{11}$$

$$h_2 U_{in} = d_2 V_2 \cos\theta. \tag{12}$$

Conservation of horizontal momentum gives:

$$\begin{aligned} -\rho_1 U_{in}^2 h_1 - \frac{1}{2}\rho_1 g_1' h_1^2 + \rho_2 U_{in}^2 h_2 + \frac{1}{2}\rho_2 g_2' h_2^2 \\ + \rho_1 V_1^2 d_1 \sin\theta\cos\theta + \rho_2 V_2^2 d_2 \sin\theta\cos\theta = 0. \end{aligned} \tag{13}$$

Rearranging this momentum equation and using Equations 11 and 12 to replace the $d\cos\theta$ terms, we find for the angle θ:

$$\sin\theta = \frac{U_{in}^2\left(\rho_2 h_2 - \rho_1 h_1\right) + \frac{1}{2}\left(\rho_2 g_2' h_2^2 - \rho_1 g_1' h_1^2\right)}{-\rho_1 V_1 U_{in} h_1 - \rho_2 V_2 U_{in} h_2}. \tag{14}$$

This is not a closed system, as the speeds V_1 and V_2 are unknown. One could use steady Bernoulli along the streamlines at the top of the gravity current to find these, but that would introduce the unknown height D to the problem.

Instead the magnitude and sign of the incoming momentum fluxes will be considered in relation to the angle. In equation 14 the denominater is always negative, therefore any changes in sign of θ must originate from the relative magnitudes of the two incoming horizontal momentum terms. Using theoretical predictions for speed and height of gravity

currents from full-depth lock releases [2, 17] we can rewrite the numerator of Equation 14 to:

$$\frac{1}{16}\left(\sqrt{g_1' H_0} + \sqrt{g_2' H_0}\right)^2 (\rho_2 - \rho_1) + \frac{1}{4}(\rho_2 g_2' - \rho_1 g_1') H_0. \tag{15}$$

For a case where $\rho_2 > \rho_1$, i.e. heavier fluid to the right, this will result in $\sin\theta < 0$ and thus $\theta < 0$. The heavier fluid pushes over the lighter fluid. All experiments have resulted in the opposite scenario, with the heavier fluid going underneath the lighter fluid: so that for $\rho_2 > \rho_1$ the measured angle θ was always positive. It can therefore be concluded that the assumptions made in the derivation of this model are incorrect. These assumptions include hydrostatic pressure everywhere in the ambient fluid, the unknown time-varying collision height D and the steady-state framework. The collision angle is not stationary in time. Close analysis of the experimental videos points towards the existence of an initial collision angle that, as time goes on, increases, i.e. rotates towards the horizontal. A steady approximation as presented here is thus not applicable.

4.2 Shear flow

Fluids with horizontal density gradients in the presence of a vertical gravitational field are known to generate a horizontal flow with vertical shear. In the experiments presented here these gradients are always present, e.g. the horizontal density gradient associated with a gravity current propagating through an ambient fluid or, after collision, the horizontal density gradient between the two fluids from the locks.

The shape of the generated horizontal shear flow can be derived in the case of a constant density gradient as shown in [19]. For an initial density profile with a constant gradient α in the horizontal direction x and gradient β in the vertical, z.

$$\rho_0 = \bar{\rho}(1 - \alpha x - \beta z), \tag{16}$$

it is found that

$$u = g\alpha z t \tag{17}$$

and

$$\rho = \rho_0 - \frac{1}{2} g \bar{\rho} \alpha^2 z t^2. \tag{18}$$

The generated flow is sheared in the vertical and accelerates linearly in time. The horizontal density gradient remains constant, the vertical stratification increases in strength. The isopycnals therefore rotate towards the horizontal,

$$\tan\theta = \frac{\beta}{\alpha} + \frac{1}{2} g \alpha t^2. \tag{19}$$

When this model is applied to the collision experiments the change in the angle is too fast. Even though it is difficult to determine precisely, the evolution of $\tan(\theta)$ and ρ seems to be more linear than quadratic. Of course the assumption of a constant linear density gradient is poor, and a continuous gradient or a piecewise gradient description would fit better. In that case the generated flow will not be constant in the horizontal, and frontogenesis will take place. An in depth analysis of these situations is beyond the scope of the work during the GFD summer.

5 Discussion

Laboratory experiments for sea breeze collision have been performed and presented. Two gravity currents from a lock-release were made to collide in a rectangular tank. Both the density of the currents and the height of the currents were varied in the different experiments, which allowed for an analysis of the influence of density differences, height differences and horizontal propagation speed difference on the collision. The main conclusions are as follows.

(i) Before collision and far apart, the gravity currents speeds match the existing theory well and propagate with a Froude number about 15% lower than energy conserving theory predicts [17].

(ii) At collision a sharp front between the two fluids develops. The angle of the front with the vertical is dependent on the ratio between the two densities (r_g) only, and no relation was found with ratios of current heights or propagation speeds. For a collision of two symmetrical currents ($r_g = 1.0$) the front is vertical. The angle of the front increases linearly with increasing density difference, up to about 20° for $r_g = 0.2$. Attempts to predict the angle of the front using horizontal momentum arguments or generated shear flows were unsatisfactory.

(iii) No conclusions can be drawn on the maximum height reached by the colored fluids during collision. The full-depth lock experiments gave different results than the half-depth and partial-depth experiments.

(iv) For colliding gravity currents of equal height energy losses due to mixing are enhanced with increasing Reynolds number, in agreement with previous experiments [5]. For meeting currents of different height no relationship was found.

In the natural environment sea breeze currents are influenced by many different factors. Over islands and peninsulas, their collisions are therefore complex. The experiments in this report were designed to give a physical description of such collisions, which are very difficult to measure in detail in nature. The initial angle of the front is the line along which moist air parcels will rise from the sea breeze into drier ambient air. Condensation of water vapor will set off heavy cloud formation and if strong enough create thunderstorms. For nearly vertical fronts all this energy and the related rainfall will be concentrated over a very small surface area, whereas in the case of a tilted front this will be spread over a much larger surface area. The precipitation rate might therefore be partly dependent on the tilt of the front. In the experiments the angle of the front was set by the difference in density. Coasts with very different land use or seas with different temperatures could generate different heating rates and thus sea breeze gravity currents with different densities. In more symmetrical configurations of peninsulas and seas one would therefore expect currents of more equal density.

Predicting the angle of the collision front and its horizontal speed are of large scientific importance. The experiments presented in this report give an initial description of the collision, but attempts to create a model to predict the tilt have not been successful so far. More information of the exact flow patterns in the gravity currents, the ambient fluid and at the collision event would be very valuable. This information could be obtained by performing similar experiments but with the added technology of particle image velocimetry. Another option would be to set up numerical experiments and model the collision event.

Both methods would provide a detailed description of the horizontal and vertical flow before, at and after the collision of two gravity currents.

Acknowledgements

Many thanks to Sarah Gille, Stefan Llewellyn Smith, Claudia Cenedese and Paul Linden, who were all involved in this project and offered great advice throughout the summer. Thanks also to Anders Jensen and Bruce Sutherland for their practical help in the laboratory. The experiments were not possible without someone helping me out, so thanks to Catherine, Kate, Barbara, Luisa and many others for lifting the second lock. Finally, all the fellows, what a great summer we had. We got it. Somehow.

References

[1] R W Arritt, *Numerical modelling of the offshore extent of sea breezes*, Quarterly Journal of the Royal Meteorological Society, 115 (1989), pp. 547–570.

[2] T B Benjamin, *Gravity currents and related phenomena*, Journal of Fluid Mechanics, 31 (1968), pp. 209–248.

[3] H R Byers and H R Rodebush, *Causes of thunderstorms of the Florida peninsula*, Journal of Meteorology, 5 (1948), pp. 275–280.

[4] R E Carbone, J W Wilson, T D Keenan, and J M Hacker, *Tropical island convection in the absence of significant topography. Part I: Life cycle of diurnally forced convection*, Monthly Weather Review, 128 (2000), pp. 3459–3480.

[5] C Cenedese and C Adduce, *Mixing in a density-driven current flowing down a slope in a rotating fluid*, Journal of Fluid Mechanics, 604 (2008), pp. 369–388.

[6] R H Clarke, *Fair weather nocturnal inland wind surges and atmospheric bores: Part I Nocturnal wind surges*, Australian Meteorological Magazine, 31 (1983), pp. 133–45.

[7] ——, *Colliding sea-breezes and the creation of internal atmospheric bore waves: two-dimensional numerical studies*, Australian Meteorological Magazine, 32 (1984), pp. 207–26.

[8] N A Crook, *Understanding Hector: The dynamics of island thunderstorms*, Monthly Weather Review, 129 (2001), pp. 1550–1563.

[9] S T Gille and S G Llewellyn Smith, *When land breezes collide: Converging diurnal winds over small bodies of water*, Quarterly Journal of the Royal Meteorological Society, (submitted).

[10] S T Gille, S G Llewellyn Smith, and S M Lee, *Measuring the sea breeze from quikSCAT scatterometry*, Geophysical Research Letters, 30 (2003), p. 1114.

[11] M W Moncrieff and C Liu, *Convection initiation by density currents: Role of convergence, shear, and dynamical organization*, Monthly Weather Review, 127 (1999), pp. 2455–2464.

[12] H Niino, *The linear theory of land and sea breeze circulation*, Journal of the Meteorological Society of Japan, 65 (1987), pp. 901–921.

[13] J A Noonan and R K Smith, *Sea-breeze circulations over Cape York Peninsula and the generation of Gulf of Carpentaria cloud line disturbances*, Journal of the Atmospheric Sciences, 43 (1986), pp. 1679–1693.

[14] J R Pacheco, A Pacheco-Vega, and S Pacheco-Vega, *Analysis of density currents using the non-staggered grid fractional step method*, in Proceedings of 5th International Symposium Stratified Flows, Citeseer, 2000, pp. 1135–1140.

[15] R A Pielke, *A three-dimensional numerical model of the sea breezes over south Florida*, Monthly Weather Review, 102 (1974), pp. 115–139.

[16] J O Shin, *Colliding gravity currents*, PhD thesis, University of Cambridge, 2001.

[17] J O Shin, S B Dalziel, and P F Linden, *Gravity currents produced by lock exchange*, Journal of Fluid Mechanics, 521 (2004), pp. 1–34.

[18] J E Simpson, *Gravity currents in the environment and the laboratory*, Journal of Fluid Mechanics, 352 (1997), pp. 376–378.

[19] J E Simpson and P F Linden, *Frontogenesis in a fluid with horizontal density gradients*, Journal of Fluid Mechanics, 202 (1989), pp. 1–16.

[20] J E Simpson, D A Mansfield, and J R Milford, *Inland penetration of sea-breeze fronts*, Quarterly Journal of the Royal Meteorological Society, 103 (1977), pp. 47–76.

[21] Z Xian and R A Pielke, *The effects of width of landmasses on the development of sea breezes*, Journal of Applied Meteorology, 30 (1991), pp. 1280–1304.

[22] H Yan and R A Anthes, *The effect of latitude on the sea breeze*, Monthly Weather Review, 115 (1987), pp. 936–956.

A Initial setup experiments

The table below provides details on the initial conditions for all experiments presented in this report.

Table 1: Initial conditions for all experiments. g'_1 and H_1 give respectively the value for reduced gravity (cm s^{-2}) and the lock height (cm) in the first lock, g'_2 and H_2 the same quantities for the second lock. Horizontal lines separate the full-depth, half-depth and partial-depth experiments.

	g'_1	H_1	g'_2	H_2	$\frac{g'_L}{g'_H}$	$\frac{g'H_1}{g'H_2}$
exp 01	9.0	20.0	8.8	20.0	0.99	1.01
exp 02	8.8	20.0	25.8	20.0	0.34	0.34
exp 03	9.7	20.0	11.3	20.0	0.86	0.86
exp 04	4.8	20.0	4.9	20.0	0.98	0.98
exp 05	5.1	20.0	9.6	20.0	0.53	0.53
exp 06	4.9	20.0	22.7	20.0	0.22	0.22
exp 07	4.8	20.0	19.4	20.0	0.25	0.25
exp 08	4.9	20.0	14.9	20.0	0.33	0.33
exp 09	14.1	20.0	18.9	20.0	0.74	0.74
exp 10	13.8	20.0	15.3	20.0	0.90	0.90
exp 11	18.5	20.0	23.5	20.0	0.79	0.79
exp 12	18.8	20.0	18.9	20.0	0.99	0.99
exp 13	9.4	20.0	15.3	20.0	0.61	0.61
exp 14	9.4	20.0	22.7	20.0	0.42	0.42
exp 15	9.7	20.0	20.3	20.0	0.48	0.48
exp 16	14.2	20.0	20.9	20.0	0.68	0.68
exp 17	4.9	20.0	7.1	20.0	0.69	0.69
exp 18	11.3	20.0	9.6	20.0	0.85	1.18
exp 19	4.9	20.0	5.2	10.0	0.94	1.88
exp 20	5.0	20.0	10.3	10.0	0.48	0.96
exp 21	9.7	20.0	5.2	10.0	0.54	3.90
exp 22	4.9	20.0	19.8	10.0	0.25	0.50
exp 23	9.5	20.0	10.0	10.0	0.95	1.90
exp 24	9.7	20.0	15.2	10.0	0.64	1.28
exp 25	9.9	20.0	21.0	10.0	0.47	0.94
exp 26	14.2	20.0	14.7	10.0	0.97	1.94
exp 27	15.0	20.0	20.1	10.0	0.75	1.49
exp 28	15.0	20.0	26.3	10.0	0.57	1.14
exp 29	9.8	20.0	24.8	10.0	0.40	0.79
exp 30	5.0	20.0	15.2	10.0	0.33	0.65
exp 31	4.7	20.0	24.3	10.0	0.19	0.39
exp 32	9.4	20.0	29.8	10.0	0.32	0.63
exp 33	5.2	20.0	20.9	5.0	0.25	0.99
exp 34	9.9	10.0	10.4	10.0	0.95	0.95
exp 35	5.0	20.0	13.5	7.5	0.37	0.99
exp 36	5.1	20.0	7.9	14.0	0.64	0.92

Granular flow in a Rotating Drum

Gregory L. Wagner

December 19, 2013

1 Introduction

Granular materials are encountered regularly in everyday life — as salt and sugar in the kitchen, as dirt on a trail underfoot, or as sand on the beach. They are agents in destructive and powerful events: vast avalanches of snow and ice, pyroclastic flows of hot dust and gas down the flanks of an erupting volcano, and landslides and mass wasting on Earth and other rocky bodies of the solar system. In human industries like the food, pharmaceutical, and semiconductor industry, granular materials are the second most manipulated substance after water [13].

An understanding of the mechanics of granular flows is necessary to interpret and predict their behavior in geophysical and industrial contexts. In general, granular flows can be divided into three regimes depending on their rate of deformation: a dense, quasi-static regime, a slowly flowing "liquid" regime, and a relatively dilute, rapidly flowing "gaseous" regime. The quasi-static regime is characterized by slow deformation and frictional interaction between particles and is well-studied in the field of soil mechanics [14]. The gaseous regime is characterized by binary collisions and can be described by a kinetic theory which accounts for dissipation in collisions [6]. The liquid regime, which is the subject of this work, is characterized both by collisions and enduring contacts and presents perhaps the greatest theoretical challenge [5].

A theoretical description of the liquid regime of granular flow based on the microscopic physics of particle interactions has proven elusive. However, empirical laws proposed relatively recently which employ the principles of mass and momentum conservation in a continuum approximation – a "hydrodynamic description" – have demonstrated some success [9, 5]. This approach decomposes the bulk stress in the granular medium into a "pressure" (often taken to be isotropic) and a deviatoric component. For the deviatoric component a "frictional" rheological law is proposed which is proportional to the pressure and coaxial with the rate of strain. In addition, the coefficient of proportionality or friction coefficient μ has a functional dependence on the "inertia number" I which is dependent on magnitude of the rate of strain, particle diameter, pressure, and bulk density of the material. We call this empirical rheology the "$\mu(I)$ law".

The $\mu(I)$ law is particularly interesting because, while it uses material parameters and has a dependence on the inertia number which is determined by shear cell and inclined plane experiments, it has provided accurate quantitative predictions for the velocity profile and flowing layer depth in an independent heap flow experiment [9] (for a description of the common experimental configurations used in the study of granular flow see [10]). In this

work, we examine whether the $\mu(I)$ law is valid for a fourth common configuration: the rotating drum.

Granular flows in rotating drums, like flows on a heap, are surface flows in that the flowing grains occupy a layer over a bed surface of static grains. One of the special characteristics of surface flows is that they exhibit two distinct regimes of behavior depending on the flow rate. At low flow rates, the system episodically avalanches: grains either accumulate (heap flow) or rotate as a solid body (rotating drum) until a critical pile inclination is reached at which they release in an avalanche. At high flow rates a continuously flowing layer of grains forms. Flow in a rotating drum is more complicated than flow on a heap because it is not necessarily homogeneous in the direction of flow. Nevertheless the rotating drum configuration uses far less granular material and permits a higher volume of experiments because grains are automatically recycled. Further, the rotating drum can access a greater range of average surface inclinations (although the shape of the surface may not remain flat) [10]. As a result much attention has been devoted to the rotating drum, including investigations into the properties of the continuously flowing layer [7], avalanches [3, 12], the transition between episodic avalanching and continuous flow [1, 4], discrete element method simulations [17, 16], explanations for the shape of the free surface [15], and studies that use experimental techniques such as MRI [16] and positron emission [11].

In this work we conduct a general investigation into the characteristics of flow in a rotating drum with an emphasis on applying the $\mu(I)$ rheology to describe both the continuously flowing layer as well as the episodic avalanches. We develop separate theories for the continuously flowing layer and for the episodic avalanching regime. We compare the predictions of the theory to experiments performed in Vancouver at the University of British Columbia as well as experiments in a second drum in the GFD lab at the Woods Hole Oceanographic Institution. We also comment on the transition from episodic avalanching and continuous flow, although it is not yet completely understood.

This report is organized as follows. In Section 2 we describe our experimental methods and materials. In Section 3 we discuss representative experimental results and introduce the main features of the flow including episodic avalanching, continuous flow, and the transition between these regimes. In addition we present our observations of the effects of drum width and drum radius on the relationship between flow rate and the inclination of grain pile. In Section 4 we give a brief introduction to the theory of the liquid regime of granular flow and the $\mu(I)$ rheology and derive two models: the "thin, shallow, slippy" (or TSS) model for the continuously flowing layer, and a "crude inertial model". In Section 5 we compare the predictions of our theory with experimental observations. We find that the TSS model appears to be valid for thin drums within a certain range of flow rates within the continuously flowing regime. However it does not appear to be valid for the wider drums (as expected), and underpredicts the angle of the flowing layer at both the high and low ends of the tested flow rates. Further we are unable to fully validate the model because it depends on material parameters which have not yet been measured. For the crude inertial model we only attempt a qualitative comparison. We find that it can produce a flow which resembles an avalanche and provides some basis for an explanation for why the system might transition from episodic avalanching to continuous flow as the flow rate is increased (but not the converse transition from continuous flow to episodic avalanching).

2 Experimental method and materials

Results are presented for experiments conducted in the GFD lab at the Woods Hole Oceanographic Institution in Woods Hole, Massachusetts during the Program in Geophysical Fluid Dynamics in the summer of 2013, as well as for experiments conducted earlier at the University of British Columbia in Vancouver, British Columbia.

2.1 Apparati

Two different drums were used for experiments: one (Vancouver) with radius 144 mm located at the University of British Columbia in Vancouver, and another (Woods Hole) with radius 69 mm located in the GFD Lab at the Woods Hole Oceanographic Institution in Woods Hole, Massachusetts. An image of each is shown in Figure 1(A) and 1(B). The exterior of both drums was composed of Perspex. The width of the Vancouver drum could be varied by fixing a Perspex plate at the desired position. The width of the Woods Hole drum was varied by inserting a circular piece of rigid, high density foam with a slightly smaller diameter than the drum. The foam was stacked on top of sheets of additional foam and Perspex against the back wall of the drum to achieve the desired width.

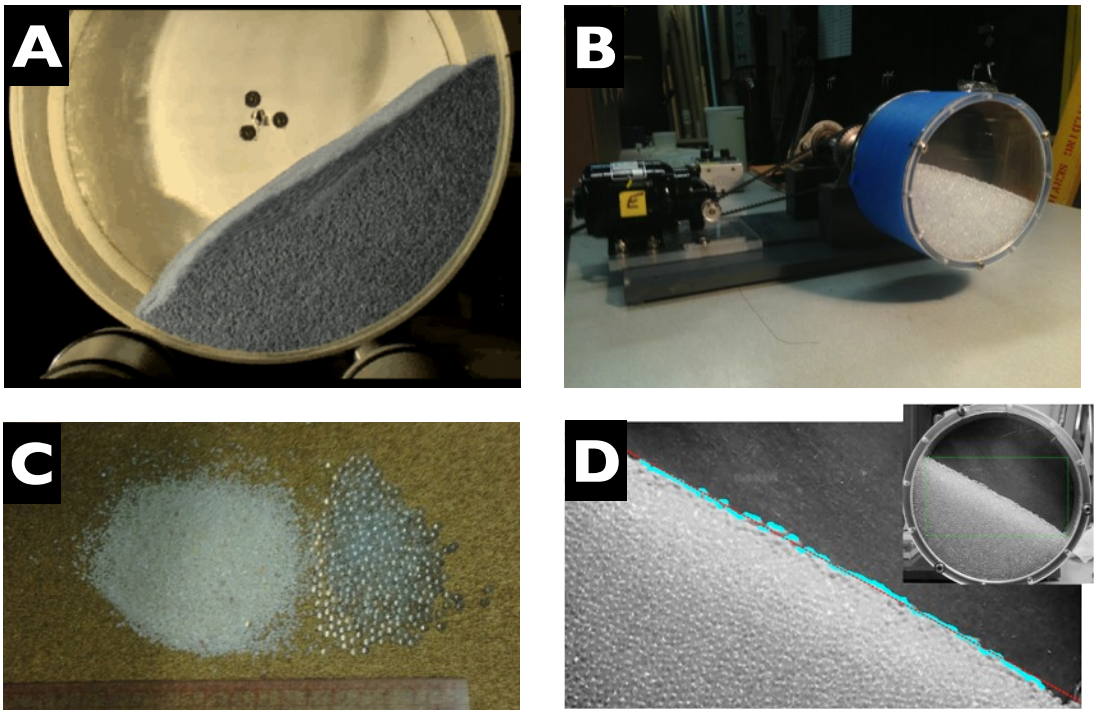

Figure 1: Experimental apparati, materials, and procedure for measuring the surface inclination. (A) Vancouver drum with radius 144 mm; (B) the entire Woods Hole set-up including the motor driving drum rotation. The Woods Hole drum has radius 69 mm and here is filled with Ballotini spherical glass beads of diameter 2 mm, (C) decorative aquarium sand (left) and 3mm spherical class beads (right), (D) illustration of the image cropping and line fitting procedure to determine the pile angle θ.

2.2 Materials

We performed experiments with four granular media: "Ballotini" spherical glass beads of diameter 1.5, 2, and 3 mm, and decorative aquarium sand of irregular shape and characteristic diameter ≈ 1 mm. An image of the decorative aquarium sand and 3mm spherical glass beads is shown in Figure 1(C).

2.3 Method

The experimental protocol for each drum was slightly different. The Vancouver drum was computer-controlled with an automated system for imaging the drum from the side and calculating the slope angle instantaneously so that many thousands of images did not have to be saved. The Woods Hole drum was controlled manually and video was taken by a camera on a tripod and analyzed later.

Because it was possible to automate the collection of large amounts of data in the Vancouver drum, very long "burn" runs were performed in which the glass beads were rotated for periods of up to 8–12 hours. From these runs it appears that the inclination of the pile does undergo a slow drift over extended runs, perhaps due to wearing of the beads and the associated accumulation of glass powder or dust. Further, if the beads were removed from the drum after a burn, washed to remove dust, and reinserted, a sudden change in the measured slopes was observed. This change in measured slope after washing would then be followed by a *second* slow drift in slope inclination before reaching a steady-state. A full characterization of the wearing properties and the apparent effect of accumulated dust is beyond the scope of this work. It is important to note, however, that all results presented for the Vancouver drum have undergone this "burning" process, whereas in the Woods Hole drum such a procedure would not have been practical.

For the Woods Hole drum, the rotation speed was set by a manual controller which was characterized to relate the scale of the controller to the rotation speed of the drum. The protocol involved starting the drum at the maximum rotation speed allowable by the controller. The rotation speed was then decreased in small increments until the minimum rotation speed for which the motor could drive the drum steadily (lower rotation speeds were possible, but "skipping" and irregular movements of the motor were observed), and then increased in small increments until the maximum rotation speed was again reached. This allowed the transition between continuous flow and episodic avalanching to be explored taking into account any potential hysteretic effects due to the history and past states of the system. For each rotation speed a short video approximately 2 minutes long was recorded for analysis.

To determine the average angle of the flowing layer from the video, a portion of each video frame containing only the layer of beads and the dark drum background was extracted. The surface of the grain pile was located according to an increase in grayscale intensity above some threshold. A line was then fit to these points from which the angle of the layer was calculated. An image of showing the cropped area of the drum image and a line fit to the layer surface is shown in Figure 1(D).

3 Experimental Results

3.1 Two regimes of flow

Figure 2 shows some representative time traces of the pile angle θ versus time for various rotation rates Ω taken from the Vancouver experiments with 2 mm glass beads. From the

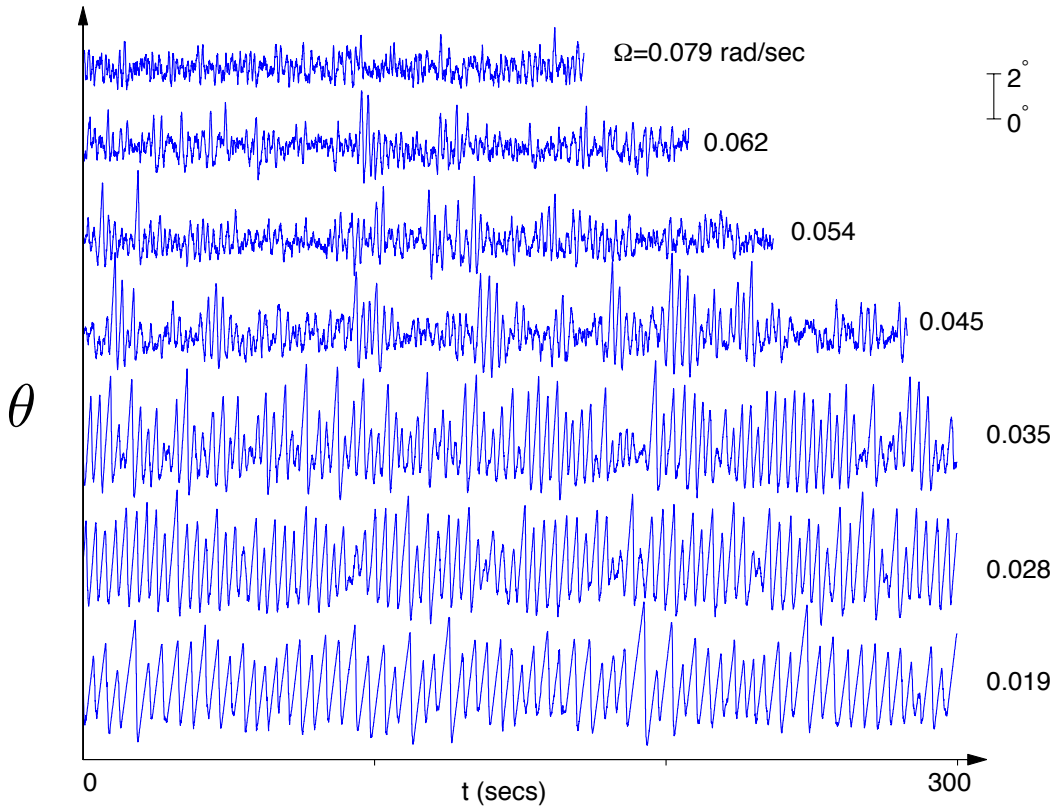

Figure 2: Representative time traces of θ at various rotation rates Ω measured in the Vancouver drum with 2 mm glass beads. At the lowest rotation rate ($\Omega = 0.019$ rad/sec) the system exhibits episodic avalanching. At the highest rotation rate ($\Omega = 0.079$ rad/sec) the system exhibits continuous flow. At intermediate flow rates the system exhibits both regimes in varying proportion.

time traces we extract the local maxima and local minima, and from these we calculate the average local maximum $\theta_{\max}$ and average local minimum $\theta_{\min}$. We also calculate the total time average θ which we denote $\langle\theta\rangle$.

The data shows the signature of the two regimes of granular flow. At the lowest rotation rate ($\Omega = 0.019$ rad/sec) the system exhibits pure avalanching with no regions of continuous flow. At the highest rotation rate ($\Omega = 0.079$ rad/sec) the system exhibits pure continuous flow with no avalanching. And at all intermediate rotation rates shown in Figure 2, the system intermittently transitions between avalanching and continuous flow.

In the episodic avalanching regime the mass of beads rotates as a solid body with the

drum until the pile reaches a critical angle θ_{start}, at which an avalanching layer of beads starts to flow. The avalanche stops when the angle of the pile reaches a second, lower critical angle θ_{stop}. These critical angles are reflected in the distinct and well-defined maximum and minimum pile angles θ_{max} and θ_{min}. We observe that θ_{max} and θ_{min} are independent of flow rate far from the transition to continuous flow for both the sand and the 3 mm glass beads.

In the continuous flow regime there is a continuously flowing layer of beads on the surface of the bead pile supported by the static, solidly rotating bulk. Far from the transition between episodic avalanching and continuous flow, the angle of the surface of the flowing layer remains relatively constant and stable in time, and the average angle of the pile increases as the flow rate increases. At low rotation rates which are just above the transition between episodic avalanching regime, the shape of the surface is almost linear. As the rotation rate increases, however, the surface begins to take on an "$\mathcal{S}$" shape. This effect is pronounced for thinner drums and there is good reason to believe it is due to the friction exerted on the flowing layer by the walls [15].

3.2 The transition between regimes: hysteresis and intermittency

Figure 3 shows plots of θ_{min}, $\langle\theta\rangle$, and θ_{max} against the flow rate $Q = \frac{1}{2}\Omega R^2$ for (A) 3 mm glass beads and (B) decorative aquarium sand. When the flow rate is very small or very

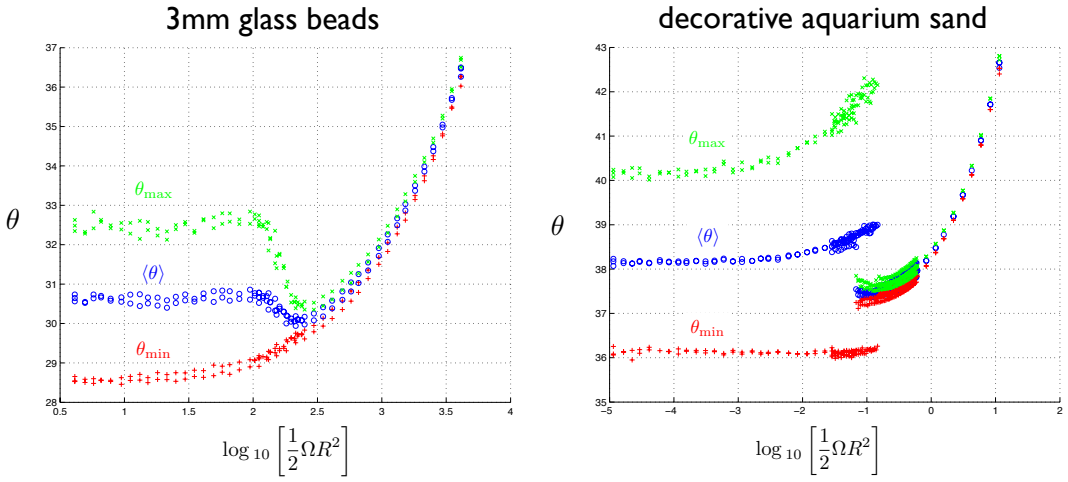

Figure 3: θ_{max}, $\langle\theta\rangle$, and θ_{min} for 3mm glass beads (left) and decorative aquarium sand (right) in the Vancouver drum for $W = 17\,\text{mm}$. Both materials exhibit episodic avalanching at low flow rates and continuous flow at high flow rates. (Left) the 3mm beads exhibit intermittent transition between avalanching and continuous flow for intermediate flow rates. (Right) the decorative aquarium sand exhibits hysteresis near the transition between avalanching and continuous flow, and no intermittency. The hysteric region was characterized thoroughly which is why there are more data points near transition.

large, the two materials exhibit qualitatively similar behavior. Overall, the sand has a significantly larger pile angle, which reflects its greater effective internal friction coefficients

and may be due to both to the irregular shape of the sand particles and greater interparticle friction forces. Both the glass beads and the sand exhibit two distinct regimes of granular flow: episodic avalanching at low flow rates, and continuous flow at high flow rates. When the pile angle θ is plotted against the flow rate Q, the signature of the avalanching regime is the widely disparate $\theta_{\min}$, $\langle\theta\rangle$, and $\theta_{\max}$. Far from the transition between avalanching and continuous flow these are independent of flow rate.

Close to the transition between episodic avalanching and continuous flow, however, the two materials exhibit qualitatively *different* behavior. For sand, there appears to be a sharp transition in θ between the continuous flow and avalanching regime. Furthermore, there is a range of flow rates for which both episodic avalanching and continuous flow is observed. In this regime we observe hysteresis; when the flow rate is increased from the avalanching regime, the system will remain in the avalanching regime until some critical maximum flow rate, and conversely for decreasing flow rate while in the continuous flow regime. Also, near the transition between the two regimes, the maximum θ for sand increases. This is because at high rotation speeds the pile angle continues to increase past θ_{start} even after the avalanche has been initiated. The same phenomenon is observed in $\theta_{\min}$.

For glass beads the transition between regimes exhibits smooth trends in $\theta_{\min}$, $\langle\theta\rangle$, and $\theta_{\max}$. This is consequence of the existence of intermittent transitions between episodic avalanching and continuous flow in this regime. These intermittent transitions are visible in the time traces plotted in Figure 2 for all but the largest and smallest rotation rates shown. The persistence time of either state before transition is dependent on the flow rate: when the flow rate is increased, the fraction of time that the system occupies the continuous flow state increases until the avalanching regime disappears altogether. Thus a smooth transition in pile angle is observed [4].

3.3 The importance of width

The pile angle is sensitive to the width of the drum when the width of the drum is smaller than the radius ($W/R \ll 1$). We observe a width dependence in the average pile angle for both the continuously flowing regime and avalanching regimes, as well as in critical angles θ_{start} and θ_{stop} for the avalanching regime. Figure 4 plots the average pile angle in the Vancouver drum for five different widths and compares the results. In the Vancouver drum we see that when $W \geq 110\,\text{mm}$ the width is no longer important.

3.4 Comparison of Woods Hole and Vancouver

Figure 5 compares the results from the Woods Hole and Vancouver drums with 3 mm glass spheres for various widths. We see that when the results for $\langle\theta\rangle$ collapse for the Woods Hole and Vancouver drums for three widths when plotted against the flow rate $Q = \frac{1}{2}\Omega R^2$. It appears therefore that even to $W/R \approx 1$ the inclination of the surface is controlled by the drum width. We note that the narrowest width in the Woods Hole drum was measured closer to 18 mm, but despite this slight difference between Woods Hole and Vancouver the data collapses impressively.

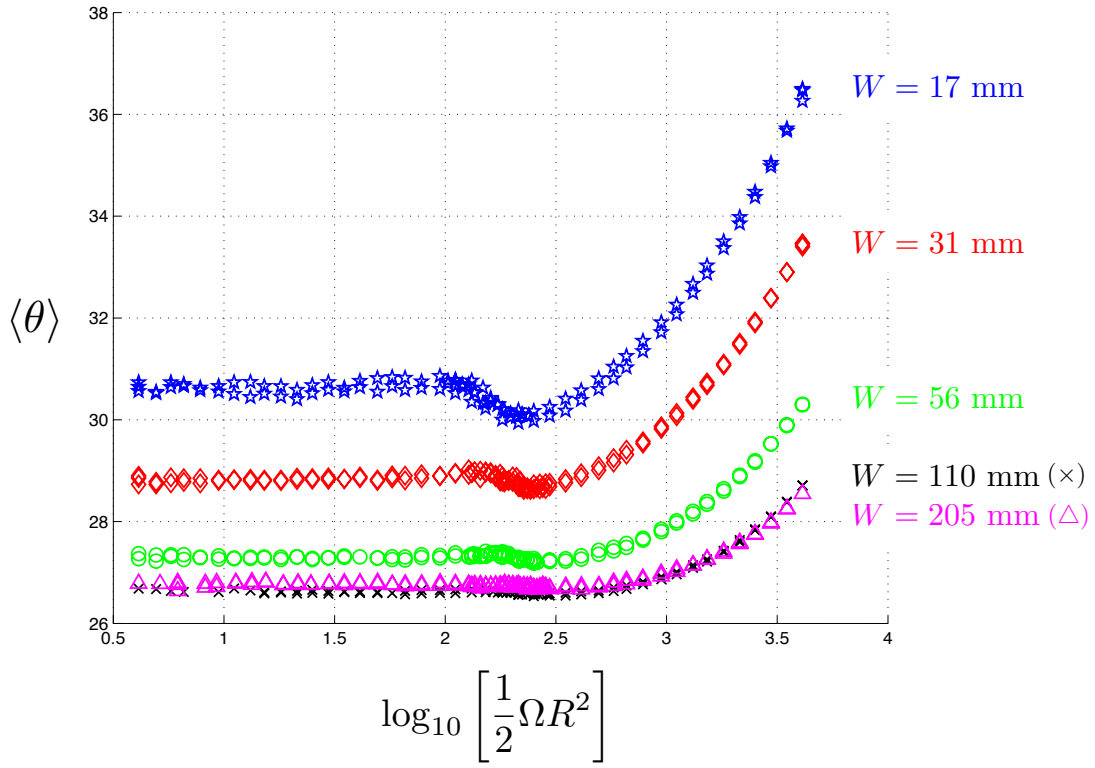

Figure 4: Average pile angle for five different widths in the Vancouver drum ($R = 144\,\text{mm}$). ($\star$, blue) $W = 17$ mm, ($\diamond$, red) $W = 31$ mm, ($\bigcirc$, green), $W = 56$ mm, ($\times$, black) $W = 110$ mm, ($\triangle$, magenta) $W = 205$ mm. The pile angle decreases as the width increases for small W/R. When W is comparable to R the pile angle appears to saturate and the width is no longer important.

4 Theory

We now attempt to develop a theoretical explanation for the observed behavior of the system. Our ultimate hope is to develop an explanation for the transition between episodic avalanching and continuous flow. We start by developing a model for the continuously flowing layer in narrow drums which relies on the fact that the width of the drum is the controlling parameter. The basis of our description is the continuum assumption and the conservation of mass and momentum for an incompressible granular fluid,

$$\nabla \cdot \mathbf{u} = 0, \tag{1}$$

$$\rho \frac{D\mathbf{u}}{Dt} = -\nabla p + \nabla \cdot \boldsymbol{\tau} + \rho \mathbf{g}, \tag{2}$$

where $\mathbf{u} = \{u, v, w\}$ is the velocity of the granular material, ρ is the bulk density, p is an isotropic pressure, $\boldsymbol{\tau}$ (τ_{ij} in indicial notation) is the deviatoric stress tensor, and $\mathbf{g}$ is gravitational acceleration. To relate the state of the system to the internal deviatoric stress τ_{ij} we employ the empirical "$\mu(I)$" law, where $\mu(I)$ is an effective friction coefficient of

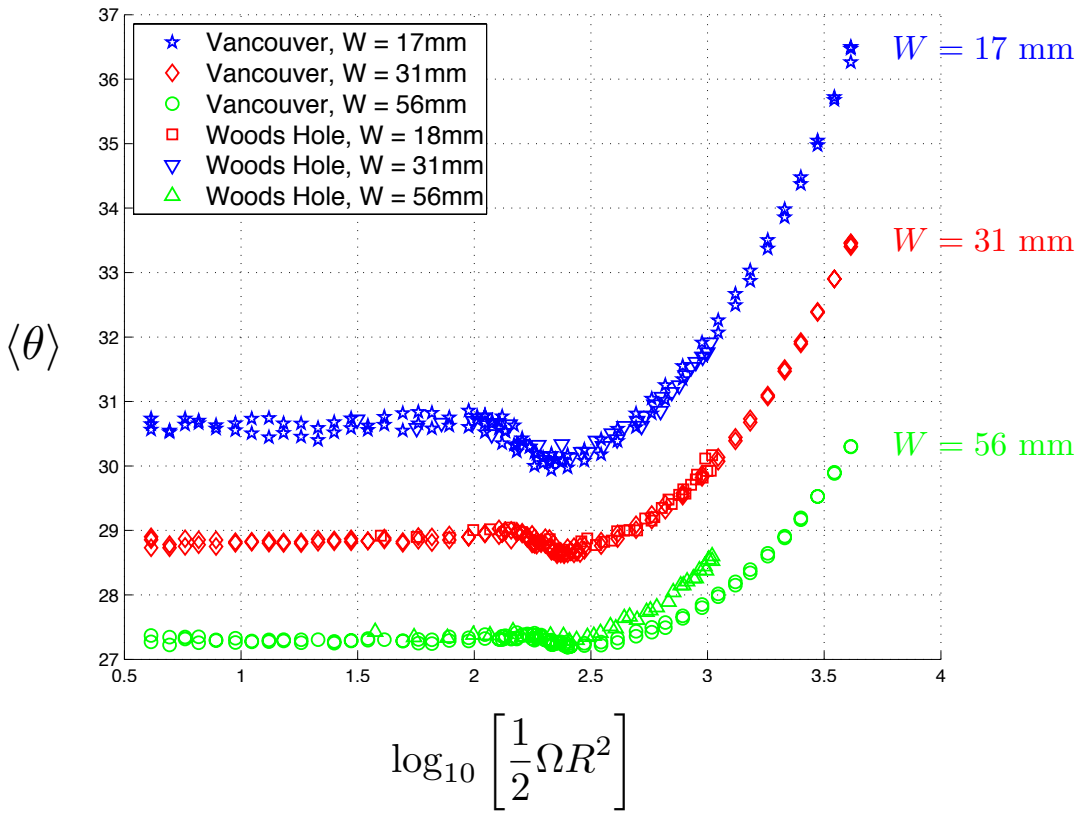

Figure 5: Comparison of the average pile angle for Woods Hole ($R = 69\,\text{mm}$) and Vancouver ($R = 144\,\text{mm}$) drums for three widths W. ($\star$, blue) Vancouver with $W = 17\,\text{mm}$, ($\triangledown$, blue) Woods Hole with $W = 18\,\text{mm}$, ($\diamond$, red) Vancouver with $W = 31\,\text{mm}$, ($\square$, red) Woods Hole with $W = 31\,\text{mm}$. ($\bigcirc$, green) Vancouver with $W = 56\,\text{mm}$, ($\triangle$, green) Woods Hole with $W = 56\,\text{mm}$. We see the observed pile angles appear to be controlled by the width of the drum even to when $W/R \approx 1$ (for the Woods Hole drum with $W = 56\,\text{mm}$): the pile angles collapse for Woods Hole and Vancouver when plotted against flow rate $Q = \frac{1}{2}\Omega R^2$.

proportionality between the deviatoric stress and the pressure, or normal force such that [9],

$$\tau_{ij} = \mu(I) p \frac{\dot{\gamma}_{ij}}{|\dot{\gamma}|}, \tag{3}$$

where $\dot{\gamma}_{ij}$ is the rate of strain tensor and I is the "inertia number". The inertia number is defined

$$I = \frac{|\dot{\gamma}| d}{\sqrt{p/\rho}}, \tag{4}$$

where $|\dot{\gamma}| = \sqrt{\frac{1}{2}\dot{\gamma}_{ij}\dot{\gamma}_{ij}}$ is the second invariant of $\dot{\gamma}_{ij}$ and d is particle diameter. The inertia number can be interpreted as the ratio of two characteristic timescales in the relative motion of two grain layers: kinematic T_{kin} and mechanical T_{mech} [10]. The kinematic timescale is a

characteristic timescale for the relative motion of the grain layers,

$$T_{\text{kin}} = \frac{d}{V_{\text{kin}}} = \frac{d}{d|\dot{\gamma}|} = \frac{1}{|\dot{\gamma}|}, \tag{5}$$

where V_{kin} is the relative velocity of the grain layers. The mechanical timescale is a characteristic timescale for the acceleration of the layers a_{mech} due to mechanical forces exerted on the layer,

$$T_{\text{mech}} = \sqrt{\frac{d}{a_{\text{mech}}}} = \sqrt{\frac{d}{F/m}} = \sqrt{d\,\frac{\rho dA}{pA}} = d\sqrt{\frac{\rho}{p}}, \tag{6}$$

where A is the area of the layer, $F = pdL$ is the normal force exerted on the layer due to the pressure p, and $m = \rho d^2 L$ is the mass of the layer. The ratio of these timescales is the inertia number,

$$I = \frac{T_{\text{mech}}}{T_{\text{kin}}} = \frac{|\dot{\gamma}|d}{\sqrt{p/\rho}}. \tag{7}$$

When the inertia number is large, the rate of deformation of the granular medium is fast relative to the rate of displacement of the medium due to mechanical forces. Experiments in shear cells and on inclined planes show that the effective friction coefficient μ collapses to a single curve when plotted against I [5]. We see that the effective coefficient has some finite value μ_1 at $I = 0$ and asymptotes to a second limiting value μ_2 as $I \to \infty$. To capture this dependence we use the formula [9]

$$\mu(I) = \mu_1 + (\mu_2 - \mu_1)\,\frac{I}{I + I_0}, \tag{8}$$

where I_0 is a material parameter which characterizes how quickly $\mu(I)$ transitions between its lower and upper values with increasing I. These equations serve as a starting point for the derivation of approximate models for granular flow in the rotating drum.

4.1 Thin, Shallow, Slippy

For our first attempt to model the flowing layer we reduce the full conservation equations greatly through a series of approximations and assumptions. We assume that the width and depth of the flow are much smaller than it's length, that we can neglect inertia, and that the internal friction coefficient $\mu(I)$ and the friction coefficient between the flowing beads and the wall are small. With these assumptions we are able to derive a single partial differential equation for the height profile of the flowing layer which is easily solved numerically. The derived model, which we call the "thin, shallow, slippy' model, or "TSS" then represents the leading order system of equations in a formal asymptotic expansion. The derivation of the model from the full detailed conservation laws illustrates clearly its approximations and limitations.

4.1.1 The momentum equation

We start by defining the characteristic dimensions for the flow: length R, depth H, and width W. A schematic of the drum, the flowing layer, and coordinate system is shown

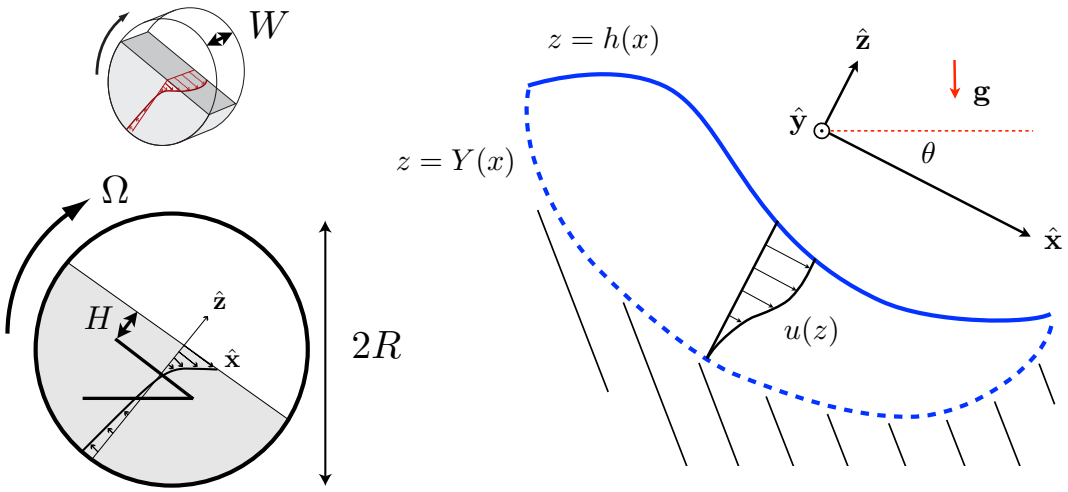

Figure 6: A schematic of the drum illustrating the characteristic dimensions and showing the coordinate system. The radius of the drum is R, the (average or characteristic) depth of the flowing layer is H, and the width of the drum is W. The surface of the flowing layer is defined at $z = h(x)$ and the yield surface dividing the flowing layer and the static bed of grains beneath is defined at $z = Y(x)$. The coordinate system is tilted at an angle θ with respect to the vertical as defined by the direction of gravity.

in Figure 6. We assume that the flow is thin and shallow such that $\epsilon = H/R \ll 1$ and $\Delta = W/H \ll 1$. These yield scalings for u, v, and w through the mass conservation equation, and from these we find scalings for $\dot{\gamma}_{ij}$ and τ_{ij}. If we substitute

$$x = Rx', \qquad y = Wy', \qquad z = Hz', \qquad u = Uu', \qquad v = Vv', \qquad w = \mathbb{W}w', \tag{9}$$

where U, V, and $\mathbb{W}$ are characteristic velocities and the primes denote a non-dimensional quantity. The mass conservation equation (1) then becomes

$$\left(\frac{U}{R}\right)\frac{\partial u'}{\partial x'} + \left(\frac{V}{W}\right)\frac{\partial v'}{\partial y'} + \left(\frac{\mathbb{W}}{H}\right)\frac{\partial w'}{\partial z'} = 0. \tag{10}$$

For each term to be of comparable magnitude, we must have that $V \sim \epsilon\Delta U$ and $\mathbb{W} \sim \epsilon U$. Next we need to non-dimensionalize the pressure and deviatoric stress tensor. We assume that the pressure is hydrostatic, which implies that

$$p = \rho g H p'. \tag{11}$$

The deviatoric stress tensor is defined as $\tau_{ij} = \mu(I)p\dot{\gamma}_{ij}/|\dot{\gamma}|$, so we need to analyze the rate of strain tensor $\dot{\gamma}_{ij}$ in order to non-dimensionalize it properly. The rate of strain tensor is defined as

$$\dot{\gamma}_{ij} = \begin{pmatrix} 2u_x & u_y + v_x & u_z + w_z \\ u_y + v_x & 2v_y & v_z + w_y \\ u_z + w_z & v_z + w_y & 2w_z \end{pmatrix}, \tag{12}$$

where we are using the shorthand $u_x = \partial u/\partial x$ here for compactness. Introducing our scalings we find

$$\dot{\gamma}_{ij} = \frac{U}{H}\begin{pmatrix} 2\epsilon u_x & \frac{1}{\Delta}u_y + \epsilon^2\Delta v_x & u_z + \epsilon^2 w_z \\ \frac{1}{\Delta}u_y + \epsilon^2\Delta v_x & 2\epsilon v_y & \epsilon\Delta v_z + \frac{\epsilon}{\Delta}w_y \\ u_z + \epsilon^2 w_z & \epsilon\Delta v_z + \frac{\epsilon}{\Delta}w_y & 2\epsilon w_z \end{pmatrix}. \tag{13}$$

We see therefore that in order for the flow to be two-dimensional at leading order, we need to assume that the y-dependence in the velocity is at most a correction at order Δ^2, or that

$$\mathbf{u}(x,y,z,t) = \mathbf{u}^{(0)}(x,z,t) + \Delta^2\mathbf{u}^{(2)}(x,y,z,t). \tag{14}$$

If we assume this then we find for $\dot{\gamma}_{ij}$,

$$\dot{\gamma}_{ij} = \frac{U}{H}\begin{pmatrix} 2\epsilon u_x & \Delta u_y + \epsilon^2\Delta v_x & u_z + \epsilon^2 w_z \\ \Delta u_y + \epsilon^2\Delta v_x & 2\epsilon\Delta^2 v_y & \epsilon\Delta v_z + \epsilon\Delta w_y \\ u_z + \epsilon^2 w_z & \epsilon\Delta v_z + \epsilon\Delta w_y & 2\epsilon w_z \end{pmatrix}. \tag{15}$$

Keeping in mind that the second invariant is $|\dot{\gamma}| = \sqrt{\frac{1}{2}\dot{\gamma}_{ij}\dot{\gamma}_{ij}}$ we then non-dimensionalize each component of τ_{ij},

$$(\tau_{xx}, \tau_{zz}) = \widehat{\mu}\rho g H\epsilon\left(\tau'_{xx}, \tau'_{zz}\right), \qquad \tau_{yy} = \widehat{\mu}\rho g H\epsilon\Delta^2\tau'_{yy}, \tag{16}$$

$$\tau_{xy} = \widehat{\mu}\rho g H\Delta\tau'_{xy} \qquad \tau_{yz}, = \widehat{\mu}\rho g\epsilon\Delta\tau'_{yz}, \qquad \tau_{xz} = \widehat{\mu}\rho g H\tau'_{xz}, \tag{17}$$

where we have substituted $\mu(I) = \widehat{\mu}\mu'$ so that $\widehat{\mu}$ represented the magnitude of $\mu(I)$. Inserting these scalings into the momentum conservation equations yields

$$\mathrm{Fr}\frac{Du}{Dt} = -\epsilon\frac{\partial p}{\partial x} + \sin\theta + \widehat{\mu}\left(\epsilon^2\frac{\partial \tau_{xx}}{\partial x} + \frac{\partial \tau_{xy}}{\partial y} + \frac{\partial \tau_{xz}}{\partial z}\right), \tag{18}$$

$$\epsilon\Delta\mathrm{Fr}\frac{Dv}{Dt} = -\frac{\partial p}{\partial y} + \widehat{\mu}\left(\epsilon\frac{\partial \tau_{xy}}{\partial x} + \epsilon\Delta\frac{\partial \tau_{yy}}{\partial y} + \epsilon\frac{\partial \tau_{yz}}{\partial z}\right), \tag{19}$$

$$\epsilon\mathrm{Fr}\frac{Dw}{Dt} = -\frac{\partial p}{\partial z} - \cos\theta + \widehat{\mu}\left(\epsilon\frac{\partial \tau_{xz}}{\partial x} + \epsilon\frac{\partial \tau_{yz}}{\partial y} + \epsilon\frac{\partial \tau_{zz}}{\partial z}\right), \tag{20}$$

where we have defined the Froude number $\mathrm{Fr} = U^2/gH$. If we assume that inertia is negligible such that $\mathrm{Fr} \ll 1$ and $\{\widehat{\mu}, \theta\} = O(\epsilon)$ (a fair assumption for many materials for which $\mu(I) \approx 0.2$–0.4), the leading order equations with dimensionality restored are

$$0 = -\frac{\partial p}{\partial x} + \rho g\sin\theta + \frac{\partial \tau_{xy}}{\partial y} + \frac{\partial \tau_{xz}}{\partial z}, \tag{21}$$

$$0 = -\frac{\partial p}{\partial y}, \tag{22}$$

$$0 = -\frac{\partial p}{\partial z} - \rho g\cos\theta. \tag{23}$$

In other words, we have that the pressure is hydrostatic, and that the x–momentum is a balance between lateral and vertical shear-induced friction, gravity, and the pressure which will come in to the equations as a shallow-water-like term dependent on the height of the flowing layer.

4.1.2 Boundary conditions

To proceed with the model we need boundary conditions at the sidewalls, at the material free surface forming the upper boundary of the flowing layer, and at the yield surface forming the lower boundary. The stress at the sidewalls is modeled as an effective friction force which opposites the velocity of the flowing layer there,

$$\boldsymbol{\tau} \cdot \mathbf{n} = \mu_{\mathrm{w}} p \frac{u\widehat{\mathbf{e}}_x + w\widehat{\mathbf{e}}_z}{\sqrt{u^2+w^2}} \left(\mathbf{n} \cdot \widehat{\mathbf{e}}_y\right), \tag{24}$$

where μ_{w} is the effective friction coefficient between the flowing beads and the wall and $\mathbf{n}$ is the surface normal which points into the flowing layer. At the confining sidewalls at $y = 0$ and $y = W$ we therefore have that

$$\tau_{xy}\big|_{y=0} = \mu_{\mathrm{w}} p \,\mathrm{sgn}(u) \qquad \text{and} \qquad \tau_{xy}\big|_{y=W} = -\mu_{\mathrm{w}} p \,\mathrm{sgn}(u). \tag{25}$$

It was observed by de Ryck and Louisnard [2] that in the case of very rough walls with a large friction coefficient we would expect to find a stationary monolayer of beads adjacent to the wall such that the effective friction coefficient between the flowing layer and the wall would simply be μ_1. This implies that μ_{w} has the constraint $\mu_{\mathrm{w}} \leq \mu_1$.

At the top of the flowing layer we define the material free surface as $z = h(x)$. Here we assume that the same free surface boundary conditions used for common fluids like water are applicable, or that,

$$p\big|_{z=h} = 0 \qquad \text{and} \qquad \tau_{xz}\big|_{z=h} = 0. \tag{26}$$

The base of the layer is a yield surface which we define as $z = Y(x)$. At this boundary the velocity of the beads equals the velocity of the beads in the static layer which rotate with the drum, or that

$$\mathbf{u}\big|_{z=Y} = u_{\widetilde{\theta}} \widehat{\mathbf{e}}_{\widetilde{\theta}}, \tag{27}$$

where $\widetilde{\theta}$ is the angle associated with the coordinate (x, Y) in the rotated coordinate frame. The tangential velocity $u_{\widetilde{\theta}}$ is simply Ωr, where Ω is the rotation rate of the drum and r is the radial position. We therefore have

$$u\big|_{z=Y} = u_{\widetilde{\theta}} \sin\widetilde{\theta} = \Omega Y, \tag{28}$$

$$w\big|_{z=Y} = u_{\widetilde{\theta}} \cos\widetilde{\theta} = -\Omega x. \tag{29}$$

If we non-dimensionalize each velocity at the boundary with ΩR such that $u = \Omega R u'$ and $Y = HY'$ we find

$$u'\big|_{z=Y} = \epsilon Y', \tag{30}$$

and so in our leading order approximation the boundary conditions at the yield surface $z = Y(x)$ are

$$u\big|_{z=Y} = 0 \qquad \text{and} \qquad w\big|_{z=Y} = -\Omega x. \tag{31}$$

4.1.3 Depth-averaged mass conservation equation

We can simplify our system of equations further by using the depth-averaged mass conservation equation commonly used for thin layers. To find this equation we first average the continuity equation across the width of the drum. Using our assumption that the flow is two-dimensional to leading order in Δ (14) and impermeability at the drum walls, we find

$$\begin{aligned} 0 &= \frac{1}{W}\int_0^W \left[\frac{\partial u}{\partial x} + \frac{\partial v}{\partial y} + \frac{\partial w}{\partial z}\right] \mathrm{d}y, \\ &= \frac{\partial u}{\partial x} + \frac{\partial w}{\partial z} + \frac{1}{W}\left(v\,\big|_{y=W} - v\,\big|_{y=0}\right), \\ &= \frac{\partial u}{\partial x} + \frac{\partial w}{\partial z}. \end{aligned} \tag{32}$$

We then integrate in z from the yield surface at $z = Y(x)$ to the upper material free surface at $z = h(x)$,

$$\int_Y^h \left[\frac{\partial u}{\partial x} + \frac{\partial w}{\partial z}\right] \mathrm{d}z = 0. \tag{33}$$

At $z = Y$ we have that $u = 0$ and $w = -\Omega x$. At $z = h$, which is a material surface, we have the kinematic condition which requires

$$w\,\big|_{z=h} = \frac{\partial h}{\partial t} + u\,\big|_{z=h}\frac{\partial h}{\partial x}. \tag{34}$$

We use Leibnitz's rule and the boundary condition at $z = Y$ to identify

$$\int_Y^h \frac{\partial u}{\partial x}\,\mathrm{d}z = \frac{\partial}{\partial x}\int_Y^h u\,\mathrm{d}z - \frac{\partial h}{\partial x}u\,\big|_{z=h} + \frac{\partial Y}{\partial x}u\,\big|_{z=Y} = \frac{\partial}{\partial x}\int_Y^h u\,\mathrm{d}z - \frac{\partial h}{\partial x}u\,\big|_{z=h}. \tag{35}$$

Noting that $\int_Y^h u\,\mathrm{d}z = Q(x)$ is the width-specific flux, we find

$$\begin{aligned} 0 &= \frac{\partial}{\partial x}\int_Y^h u\,\mathrm{d}z - \frac{\partial h}{\partial x}u(z=h) + \frac{\partial Y}{\partial x}u(z=Y) + w(z=h) - w(z=Y), \\ &= \frac{\partial h}{\partial t} + \frac{\partial Q}{\partial x} + \Omega x, \end{aligned} \tag{36}$$

which we write

$$\frac{\partial h}{\partial t} + \frac{\partial Q}{\partial x} = -\Omega x. \tag{37}$$

Furthermore, we place the origin of the coordinate system at the center of the drum. When the drum is half-filled and we neglect any changes in volume fraction of the flowing grains, the total conservation of granular material along with our choice of origin implies that

$$\int_{-R}^{R} h(x)\,\mathrm{d}x = 0. \tag{38}$$

Another way to state this condition is that the addition of material in one part of the drum requires a subtraction of material elsewhere.

4.1.4 Width-averaged momentum equation

To simplify the x–momentum equation further we observe that our "2D" assumption that the $y-$dependence of u is at most a correction of $O(\Delta^2)$ permits us to average the x–momentum equation in y. This leaves all terms unchanged except for $\partial\tau_{xy}/\partial y$, which is replaced by the boundary conditions at either bounding wall. Because the velocity is unidirectional we find

$$\frac{1}{W} = \int_0^W \frac{\partial \tau_{xy}}{\partial y}\,\mathrm{d}y = \frac{1}{W}\left(\tau_{xy}\,\big|_{y=W} - \tau_{xy}\,\big|_{y=0}\right) = -2\delta p, \tag{39}$$

where we have defined the wall friction parameter $\delta = \mu_\mathrm{w}/W$ is the friction coefficient between the flowing bead layer and the sidewall. The other terms in the x-momentum equation are unchanged and so it becomes

$$0 = -\frac{\partial p}{\partial x} + \rho g \sin\theta - 2\delta p + \frac{\partial \tau_{xz}}{\partial z}. \tag{40}$$

4.1.5 A note on θ

In the theory, we have defined θ as the inclination of our coordinate system, while in the experiments θ is defined by a linear fit to its surface in the cropped region of the image in Figure 1(D). In the solution of the model, we found that is was slightly more convenient to define the inclination of the coordinate system as the *average* inclination of the slope, rather than the inclination of the slope over some region of the surface in the center of the drum. Despite the confusion caused by the different definitions, it seems that these θ are nevertheless approximately the same. The definition that θ in the model is the average slope of the surface implies that $h(x)$ must satisfy

$$\frac{1}{2R}\int_{-R}^{R} \frac{\partial h}{\partial x}\,\mathrm{d}x = \frac{1}{2R}\left(h(R) - h(-R)\right) = 0. \tag{41}$$

4.2 Solution of TSS

To solve the TSS model we first observe that Equation (23) implies that pressure is hydrostatic, or

$$p = \rho g \cos\theta (h - z), \tag{42}$$

where we have applied the boundary condition $p\,|_{z=h} = 0$. Inserting this into the width-averaged x–momentum equation (40) yields

$$0 = -\rho g \cos\theta \frac{\partial h}{\partial x} + \rho g \sin\theta - 2\delta\rho g \cos\theta (h - z) + \frac{\partial \tau_{xz}}{\partial z}. \tag{43}$$

Rearranging and integrating from z to h yields

$$\tau_{xz} = -\rho g \cos\theta (h - z)\left[h_x - \tan\theta + \delta(h - z)\right]. \tag{44}$$

We note that to leading order $\tau_{xz} = \mu(I)p = \mu(I)\rho g\cos\theta(h-z)$, which implies

$$\mu(I) = -h_x + \tan\theta - \delta(h - z). \tag{45}$$

The definition of $\mu(I)$ is

$$\mu(I) = \mu_1 + (\mu_2 + \mu_1)\,\frac{I}{I + I_0}, \tag{46}$$

and substitution this into Equation (45) and solving for I yields

$$I = I_0 \left[\frac{\tan\theta - \mu_1 - h_x - \delta(h - z)}{\mu_2 - \tan\theta + h_x + \delta(h - z)}\right]. \tag{47}$$

We can write this in a simpler way in terms of the yield surface $z = Y$. In order for the granular material to flow we must have that the shear stress exceeds $\mu_1 p$, or that

$$\tau_{xz} > \mu_1 p. \tag{48}$$

This implies that in the flowing layer we have

$$-h_x + \tan\theta - \delta(h - z) > \mu_1, \tag{49}$$

and that the yield surface $z = Y$ is defined by

$$Y = h - \frac{\tan\theta - \mu_1 - h_x}{\delta}. \tag{50}$$

We can therefore rewrite the relation for I as

$$I = I_0 \left[\frac{\delta(z - Y)}{\Delta\mu - \delta(z - Y)}\right], \tag{51}$$

where we have defined $\Delta\mu = \mu_2 - \mu_1$. To leading order we have

$$I = \frac{|\dot{\gamma}|d}{\sqrt{p/\rho}} = \frac{u_z d}{\sqrt{g\cos\theta(h - z)}}, \tag{52}$$

and combining this with (51) and rearranging provides an equation for $\partial u/\partial z$,

$$\frac{\partial u}{\partial z} = \frac{\delta I_0\sqrt{g\cos\theta}}{d\Delta\mu}\left[\frac{\sqrt{h - z}(z - Y)}{1 - \frac{\delta}{\Delta\mu}(z - Y)}\right]. \tag{53}$$

With this equation we are then able to calculate the flow rate Q and are then in a position to solve the depth-averaged momentum equation. To calculate $Q = \int u\,\mathrm{d}z$, we first observe that through integration by parts,

$$\int_Y^h (h - z)\frac{\partial u}{\partial z}\,\mathrm{d}z = u(h - z)\Big|_Y^h + \int_Y^h u\,\mathrm{d}z = Q, \tag{54}$$

which means that we have to calculate only one integral for Q,

$$Q = \frac{\delta I_0\sqrt{g\cos\theta}}{d}\int_Y^h \frac{(h - z)^{3/2}\,(z - Y)}{\Delta\mu - \delta(z - Y)}\,\mathrm{d}z. \tag{55}$$

This integral can be calculated analytically. We find

$$Q = \frac{2I_0\sqrt{g\cos\theta}}{d}\left(\frac{\Delta\mu}{\delta}\right)^{5/2} q\left(\frac{\tan\theta - \mu_1 - h_x}{\Delta\mu}\right), \tag{56}$$

where

$$q(s) = (1-s)\left[\sqrt{1-s}\tan^{-1}\left(\sqrt{\frac{s}{1-s}}\right) - \sqrt{s} + \frac{1}{3}s^{3/2}\right] + \frac{2}{15}s^{5/2}. \tag{57}$$

Note that

$$q(s \to 0) \approx \frac{2}{35}s^{7/2} + O\left(s^{9/2}\right). \tag{58}$$

From the expression for $q(s)$ we see that s cannot be greater than 1, or that $\tan\theta - h_x$ cannot be greater than μ_2. This reflects our assumption that inertia is negligible and the flow is not accelerating. If $\tan\theta - h_x > \mu_2$, then the pile is too steep for friction forces to balance gravitational forces and the flow must accelerate. Further, we can easily calculate that $q(s=1) = 2/15$, which implies that

$$\frac{d\Omega R^2}{4I_0\sqrt{g\cos\theta}}\left(\frac{\delta}{\Delta\mu}\right)^{5/2} < \frac{2}{15}, \tag{59}$$

for the existence of a solution without taking into account inertial terms.

This expression for Q yields a partial differential equation for $h(x,t)$ when inserted into the depth-averaged mass conservation equation (37). The steady solution satisfies

$$\frac{\partial Q}{\partial x} = -\Omega x. \tag{60}$$

The impermeability boundary condition at the boundaries of the drum require that $u\,|_{x=\pm R} = 0$, which implies that

$$Q\,\big|_{x=\pm R} = 0. \tag{61}$$

Integrating Equation (60) from $x = -R$ to x yields

$$Q = \frac{1}{2}\Omega\left(R^2 - x^2\right) = \frac{\Omega R^2}{2}\left(1 - \left(\frac{x}{R}\right)^2\right). \tag{62}$$

The general steady problem is then to solve the nonlinear ordinary differential equation

$$q\left(\frac{\tan\theta - \mu_1 - h_x}{\Delta\mu}\right) = \frac{\Omega R^2 d}{4I_0\sqrt{g\cos\theta}}\left(\frac{\delta}{\Delta\mu}\right)^{5/2}\left(1 - \left(\frac{x}{R}\right)^2\right), \tag{63}$$

under the constraint that

$$\int_{-R}^{R} h(x)\,\mathrm{d}x = 0. \tag{64}$$

4.2.1 The "low-flux" limit

The problem is simplified in the limit when $s = \frac{1}{\Delta\mu}(\tan\theta - \mu_1 - h_x)$ in $q(s)$ is small. We have $q(s \to 0) = (2/35)s^{7/2} + O(s^{9/2})$, which means that

$$\frac{2}{35}\left(\frac{\tan\theta - \mu_1 - h_x}{\Delta\mu}\right)^{7/2} = \frac{\Omega R^2 d}{4I_0\sqrt{g\cos\theta}}\left(\frac{\delta}{\Delta\mu}\right)^{5/2}\left(1 - \left(\frac{x}{R}\right)^2\right). \tag{65}$$

Solving for h_x, we find,

$$\frac{\partial h}{\partial x} = \tan\theta - \mu_1 - \Delta\mu\left(\frac{35\Omega R^2 d}{8I_0\sqrt{g\cos\theta}}\right)^{2/7}\left(\frac{\delta}{\Delta\mu}\right)^{5/7}\left(1 - \left(\frac{x}{R}\right)^2\right)^{2/7}. \tag{66}$$

A single integration yields $h(x)$,

$$\begin{aligned} h(x) - h(-R) = {} & \tan\theta - \mu_1 (x + R) \\ & - \Delta\mu\left(\frac{35\Omega R^2 d}{8I_0\sqrt{g\cos\theta}}\right)^{2/7}\left(\frac{\delta}{\Delta\mu}\right)^{5/7}\int_{-R}^{x}\left(1 - \left(\frac{x'}{R}\right)^2\right)^{2/7}\,\mathrm{d}x', \end{aligned} \tag{67}$$

where $h(-R)$ is determined by the total conservation of mass expressed by Equation (64).

4.2.2 General solution

The function $q(s)$ cannot be inverted analytically, which means that without approximation we cannot find a closed-form expression for $\partial h/\partial x$. Thus we must turn to numerics. We can express the general problem given by Equation (63) by writing

$$q(s) = C\left(1 - \left(\frac{x}{R}\right)^2\right). \tag{68}$$

Our strategy is to map $q(s)$ as a function of s, invert the mapping, and then integrate the inverted mapping to find $h(x)$. If we substitute a function $x^*(s)$ for x in (68), we can write

$$x = \pm R\sqrt{1 - \frac{1}{C}q(s)}. \tag{69}$$

We then find numerically the x which correspond to all valid s, and therefore also $s(x)$ as a function of x. Formally then,

$$q^{-1}\left(C\left[1 - \left(\frac{x}{R}\right)^2\right]\right) = s(x) = \frac{1}{\Delta\mu}\left(\tan\theta - \mu_1 - \frac{\partial h}{\partial x}\right), \tag{70}$$

so

$$h(x) - h(-R) = (\tan\theta - \mu_1)(x + R) - \Delta\mu\int_{-R}^{x} s(x)\,\mathrm{d}x', \tag{71}$$

where condition (64) then yields $h(-R)$. In practice, we use MATLAB's `cumtrapz` to calculate the integral in (71) using the mapping between s and x and find the difference $h(x) - h(-R)$. Integrating this difference yields $h(-R)$, since (64) implies

$$h(-R) = -\frac{1}{2R}\int_{-R}^{R} h(x) - h(-R)\,\mathrm{d}x. \tag{72}$$

Finally, after finding $h(x)$ for this initial choice of θ, we must iterate until the condition (41) is met. An example of $h(x)$ is shown in Figure 7 in the rotated frame (A) and lab frame (B).

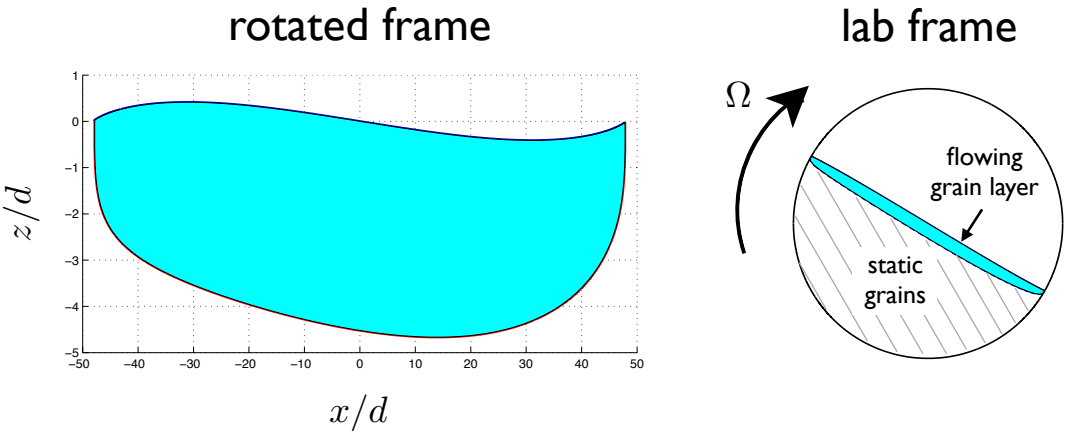

Figure 7: An example of the geometry of a predicted grain layer as defined by the upper free surface $h(x)$ and the lower yield surface $Y(x)$. (Left) the calculated geometry of the grain layer, shaded in blue, in the rotated frame with an exaggerated vertical dimension. (Right) the calculated geometry of the grain layer, shaded in blue, as it looks in the lab frame inserted into the drum.

4.3 Crude inertial model for avalanches

By neglecting inertial terms in the momentum equation, we preclude the possibility for avalanches, despite the fact that we might still consider time-dependent behavior by retaining the time-derivative in the depth-averaged continuity equation (37). More on why...

To consider inertia, we could solve the full equations, but this would involve significant computational effort. Instead we develop a crude "depth-averaged model" which, upon assuming a functional form for the velocity profile $u(z)$ that does not change in time or along the layer, yields a partial differential equation for the average velocity $U(x,t) = \frac{1}{h-Y}\int_Y^h u\,\mathrm{d}z$, and the height of the layer $h(x,t)$. If we use the same scaling as for the "thin, shallow, slippy" model, we still find from the z-momentum equation that pressure is hydrostatic,

$$p = \rho g \cos\theta (h - z). \tag{73}$$

However this time we retain all terms in the (y-averaged) x-momentum equation. Using the continuity equation we have the identity

$$\frac{\partial}{\partial x}\left(u^2\right) + \frac{\partial}{\partial z}(uw) = u\frac{\partial u}{\partial x} + u\frac{\partial w}{\partial z} + u\left(\frac{\partial u}{\partial x} + \frac{\partial w}{\partial z}\right) = u\frac{\partial u}{\partial x} + u\frac{\partial w}{\partial z}, \tag{74}$$

which means that the y-averaged x-momentum equation can be written

$$\rho\left(\frac{\partial u}{\partial t} + \frac{\partial}{\partial x}\left(u^2\right) + \frac{\partial}{\partial z}(uw)\right) = -p_x + \rho g \sin\theta - 2\delta p + \frac{\partial \tau_{xz}}{\partial z}. \tag{75}$$

Inserting hydrostatic pressure yields

$$\rho\left(\frac{\partial u}{\partial t}+\frac{\partial}{\partial x}\left(u^2\right)+\frac{\partial}{\partial z}\left(uw\right)\right)=\rho g\cos\theta\left(\tan\theta-h_x-2\delta(h-z)\right)+\frac{\partial\tau_{xz}}{\partial z}. \tag{76}$$

Integrating in z from $z=Y$ to $z=h$ and applying Leibniz's rule to remove derivatives from integrals yields

$$\rho\left[\frac{\partial}{\partial t}\int_b^h u\,\mathrm{d}z-\frac{\partial h}{\partial t}u(z=h)+\frac{\partial Y}{\partial t}u(z=b)\right]+\rho\left[\frac{\partial}{\partial x}\int_Y^h u^2\,\mathrm{d}z-\frac{\partial h}{\partial x}u^2(z=h)+\frac{\partial Y}{\partial x}u^2(z=Y)\right]\cdots$$
$$+\rho uw\Big|_{z=h}-\rho uw\Big|_{z=Y}=\rho g(h-Y)\cos\theta\left[\tan\theta-h_x-\delta(h-Y)\right]+\tau_{xz}\Big|_{z=h}-\tau_{xz}\Big|_{z=Y}. \tag{77}$$

Using the kinematic condition for w at $z=h$ and applying $\tau_{xz}=0$ at $z=h$, $u=0$ at $z=Y$, and $\tau_{xz}\big|_{z=Y}=\mu_1\rho gD\cos\theta$ where $D=h-Y$ is the depth of the layer, yields the depth-averaged momentum equation

$$\frac{\partial}{\partial t}\int_Y^h u\,\mathrm{d}z+\frac{\partial}{\partial x}\int_Y^h u^2\,\mathrm{d}z=gD\cos\theta\left(-\frac{\partial h}{\partial x}+\tan\theta-\delta D-\mu_1\right), \tag{78}$$

At this stage we need to assume a form for the velocity profile $u(z)$ in order to proceed. We derive our velocity profile from the Thin, Shallow, Slippy model, which is undoubtedly a crude approximation, but perhaps slightly less crude than assuming either a constant or a linear velocity profile. In this model we find a relation for the gradient $\partial u/\partial z$,

$$\frac{\partial u}{\partial z}=\frac{\delta I_0\sqrt{g\cos\theta}}{d\Delta\mu}\left[\frac{\sqrt{h-z}(z-Y)}{1-\frac{\delta}{\Delta\mu}(z-Y)}\right]. \tag{79}$$

The "low flux" assumption, or the assumption that Ω (and therefore $Q=\frac{1}{2}\Omega R^2$) is small is equivalent to assuming that the depth of the layer is small, and therefore $z-Y\ll 1$. If we assume this we find a simpler relation for $\partial u/\partial z$,

$$\frac{\partial u}{\partial z}=\frac{\delta I_0\sqrt{g\cos\theta}}{d\Delta\mu}\sqrt{h-z}(z-Y), \tag{80}$$

from which we can obtain a well-behaved velocity profile $u(z)$,

$$u(z)=\frac{\delta I_0\sqrt{g\cos\theta}}{d\Delta\mu}\left\{\frac{4}{15}\left[(h-Y)^{5/2}-(h-z)^{5/2}\right]-\frac{2}{3}(z-Y)(h-z)^{3/2}\right\}, \tag{81}$$

which, upon integration, yields a unique relation between the average velocity U and the depth of the layer D,

$$\int_Y^h u\,\mathrm{d}z=\frac{4}{35}\frac{\delta I_0\sqrt{g\cos\theta}}{d\Delta\mu}D^{7/2}\implies U=\frac{1}{D}\int_Y^h u\,\mathrm{d}z=\frac{4}{35}\frac{\delta I_0\sqrt{g\cos\theta}}{d\Delta\mu}D^{5/2}. \tag{82}$$

We also have

$$\int_Y^h u^2\,\mathrm{d}z=\frac{11}{525}\left(\frac{\delta I_0\sqrt{g\cos\theta}}{d\Delta\mu}\right)^2D^6. \tag{83}$$

Inserting this into the depth-average x-momentum equation yields

$$\frac{\partial U}{\partial t} + \frac{11}{4} U \frac{\partial U}{\partial x} = \frac{5}{7} g \cos\theta \left(-\frac{\partial h}{\partial x} + \tan\theta - \delta \left(\frac{35 d \Delta\mu}{4\delta I_0 \sqrt{g \cos\theta}} \right)^{2/5} U^{2/5} - \mu_1 \right), \tag{84}$$

which forms a system of equations with the depth-average continuity equation, which, recognizing the flux as $Q = UD$, is

$$\frac{\partial h}{\partial t} + \frac{7}{5} \left(\frac{35 d \Delta\mu}{4\delta I_0 \sqrt{g \cos\theta}} \right)^{2/5} U^{2/5} \frac{\partial U}{\partial x} = -\Omega x. \tag{85}$$

4.3.1 Modeling the avalanching regime

While the crude depth-averaged model includes inertia and can accommodate unsteady solutions, it contains no ingredients which can predict the critical angle θ_{start} at which avalanches start. Because of this the model is not fully predictive and θ_{start} is a parameter (depending in general on drum width, drum radius, and granular material) which we must measure in a rotating drum experiment. To capture the full dynamics of the episodic avalanching regime, we insert a condition into our model which specifies that if the total flow across the layer is 0 (the grain pile is at rest) then it cannot flow again until solid body rotation causes the pile angle to reach θ_{start}. At this point the flow is released, which develops into an avalanche. If the rotation rate is slow enough, the avalanche then proceeds until the depth of the layer shrinks to zero first at the toe of the avalanche, and then propagating upwards to the front. The minimum angle of the pile which is achieved when there is no flow corresponds to θ_{stop}. A series of images depicting an avalanche are shown in Figure 8.

5 Comparison with experiment

5.1 Continuous flow and "thin, shallow, slippy"

The thin shallow slippy model yields a prediction for the free surface $h(x)$, and therefore for the average inclination of the flowing layer $\langle\theta\rangle$. Further, the form of the predicted flux Q,

$$Q = \frac{2 I_0 \sqrt{g \cos\theta}}{d} \left(\frac{\Delta\mu}{\delta} \right)^{5/2} q \left(\frac{\tan\theta - \mu_1 - h_x}{\Delta\mu} \right), \tag{86}$$

implies that scaling Q with $W^{5/2}$ eliminates the drum width from the problem (recall $\delta = \mu_{\text{wall}}/W$). To test this prediction of the model we plot of the average angle of the flowing layer $\langle\theta\rangle$ against the $Q/W^{5/2}$ in Figure 9. We observe what appears to be a collapse of the data for widths narrower than $W = 56$ mm. Further, the prediction of the TSS model corresponds well to a portion of the experimental data with the material parameters $\theta_1 = \tan^{-1}\mu_1 = 24.5°$, $\theta_2 = \tan^{-1}\mu_2 = 40°$, and $\mu_{\text{wall}} = 0.38\mu_1$. In this case, we have used the material parameters like fitting parameters and chosen those which best fit the experimental data. It is important to note, however, that the material parameters can and should be measured independent from the drum experiments; further it is only with such measurements that we can make a rigorous test of the fidelity of the model.

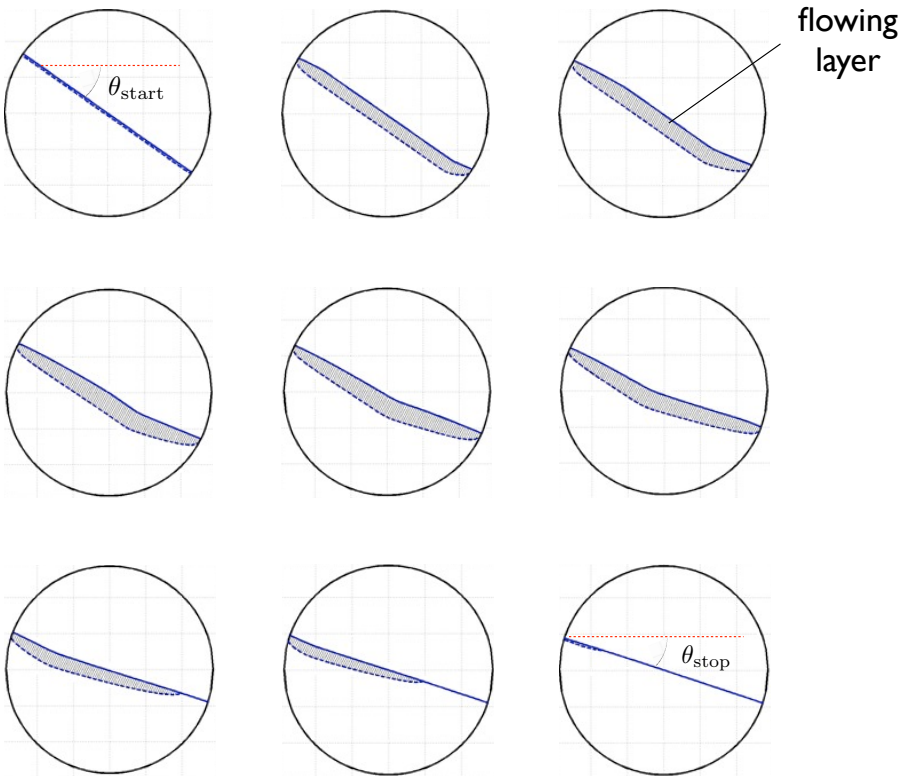

Figure 8: Series of images of a model avalanche calculated using the crude depth-averaged model.

The experimental data differs from the scaling $Q/W^{5/2}$ and the prediction of the model at the upper and lower limits of flow rates explored in the experiment. In both limits the slope of the flowing layer is greater than predicted. At high flow rates, a possible explanation for the discrepancy is the effect of inertia, which should become more important at high flow rates. At the lower flow rates plotted in Figure 9 the system is approaching the transition to episodic avalanching. The failure of the model here may be linked to the transition, which the model does not describe. Finally, for the wide drums $W = 110\,\text{mm}$ and $W = 205\,\text{mm}$, we see that the scaling predicted by the model is no longer valid. This may be due to the fact that the model assumes that W/H is small that the velocity u is uniform across the drum.

Further, the TSS model fails to predict the transition to episodic avalanching. Indeed, the TSS model predicts some pile angle for arbitrarily small flow rates. Of course for a low enough flow rate the predicted thickness of the flowing layer will be smaller than a single particle diameter and the continuum approximation cannot possibly be valid. It is unclear whether it is critical to understand the failure of the continuum assumption and finite size effects in order to predict transition, or if other factors which the model neglects are becoming important.

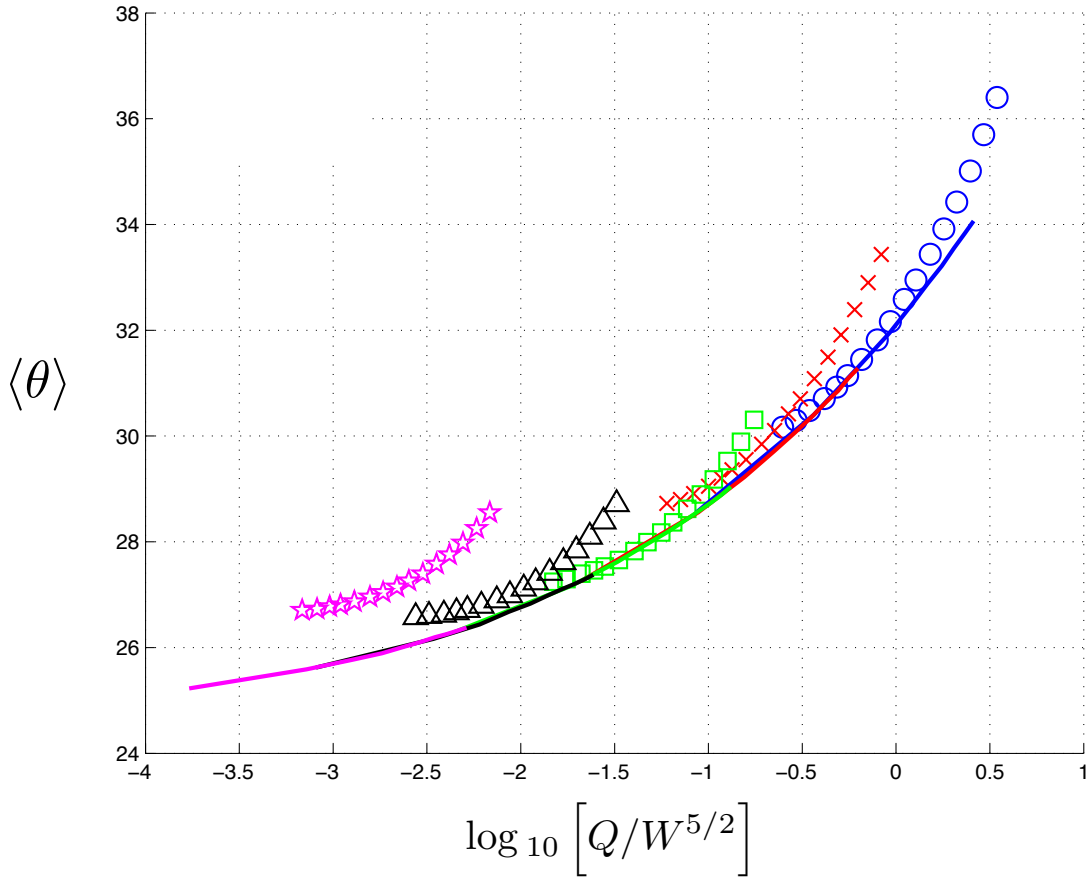

Figure 9: Angle of the flowing layer versus $Q/W^{5/2}$ for five different widths in the Vancouver drum with 3mm diameter glass spheres. Results are shown only for the continuous regime as determined by the minimum value for $\theta_{\max}$. Experimental results: ($\bigcirc$, blue) $W = 17$ mm, ($\times$, red) $W = 31$ mm, ($\square$, green) $W = 56$ mm, ($\triangle$, black) $W = 110$ mm, ($\star$, magenta) $W = 205$ mm. The line is the prediction of the "thin, shallow, slippy" theory the material constants $\theta_1 = \tan^{-1}\mu_1 = 24.5°$, $\theta_2 = \tan^{-1}\mu_2 = 40°$, $\mu_{\text{wall}} = 0.38\mu_1$.

5.2 Episodic avalanching and the crude inertial model

The "thin, shallow, slippy" model is inadequate for modeling the avalanching regime of flow in a rotating drum because it neglects inertial terms in the x-momentum equation. The crude inertial model appears to have the capacity to model an avalanche, but we have not yet had the chance to compare the predicted avalanches with observations. Because it seems plausible that the transition from avalanching to continuous flow with increasing flow rate is linked to the comparative magnitude of the rotation time scale and the avalanche duration, it may be especially important to predict the avalanche duration properly.

Nevertheless, avalanches in the crude inertial model seem reasonable at first glance: the duration is on the order of 0.5 to 1 second, and the halting of the avalanche resembles a wave which begins at the foot of the avalanche and propagates upstream. In addition to this, the model predicts a critical flow rate at which an persistent avalanching solution no longer exists. This transition depends on our model choice of θ_{start} and occurs because the rotation of the drum is fast enough (and the avalanche duration long enough) such that the flow incurred in the avalanche never decreases all the way to zero. Figure 10 shows a plot of θ versus Q and a phase space plot in $\{\dot{\theta}, \theta\}$-space for the crude inertial model. In the plot of θ versus Q, a transition from episodic avalanching to continuous flow is predicted around $Q \approx 300\,\text{mm}^2/\text{sec}$. The plot in $\{\dot{\theta}, \theta\}$-space shows two phase space trajectories. The blue solid line plots a trajectory taken by the system in in its episodic avalanching state and the red dotted line plots a trajectory taken by the system for a higher flow rate at which the system reaches the continuous flow state even when an avalanche is initiated at θ_{start}. We see in the trajectory taken by the system with a higher flow rate that the rate of change of the pile angle, which is analogous to the inertia contained in the avalanche, is diminished. Further, the minimum pile angle achieved on the trajectory for the higher flow rate is not quite as low as the minimum pile angle achieved for the system with a smaller flow rate. In the trajectory shown here, the system nearly reaches the cessation of flow as the rate of change of the pile angle approaches its value for solid body rotation, but subsequently drifts into the continuous flow solution.

6 Discussion

With the results of the two models in hand we can begin to sketch out a global understanding of the system. We see first of all that the thin, shallow, slippy model appears to accurately describe the dependence of the pile slope on flow rate for a certain range of flow rates. This lends confidence to the validity of $\mu(I)$ frictional rheology. At high flow rates, the thin shallow slippy model fails, but this is likely because of the importance of inertial terms and not a failure of the $\mu(I)$ law. Near the transition to episodic avalanching, however, it appears that the thin, shallow, slippy model begins to slightly underestimate the angle of the pile. We can only speculate to the reason for this discrepancy, but it seems possible that it is linked to the same physics that leads eventually to the disappearance of the continuous flow regime. One possible explanation for this discrepancy (and perhaps the transition as well [8]) is the finite thickness of the flowing layer.

Secondly, while the crudity and incompleteness of the crude inertial model mean it cannot be used as a quantitative and predictive model, it provides some basis for the notion

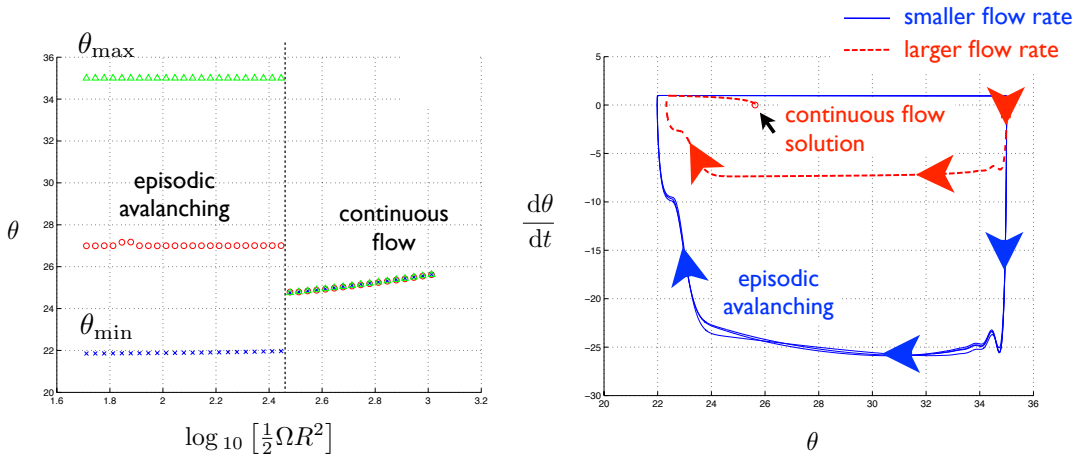

Figure 10: A θ versus Q plot (left) and a phase space plot (right) for the crude inertial model. (Left) a θ versus Q plot as predicted by the crude inertial model with $\theta_{\text{start}} = 35°$. Episodic avalanching cannot be observed as a steady solution in the model after $Q \approx 300\ \text{mm}^2/\text{sec}$. (Right) a plot showing transient phase space trajectories of episodic avalanching and continuous flow solutions in $\{\dot{\theta}, \theta\}$-space. When episodic avalanching is observed we see that $\dot{\theta}$ and the inertia of the avalanche are large enough to bring the avalanching to a small value of θ at which the flow stops completely. At larger flow rates, the $\dot{\theta}$ and the inertia of the avalanche are insufficient to bring the pile angle low enough to halt the avalanche.

that an increase in rotation rate can decrease the grain inertia which builds during an avalanche. This is important because the inertia contained in the avalanche controls the amount of material it moves; and the more material which is moved, the more the angle of the pile is decreased. Finally, the pile angle must decrease sufficiently for the flow to cease completely. If too little material is carried by the avalanche, the pile angle will remain high enough to continue driving flow, and the system will undergo damped oscillations in flow rate until settling into a continuous flow state. This implies that there is some critical flow rate which diminishes avalanche inertia enough such that the episodic avalanching solution no longer exists.

A sketch of our current understanding of the system — the "big picture" — is shown in Figure 11. At low flow rates, $Q < Q_1$, only episodic avalanching is observed. Below this critical flow rate, the continuous flow solution cannot exist in steady-state; this perhaps can be linked to a minimum thickness for the flowing layer, or an increase in effective friction for layers on the order of a particle diameter. At intermediate flow rates, $Q_1 < Q < Q_2$, both the episodic avalanching regime and the continuous flow solution are observed. At high flow rates, $Q > Q_2$ only continuous flow is observed. The episodic regime can no longer exist in steady-state because the rotation of the drum prevents any avalanche from building up enough inertia to cause cessation of flow.

Further, we can speculate as to why hysteresis is observed in sand where intermittency is observed with spherical glass beads. It may be true that for any granular material there are stochastic fluctuations in the volume fraction of the flow (affecting the effective internal

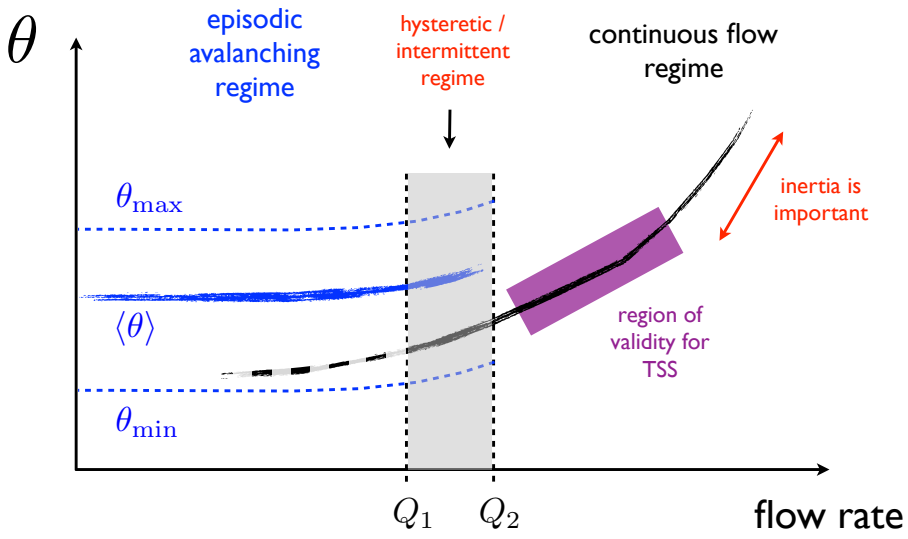

Figure 11: The big picture: a sketch of our current understanding

friction coefficient), velocity profile, and pressure forces. These stochastic fluctuations could imply that the critical flow rates Q_1 and Q_2 fluctuate as well, which could result in intermittent transition between regimes at intermediate flow rates. In this theory, stochasticity would still be present for sand but would be relatively small compared to other forcings in the system. An explanation for the relative unimportance of stochasticity is perhaps related to the larger effective friction coefficient observed with sand.

Much work remains. For the thin, shallow, slippy model, it should be verified that discrepancies at high flow rates are due to inertia. This could be done preliminarily by including the effects of inertia as a correction to the $\mathrm{Fr} = 0$ solution. An asymptotic expansion can only be extended so far, however, as it is still unable to accommodate flow rates which result in pile angles $\theta > \theta_2$, as the leading order inertialess solution no longer exists in this case. Accommodating higher flow rates than this would likely require two-dimensional simulations.

Further, the initial aim of this work was to describe the transition from continuous flow to episodic avalanching, a goal which remains unfulfilled. Now that it is known that the $\mu(I)$ frictional rheology is inadequate by itself to predict this transition (as well as underpredicting the angle of the flowing layer close to transition), some creativity is necessary to proceed. Perhaps most promising approach would be to consider effects of the finite thickness of the flowing layer depth and the failure of the continuum approximation. This may prove difficult, as connecting microscopic physics to the observed macroscopic behavior of granular flows is a long-standing problem. Discrete element numerical simulations may aid greatly in this pursuit.

For the crude avalanching model, it must first of all be confirmed that the avalanche dynamics are captured correctly. If the dynamics are incorrect, the model must be refined. Capturing avalanches correctly may require two-dimensional simulations. The proposed hypothesis for the transition from episodic avalanching to continuous flow is that increasing

flow rates limit the build up of inertia in the avalanche, which in turn limits the change in pile angle. An accurate model for avalanching could explore this hypothesis fully. Finally, it would be desirable to be able to predict the width-dependent θ_{start}, the angle at which avalanches are initiated. With a method to predict θ_{start}, and accurate avalanching model could potentially be fully predictive and dependent only on independently measured material parameters.

7 Acknowledgements

I would like to extend a hearty thanks to the directors Stefan Llewellyn Smith, Claudia Cenedese, and Eric Chassignet, the principle lecturer Paul Linden, and staff of the 2013 WHOI program in Geophysical Fluid Dynamics. It was an unforgettable summer. I would like to thank Neil Balmforth for proposing the project and yielding a great deal of time to work closely with me, perform experiments over the summer and for contributing results from his lab in Vancouver. I would like to thank Anders Jensen for helping to set-up the rotating drum in Woods Hole and tolerating the peculiarities of experiments with granular materials and glass beads with low interparticle friction coefficients. Finally, it is with great understatement that I thank the other Fellows of the program, whose friendship was forged through trials of both mind and matter, in the sublime highs and devastating lows of WHOI softball, and the blackboard-lined crucible of Walsh Cottage.

A Data for 2 mm and 1.5 mm glass beads

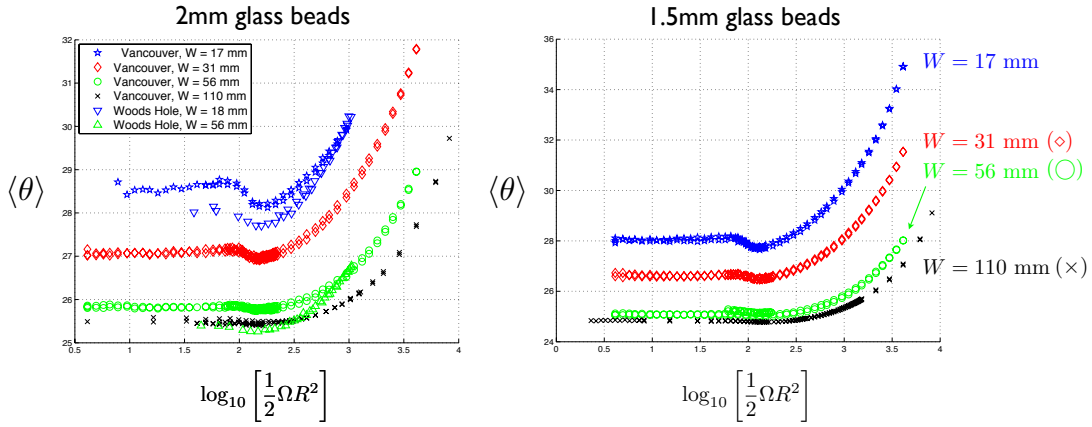

Figure 12: (Left) θ versus Q for 2 mm from experiments in Vancouver and Woods Hole. The Woods Hole results do not line up as well with the Vancouver results as for the 3 mm glass beads. This may have to do with errors associated with the alignment of the Woods Hole camera. It also appears that θ is increasing much faster with Q for both $W = 17$ mm ($W = 18$ mm for Woods Hole) and $W = 56$ mm. The cause of this is unknown. (Right) θ versus Q for the 1.5 mm glass beads from experiments in Vancouver.

References

[1] M Caponeri, S Douady, S Fauve, and C Laroche, *Dynamics of avalanches in a rotating cylinder*, Mobile Particulate Systems, (1995), pp. 331–366.

[2] Alain de Ryck and Olivier Louisnard, *Depth and minimal slope for surface flows of cohesive granular materials on inclined channels*, Journal of Fluid Mechanics, 727 (2013), pp. 191–235.

[3] Raphaël Fischer, Philippe Gondret, Bernard Perrin, and Marc Rabaud, *Dynamics of dry granular avalanches*, Phys. Rev. E, 78 (2008), pp. 1–4.

[4] Raphaël Fischer, Philippe Gondret, and Marc Rabaud, *Transition by intermittency in granular matter: From discontinuous avalanches to continuous flow*, Phys. Rev. Lett., 103 (2009), pp. 1–4.

[5] Yoël Forterre and Olivier Pouliquen, *Flows of dense granular media*, Annu. Rev. Fluid Mech., 40 (2008), pp. 1–24.

[6] Isaac Goldhirsch, *Rapid granular flows*, Annual Review of Fluid Mechanics, 35 (2003), pp. 267–293.

[7] Nitin Jain, J M Ottino, and R M Lueptow, *An experimental study of the flowing granular layer in a rotating tumbler*, Physics of Fluids, 14 (2002), pp. 1–12.

[8] Pierre Jop, Yoël Forterre, and Olivier Pouliquen, *Crucial role of sidewalls in granular surface flows: consequences for the rheology*, J. Fluid Mech., 541 (2005), p. 167.

[9] ——, *A constitutive law for dense granular flows*, Nature, 441 (2006), pp. 727–730.

[10] GFD MiDi, *On dense granular flows*, Eur. Phys. J. E, 14 (2004), pp. 341–365.

[11] D J Parker, A E Dijkstra, T W Martin, and J P K Seville, *Positron emission particle tracking studies of spherical particle motion in rotating drums*, Chemical Engineering Science, 52 (1997), pp. 2011–2022.

[12] Sylvain Courrech Du Pont, Raphaël Fischer, Philippe Gondret, Bernard Perrin, and Marc Rabaud, *Instantaneous velocity profiles during granular avalanches*, Phys. Rev. Lett., 94 (2005), pp. 1–4.

[13] Patrick Richard, Mario Nicodemi, Renaud Delannay, Philippe Ribière, and Daniel Bideau, *Slow relaxation and compaction of granular systems*, Nat Mater, 4 (2005), pp. 121–128.

[14] Jean-Noel Roux and Gael Comb, *Quasistatic rheology and the origins of strain*, Physics of Granular Media, 3 (2002), pp. 131–140.

[15] Nicolas Taberlet, Patrick Richard, and E John Hinch, *S shape of a granular pile in a rotating drum*, Phys. Rev. E, 73 (2006), pp. 1–4.

[16] K Yamane, M Nakagawa, S A Altobelli, T Tanaka, and Y Tsuji, *Steady particulate flows in a horizontal rotating cylinder*, Physics of Fluids, 10 (1998), pp. 1419–1427.

[17] R Y Yang, R P Zou, and A B Yu, *Microdynamic analysis of particle flow in a horizontal rotating drum*, Powder Technology, 130 (2003), pp. 138–146.

The Stokes drift of internal gravity wave groups

Ton S. van den Bremer*

October 18, 2013

1 Introduction

When periodic surface gravity waves propagate they have associated with them a wave-induced mean flow known as the Stokes drift after George Gabriel Stokes who first derived a theoretical description for this drift in 1847. For periodic surface gravity waves, the drift manifests itself as a net horizontal velocity of a Lagrangian particle that remains after the periodic part of the motion has been averaged out. The latter motion corresponds to elliptic particle trajectories when the wave length associated with the periodic motion is of comparable magnitude to the water depth (intermediate depth) and to circular particle trajectories when the depth is large compared to the wave length (so-called deep water waves). As a result of the drift, these orbits do not close perfectly, as illustrated by a few orbits in figure 1. Multiplied by the density of water, the Stokes drift of periodic surface gravity waves is associated with wave momentum. Taking a Lagrangian approach, Stokes (1847) found the following expression for the horizontal drift velocity at the free surface for regular waves in deep water and to second order of approximation:

$$\overline{u} = \frac{1}{T}\int_0^T u\big(x(t),\eta(t),t\big)dt = c(ka)^2 + O\big((ka)^4\big), \tag{1}$$

where $c = \sqrt{g/k} =$ is the wave celerity or phase speed, g is the gravitational constant, $k = 2\pi/\lambda$ is the wave number of the regular wave, and a its linear amplitude. Stokes drift is thus a non-linear phenomenon (cf. $(ka)^2$) that can be derived from linear theory. Stokes (1847) considered both the effect of horizontal displacement $x(t) = x_0 + \Delta x(t)$ and vertical displacement at the free surface $z(t) = \xi(t)$ on the drift velocity (1) , equal to the displacement per wave period T. Compatible results were first derived in an Eulerian framework by Starr (1947).

For packets or groups of surface gravity waves, the Stokes drift near the surface and its associated momentum in the direction of propagation of the packet is balanced by a return flow at depth below the surface in the opposing direction and of opposite sign and equal magnitude, as first shown by Longuet-Higgins & Stewart (1962). Their derivation is reproduced in appendix A for completeness and the streamlines of the return flow are shown in

*I would like to thank my GFD programme advisor Bruce Sutherland (University of Alberta) and Basile Gallet (Laboratoire FAST) and Jean-Marc Chomaz (CNRS-Ecole Polytechnique) for the helpful discussions.

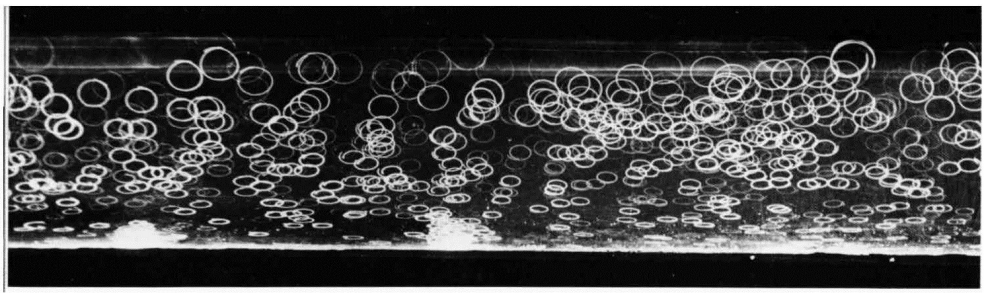

Figure 1: Particle trajectories underneath two-dimensional periodic surface gravity waves from Wallet & Ruellan (1950) reproduced in Van Dyke (1982). The waves are only moderately non-linear and the net horizontal drift is only visually apparent for a few orbits.

figure 2. Combining the Stokes drift and the return flow, leads to a zero vertically-integrated momentum associated with the travelling wave packet as emphasized by Mcintyre (1981). In the terminology of the derivation of Longuet-Higgins & Stewart (1962), the different wave number components that make up the linear multi-chromatic wave packet, interact to produce frequency sum and frequency difference components at the next order in amplitude. The frequency difference components, in turn, are responsible for the return flow. In physical terms, the kinematic and dynamic free surface boundary conditions, requiring no flow through the free surface and a uniform pressure on this surface, prevent a net deposition of fluid at the leading edge of the packet due to Stokes drift. It can be shown (van den Bremer & Taylor (in preparation)) that for deep water and in the limit of a narrow-banded spectrum the return flow is equal to the potential flow field corresponding to a series of sources and sinks of mass placed at the still water level, respectively, upstream and downstream of the centre of the wave packet with their strength determined by the local variation of the mass flux associated with the horizontal Stokes drift. As a result, a spatial separation of the two effects takes place: Stokes drift, the strength of which varies rapidly (exponentially) with depth, is the dominant effect at the free surface, whereas the return flow, which displays a much more slow decay with depth, dominates at a distance below.

For internal gravity waves on the continuum of equidensity surfaces in a stably stratified fluid the story is markedly different. In contrast to periodic surface gravity waves, horizontally and vertically periodic internal gravity waves that exist on stably stratified fluids do not display Stokes drift. In fact, the linear horizontally and vertically periodic (or planar) wave solutions satisfy the non-linear governing equations exactly, with no requirement for higher order corrections or induced-mean flow arising, unlike the case of surface gravity waves. The individual trajectory of a Lagrangian particles forms a straight line inclined at an angle to the horizontal, and the trajectory is completed as the local equidensity surface is displaced sinusoidally in time. The magnitude of the angle of inclination of the straight trajectory is determined by the ration of the frequency of the wave and the buoyancy frequency associated with the stratification.

For internal gravity wave groups that are vertically compact but remain periodic in

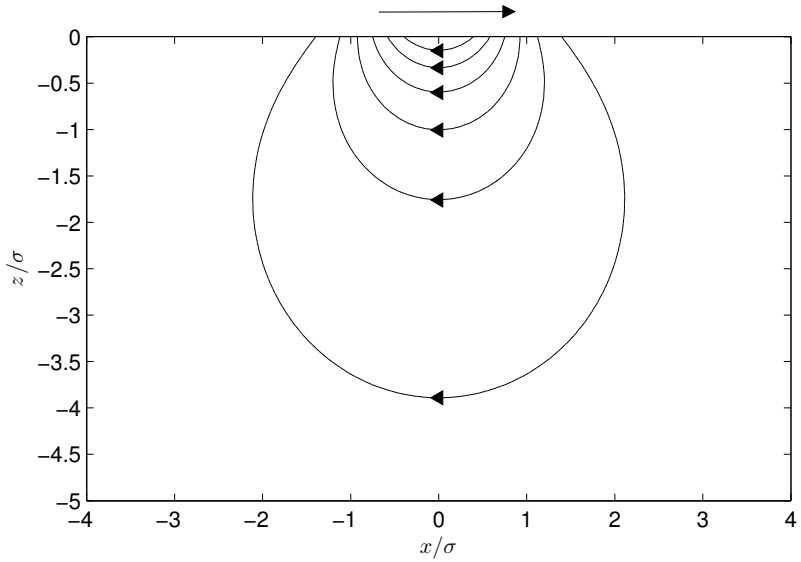

Figure 2: Streamlines corresponding to the (leftward) return flow below a (rightward) travelling surface gravity wave group from Longuet-Higgins & Stewart (1962) (see appendix A) for a Gaussian linear spectrum with bandwidth $\epsilon = (k_0\sigma)^{-1} = 1$ with σ denoting the bandwidth of the spectrum or the Gaussian half-width of the linear wave group and k_0 denoting the wave number of the peak of the spectrum (cf. figure 2 of Mcintyre (1981)).

the horizontal, it is well established that a wave-induced mean flow (or a Stokes drift) exists and, in fact, plays a large role in determining the stability properties of such groups. Using Hamiltonian fluid mechanics, Scinocca & Shephard (1992) show that the horizontal wave-induced mean flow for such groups is given by:

$$\overline{u} = -\langle \xi\zeta \rangle, \tag{2}$$

where the angular brackets denote averaging over one horizontal wave length, $\xi(x, z, t)$ denotes the vertical displacement and $\zeta(x, z, t)$ denotes the vorticity. As for the Stokes drift for surface gravity waves (1), the induced mean flow in (2) is quadratic in the amplitude of the vertical displacement. Alternative means of deriving equivalent expressions to (2) include but are not limited to Stokes' circulation theorem (Sutherland (2010), §3.4.5) , energy conservation relation (Bretherton (1969)) or from momentum flux divergence (see §3.1). Using the polarization relationships for linear internal gravity waves it can be shown that the induced mean flow $\overline{u}$ in (2) is positive in the direction of the horizontal component of the group velocity.

Weakly nonlinear theory and fully nonlinear simulations have demonstrated that this wave-induced mean flow transiently Doppler-shifts the wave packet as it evolves, changing its structure and significantly altering where the wave packet breaks through modulational instability of the waves resulting from interaction with the self-induced mean flow. As for surface gravity waves (see for example Dysthe (1979)), the interaction with the horizontal

induced mean flow of horizontally periodic but vertically compact wave groups is well-captured by non-linear Schrödinger type evolution equations subject to an instability of the Benjamin-Feir type (Benjamin & Feir (1967)). For Boussinesq, non-Boussinesq and anelastic horizontally periodic wave packets Sutherland (2006) and Dosser & Sutherland (2011a, 2011b) have derived such equations and compared their predictive ability to fully non-linear simulations.

The framework of Lagrangian-mean flow, which underlies some of the terminology used in this report, was not formalized until Andrews & McIntyre (1978), who provided a generalized theory for the back effect of oscillatory disturbances upon the mean state termed the 'generalized Lagrangian-mean' (GLM). As noted by these authors, the concept of 'Lagrangian mean' is often required in a more general sense than its classical sense of the mean following a single fluid particle. What is of interest is the Lagrangian-mean flow described in terms of equations in Eulerian form, i.e. potentially as a function of position (x,z) and time t. When we refer to the Stokes drift velocity (cf. equation (2), which not a function of x only due to the periodic nature in that direction, but is a function of z) or the mass flux at a certain position x and time t, it is in fact the 'generalized Lagrangian-mean' of Andrews & McIntyre (1978), a hybrid Eulerian-Lagrangian description of wave mean-flow interaction, we implicitly adopt.

Internal gravity waves are widespread in both the ocean, in which the variation of salinity and temperature are responsible for the gradient in density with depth, and the atmosphere, which displays very significant temperature and density variation with height, where they may be generated by wind flow over mountain ranges or storms in the troposphere. Stokes drift associated with internal gravity wave packet may affect momentum transport and deposition indirectly through changing the criteria for breaking and resulting deposition of momentum to the environment , inclusion of which has improved predictions of mean zonal winds and temperatures in the middle atmosphere (McLandress (1998)). Its effects may also be direct through dispersion of tracers in the ocean ((Sanderson & Okubo (1988) and Holmes-Cerfon, Bühler & Ferrari (2011)).

This report considers the Stokes drift for a vertically and horizontally confined Boussinesq internal gravity wave packet in a linearly and stably stratified two-dimensional fluid of infinite vertical and horizontal extent and examines the existence and nature of a predicted return flow. It asks the question whether the results from horizontally periodic wave packets can be readily extended to the vertically and horizontally compact case or whether the wave-induced mean flow is accompanied by a return flow in a similar way to the surface gravity wave packet. For the benefit of simplicity, we apply the Boussinesq approximation, an assumption that is omnipresent in the literature on buoyancy driven flow and that assumes density variations are small and can be ignored except where they are responsible for the existence of the buoyancy force itself. The Boussinesq approximation is typically adequate for internal gravity waves in the ocean, in which the density may only vary by a small amount across the ocean's depth, but inadequate in the atmosphere, in which individual waves will experience a significant decrease in background density as they rise and non-Boussinesq effects become important.

This report is laid out as follows. First §2 introduces the governing equations and discussed the assumptions made in their derivation. First, §3.1 reviews established results for wave packets that are compact in the vertical direction, but periodic in the horizontal direction and shows that for such packets there is an unbalanced induced mean flow in the horizontal direction. §3.2 extends this analysis based on momentum flux divergence to wave packets that are both vertically and horizontally compact. Using a separation of scales argument, we show that at leading order in bandwidth of the spectrum Stokes drift can only induce a global response in the horizontal direction and there can be no flow in the vertical direction, even if this flow is balanced by a return flow. In §4 we complete the discussion by deriving expressions for the local response in the vain of Longuet-Higgings & Stewart (1962), which would arrive at higher order in bandwidth in the perturbation expansion of §3.2. Finally, conclusions are drawn in §5.

2 Governing equations

We begin by making the usual Boussinesq approximation, that is, we ignore variation of density in the conservation equations except where it is responsible for the existence of the buoyancy force itself (cf. Spiegel & Veronis 1960). In a two-dimensional coordinate system (x,z), where x denotes the horizontal coordinate and z denotes the vertical coordinate, the momentum equations in the x and z directions then become, respectively:

$$\frac{Du}{Dt} = -\frac{1}{\rho_0}\frac{\partial p}{\partial x}, \tag{3}$$

$$\frac{Dw}{Dt} = -\frac{1}{\rho_0}\frac{\partial p}{\partial z} - g\frac{\Delta\rho}{\rho_0}, \tag{4}$$

where u and w denote the horizontal and vertical velocity, respectively, p the pressure, and gravity g acts in the negative z direction. The total density of the fluid ρ is the sum of background stratification density $\overline{\rho}$ and small variations from the background $\Delta\rho$, so that $\rho = \rho_0 + \Delta\rho$. Mass is conserved:

$$\frac{\partial\rho}{\partial t} + \nabla\cdot(\rho\mathbf{u}), \tag{5}$$

where $\mathbf{u} = (u, w)$ and the fluid is assumed to be incompressible:

$$\frac{D\rho}{Dt} = 0. \tag{6}$$

Incompressibility (6) can be viewed as an additional assumption or as an implication of conservation of mass under the Boussinesq approximation. It is common to combine the (5) and (6) to give:

$$\nabla\cdot\mathbf{u} = 0. \tag{7}$$

We further assume the ambient is linearly stratified with (constant) buoyancy frequency N_0:

$$N_0^2 = -\frac{g}{\rho_0}\frac{d\rho_0}{dz}. \tag{8}$$

Equation (6) can then be rewritten to give an equation for the density perturbation $\Delta\rho$:

$$\frac{D\Delta\rho}{Dt} = -w\frac{d\rho_0}{dz}. \tag{9}$$

It is convenient to rewrite density perturbations $\Delta\rho$ into a corresponding vertical displacement field:

$$\xi = -\frac{\Delta\rho}{\rho_0'(z)}, \tag{10}$$

so that (9) can be rewritten as:

$$\frac{D\xi}{Dt} = \frac{\partial\psi}{\partial x}, \tag{11}$$

where $\psi(x,z,t)$ is a stream function defined so that $u = -\partial\psi/\partial z$ and $w = \partial\psi/\partial x$. It is convenient to combine the horizontal and vertical momentum equations (3) and (4) into one equation in terms of two variables: the stream function ψ and the vertical displacement ξ. By taking the curl of momentum equation in the x and z direction, we obtain the equation for (baroclinic) generation of vorticity:

$$\frac{D\nabla^2\psi}{Dt} = -N_0^2\frac{\partial\xi}{\partial x}, \tag{12}$$

where the right hand side denotes the total derivative of vorticity $\zeta = -\nabla^2\psi$. Finally, (12) and (11) can be combined into one:

$$\underbrace{\left[\frac{\partial^2}{\partial t^2}\Big[\frac{\partial^2}{\partial x^2} + \frac{\partial^2}{\partial z^2}\Big] + N_0^2\frac{\partial^2}{\partial x^2}\right]}_{\equiv\, L}\psi = \nabla\cdot\underbrace{\Big[\frac{\partial}{\partial t}\big[\zeta\nabla\times\psi\big] + N_0^2\frac{\partial}{\partial x}\big[\xi\nabla\times\psi\big]\Big]}_{\equiv\, \mathbf{F}}, \tag{13}$$

where the cross product of the stream function is the velocity vector in the (x,z) direction $\mathbf{u} = \nabla\times\psi$. We have thus defined the linear wave operator L and the non-linear vector $\mathbf{F}$. Together (11) and (13) can be used to capture the entire dynamics of the problem without further approximation compared to the governing equation for momentum (3), (4) mass (5) and incompressibility (6).

3 Global wave-induced mean flow

We begin (§3.1) by deriving an expression for the wave-induced mean flow for a wave group that is compact in the vertical direction but periodic in the horizontal direction, as illustrated in figure 3a, that is consistent with expression (2) derived by Scinocca & Shephard (1992) (see Sutherland (2010)). We extend this result to a group that is both compact in the vertical and the horizontal direction, as illustrated in figure 3b giving rise to what we show is a misleading result (§3.2.1). We then take a step back in §3.2.2 and pursue a separation of scales perturbation expansion in two variables: the amplitude of the displacement field and the bandwidth of the spectrum. Throughout we assume a Gaussian amplitude spectrum to produce the figures.

3.1 Vertically compact and horizontally periodic wave packets (review)

For internal gravity wave packets that are vertically compact but horizontally periodic, we consider the following vertical displacement:

$$\xi = \mathrm{Re}\big[A(Z,T)e^{i(k_x+k_z z-\omega t)}\big], \tag{14}$$

where $A(Z,T)$ is the (complex) envelope of the packet (in the z-direction) with units of vertical displacement that evolves on the slow scale $Z = \epsilon_z(z - c_{g,z}z)$, where $c_{g,z}$ is the vertical group velocity and $\epsilon_z = (k_z\sigma_z)^{-1}$ is the (small) bandwidth parameter with k_z denoting the peak of the quasi-monochromatic spectrum and σ_z its bandwidth. The effects of dispersion are assumed to come in at higher order via the slow time scale $T = \epsilon_z^2 t$. From (11), we obtain expressions for the horizontal and vertical velocity at the same order:

$$u = \mathrm{Re}\big[iA(Z,T)N_0\sin(\theta_0)e^{i(k_x+k_z z-\omega t)}\big], \tag{15}$$

$$w = -\mathrm{Re}\big[iA(Z,T)N_0\cos(\theta_0)e^{i(k_x+k_z z-\omega t)}\big], \tag{16}$$

where we use the angle θ_0 to denote the angle between the horizontal and vertical components of the wave number vector of the carrier wave $\tan(\theta_0) = k_z/k_x$. Invoking the incompressibility assumption, the horizontal momentum conservation equation (3) can be written in flux form:

$$\frac{\partial u}{\partial t} + \frac{\partial uu}{\partial x} + \frac{\partial uw}{\partial z} = -\frac{1}{\rho_0}\frac{\partial p}{\partial x}, \tag{17}$$

Because the packet has remained periodic in the x-direction, we average over the fast variation in that direction to obtain from (17):

$$\frac{\partial}{\partial t}\langle u\rangle + \frac{\partial}{\partial z}\langle uw\rangle = 0, \tag{18}$$

where the angular brackets denote averaging in the x-direction. Continuing the informal separation of scales argument, we replace the temporal derivative on the left-hand side by a derivative with respect to the slow vertical scale Z, $\partial/\partial t = \epsilon_z^2\partial_T - \epsilon_z c_{g,z}\partial_Z$, where we ignore the ϵ_z^2 term. Due to the averaging over the derivative $\partial/\partial z$ has become a slow derivative $\partial/\partial Z$ as well and we have to leading order in ϵ:

$$\langle u\rangle = \frac{1}{c_{g,z}}\langle uw\rangle. \tag{19}$$

Substituting in for the horizontal and vertical velocities from (15) and (16), we obtain:

$$\langle u\rangle = \frac{k_x N_0}{2\cos(\theta_0)}A^2(Z,T). \tag{20}$$

Using the polarization relationship for linear waves (in amplitude) it can be shown that (20) is equivalent to (2). We thus have a induced mean flow that arises because of the vertical divergence of the flux of horizontal momentum.

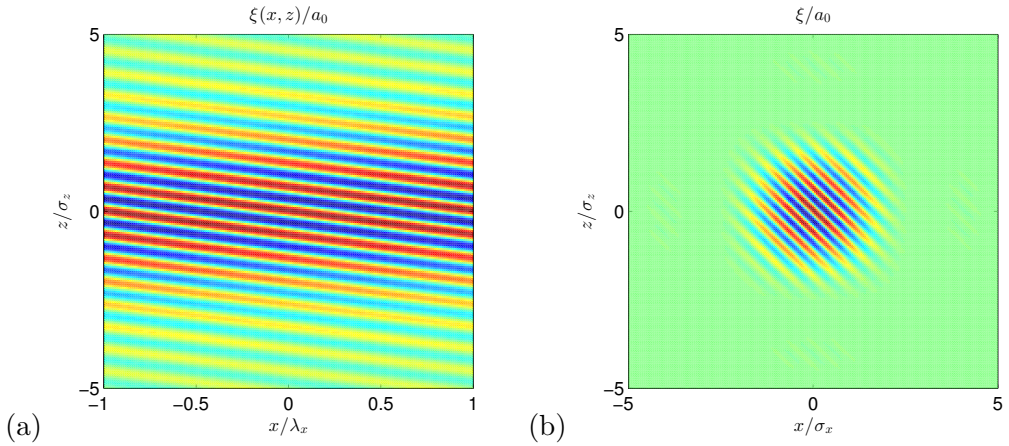

Figure 3: Linear vertical displacement ξ in (x, z)-space for (a) vertically compact but horizontally periodic Gaussian internal wave packet with $\epsilon_z = (\sigma_z k_{z,0})^{-1} = 0.1$ and (b) vertically and horizontally compact Gaussian packet with $\epsilon_x = (\sigma_x k_{x,0})^{-1} = \epsilon_z = (\sigma_z k_{z,0})^{-1} = 0.1$. In both cases $\omega_0/N_0 = 1/\sqrt{2}$ so that the group velocity vector points in the positive x and negative z direction at an angle of 45°.

3.2 Vertically and horizontally compact wave packets

3.2.1 Momentum flux divergence: a misleading picture

By introducing an additional slow scale $X = \epsilon_x(x - c_{g,x}t)$ and setting $\epsilon = \epsilon_x = \epsilon_z$, we extend the analysis in §3.1 to vertically and horizontally compact groups. The vertical displacement is given by:

$$\xi = \mathrm{Re}\big[A(Z, X, T)e^{i(k_x + k_z z - \omega t)}\big], \tag{21}$$

and the horizontal and vertical velocities can be found accordingly. Following a similar procedure to the one in §3.1, but now averaging over the fast time scale instead of the fast x scale and considering both the horizontal (3) and the vertical (4) momentum equation (in flux form), we obtain:

$$(u_{SD}, w_{SD}) = \frac{1}{2}|\mathbf{k}||A|^2\Big(1, \frac{c_{g,z}}{c_{g,x}}\Big). \tag{22}$$

The velocity field (22) is illustrated in figure4a and shows a field that is local to the Gaussian wave packet (unsurprisingly). As is evident from (22) its direction is that of the group velocity vector. Computing the (negative) divergence of this second-order (in amplitude) flow field (22) shows that it transports mass and deposits it at the leading edge of the wave packet. Evidently, the flow field cannot represent the entire picture: it is unbalanced in terms of mass and in terms of energy, as particles are transported against the stratification.

3.2.2 Separation of scales expansion in amplitude and bandwidth

We take a step back and consider a new separation of scales argument with the fast spatial and temporal scales denoted by x, z and t and the slow scales denoted by $X = \epsilon x$, $Z = \epsilon z$

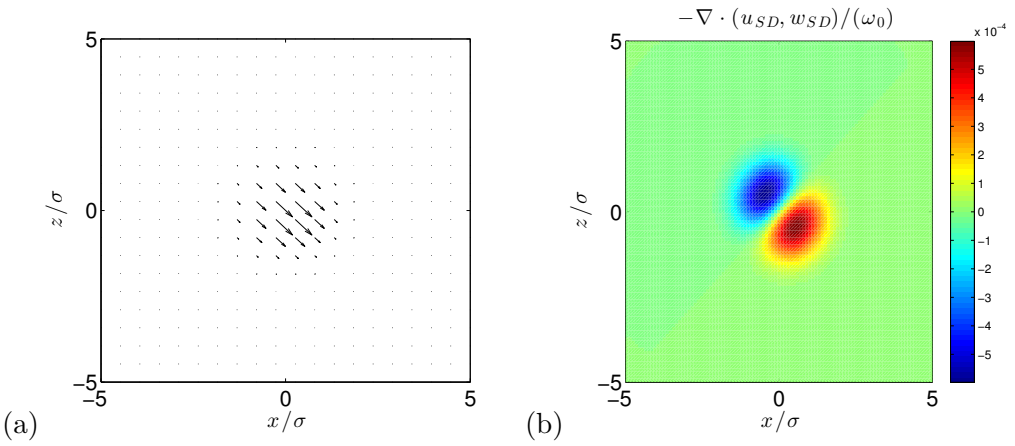

Figure 4: Unbalanced Stokes drift of a vertically and horizontally compact Gaussian packet with $\epsilon_x = (\sigma_x k_{x,0})^{-1} = \epsilon_z = (\sigma_z k_{z,0})^{-1} = 0.1$ showing (a) the flow field corresponding to (22) and (b) the negative divergence of this flow field illustrating there is a net transport of fluid in the direction of the group velocity. $\omega_0/N_0 = 1/\sqrt{2}$ so that the group velocity vector points in the positive x and negative z direction at an angle of 45°. The magnitude of the largest vector in (a) is $|\mathbf{u}_{SD}| = 1.2 \cdot 10^{-1} a_0 \omega_0$.

and $T = \epsilon t$. For tractability, we assume one universal bandwidth parameter $\epsilon = (k_x \sigma_x)^{-1} = (k_z \sigma_z)^{-1}$ with σ_x and σ_z denoting the horizontal and vertical bandwidth. We keep track of both the order in the bandwidth parameter ϵ, which we denote by a subscript, and the order in the amplitude of the signal, which we denote by a superscript. For example, $\xi^{(2)}_{(1)}$ denotes the component of the vertical displacement that is first order in bandwidth ϵ and second order in amplitude A. We do not make the assumption that $\epsilon = \alpha$, where $\alpha = kA$ with k denoting the magnitude of the wave number vector, an assumption that is commonly made to derive non-linear Schrödinger type of equations. We restrict our attention to first and second-order in amplitude, which we consider in turn.

Linear in amplitude $O(A)$

Our starting point is to assume the following form for the component of the vertical displacement that is first-order in amplitude:

$$\xi^{(1)} = \xi^{(1)}_{(0)} = \mathrm{Re}\big[A(X,Z,T)e^{i(k_x x + k_z z - \omega t)}\big] \tag{23}$$

where the amplitude of the envelope A may be complex and we have set $\xi^{(1)}_{(n)} = 0$ for $n \geq 1$. From (11) we readily identify the counterpart of (23) that does not take any of the slow variation into account:

$$\psi^{(1)}_{(0)} = -\mathrm{Re}\big[\frac{\omega}{k_x} A(X,Z,T)e^{i(k_x x + k_z z - \omega t)}\big]. \tag{24}$$

In order to satisfy (11) at every order in bandwidth we need to consider the effect of the derivatives acting on the slowly varying envelope. We use the following notation: we use

$\partial/\partial x$ to denote the combined effect of slow and fast derivatives, but let the subscripts in ∂_x and ∂_X denote only fast or slow derivatives, respectively. At first order in ϵ (11) becomes:

$$\epsilon\partial_T\xi^{(1)}_{(0)} = \epsilon\partial_X\psi^{(1)}_{(0)} + \partial_x\psi^{(1)}_{(1)}, \tag{25}$$

where we have used our assumption that $\xi^{(1)}_{(n)} = 0$ for $n = 1$. From (25) we have:

$$\psi^{(1)}_{(1)} = -\mathrm{Re}\Big[\frac{i}{k_x}\epsilon\Big(A_T + \frac{\omega}{k_x}A_X\Big)e^{i(k_x x + k_z z - \omega t)}\Big]. \tag{26}$$

Equation (25) can be generalized for nth order in ϵ for $n > 1$:

$$\epsilon\partial_X\psi^{(1)}_{(n-1)} + \partial_x\psi^{(1)}_{(n)} = 0 \quad \text{for } n > 1, \tag{27}$$

which can be solved iteratively in combination with (26) to give:

$$\psi^{(1)}_{(n)} = -\mathrm{Re}\Big[\frac{i^n}{k_x^n}\epsilon^n\Big(A_{X^{(n-1)T}} + \frac{\omega}{k_x}A_{X^{(n)}}\Big)e^{i(k_x x + k_z z - \omega t)}\Big] \quad \text{for } n > 1. \tag{28}$$

Having satisfied (11) at first-order in A and every order in ϵ, we turn to (13) and obtain the linear dispersion relation at zeroth order:

$$\frac{\omega^2}{N_0^2} = \frac{k_x^2}{k_x^2 + k_z^2}. \tag{29}$$

the envelope travelling at the group velocity at first order in ϵ and the effects of linear (in amplitude) dispersion at the next orders.

Second-order in amplitude $O(A^2)$

At second-order in amplitude we have from (13):

$$L\psi^{(2)} = \nabla\cdot\Big[\frac{\partial}{\partial t}\big[\zeta^{(1)}\nabla\times\psi^{(1)}\big] + N_0^2\frac{\partial}{\partial x}\big[\xi^{(1)}\nabla\times\psi^{(1)}\big]\Big] \tag{30}$$

where the linear operator L is defined in (13) and we have so far included all terms in ϵ. Using the expressions for ψ^1_n and ξ^1_n for $n \geq 0$ derived above and after considerable manipulation, it can be shown that the right hand side is equal to zero at zeroth and first order in ϵ and periodic at second order and hence unable to provide the forcing required for a mean flow. The first non-zero and non-periodic only arise at even higher order.

3.2.3 Resulting gobal response

Considering the order (in the bandwidth ϵ) of all the terms in (30) we have:

$$\Big[\underbrace{\frac{\partial^2}{\partial t^2}\Big[\frac{\partial^2}{\partial x^2} + \frac{\partial^2}{\partial z^2}\Big]}_{O(\epsilon^4)} + \underbrace{N_0^2\frac{\partial^2}{\partial x^2}}_{O(\epsilon^2)}\Big]\psi^2(X,Z,T) = \underbrace{\nabla\cdot\Big[\frac{\partial}{\partial t}\big[\zeta^{(1)}\nabla\times\psi^{(1)}\big] + N_0^2\frac{\partial}{\partial x}\big[\xi^{(1)}\nabla\times\psi^{(1)}\big]\Big]}_{O(\epsilon^4)}. \tag{31}$$

We thus have to leading order (second):

$$\partial_{XX}\psi^2 = 0, \rightarrow \psi^2 = f(Z)X + g(X), \tag{32}$$

where $f(Z)$ and $g(X)$ are arbitrary function of the slow scales X and Z. In combination with incompressibility (7), it is then easy to show that the only possible flow field at second order in ϵ, the order at which the Stokes drift in §3.2.1 is derived, that is not periodic and does not grow indefinately in x or z, is the following:

$$u_2^2 = g(z), \quad w_2^2 = 0. \tag{33}$$

In words, at leading order in bandwidth the total (non-periodic) horizontal velocity that is the sum of the Stokes drift derived in §3.2.1 and a "return flow" $u^2 = u_{SD}^2 + u_{RF}^2$ can only be a function of the vertical coordinate z. It cannot display any variation in the horizontal direction. The total vertical velocity that is the sum of the Stokes drift velocity derived in §3.2.1 and "return flow" is zero $w^2 = w_{SD}^2 + w_{RF}^2 = 0$. The return flow thus exactly cancels out the vertical component of the Stokes drift at all points in space (x, z) but leaves long disturbances in the x-direction:

$$(u_{RF}, w_{RF}) = \Big(- u_{SD} + \frac{1}{L_x}\int_0^{L_x} u_{SD} dx, -w_{SD} \Big) \tag{34}$$

where L_x is the length of the domain in the x-direction. The Stokes drift is spread out horizontally over the domain and decreases with the size of the domain considered. In the limit of an infinite (computational) domain $L_x \rightarrow \infty$ the induced mean flow goes to zero, but may be finite in magnitude even in infinite domains provided the number of wave groups per unit length is finite. In reality, the horizontal extent of the disturbance is limited by the time scale for vertical propagation and the horizontal group velocity for long waves, effects both not considered herein.

4 Local circulation for broadbanded packets

4.1 Lagrangian effects

The presence of a second local and potentially much smaller effect becomes apparent from numerically integrating the equations of motion of a Lagrangian particle with respect to time:

$$\frac{d\Delta x}{dt} = u(x, z, t), \quad \frac{d\Delta z}{dt} = w(x, z, t), \tag{35}$$

where we obtain the horizontal and vertical velocities from linear theory:

$$u = \mathrm{Re}\big[iA(Z, X, T)N_0 \sin(\theta_0) e^{i(k_x + k_z z - \omega t)}\big], \tag{36}$$

$$w = -\mathrm{Re}\big[iA(Z, X, T)N_0 \cos(\theta_0) e^{i(k_x + k_z z - \omega t)}\big], \tag{37}$$

use a bivariate Gaussian distribution for $A(X, Z)$ and ignore the effects of dispersion via the additional slow scale T. Figure 5 shows the motion the Lagrangian particles undergo during the passing of the wave group. What is also evident from the figure is that the

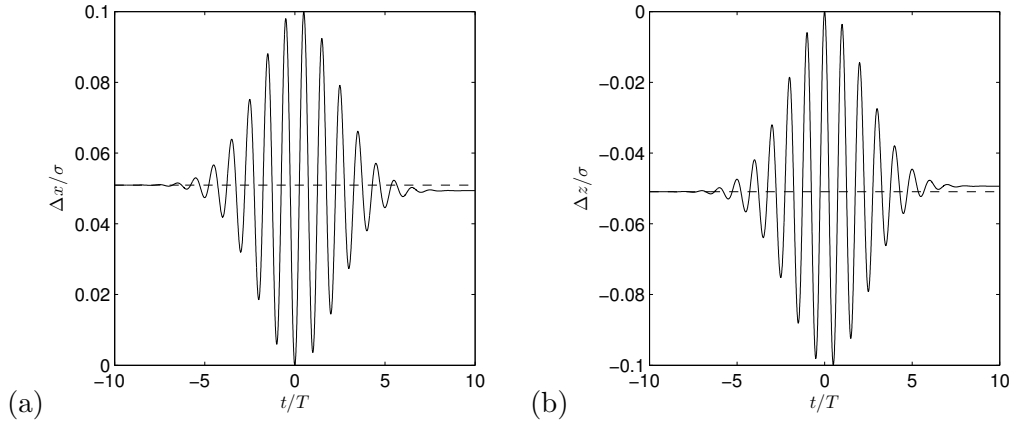

Figure 5: Displacement of Lagrangian particles in the (a) horizontal and (b) vertical direction due to the passing of an internal wave group obtained from time integration of (35) with linear (in amplitude) vertical and horizontal velocities (36-37). The Lagrangian particles are located at the focus point $x = 0$, $z = 0$ of the Gaussian wave group at the time of focus $t = 0$.

particles undergo a net displacement. Figure 6 shows the actual particle trajectory, which still forms a straight line in (x, z)-space, but a net displacement in the direction opposite to the group velocity vector. We set out to find the accompanying return flow, which must occur at higher order in bandwidth than the global effects discussed in §3.

4.2 Derivation of local circulation

A third order in ϵ and above the separation of scales argument laid out in §3.2 becomes very cumbersome involving a very large number of different terms. It becomes advantageous to pursue the expansion in Fourier space. As an analogue to the derivation for the return flow of surface gravity waves by Longuet-Higgins & Stewart (1962) reproduced in appendix A for completeness, we define the solution to the linearised equations for vertically and horizontally compact internal wave packet as the sum of individual terms:

$$\xi^{(1)} = \sum_{n=1}^{\infty}\sum_{m=1}^{\infty} A_{nm}\cos\big(k_{x,n}x + k_{z,m}z - \omega_{nm}t + \mu_{nm}\big), \tag{38}$$

where A is the two-dimensional matrix of amplitude coefficients. In contrast to the surface gravity wave case, where a single summation suffices, a double summation is required to represent the spatial structure of the linear internal wave packet. From the linearised version of (11), we obtain:

$$\psi^{(1)} = -\sum_{n=1}^{\infty}\sum_{m=1}^{\infty} \frac{A_{nm}\omega_{nm}}{k_{x,n}}\cos\big(k_{x,n}x + k_{z,m}z - \omega_{nm}t + \mu_{nm}\big), \tag{39}$$

The inclusion of all the different spectral terms ensures the linearised (in amplitude) version of (11) is effectively satisfied at all order in the bandwidth parameter ϵ. In addition, all

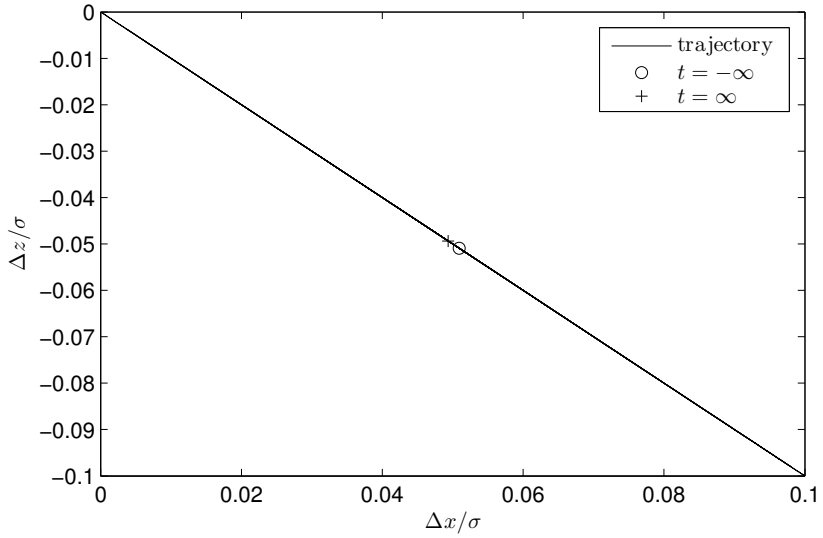

Figure 6: Trajectories of Lagrangian particles due to the passing of an internal wave group obtained from time integration of (35) with linear (in amplitude) vertical and horizontal velocities (36-37). The Lagrangian particles are located at the focus point $x = 0$, $z = 0$ of the Gaussian wave group at the time of focus $t = 0$. The initial particle, prior to the arrival of the wave group is denoted by an open circle and the final position is denoted by a + symbol. The net displacement is in the direction opposite to the group velocity vector.

the individual components satisfy the linear dispersion equation (29). From the linearised version of (13):

$$\frac{\omega_{nm}^2}{N_0^2} = \frac{k_{x,n}^2}{k_{x,n}^2 + k_{z,n}^2} \quad \text{for } \forall n, m \tag{40}$$

The full solution up to second-order in amplitude is given by:

$$\xi = \xi^{(1)} + \xi^{(2)} + O(A^3), \quad \psi = \psi^{(1)} + \psi^{(1)} + O(A^3), \tag{41a,b}$$

We set out to find $\xi^{(2)}$ and $\psi^{(2)}$ corresponding to $\xi^{(1)}$ (38) and $\psi^{(1)}$ (39). From (13) we have for $\phi^{(2)}$:

$$L\psi^{(2)} = \nabla \cdot \underbrace{\Big[\frac{\partial}{\partial t}\big[\zeta^{(1)}\nabla \times \psi^{(1)}\big] + N_0^2 \frac{\partial}{\partial x}\big[\xi^{(1)}\nabla \times \psi^{(1)}\big]\Big]}_{\equiv\ \mathbf{F}^{(2)}}, \tag{42}$$

where the linear operator L is defined in (13) and all the individual terms on the right hand side are linear in amplitude so that the right hand side itself becomes second-order in amplitude (cf. $\mathbf{F}^{(2)}$). After considerable manipulation it can be shown that the right hand side of (42) takes the form:

$$L\psi^{(2)} = \frac{N_0^2}{2} \sum_{n_1=1}^{\infty} \sum_{m_1=1}^{\infty} \sum_{n_2=1}^{\infty} \sum_{m_2=1}^{\infty} A_{n_1 m_1} A_{n_2 m_2} \Gamma_1 \Gamma_2 \sin\big(\Omega_{n_1 m_1} - \Omega_{n_2 m_2}\big), \tag{43}$$

where the phases are given by:

$$\Omega_{n_1 m_1} = k_{x,n_1} x + k_{z,m_1} z - \omega_{n_1 m_1} t + \mu_{n_1 m_1}, \quad \Omega_{n_2 m_2} = k_{x,n_2} x + k_{z,m_2} z - \omega_{n_2 m_2} t + \mu_{n_2 m_2}. \tag{44}$$

The coefficients Γ_1 and Γ_2 are given by:

$$\Gamma_1 = \omega_{n_1 m_1} k_{x,n_2} \Big(\frac{\omega_{n_1 m_1}}{\omega_{n_2 m_2}} + \frac{k_{x,n_1}}{k_{x,n_2}} - 2\Big), \quad \Gamma_2 = k_{z,m_2} - k_{z,m_1} \frac{k_{x,n_2}}{k_{x,n_1}}. \tag{45}$$

Before we invert the linear operator in (43), we set out to simplify the right hand side of (43) by considering only its leading order variation in bandwidth, that is we only include the lowest order non-zero terms in $\Delta\omega = \omega_{n_1 m_1} - \omega_{n_2 m_2}$. The coefficients Γ_1 and Γ_2 (45) simplify to:

$$\Gamma_1 = \frac{2\tan(\theta_0)}{c_{g,x}} \Delta\omega + O\big((\Delta\omega)^2\big), \quad \Gamma_2 = \frac{\omega_{n_1 m_1}}{c_{g,x}} \big(1 + \tan^2(\theta_0)\big) \Delta\omega + O\big((\Delta\omega)^2\big). \tag{46}$$

Inverting the linear operator in (43) requires multiplication of the right-hand side of (43) in Fourier space by:

$$L^{-1} \longleftrightarrow \frac{1}{(\omega_{n_2 m_2} - \omega_{n_1 m_1})^2 \big((k_{x,n_2} - k_{x,n_1})^2 + (k_{z,m_2} - k_{z,m_1})^2\big) - N_0^2 (k_{x,n_2} - k_{x,n_1})^2}. \tag{47}$$

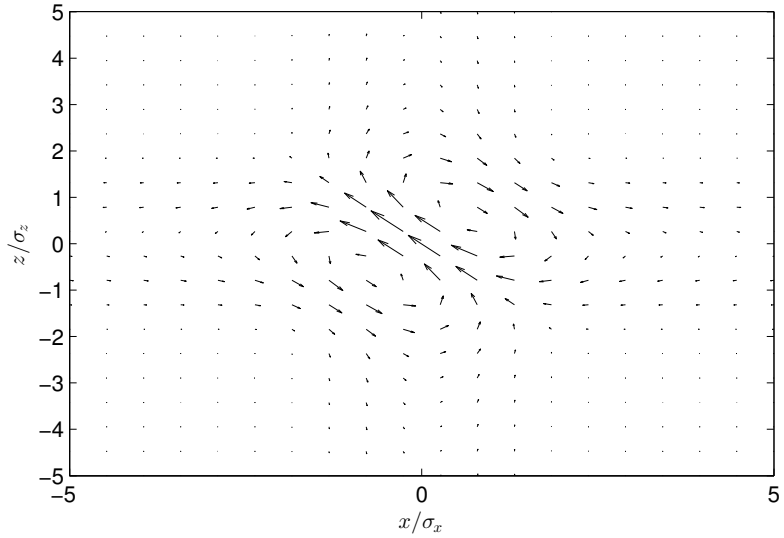

Figure 7: Local circulation flow field (u, w) corresponding to the stream function (48) for a Gaussian wave packet with bandwidth parameter $\epsilon_x = (\sigma_x k_{x,0})^{-1} = \epsilon_z = (\sigma_z k_{z,0})^{-1} = 0.1$ with $\sigma_x = \sigma_z$ denoting the bandwidth and $k_{x,0} = k_{z,0}$ denoting the peak of the spectrum. In particular, $\omega_0/N_0 = 1/\sqrt{2}$ so that the group velocity vector points in the positive x and negative z direction at an angle of 45°, exactly opposite to the largest arrows at the centre of the packet. The magnitude of the largest vector $|\mathbf{u}| = 5.6 \cdot 10^{-3} a_0 \omega_0$.

It is evident that the left-hand side term in the denominator is $(\Delta\omega)^4$, whereas the right-hand side is only $(\Delta\omega)^2$. Ignoring the former, the linear operator can be inverted to give the following leading-order stream function:

$$\psi^{(2)} = -\sum_{n_1=1}^{\infty}\sum_{m_1=1}^{\infty}\sum_{n_2=1}^{\infty}\sum_{m_2=1}^{\infty} A_{n_1 m_1} A_{n_2 m_2} \tan(\theta_0)\big(1+\tan^2(\theta_0)\big)\omega_{n_1 m_1} \sin\big(\Omega_{n_1 m_1} - \Omega_{n_1 m_1}\big), \tag{48}$$

where the term includes information about both the velocity at which this flow field travels, namely the group velocity, and the local structure of the re-circulatory flow. Figure 7 shows the spatial structure of flow field $(u,\, w)$ corresponding to the stream function (48). What is evident from this figure is a strongly localized flow through the centre of the wave packet and in the direction opposite to the group velocity vector, and a return flow in the opposite direction around the packet that is more spread out. Evidently, the flow field (48) is divergence free (volume is conserved), and leaves the energy of the system unchanged.

In our search for the leading order variation after (43), we have only excluded terms that describe the effect of linear (in amplitude) dispersion that could in principle be included but would modify the local circulation, a higher order phenomenon in bandwidth than the global induced mean flow of §3, slightly by introducing even higher order terms in bandwidth.

5 Conclusions

For vertically and horizontally compact internal wave groups in a linearly stratified ambient we have shown that two types of wave-induced mean flow can be distinguished: a global response consisting of horizontally long disturbances and no vertical motion and a local circulation that is associated with balanced horizontal and vertical motion. Both phenomena are second-order in amplitude, but the local circulation occurs at higher order in the bandwidth of the spectrum.

In the terminology of the surface gravity wave group, for which Stokes drift at the free surface is balanced by a return flow at depth giving rise to zero net depth-integrated momentum, the vertical component of the induced mean flow for internal wave packets is cancelled out locally by a return flow of equal magnitude and opposite sign with no motion in vertical as a result. In the horizontal direction the "return flow" acts to cancel out the horizontal structure of the Stokes drift, which is local to the packet, so that any variation of the horizontal induced mean flow along the horizontal direction disappears: the wave group induces long disturbances. As the domain under consideration is increased to infinity, the magnitude of these disturbances goes to zero. The local circulation, on the other hand, displays a behaviour that is reminiscent of that of surface gravity wave packets, and consists of a Stokes drift through the centre of the packet (in the direction opposite to the group velocity) that is balanced by a return flow around the packet.

A The return flow for surface gravity wave groups following Longuet-Higgins & Stewart (1962)

Longuet-Higgins & Stewart (1962) derive an expression for the return flow underneath a surface gravity wave group in finite water depth d without making any assumptions about the bandwidth of the underlying linear spectrum. We reproduce the derivation below assuming the water depth is large relative to all the linear components of the spectrum (the deep-water assumption).

A.1 Governing equations and boundary conditions

A two-dimensional body of water of infinite depth and indefinite lateral extent is assumed with a coordinate system (x,z), where x denotes the horizontal coordinate and z the vertical coordinate measured from the undisturbed water level upwards. Inviscid, incompressible and irrotational flow is assumed and, as a result, the velocity vector can be defined as the gradient of the velocity potential $\mathbf{u} = \nabla\phi$, and the horizontal and vertical velocity as $u = \partial\phi/\partial x$ and $w = \partial\phi/\partial z$, respectively. The governing equation within the domain of the fluid is then Laplace:

$$\nabla^2\phi = 0 \quad \text{for } z \leq \eta(x,t), \tag{49}$$

where $\eta(x,t)$ denotes the free surface. The no-flow bottom boundary condition is:

$$\lim_{z\to-\infty} \frac{\partial\phi}{\partial z} = 0. \tag{50}$$

The kinematic free surface boundary condition (KFSBC) defines the free surface as moving with the particles located at the free surface such that particles located at the free surface stay there, i.e. $D(z-\eta)/Dt = 0$ or:

$$w - \frac{\partial\eta}{\partial t} - u\frac{\partial\eta}{\partial x} = 0 \quad \text{at } z = \eta(x,t). \tag{51}$$

Finally, the dynamic free surface boundary condition (DFSBC), which states that pressure at the free surface is constant and zero, fully closes the problem:

$$g\eta + \frac{\partial\phi}{\partial t} + \frac{1}{2}\left(u^2 + w^2\right) = 0 \quad \text{at } z = \eta(x,t), \tag{52}$$

where gravity g acts in the negative z direction.

A.2 The solution to second-order in amplitude

A multi-chromatic solution to the governing equation (49) that satisfies the bottom boundary condition (50) exactly and satisfies the free surface boundary conditions (51) and (52) at first-order in amplitude is given by:

$$\xi^{(1)}(x,z,t) = \sum_{n=1}^{\infty} a_n \cos(k_n x - \omega_n t + \mu_n), \tag{53}$$

$$\xi^{(1)}(x,z,t) = \sum_{n=1}^{\infty} \frac{a_n \omega_n}{k_n} \sin(k_n x - \omega_n t + \mu_n), \tag{54}$$

where a_n, k_n, ω_n, μ_n denote the amplitude, wave number, wave frequency and phase of the individual components. All the individual components satisfy the linear dispersion equation:

$$\omega_n^2 = g k_n \quad \text{for } \forall n. \tag{55}$$

Retaining only terms that are second order in amplitude, the kinematic boundary condition (51) can be rewritten as:

$$\frac{\partial \phi^{(2)}}{\partial z} - \frac{\partial \eta^{(2)}}{\partial z} = \frac{\partial}{\partial x}\Big(\eta^{(1)} \frac{\partial \phi^{(1)}}{\partial x}\Big) \quad \text{at } z = 0, \tag{56}$$

where we have used $\partial^2 \phi^{(1)}/\partial x^2 = -\partial^2 \phi^{(1)}/\partial z^2$ from (49). The second-order solution still has to satisfy the linearised dynamic boundary condition (52):

$$\frac{\partial^{(2)}}{\partial t} + g\eta^{(2)} = 0. \quad \text{at } z = 0, \tag{57}$$

Combining (56) and (57), gives:

$$\frac{\partial \phi^{(2)}}{\partial z} + g\frac{\partial^2 \phi^{(2)}}{\partial t^2} = \frac{\partial}{\partial x}\Big(\eta^{(1)} \frac{\partial \phi^{(1)}}{\partial x}\Big) \quad \text{at } z = 0. \tag{58}$$

Equation (58), as pointed out by Dysthe (1979), in combination with the bottom boundary condition (50) and the governing equation (49), fully specify the solution for $\phi^{(2)}$. This solution is:

$$\phi^{(2)} = \sum_{n=1}^{\infty} \sum_{m=n+1}^{\infty} a_n a_m \omega_m e^{(k_m - k_n)z} \sin\big((k_n - k_m)x - (\omega_n - \omega_m)t + (\mu_n - \mu_m)\big), \tag{59}$$

where the requirement that $m > n$ ensures that the bottom boundary condition is met. Equation (59) can also be rewritten in terms of the corresponding stream function:

$$\psi^{(2)} = \sum_{n=1}^{\infty} \sum_{m=n+1}^{\infty} a_n a_m \omega_m e^{(k_m - k_n)z} \cos\big((k_n - k_m)x - (\omega_n - \omega_m)t + (\mu_n - \mu_m)\big), \tag{60}$$

Contours of constant values of the stream function (60) in (x,z)-space are shown in figure 2.

References

[1] Andrews, D.G. & McIntyre, M.E., 1978. An exact theory of nonlinear waves on a Lagrangian mean flow. *J. Fluid Mech.*, **89**, 609-646.

[2] Benjamin, T. Brooke & Feir, J.E., 1967. The disintegration of wave trains on deep water. Part 1. Theory *J. Fluid Mech*, **27**, 417-430.

[3] Bretherton, F.P., 1969. On the mean motion induced by internal gravity waves. *J. Fluid Mech.*, **36**, 785-803.

[4] Dysthe, K.B., 1979. Note on a Modification to the nonlinear Schrödinger equation for application to deep water waves. *Proc. R. Soc. Lond. A*, **369**, (1736), 105-114.

[5] Grimshaw, R., 1975. Nonlinear Internal Gravity Waves and Their Interaction with the Mean Wind. *J. Atmos. Sci.*, **32**, 1779-1793.

[6] Holmes-Cerfon, M., Bühler, O. & Ferrari, R., 2011. Particle dispersion by random waves in the rotating Boussinesq system. *J. Fluid Mech.*, **670**, 150-175.

[7] Longuet-Higgins, M.S. & Stewart, R.W., 1962. Radiation stress and mass transport in gravity waves, with applications to 'surf beats'. *J. Fluid Mech.* **13**, 481-504.

[8] Mcintyre, M.E., 1981. On the 'wave momentum' myth. *J. Fluid Mech.*, **106**, 331-347.

[9] McLandress, C., 1998. On the importance of gravity waves in the middle atmosphere and their parameterization in general circulation models. *J. Atmos. So.-Terr. Phy.*, **60**, (14), 1357-1383.

[10] Sanderson, B. G.& Okubo, A., 1988. Diffusion by internal waves. *J. Geophys. Res.*, **94**(C4), 3570-3582.

[11] Scinocca, J.F. & Shepherd, T.G., 1992. Nonlinear wave-activity conservation laws and Hamiltonian structure for the two-dimensional anelastic equations. *J. Atmos. Sci.*, **49**, 5-28.

[12] Spiegel, E.A. & Veronis, G., 1960. On the Boussinesq approximation for a compressible fluid. *Astrophys. J.*, **131**, 442-447.

[13] Sutherland, B.R., 2006. Weakly nonlinear internal gravity wavepackets. *J. Fluid Mech.*, **569**, 249-258.

[14] Dosser, H.V. & Sutherland, B.R., 2011a. Weakly nonlinear non-Boussinesq internal gravity wavepackets. *Physica C.*, **240** (3), 346-356.

[15] Dosser, H.V. & Sutherland, B.R., 2011b. Anelastic internal wavepacket evolution and stability. J. Atmos. Sci., **68**, 2844-2859.

[16] Starr, V.P., 1947. A momentum integral for surface waves in deep water. *J. Mar. Res.* **6**, 126-135.

[17] Stokes, G.G., 1847. On the theory of oscillatory waves. *Trans. Camb. Philos. Soc.* **8**, 441-455. Reprinted in: Stokes, G.G. (1880). Mathematical and Physical Papers, Volume I, Cambridge University Press. 197-229.

[18] Sutherland, B.R., 2010. Internal gravity waves. Cambridge University Press, Cambridge, UK.

[19] van den Bremer, T.S. & Taylor, P.H., (in preparation). Stokes drift and induced mean flow for weakly non-linear surface gravity wave packets.

[20] Van Dyke, M., 1982. An album of fluid motion. The Parabolic Press, Stanford, USA.

[21] Wallet, A. & Ruellan, F., 1950. *Houille blanche*, **5**, 483-489.